The exploitation of acoustic-to-seismic coupling for the determination of soil properties

Thesis

The Exploitation of Acoustic-to-Seismic Coupling for the Determination of Soil Properties

Thesis Submitted by

Nicholas Harrop BEng(Hons) MSc

For the Degree of

Doctor Of Philosophy

November 1999

Department of Environmental and Mechanical Engineering,

Faculty of Technology,

The Open University,

Milton Keynes,

United Kingdom

Abstract

Laboratory measurements of three predicted wave types (two compressional or P-waves and one shear S-wave) have been made in artificial soils. The Type-I P and S-wave are predicted to be most sensitive to the macroscopic elastic properties of the frame, whilst the Type II P-wave is predicted to be most sensitive to the hydrodynamic material properties.

A loudspeaker source has been used for the preferential excitation of the Type II P-wave whilst preferential excitement of the Type-I P-wave has been accomplished using a mechanical shaker. Probe microphone measurements of the Type-II wave allowed the flow resistivity and tortuosity of the material to be determined using a rigid frame model, whilst deduction of elastic moduli has been made from signals received at buried geophones. It has been shown that microphone signals include Type-I P-wave energy in a high flow resistivity soil. Acoustically deduced soil properties are consistent with mechanically derived values.

A systematic investigation of outdoor measurements of acoustic-to-seismic coupling ratio has been made. From the measurements, it has been found that the geophone-ground coupling has a great effect upon the measured coupling ratio. In-situ calibration methods have been developed to overcome this problem, whilst the novel use of a Laser Doppler Vibrometer has been proposed to provide a completely non-invasive method of measuring motion in soils.

The measured coupling ratio has been compared with theoretical predictions, using a modified Biot-Stoll formulation. The model can be used to predict values of flow resistivity, porosity, bulk and shear moduli and layer depths. Reasonable agreement has been obtained between the model and data.

Procedures that exploit acoustic-to-seismic coupling data and models to determine soil properties have been developed and used to measure the soil properties of friable agricultural soils where more standard investigation techniques have proved unsuitable.

" . . . and we can save 700 lire by not taking soil tests."

Acknowledgements

Over the four years of toil in undertaking this project a great many people have come to my aid in a myriad of differing ways. Friends and family provided much needed encouragement for the soul, whilst colleagues from the academic world provided the input and guidance needed by all students undertaking their doctorates. All of whom have my most sincere gratitude.

It seems difficult when writing ones acknowledgements not to make it sound like an Oscars acceptance speech. Where, once a year a tearful actor blurts out a list of friends and colleagues, punctuated by sniffle and sobs, without whom they feel their lives would have been much poorer and they wouldn't be there on the podium. As such I'd just like to say:

"Well, this is a great surprise, err, I hadn't anything prepared, err, wow! This is all so last minute. Well where to start? I'll try and keep this short but first and foremost I'd like to thank Professor Keith Attenborough, ~~my agent~~, sorry, my supervisor throughout the last four years for his permanent guidance, support and understanding. I am profoundly grateful to Dr Shahram Taherzadeh. He worked with me through nearly all the phases of this project, rewarding or frustrating, had great patience and shared with me a lot of his wisdom.

Also at the Open University Tim Waters-Fuller helped out enormously when I was just starting out, whilst Simon Moss was ever a great source of information and advice, especially on Labview. Pete Seabrook with whom I shared an office has had to put up with a great deal (usually in the mornings) apart from giving his invaluable advice and expertise in all things practical. A mention must also go to Brendan Aegenheister for his help with some of the electronics and of course to Sharon Lumbers and rest of secretaries.

I have spent some little time at several other facilities during the course of my doctorate, including trips across the pond to the US to visit the National Centre for Physical Acoustics at the University of Mississippi. Here again I gained great help and insight into the subject of acoustic-to-seismic coupling from Dr Jim Sabatier and Dr Craig Hickey, whilst grad student Mike Troutman gave me a place to stay as well as providing me with a glimpse of the trials and tribulations that can beset those who.....(censored)

Soil testing was undertaken at my old university at Bangor, North Wales. Here, Dr Dei Huws allowed me unrestricted access to the soil labs, whilst my presence was tolerated by the soils technician Geraint Williams, whom I must thank for his patience and his freely given advice. More help once again came from my old supervisor and good friend Sinclair Buchan who has passed on his wisdom to me for many years now, whilst Dr Jim Bennell provided invaluable help and explanation concerning the resonant column procedure.

At Horticultural Research International, Dr Bill Finch-Savage kindly provided me with access to the test area that was used as part of the outdoor acoustic-to-seismic coupling experiments.

Friends can be almost as big a help during the time of ones doctorate (its not all work! work! work!). Much social diversion has been given by all my friends at the OU a list of whom would go on for many pages. However, special mention must go to Mark Davies, Simon Sheridan, Giles Graham and Sarah Sherlock and to their respective partners. Thanks also to Dave Sharp, Jim Whitehouse, Kevan Ellis and to Richie Wheeler. Finally, (and you know I'm getting near the end now) my Mum and Dad who have given me their wholehearted support throughout the now many years of my graduate education.

Oh and before I go (if you're still awake) there is one very special person who I must thank - my fiancee Lou. Her great patience, understanding and encouragement throughout the last four years have kept me going to the end."

Table of Contents

List of Figures

List of Tables

List of Symbols

Symbol	*Meaning*
c_i	Speed of sound in ground layer i
c_o	Speed of sound in air
e	Void ratio
E	Young's modulus
f	Frequency
F	Formation factor
g	Acceleration due to gravity
G_s	Specific gravity of sediment solid particles
i	Hydraulic gradient
k	Coefficient of permeability, Wavenumber
k_b	Bulk propagation constant
k_i	Intrinsic permeability
k_p	P-wave wavenumber
k_{sh}	Shear wavenumber
K	Bulk modulus
K_{ud}	Undrained bulk modulus
$L.I.$ or I_L	Liquidity index
$L.L.$	Liquid limit
N_{pr}	Prandtl number
$P.I.$ or I_p	Plasticity index
$P.L.$	Plastic limit

P_a	Atmospheric pressure
R_s	Flow Resistivity
s	Shear strength
S_p	Pore shape factor
v_p	Compressional wave velocity
v_r	Rayleigh wave velocity
v_s	Shear wave velocity
V_t	Total volume occupied by granular material
V_f	Total volume occupied by fluid
V_a	Total volume occupied by air
V_w	Total volume occupied by water
z	Depth. Vertical Component

Greek Symbols

Symbol	*Meaning*
δ	Electrical conductivity
ϕ	Grain particle diameter
γ	Ratio of specific heat
γ_d	Damping coefficient
η	Fluid viscosity
η_d	Damping parameter
λ	Wavelength
λ'	Lamé constant
μ	Lamé constant (often referred to as shear modulus)
θ	Cubic dilatation, Angle of internal friction

ρ	Density (general)
ρ_b	Bulk density
ρ_g	Density of solid grains
ρ_f	Density of fluid
ρ_o	Density of air
ρ_w	Density of water
σ	Poisson's ratio
σ_{eff}	Effective flow resistivity
τ	Tortuosity, Shear stress
ω	Angular frequency, moisture content
ω_0	Angular frequency of planted geophone
ω_0	Angular ping frequency (measured)
ξ_f	Bulk viscosity of air
ψ	Axial modulus
Ω	Porosity

Chapter 1

Introduction

1 Introduction

Over the past decades the increasing strain being placed on the agricultural resources of the world, has generated interest into an improved understanding of the structural and hydrodynamic properties of soils. There are already a number of direct and indirect methods for the determination of the material properties. However, with a growing concern for both the accuracy and the environmental impact of these methods there is a need for a cheap, reliable, non-invasive method for the determination of bulk and hydrodynamic soil properties.

Soil strength and rigidity are important bulk properties that control many factors including seed emergence, erodibility and tillage. Hydrodynamically, knowledge of the proportion of air-filled and air-connected pores, total porosity and pore-size distribution, tortuosity, air permeability and their variation with depth is desirable to indicate the structural compaction and aeration of a soil. Although, the precise dependence of these parameters on crop growth is not yet fully understood, it is known that poor structure, such as small air-filled porosity and poor drainage, will inhibit plant development.

Over the past fifty years, there has been considerable effort, in both civil and agricultural engineering, into the development of techniques to determine soil properties. Shear box or triaxial tests have long been the standard techniques for soil strength determination (Smith, 1994). Direct characterisation of the structural properties of soils has been developed using image analysis techniques (Ringrose-Voase, 1991), whilst indirectly there are several techniques that use liquid or gas flow measurements for characterising pore properties (Stinson and Daigle, 1988).

Most of these techniques involve the removal of a soil packet to be tested later in a laboratory. This removal either alters or totally destroys the in-situ soil structure, making the results difficult to interpret. These tests are also labour and time intensive and since many of the soil parameters of interest vary continuously with time, there is a need for

continuous monitoring in a tolerably non-invasive manner. Wave propagation techniques can provide a means for determining the physical properties of soils with minimum soil disturbance. The measurement techniques align themselves to being portable and so suitable for field sites. Furthermore, measurements can be performed continuously without sample alteration once the source and receivers have been placed.

The propagating waves can be either seismic or acoustic. Seismic waves propagate in the bulk soil and are most sensitive to the macroscopic elastic properties of the soil frame. Seismic waves are primarily excited through direct contact with the soil surface, using mechanical vibrators, drop weights or explosive charges. Seismic investigations are commonly used to obtain information about the depth to the interface separating materials of different properties, and to obtain information about various physical properties of each material (Telford *et al.*, 1976).

Acoustic waves propagate predominantly through the soil pore space and are sensitive to the hydrodynamic properties of the soil. Acoustic waves in the pores are excited by insonifying the ground using loudspeakers. Several authors (Moore and Attenborough, 1992; Sabatier *et al.*, 1996) have used acoustic waves to determine the air permeability and porosity of soils.

In principle however, acoustic waves can be used as the principal source of induced ground motion in porous elastic materials. Theoretical models of acoustic and seismic wave propagation in porous elastic materials predict the existence of two types of dilatational and one rotational wave. The first dilatational wave is primarily transmitted through the bulk soil and the second is primarily transmitted through the soil pores. This method of excitation has the advantage that the input source energy is non-invasive, especially when compared to the use of explosives in seismic exploration.

In light of this, there have been several studies in recent years that have involved the phenomena of acoustic-to-seismic coupling (Albert and Orcutt, 1989; Bass *et al.*, 1980; Sabatier *et al.*, 1986a). The acoustic-to-seismic coupling ratio is the ratio of the pressure exerted by an acoustic wave at a point on the surface to the acoustic particle velocity generated at the surface at that point and forms the main focus of this dissertation.

A study has been made into the extent to which acoustic-to-seismic coupling can be used in the determination of soil properties. In general, this project is concerned with the problem of making inferences about physical systems from data. To make these inferences quantitative, one must answer three fundamental questions.

1) How accurate is the data?

   (Is the data reliable? Have all errors in the data collection been minimised?)

2) How accurately can we model the response of the system?

   (Have we included all the physics in the model that contribute significantly to the data?)

3) What is known about the system independently of the data?

   (This is called a priori information and is essential for optimisation of a system. There will be unreasonable values of parameters that can be used in the models that will allow the model to fit the known data. Prior information is the means by which we reject or give less credence to unreasonable models.)

Of these three fundamental questions it is the first which is of most importance in this project. There has been a great deal of time spent developing and improving the theoretical models to describe the ground response to an external acoustic disturbance. In contrast, very little work has been undertaken into a coherent investigation into the experimental measurement of acoustic-to-seismic coupling and its subsequent use in the deduction of soil properties. To the author's knowledge, this thesis is the first to explore the possibility of obtaining structural (i.e. elastic constant) information as well as information about pore properties from acoustic-to-seismic coupling measurements.

Since the study is multi-disciplinary in nature, covering acoustics, seismics and soil mechanics, it has been found necessary to give brief outlines of background information in the text. It is hoped that this will provide a clearer understanding of the project for those unfamiliar with each of the relevant disciplines.

The majority of the experiments undertaken as part of this study involved the use of the Labview programming language for the acquisition and partial analysis of the experimental data. All the programs used were written specifically for the project by the author. A brief note on the fundamentals of FFT based signal analysis and measurement, with specific relation to Labview has been given in Appendix A.

1.1 Thesis Outline

The background to this study is described in the remainder of Chapter 1 in the form of a literature review of published material relating to two topic areas. Firstly, the development of theoretical formulae that have been used to describe the ground response to an external acoustic disturbance and secondly, a summary of the experimental investigations that have included, to some degree, measurements of acoustic-to-seismic coupling.

Chapter 2 then gives a more detailed description of some of the theoretical models that have been outlined in the literature survey. The models are described in sequence of increasing complexity. Numerical predictions are given to outline differences between the models.

Several differing experimental techniques have been used throughout the study from which soil properties have been deduced. Chapter 3 outlines the procedures and techniques used for each set of experiments from which soil property deduction have been made.

Chapter 4 gives a description of each experimental location both in and outdoor. A description of the mechanical properties of the materials used throughout the project is given which is later used as a comparison to those calculated using the wave propagation techniques. At the beginning of this chapter a brief introduction to soil properties and mechanical testing techniques is given.

Chapter 5 provides a detailed description of the indoor experiments undertaken. This work covers the measurement of the two dilatational waves and one rotational wave predicted by poro-elastic theory and their use in soil property deduction. A description is given of the calibration of the sensors used throughout the project. Finally, an account of the use of a Laser Doppler Vibrometer (LDV) in acoustic-to-seismic coupling measurements is detailed.

Chapter 6 gives the results and analysis of the experiments outlined in Chapter 5.

Chapter 7 is similar to Chapter 5 in that it provides a detailed description of the outdoor experiments undertaken, at locations described in Chapter 4. The experiments cover the seismic refraction method for the deduction of ground layering and wave velocities (plus a brief introduction to seismic investigation theory); the measurement of acoustic-to-seismic coupling in varying materials, including the reliability of these

measurements and the effect of experimental set-up on the recorded spectra; and the in-situ geophone calibration method.

Chapter 8 gives the results and analysis of the experiments outlined in Chapter 7.

Finally a summary of the project and implications of the work for an applied use and for further areas of research and investigation are presented in Chapter 9.

1.2 Previous Work

In the following section a literature survey is given which, though not exhaustive, provides background information on the theoretical models to describe the interaction of airborne sound with the ground. The second section highlights some of the experimental work undertaken. Since experimentally, acoustic-to-seismic coupling has received comparatively little attention, available data comes from a variety of indirect and direct investigations.

1.2.1 Theoretical Models

The influence of the presence of the ground surface on outdoor sound propagation has received considerable attention including Embleton *et al.*, 1976; Bolen and Bass, 1981; Delaney and Bazely, 1970; Attenborough, 1983 and Attenborough, 1985. These models assume that the ground is locally reacting so that its acoustical properties are described adequately by its normal acoustic surface impedance.

A common assumption of all the models is that the frame of the porous material is rigid, so that for acoustical purposes, the porous medium may be regarded as that of an effective or modified fluid. For many ground surfaces, this assumption appears to be satisfactory, but is clearly unsatisfactory when describing the response of buried geophones and microphones to sound waves in the air.

Air-ground coupling has been of considerable interest in geophysics, both because of the measured ground-roll caused by intense acoustic sources and the possible use of air sources in ground layering studies. Theoretical analyses have been carried out for

spherical wave incidence on a ground consisting either of a fluid or solid layer above a fluid or solid half-space (Press and Ewing, 1951; Jardetsky and Press, 1952). Hastrup (1980) investigated cases of shallow wave propagation where the sea bottom consists of a layer of soft unconsolidated sediments above a high velocity layer and this model was applied to acoustically induced ground motion by Attenborough (1986).

In seismic geophysics, the ground has been modelled as that of a layered elastic medium. The theory of motion in an elastic medium has been treated widely and can be found in many reference books (Ewing *et al.*, 1957; Aki and Richards, 1980). However, to accurately describe the phenomenon of acoustic-to-seismic coupling it has been found that the ground must be modelled as an elastic porous material (Attenborough *et al.*, 1986; Sabatier *et al.*, 1986a,b; Tooms, 1990; Taherzadeh, 1997).

Biot undertook the seminal work in the modelling of propagation in porous elastic media. Starting with a paper on consolidation of porous elastic materials in 1941 (Biot, 1941), he developed a comprehensive theory for the static and dynamic response of linear, porous materials containing a compressible fluid. He considered both low and high frequency behaviour (Biot, 1956a, b), and has included the possibility of viscoelastic or viscodynamic response in various components of his model (Biot, 1962a, b).

At around the same period Frenkel (1944) and Brandt (1955) had discussed wave propagation in porous media, although in a less rigorous manner. Beranek (1947) and Zwikker and Kosten (1949) had also made consideration of consolidated material with an elastic frame, although in both cases shear motion was ignored. Their theories were based upon the use of impedances.

Brutsaert (1964) considered a three-phase material and predicted the possibility of three kinds of dilatational waves. Bolton (1984) modified the model of Rosin (1973) to include frequency dependent viscous and thermal effects, although Allard has indicated that the Biot theory is more self-consistent than the models of Rosin, Baranek or Zwikker and Kosten.

The above models essentially describe the medium by conceptual pore microstructure. Attenborough (1982) undertook a review of theories that specify a model microstructure for the solid constituent. This delineation covered a wide range of materials including parallel and stacked fibres, packed spheres, arrays of solid cubes or cylinders, and a lattice of arbitrarily shaped mass elements with viscoelastic connections. One common feature of all these models, however, is their unsuitability for wide application due to the assumptions made about the microstructure.

1.2.1.1 The Biot Theory

Biot's 1956 papers began by examining the stress-strain relationships in an isotropic elastic solid containing a fluid. This showed that in the absence of dissipation the material could be described by four distinct elastic constants; two corresponding to solid Lamé constants, one corresponding to the modified bulk modulus of the fluid and a fourth corresponding to a coefficient of coupling between the volume change in the solid, and that in the fluid.

The kinetic energy in the medium was described in terms of three mass coefficients and, via Lagrange's equations, equations of motion for dilatational and rotational (shear) waves in the medium in the absence of dissipation were derived. It was shown that, assuming the pore fluid to be an ideal fluid, one rotational and two dilatational waves exist, and equations for their velocities were derived.

The derivation for the equations of propagation was then repeated, using a dissipative term in the LaGrange equations, as a function of the velocity difference between the solid and fluid, and hence as a function of the frictional forces on the walls of the pores due to the viscosity of the flow. Poiseuille flow in the pores was assumed to occur, thus the dissipative terms were given a simple form. An approximate limiting frequency above which Poiseuille flow breaks down was then derived as a function of pore diameter and fluid viscosity.

In the second paper (Biot, 1956b) the viscous forces on the pore walls were examined for two pore shapes at frequencies above which Poiseuille flow breaks down. Biot showed that for flows at these frequencies a modified viscosity coefficient could be calculated which corrected for non-Poiseuille flow.

Biot (1962a) went on to derive detailed stress-strain relations for porous elastic media. In this paper, he also considered the problem of the attenuation of waves due to the movement of fluid into and out of cracks in the solid frame and the areas of intergranular contact were also considered.

In the following paper (Biot, 1962b), the derivations of the equations of propagation were modified and a "viscodynamic operator" was introduced. This included the effects of both the viscous and the inertial forces between the solid and fluid, including the modified viscosity on the breakdown of Poiseulle flow.

Stoll (1974) developed a theory of elastic wave propagation in porous media based on the work of Biot. Stoll attempted to include in the calculation of attenuation, the effect

not only of viscous forces due to the relative movement of solid and fluid, but also the effect of the movement of fluid into and out of the contact areas between grains as the frame expands and contracts. Stoll also attempted to relate the fast longitudinal and shear wave velocities of a porous solid to the static stress on the solid. This could be related to the depth of burial and hence theoretical velocity-depth relations were derived.

The Biot-Stoll model predicts the existence of three wave types in the porous medium. These are two dilatational waves and one rotational. In a material consisting of a dense solid frame with a low density fluid saturating the pores, the first kind of dilatational wave has a velocity very similar to the dilatational wave (or geophysical "P" wave) travelling in the drained frame. The attenuation of the first dilatational wave type is however, higher than that of the P wave in the drained frame. The extra attenuation comes from the viscous forces in the pore fluid acting on the pore walls. This wave has negligible dispersion and the attenuation is proportional to the square of the frequency, as is the case for the rotational wave. This viscous coupling leads to some of the energy in this propagating wave being carried in the pore fluid as a second type of dilatational wave.

The second dilatational wave has a much lower velocity than the first in most cases relevant to air-saturated soils. Its attenuation also stems from viscous forces acting on the pore walls. Its rigid-frame limit is very similar to the pore wave, which travels through the fluid in the pores of a rigid-porous solid in the Rayleigh-Attenborough propagation model (Attenborough, 1987). Most of the energy in this wave type is carried in the pore fluid. However, the viscous coupling through the pore walls leads to some propagation within the solid frame. At low frequencies, it has the nature of a diffusion process rather than a wave, being analogous to heat conduction. The attenuation for this second dilatational wave is higher than that of the first in most materials and the real and imaginary parts of the propagation constant are nearly equal.

The rotational wave has a very similar velocity to the rotational (or geophysical "S") wave carried in the drained frame. Again there is some extra attenuation due to the viscous forces, and there is some differential movement between solid and pore fluid. The fluid is unable to support rotational waves, but is driven by the solid.

The propagation of each wave type is determined by a number of parameters relating to the elastic properties of the solid and fluid components. Considerable work has been undertaken to identify these parameters and determine appropriate forms for specific materials. Although Biot developed his theory in the 1950's, its practical application was limited until Stoll and Bryan (1970) and Stoll (1974) applied the theory to attenuation in

marine sediments, including terms to accounts for losses due to grain-to-grain contacts and a viscous fluid loss.

Plona (1980) first observed slow wave propagation in water-saturated porous ceramics and correlation with the Biot theory was provided by Berryman (1980) and Dutta (1980). The theory has found wide application in understanding the propagation and attenuation of the fast and shear modes in sediments (Stoll, 1977) and rocks. The presence of the slow wave in rocks has recently begun to be measured (Hunt and Worthington, 1999) along the interface between layers, although it has been shown theoretically to have a decay radius in the order of centimetres (Norris, 1985).

The Biot theory has also been applied to partially consolidated media (Johnson and Plona, 1982; Berryman, 1981), whilst Ogushwitz (1985a, b, c) gave an overview of the field with emphasis on the prediction of the attenuation properties of sediments and suspensions.

Santos *et al.* (1990) derived a model for wave propagation in a porous solid saturated by two immiscible fluids, and considered the case of oil and water in sandstone, while Bardet and Sayed (1993) compared the Biot theory to a three-phase model in relation to the attenuation and speed of the frame wave in nearly saturated soils. A recent extension to the theory predicts three compressional and two shear waves in a medium consisting of ice, liquid water and rock (LeClaire, 1994).

Overall, Biot theory has been used to model outdoor ground surfaces for impedance predictions (Sabatier, 1986b; Tooms *et al.* 1993; Tooms and Attenborough, 1989), transmission of sound into the ground (Attenborough *et al.* 1986), acoustic-to-seismic coupling (Attenborough *et al.* 1986; Sabatier *et al.* 1986a, b, c; Tooms, 1990; Taherzadeh, 1997), and acoustically induced surface waves (Attenborough and Chen, 1990).

An alternative theory of wave propagation to the Biot theory has been proposed by de la Cruz & Spanos (1985, 1989a, b). In this model an allowance is made for vorticity in the permeating fluid, so that two rotational waves are predicted in comparison to the one predicted by Biot. Another important difference between the two theories is that in the de la Cruz & Spanos formulation porosity is no longer taken as a constant property but is treated as a dynamic variable.

They started by considering equations of continuity at the pore scale and also the boundary conditions at the pore wall. They then used averaging theorems to obtain mass-averaged macroscopic equations of state for the porous medium.

A further approach to the prediction/simulation of ground vibration from airblasts is the *moving-load* formulation (Miles, 1960). More details on the solution scheme have also been given by Siddharthan *et al.* (1993) and Montcourt (1995). This approach is based on the observation that at large distance from a blast point, the air pressure wave front propagates nearly horizontally over the ground surface and hence acts as a moving normal load. Although such models ignore atmospheric refraction, which in many cases has significant effect on the induced ground vibration, they nevertheless provide an effective means to gain insight into the mechanism of ground vibration and interplay of the various environmental parameters (Hole *et al.* 1998).

As part of an investigation into the moving load model, Hole *et al.* (1998) made measurements of acoustic pulses out to a range of 1400m using 1kg unconfined charges of C4 plastic explosive as sound sources. These data were compared with viscoelastic and poro-elastic FFP models and the moving load formulation.

He concluded that both versions of the FFP model gave realistic values of the magnitude of the ground oscillations, although the viscoelastic version predicted too high a frequency. He also concluded, that the moving load simulation did not give a complete representation of all the physical processes involved, even if a layered ground was included in the calculation. When the moving load propagates with a speed higher than the ground speeds (i.e. the superseismic case), ensuing motion is not predicted, although magnitude and frequency of the directly induced motion seemed to be of the correct order-size.

In order to make numerical predictions of acoustically induced ground motion several authors have produced computer programs based around the Biot model. Of most interest to this study are the FFLAGS and OASES programs (or more notably SAFARI). Both these programs are general purpose computer codes for modelling seismo-acoustic propagation in horizontally stratified waveguides using wavenumber integration in combination with the Direct Global Matrix solution technique.

FFLAGS, or Fast Field Program for Layer Air Ground Systems was originally developed by Tooms (1990) working at The Open University, with Taherzadeh (1997) making further improvements.

OASES (Ocean Acoustics and Seismic Exploration Synthesis) was developed by Schmidt (1988) from his original SAFARI (Seismo-Acoustic Fast Field Algorithm for Range Independent Environments) code (Schmidt, 1986). SAFARI was based around a viscoelastic approximation of the ground, whilst OASES incorporated the full Biot solution for poro-elastic materials.

1.2.2 Experimental Studies

Exploration seismic methods were developed out of pioneering earthquake studies in the mid-to-late nineteenth century. The first use of an artificial energy source in a seismic experiment was in 1846 by Robert Mallet an Irish physicist, who was also the first to use the word "seismology". John Milne introduced the drop weight as an energy source in 1885. His ideas were further developed by August Schmidt, who in 1888 devised travel-time distance graphs for the determination of seismic velocities. In 1899, G.K. Knott explained the propagation, refraction and reflection of seismic waves at discontinuity boundaries.

Both the Allies and Axis powers made significant developments in the refraction method during the First World War, particularly by Ludger Mintrop. Research was undertaken at the time to develop methods by which the location of heavy artillery could be achieved by studying the waves generated by the recoil of the guns on firing. As with most geophysical methods, the Second World War provided advances in technology that increased the usefulness of the various seismic methods.

Since the 1980's, of the two main seismic methods available (refraction and reflection), there has been a major shift towards using high-resolution seismic reflection surveying in shallow investigations (i.e. to depths less than 50m). Previously refraction surveying had been principally used within engineering site investigations. However, extremely shallow investigations are still difficult, due to the lack of a suitably high frequency source. In studies of this nature the depth of interest is approximately the first 2m, where typical propagation velocities are less than 1000m/s. In an attempt to overcome this problem, higher frequency sources were investigated.

Early work was undertaken by Press and Ewing (1951) who investigated the effect in seismic exploration of using airborne explosive sources. A typical vertical component geophone trace for a shot below the surface showed a sequence of P, S, and R waves. The R waves being distinguished by their retrograde elliptical motion, characteristic dispersion, and low velocity. A trace for a shot above the ground gave only a later primary pulse followed by a non-dispersive R-wave train whose phase velocity was approximately equal to that of sound in air. The frequency of these R waves from the air shot matched that of the section of the dispersive train from the ground shot which was travelling along the surface at the velocity of sound. It was therefore inferred that there was a resonant coupling between the airwave and the R-wave, this was modelled as a succession of

infinitesimal impulses incident on the surface producing dispersive waves in the surface along the path of the airwave. The induced wave train will thus be of constant frequency and non-dispersive, in contrast to the dispersive Rayleigh wavetrain produced by a below surface source (Press and Ewing, 1951).

Mooney and Kasai (1962) also found that appreciable energy was transferred to the ground as the acoustic wavefront traversed the surface without this resonance condition being satisfied. The induced ground signal took the form of a short pulse followed by several cycles of nearly the same frequency but considerably smaller amplitude.

Sonic boom effects provided a brief area of interest in the study of acoustic-to-seismic coupling (Goforth and MacDonald, 1970), where typical seismograms revealed constant-frequency air-coupled Rayleigh waves. Rocket launchings have also provided further data with Heller and Weiss (1967). They studied the frequency distribution of the ground-induced motion due to a launching 800m away, but yielded no quantitative value of the coupling as the acoustic-seismic component was obtained by subtracting the theoretical contribution due to ground motion coming directly from the launch pad.

McCarty and Dalius (1971) found that the air coupled seismic system was much larger in amplitude than that produced directly from the vibration of the launch pad during the launch of a rocket. Crowley and Ossing (1969) examined the seismic signals from rocket firings to assess their effect on a "natural" runway surface 8km away as a possible means of detecting rocket firings. Static firings were found to produce very weak broad band seismic, but they found that in geologically suitable areas air coupled waves were significant and would allow seismic detection ranges of up to tens of kilometres in moderate seismic noise conditions. The filtering actions of the ground layers served to reduce the source broadband signal to narrow band of approximately 5Hz, with effects due to the thinning of the surface layer.

The US Air Force Geophysics Laboratory has been studying seismo-acoustic coupling for many years with their interest being in the coupling of low frequency acoustics in the ground and structures. They are particularly interested in the detection and tracking of low flying subsonic aircraft by use of the acoustic-coupled phase (Crowley and Blaney, 1987) and the acoustic induced effects on structures, primarily archaeological sites, by very low flying aircraft (<200m).

Earlier Crowley (1985) had studied the forecasting and measurement of the vibro-acoustic environment for Shuttle launches at the Vandenburg Air Force Base in support of facility design, operation and lifetime prediction. This report was part of a comprehensive

review of all Shuttle launch sites, as the launch complex and natural setting for Shuttle operations between sites are markedly different in many ways.

Acoustic-to-seismic coupling has been found to be an important parameter in the monitoring of sub-surface conditions, especially in the detection of buried objects or cavities. Cook and Wormser (1973) found ground-induced vibrations due to a suspended loudspeaker source to be easily detectable by a geophone buried 300mm deep. Local changes in the surface (such as digging a hole and refilling) produced an increase in vibration level. Triaxial geophones confirmed that R-waves formed the main propagation mode.

The frequency spectra of the coupling was found using a swept sine up to 300Hz and showed the peaks in spectra to be independent of source height. There was also a fall off in the spectra over 200Hz, which they considered to be either real or due to the geophones. The detecting geophone used was at an angle of grazing, and this may partly explain the contrasting results of Antmann (1970) who undertook measurements at normal incidence and found a strong dependence on source height, though this effect could possibly be due to near field effects of the speaker.

The total propagation loss from the source to the geophone included an unknown contribution from the air-ground interface. They also found this unknown contribution in further measurements, where they suspended a loudspeaker in a hole beneath the ground surface. The hole was blocked to prevent a direct airborne path to the geophone and was calculated using the standard plane wave normal incidence rigid boundary relation for the transmission coefficient. A further assumption made was that the velocity in the soil was equal to the speed of sound in the air. They calculated a frequency-independent interface loss of 27dB and hence a loss in the soil of 14dB/m at 100Hz. This was taken to indicate shear wave propagation.

More directly, several experimental investigations have used arrays of geophones and microphones at various distances from the sources emitting acoustic waves and mechanically isolated from the ground, and from vehicles constituting combined acoustic and seismic sources, over various ground surfaces in order to characterise acoustic coupling as a function of ground type (Flohr and Cress, 1979; Peck, 1987; Bass *et al.* 1980).

In the work by Bass *et al.* (1980), seismic coupling was investigated in the frequency band 20 to 300Hz. A loudspeaker was suspended a measured distance from the ground (between 1m and 10m). The source signal was a swept frequency of between 20

and 700Hz. The microphone receivers were varied in height between 0.0 and 2.0m, with the geophones buried to approximately 0.05m. Results for vertical, horizontal and radial motion indicated that the coupled seismic signal is greatest for vertical, next for radial and least for transverse, though the difference between radial and vertical displacement velocities was not great and depended upon speaker altitude. The seismic structure of the ground was determined using standard seismic refraction techniques.

The recorded ratios exhibited peaks at certain low frequencies (less than 100Hz). It was found that the peaks in the seismic coupling coefficient altered in frequency when the height of the source was altered. It was also found that some of the peaks were near the frequencies predicted by a simple waveguide model (Espanosa and Sierra, 1967), although for other peaks the alteration in frequency could not be explained.

Bass and Bolen's (1984) further work included the measurement of seismic structure of two ground surfaces, together with measurement of soil samples for bulk density and flow resistivity, and the use of probe microphones to measure the acoustic propagation in the soil. The acoustic-seismic transfer function was then measured and compared to the transfer function predicted by a single layer Biot model. Although agreement was reasonable, much of the fine structure in the coupling could not be predicted.

Further work (Flohr and Cress, 1979) up to 600Hz gave coupling data differing from the earlier work and revealed a significant variation of the results between geophones depths of 0.5 and 1.0m in the range 100-200Hz. The magnitude of the coupling also increased with bandwidth, giving a different response to an impulsive or limited-bandwidth continuous signals.

In a follow-up to the previous work undertaken by the US National Centre for Physical Acoustic (NCPA), Sabatier *et al.* (1986c) undertook a more systematic investigation to determine the location and magnitude of maxima in the acoustic-to-seismic transfer function. In this paper, the seismic transfer function for a desert site is compared to the seismic transfer function for holes dug in the desert floor, which were filled with pumice. The hole geometry was rectangular and hole depths varied from 0.25m to 2.0m. The p- and s-wave speeds, densities, porosities and flow resistivities for the desert floor were all measured

By varying the hole depth and the fill material, the maxima in the seismic transfer function was shifted in frequency and location. The results compared reasonably with that of a hard-backed layer calculation.

In a similar manner, Van Hoof (1986) carried out a series of experiments to determine the acoustic attenuation and propagation velocity for several materials. To achieve this $1m^3$ holes were cut and filled. The main implication of the work was to study the application of unattended ground sensors to detect, locate and classify targets of interest and was a continuance of previous work (Van Hoof and Doorman, 1983).

The measurements were carried out on a military terrain in Wezep, NL. The site was first characterised with boreholes dug to determine the ground profile and soil property measurements taken on the materials. It was shown that inconsistencies were found in the results with time and between geophones buried at differing depths. Although, it was experienced that the deeper geophones responded more consistently under various distances, source heights and meteorological conditions.

From a number of these experimental investigations it seemed clear that large differences were being found in the coupling ratio with geophone positioning and with time. Although, this could be attributed to either, meteorological effects on the microphone or errors in microphone positioning, experiments by the author led to the conclusion that variations in the geophone signal were causing the recorded differences in the spectra. An investigation was therefore made into the phenomena of geophone-ground coupling.

The subsequent review showed that this was a problem that had occurred in seismic data acquisition. It appears that the first investigation was made by Washburn and Wiley (1941), who discovered that geophone ground coupling is a resonant phenomenon and demonstrated that the coupling could distort the seismic signal by altering both the amplification and phase of the higher frequencies. Fail *et al.* (1962) made both field and laboratory measurements of coupling.

It appears that there has been more theoretical modelling of geophone ground coupling than actual experimental work (Wolf, 1944; Miller and Pursey, 1954; Lamar, 1970; Asten, 1977; and Hoover and O'Brien, 1980). This list would be even longer if it included those who solved some of the mathematics relating to a point force near a surface. However, all the work modelled the coupling as a rigid cylinder resting upon a isotropic elastic half-space. The models do vary in the form of attachment, choosing either a uniform normal stress distribution under the cylinder or using a stress distribution for static loading. With either form, a complex mixed boundary value problem is formulated in terms of integral equations that are solved numerically.

Krohn (1984) has made a comprehensive study of geophone-ground coupling both theoretically and with laboratory experiments. He showed that the coupling is adequately modelled by a simple resonant system in terms of a single coupling resonant frequency and damping factor. The vertical coupling resonant frequency and damping depends upon the firmness of the soil in which the geophones are planted. He concluded that burying the geophones or using longer spikes would increase the resonant frequency coupling, although the damping factor is greater for buried geophones.

Krohn also showed that the coupling resonances are insensitive to changes in mass or diameter of the geophone, although this disagrees with the results of Hoover and O'Brien (Hoover and O'Brien, 1980) and Omata (1983). Both these studies showed that if vibration transducers with different weights and base areas were placed on the same soil surface, the values measured by each transducer would be different for the same ground motion.

However, the Hoover and O'Brien conclusions of base size dependence of the coupling were based upon experimental work that included three points in sand and clay. Although, they reported an increase with base size of resonant frequency in sand, their work with clay did not show a change. The differences in the results may be due to the Hoover and O'Brien work being based upon large seismometers mounted on a flat base. Whereas, the geophones used by Krohn were based on the more modern design which incorporates a long spike on the base. The modern geophone is dominated by it spike, which has a very different set of stress distributions than a flat base. With a spike it is likely that variations of soil conditions near the surface become very important.

It appears the calibration of the geophone is an important factor for measurements requiring accurate amplitude data and for frequencies higher than those used in standard seismic investigations (>200Hz). This could be either the determination of the frequencies and characteristic modes of vibration of an arch dam using data obtained from geophones attached to the dam or more importantly for this study, acoustic-to-seismic coupling measurements.

The most direct method of calibrating a geophone is to drive it with a shaker table having a well-defined mode of vibration and amplitude over the required frequency range. MacArthur (1985) describes a system of geophone frequency calibration using a shaker table after his search of the literature did not reveal a suitable frequency calibration procedure. Although, it has been noted that further experimental testing is required to calibrate shaker tables precisely (Hudson, 1984). Hence, indirect methods are used for in-

situ calibration of geophones. The release test (Krohn, 1984) and the phase-ellipse test (Liu and Peselnick, 1986) are the two most practical methods.

To overcome the problems associated with the use of geophones for ground vibration measurements, non-invasive measurement systems have been investigated. Arnott and Sabatier (1990) undertook an investigation into the use of a Laser Doppler Vibrometer (LDV) in acoustic-to-seismic coupling measurements.

The use of the frequency shift of laser light (or Doppler shift) to measure flow velocities was first demonstrated experimentally in 1964 and has since undergone continued development (Bouchard and Bogg, 1985). Various Laser Doppler Vibrometers (LDV) were built in the late sixties (Massey, 1967; Whitman *et al.*, 1968) and are intended for non-contact vibration measurement from diffuse or specularly reflective surfaces. The LDV measures the moving velocity of an object by detecting the frequency shift of the laser.

The work by Arnott and Sabatier (1990) compared the response of a geophone to a propane cannon burst and to continuous waves from a speaker system. Measurements were in the frequency range 100 to 500Hz. The geophones were positioned in a well-packed consolidated soil, which had been manicured with a straight edge to be horizontal so that the scattered light followed the path of the incident light.

They showed that the response of the LDV followed the geophone when the LDV probe beam was focussed on the geophone and that a similar response was seen when the probe beam was focussed directly onto the soil 0.10m away. They also gave a description of the modifications necessary to use an off-the-shelf LDV system in outdoors acoustic-to-seismic coupling measurements. They did show however, that the quality of the LDV signal was detrimentally affected by wind noise by causing the laser beam to sample many different soil parcels.

LDV's have been used by several other workers, investigating or utilising elastic wave motion. Bouchard and Bogy (1985) developed a technique for the experimental measurement of scattered surface waves. The primary motivation of the work was in the field of non-destructive evaluation (NDE). In NDE, piezoelectric disks are used as active elements of transducers, which are usually mounted on the test piece with a viscous couplant. These transducers allow the detection of the ultrasonic wave motion scattered from passive flaws or generated by actively growing flaws, yielding information about the geometry and orientation of these flaws.

The mechanical detection of the incident and scattered waves using piezoelectric transducers is problematic due to the narrow bandedness and the poor characterisation of the transducers. However, they found that the LDV avoided problems with reproducibility due to mechanical contact of the detector and the detection was very versatile in terms of frequency and amplitude.

Laboratory studies of seismic wave propagation in inhomogeneous media using a LDV has been undertaken by Nishizawa *et al.* (1997, 1998). In the first paper they developed the system for studying elastic wave propagation and showed important features of the waveforms that were due to the inhomogeneities, such as the change in P-wave particle motion caused by scattering. The second paper deals specifically with the detection of shear waves in rock samples.

Their measurements were accomplished by attaching a commercially available reflective sheet, covered with 60μm spherical glass lens, to the rock sample. Since the spherical lens strongly reflects the laser beam along its incident direction, the vibration of the sample surface along the beam direction can be detected. Measurements were taken of surface motion in three different directions to derive the three-component elastic waveform.

An investigation has also been made by Hickey and Sabatier (1986) into the use of in-situ microphones for the measurement of elastic waves. This was undertaken as part of a set of measurements of phase velocity and attenuation of the two dilatational waves (Biot Type-I and Type-II) and one rotational wave, predicted by the Biot theory, in an air filled unconsolidated sand for the deduction of the bulk elastic properties of the material.

They showed that for the material used that the microphones produced the same Type-I P-wave phase velocity as that measured by vertical component geophones, using a mechanical shaker source and that a loudspeaker source produced selective excitation of the Type-II P-wave which could be detected by both the microphones and geophones.

Using the measured Type-I P-wave phase velocity an inversion was made for values of the undrained bulk modulus of the material using an "elastic" wave theory and a limit of the dual wave theory. It was shown that dual wave theory does not incorporate the proper attenuation mechanisms and the values determined for the undrained bulk modulus were larger.

They also used the loudspeaker source in conjunction with a probe microphone. From these measurements, values for the tortuosity and permeability of the sand were

determined using the rigid frame model. This work was a continuance of previous work by Sabatier *et al.* (1996) which describes the development of the technique that had begun with work by Moore and Attenborough (1992) and Sabatier *et al.* (1990).

1.2.3 Conclusions

It appears from the literature review that considerable effort has been made to theoretically describe acoustically induced motion. Models range from those based on simple resonances in a layer through to more complex models using wavenumber integration in combination with the Direct Global Matrix solution technique. These models have described the ground as either elastic or porous elastic materials.

Experimentally, although a number of workers have considered acoustic-to-seismic coupling, much of this work has been carried out for the development of detection systems. Very few workers have undertaken a coherent investigation into the use of acoustically induced ground motion to determine the physical properties of the ground. These studies have raised a number of questions concerning the influence of the experimental configuration on the recorded spectra and the overall reliability of the data.

It is hoped that the present work will go some way to resolving these issues.

Chapter 2

The Prediction of Acoustically-Induced Ground Motion

2 Introduction

There have been several theoretical models formulated for the prediction of acoustically induced ground motion. These range from simplistic models based on plane waves and non-porous elastic layer resonances to more complicated models which consider full-wave propagation in layered porous and elastic solids. Measurements of the acoustic-to-seismic coupling ratio in soils show the variation in magnitude of the coupling with frequency. Models therefore need to predict the frequencies at which the maxima and minima occur as well as the magnitude of the extrema.

This chapter will outline the mathematical formulations for four of the available models in order of increasing complexity. The first two models, based around layer resonance, predict only the frequencies at which the maxima and minima occur. Models that are more complex are required to also calculate the magnitudes and two of these will be described.

As stated above and outlined in the literature review in Chapter 1, a number of models are available for the prediction of acoustically induced ground motion. It is beyond the scope of this study to address all models; the models presented here are the most widely accepted.

2.1 Single Rigid-Backed Layer

This model is the most simplistic available and is based on wave interference within a single layer. It is assumed that the layer is a homogeneous elastic layer, bounded by a pressure release boundary at the air-ground interface and a rigid solid half space with a totally reflecting interface at the base (Figure 2-1).

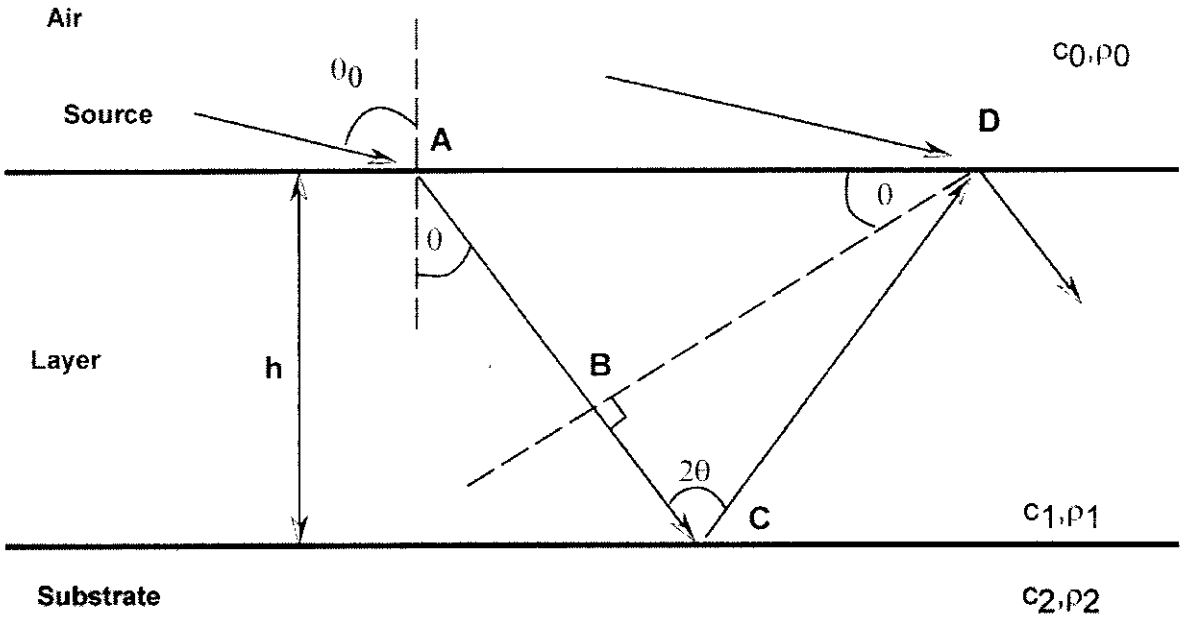

Figure 2-1. Ray diagram used for p- and s-wave interference with a layer.

An airborne acoustic plane wave is incident at the ground surface, it is partially reflected back into the atmosphere, but also excites elastic vibrations in the ground. The elastic waves are incident on the rigid half space and are totally reflected. The reflected waves travel through the layer and upon meeting the pressure release boundary interfere with further incoming waves.

The condition for constructive interference is that the extra path length travelled by the first wave is exactly an integral number of wavelengths. Furthermore, since the upper surface is assumed to be a pressure release boundary it produces an additional phase shift equal to π. This is equivalent to an extra path length of ½ the wavelength. Therefore, the condition for constructive interference can be written as:

$$\delta PL = n\lambda + \tfrac{1}{2}\lambda \qquad \textit{(Eq. 2-1)}$$

where:

δPL = Path length difference

λ = Wavelength

To calculate δPL, we can make use of simple trigonometrical relationships. Referring to Figure 2-1, δPL can be determined from the lengths BC + CD. It can be seen that:

$$CD = \frac{h}{\cos\theta} \qquad \textit{(Eq. 2-2)}$$

$$AD = 2h(\tan\theta) \qquad \textit{(Eq. 2-3)}$$

and that:

$$AB = AD(\sin\theta) = \frac{2h\sin^2\theta}{\cos\theta} \qquad \textit{(Eq. 2-4)}$$

$$BC = CD - AB = \frac{h}{\cos\theta} - \frac{2h\sin^2\theta}{\cos\theta} \qquad \textit{(Eq. 2-5)}$$

We have stated that δPL can be determined from the lengths BC + CD:

$$\delta PL = BC + CD = \frac{2h}{\cos\theta} - \frac{2h\sin^2\theta}{\cos\theta} = \frac{2h}{\cos\theta}\left(1 - \sin^2\theta\right) = 2h\cos\theta \qquad \textit{(Eq. 2-6)}$$

Using Snell's law it can be seen that:

$$\sin\theta = \frac{c_1}{c_0}\sin\theta_0 \qquad \textit{(Eq. 2-7)}$$

and

$$\cos\theta = \sqrt{1 - \left(\frac{c_1}{c_0}\sin\theta_0\right)^2} \qquad \textit{(Eq. 2-8)}$$

Then

$$\delta PL = 2h\sqrt{1 - \left(\frac{c_1}{c_0}\sin\theta_0\right)^2} \qquad \textit{(Eq. 2-9)}$$

Using the expression for δPL shown in Equation 2-1 and $\lambda = c_1/f$

$$\delta PL = \left(\frac{2n+1}{2}\right)\frac{c_1}{f} = 2h\sqrt{1 - \left(\frac{c_1}{c_0}\sin\theta_0\right)^2} \qquad \textit{(Eq. 2-10)}$$

$$f = \left(\frac{2n+1}{4h}\right)\frac{c_1}{\sqrt{1 - \left(\frac{c_1}{c_0}\sin\theta_0\right)^2}} \qquad \text{for } n=0,1,2\ldots \quad \textit{(Eq. 2-11)}$$

where

f = Resonance frequency

c_1 = Wave speed in the ground layer (compressional or shear speed)

c_0 = Speed of sound in air

This then gives the frequencies of the first and subsequent harmonics for either compressional or shear waves.

Two simplifying assumptions are made in this model. The first is that the upper interface of the layer is a pressure boundary and the second is that the bottom interface is a totally reflecting surface. The latter assumption has been relaxed by Hastrup (1980) whose model is the second to be described.

2.2 *Single Soft-Backed Layer*

Attenborough (1986) used a model developed by Hastrup (1980) to improve on the single rigid backed layer model. In this model, it is assumed that the bottom interface need not be totally reflecting. It is also assumed that the wave speed in the underlying substrate is greater than the comparable wave speed in either the upper layer or the air (See Figure 2-1), such that:

$$c_2 > c_0 > c_1 \qquad \textit{(Eq. 2-12)}$$

and that shear waves are negligible in this case. Since the substrate is no longer totally reflecting, the equation for the determination of the path length difference must be modified to include the added phase shift at the bottom interface.

$$\delta PL = n\lambda + \tfrac{1}{2}\lambda + \left(\frac{\phi}{2\pi}\right)\lambda \qquad \textit{(Eq. 2-13)}$$

The reflection coefficient at the bottom interface can be written as

$$R = e^{i(S(\pi/2-\theta))} \qquad \textit{(Eq. 2-14)}$$

where

$$S = \frac{2\rho_2/\rho_1}{\sqrt{1-(c_1/c_2)^2}} \qquad \textit{(Eq. 2-15)}$$

Thus, the phase shift can be expressed as:

$$\phi = S(\pi/2 - \theta) \qquad \textit{(Eq. 2-16)}$$

Combining Equation 2-13 and Equation 2-14 together with Equation 2-6 gives an expression for the path length difference, δPL, such that:

$$2h\cos\theta = \left(\frac{2n+1}{2}\right)\frac{c_1}{f} + \left(\frac{S(\pi/2 - \theta)}{2\pi}\right)\frac{c_1}{f} \qquad \textit{(Eq. 2-17)}$$

$$2h\cos\theta = \frac{(2n+1)\pi + S(\pi/2 - \theta)}{2\pi}\frac{c_1}{f} \qquad \textit{(Eq. 2-18)}$$

$$f = \frac{c_1}{4h}\frac{(2n+1)\pi + S(\pi/2 - \theta)}{\pi\sqrt{1 - \left(\frac{c_1}{c_0}\sin\theta_0\right)^2}} \qquad \text{for } n=0,1,2\ldots \qquad \textit{(Eq. 2-19)}$$

The two resonance models have been compared (Attenborough, 1986) with data measured by Van Hoof (1986). Table 2-1 shows the predicted and measured frequencies of interference maxima in the acoustic-to-seismic coupling ratio.

Measured (Van Hoof, 1986)	**Single Rigid-Backed Layer** (Sabatier, 1986a)	**Single Soft-Backed Layer** (Attenborough, 1986)
105*		108.3(s2)
116*		122.9(p1)
155	142.5(s2)	
	164.1(p1)	165.36(s3)
174*		
	199.5(s3)	
220*		222.4(s4)
235		231.6(p2)
250	256.6(s4)	
275	273.5(p2)	279.5(s5)
303	313.5(s5)	
330*		
335		340.95(p3)

Table 2-1. Measured and predicted peak frequencies of acoustic-to-seismic coupling ratio. Asterisks refer to major peaks, Sn and Pn to the nth harmonics of s- and p-waves respectively.

It can be seen in Table 2-1 that the softness of the substrate reduces frequencies of the peaks. It is also clear that for this data set that single soft-backed layer model gives the more accurate predictions, even when applied to shear wave resonances.

2.3 Layered Elastic Media

The remaining two models that will be described are based on wave propagation theory. The first, described here, concerns the modelling of the ground as a homogeneous, isotropic elastic solid, whilst the second method introduces ground porosity. This will be described in Section 2.4.

The following is a brief background to the theory of motion in an elastic medium. A more detailed treatment can be found in reference books (Ewing *et al.*, 1957, Aki and Richards, 1980).

Seismic waves which consist of tiny packets of elastic strain energy, travel away from any seismic source at speeds determined by the elastic moduli and the densities of the media through which they pass. There are two main types of seismic waves: those that pass through the bulk of the medium, known as *body waves*; those confined to the interfaces between media with contrasting elastic properties, particularly the ground surface, are called *surface waves*.

A) Body Waves

Two types of body wave can travel through an elastic medium. *P-waves*, which are the most important in exploration seismology, are also known as *longitudinal, primary, push* or *compressional* waves. Material particles oscillate about fixed points in the direction of wave propagation (Figure 2-2A) by compression and dilatational strain. The second type of wave is the *S-wave*, also known as the *transverse, secondary* or *shear wave*. Particle motion is at right angles to the direction of wave propagation and occurs by pure shear strain (Figure 2-2B).

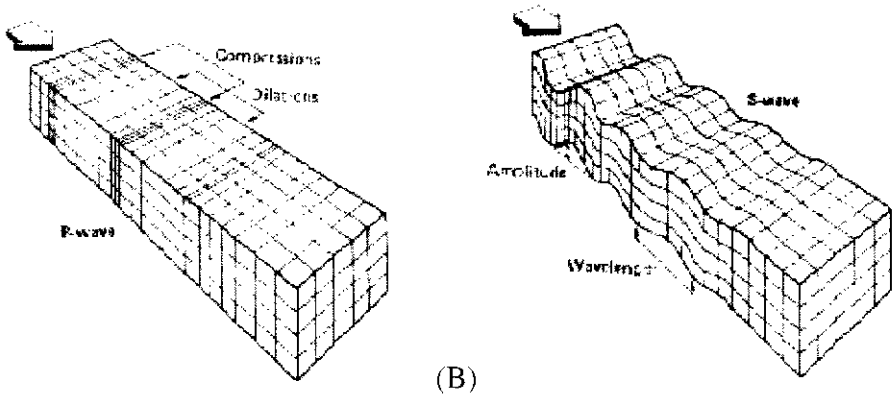

(A) (B)

Figure 2-2. Elastic deformations and ground particle motions associated with the passage of body waves (A) a P-wave and (B) an S-wave. P-waves have short wavelengths and a relatively high frequency. They are longitudinal waves and can travel through the whole earth, including the molten core. S-waves also have short wavelengths and a relatively high frequency. They are transverse waves and are unable to travel through the liquid parts of the earth.

All the frequencies contained within body waves travel through a given material at the same velocity, subject to the consistency of the elastic moduli and density of the medium through which the waves are propagating

B) Surface Waves

Waves that do not penetrate deep into the sub-surface media are known as surface waves, of which there are two types, *Rayleigh* and *Love waves*. Rayleigh waves travel along the free surface of the Earth with amplitudes that decrease exponentially with depth. Particle motion is in a retrograde elliptical sense in a vertical plane with respect to the surface (Figure 2-3A) and as shear is involved, Rayleigh waves can only travel through a solid medium. Love waves occur only where a medium with a low S-wave velocity overlies a layer with a higher S-wave velocity. Particle motion is at right angles to the direction of wave propagation but parallel to the surface. These are thus polarised shear waves (Figure 2-3B).

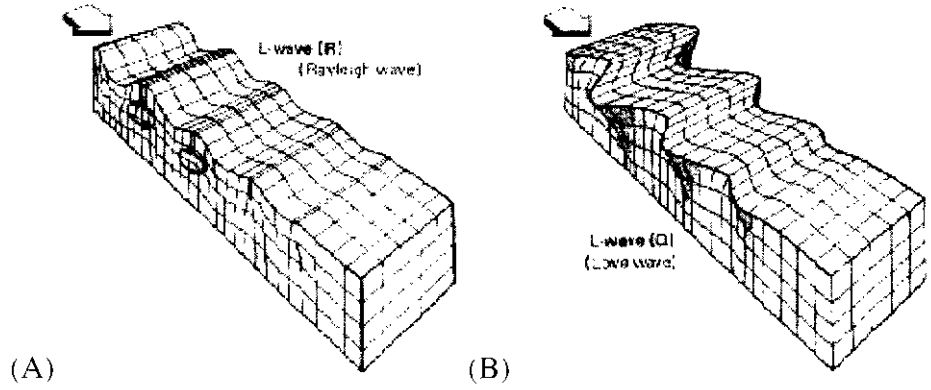

Figure 2-3. Elastic deformations and ground particle motions associated with the passage of surface waves (A) an R-wave and (B) a Q-wave. Surface waves occur only in the earth's crust. They have long wavelengths and a relatively low frequency, confined to the skin of the earth's crust; at high amplitudes they cause the most damage. Surface waves occur in two forms:

-Love waves (Q Waves) where there is a strong horizontal movement perpendicular to the direction of the wave.

-Rayleigh waves (R waves) where there is a vertical motion in the wave's direction

Surface waves have the characteristic that their waveform changes as they travel because different frequency components propagate at different rates, a phenomenon known as *wave dispersion*. The dispersion patterns are indicative of the velocity structure through which the waves travel. Surface wave dispersion has been described in detail elsewhere (Grant and West, 1965; Sheriff and Geldert, 1982).

Body waves are non-dispersive. In exploration seismology, Rayleigh waves manifest themselves normally as large amplitude low-frequency waves called *ground-roll*. Rayleigh waves can mask reflections on a seismic record and are usually considered as noise. Seismic surveys are usually constructed to minimise ground roll, which can be further reduced by filtering during later data processing.

The equations of motion in terms of displacements u, v, w, of a point in an elastic solid in the absence of body forces is expressed as:

$$\rho \frac{\partial^2 u}{\partial t^2} = (\lambda'+\mu)\frac{\partial \theta}{\partial x} + \mu \nabla^2 u \qquad \textit{(Eq. 2-20)}$$

$$\rho \frac{\partial^2 v}{\partial t^2} = (\lambda' + \mu) \frac{\partial \theta}{\partial x} + \mu \nabla^2 v \qquad \textit{(Eq. 2-21)}$$

$$\rho \frac{\partial^2 w}{\partial t^2} = (\lambda' + \mu) \frac{\partial \theta}{\partial x} + \mu \nabla^2 w \qquad \textit{(Eq. 2-22)}$$

where:

λ' = Lamé constant

μ = Lamé constant

θ = Cubic dilatation

For displacements in a solid body, it is convenient to define the displacements u, v, w in terms of a scalar potential, φ, and vector potential ψ (ψ_1, ψ_2, ψ_3) as follows:

$$u = \frac{\partial \varphi}{\partial x} + \frac{\partial \psi_3}{\partial y} - \frac{\partial \psi_2}{\partial z} \qquad \textit{(Eq. 2-23)}$$

$$v = \frac{\partial \varphi}{\partial y} + \frac{\partial \psi_1}{\partial z} - \frac{\partial \psi_3}{\partial x} \qquad \textit{(Eq. 2-24)}$$

$$w = \frac{\partial \varphi}{\partial z} + \frac{\partial \psi_2}{\partial x} - \frac{\partial \psi_1}{\partial y} \qquad \textit{(Eq. 2-25)}$$

or in vector form:

$$s(u, v, w) = \nabla \varphi + \nabla \times \psi(\psi_1, \psi_2, \psi_3) \qquad \textit{(Eq. 2-26)}$$

From this we can obtain:

$$\theta = \nabla^2 \varphi \qquad \textit{(Eq. 2-27)}$$

In general, the equations of motion, given in Equations 2-20, 2-21 and 2-22 represent the propagation of a disturbance that involves both equivoluminal and irrotational motion. However, by introducing the potentials φ and ψ_1, separate wave equations are obtained for these two types of motion. Substituting Equation 2-26 and Equation 2-27 into the equations of motion, we obtain, using Equation 2-20 for example:

$$\rho \frac{\partial^2}{\partial t^2} \left(\frac{\partial \varphi}{\partial x} + \frac{\partial \psi_3}{\partial y} - \frac{\partial \psi_2}{\partial z} \right) = (\lambda' + \mu) \frac{\partial}{\partial x} \nabla^2 \varphi + \mu \nabla^2 \left(\frac{\partial \varphi}{\partial x} + \frac{\partial \psi_3}{\partial y} - \frac{\partial \psi_2}{\partial z} \right) \qquad \textit{(Eq. 2-28)}$$

Rearranging gives:

$$\frac{\partial}{\partial x}\left[\rho\frac{\partial^2\varphi}{\partial t^2}-(\lambda'+\mu)\nabla^2\varphi-\mu\nabla^2\varphi\right]=$$

$$\frac{\partial}{\partial y}\left[-\rho\frac{\partial^2}{\partial t^2}\psi_3+\mu\nabla^2\psi_3\right]-\frac{\partial}{\partial z}\left[-\rho\frac{\partial^2}{\partial t^2}\psi_2+\mu\nabla^2\psi_2\right] \qquad \textit{(Eq. 2-29)}$$

If each square bracket is zero independently. then the equality will be valid for all u, v and w, such that:

$$\rho\frac{\partial^2\varphi}{\partial t^2}-(\lambda'+2\mu)\nabla^2\varphi=0 \qquad \textit{(Eq. 2-30)}$$

$$\nabla^2\varphi=\frac{1}{v_p^{\,2}}\frac{\partial^2\varphi}{\partial t^2} \qquad \textit{(Eq. 2-31)}$$

where $$v_p=\sqrt{\frac{\lambda'+2\mu}{\rho}} \qquad \textit{(Eq. 2-32)}$$

And $$\nabla^2\psi_i=\frac{1}{v_s^{\,2}}\frac{\partial^2\psi_i}{\partial t^2} \qquad \text{for } i = 1, 2, 3 \qquad \textit{(Eq. 2-33)}$$

where $$v_s=\sqrt{\frac{\mu}{\rho}} \qquad \textit{(Eq. 2-34)}$$

Similar results can be found using Equations 2-21 and 2-22. The solution to these wave equations is simple if the medium is homogeneous. For a medium in which the wave speeds vary with height. the medium can be divided into layers. Within each, the wave speed is constant. The wave amplitudes in each layer are evaluated by forming and solving the boundary equations between successive layers.

For spherical waves, the solution can be written in terms of a Hankel transform integral. In physical terms, the Hankel integral represents the solution as a summation of plane waves. This method will be described in greater detail in the following section.

2.4 *Layered Porous Elastic Media*

In the final model to be described, the ground is modelled as an air-filled poro-elastic layer above a non-porous semi-infinite, elastic substrate. The poro-elastic layer supports two kinds of compressional waves and one shear wave as opposed to the single compressional and shear wave that has been shown to propagate in an elastic medium.

The formulation given is a modified Biot model. The Biot equations of motion are used to determine the propagation constants in the layer material. The following is a description of the method used to determine the equations describing the two dilatational waves. A similar procedure may be followed to obtain equations describing shear waves.

The coupled equations governing the propagation of dilatational waves as given by Biot-Stoll (Stoll, 1980) can be written as

$$\nabla^2(He - C\xi) = \frac{\partial^2}{\partial t^2}(\rho e - \rho_f \xi) \qquad \textit{(Eq. 2-35)}$$

$$\nabla^2(Ce - M\xi) = \frac{\partial^2}{\partial t^2}(\rho_f e - m\xi) - \frac{\eta}{k}\frac{\partial \xi}{\partial t}F(\lambda) \qquad \textit{(Eq. 2-36)}$$

where $$e = \nabla . u \qquad \textit{(Eq. 2-37)}$$

and is the dilatation or volumetric strain of the skeletal frame, and

$$\xi = \Omega \nabla . (u - U) \qquad \textit{(Eq. 2-38)}$$

and is the relative dilatation between the frame and the fluid. Also, where

u = Displacement vectors of the frame

U = Displacement vectors of the fluid

$F(\lambda)$ = Biot viscosity correction function

ρ = Total density of the medium

ρ_f = Fluid density

η = Dynamic fluid viscosity

k = permeability

The term

$$\frac{\eta}{k}\frac{\partial \xi}{\partial t}F(\lambda) \qquad \textit{(Eq. 2-39)}$$

allows for the damping through viscous drag as the fluid and matrix move relative to one another. In Stoll's notation (Stoll, 1980), m is a dimensionless parameter that accounts for the fact that not all the fluid moves in the direction of macroscopic pressure gradient as not all the pores run normal to the surface, and is given by:

$$m = \frac{\tau \rho_f}{\Omega} \qquad \textit{(Eq. 2-40)}$$

where

τ = Tortuosity

Ω = Porosity

H, C and M are elastic constants that can be expressed in terms of the moduli of the grains, fluid and frame.

$$H = \left[\frac{(K_s - K_b)^2}{D - K_b}\right] + K_b + \tfrac{4}{3}\mu \qquad \textit{(Eq. 2-41)}$$

$$C = K_s\left(\frac{K_s - K_b}{D - K_b}\right) \qquad \textit{(Eq. 2-42)}$$

and

$$M = \frac{K_s^2}{(D - K_b)} \qquad \textit{(Eq. 2-43)}$$

where

$$D = K_s\left[1 + \left(\frac{K_s}{K_f} - 1\right)\Omega\right] \qquad \textit{(Eq. 2-44)}$$

K_s, K_f, K_b are the bulk moduli of the discrete grains, the fluid, and the frame, with μ being the shear modulus of the frame.

The bulk and shear moduli of the frame can be determined from measurements of the compressional and shear wave speeds in the porous frame, the frame density and the expressions for these waves in a poro-elastic solid. For air-filled porous media, K_f can be calculated using the Zwikker and Kosten expression for the dynamic fluid modulus, $K(\omega)$

(Sides *et al.*, 1971; Sabatier *et al.* 1986a). It should be noted, however, that the expression for $K(\omega)$, represents the effective bulk modulus that the medium presents to an incident wave and hence differs by a factor of $1/\Omega$ to the intrinsic bulk modulus, K_f, of the fluid, i.e. $K_f=\Omega K(\omega)$.

The term $F(\lambda)$ in Equation 2- 36 represents a viscosity correction factor, where λ is a dimensionless quantity that is related to the thickness of the viscous boundary layer at the pore wall. Biot (1956b) developed expressions for $F(\lambda)$ for cylindrical and parallel sided pores in terms of the fluid viscosity and pore diameter. Subsequent work (Attenborough, 1983) has shown that for an arbitrary pore shape the expression for the dimensionless parameter λ is:

$$\lambda = \frac{1}{S_p}\left[\frac{(8\rho_f q^2 \omega)}{\Omega \eta / k}\right]^{1/2} \qquad \textit{(Eq. 2-45)}$$

where S_p = Pore shape factor ratio.

Here, S_p, is used as a scaling factor to equate the fluid velocity profile in the arbitrary pore shape to that in a regular pore cross-section. The viscosity correction factor $F(\lambda)$ is a complex function and is written as

$$F(\lambda) = -\frac{1}{4}\left(\frac{\sqrt{i}\lambda T\left(\sqrt{i}\lambda\right)}{1-\left(2\sqrt{i}\lambda\right)\left[T\left(\sqrt{i}\lambda\right)\right]}\right)\frac{1}{S_p} \qquad \textit{(Eq. 2-46)}$$

where

$$T\left(\sqrt{i}\lambda\right) = \frac{J_1\left(\sqrt{i}\lambda\right)}{J_0\left(\sqrt{i}\lambda\right)} \qquad \textit{(Eq. 2-47)}$$

and J_0 and J_1 are the zero and first-order Bessel functions of the first kind. This expression for $F(\lambda)$ differs from the version given by Biot (1956b) by the factor S_p. This factor is required to ensure equivalence between Equation 2-36, when e=0, and the corresponding wave equation in a rigid porous medium of arbitrary shape.

Assuming that e and ξ vary as $e^{-i(\omega t)}$, $\partial/\partial t$ can be replaced by $-i\omega$, and Equation 2-36 can be written (Attenborough, 1987) as

$$\nabla^2\left(Ce - M\xi\right) = -\omega^2\left(\rho_f e - \rho(\omega)\xi\right) \qquad \textit{(Eq. 2-48)}$$

where $$\rho(\omega)=\frac{\tau\rho_f}{\Omega}+\frac{i\eta}{\omega k}F(\lambda) \qquad \textit{(Eq. 2-49)}$$

is the dynamic fluid density. If plane waves:

$$e = A\exp(i(lx-\omega t) \qquad \textit{(Eq. 2-50)}$$

$$\xi = B\exp(i(lx-\omega t) \qquad \textit{(Eq. 2-51)}$$

are chosen as solutions to Equations 2-36 and 2-48, then the dispersion equations for the propagation constants may be derived. These are:

$$A(l^2H-\omega^2\rho)+B(\omega^2\rho_f-l^2C)=0 \qquad \textit{(Eq. 2-52)}$$

and

$$A(l^2C-\omega^2\rho_f)+B\left(m\omega^2-l^2M+i\omega F(\lambda)\eta/k\right)=0 \qquad \textit{(Eq. 2-53)}$$

A non-trivial solution of Equation 2-52 and 2-53 exists only if the determinant of the coefficient vanishes, giving

$$\begin{vmatrix} l^2H-\omega^2\rho & \omega^2\rho_f-l^2C \\ l^2C-\omega^2\rho_f & m\omega^2-l^2M+i\omega F(\lambda)\eta/k \end{vmatrix} \qquad \textit{(Eq. 2-54)}$$

The sign of the term including $F(\lambda)$ is dictated by the sign in the in the time convention.

There are two complex roots of this equation from which both the attenuation and phase velocities of the two dilatational waves are calculated. These dilatational wave modes propagate simultaneously in both constituents of the porous medium, however, in general one of the waves travels predominantly in the frame whilst the other is borne mainly by the fluid. These waves are commonly termed "fast" and "slow", although in materials with high porosity and at high frequencies the "fast" wave can travel more slowly that the "slow" wave and so for clarity it is preferable to term "Type-I" and "Type II" waves or "frame" and "fluid" waves.

From Equation 2-52, the relation between the fluid and matrix wave amplitudes for each wave type is expressed as

$$m_i=\frac{B}{A}=\frac{(l^2H-\rho\omega^2)}{(\rho_f\omega^2-l^2C)} \qquad \textit{(Eq. 2-55)}$$

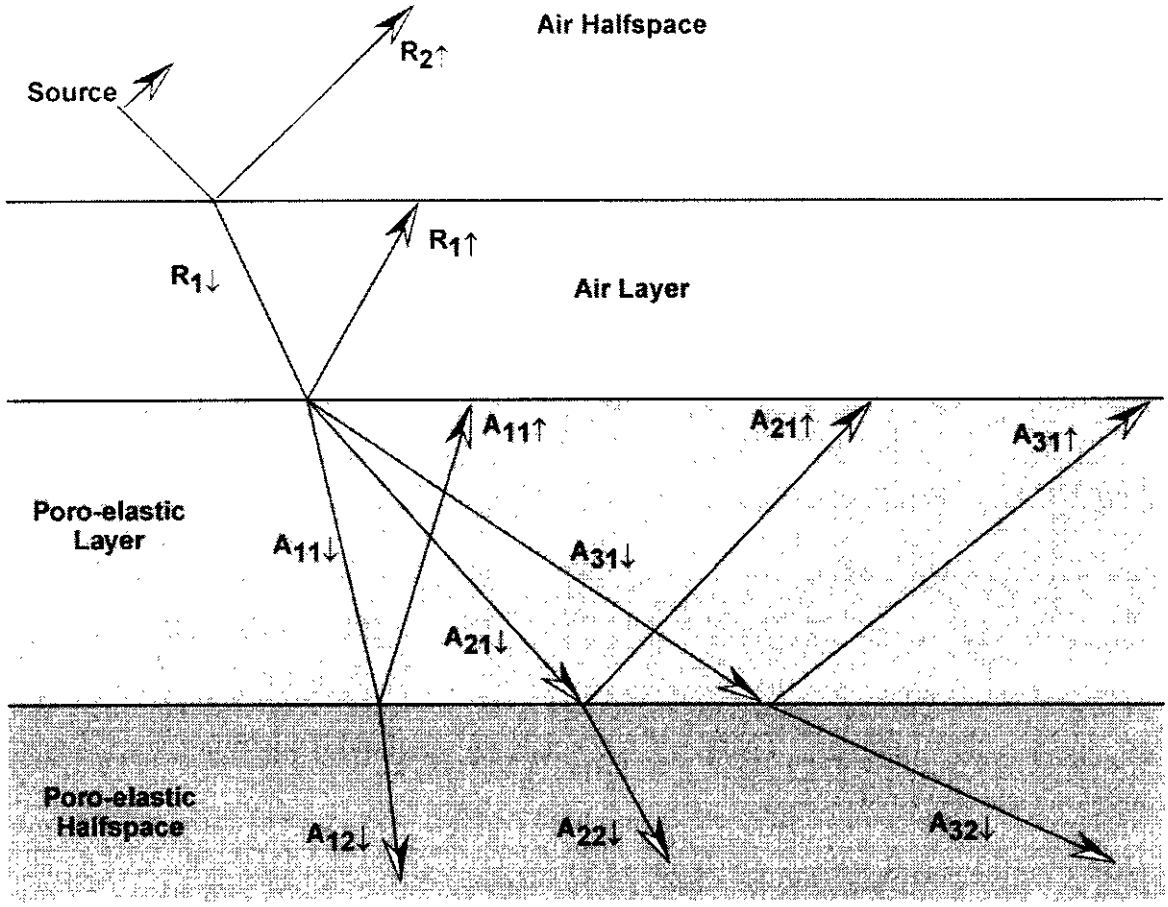

Figure 2-4. An example environment used in the porous elastic theory. This shows the notation for the amplitudes of the predicted wave types.

The solution to the wave equations can be written in terms of displacement potentials. In terms of these potentials the solid and fluid displacement can be written as:

$$u = \nabla\Phi_1 + \nabla \times x_1, \qquad \textit{(Eq. 2-56)}$$

$$\omega = \nabla\Phi_2 + m_3 \nabla \times x_1, \qquad \textit{(Eq. 2-57)}$$

here, ω is the relative fluid displacement and u is the solid matrix displacement. The vector potential can be written simply in terms of a third scalar potential (Attenborough, 1980), such that:

$$x_1 = \bar{\theta}\frac{\partial\Phi_3}{\partial r}, \qquad \textit{(Eq. 2-58)}$$

$$x_2 = m_3 x_1, \qquad \textit{(Eq. 2-59)}$$

In a porous-elastic layer, bounded by interfaces at depths d_1 and d_2, in the absence of a source, the Φ_i's at a depth z are given by :

$$\Phi_1 = A_{1\downarrow} e^{i(z-d_1)\beta_1} + A_{1\uparrow} e^{i(d_2-z)\beta_1} + A_{2\downarrow} e^{i(z-d_1)\beta_2} + A_{2\uparrow} e^{i(d_2-z)\beta_2} \qquad \textit{(Eq. 2-60)}$$

$$\Phi_2 = m_1\left(A_{1\downarrow} e^{i(z-d_1)\beta_1} + A_{1\uparrow} e^{i(d_2-z)\beta_1}\right) + m_2\left(A_{2\downarrow} e^{i(z-d_1)\beta_2} + A_{2\uparrow} e^{i(d_2-z)\beta_2}\right) \qquad \textit{(Eq. 2-61)}$$

$$\Phi_3 = A_{3\downarrow} e^{i(z-d_1)\beta_3} + A_{3\uparrow} e^{i(d_2-z)\beta_3} \qquad \textit{(Eq. 2-62)}$$

where β is the vertical component of the wavenumber. The amplitudes $A_{n\uparrow\downarrow}$ are described in Figure 2-4.

The m_i's given in Equations 2-60 to 2-62 are the ratios of fluid to solid displacement. To determine the unknown amplitudes, boundary conditions between layers have to be set and solved. There are six unknown amplitudes requiring six boundary conditions and these are

1) Continuity of total normal stress

2) Continuity of normal displacement

3) Continuity of fluid pressure

4) Continuity of tangential stress

5) Continuity of normal fluid displacement,

6) Continuity of tangential frame displacement

For the interface between a fluid and the poroelastic layer there are only four unknowns requiring four boundary conditions and these are:

1) Continuity of total normal stress.

2) Continuity of normal displacement,

3) Continuity of fluid pressure,

4) Continuity of tangential stress,

So far, the solution is for plane waves, for spherical waves one can transform the wave equation by Hankel transform to express the potentials in terms of an integral.

$$\Phi_1 = \int_0^\infty \overline{\Phi}_1 J_0(k_h r) k_h dk_h \qquad \textit{(Eq. 2-63)}$$

$$\Phi_2 = \int_0^\infty \overline{\Phi}_2 J_0(k_h r) k_h dk_h \qquad \textit{(Eq. 2-64)}$$

$$\Phi_3 = \int_0^\infty \overline{\Phi}_3 J_0(k_h r) k_h dk_h \qquad \textit{(Eq. 2-65)}$$

Φ_1 is the longitudinal displacement potential in the solid, Φ_2 is the longitudinal displacement potential in the fluid. Φ_3 is the transverse displacement potential in the solid, to which the fluid transverse displacement potential is directly proportional. Here $\overline{\Phi}$ is the same as Φ in Equations 2-60 to 2-62. These now have to be evaluated for all k_h, since in Equations 2-63 to 2-65 the vertical wavenumber β_i can now be written as

$$\beta_i = \left(k_0^2 - k_h^2\right) \qquad \textit{(Eq. 2-66)}$$

where k_0 is the propagation constant in the medium, thus allowing for the dependence of k_h.

In the far field, the Bessel functions in the integrals can be approximated by their large argument expression (Abramowitz and Stegun, 1970) and the Hankel integral can be approximated by a Fourier transform. The resulting integral can be solved efficiently by Discrete Fourier Transform methods.

This method has been detailed explicitly elsewhere (Tooms, 1990; Taherzadeh, 1997).

Table 2-2 is a reproduction of Table 2-1 giving the comparison of the single soft-backed layer model with the measured data. The table now gives the predictions made using programs that model the ground as either an elastic or poroelastic medium. The results given are based around full spherical wave solutions. The measured ground parameters are those listed in Table 2-3 with the plot of the predicted spectra shown in Figure 2-5.

Measured (Van Hoof, 1986)	**Single Soft-Backed Layer** (Attenborough, 1986)	**Elastic**	**Poroelastic**
105*	108.3(s2)	105*	105*
116*	122.9(p1)	130	130
155		155	155
	165.36(s3)		
174*		174*	174*
		202	202
220*	222.4(s4)		
235	231.6(p2)		
250		264	264
275	279.5(s5)		
303			
330*		330*	330*
335	340.95(p3)		

Table 2-2. Measured and predicted peak frequencies of acoustic-to-seismic coupling ratio. Asterisks refer to major peaks, Sn and Pn to the nth harmonics of s- and p-waves respectively.

	Layer	**Substrate**
P-wave speed (m/s)	270.0	500.0
S-wave speed (m/s)	190.0	330.0
Flow resistivity (Pa sm^{-2})	366000	3660000
Porosity	0.27	0.001
Grain shape factor	0.5	0.5
Soil density (kg/m^3)	1700.0	2650.0
Layer thickness (m)	2.0	∞
Attenuation	0.02	0.02
Dynamic viscosity of air (Nsm^{-2})	1.81×10^{-5}	
Source height (m)	2.0	
Microphone height (m)	0.10	
Geophone depth (m)	-0.10	
Range (m)	50	
Frequency range (Hz)	100 – 400	
Speed of sound in air (m/s)	344.0	

Table 2-3. Parameters taken by van Hoof (1986) and used in the predictions shown in Table 2-2.

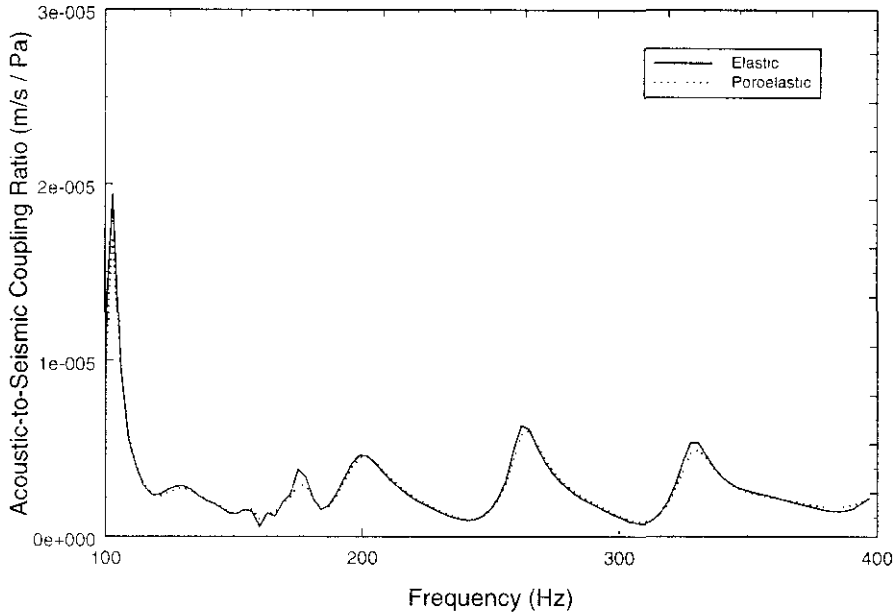

Figure 2-5. Prediction of acoustic-to-seismic coupling ratio using an elastic and poroelastic model. Data is based on van Hoof (1986). Range = 50.0m.

It can be seen in Table 2-2, that there are some measured maxima that are not predicted by the full-wave solution models, most notably the major peaks at 116Hz and 220Hz. There are also several minor peaks measured at 235, 250, 275, 303 and 335Hz that have not been predicted, although it is likely that these are due to a finer ground structure at the site that has not been reported.

The results show that overall the predictions made using the elastic and porous elastic models give an increased accuracy over predictions made using the model based upon layer resonance. It can be noted that the predicted values for the porous elastic formulation differ slightly from those given previously (Taherzadeh, 1997). The prediction based upon elastic theory shown in Table 2-2 and Figure 2-5 was made using a low porosity/high flow resistivity approximation of the porous-elastic model using the FFLAGS computer program.

It has been shown previously (Tooms, 1993) that predictions using the FFLAGS program for the vertical particle velocity (due to an elevated source) at the surface of a layered porous and elastic ground in which the porosity is allowed to decrease to zero, and

the flow resistivity allowed to increase correspondingly, approach those from a similar model that allows for a layered elastic ground but excludes porosity. The model used for comparison was SAFARI (Schmidt, 1986).

Subsequent calculations have shown that the same is true for predictions of acoustic-to-seismic coupling ratio made using the FFLAGS and SAFARI computer models. Figure 2-6 and Figure 2-7 show predictions of acoustic-to-seismic coupling ratio using the elastic (SAFARI) and low porosity limit of porous elastic theory (FFLAGS). The parameters used to describe the ground are given in Table 2-4.

	SAFARI		**FFLAGS**	
	Layer	**Substrate**	**Layer**	**Substrate**
P-wave speed (m/s)	500.0	1000.0	500.0	1000.0
S-wave speed (m/s)	320.0	640.0	320.0	640.0
Flow resistivity (Pa sm^{-2})	---	---	500000	500000000
Porosity	---	---	0.04	0.0004
Grain shape factor	0.375	0.375	0.375	0.375
Soil density (kg/m^3)	1300	2700	1300	2700
Attenuation	0.675	0.675	0.0125	0.0125
Layer thickness (m)	2.0	∞	2.0	∞
Dynamic viscosity of air (Nsm^{-2})	1.81×10^{-5}		1.81×10^{-5}	
Source height (m)	1.0		1.0	
Microphone height (m)	0.05		0.05	
Geophone depth (m)	-0.05		-0.05	
Speed of sound in air (m/s)	344.0		344.0	

Table 2-4. Parameters used for the comparison of elastic theory with poroelastic theory.

Figure 2-6 shows the prediction of change in acoustic-to-seismic coupling ratio with range at a frequency of 50Hz. It can be seen that the two predictions give excellent agreement, with some small differences occurring at long ranges, i.e. those greater than 250m. Figure 2-7 shows the predictions made for a frequency of 250Hz. Excellent agreement is found, although again, small differences can be seen at the longer ranges. It seems therefore, that using a low porosity / high flow resistivity limit in the porous elastic model, the FFLAGS program can be used to model the ground as if it behaved as an elastic medium.

It can be observed in Table 2-4 that the values of attenuation used in each model were dissimilar. This is a consequence of the two models use differing expressions for attenuation.

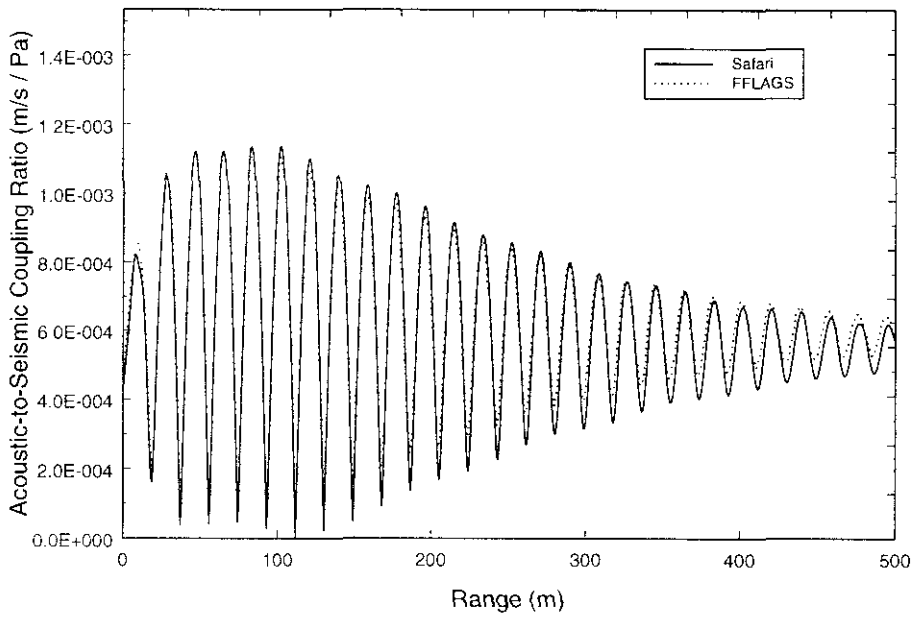

Figure 2-6. A comparison of elastic and low porosity limit of the poroelastic theory with range at a frequency of 50Hz with range. Using parameters in Table 2-4.

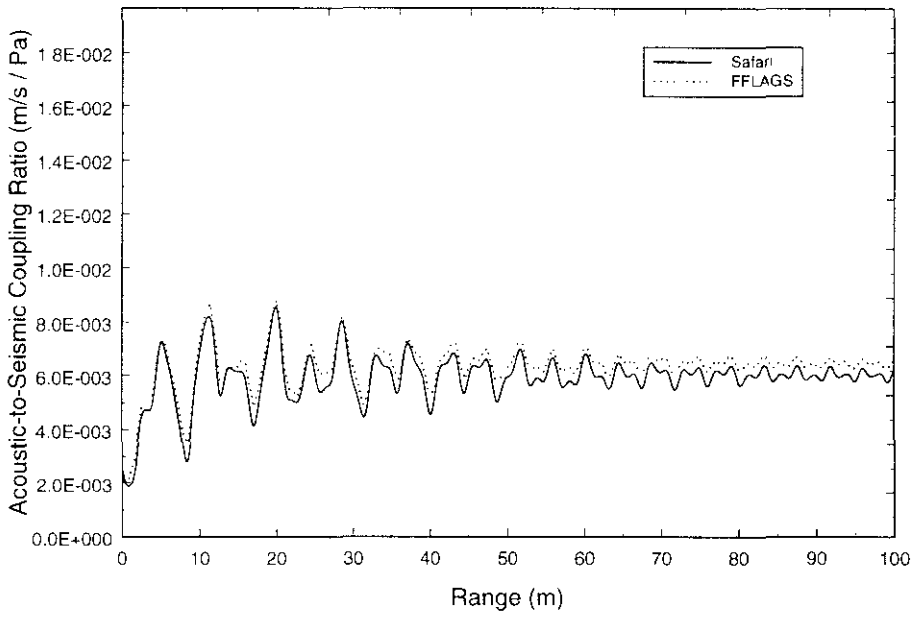

Figure 2-7. A comparison of elastic and low porosity limit of the poroelastic theory with range at a frequency of 250Hz. Using parameters in Table 2-4

It is well known that sound propagating in a ground layer undergoes significant attenuation due to the dissipation of the seismo-acoustic energy into heat. It is therefore crucial to a realistic prediction of the propagation characteristics that volume attenuation be taken into account.

Consider a harmonic wave of angular frequency (ω) propagating in a homogeneous medium along the positive axis of a Cartesian coordinate system,

$$F(x,t) = Ae^{i(\omega t - k_m x)} \qquad \textit{(Eq. 2-67)}$$

where k_m is the medium wavenumber for either the compressional or shear waves and A is the amplitude. If k_m is real, this wave has a constant amplitude for all ranges of x. However, attenuation can be accounted for by letting the medium wavenumber k_m be complex, such that:

$$\tilde{k}_m = k_m(1 - i\delta), \delta > 0 \qquad \textit{(Eq. 2-68)}$$

Then the wavefield becomes:

$$F(x,t) = Ae^{-\delta k_m x} e^{i(\omega t - k_m x)} \qquad \textit{(Eq. 2-69)}$$

and the amplitude decays exponentially with range. Since the medium wavenumber is now complex, the Lamé constants must also be complex, such that:

$$\tilde{\lambda}' = \lambda'_{\mathrm{Re}} + i\lambda'_{\mathrm{Im}} \qquad \textit{(Eq. 2-70)}$$

$$\tilde{\mu} = \mu_{\mathrm{Re}} + i\mu_{\mathrm{Im}} \qquad \textit{(Eq. 2-71)}$$

It has been shown experimentally (Ewing *et al.*, 1957) that most solid media are Voigt solids which exhibit an attenuation increasing linearly with frequency. For a Voigt solid:

$$\frac{\lambda'_{\mathrm{Im}} + 2\mu_{\mathrm{Im}}}{\lambda'_{\mathrm{Re}} + 2\mu_{\mathrm{Re}}} = \frac{1}{Q_c} \qquad \textit{(Eq. 2-72)}$$

$$\frac{\mu_{\mathrm{Im}}}{\mu_{\mathrm{Re}}} = \frac{1}{Q_s} \qquad \textit{(Eq. 2-73)}$$

where Q_c and Q_s are constants. By inserting the complex Lamé constants into Equation 2-32, 2-68 and using the relationship:

$$k_m(r,z) = \frac{\omega}{c(r,z)} \qquad \textit{(Eq. 2-74)}$$

this leads to the following value of δ for compressional and shear waves respectively, assuming Q_c and Q_s >>1:

$$\delta_c = \frac{1}{2Q_c} \qquad \textit{(Eq. 2-75)}$$

$$\delta_s = \frac{1}{2Q_s} \qquad \textit{(Eq. 2-76)}$$

It is more common to express the linearly frequency dependent attenuation in dB/Λ, where Λ is the wavelength:

$$\gamma = -20\log\left|\frac{F(x+\Lambda,t)}{F(x,t)}\right| = -20\log\left[e^{-\delta k_m \Lambda}\right] = 40\pi\delta\log e \equiv \frac{27.29}{Q} \qquad \textit{(Eq. 2-77)}$$

The SAFARI model uses γ as the value of attenuation whilst, FFLAGS uses δ. It can be seen however, that they can be resolved through:

$$\gamma = (2\times 27.29)\delta \qquad \textit{(Eq. 2-78)}$$

The use of this relationship allowed the direct comparison of the two models, shown in Figure 2-6 and Figure 2-7, to be made.

Since it has now been shown that using a low porosity / high flow resistivity limit in the porous elastic model, the FFLAGS program can be used to model the ground as if it behaved as an elastic medium, numerical differences between the two models have been investigated.

Figure 2-8 shows the effect of increasing porosity (and subsequently decreasing flow resistivity) on predicted values of acoustic-to-seismic coupling ratio. The figure shows that overall, increasing porosity leads to an increase in the magnitude of the coupling ratio. However, below 125Hz, there is little difference in the predictions. These predictions were made for a range of 5m and a grazing angle of 2°. The ground was described using the parameters given in Table 2-5 and for each subsequent plot, the only parameters altered were the porosity and flow resistivity.

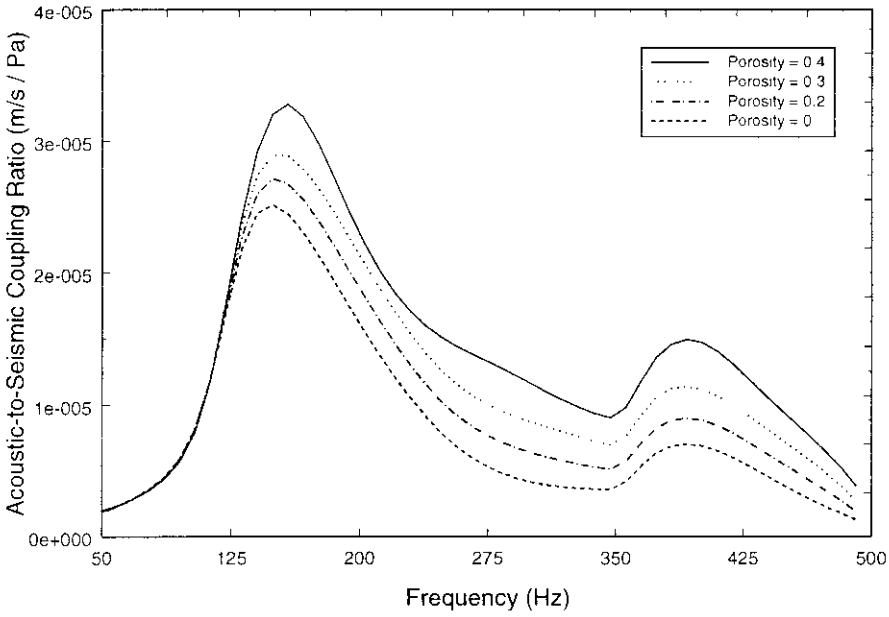

Figure 2-8. Variation in acoustic-to-seismic coupling ratio with differing porosity (range =5.0m and grazing angle=2°).

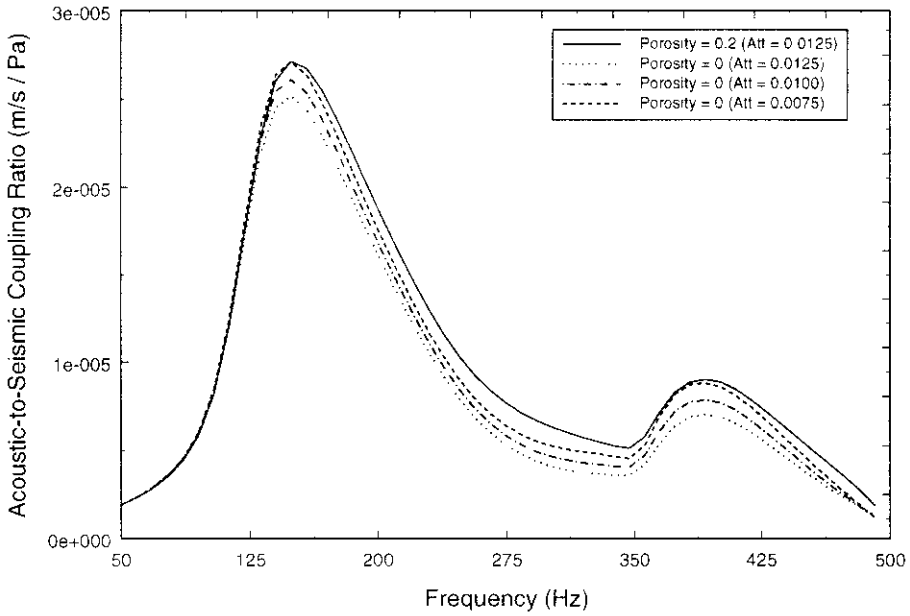

Figure 2-9. Effect of variation in attenuation on predicted acoustic-to-seismic coupling ratio (range =5.0m and grazing angle=2°).

	Layer	Substrate
P-wave speed (m/s)	500.0	1000.0
S-wave speed (m/s)	320.0	640.0
Flow resistivity (Pa sm^{-2})	5000 25000 50000 500000	50000000
Porosity porous elastic	0.4 0.3 0.2 0.04	0.0004
Grain shape factor	0.5	0.5
Soil density (kg/m^3)	1700.0	2650.0
Layer thickness (m)	2.0	∞
Attenuation porous elastic	0.0125 0.0125 0.0100 0.0075	0.0125 0.0125 0.0100 0.0075
Dynamic viscosity of air (Nsm^{-2})	1.81×10^{-5}	
Source height (m)	0.15 0.75	
Microphone height (m)	0.10	
Geophone depth (m)	-0.10	
Range (m)	5, 25	
Frequency range (Hz)	100 – 500	
Speed of sound in air (m/s)	344.0	

Table 2-5. Parameters used to describe the ground to show the differences between elastic and porous elastic models.

Figure 2-9 shows the predicted acoustic-to-seismic coupling ratio spectra for a porosity of 0.2. Also shown in the figure, are plots of coupling ratio calculated for the elastic model, i.e. zero porosity. The plot shows the sensitivity of the predictions to the value of attenuation input into the model. It can be seen how the prediction based on elastic theory can be made to match the coupling ratio spectra for a porous ground (with a porosity of 0.2) by altering the attenuation value.

Figure 2-10, in a similar manner to Figure 2-8, shows the effect of increasing porosity (decreasing flow resistivity) on predicted values of acoustic-to-seismic coupling ratio. However, here calculations are based on a range of 25m and a grazing angle of 2°. Again, the ground was described using the parameters given in Table 2-5.

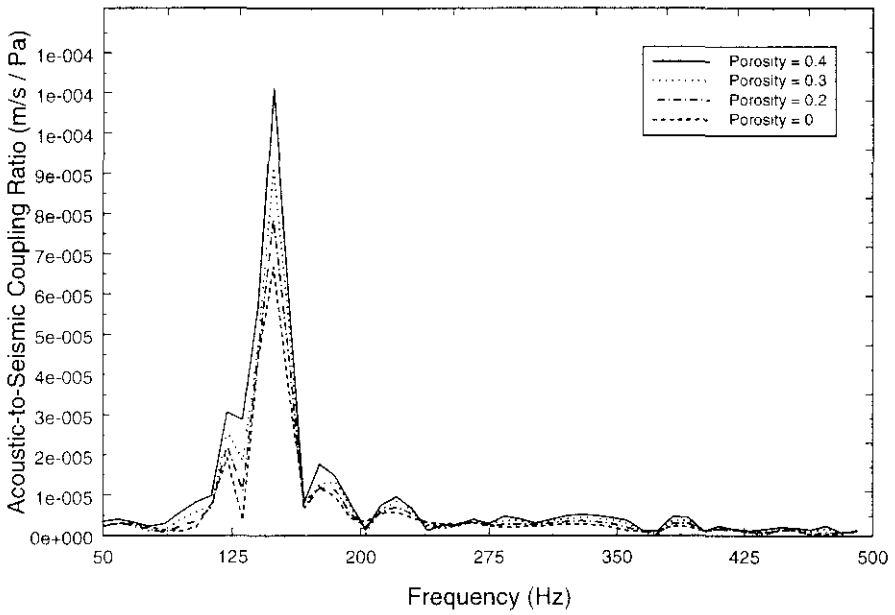

Figure 2-10. Variation in acoustic-to-seismic coupling ratio with differing porosity (range =25.0m and grazing angle=2°).

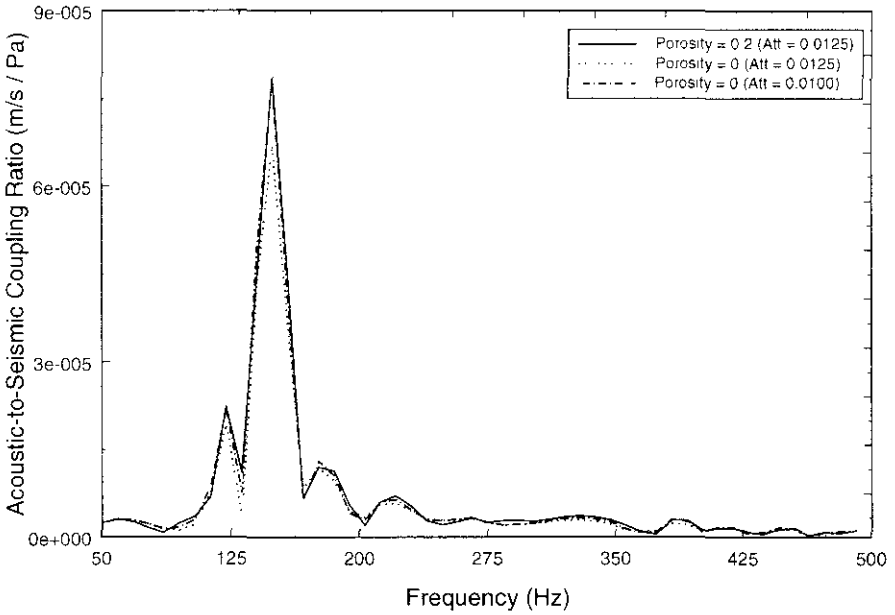

Figure 2-11. Effect of variation in attenuation on predicted acoustic-to-seismic coupling ratio (range =25.0m and grazing angle=2°).

It can be seen that, at this longer range, the differences between predicted values of coupling ratio are much smaller. The main difference between the plots is the magnitude of the peak at roughly 150Hz. Figure 2-11, again shows how alteration of the level of attenuation used, can enable the prediction based upon the elastic model to fit the prediction based around porous elastic theory.

Predictions made at greater grazing angles show similar results to those already shown. That is, at short ranges there is a large overall increase in magnitude of acoustic-to-seismic coupling ratio with increasing porosity (decreasing flow resistivity), whilst with increasing range the difference is much reduced.

Predictions previously shown have been based upon a spherical wave solution. The use of the full spherical wave solution requires extra computation time, due to the extra numerical calculations involved. There has been some discussion, therefore, concerning the merits of using a less computationally exhaustive plane wave solution.

The major difference between the two models is that in outdoor sound propagation plane waves at grazing angles do not predict the groundwave caused by the boundary loss factor ($F(\omega)$). This term makes significant contributions to the total field at grazing angles. At near normal incidence, however, there is little difference. Similarly, in seismic excitations, spherical waves impinging on a boundary at near grazing angles will excite extra boundary waves that will be significant at shorter distances.

This effect can be seen in Figure 2-12 and Figure 2-13. Figure 2-12 shows a prediction of acoustic-to-seismic coupling ratio using plane wave and spherical wave solutions. Here, the geophone receiver is placed close to the air-ground interface. It can be seen that at low frequencies, especially less 150Hz, there are significant differences between the two predictions.

Figure 2-13 again shows a prediction of acoustic-to-seismic coupling ratio using plane wave and spherical wave solutions, but here the geophone was placed close to the centre of the ground layer. It can be seen that both predictions give almost identical solutions. Both plots use values given in Table 2-6 to describe the ground.

A more thorough investigation was undertaken to highlight numerical differences between spherical and plane wave porous elastic theory. Here, the variation of compressional and shear wave velocity, flow resistivity and porosity on the acoustic-to-seismic coupling spectra predicted by each model was studied.

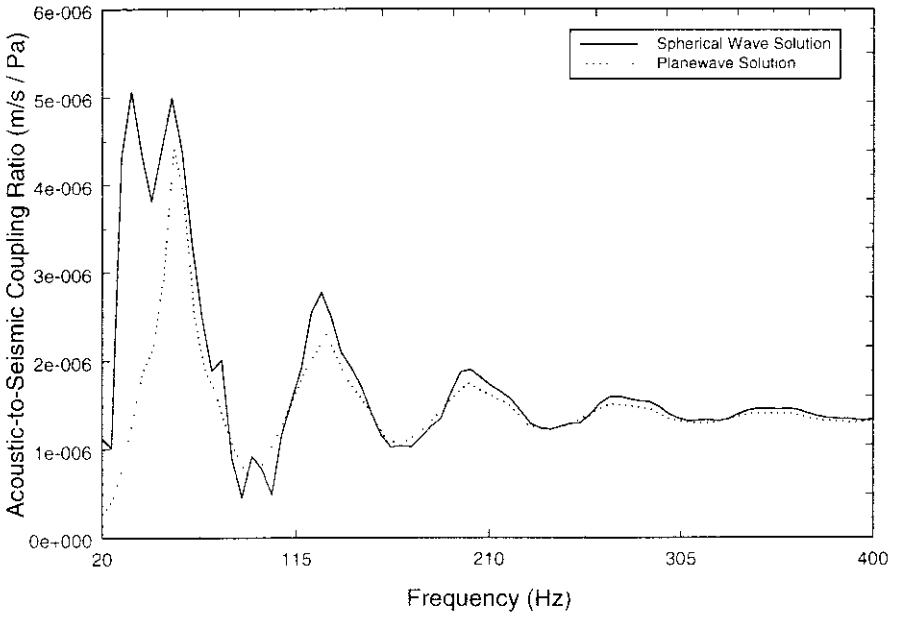

Figure 2-12. Prediction of acoustic-to-seismic coupling ratio using planewave and spherical wave solutions. Geophone is close to the air-ground boundary.

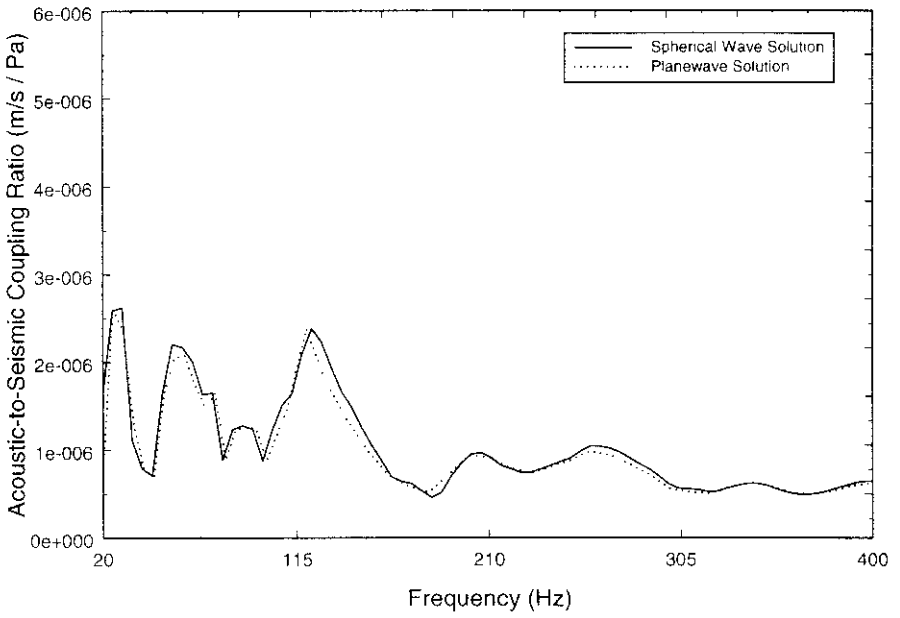

Figure 2-13. Prediction of acoustic-to-seismic coupling ratio using planewave and spherical wave solutions. Geophone is at the center of the ground layer.

	Layer	Substrate
P-wave speed (m/s)	270	530
S-wave speed (m/s)	190	325
Flow resistivity (Pa sm^{-2})	360000	36000000
Porosity	0.27	0.0027
Grain shape factor	0.5	0.5
Soil density (kg/m^3)	1700.0	2650.0
Layer thickness (m)	4.0	∞
Attenuation (V_p)	0.048	0.048
Attenuation (V_s)	0.0175	0.0175
Dynamic viscosity of air (Nsm^{-2})	1.81×10^{-5}	
Source height (m)	0.2	
Range (m)	5.0	
Microphone height (m)	0.05	
Geophone depth (m)	-0.05	
Frequency range (Hz)	20 – 400	
Speed of sound in air	344.0	

Table 2-6. Parameters used to highlight the differences between spherical and plane wave porous elastic theory (Figure 2-12 and Figure 2-13).

It was believed that large differences would occur at compressional wave velocities in the ground close to that of the speed of sound in air and low flow resistivites. As such, P-wave velocities used for the calculations ranged from 300 to 1000m/s in 50m/s intervals, with a V_s/V_p ratio of 0.5 used throughout. The range of flow resistivities used was from 10000 to 100000 MKS Rayls in 9000 MKS Rayls intervals with the respective porosities calculated using (Hovem and Ingram, 1979):

$$R_s = \frac{180\eta}{d^2} \times \frac{(1-\Omega)^2}{\Omega^3} \qquad \textit{(Eq. 2-79)}$$

where:

R_s = flow resistivity

η = kinematic fluid viscosity

Ω = porosity

and it is assumed that the solid grains are spherical.

For this investigation the ground was described using the parameters given in Table 2-7.

	Layer	Substrate
P-wave speed (m/s)	Variable	2000.0
S-wave speed (m/s)	Variable (dependent upon Vp)	1200.0
Flow resistivity (Pa sm^{-2})	Variable	1000000
Porosity	Variable (dependent upon R_s)	0.0027
Grain shape factor	0.5	0.5
Soil density (kg/m^3)	1700.0	2650.0
Layer thickness (m)	2.0	∞
Attenuation (V_p)	0.048	0.048
Attenuation (V_s)	0.0175	0.0175
Dynamic viscosity of air (Nsm^{-2})	1.81×10^{-5}	
Source height (m)	5.0	
Microphone height (m)	0.05	
Geophone depth (m)	-0.05	
Angles of incidence (^{0})	1, 2, 3, 4, 5, 10, 15, 30, 45, 60, 75	
Frequency range (Hz)	100 – 500	
Speed of sound in air (m/s)	344.0	

Table 2-7. Parameters used to highlight differences between spherical and place wave solutions.

Figure 2-14 to Figure 2-19 give an example set of results from this study. The figures show the differences in acoustic-to-seismic coupling ratio between predictions based upon plane wave and spherical wave solutions with increasing flow resistivity for a range of compressional wave velocities and frequencies and for a range of grazing angles.

The examples shown give the results of the lower compressional wave velocities of 300m/s and 400m/s at frequencies of 100, 200 and 300Hz over the range of flow resistivities used.

Figure 2-14 shows the predicted acoustic-to-seismic coupling at 100Hz for a ground having a compressional wave speed of 300m/s. The plot shows that there is little variation in the coupling magnitude predicted using the plane wave model, yet there appears some variation between the coupling ratio as defined by the spherical wave solution. There does not appear to be any relationship between the difference in the predictions of the two models and the grazing angle, although the difference is greater at lower flow resistivities.

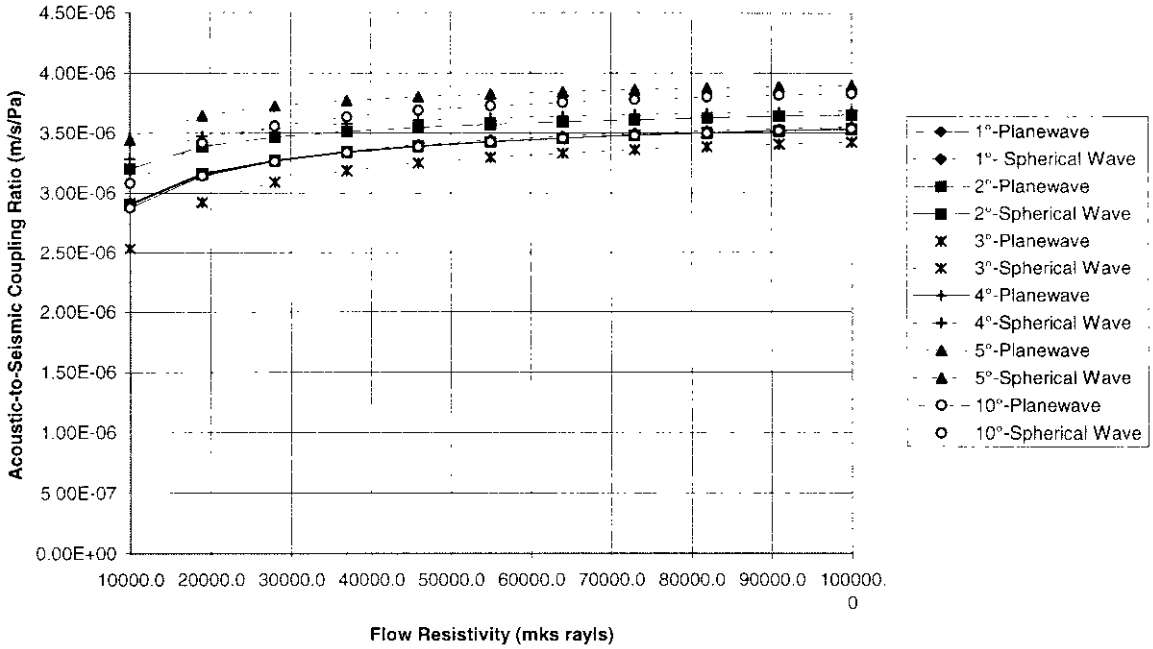

Figure 2-14. Differences in acoustic-to-seismic coupling ratio between predictions based upon plane wave and spherical wave solutions. (P-wave = 300m/s, Frequency = 100Hz).

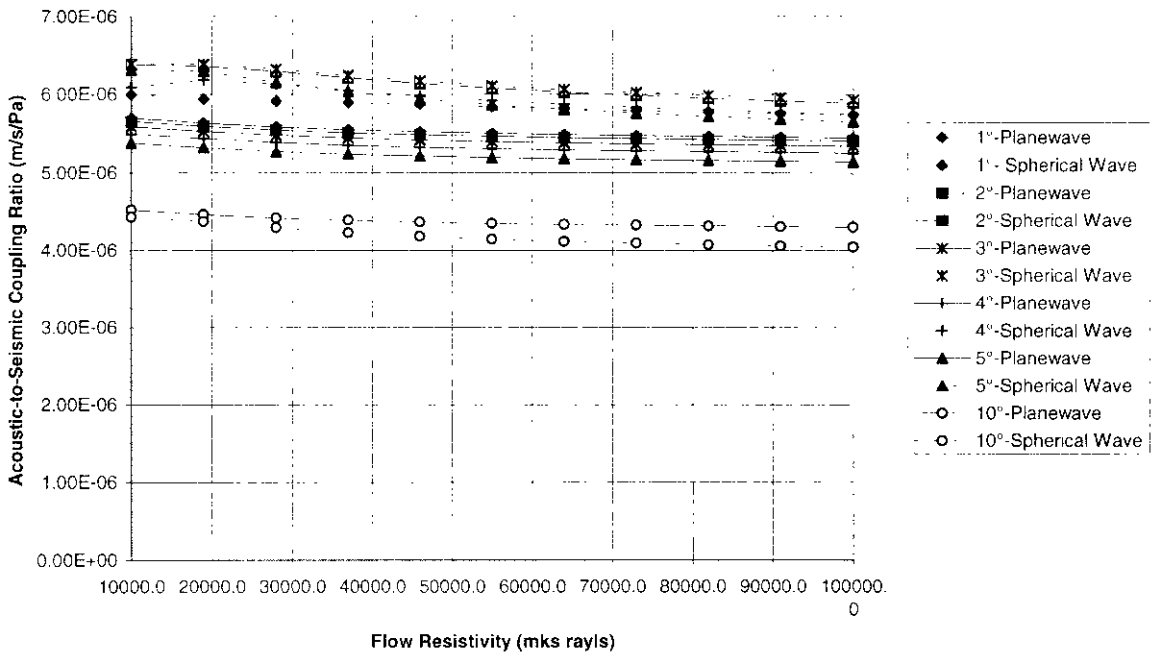

Figure 2-15. Differences in acoustic-to-seismic coupling ratio between predictions based upon plane wave and spherical wave solutions. (P-wave = 400m/s, Frequency = 100Hz).

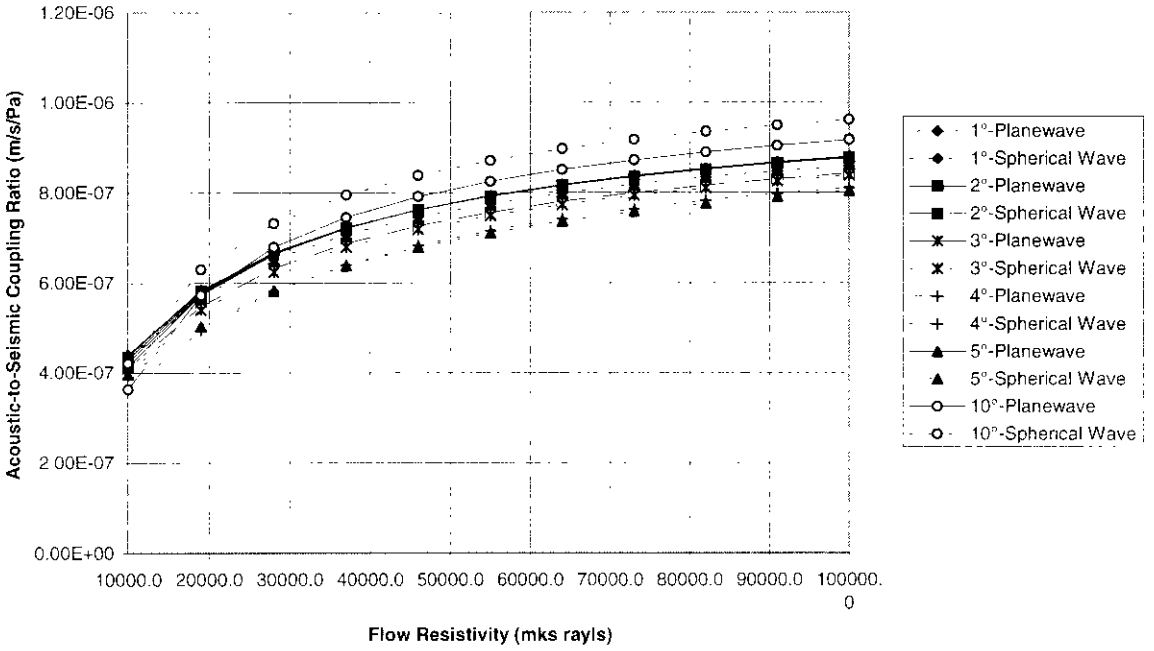

Figure 2-16. Differences in acoustic-to-seismic coupling ratio between predictions based upon plane wave and spherical wave solutions. (P-wave = 300m/s, Frequency = 200Hz).

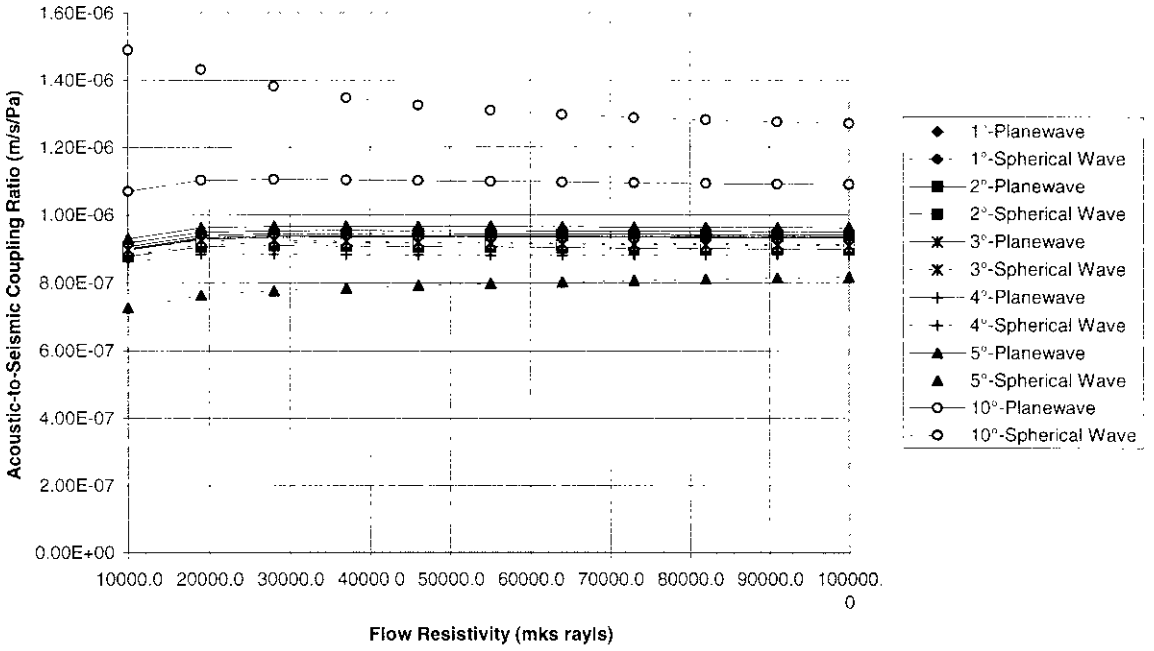

Figure 2-17. Differences in acoustic-to-seismic coupling ratio between predictions based upon plane wave and spherical wave solutions. (P-wave = 400m/s, Frequency = 200Hz).

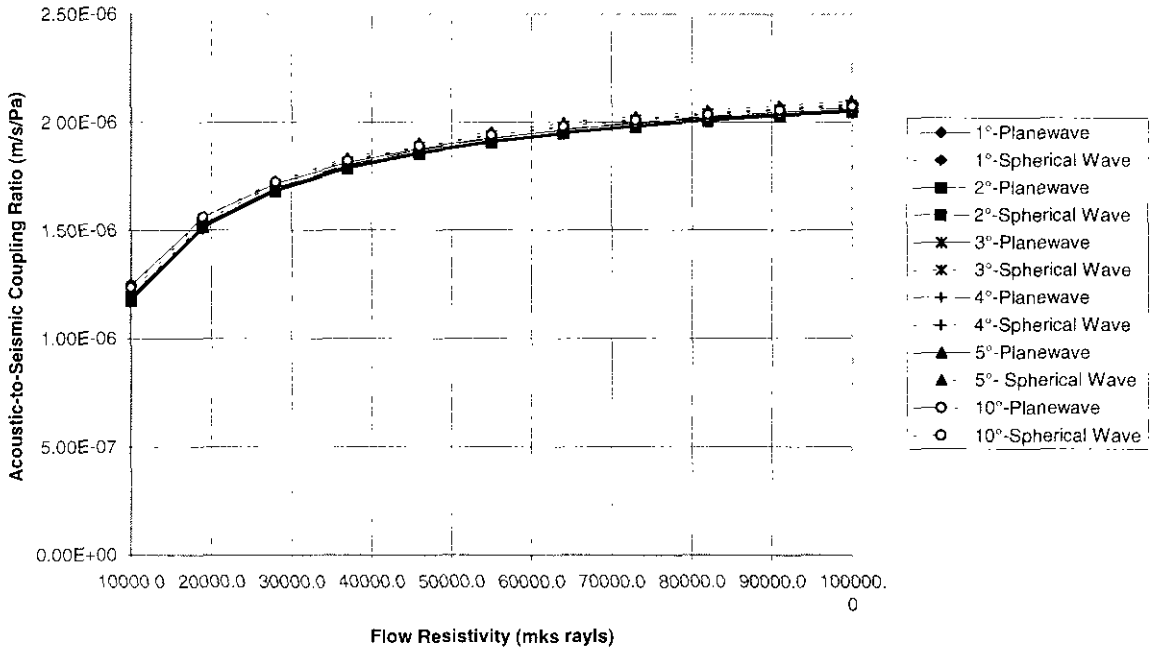

Figure 2-18. Differences in acoustic-to-seismic coupling ratio between predictions based upon plane wave and spherical wave solutions. (P-wave = 300m/s, Frequency = 300Hz).

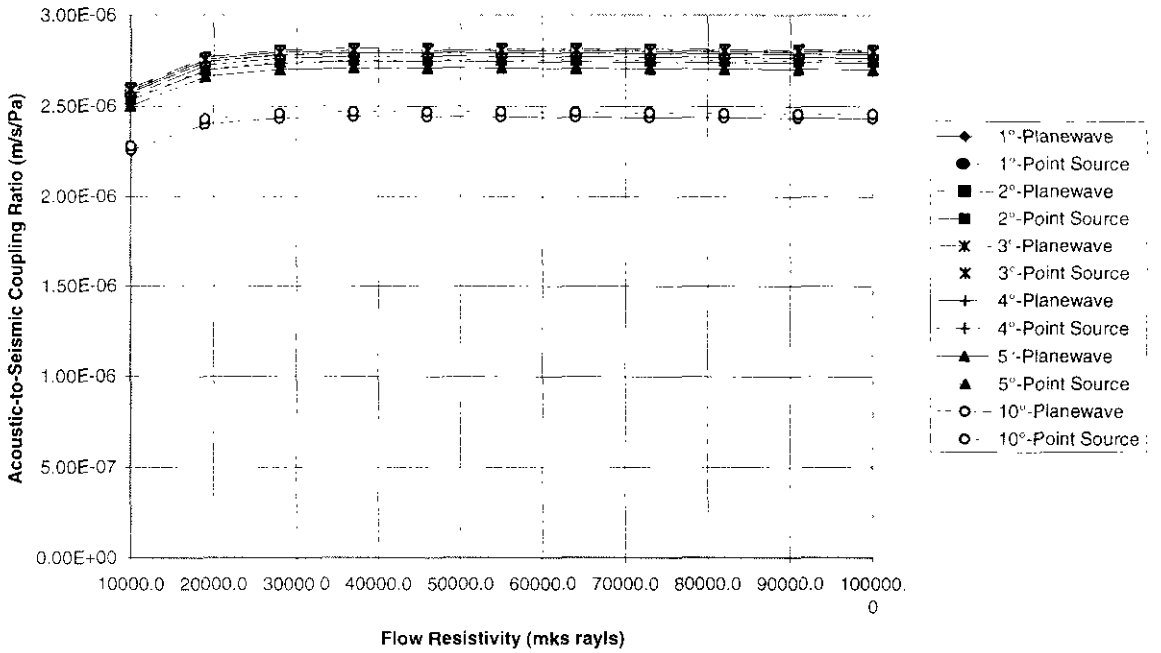

Figure 2-19. Differences in acoustic-to-seismic coupling ratio between predictions based upon plane wave and spherical wave solutions. (P-wave = 400m/s, Frequency = 300Hz).

Increasing the compressional wave velocity to 400m/s, shown in Figure 2-15, shows that again, plane wave theory predicts roughly equal magnitudes of coupling ratio with increasing flow resistivity, with the spherical wave coupling ratio showing a larger magnitude. The exception is the result for a grazing angle of 10°, where both models show a result much lower than the previous grazing angles. Again, there is a small decrease in the difference between the two models for each grazing angle with increasing flow resistivity.

With increasing frequency the difference between the predictions, made using the two models becomes closer. This can be seen in Figure 2-16 which shows the predictions for a frequency of 200Hz, with a ground layer having a compressional wave velocity of 300m/s. Again, the predictions made using the plane wave model show similar magnitudes for increasing flow resistivity, with the difference between the two models being smaller than at 100Hz.

Figure 2-17 which shows the results of a 400m/s ground layer at 200Hz shows a similar narrowing of the difference between the two models, which can also be seen at the higher frequencies shown in Figure 2-18 and Figure 2-19.

The overall results follow the trends observed in the example figures. It appears that at the grazing angles considered that the plane wave model predicts very little variation in acoustic-to-seismic coupling with increasing grazing angle. The difference between the two models appears greatest where the ground compressional wave velocity is close to the speed of sound in air and that the difference becomes less as this velocity increases. Also, that the differences also decrease with increasing frequency.

2.5 Conclusions

Four models have been described which can be used for the prediction of acoustically-induced ground motion. These ranged from simplistic models based on plane waves and non-porous elastic layer resonances to more complicated models which consider full-wave propagation in layered porous and elastic solids.

Comparisons with previously published data (Van Hoof, 1986) show that those models based upon full-wave propagation give a more accurate description of the acoustic-

to-seismic coupling ratio. Both the full-wave propagation model based upon elastic porous media and the model based upon elastic media predict the same values of extrema.

In the porous elastic model the predicted magnitude of the coupling ratio has been found to be dependent upon the ground parameters, porosity and flow resistivity, and upon the value of attenuation of the compressional and shear waves. Alteration of the value of attenuation input into either model allows agreement of the magnitude of the coupling ratio between the two models.

Since the value of attenuation used is an arbitrary value and since the difference between the two values used in each model is within the reasonable range of values of attenuation, claims of the superiority of one model against the other can not be justified on this ground. However, Attenborough *et al.* (1995) showed that the porous elastic model can be used to predict acoustic propagation above a rigid porous ground, whereas the elastic model is mutually exclusive with the rigid porous theory.

Figure 2-20 shows a plot of excess attenuation predicted using rigid porous, porous elastic and elastic theories. The plot shows the analogous predictions of the rigid porous and porous elastic models. The plot also shows the marked difference between the two models and the elastic model. The almost flat 6dB prediction of the elastic model shows that, here the ground is taken at totally reflecting.

	Rigid Porous Layer	**Porous Elastic Layer**	**Elastic Layer**	**Substrate**
P-wave speed (m/s)	5000.0	500.0	500.0	1000.0
S-wave speed (m/s)	3200.0	320.0	320.0	640.0
Flow resistivity (Pa sm^{-2})	5000	5000	---	5000000
Porosity	0.4	0.4	---	0.004
Grain shape factor	0.5	0.5	0.5	0.5
Soil density (kg/m^3)	130000	1300	1300	2700
Attenuation	100.325	0.0325	0.325	0.0125
Layer thickness (m)	1.0	1.0	1.0	∞
Dynamic viscosity of air (Nsm^{-2})	1.81×10^{-5}	1.81×10^{-5}	1.81×10^{-5}	
Source height (m)	0.5	0.5	0.5	
Microphone height (m)	0.1	0.1	0.1	
Speed of sound in air (m/s)	344.0	344.0	344.0	

Table 2-8. Parameters used for the prediction of excess attenuation using rigid porous, porous elastic and elastic theories.

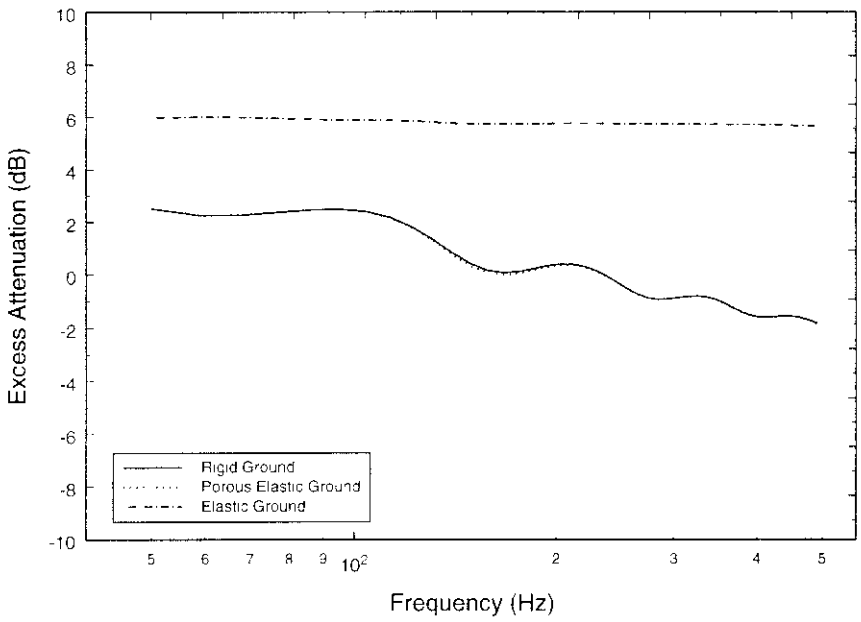

Figure 2-20. Prediction of excess attenuation using rigid porous, porous elastic and elastic models.

Thus, it appears that the porous elastic model is a more complete theory for the modelling of acoustic and acoustic-to-seismic data. In view of this, it has been decided to use the porous-elastic model to predict measurements of acoustic-to-seismic coupling ratio taken as part of this thesis.

A numerical investigation into differences between spherical wave and a plane wave approximation of the porous elastic model shows that close to the air-ground boundary predictions of acoustic-to-seismic coupling ratio show marked difference between the two. The major differences are seen at lower frequencies, below 150Hz, where peaks in the coupling ratio, most likely attributed to the presence of acoustically-induced interface waves, are not predicted by the plane wave solution.

Measurements taken close to the centre of a deep ground layer show very little difference between the two models.

The more detailed numerical search shows that the largest differences occur between the models at low frequencies, less than 300Hz, and where the ground compressional wave velocity is close to the speed of sound in air.

Chapter 3

Algorithms for the Deduction of Soil Properties

3 Introduction

This chapter is concerned with the methods for deducing soil properties from acoustic-to-seismic measurements. In acoustic-to-seismic analysis there are basically two sources of information concerning the subsurface: wave travel times and amplitude. From these parameters, material properties can be deduced using either empirical or theoretical expressions.

The emphasis of this project was the measurement of both of these two basic sources of information. Measurements were taken both indoors and outdoor. The majority of the indoor study consisted of laboratory measurements of the two dilatational waves and the one rotational wave propagating through an air-filled unconsolidated soil. The outdoor study consisted of measurements of the acoustic-to-seismic coupling ratio, i.e. the ratio of the sound pressure amplitude at the surface to the vertical particle velocity amplitude measured at some depth in the ground. Preliminary measurements were also made of acoustically induced surface waves, with the travel time and subsequent phase velocity being of most interest.

3.1 Algorithms Used For Indoor Measurements

This study focused on the measurement of the bulk elastic properties and hydrodynamic properties of an unconsolidated air filled porous medium.

Measurements were made of the three possible body waves in the material (shear wave (S), Type I dilatational (P) and Type II dilatational (P)). The wave speed and attenuation of the Type II P-wave is most sensitive to the hydrodynamic properties of the material. Flow resistivity and tortuosity can be evaluated using a rigid frame model. The

wave speed of the Type I P-wave and S-wave are controlled largely by the bulk elastic properties and the density of the component phases.

Two main experiments were undertaken in the Indoor Tank. Five cycle tone bursts were used for the measurement of Type I P-wave and S-wave, whilst MLS (Maximum Length Sequence) was used for the measurement of Type II P-wave. These experiments will be described in detail in Chapter 5 with the results and analysis given in Chapter 6.

Elastic wave models of wave propagation predict the presence of one compressional (P-Wave) and one shear (S-Wave) wave. Both these waves are "Body Waves" and are non-dispersive, i.e. all frequency components in a wave-train or pulse travel though any material at the same velocity, determined only by the elastic moduli (bulk and shear) and density of the material. In an ideal material there is no attenuation.

Attenuation may be introduced by allowing the elastic moduli of the material to be complex valued. However, studies show that it is very difficult to associate the measured attenuation (imaginary part of the moduli) and the actual physical mechanism responsible. Most soils are porous and contain a mixture of fluids. This simplified approach cannot adequately account for the interaction of solid and fluid.

Theoretical models have therefore been produced for wave propagation which involve two coupled and interacting continua. The most popular of these "dual wave models" was developed by Biot. The model predicts the presence of two dilatational waves and one shear wave and has been incorporated into the FFLAGS model described in Chapter 2. The two dilatational waves are usually referred to as the fast or Type I and the slow or Type II wave.

The complete description of wave propagation through porous media requires between six and thirteen macroscopic parameters. Solving of the coupled differential equations makes obtaining relationships for wave speeds and attenuation extremely difficult. Inverting these expressions for material properties is even more difficult and error prone. In view of this, some limiting case must be considered to allow inversion for the material parameters to be undertaken.

Limiting Case 1: A Model of Phase Constituent Motion

Numerical calculations (Hickey, 1990; Albert, 1993b) of the Type I P-wave and S-wave using dual wave theories have shown that for many consolidated porous materials the solid and fluid phase are strongly coupled. The component displacements associated with the deformation of these waves have approximately the same magnitude and phase. The coupling does not degenerate with increasing frequency with some occurrence of relative motion. However, an approximate low frequency model (below a few kilohertz) for the Type I P-wave and S-wave assumes that the solid and fluid displacements or velocities are equal, i.e.,

$$u_s = u_f = u. \qquad \textit{(Eq. 3-1)}$$

In such a limit the dissipation associated with fluid flow, as predicted by Biot theory, is zero. In the de la Cruz & Spanos model (1985, 1989b), however, the equations contain several terms representing dissipation associated with the viscosity of the fluid. Using Equation 3-1 and combining the standard equations of motion it is possible to construct the wave equation

$$\rho_m \frac{\partial^2 u}{\partial t^2} = K_m^* \nabla\nabla . u + \mu_m^* (\nabla^2 u + \frac{1}{3}\nabla\nabla . u) \qquad \textit{(Eq. 3-2)}$$

where the material density is

$$\rho_m = (1-\eta_0)\rho_s + \eta_0 \rho_f \qquad \textit{(Eq. 3-3)}$$

The complex material shear modulus (assuming $e^{-i\omega t}$ time dependence) is given by

$$\mu_m^* = \mu_m - i\omega\mu_f \left(1 - \frac{\mu_m}{\mu_s}\right) \qquad \textit{(Eq. 3-4)}$$

where μ_m is the macroscopic frame shear modulus. The complex bulk modulus is given by:

$$K_m^* = K_{md} - i\omega\xi_f \left(\frac{K_{md} - K_s}{K_f - K_s}\right) \qquad \textit{(Eq. 3-5)}$$

The calculation of phase velocity of a wave propagating through a medium described by complex material coefficients is cumbersome because one has to take the square root of complex number, more useful expressions are obtained for the wavenumber squared.

Assuming a plane shear wave propagating in the x direction, the shear wavenumber calculated using Equation 3-2, is

$$k_{sh}^2 = \frac{\omega^2 \rho_m \left[\mu_m - i\omega\mu_f \left(1 - \frac{\mu_m}{\mu_s} \right) \right]}{\mu_m^2 + \omega^2 \mu_f^2 \left(1 - \frac{\mu_m}{\mu_s} \right)^2} \qquad \textit{(Eq. 3-6)}$$

For all porous materials $\mu_m \leq (1-\eta_0)\mu_s$. For air, the viscosity is of the order of 10^{-5} Pa.s so that for low frequency the second term in the denominator is much less than the first term and may be disregarded. The real part of the shear wavenumber squared then becomes

$$\mathrm{Re}(k_{sh}^2) = \frac{\omega^2 \rho_m}{\mu_m} \qquad \textit{(Eq. 3-7)}$$

Knowing the bulk density of the material Equation 3-7 can be inverted to obtain the material shear modulus. The imaginary part of the shear wavenumber squared is

$$\mathrm{Im}(k_{sh}^2) = \frac{\omega^2 \rho_m}{\mu_m^2} \left[\omega\mu_f \left(1 - \frac{\mu_m}{\mu_s} \right) \right] \qquad \textit{(Eq. 3-8)}$$

Equation 3-8 might be used to obtain a value for the shear modulus of the solid grains. In the case of unconsolidated sands $\mu_m << \mu_s$ and Equation 3-8 then becomes

$$\mathrm{Im}(k_{sh}^2) = \frac{\omega^2 \rho_m}{\mu_m^2} \left[\omega\mu_f \right] \qquad \textit{(Eq. 3-9)}$$

and the ratio of imaginary to real part of the shear wavenumber is

$$\frac{\mathrm{Im}(k_{sh}^2)}{\mathrm{Re}(k_{sh}^2)} = \frac{\omega\mu_f}{\mu_m} \qquad \textit{(Eq. 3-10)}$$

This can be inverted for the material shear modulus without knowing the bulk density of the material. However, the use of the imaginary part of the shear wavenumber squared, i.e. Equations 3-8 to 3-10, requires that the dominant attenuation mechanism be associated solely with fluid viscosity. Hickey and Sabatier (1996) have shown that for air and water-filled porous materials this type of attenuation accounts only for a small amount of the measured shear wave attenuation. Therefore, alternate attenuation mechanisms must be examined and incorporated before the imaginary part is of any use.

Following the same procedure as above, the compressional wavenumber squared is:

$$k_p^2 = \frac{\omega^2 \rho_m \left[K_{ud} + \frac{4}{3}\mu_m + i\omega \left(\xi_f \left(\frac{K_s - K_{ud}}{K_s - K_f} \right) + \frac{4}{3}\mu_f \left(1 - \frac{\mu_m}{\mu_s} \right) \right) \right]}{\left(K_{ud} + \frac{4}{3}\mu_m \right)^2 + \omega^2 \left(\xi_f \left(\frac{K_s - K_{ud}}{K_s - K_f} \right) + \frac{4}{3}\mu_f \left(1 - \frac{\mu_m}{\mu_s} \right) \right)^2} \qquad \textit{(Eq. 3-11)}$$

It has been deduced (Greenspan, 1959) from acoustic absorption experiments that the bulk viscosity of air $\xi_f \cong 0.60\mu_f$. Therefore, for low frequencies the second term in the denominator may be ignored. The real part of k_p^2 is then given by

$$\mathrm{Re}(k_p^2) = \frac{\omega^2 \rho_m}{K_{ud} + \frac{4}{3}\mu_m} \qquad \textit{(Eq. 3-12)}$$

and the imaginary part of k_p^2 is

$$\mathrm{Im}(k_p^2) = \frac{\omega^3 \rho_m \left(\xi_f \left(\frac{K_s - K_{ud}}{K_s - K_f} \right) + \frac{4}{3}\mu_f \left(1 - \frac{\mu_m}{\mu_s} \right) \right)}{\left(K_{ud} + \frac{4}{3}\mu_m \right)^2} \qquad \textit{(Eq. 3-13)}$$

Knowing the bulk density and the material shear modulus, equation 3-12 can be used to determine the undrained bulk modulus of the porous frame. Again, forward model calculations for air- and water-filled porous materials show that the attenuation incorporated above accounts for only a very small amount of the measured compressional wave attenuation.

Using the equations above, the material shear modulus and undrained bulk modulus of a porous material may be determined if the bulk density of the material is already known. It is preferable to use the real part of the wavenumber squared, and not the imaginary part as it is strongly dependent upon the attenuation mechanisms accounted for in the model. These mechanisms are not sufficient to account for the measured attenuation and therefore use of the imaginary parts would lead to the results being suspect.

Ignoring attenuation reduces the inversion to that based on simple elastic theory. This approach uses seismic wave velocities and material densities. It can be shown that the rates at which seismic waves propagate through elastic media are dictated by the elastic moduli and densities of the materials through which they pass. As a broad generalisation, velocities increase with increasing density. The velocity of propagation V, through an elastic material is:

$$v = (Appropriate\ elastic\ moduli\ /\ density\ (\rho)\ )^{1/2} \qquad (Eq.\ 3\text{-}14)$$

Velocity of P-Waves is:

$$v_p = \left(\frac{K + 4/3\mu}{\rho} \right)^{1/2} \qquad (Eq.\ 3\text{-}15)$$

Velocity of S-Waves is:

$$v_S = \left(\frac{\mu}{\rho} \right)^{1/2} \qquad (Eq.\ 3\text{-}16)$$

Determination of the s-wave velocity and knowledge of the material density allows the shear modulus to be determined. This can then be used in conjunction with the p-wave velocity for the determination of the bulk modulus.

Limiting Case 2: Rigid Frame Limit

The acoustical properties of the ground may be modelled as those of a rigid-porous material and characterised by a complex density, containing the influence of viscous effects, and a complex compressibility, containing the influence of thermal effects. Thermal effects are much greater in air-filled materials than in water-filled materials. The precise forms of these quantities may be obtained by considering a microstructure of narrow pores or tubes. This offers a more rigorous basis for ground impedance and propagation constant prediction than the semi-empirical approaches.

It has been shown (Stinson, 1991) that the complex density in a uniform pore of arbitrary shape can be written as

$$\rho(\omega) = \frac{\rho_0}{H(\lambda)} \qquad (Eq.\ 3\text{-}17)$$

where λ is a dimensionless parameter. The complex compressibility is then given by:

$$C(\omega) = (\gamma P_0)^{-1} \left[\gamma - (\gamma - 1) H\left(\lambda \sqrt{(N_{pr})} \right) \right] \qquad (Eq.\ 3\text{-}18)$$

where $(\gamma P_0)^{-1} = (\rho_o c_o^2)^{-1}$ is the adiabatic compressibility of air.

$H(\lambda)$ has been calculated for many ideal pore shapes (Stinson, 1991; Champoux and Stinson, 1992; Allard, 1993; Attenborough, 1993) including circular, capillary, infinite sided slit, equilateral triangle and rectangle. Having calculated the complex density $(\rho(\omega))$ and complex compressibility $(C(\omega))$ of the individual pores then the bulk propagation constant $(k_b(\omega))$ and relative characteristic impedance $(Z_c(\omega))$ of the bulk porous material can be calculated from

$$k_b(\omega) = \omega\left[(\tau^2)\rho(\omega)C(\omega)\right]^{0.5} \qquad \textit{(Eq. 3-19)}$$

$$Z_c(\omega) = (\rho_f c_f)^{-1}\left[(\tau^2/\Omega^2)\rho(\omega)/C(\omega)\right]^{0.5} \qquad \textit{(Eq. 3-20)}$$

Attenborough (1983) scaled the complex density function directly between pore shapes and introduced an adjustable dynamic pore shape parameter (s_A). For example, the bulk complex density function for cylindrical pore functions is

$$\rho_b(\lambda) = (\tau^2/\Omega)\rho_0\left[1-(2/\lambda\sqrt{i})J_1(\lambda\sqrt{i})/J_0(\lambda\sqrt{i})\right] \qquad \textit{(Eq. 3-21)}$$

Where

$$\lambda = s_A\left(\frac{8\rho_f\omega\tau^2}{\Omega R_\backslash}\right)^{1/2}$$

From these equations simple approximations for characteristic impedance and propagation constant in the limit of small λ (corresponding to low frequencies and high flow resistivities) can be deduced. The approximation (based on approximation of cylindrical pore functions) for the propagation constant may be written as,

$$k_b(f) = \frac{2\pi f}{c_0}\sqrt{\gamma}\left[\left(\frac{4}{3}-\frac{(\gamma-1)}{\gamma}N_{pr}\right)\tau+\frac{i2\sigma_{eff}}{\pi f\rho_0}\right]^{1/2} \qquad \textit{(Eq. 3-22)}$$

Where

γ= the ratio of specific heats

N_{pr} = the Prandtl number

c_o = speed of sound in air

ρ_o = the density of air

In this form k_b is complex and thus solving for ρ or σ_{eff} would be difficult. However, squaring Equation 3-22 gives

$$\mathrm{Re}(k_b^2) = k_r^2 - k_i^2 = \gamma \frac{4\pi^2 f^2}{c_o^2} a\tau \qquad \textit{(Eq. 3-23)}$$

$$\mathrm{Im}(k_b^2) = 2k_r k_i = \gamma \frac{8\pi f \sigma_{eff}}{c_o^2 \rho_0} \qquad \textit{(Eq. 3-24)}$$

where

$$a = \left(\frac{4}{3} - \frac{(\gamma - 1)}{\gamma} N_{pr} \right)$$

Combining these two equations with phase and magnitude measurements, gives τ and σ_{eff} in terms of measurable and known quantities.

$$\tau = \frac{c_0^2 \left(k_r^2 - k_i^2\right)}{\gamma 4\pi^2 f^2 a} \qquad \textit{(Eq. 3-25)}$$

$$\sigma_{eff} = \frac{c_0^2 \rho_0 k_r k_i}{\gamma 4\pi f} \qquad \textit{(Eq. 3-26)}$$

For this approximation $\sigma_{eff} = \Omega S_p^2 R_s$

where

S_p = Pore shape factor

R_s = Flow resistivity

The above formulation is for normal incidence. However, when the speaker is positioned off to one side then a modification to the theory must be made. The set-up is more typical for outdoor experiments. Where the angle of incidence is θ_i, the tortuosity (τ') becomes

$$\tau' = \tau + \frac{\sin^2 \theta_i}{\left(\frac{4}{3} - \frac{(\gamma - 1)}{\gamma} N_{pr} \right) \gamma} \qquad \textit{(Eq. 3-27)}$$

The flow resistivity remains unchanged. For more details of the formulation see Sabatier *et al.* (1996).

3.1.1 Measurements

The MLS measurement consists of a measurement of phase difference and relative magnitude of the signal at the appropriate sensor with respect to some other sensor.

A time harmonic plane wave propagating in the x direction with a complex wave number Re(k)+i Im(k) is written as,

$$e^{-\mathrm{Im}(k)x}e^{i(\mathrm{Re}(k)x-\omega t)} \qquad \textit{(Eq. 3-28)}$$

The real part of the wavenumber can be determined from the phase difference, $\Delta\Phi$, by,

$$\mathrm{Re}(k)=\frac{\Delta\Phi}{\Delta x} \qquad \textit{(Eq. 3-29)}$$

where Δx is the distance between receivers. The imaginary part of the wavenumber can be obtained from the relative magnitude, $\ln|A_2/A_1|$, by,

$$\mathrm{Im}(k)=-\frac{\ln|A_2/A_1|}{\Delta x} \qquad \textit{(Eq. 3-30)}$$

For the five cycle tone burst measurements, first break arrival time and peak-to-peak amplitudes were measured, from the signal received by the probe and the various geophones and microphones. Knowing the spatial separation between the sensors and the difference in arrival time, the wave speed or Re(k) may be determined by

$$\mathrm{Re}(k)=\frac{\omega}{c}=\frac{\omega\Delta t}{\Delta x} \qquad \textit{(Eq. 3-31)}$$

Table 3-1 gives a summary of the measurements undertaken in the Indoor Tank and the subsequent reduction of the data to give a number of soil properties.

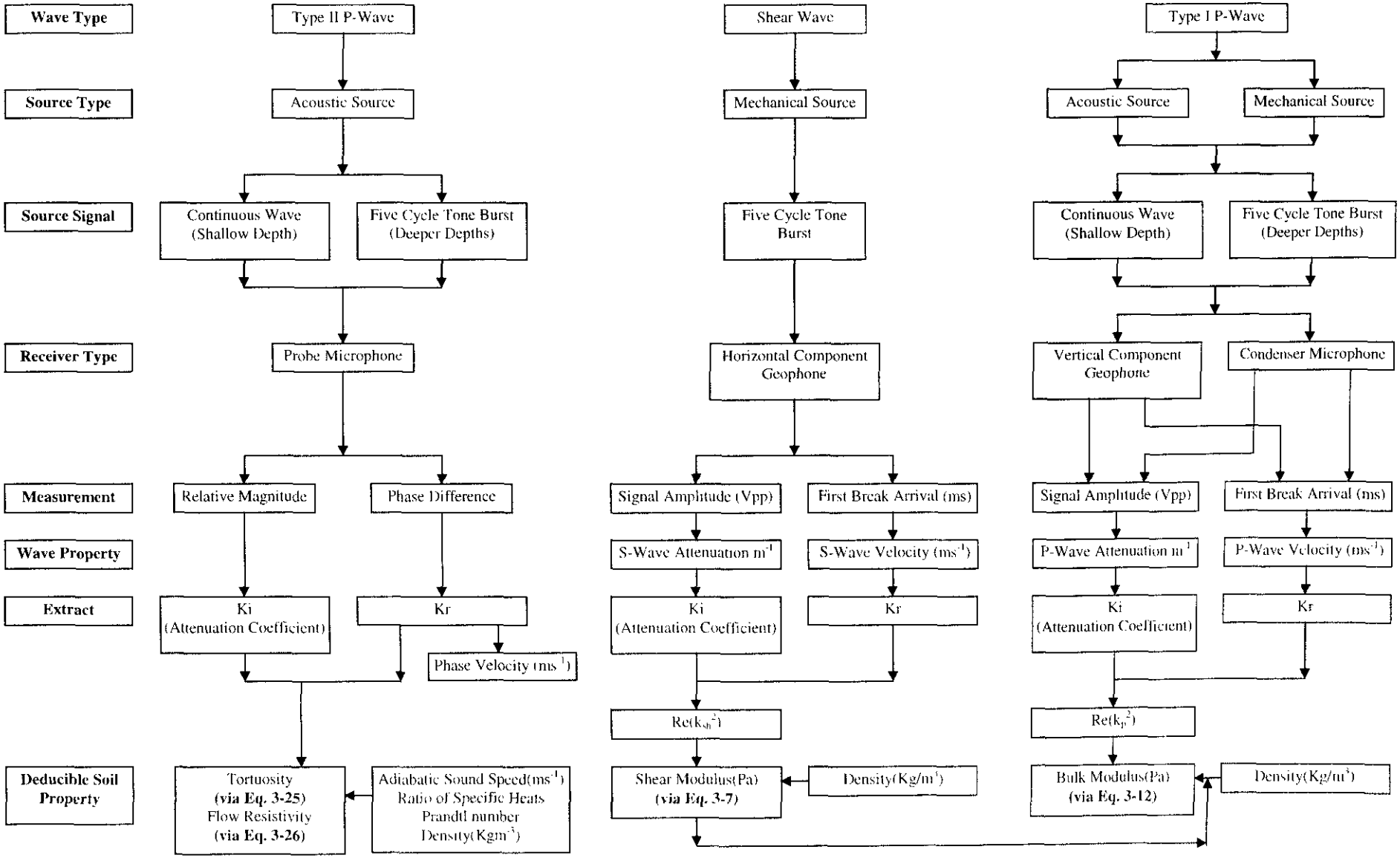

Table 3-1. Determination of Soil Properties Using Acoustic Techniques.

3.2 *Algorithms Used For Outdoor Measurements*

3.2.1 Acoustic-to-seismic coupling ratio

The theoretical formulations for predicting levels of acoustic-to-seismic coupling have been discussed in detail in Chapter 2.

The FFLAGS computer code for predictions of acoustic-to-seismic coupling in poro-elastic media has been shown to give the closest agreement with experimental data. Fitting the theoretical prediction to the experimental data requires the input of a number of soil properties. They are:

1. Number of ground layers
2. Flow Resistivity
3. Porosity
4. Compressional wave velocity
5. Shear wave velocity
6. Soil density
7. Layer thickness
8. Soil bulk modulus

As in the indoor tank experiment, knowledge of the material shear wave velocity and soil density allows the shear modulus to be determined.

3.2.2 Acoustically induced surface waves

Measurements were made of acoustically induced surface waves. The process will be described in Chapter 7 with the results and analysis to be found in Chapter 8.

The measurements include phase speed and wavelength determination for each input frequency. The process of converting the field dispersion curve to a Rayleigh velocity-depth relationship was undertaken using the wavelength-depth technique.

This technique is the simplest, and as such the least exact of the available methods. Its value is in its ease and quickness of use. To establish the depth profile, it is necessary to determine at what depth, z, the calculated phase velocity is representative of the propagation properties of the ground. Recall, that the amplitude of a Rayleigh wave diminishes with depth. In the wavelength-depth method the representative depth is taken as a fraction of the wavelength (λ). That is, λ / z is assumed to be a constant. A ratio of 2 is commonly used (Matthews *et al.*, 1996). Gazetas (1982) recommends that 4 is used at sites where the stiffness increases with depth, and that 2 is suitable at more homogeneous sites. He suggests that $\lambda / z = 3$ is a reasonable compromise.

To calculate the stiffness profile, the standard relationship between shear wave and Rayleigh wave velocity must be used, such that

$$v_s = p v_r \qquad \textit{(Eq. 3-32)}$$

where p is a constant derived from the solution of the Rayleigh equation, being dependent upon the value of Poisson's ratio (σ). For a value of σ=0.25 then p=1.088, whilst for σ=0.5 then p=1.047, showing that a poor estimation of σ has little effect on v_s. The shear modulus, μ, is related to the shear wave velocity by

$$\mu = \rho_b v_s^{\,2} \qquad \textit{(Eq. 3-33)}$$

Hence,

$$\mu = \rho_b p^2 v_r^{\,2} \qquad \textit{(Eq. 3-34)}$$

This permits a conversion from Rayleigh velocity depth profile to stiffness-depth profile. The stiffness values derived are usually denoted by μ_{max}. The values represent the very small strain stiffness, that is considered to be the maximum shear modulus exhibited by a material. μ_{max} can be used in subsequent calculations with only minor modifications.

Chapter 4

Experimental Site Location and In-situ Material Properties

4 Materials Used in the Study

One of the aims of this study was the development of a non-invasive acoustic method of determining soil properties. Consequently, it was necessary to directly ascertain the mechanical properties of the soils utilised, so that comparisons could be made with the acoustically derived values. Experiments were therefore undertaken, to assess soil properties for comparison purposes and for general classification. Throughout the project, eight different sediments were used. These included a coarse pea-gravel, fine and coarse sands and four agricultural soils.

As part of any engineering or sedimentological investigation, a description of the material under analysis is required both in the field and in the laboratory. In the light of this, materials used in the outdoors experimental portion of the study were given in-situ descriptions and then sampled. A sample of the material was taken to the soils laboratory of the University of Wales, Bangor for sedimentological classification. The work was carried out during the period November 1998 to January 1999.

The tests undertaken to assess soil properties for comparison purposes were air and water permeability (constant head test for the unconsolidated materials and a modified Aberdeen test for the consolidated materials), porosity (gravimetric method), and tortuosity (Jackson cell). In addition, a modified Drevnich resonant column test was carried out upon several of the materials for the measurement of dynamic shear modulus.

As well as those tests required for general classification (particle size analysis and consistency), a number of further tests were carried out. These included natural sediment properties (natural moisture content, specific gravity and colour) and shear strength determination. The consolidated materials were also tested for organic content.

Indoor measurements were undertaken at the Open University and the American National Centre for Physical Acoustics (NCPA), based at the University of Mississippi. Experiments at the Open University were conducted using a graded coarse dried silica sand

and a relatively poorly graded medium sand. This medium sand was from the HMC Stone Lane Quarry that will be described in Section 4.1.2.

The material used at NCPA, was an agricultural Loam found locally to Oxford, Mississippi that had been sieved to remove the coarse particles and then crushed until it was a fine powder. Unfortunately, due to constraints only a small sample of this material was available and so was only tested for a limited number of parameters.

Outdoor measurements were performed at three sites; the Acoustics Research Group test area at the Open University, where the in-situ material is a medium Gravel; HMC Stone Lane Quarry where the in-situ material is a medium Sand; and at HRI Wellesbourne, where the in-situ material consisted of three differing agricultural soils.

4.1 Outdoor Study Areas

4.1.1 Acoustics Research Group Test Site

Provisional outdoor experiments were conducted in a trial pit at the Open University. The pit is approximately 3.5m x 3m x 2.0m. As part of the design, a drainage system was provided to minimise the build up of ground water. It is surrounded on all sides by an area of flat grassland for approximately 10m, where on one side there is a line of trees and on another, there is a small building. A view of the site can be seen in Figure 4-1. The pit is filled with a coarse pea-gravel.

Field Description: Loose light grey subangular sandy fine to coarse GRAVEL with occasional presence of roots. (BS 5930, 1981)

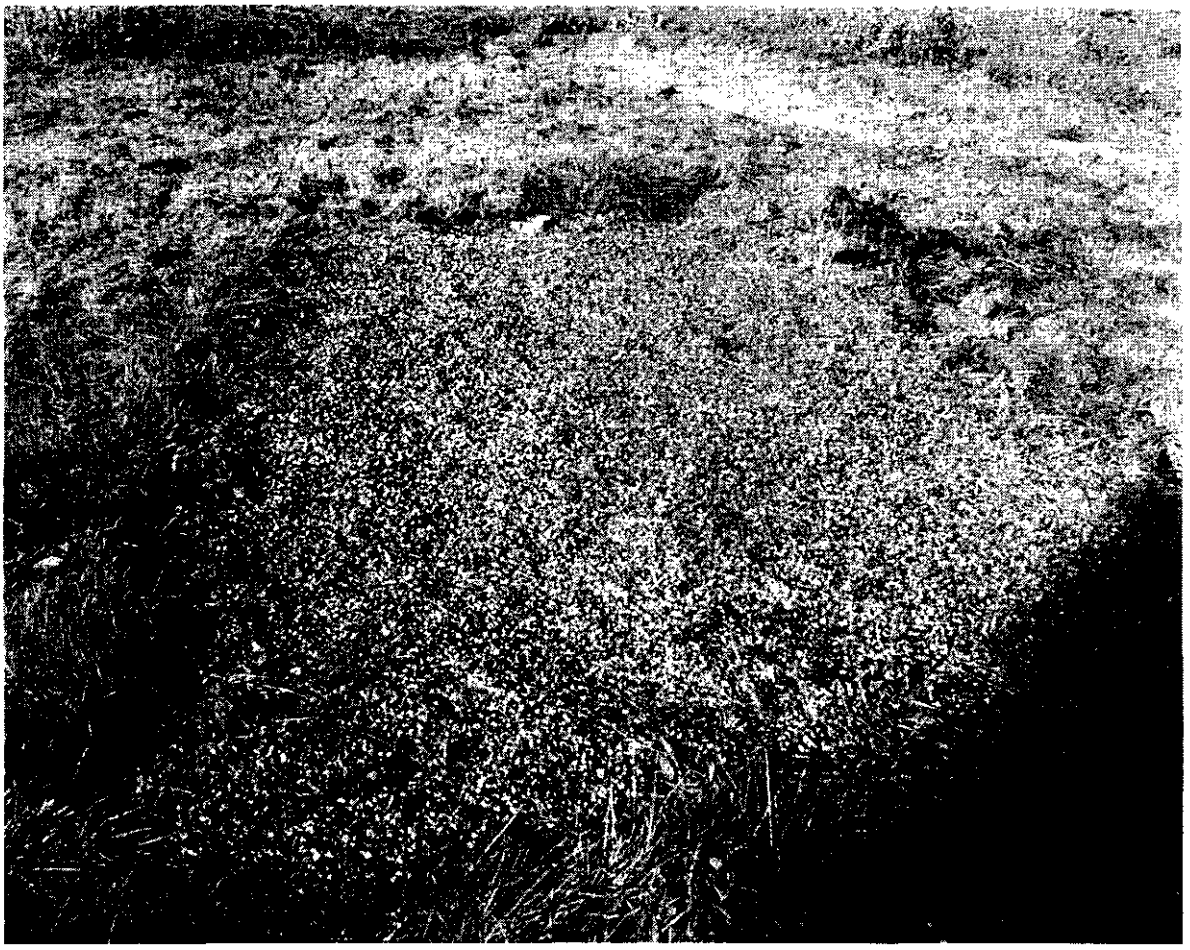

Figure 4-1. Acoustics Research Group test area.

4.1.2 HMC Stone Lane Quarry

The second field site was at the Hepworth, Minerals and Chemicals, Stone Lane Quarry, Heath and Reach, Bedfordshire and can be seen in Figure 4-2.

The quarry lies in a region of Lower Cretaceous sediments that consist of Lower Greensand and Gault Clay. This outcrop is up to 8km wide, and the unit dips gently (approximately 0.6^{o}) to the Southeast, although dip is variable and on a very local scale may be more. The Lower Greensand in the Leighton Buzzard area is late Aptian in age and is known in Bedfordshire area as the Woburn Sands, due to its maximum development in the Woburn area.

In most areas, division of the Lower Greensand is not possible, however, in Leighton Buzzard region it can be divided as follows:

		- 'Red' Sands *
	'Upper Woburn' Sands	
Lower Greensand (Woburn Sands)		- 'Silver' Sands
	'Lower Woburn' Sands	- 'Brown' Sands

Table 4-1. Division of the Lower Greensand in the Leighton Buzzard Area. (BGS terms: see for instance (Shephard-thorn et al., 1986))

At Stone Lane, the main outcropping formation is the "silver sand" beds of the Upper Woburn sands. In this area, the Lower Greensand is approximately 50m thick, with the 'silver' sands being up to 20m in thickness.

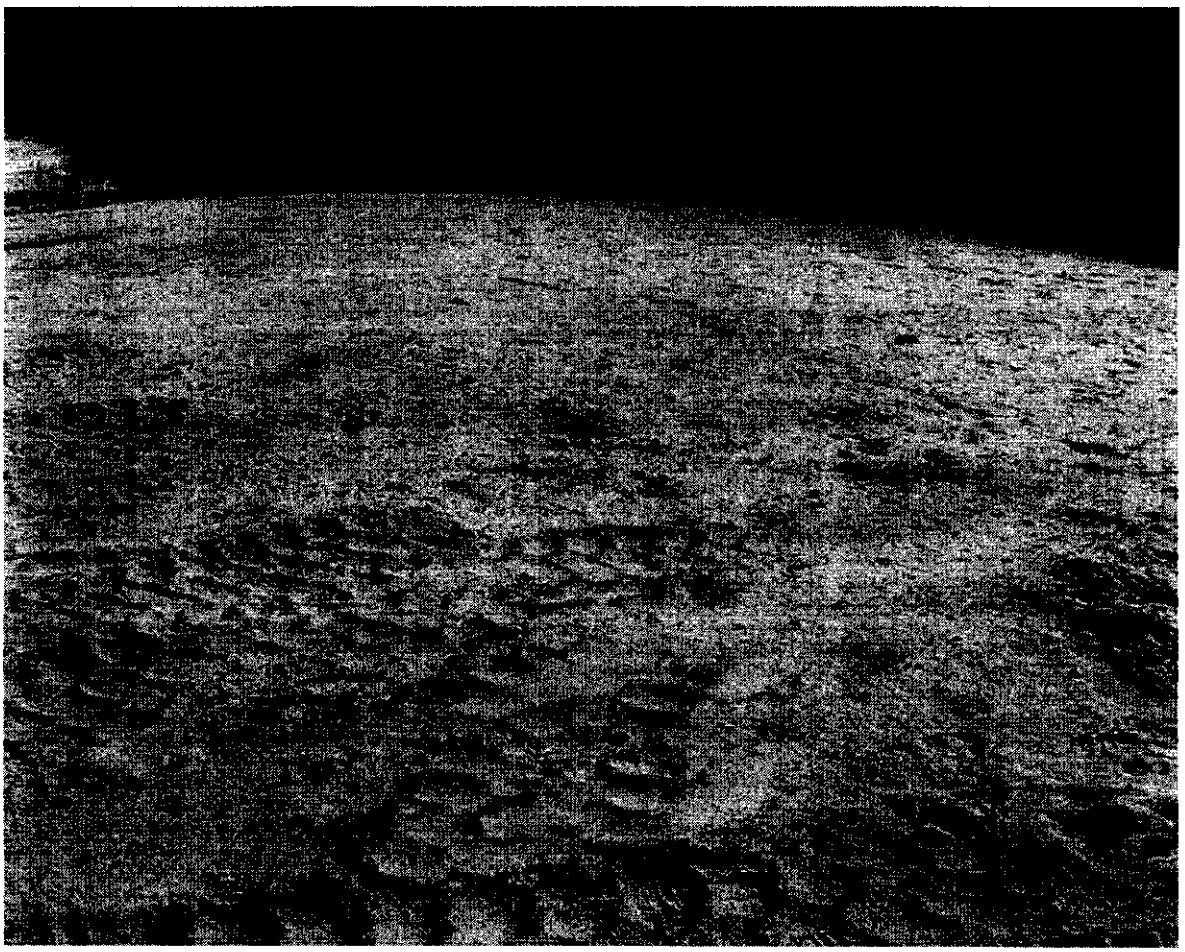

Figure 4-2. HMC. Stone Lane Quarry.

The 'Silver' sands are characteristically white but are often iron-stained to give yellow, orange or red colouration. The are very pure quartz sands that contain pebbly lenses or laminae of quartz and chert. Eyers (1992) reported they had medium to coarse, well rounded grains, which showed moderately well sorting.

Field Description: Loose yellowish rounded fine to medium SAND. (BS 5930, 1981)

4.1.3 HRI Wellesbourne

Finally, a case study was undertaken at Horticultural Research International (HRI) based at Wellesbourne, Warwickshire. Measurements were undertaken on a specially prepared experimental plot that was being used by HRI as part of a seed emergence monitoring experiment.

The site consisted of an artificial seedbed 6m wide by 26m length with three different soil types A, B and C in 2-m wide bands, with each bed being between 0.25m and 0.50m thick (See Figure 4-3). As part of the HRI experiments the area is permanently covered, as can be seen in Figure 4-3.

The soil (B) is the original soil sequence on the station; a shallow phase over calcareous gravels of the Wick series. Whitfield (1974) described the top soil (B) as a very friable sandy loamy soil with 67% sand, 14% clay, 19% silt and 0.9% of organic carbon, with an available water content of a typical plough layer about 17%.

Topsoil, up to 25cm, in bands A and C was removed and replaced by non-native topsoil. In band (C), a sandier end of the same Wick series collected locally on the research station was used. This loamy sand contains 80% sand, 9% clay and 11% silt. The topsoil in (A) with 8% sand, 20% clay and 72% silt is a silty loam soil that has developed originally over marine alluvium in the marsh of Lincolnshire. This deep stoneless calcareous fine silty loam belongs to the Tanvats association. All the three soils are commonly used for vegetable crops.

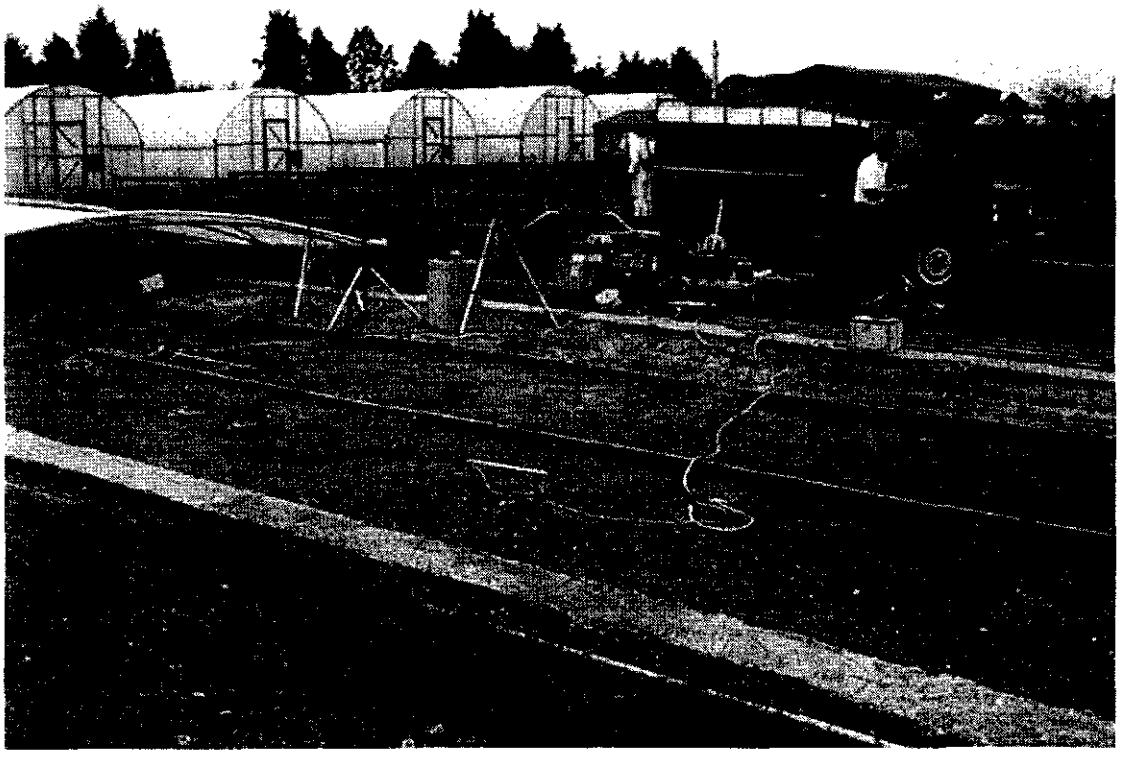

Figure 4-3. The HRI experimental site. Soils A, B and C are described in text.

Soil A - Field Description: Stiff to very stiff yellowish brown very friable fissured slightly clayey SILT with occasional presence of roots. (BS5930, 1981).

Soil B - Field Description: Very stiff light brown very friable fissured very silty SAND with occasional presence of roots. (BS5930, 1981).

Soil C - Field Description: Stiff to very stiff brown very friable fissured slightly silty fine SAND with occasional presence of roots. (BS5930, 1981).

4.1.4 Sampling Techniques

Two types of soil sample can be obtained: a disturbed sample and an undisturbed sample. In practice, no matter how careful the technique employed there will inevitably be some disturbance of the soil during its collection as an "undisturbed" sample. With sample tubes, jacking is preferable to hammering although if the blows are applied in a regular pattern there is little difference between the two (Smith, 1994).

Collection of undisturbed samples of the cohesionless soils, such as gravel and sand, is extremely difficult. If the sample is damp and there is enough temporary cohesion, samples can be collected in sample tubes. Various techniques involving chemicals or temporarily freezing the ground have been tried, but they are expensive and have been found not to be satisfactory. Also, even if an undisturbed sample can be extruded, then transportation can easily disturb the sample

Therefore, the cohesionless materials used throughout the project were all taken as disturbed samples. After sampling, the material was placed in plastic sample bags which were immediately sealed to ensure that the natural moisture content of the material remained constant until it was ready for testing.

For the cohesive sediments found at HRI Wellesbourne, two specially designed samplers were used for the collection of undisturbed material. The sampler used for the collection of material for the shear strength determination test consisted of an open ended metal sided box, 0.20m x 0.20m and 0.05m deep, with one side having a sharpened edge for easier intrusion. The sampler used for the collection of material for the resonant column test, consisted of metal tubes, 0.038m in diameter and between 0.175m and 0.250m in length.

The sampler was employed by first removing the top surface of the sample point to achieve a clean horizontal surface, free from large pebbles and fractures. It was then driven into the sediment with the aid of a hammer and piece of wood. Finally the material surrounding the sample box was carefully removed, to produce as little disturbance as possible, and the sampler removed. The ends were then sealed to the atmosphere using plastic caps, to ensure that the natural moisture content of the material was kept.

Material for the index property tests was taken from the material extruded around the sample tubes, as the non-disturbance of this material is unessential. This material was placed in plastic sample bags, which were immediately sealed, again to ensure that the natural moisture content of the material remained constant until it was ready for testing.

4.2 *Comparative Tests*

4.2.1 Permeability

Permeability is a measure of the ease with which a fluid moves through a soil medium. Soil scientists prefer to measure this function using water and give it the title permeability, whilst acousticians tend to measure this function using air and give it the title flow resistivity.

4.2.1.1 Water Permeability

Water may pass through the voids of soils, the pores, or through the discontinuities such as the fissures found in an overconsolidated clay. This behaviour will affect the value of the coefficient of permeability that can be determined by either laboratory or in-situ testing.

Darcy (1856) showed experimentally that a fluid's velocity of flow through a porous medium is directly related to the hydraulic gradient causing the flow. That is:

$$v \alpha i \qquad \textit{(Eq. 4-1)}$$

where i = hydraulic gradient (the head loss per unit length). Thus:

$$v = Ci \qquad \textit{(Eq. 4-2)}$$

where C = a constant involving the properties of both the fluid and the porous material. When the constant C is determined using water as the permeant, the value obtained is known as the coefficient of permeability and is the given the symbol k.

It is important to note that when the soil is said to have a certain coefficient of permeability this value only applies to water (at 20°C). If another fluid is used as the permeant, the value of C would be considerably different.

The conversion of a permeability of a soil, measured with a fluid of the same viscosity and unit weight as water, from permeability in cm/sec, to an intrinsic permeability constant k, which is independent of fluid properties is

$$k_i = k\frac{\eta}{\rho g} \qquad \textit{(Eq. 4-3)}$$

where:

k = permeability (cm/sec)

ρ = Density of water = 0.9982 g/cm^3 at 20°C

g = Acceleration of gravity = 980 cm/sec^2

η = Dynamic viscosity of water = 0.01 g / cm sec at 20°C

k_i = Intrinsic permeability (in units of cm^2)

(conversion factor: 9.87x10^{-9} cm^2/darcy)

This intrinsic permeability is really only applicable to inert particles such as sands and gravels. With clays, the chemical interaction between different fluids and the soil can be much more complex than described by viscosity and unit weight.

The value of permeability of a soil depends upon a number of factors, with the main ones being

1) The size of the soil grains. It has been found that permeability appears to be proportional to the square of an effective grain size. This is known as Hazen's Formula, but is only applicable for single sized sands.

$$k = 10\,D_{10}^2\ mm/s \qquad \textit{(Eq. 4-4)}$$

where D_{10} = the effective particle size in mm.

2) *The properties of the pore fluid.* The only important variable of water is viscosity, which in turn is sensitive to changes in temperature.

3) *The void ratio of the soil.*

4) *The shapes and arrangements of pores.*

5) *The degree of saturation.* An increase in the degree of saturation of a soil causes an increase in permeability.

It can be seen that it is possible to evaluate permeability of a soil given its particle size distribution, and various formulae have been produced (Loudon, 1952). Typical values of permeability can be found in Table 4-2.

Gravel	$>10^{-1}$ m/s
Sands	10^{-1} to 10^{-5} m/s
Fine sands, coarse silts	10^{-5} to 10^{-7} m/s
Silts	10^{-7} to 10^{-9} m/s
Clays	$< 10^{-10}$ m/s

Table 4-2. Typical values of water permeability

4.2.1.1.1 Available Methods

At least four laboratory methods of measuring the permeability of a soil are available. These are, constant head, falling head, capillarity and consolidation test.

Of these methods, the constant head permeameter is the most widely accepted apparatus for the determination of permeability for cohesionless materials, whilst the falling head permeameter is the most widely accepted apparatus for the determination of permeability for cohesive materials.

4.2.1.2 Flow Resistivity

Soil flow resistivity is a measure of the difficulty with which air moves through a soil medium and is the inverse of air permeability. Measurements of air permeability are based on Poiseuille's Law of fluid flow through a cylindrical pore with a tube radius r, as shown

$$Q = \frac{\pi r^4}{8\eta} \rho_f g \, \mathrm{grad}\phi \qquad \textit{(Eq. 4-5)}$$

where: -

Q = Volume/time = Volume flow rate

η = Viscosity of the fluid

$grad\ \phi$ = Potential gradient

ρ_f = Density of the fluid

g = Acceleration due to gravity

From Childs (1969) for a number (n) of pores, this can be written as

$$v = \frac{n}{A} Q = \frac{n\pi r^4}{8\eta} \rho_f \, g \, \text{grad}\phi \qquad \textit{(Eq. 4-6)}$$

Taking into account porosity Ω, where Ω is equal to the area of the pore per unit area of cross-section ($n\pi r^2/A$), then,

$$v = \frac{n}{A} Q = \frac{\Omega r^2}{8\eta} \rho_f \, g \, \text{grad}\phi \qquad \textit{(Eq. 4-7)}$$

When gravitational potential is negligible (assuming horizontal flow) compared to the pressure potential, then

$$v = \frac{n}{A} Q = \frac{\Omega r^2}{8\eta} \frac{\Delta P}{L} \qquad \textit{(Eq. 4-8)}$$

where L is the length of the pore. This is analogous to Darcy's Law of flow through a single capillary tube.

$$Q = K \frac{\Delta P}{L} A \qquad \textit{(Eq. 4-9)}$$

where A is the area of the tube. Childs (1969) expresses k the conductivity of the body as

$$k = \frac{\Omega r^2}{8\eta} = \frac{k_i}{\eta} \qquad \textit{(Eq. 4-10)}$$

where $K_i = \Omega r^2/8$ and is the intrinsic permeability and is an exclusive property of the porous medium dependent upon porosity and pore radius. k is the conductivity and is also called the permeability. It is dependent upon both k_i and the viscosity of the fluid. In this case, k_i is expressed in dimensions of area m^2. In acoustics, the specific air flow resistance (or resistivity) is:

$$R_s = \frac{\eta}{k_i} = \frac{8\eta}{\Omega r^2} \qquad \textit{(Eq. 4-11)}$$

and is measured in Pa s m^{-2} where 1Pa s m^{-2} = 1 mksrayls/m.

Typical values for flow resistivity of soils can be found in Table 4-3, Table 4-4 and Table 4-5.

Ground Type	Flow resistivity kPa s m^{-2}	Porosity – total or (air-filled / water-filled) (%)
Loamy sand beneath lawn (no roots)	677 ± 93	28.8/13.7
Grass covered compact sandy soil	463 ± 122	41.7/5.2
Grass-covered field	300	34.5/16.0
Loamy sand beneath lawn (0.06 m thick with roots)	237 ± 77	50.5
Grass	220	----
Grass root-filled layer	189 ± 91	----
loamy sand with roots (mixed overgrowth)	114 ± 52	21.1/27.1

Table 4-3. Typical values of the flow resistivity and porosities for grasslands.

Ground Type	Flow resistivity kPa s m^{-2}	Porosity –total or (air-filled / water-filled)
Wet sandy loam	1501	11
Compacted silt	1477	12
Mineral layer beneath mixed deciduous forest	540 ± 92	36.5/15.0
Sand (moistened)	479	37.0
Loamy sand on plain	422 ± 165	37.5/11.2
Hard clay field	400	-----
Sand (dry)	376	35.0
Bare sandy plain	366 ± 108	26.9/9.3
Dry sandy loam	259	50.0
Humus on pine forest floor	233 ± 223	58.1/16.1
Sand (dry)	134	47.0
Sand (grain dia. 0.25 - 0.33 mm)	95.9	47.0
Sand (dry)	70.9	34.0
Sand (grain dia. 0.33 - 0.5 mm)	61.2	40.0

Table 4-4. Typical values of the flow resistivity and porosities for soils and sands.

Ground Type	Flow resistivity kPa s m^{-2}	Porosity (volume %)
bare loamy sand	422 ± 165	48.3 ± 1.7
grass root layer in loamy sand	153 ± 91	47.9 ± 4.4
grass root layer in loamy sand	237 ± 77	50.5 ± 9.3
loamy sand beneath root-zone	677 ± 93	42.5 ± 1.7
loamy sand with roots	114 ± 52	55.2 ± 4.5

Table 4-5. Influence of root zones on flow resistivities and porosities.

Table 4-5 indicates that the presence of an acoustically-soft organic *root layer* (the root zone) above rootless mineral soil reduces the flow resistivity near the surface by a factor of between 2 and 5 compared with that in the substrate. The measured effects of roots on porosity are less dramatic.

The values given in the above tables are taken from Martens *et al.* (1985) and Moore and Attenborough (1992)

4.2.1.2.1 Available Methods

Measurements of the flow resistivity are extremely difficult to make. In doing so porosity and structure of the soil particles and crumbs, that are probably the most important physical soil properties governing its flow resistivity, are usually unavoidably changed.

In the laboratory, the most practised method involves the use of compressed air apparatus in conjunction with manometers. An alternative comparative method (Stinson and Daigle, 1988) makes use of a calibrated known resistance (a laminar flow element) placed in series with the test sample. Variable-capacitance pressure transducers are used to measure pressure differences across both the test sample and the calibrated resistance. For steady non-pulsating flow, the ratio of flow resistances equals the ratio of measured pressure differences that may be obtained with variable electronic capacitances. The airflow may also be controlled electronically.

Laboratory techniques involve the disturbance of cores during sampling, transportation to the laboratory and insertion into the resistivity rig itself. This is particularly true for cohesionless materials, where sampling of undisturbed samples is extremely difficult.

Various in-situ flow resistivity techniques, known as air permeameters are available. All these techniques require the insertion of a sampling container and the sealing of the surrounding soil surface with paraffin wax or similar. They also require individual calibration to account for boundary conditions peculiar to each specific apparatus. There are a number of methods for in-situ measurement of flow resistivity but they can be broadly divided into two groups.

1. Variable pressure methods

The original variable pressure method was developed by Kirkham (1947) and uses a constant volume air tank. Air at a given initial pressure P_e (and registered on a manometer as y) is allowed to discharge through a soil sample of known dimensions located in-situ. The dimensions of the permeameter and the volume and initial pressure of the air tank (regulated by a bicycle pump) can be varied to give a conveniently low rate of pressure drop during the test. The lower the rate of pressure change the more nearly the conditions approximate to the isothermal expansion of air. As the tank pressure drops, various values of y and time are recorded. A plot of y against time on semilog paper reveals a straight line of slope S. The intrinsic permeability can be calculated from: -

$$k_i = \frac{2.30\eta.L.V.S}{A.P_a} \qquad (Eq.\ 4\text{-}12)$$

where

k_i = Intrinsic permeability

η = Viscosity of the fluid

L = Length of the sample

V = Volume of the tank (cm^3)

A = Area of the sample

P_a = Atmospheric pressure ($dynes/cm^3$)

The chief limitation of the variable pressure methods, is the volume of the air tank. It is necessary for the tank to be large enough to cover a representative area (to eliminate variation in readings). However, in practice the size of the tank is limited by the requirement that it be portable enough to carry into the field. The restricted volume of air in turn limits the range of soils that can be studied, since a highly permeable sand would require a large volume of air as it would pass through it very quickly. This technique is therefore suited to soils with an expected high flow resistivity.

2. Constant pressure methods

Constant pressure methods were designed for low permeability soils, where low pressures are required to prevent disturbance of the liquid phase and to avoid turbulent flow (Alpan, 1962). The original idea was developed for the field by Grover (1955). It consisted of an

inverted cylinder of air, floating in an annular water chamber and an inlet tube positioned in the soil. Air in the chamber was at a known, constant pressure, recorded as a water head in cm on a manometer. As the float falls, air from the chamber is passed through the pipe into the soil. The weight of the float maintained a constant pressure independent of the rate of fall.

$$k_i = \frac{\eta Q}{C\Delta P} \qquad (Eq.\ 4\text{-}13)$$

where

Q = volume of air (V) entering the soil in time (t)

ΔP = a known constant pressure

C = a constant factor determined for differing sampling cylinders and boundary conditions

Although it appears that in-situ permeameters are preferable to laboratory measurements there are a number of problems associated with their use including: -

1. Boundary conditions
2. Disturbance of the soil
3. Sample size
4. Drying of samples
5. Variability of data

4.2.2 Porosity

Soils can be regarded as a three phase system as shown in Figure 4-4, consisting of solids, that are either mineral or organic matter; water and solutes; and air. The size and arrangement of solid particles determines the total amount of pore space that is occupied by water or air, which usually accounts for 30 to 60% of the volume of the soil, (Hillel, 1982). In acoustics, it is important to study the proportion of the total porosity (V_f) occupied by air, the air-filled porosity (V_a). The volume of air-filled porosity is related to water volume (V_w) as they compete for the same pore space.

The air-filled porosity is of great interest in terms of soil aeration for agricultural purposes, as it affects such phenomena as crop growth and root development.

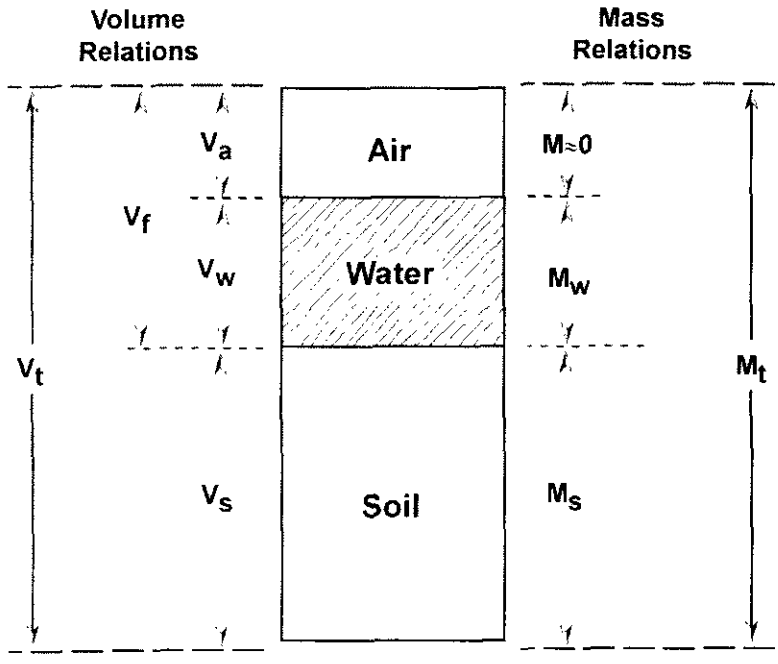

Figure 4-4. Schematic diagram of a soil as a three phase system.

$$V_f = V_w + V_a \qquad \textit{(Eq. 4-14)}$$

The standard technique for measuring total porosity, water content and air filled porosity is called gravimetric or difference method. The water content in a known volume of soil V_t is dried off by placing samples in an oven at 105°C for 24 hrs. The ratio of the mass of the dried soil M_s to its volume V_t is the dry bulk density and is given by

$$\rho_s = \frac{M_s}{V_t} \qquad \textit{(Eq. 4-15)}$$

The dry bulk density is always lower than the soil particle density, ρ_g. In most mineral soils, the soil particle density has a short range of 2.6-2.7 g/cm^3 (Hillel, 1982). This density is close to that of quartz, which is usually the predominant constituent of sandy soils. A typical value of 2.65 g/cm^3 has been suggested to characterise the soil particle density of a general mineral soil (Freeze and Cherry, 1979). Aluminosilicate clay minerals have particle density variations in the same range. The presence of iron oxides and other heavy minerals increases the value of the soil particle density. The presence of solid organic materials in the soil decreases the value.

Since ρ_s is lower than ρ_g this means that only part of the bulk volume is occupied by solid particles, the rest is pore space. Total porosity can then be expressed as

$$V_t = 1 - \frac{\rho_s}{\rho_g} \qquad \textit{(Eq. 4-16)}$$

By calculating the mass of water M_w as the difference between wet and dry sample weight and assuming the density of water ρ_w to be 1000 kg/m^3, the volume of air-filled porosity V_a is found by subtraction of the calculated fractional volumes of the water V_w and the solids V_s as shown in equations, 4.17, 4.18 and 4.19.

$$V_w = \frac{(M_w / \rho_w)}{V_t} \qquad \textit{(Eq. 4-17)}$$

$$V_s = \frac{(M_s / \rho_g)}{V_t} \qquad \textit{(Eq. 4-18)}$$

$$V_a = 1 - (V_w + V_s) \qquad \textit{(Eq. 4-19)}$$

The gravimetric technique has several drawbacks. Like all mechanical tests it is destructive, labour intensive and slow. It requires replication of at least three soil cores from any one soil depth to give a representative value of V_a (Avery and Bascombe, 1982). As mentioned in Section 4.1.4, the extraction of undisturbed samples is difficult to achieve in cohesionless materials. Problems also arise from coarse cohesionless materials as stones within the samples affect the volume and may give misleading results (Low, 1954).

Problems can also occur with fine-grained cohesive sediments. It is assumed that, after the 24 hour period of oven drying, all moisture has been removed from the samples. However, clay soils often retain appreciable quantities of water at that state of dryness. Clay soils also prove problematic due to volume shrinkage on drying.

Typical values of porosity can be found in Table 4-3, Table 4-4 and Table 4-5.

4.2.3 Tortuosity

In-situ electrical resistivity techniques are used in the oil industry to give estimations of porosity. These methods are based on the relationship between formation factor, F, and porosity Ω, discovered during the 1940's (Archie, 1942) who developed Archie's Law.

This work was based around the fact that the degree to which a sediment conducts electricity can be related to the nature of the pore spaces, and in particular the nature of the fluid contained within them.

When an electric current passes through a porous medium most of the conduction is via the pore fluid, since the constituent minerals of the material are insulators. The electrical resistivity of the sediment is therefore dependent on the resistivity and salinity of the pore fluid present, together with its quantity and distribution throughout the sediment.

The amount and nature of the pore fluid is dependent upon the structure of the sediment e.g. porosity. Direct relationships exist between resistance and porosity, such that the resistance varies as the inverse square of the porosity. However, relating direct sediment resistance measurements to the porosity produces inaccuracies due to the effect of the resistivity of the pore fluid. To remove dependence of the pore fluid, a formation factor may be defined in that for a given porosity, the ratio of the sediment resistance to pore fluid resistance should be constant. F is a function of the material texture and is given by

$$F = \frac{\delta f}{\delta s} \qquad \textit{(Eq. 4-20)}$$

where δf is the conductivity of the fluid and δs that of the fluid saturated sample.

A relationship now exists between the formation factor and porosity, since the formation factor is completely independent of the resistivity of the pore fluid. However, the quantity and distribution of the pore fluid is still a factor, i.e. it is a function of the structure of the sediment particles.

Porosity and formation factor are related by

$$F = a\Omega^{-m} \qquad \textit{(Eq. 4-21)}$$

where Ω is porosity, a is an empirical constant specific to the materials of interest and is taken as 1 for sands, and m is a constant known as the cementation factor which depends on the grain size and tortuosity.

The tortuosity of a porous material is a measurement of the increased path length through the material due to the deviation from a straight line. The tortuosity of a sample has been related to its porosity and formation factor (Brown, 1980). Hence,

$$\tau = F\Omega \qquad \textit{(Eq. 4-22)}$$

where Ω is the porosity and F is the formation factor. Combining Equation 4-21 and 4-22 shows that:

$$\tau = a\Omega^{1-m} \qquad \textit{(Eq. 4-23)}$$

assuming a = integer and $\tau > 1$, then m must be greater than 1.

4.2.3.1 Available methods

The majority of methods for the determination of tortuosity are based upon the electrical conductivity of a conductive fluid saturated material.

A sample is saturated in an electrically conductive fluid (e.g. brine solution). For cohesionless materials such as sands, this can easily be achieved through natural permutation, but for fine grained more cohesive materials the application of a vacuum enhances saturation. Some agitation of the sample may be necessary if the pore sizes are small. An *AC* voltage is then applied across the sample and the current measured. A measurement of the conductivity of the brine is also required.

It must be noted however, that Archie's Law is not valid for sediments containing a significant percentage of clay. Clay provides a conductive matrix, rendering a fundamental assumption made in the Archie's Law invalid. Graphite, native metals, and minerals with metallic lustres are also electrical conductors, but these are far scarcer than clays.

The use of separate current and voltage probes assures a reliable contact between the end of the sample and the electrodes. This eliminates a voltage drop at the current electrodes and allows simultaneous measurement of the resitivities of the fluid and saturated porous material.

It has been found (Sens *et al.*, 1981) that the tortuosity of a random stacking of glass spheres is given by $1/\sqrt{\Omega}$. This has been verified for a range of porosities from 0.33 and 0.38 and is a special case of the Bruggeman relationship.

$$\tau = \Omega^{-n} \qquad \textit{(Eq. 4-24)}$$

Where n depends on grain shape (Attenborough, 1987) and is usually given a value of 1 for soils.

4.2.4 Elastic Moduli

When external forces are applied to a body, balanced internal forces are set up within it. Stress, is a measure of the intensity of these balanced internal forces. The stress acting in an area of any surface within the body may be resolved into a component of normal stress perpendicular to the surface and a component of shearing stress in the plane of the surface.

A body subjected to stress undergoes a change of shape and/or size known as strain. Up to a certain limiting value of stress, known as the yield strength of a material, the strain is linearly related to the applied stress (Hooke's Law). This elastic strain is reversible so that removal of stress leads to a removal of strain. If the yield strength is exceeded the strain becomes non-linear and partly irreversible (i.e. permanent strain results), and is known as plastic or ductile strain. If the stress is increased still further the body fails by fracture. A typical stress-strain relationship can be found in Figure 4-5.

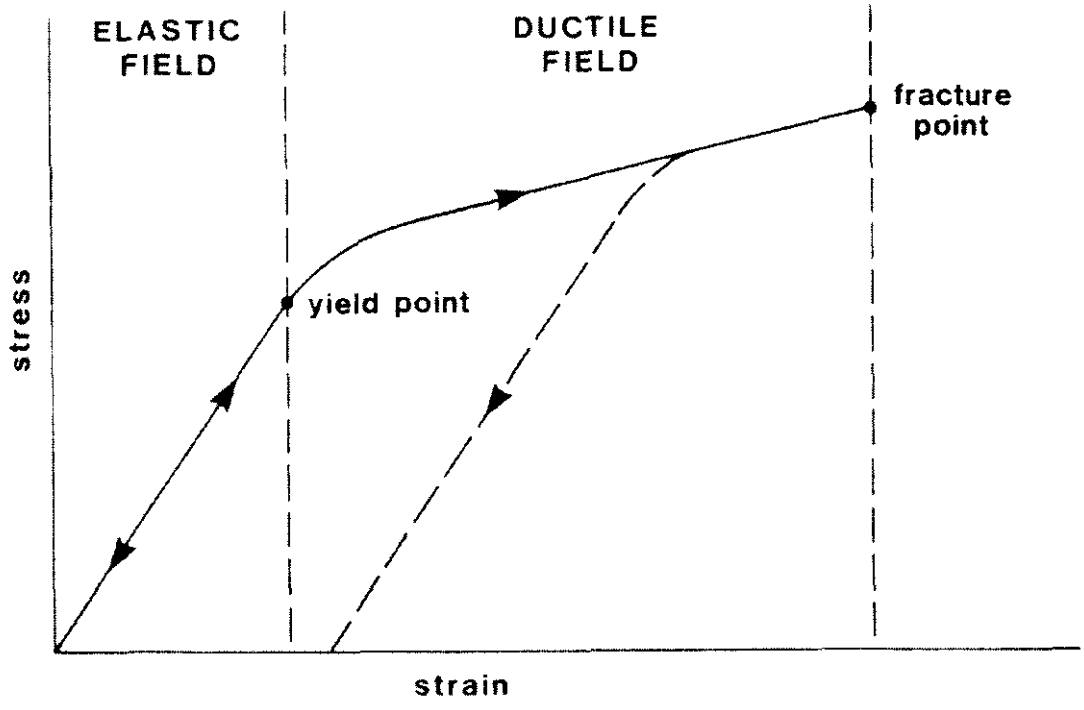

Figure 4-5. A typical stress-strain curve for a typical body

The linear relationship between stress and strain in the elastic field is specified for any material by its various elastic moduli, each which expresses the ratio of a particular type of stress to the resultant strain.

Consider a rod of original length, l, and cross-sectional area, A, that is extended by an increment, Δl, through the application of a stretching force, F, to its end faces (See Figure 4-6a). The relevant elastic modulus is Young's modulus E, defined by

$$\text{Young's modulus } E = \frac{\text{longitudinal stress } F/A}{\text{longitudinal strain } \Delta l/l} \qquad \textit{(Eq. 4-25)}$$

With the extension in the rod there will be an accompanied reduction in its diameter, i.e. the rod will suffer lateral as well as longitudinal strain. The ratio of the lateral to longitudinal strain is known as the Poisson's ratio.

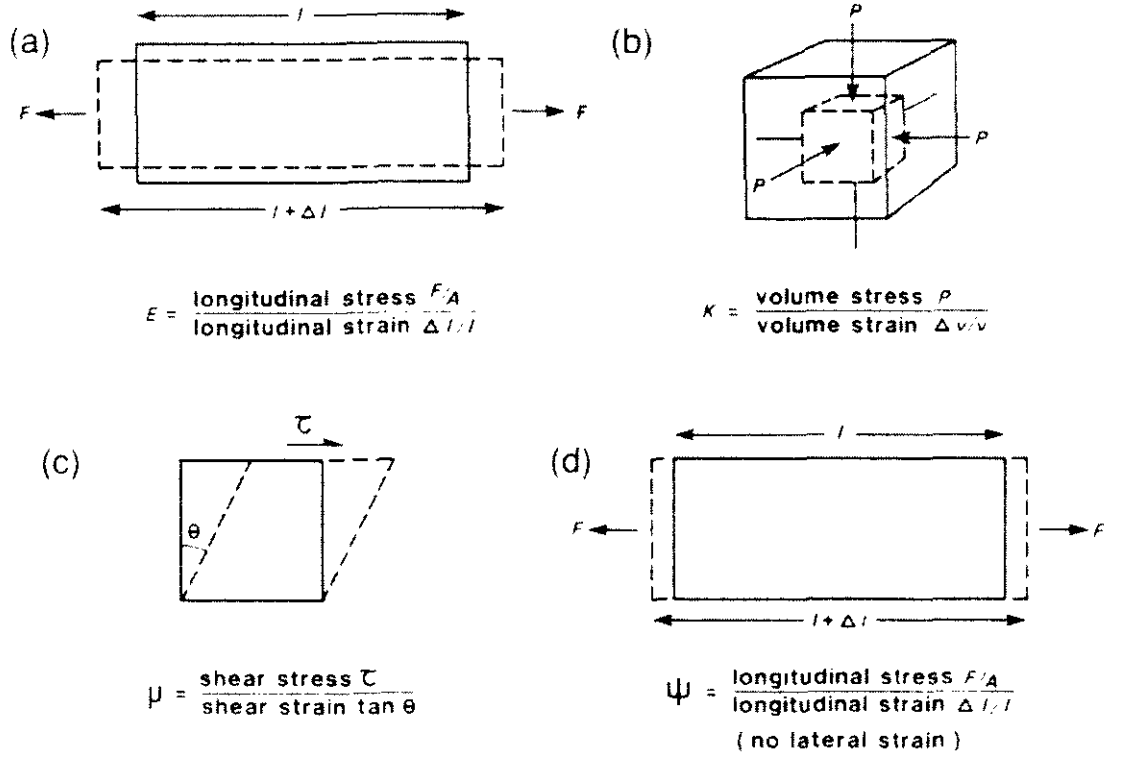

Figure 4-6. The elastic moduli. (a) Young's modulus E. (b) Bulk modulus K. (c) Shear modulus μ. (d) Axial modulus ψ.

The Bulk modulus, K, expresses the stress-strain ratio in the case of a simple hydrostatic pressure, P, applied to cubic element (Figure 4-6b), the resultant volume strain being the change in volume Δv divided by the original volume, v,

$$\text{Bulk modulus } K = \frac{\text{volume stress } P}{\text{volume strain } \Delta v/v} \qquad \textit{(Eq. 4-26)}$$

In a similar manner the shear modulus (μ) is defined as the ratio of shearing stress (τ) to the resultant shear strain *tan* θ (See Figure 4-6c).

$$\text{Shear modulus } \mu = \frac{\text{shear stress } \tau}{\text{shear strain } \tan\theta} \qquad \textit{(Eq. 4-27)}$$

Finally, the axial modulus ψ defines the ratio of longitudinal stress to longitudinal strain in the case where there is no lateral strain, i.e. when the material is constrained to deform laterally (Figure 4-6d).

$$\text{Axial modulus } \psi = \frac{\text{longitudinal stress F/A}}{\text{longitudinal strain (uniaxial) } \Delta l/l} \qquad \textit{(Eq. 4-28)}$$

There are also inter-relationships between the elastic moduli which can be used to calculate an unknown moduli having knowledge of two others.

$$\text{Young's modulus } E = \frac{\mu(3\lambda'+2\mu)}{\lambda'+\mu} \qquad \textit{(Eq. 4-29)}$$

$$\text{Poissons Ratio } \sigma = \frac{\lambda'}{2(\lambda'+\mu)} \qquad \textit{(Eq. 4-30)}$$

$$\text{Bulk modulus } K = \frac{3\lambda'+2\mu}{3} \qquad \textit{(Eq. 4-31)}$$

Where λ' is one of the Lame constants.

The elastic constants are defined in such a way that they are positive numbers. As a consequence, σ must have values between 0 and 0.5 (because in Eq. 4-30 $\lambda'/(\lambda'+\mu)$ is less than unity). Values range from 0.05 for very hard, rigid rocks to about 0.45 for tight sand, with loose sand and snow about 0.49. Liquids have no resistance to shear and they therefore have a value of $\mu = 0$ and σ=0.5. For most materials E is generally the largest of the moduli and μ the smallest of the three.

4.2.4.1 Available methods

The resonant bar technique, in various vibration modes (longitudinal, torsional or flexural), has been used for many years on rock samples for the determination of elastic moduli. This principle has also been employed in soil dynamics, with the use of the resonant

column device. In the USA, the test has now become the ASTM standard method for determining the shear modulus and damping capacity of soils.

The resonant column test involves vibrating a cylindrical specimen or column of soil in its first torsional mode to determine its shear modulus and in its first longitudinal mode to determine its dynamic compression modulus. Measurement of the specimen's end displacements can be determined as a function of the resonant frequency at which the sinusoidal excitation force is in phase with the velocity of vibration at the end of the specimen. This, together with the sample length allows the computation of the wave velocity through the specimen (Figure 4-7). The damping ratio, which can be related to attenuation, can be determined from the steady state magnification factor at resonance, the width of the resonant response curve, or the logarithmic decay of free vibrations.

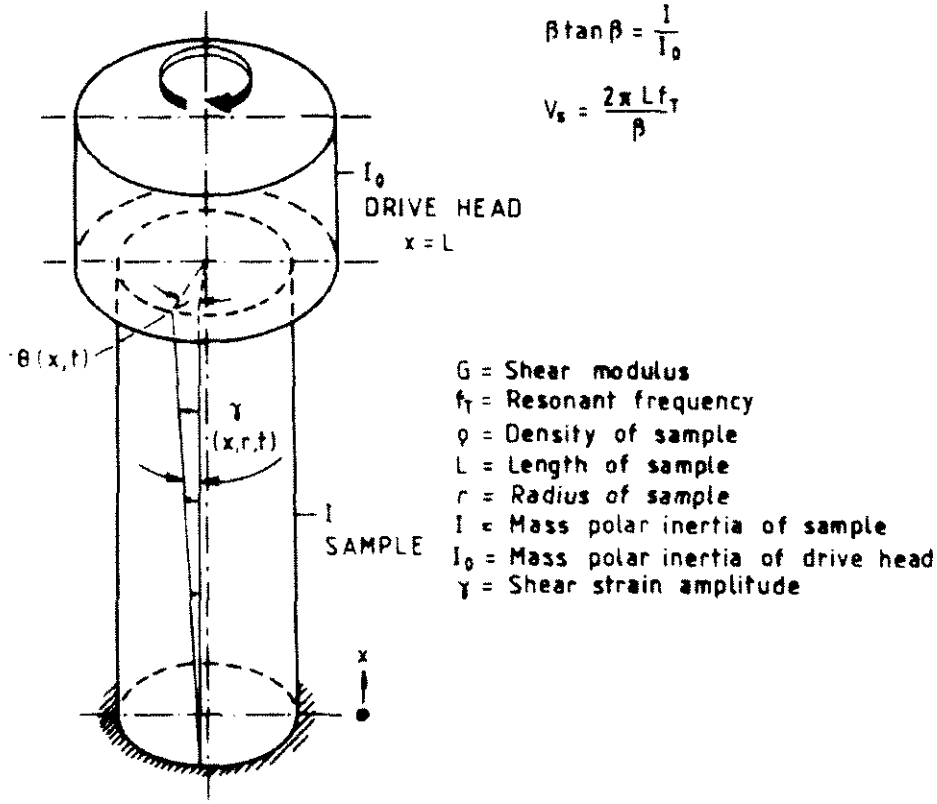

Figure 4-7. Principle of operation of the resonant column test.

4.3 *Soil Classification*

Soil classification systems have been in use for centuries, the first being developed some 4000 years ago by a Chinese engineer (Smith, 1994). More recently in 1896, the Bureau of Soils, United States Department of Agriculture, devised a system in which the various soil types were classified purely upon particle size. Further improved systems allowed for the plasticity characteristics of soil and a modified form of the system proposed by Casegrande (1947) forms the basis of the soil classification used in Britain.

The British Soil Classification System (BSCS) is given in BS5930, Code of practice for site investigation (BS5930, 1981). The system divides soils into two main categories. If at least 35 per cent of a soil can pass through a 63 μm sieve then it is a fine soil. Conversely, if the amount of soil that can pass through a 63 μm sieve is less than 35 per cent then the soil is coarse. Each category is divided into groups depending upon the grading of the soil particles not passing the 63 μm sieve and upon the plasticity characteristics of the soil particles passing a 425 μm sieve.

A summary of the BSCS is shown in Table 4-6 and its associated plasticity chart in Figure 4-8. This classification is useful in the field, however in the laboratory a standardised system of classification helps to eliminate human error.

To use the plasticity chart it is necessary to plot a point whose co-ordinates are the liquid limit and the plasticity index of the soil to be identified. The soil is classified by observing the position of the point relative to the sloping straight line drawn across the diagram. This line, known as the A-line, is an empirical boundary between inorganic clays, whose points lie above the line, and organic silts and clays whose points lie below.

The A-line goes through the base line at $P.I.=0$, $L.L.=20\%$ so that its equation is:

$$P.I. = 0.73(L.L. - 20\%) \qquad (Eq.\ 4\text{-}32)$$

$$P.I. = 0.73(W_l - 20\%) \qquad (Eq.\ 4\text{-}33)$$

Soil groups			Subgroups and laboratory identification				
GRAVEL and SAND may be qualified Sandy GRAVEL and Gravelly SAND etc. where appropriate			Group symbol	Subgroup symbol	Fines)% less than 0.06 mm)	Liquid limit %	Name
COARSE SOILS - Less than 35% of the material is finer than 0.06 mm	GRAVELS - More than 50% of coarse material is of gravel size	Slightly silty or clayey GRAVEL	GW G GP	GW GPu GPg	0 to 5		Well graded GRAVEL Poorly graded/Uniform/Gap graded GRAVEL
		Silty GRAVEL	G-M G-F G-C	GWM GPM GWC GPC	5 to 15		Well graded/Poorly graded silty GRAVEL Well graded/Poorly graded clayey GRAVEL
		Very Silty GRAVEL Very Clayey GRAVEL	GM GF GC	GML etc. GCL GCI GCH GCV GCE	15 to 35		Very silty GRAVEL: subdivide as for GC Very clayey GRAVEL (clay of low, intermediate, high very high extremely high plasticity)
	SANDS - More than 50% of coarse material is of sand size (finer than 2 mm)	Slightly silty or clayey SAND	SW S SP	SW SPu SPg	0 to 5		Well graded SAND Poorly graded/Uniform/Gap graded SAND
		silty SAND clayey SAND	S-M S-F S-C	SWM SPM SWC SPC	5 to 15		Well graded/Poorly graded silty SAND Well graded/Poorly graded clayey SAND
		Very silty SAND Very clayey SAND	SM SF SC	SML etc SCL SCI SCH SCV SCE	15 to 35		Very silty SAND: subdivide as for SC Very clayey SAND (clay of low, intermediate, high very high extremely high plasticity)
FINE SOILS	Gravelly or sandy SILTS and CLAY 35% to 65% fines	Gravelly SILT Gravelly CLAY	MG FG CG	MLG etc CLG CIG CHG CVG CEG		< 35 35 to 50 50 to 70 70 to 90 > 90	Gravelly SILT; subdivide as for CG Gravelly CLAY of low plasticity of intermediate plasticity of high plasticity of very high plasticity of extremely high plasticity
	SILT and CLAYS - 65% to 100% fines	Sandy SILT Sand CLAY	Ms FS CS	MLS etc. CLS etc.			Sandy SILT; subdivide as for CG Sandy CLAY; subdivide as for CG
		SILT (M-SOIL) CLAY	M F C	ML etc Cl Ci CH CV CE		< 35 35 to 50 50 to 70 70 to 90 > 90	SILT, subdivide as for C CLAY of low plasticity of intermediate plasticity of high plasticity of very high plasticity of extremely high plasticity
ORGANIC SOILS		Descriptive letter "O" suffixed to any group or subgroup letter	Organic matter suspected to be a significant constituent. Example MHO: Organic SILT of high plasticity.				
PEAT		Pt Peat soils consist predominantly of plant remains which may be fibrous or amorphous.					

Table 4-6. British Soil Classification System for Engineering Purposes

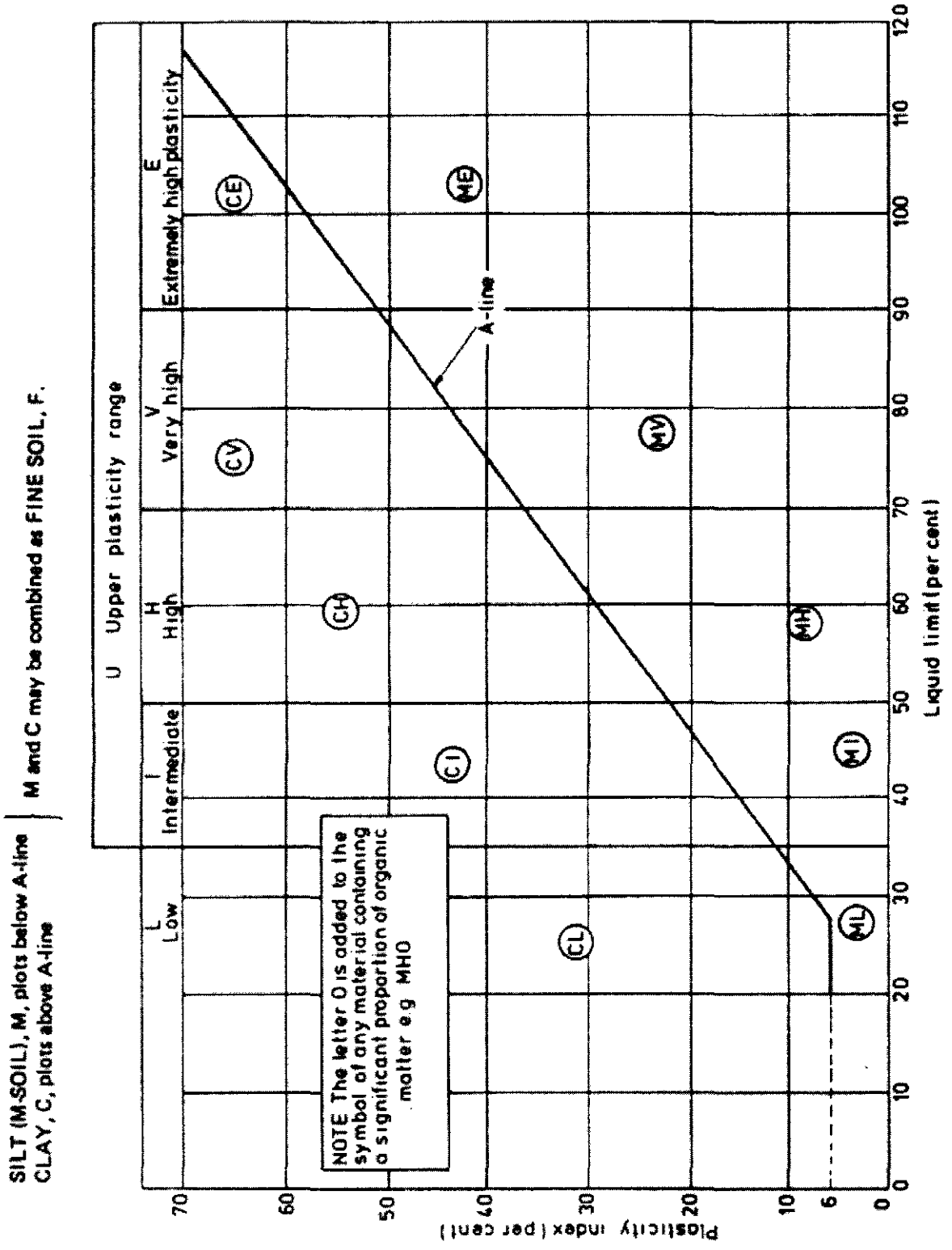

Figure 4-8. Plasticity Chart for the BSCS

The main soil types are designated by capital letters:

G	Gravel	**M**	Silt, M-Soil
S	Sand	**C**	Clay
F	Fine soil, Fines	**Pt**	Peat

Table 4-7. Soil type designation letters.

The classification "*F*" is intended for use when there is difficulty in determining whether a soil is a silt or a clay. Originally, all soils that plotted below the A-line of the plasticity charts were classified as silts. The term M-Soil has been introduced to classify soils that plot below the A-line but have a particle size distribution not wholly in the range of silt sizes.

After the letter designating the main soil type, additional letters are added to further describe the soil and to denote its grading and plasticity. The letter "*O*" is applied at the end of the group symbol for a soil if the soil has a significant amount of organic matter within it. These letters are:

W	Well graded	**L**	Low plasticity ($LL < 35\%$)
P	Poorly graded	**I**	Intermediate ($35 \leq LL \leq 70$)
$\mathbf{P_u}$	Uniform	**H**	High plasticity ($50 \leq LL \leq 70$)
$\mathbf{P_g}$	Gap graded	**V**	Very high ($70 \leq LL \leq 90$)
O	Organic	**E**	Extremely high ($LL \geq 90\%$)

Table 4-8. Additional letters used as part of the soil classification.

4.3.1 Size Analysis

An analysis of the size distribution of any soil is carried out for various reasons, some of which are to provide: -

1. a simple means of classifying a soil (such as a fine sand, a coarse silt, a medium sand, or as a silty clay, a sandy silt etc).
2. an understanding of the bulk mechanical properties of a sediment and its acoustic properties.

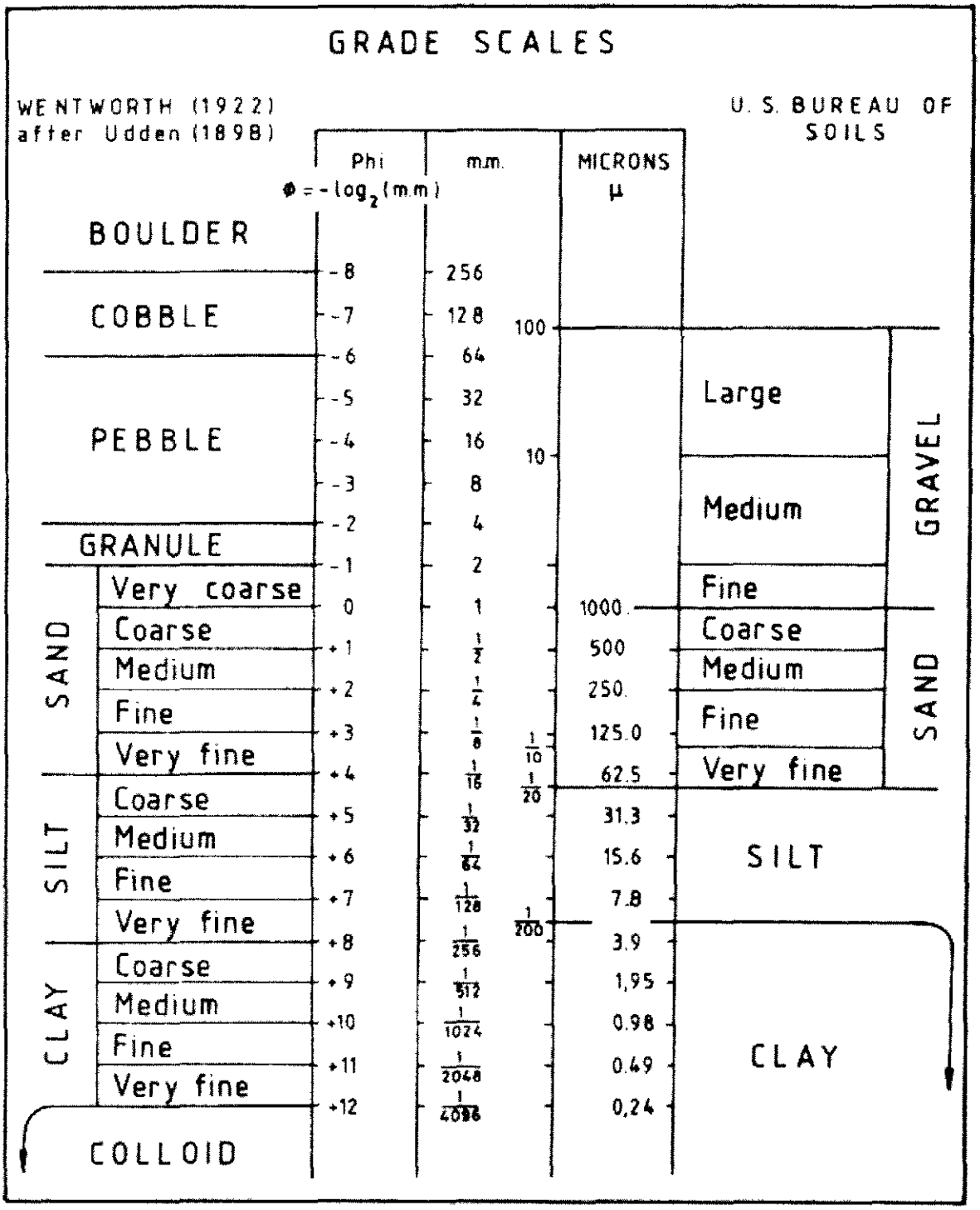

Table 4-9. Grain size scales for sediments

The first step in size analysis is the selection of the grade scale. Various scales have been used in sediment analysis, some of which are shown in Table 4-9. The most useful grade scales are those based on a true geometric scale: they offer advantages in the statistical analysis of the data and in the ease of conversion from one scale to another.

The Wentworth scale has become the standard grade scale used. Here particle diameters are expressed in terms of phi diameters as defined by the equation

$$\phi = -\log_2 d \qquad \textit{(Eq. 4-34)}$$

where d = the diameter of the particle in millimetres.

From Table 4-9, it can be seen that a difference of 1 phi between the sizes of two particles means that the diameter is twice that of the other. The limits of the various grades on the Wentworth scale (see Table 4-9) are selected at intervals of 1 phi. The general boundaries between classes, however, are somewhat controversial but for most purposes may be defined as in Table 4-10.

Sediment Class	phi	Microns
Gravel	-7 to 0	128×10^3 to 1×10^3
Sand	0 to 4	1×10^3 to 62.5
Silt	4 to 8	62.5 to 3.9
Clay	8 to 12	3.9 to 0.24
Colloid	>12	<0.24

Table 4-10. Sediment Grade Boundaries

4.3.1.1 Available Methods

A number of methods of analysis are available, the choice depending primarily on the size range of particles being analysed.

4.3.1.1.1 Sieving

The most common method used for the size analysis of large particles (sand and gravels) is sieving. Inaccuracies are due to a number of factors including

1. sieves sort according to shape as well as to size

2. sieving may be incomplete i.e. material retained in the sieve mesh

3. non-uniformity of the apertures of the sieve mesh, particularly with the smaller meshes

Sieving is only effective down to the lower size limit of about 50 microns (and is rarely continued below the sand sizes), but it has the advantages of simplicity and ease of handling (especially of large samples) so that sampling errors are reduced to a minimum. Sieves are usually spaced at half-phi or quarter-phi intervals.

4.3.1.1.2 Methods based upon Stokes Law

The rate of fall of a spherical body in a liquid is governed by Stokes' Law, which is expressed as: -

$$v = \frac{2gr^2(\rho_g - \rho_f)}{9\eta} \qquad \textit{(Eq. 4-35)}$$

where v = velocity of the sedimentation (cm/sec)

g = acceleration due to gravity (cm/sec^2)

r = radius of the particle which is assumed to be spherical (cm)

ρ_g = density of the solid particle (g/cm^3)

ρ_f = density of the fluid (g/cm^3)

and η = viscosity of the fluid (dyne sec/cm^2)

Table 4-11 shows the time of settling of particles of silt and clay sizes for different temperatures. These show that all other things being equal it is possible to distinguish between two particles of differing sizes based on their settling velocities.

Generally speaking these methods are used only for the analysis of material finer than the sand size (i.e. silts and clays), although techniques do exist for using settling velocities to grade sand sizes as well; these later techniques require very tall settling columns and can usually only accommodate sand sizes up to 0.5cm. The methods include elutriation, sedimentation, centrifugation, pipette and hydrometer techniques.

Inaccuracies occur in all these methods based upon Stokes' Law because of certain assumptions that are not exactly true. These include: -

1. The particles are never truly spherical; in fact, the actual shapes may bear little resemblance to spheres. Neither are the particles smooth or rigid.
2. The body of water is not infinite in extent, and, since many particles are present, the fall of any particles is influenced by the presence of other particles; similarly, particles near the side walls of the container are affected by the presence of the wall.
3. An average value for specific gravity of particles is used; the value for some particles may differ appreciably from the average value.

Nevertheless, the hydrometer method is adequate for analysis of sizes down to about 2 microns, but for smaller size grades centrifugation is necessary because of the long settling times and the effects of Brownian movement in grades smaller than about 1 micron.

4.3.1.1.3 Direct Measurement

Various techniques exist for the direct measurement of particle size; in most of them, particularly in the smaller sizes, use must be made of sediment thin sections or grain mounts for microscopic examination. These methods are extremely time-consuming and thus are never standard sedimentological practice.

4.3.1.2 Presentation of the data

Presentation of the size analysis data should be such that it represents at a glance as much information as is possible and facilitates interpretation of the data.

4.3.1.2.1 Two Variables

In theses, one of the variables, the diameter of the particle (usually in Phi), is plotted against another variable, the amount (or number or frequency) of particles of that size.

Diameter	mm	Depth	14-15°C	16°C	17°C	18°C	19°C	20°C	21°C
1/16	0.625	20 cm	1m 6s	1m 4s	1m 2s	1m 0s	59s	58s	57s
1/32	0.312	10 cm	2m12s	2m 8s	2m 3s	2m 0s	1m 58s	1m 56s	1m 54s
1/64	0.0156	10 cm	8m 46s	8m 32s	8m 18s	8m 12s	7m 51s	7m 44s	7m 33s
1/128	0.0078	10 cm	35m 3s	34m 8s	33m 12s	32m 49s	31m 24s	30m 48s	30m 14s
1/256	0.0039	10 cm	2h20m16s	2h 16m 23s	2h12m25s	2h 11m 4s	2h 5m 43s	2h 3m 4s	2h 0m 7s
1/512	0.00195	10 cm	9h 20m 0s	9h 1m 0s	8h 46m 0s	8h 40m 0s	8h 14m 0s	8h 1m 0s	7h 52m 0s

Table 4-11. Settling times for silt and clay at depths indicated (specific gravity =2.65).

1. Histograms

Diameters are plotted along the horizontal axis either arithmetically or logarithmically; if phi units are used, each grade unit is of equal width on the horizontal axis, even if each does not represent an equal range of diameters. A vertical block is set above each grade proportional in height to the weight percentage of the whole occupying that grade. It should be remembered that if, for some reason, arithmetic plotting of diameters (i.e. not phi units) is carried out, the various rectangles will be of different widths, and care must be taken to ensure that the area of each rectangle represents the frequency in that grade.

2. Frequency Curves

These are simply smooth curves showing the variation of one variable against the other. An approximation of such curves can be produced by joining the midpoints of the topsides of the histogram rectangles by a smooth curve; the narrower the rectangles the closer will this curve represent the true frequency curve

3. Cumulative Curves

The cumulative frequency curve is a curve based on the original histogram data, and is obtained by plotting ordinates which represent the total amount of material larger or smaller than a given diameter. Briefly the cumulative curve is equivalent to setting one histogram block above and to the right of its predecessor, so that the height of the base of each block is the total height of the all the proceeding blocks.

A smooth curve is then drawn through the resulting step diagram, as in the frequency curve case, to provide an approximation to the true cumulative curve. In practice, it is not necessary to draw the histograms to provide the cumulative curves the computation form provide the frequency information directly.

Cumulative curves have come into wide use in sedimentary work because of the convenience with which statistical values can be drawn from them.

4.3.1.2.2 Three Variables

1. Isopleth Maps

An isopleth is a line drawn on a chart or map showing equal abundance or magnitude of some quantity (grain size, density, porosity etc). With respect to grain size analysis, such a map would show the aerial distribution of grain sizes in the region under survey

2. Triangular Diagrams

The apices of the triangle represent one of each of the three variables being considered. In grain size analysis, the variables are usually the percentage sand, silt and clay fractions of the whole sediment. The total quantity of each fraction, expressed as a percentage of the whole, is plotted on the diagram (along a line parallel to the appropriate base, the particular component being the apex) and the particular region into which the point of trisection falls, defines the sediment.

3. Pie Diagrams

These indicate the relative magnitudes of any number of variables by the size of sediment of a circle.

4.3.1.3 Examination of the Data

The cumulative frequency curve described above provides information that can be analysed statistically and, from the values obtained, inference may be drawn about the sediment. Four statistical parameters are sufficient to adequately describe the sediment.

1) Central Tendency

Probably the most important measure as it provides the value about which all the other values cluster. The value corresponds to the size that is most frequent, although in asymmetrical curves this may not be so. For this reason it is preferable to obtain both the median and mean diameter. Inman (1952) proposed that:

$$Mean = \frac{\Phi_{16} + \Phi_{50} + \Phi_{84}}{3} \qquad (Eq.\ 4\text{-}36)$$

The 16^{th} and 84^{th} percentiles are chosen as they represent the diameters one standard deviation either side of the mean on a normal distribution curve. For skewed and bimodal distributions this is probably inadequate and the median diameter has been introduced.

$$Median = \Phi_{50} \qquad (Eq.\ 4\text{-}37)$$

2) Standard Deviation (Degree of Sorting)

Two frequency curves with the same average size may have entirely different degrees of spread. Consequently, the standard deviation indicates the degree of scatter or dispersion or spread of data about the central tendency.

$$Sorting = \frac{\Phi_{84} - \Phi_{16}}{4} + \frac{\Phi_{95} - \Phi_{5}}{6.6} \qquad (Eq.\ 4\text{-}38)$$

The lower the value of sorting, the increased sorting represented in the material (<1 – good sorting, >1 – poor sorting).

3) Kurtosis (B_Φ)

This is a measure of the peakedness of the frequency curve. Folk and Ward (1966) defined it as

$$Kurtosis = \frac{\Phi_{95} - \Phi_{5}}{2.44(\Phi_{75} - \Phi_{25})} \qquad (Eq.\ 4\text{-}39)$$

For a normal distribution the kurtosis has a value of 0.65. If the distribution is less peaked than normal, then $B_\Phi > 0.65$ and if the distribution is more peaked than normal $B_\Phi < 0.65$.

4) Skewness

The average size and the degree of spread of two curves may be the same but their symmetry may be different. A measure of the tendency of the data to spread on one side or another of the average is the called the skewness of the curve. Because skewness may be either to the left or the right, a positive or negative sense is usually assigned to it. Skewness is defined as the difference between the mean and the median divided by the standard deviation.

$$Skewness = \frac{\Phi_{16} + \Phi_{84} - 2\Phi_{50}}{2(\Phi_{84} - \Phi_{16})} + \frac{\Phi_{5} + \Phi_{95} - 2\Phi_{50}}{2(\Phi_{95} - \Phi_{5})} \qquad (Eq.\ 4\text{-}40)$$

This skewness measure is zero for a symmetrical size distribution. If the distribution is skewed towards smaller phi values (coarser diameters); the skewness is negative, and positive if skewed to the finer sizes.

4.3.2 Consistency

Consistency is a term that is frequently used to describe the condition of a soil. It denotes the degree of firmness of the soil and is indicated by such terms as soft, firm or hard. In practice, only the finer soils or fine fractions of coarser soils are so described, i.e. soils whose condition is markedly affected by changes in moisture content.

As a soil changes consistency, its engineering properties also change. Shear strength and bearing capacity, for example, vary significantly with consistency. Thus a textural classification indicating that a certain material is a clay is not sufficient for engineering purposes: it is also necessary to determine the condition of the clay.

To aid eliminating the personal factor in describing soil consistency, Atterberg (1911) arbitrarily established four states of consistency for fine-grained soils. These are the liquid, the plastic, the semisolid and the solid states. Atterberg developed a number of tests to determine the liquid limit, plastic limit and shrinkage limit of these materials. The cone penetrometer and plastic limit method are widely used in accordance with BS1377, 1990, Part 2 to determine the Atterberg Limits of consolidated materials.

The principles that lie behind the Atterberg Limits are that with addition of water to a fine grained sediment, particularly clays, a film of absorbed water is produced that covers each particle. If the percentage of water held in the structure of the material is high enough, the particles will have the potential to slide past one another with greater ease than normal, and the soil will begin to act as a liquid with no resistance to shear.

As the soil dries from the liquid state of consistency, a moisture content is reached at which it begins to attain a slight shear resistance. It is then said to have reached the limit of the liquid state of consistency, or more simply, it reaches its liquid limit (*L.L* or W_L). Similarly further loss of water will increase the shear resistance to a point where the material begins to behave as a semisolid. This limit is termed the plastic limit (*P.L.* or *Wp*). The convention is to evaluate or express the Atterberg Limits for a soil in terms of the moisture contents at these limits.

Knowledge of the liquid and plastic limit enables the plasticity index (*P.I.* or *Ip*) to be determined. The plasticity index measures the amount of water which is required to change the state of a sediment from its plastic limit to its liquid limit and is defined as the range over which the soil is plastic. It is calculated from the equation below: -

$$P.I. = L.L. - P.L. \qquad \textit{(Eq. 4-41)}$$

A final property that relates the in-situ condition of the sediment to its natural moisture content (ω) is the liquidity index (*L.I.* or I_L). This is calculated from the equation below: -

$$L.I = \frac{\omega - P.L.}{P.I} \qquad (Eq.\ 4\text{-}42)$$

This index property more usefully reflects the properties of plastic soils than the generally used consistency limits (*L.L.* or *P.L.*). Liquid and plastic limit tests are carried out upon remoulded soil, but the same soil, in its undisturbed in-situ state, may exhibit a different consistency at the same moisture content as the laboratory specimen, due to sensitivity effects. It does not mean therefore that a soil found to have a liquid limit of 50% will be in the liquid state if its in-situ moisture content is also at 50%.

If the in-situ moisture content of the sample is greater than the test value of *L.L.* then the *L.I.* is greater than 1.0 and it is obvious that if the soil were remoulded it would be transformed into a slurry. In such a case, it is likely that the soil is an unconsolidated sediment with an undrained shear strength of between 15 and 50 kN/m^2.

Most cohesive sediments have a *L.I.* value that is between 1.0 and 0.0. The lower the value of in-situ moisture content, the greater the amount of compression that must have taken place and the nearer *L.I.* will be to zero.

If the value of in-situ moisture content is less than the test value of the plastic limit then the *L.I.* will be less than 0.0 and the soil cannot be remoulded, since it is outside the plastic range. In this case, the soil will no longer exhibit permanent deformation and simply fractures with no plastic limit, i.e. it acts as a brittle solid. Soils in this state will have an undrained shear strength ranging from 50 to 250 kN/m^2 (Smith, 1990).

The Atterberg Limits classify a sediment mainly in terms of its shear strength. However, factors such as chemical and mineralogical composition, grain size and shape, will influence the amount of water that can be held in the sediment and hence will affect the Atterberg Limits.

After calculation of the liquid limit and the plastic limit, a classification of the sediment can be made. This is determined by plotting liquid limit against plasticity index on Casagrande's Classification Chart. The A-line is given by the equation: -

$$P.I. = 0.73(L.L. - 20) \qquad (Eq.\ 4\text{-}43)$$

This line separates inorganic clays (above the A-line) from organic clays (below the A-line). This plot classifies the plasticity class of the sediment.

4.4 *Other Tests*

4.4.1 Natural Sediment Properties

4.4.1.1 Natural Moisture Content

The determination of the natural moisture content of a sediment is of great importance, since the natural moisture content can give a preliminary indication of how the sediment will behave. For example, the shear strength of a sediment will vary greatly due to varying moisture contents.

In principle, the moisture content of a sediment can be defined as the ratio, in percent, of the weight of water in a given mass of sediment sample to the oven-dry (105°C) weight of solid particles. In the case of marine/coastal sediments, either the salt content must be completely removed prior to testing, or the amount of salt, determined from salinity tests must be accounted for in any of the subsequent calculations. In the case of the sediments in this study, this precaution is unnecessary.

4.4.1.2 Particle Specific Gravity

When given, the specific gravity, *Gs*, of a sediment is the specific gravity of the sediment solid particles. It can be defined as the ratio of the weight of a given volume of oven-dry (105°C) sediment at 20°C to the weight of an equal volume of de-aired distilled water at 20°C.

The specific gravity of a soil is often used in relating a weight of soil to its volume. Thus knowing the void ratio, the degree of saturation, and the specific gravity, the unit weight of a moist soil can be computed. Unit weights are needed in nearly all pressure, settlement, and stability problems in soil engineering. The specific gravity is also used in the computations of most of the laboratory tests.

Since most sediments contain particles of differing minerals, the final figure calculated is an average value of all the constituent particles of a sediment carried out upon a representative sample. The measurement of specific gravity requires a very careful

technique as all weighing has to be accurate to 0.001g. The tests were carried out in duplicate to detect any erroneous data.

The specific gravity of most soils lies within the range of 2.65 to 2.85. Soils with measurable organic content or soils with porous particles may have a specific gravity value below 2.0. Conversely, soils containing heavy substances, such as iron, may have specific gravity values over 3.0.

The specific gravity of a natural soil often depends upon how representative the test specimen is, because most soils are far from homogeneous. For example, the Quaternary boulder clays of Porth Neigwl, often contain lenses of silt which may cause the specific gravity to vary from 2.70 to 2.74 depending on the percentage of silt in the test specimen (Harrop, 1994)

4.4.1.3 Colour

Standard colour descriptions, as outlined in the British Standard (BS 5930, 1981), were used in the field. In the laboratory a more detailed description of the colour of the sediment samples was undertaken using a Munsell Colour Chart.

The Munsell colour-order system is a way of precisely specifying colours and showing the relationships among colours. Every colour has three qualities or attributes: hue, value and chroma. Munsell established numerical scales with visually uniform steps for each of these attributes. The Munsell Book of Colour displays a collection of coloured chips arranged according to these scales. Each chip is identified numerically using these scales. The colour of any surface can be identified by comparing it to the chips, under proper illumination and viewing conditions. The colour is then identified by its hue, value and chroma. These attributes are given the symbols H, V, and C and are written in a form H V/C, which is called the Munsell notation.

Soil colour is one of the characteristics used to identify properties of soil horizons within a pedon. Soil colour is the most obvious characteristic to distinguish soil horizons. Each horizon is made of different mineral and organic components. Therefore, the colour of a soil horizon is a composite of the colours of each of its components and is related to the surface area of particles. This means that colloidal materials have the greatest impact on soil colour. For example, humus is black or brown while iron-oxides may be red, rust-brown or yellow depending on the degree of hydration. Reduced iron is blue green. Other

common materials in soil have a range of colours: quartz is mostly white, limestones are white, grey or sometimes olive-green. Feldspars are predominantly red while clays are grey, white or red. The colours of clays are largely determined by the type and amount of iron coatings (Kohnke, 1968).

Soil colour can be used to determine the regime of water and air in soil. When a soil is saturated, water completely replaces the soil air. The absence of oxygen causes reduction of iron and manganese compounds which become soluble. When the soil dries, iron and manganese compounds are oxidized and precipitate out of the soil solution. Light-coloured patches of soil are low in iron and manganese while dark coloured patches show where the iron or manganese have been precipitated. The pattern of spots or blotches of different colour or shades of colour interspersed with the dominant colour is called mottling.

Wet and moist soils look darker than dry soils. Therefore, the soil colour description includes a symbol to indicate the moisture content of soil. Soil colour of surface horizons is correlated with organic matter content. Soils with a higher amount of organic matter have a greater nutrient supplying power and support greater plant productivity. Light colour frequently results from the preponderance of quartz, a mineral which has no nutritional value. Generally the sequence of productivity decreases as soils become lighter according to the following sequence: black, brown, rust-brown, grey-brown, red, grey, yellow and white (Kohnke, 1968). It is important to note that plant productivity is controlled by soil texture, structure, moisture and temperature regime and many other factors. Therefore, soil colour alone should not be used to predict plant productivity in different ecosystems. Soil colour is a good indicator of soil characteristics and is used with other soil characteristics to describe the processes of soil formation.

In generally, well aerated soils have bright colours while poorly aerated soils have darker colours. Soils in depressions have darker colours because they have higher amounts of organic matter. Practically all soil profiles show a change of colours from one horizon to the next and can be used to identify horizon sequences in a pedon.

4.4.2 Shear Strength

All failures in soils result from failure of the soil structure due to shear stresses. It is therefore very important to have knowledge of the shear strength parameters of materials. The shear strength is generally required for slope stability analyses and for foundation and piling bearing capacity assessments. Knowledge of soil strength is also important in an agricultural context, as it will greatly affect the type of plough used.

Depending upon the source of its strength, a soil can be placed in one of two groups, namely cohesionless and cohesive. Here, cohesionless soils have no cohesion, or attraction, between individual particles, whilst in cohesive soils the particles exhibit inter-attraction.

4.4.2.1 Strength Theory of Cohesionless Soils

The resistance to shear of a cohesionless soil is derived from the friction between grains and the interlocking of the grains. Friction between soil grains is similar to friction between any surfaces, as for example can be seen in Figure 4-9.

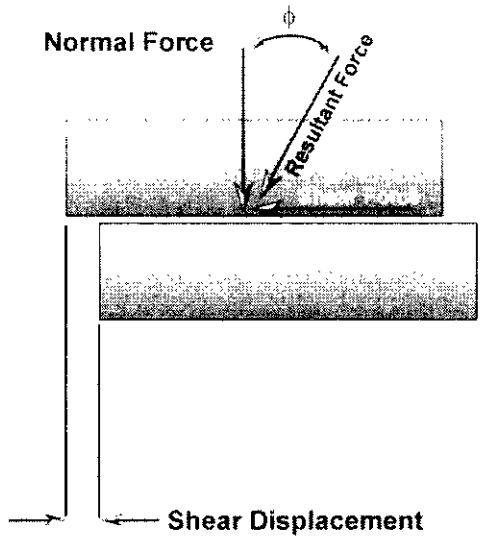

Figure 4-9. Friction between blocks.

When the top block is sliding along the bottom block, a shear force is applied to the surface of the bottom block that is equal to the normal force acting upon the blocks multiplied by a coefficient that is known as "the coefficient of friction". In soils, the friction may either be

a sliding friction, as shown in Figure 4-9, or rolling friction. For example, if a large enough shear force were applied to a soil grain A (See Figure 4-10), it could be moved to Position B by either sliding or rolling, or a combination of the two. Normally, no attempt is made to distinguish between sliding or rolling friction.

To move from Position B to Position C (Figure 4-10) against the applied normal force requires work. This work is the quantitative measure of the phenomenon termed interlocking.

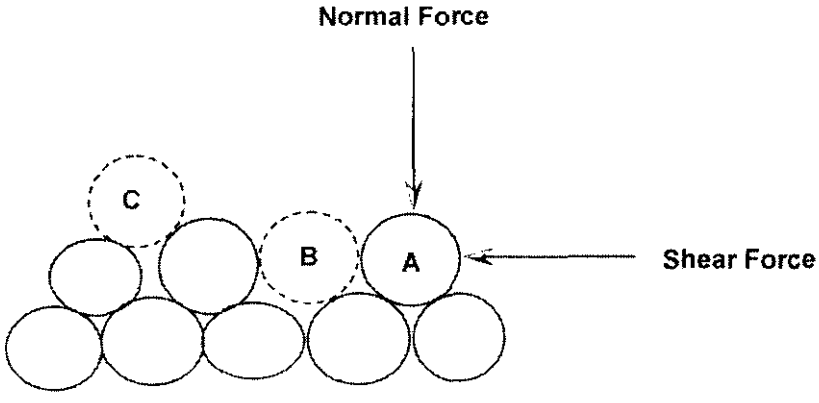

Figure 4-10. Friction in soil.

Because interlocking occurs to a greater extent when soil grains are closer together, dense soils show a higher shear strength at small shear displacements than loose soils. During the initial part of shear on a dense sand the volume of the soil increases, with the result that the effects of interlocking at reduced.

Figure 4-11 shows an element of soil being subjected to a shear force, which is equal to the normal force times *tan* α. If the area of the potential shear surface is A, then the shear stress, τ, is equal to the shear force divided by A; the normal stress, σ is equal to the normal force divided by A. It can be seen that

$$\tau = \sigma \tan \alpha \qquad \textit{(Eq. 4-44)}$$

The shear strength, s, is the shear stress that is necessary to cause slippage on a surface through the soil; or

$$s = \sigma \tan \phi \qquad \textit{(Eq. 4-45)}$$

where ϕ is the angle α at slippage. The shear strength of the soil can be expressed as s ("shear strength") or $tan\ \phi$ ("coefficient of friction") or ϕ ("angle of internal friction" or "friction angle").

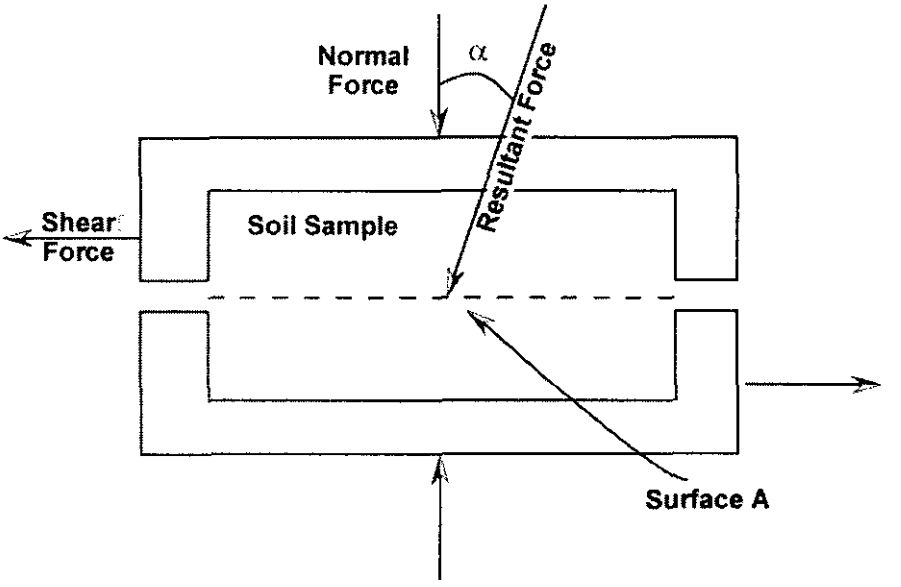

Figure 4-11. Shear of soil in a box.

Because of the phenomenon of interlocking, the strength of a dense cohesionless soil tends to be greater at small displacements than at large displacements, where the effects of interlocking have been overcome. The higher strength is called "peak" or "maximum" strength; the lower strength is known as "ultimate" strength.

Typical values of shear strength for cohesionless materials range from approximately 30 to 200kN/m^2 whilst peak friction angles in a dense well-graded, coarse sand usually range from 37° to 60°; for a dense, uniform, fine sand they are usually between 33° and 45°. There is less variation in the values of ultimate friction angle.

4.4.2.2 Strength Theory of Cohesive Soils

The elements of shear strength are considerably more complicated in cohesive soils than in cohesionless ones. This is due to the more complex arrangement of cohesive soils. Cohesionless soils are composed of particles that, because of their size and shape, have a small specific surface (the ratio of surface area to mass). The mass forces such as gravity control their behaviour rather than surface forces. Particles of cohesive soils, however,

because of their size and shape (usually small platelets) have a large specific surface. Their behaviour, therefore, can be influenced more by surface forces than by mass forces.

The shear strength of cohesive soil is made up of two components: friction, as in a cohesionless soil, and a second component called "cohesion", which is all the strength not due to friction. The exact nature of the surface forces that cause cohesion is not known. The cohesion of a soil is not a constant soil property but is a function of the load carried by the soil structure, or intergranular load, as well as of the details by which it is determined. The term cohesion is often used loosely for the shear strength of a soil when tested with no lateral load applied to the sample.

The following analogy will help to clarify this. Figure 4-12b shows the shear force required to move the block shown in Figure 4-12a, for differently applied normal forces. If the weight of the block is ignored, the relationship between normal force and shear force required to move the block is shown by line OA. Line OA is analogous to a plot of normal strength against shear strength for a cohesionless soil.

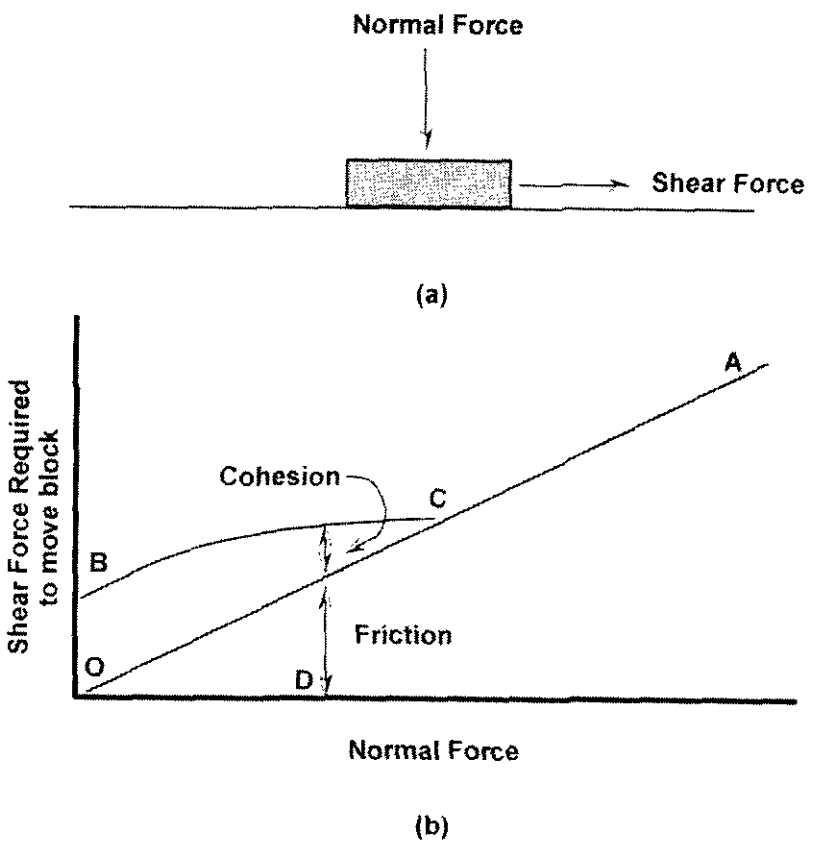

Figure 4-12. Analogy of cohesion.

If the block in Figure 4-12a is then stuck to the surface on which it is resting with an adhesive that can be squeezed out by pressure, line BCA in Figure 4-12b represents the relationship between an applied normal force and the shear force required to move the block. At any normal force, D, the resistance to movement is due to the friction between the block and the surface (corresponding to friction between particles in soil) plus the strength of the adhesive (corresponding to cohesion in the soil). At a normal force of C, the entire adhesive is squeezed out of the space between the block and the surface. In like manner, the cohesion of a soil can be reduced to zero at large normal pressures. The loose definition of cohesion mentioned previously would be represented by OB, which is the shear force required to move the block when no normal force is applied.

The portion of the load applied to a cohesive soil that is carried by the soil structure depends on the degree to which the pore water is permitted to drain and thus release its hydrostatic excess pressure (i.e. consolidate). Since the load carried by the water is not able to mobilise friction between soil particles, the shear strength of clay is higher (in most circumstances) if drainage occurs than if it is prevented. The two limiting drainage possibilities are:

1) Shear where there is complete pore water drainage making the excess pressure in the water zero.

2) Shear where no water drainage occurs.

The first type of shear is named "drained" or "slow" shear; the second type is called "undrained" or "quick" shear. Although both drained and undrained shear are possible in nature, most actual cases lie between the two.

4.4.2.3 Methods of Shear Testing

The three common methods of shear testing are direct shear, cylindrical (or triaxial), compression and torsional shear.

In a direct shear test, the soil is stressed to failure by moving one part of the soil container relative to another. This type of shear is illustrated in Figure 4-11. When a shear force of sufficient magnitude is applied, the top of the box moves relative to the bottom, causing the soil to shear along surface A. The triaxial test subjects the soil sample to three compressive stresses at right angles to each other, one of the three stresses being increased

until the sample fails in shear. Its great advantage is that the place of shear failure is not predetermined as in the shear box test.

Since the purpose of any laboratory shear test is to gain information on the effective shear strength of a soil in the field, the most appropriate test would be one that duplicates field conditions. However, the pressure systems existing in soils in the field are not completely understood to date, so that the better test type is the one in which the conditions of stress and strain are understood and controlled. On this reasoning, the triaxial test is preferable to the direct shear box. However, the speed and simplicity of the direct shear box justify its continued use.

The advantages of the triaxial test over the direct shear test are:

1) Progressive effects are smaller in the triaxial test.

2) The measurement of specimen volume changes are more accurate in the triaxial test.

3) The complete state of stress is known at all stages during the triaxial test, whereas only the stress at failure is known in the direct shear test.

4) The triaxial machine is more adaptable to special requirements.

However, there are several advantages to the direct shear test:

1) It is possible to test clays, sands and gravels.

2) It can be used to determine the residual shear strengths of materials. This is achieved by reversing the direction of travel of the machine.

3) A thinner sample is used in the direct shear test, thus facilitating drainage of the pore water from a saturated specimen.

4.4.3 Organic Matter Content

Surface soils and many underlying formations may contain significant amounts of solid matter derived from organisms. While shell fragments and similar solid matter are found at some locations, organic matter in soil is usually derived from plant or root growth and consists of almost completely disintegrated matter, such as peat.

The percentage of organic matter is vital to quantify since, under certain conditions of construction, the organic matter contained within the sediment may decompose leaving

voids in the soil mass. These voids, if founded under building foundations may cause instability and failure at worse, or at best the decomposition of the soil may produce a significant drop in the shear strength.

4.5 Results and Analysis of Unconsolidated Materials

The unconsolidated materials tested were taken from:

1) ARG test site

2) Indoor Tank

3) HMC, Stone Lane Quarry

4) NCPA

All these materials can be classed as cohesionless materials, except for the material from NCPA. This material is an agricultural loam that, in its original state would be classified as being a cohesive soil. However, the material has been specially prepared by sieving it to remove the coarse particles, then being crushed to a fine powder and finally oven dried. The drying of the material led to the removal of moisture from the structure, thus removing any cohesion between the particles. It has therefore been included in this section.

4.5.1 Comparative Tests

4.5.1.1 Permeability

4.5.1.1.1 Water Permeability

The most widely used technique for the determination of the permeability of cohesionless materials is the constant head permeameter test. This technique was undertaken upon the test materials and was carried out in accordance with procedures to be found in BS 1377, 1990, Part 5.

For each test, three differing flow rates were used. The permeability for each flow rate was determined from the average permeability from the bottom-to-middle and the middle-to-top of the sample. An average of the three flow rates was then calculated to give the mean overall permeability for that sample.

For each material two samples were tested with the average of the two tests given. The results of the constant head permeability test can be found in Appendix B. Table 4-12 shows the results of the test and also shows values of intrinsic permeability calculated using Equation 4-3.

Sample	Permeability (m/s)	Intrinsic Permeability (m^2)
ARG test site	$5.31x10^{-2} \pm 0.39x10^{-2}$	$5.43x10^{-9} \pm 3.97x10^{-10}$
Indoor tank	$6.76x10^{-3} \pm 8.10x10^{-5}$	$6.91x10^{-10} \pm 8.28x10^{-12}$
HMC Stone Lane	$2.22x10^{-4} \pm 2.50x10^{-6}$	$2.26x10^{-9} \pm 2.55x10^{-11}$

Table 4-12. Values of permeability and intrinsic permeability measured using the constant head permeameter.

It can be seen in Table 4-2 that a typical permeability for a gravel is in the range $>10^{-1}$m/s, whilst the value gained from the constant head permeameter was $5.31x10^{-2} \pm 0.39x10^{-2}$m/s and lies slightly below this range. Table 4-2 shows that typical values for the permeability of sand lie in the range $>10^{-1}$ to 10^{-5}m/s and both the Indoor tank and HMC Stone Lane materials lie within this range.

4.5.1.1.2 Flow Resisitivity

The flow resistivity of the samples was measured using a flow rig, following ASTM standard C522-60. The apparatus is primarily designed for the measurement of foams and materials with an integral structure. A schematic diagram of the flow rig can be seen in Figure 4-13. Since the original apparatus was design for materials with an integral structure, this meant that measurements of the cohesionless materials led to a slight modification of the apparatus.

Whereas in the standard apparatus the sample holder is placed horizontally in the airflow, this was not practical for the cohesionless materials. A metal L-section of the same diameter as the original pipework was placed in the rig and the sample holder positioned vertically. A fine mesh (~63 μm) was then placed to stop any of the sample

under test being pushed through the apparatus. It was thought that although the presence of the mesh would result in a slightly higher value of the flow resistivity, this set-up would provide an indicative value.

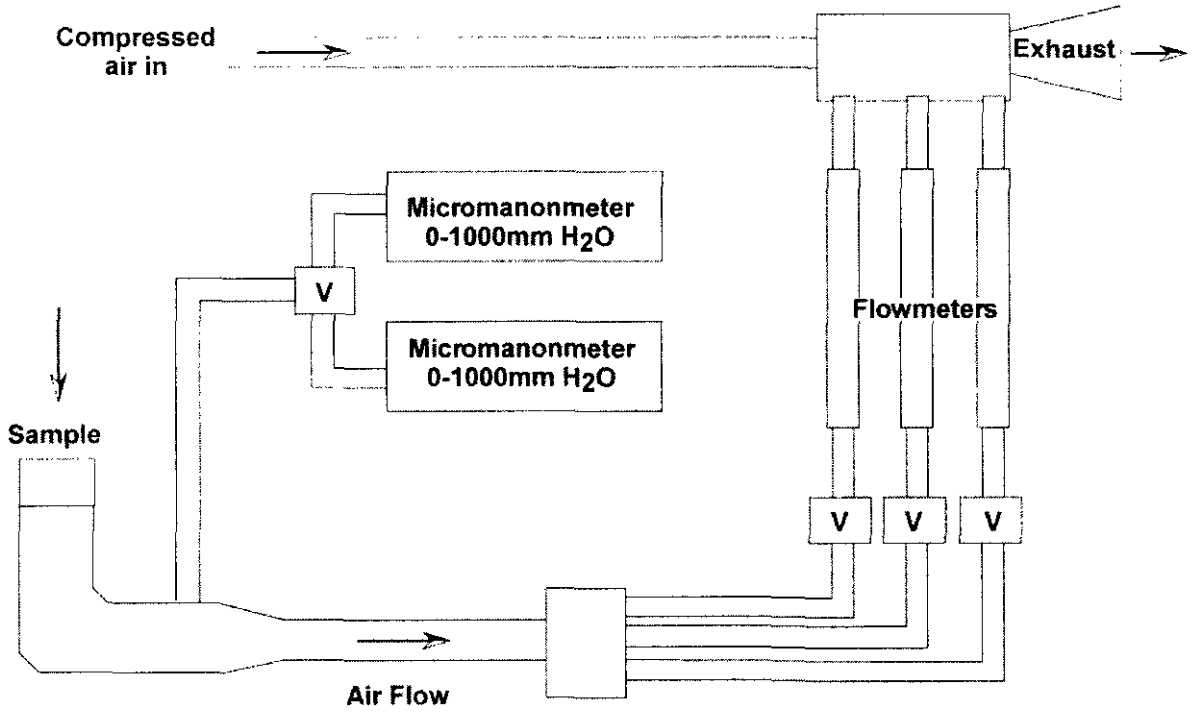

Figure 4-13. Schematic diagram of the flow rig.

Once the sample under test had been placed into the sample holder, a pressure differential was created on one side of the sample by the venturi effect, using a compressed air source. Hence, air flowed through the sample to equalise the induced pressure differential. The flow rate was regulated and measured by a set of three flow meters. The pressure drop across the sample was measured using two micromanometers.

Starting with a flow rate of approximately three litres per minute the pressure was noted. The flow rate was then reduced in steps and the measured flow rate and pressure drop noted. At each step the flow resistivity of the sample was calculated using: -

$$R = \frac{C_1 A \delta P}{QL} \qquad \textit{(Eq. 4-46)}$$

where: -

C_1 = a conversion factor of 2940

A = the cross sectional area of the sample in cm^2

δP = the pressure drop in mm of H_2O

L = the sample thickness in cm

Q = the flow rate in cm^3s^{-1}

Since outdoor testing was undertaken over a period of time two flow resistivity measurements were taken.

The results of the air flow resistivity experiments can be found in Appendix B, with Table 4-13 showing the results of the test. Table 4-13 also show values of intrinsic permeability calculated using Equation 4-11.

Sample	Flow Resistivity (MKS Rayls)		Intrinsic Permeability (m^2)	
	Test 1	Test 2	Test 1	Test 2
ARG test site	925 ± 83	1072 ± 53	$1.96\text{x}10^{-8} \pm 1.90\text{x}10^{-9}$	$1.69\text{x}10^{-8} \pm 8.00\text{x}10^{-10}$
Indoor Tank	16545 ± 726	16802 ± 148	$1.09\text{x}10^{-9} \pm 5.00\text{x}10^{-11}$	$1.08\text{x}10^{-9} \pm 6.82\text{x}10^{-12}$
HMC Stone Lane	21748 ± 598	17927 ± 433	$8.32\text{x}10^{-10} \pm 1.38\text{x}10^{-11}$	$1.01\text{x}10^{-9} \pm 2.46\text{x}10^{-11}$
NCPA	419855±264044	320789±135587	$4.31\text{x}10^{-11} \pm 1.66\text{x}10^{-11}$	$5.64\text{x}10^{-11} \pm 4.13\text{x}10^{-11}$

Table 4-13. Values of measured flow resistivity and calculated intrinsic permeability.

Whilst Table 4-4 does not show any values for gravels, it does show a wide range of values for a typical air flow resistivity of a dry sand. These range from 60000 MKS Rayls up to 376000 MKS Rayls, whereas the value for the indoor tank material is approximately 16500 MKS Rayls and is approximately 18000 MKS Rayls for the HMC Stone Lane material.

The results show that there is a slight variation between the measured values. This and the low measured values are probably due to variations in moisture content of the samples.

A larger variation is seen in the results for the NPCA material. This difference can most likely be attributed to the fact that, since the material is extremely fine grained with increasing air flow velocity preferred flow paths are being generated in the material. From the results of the test (See Appendix B) it can be seen that there is a sharp drop in the measured flow resistivity with increasing air flow velocity, thus giving the wide range of values.

4.5.1.2 Porosity

The porosity of the cohesionless sediments was determined using the procedure outlined in Section 4.2.2, with the measured values shown in Table 4-14.

Sample	Porosity (%)
ARG Test Site	45.88±0.13
Indoor Tank	38.92±0.31
HMC Stone Lane	37.31±0.96
NCPA	22.12±1.12

Table 4-14. Measured values of porosity for the cohesionless materials.

It can be seen in Table 4-4, that a range of values for the porosity of sands has been reported from 34% to 47% and that the values for the Indoor Tank and the HMC Stone Lane material, shown in Table 4-14, lie within this range. The higher value for the ARG test site material is expected for an angular coarse material such as this.

4.5.1.3 Tortuosity

The materials under test were placed in a Jackson cell (See Figure 4-14) and the resistivity values of the sediments for varying degrees of compaction were taken. From these resistivity values the formation factor and porosity ware calculated. Using the porosity previously measured, in conjunction with the formation factor, leads to the calculations of the tortuosity using Equation 4-22.

4.5.1.3.1 Equipment

The apparatus consisted of a Jackson resistivity cell (See Figure 4-14) and ABEM AC Terrameter. The cell comprises a large Perspex cylinder with a widened portion at its base. A graduated neck gives volume readings and acts as a reservoir for the electrolyte.

In the base area are placed two steel plates on opposing sides of the cell, each having two electrodes attached to them. Each plate consists of a matrix of stainless steel

screws, wired alternatively in series to produce one current electrode and one voltage electrode.

The two current electrodes are used to pass current through the sample, whilst the voltage electrodes measure the potential difference produced. Both current and voltage electrodes are necessary to avoid spurious readings due to contact impedances' at the current electrode surface.

The ABEM AC Terrameter is connected to the four electrodes in the Jackson cell. The Terrameter is primarily a field instrument, used essentially to measure ground resistance, which when multiplied by a factor dependent on the geometry of the electrode arrangement can be converted to ground resistivity.

A funnel was used to ensure no spillage of the electrolyte occurred. The funnel also ensured that the initial porosity of the sediments was as high as possible. A standard thermometer was used to provide temperature readings. Changes in temperature will alter the overall bulk resistance of the sediment; i.e. the resistance of the pore fluid will vary. The pore fluid resistance must therefore be corrected to the original temperature of the electrolyte before the formation factor can be calculated.

4.5.1.3.2 Procedure

The samples to be investigated were placed into large evaporating basins filled with the electrolyte (in this case seawater was used) and left overnight to saturate.

The Terrameter was connected to the Jackson cell by way of the two current and two voltage electrodes. Then using the funnel provided, the electrolyte was carefully poured into the cell. Care must be taken at this point to remove any air bubbles that may be trapped within the cell, as these will alter the resistance readings.

A current was then passed through the fluid and the resistance noted. The temperature of the electrolyte is also noted at this point.

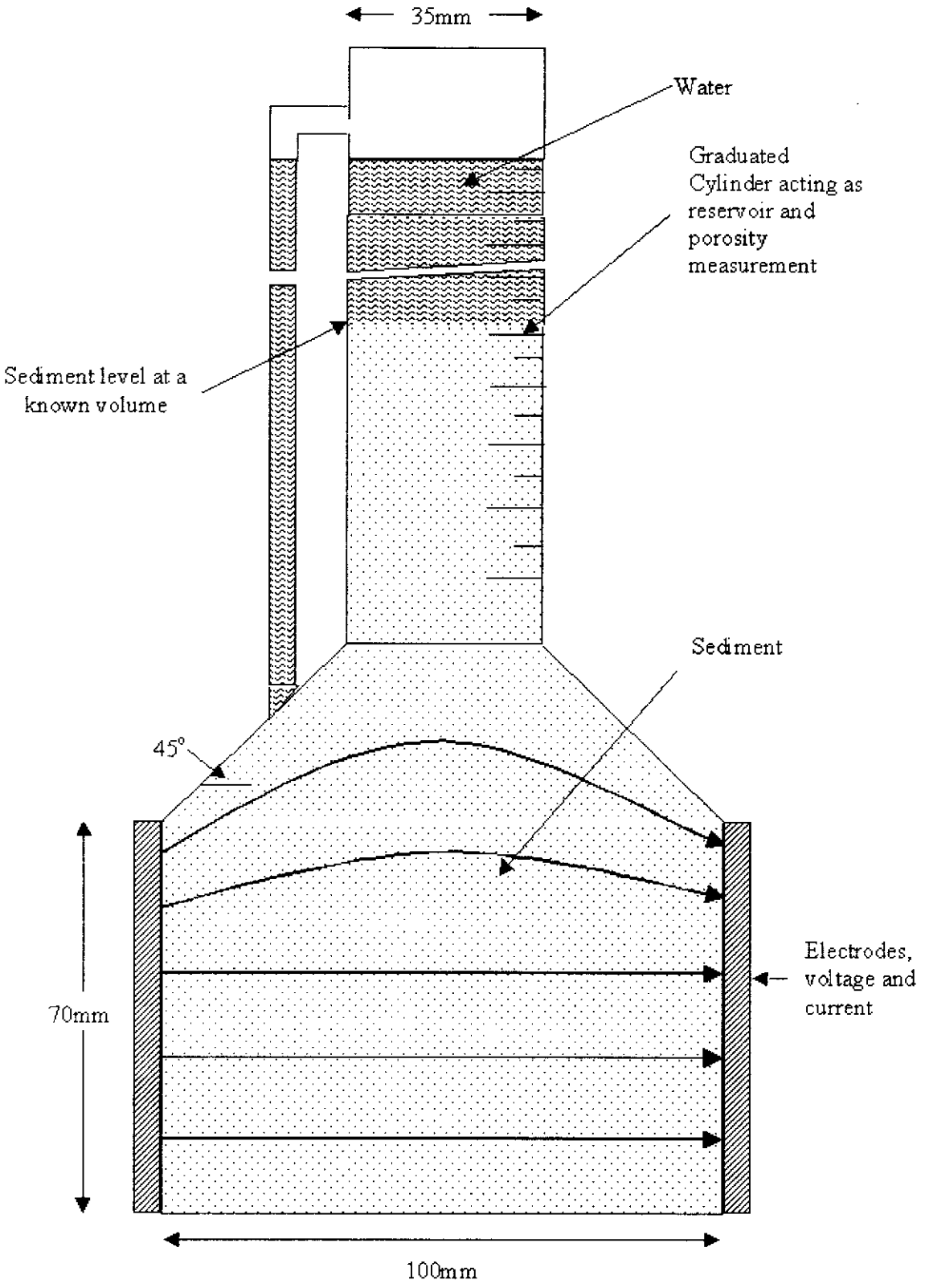

Figure 4-14. The Jackson Cell, showing the bypass system, and the volume-measuring device.

At this point, the sample was placed into the cell. It was important when adding the sediment that it was entered into the cell as slowly as possible, since the slower the grains are allowed to settle, the higher the initial porosity. This was achieved by using a spoon to place the grains into the funnel. This method also ensured that there was a uniform distribution of the moisture content through the sample.

Once all the sediment had been entered, the excess electrolyte was siphoned from the funnel, leaving the neck of the cell full. The level of the sediment below the zero mark on the graduated neck was noted. A resistivity reading and the temperature were then noted.

The sediment was then compacted to reduce its porosity. This was achieved by gently tapping the cell with a hammer until the sediment had been compacted by approximately 10ml. At lower compactions it was only necessary to gently tap the cell. N.B. Any major vibration will cause liquefaction in the cell neck as the increase in pore pressure caused by the interchange of the grains and the pore fluid exceeds the gravitational forces acting upon the grains. The overall result of this, is piping of the sediment and production of non-uniform porosity in the cell.

At higher compactions the hammer blows, when applied, were continuous around the perimeter top of the cell, ensuring the cell was resting on a firm surface. Due to differential settlement of the sediment, averages of the volume were taken. Temperatures were taken away from the sides of the cell.

Compaction of the sediment, with associated resistivity and temperature readings, was carried out until maximum compaction was achieved. Once this had been achieved the cell was emptied into the original container, placed into an oven for 24hrs, and weighed.

Temperature corrections were applied as necessary to the pore fluid resistance and the porosity of each reading calculated. Since the porosity of the fully saturated sediment can be defined as the ratio of pore space volume to the total volume.

$$\Omega = \frac{V_v}{V_t} \qquad \textit{(Eq. 4-47)}$$

where:-

Ω= porosity

V_v = volume of the pore spaces

V_t = total volume

For the cell, the porosity can also be computed using:-

$$\Omega = 1 - \frac{W_s}{\rho_s (V_t - dV)} \qquad \textit{(Eq. 4-48)}$$

where:-

W_s = dry weight of the sample

ρ_s = specific gravity of the grains

V_t = total volume of the cell to the zero mark

dV = volume of fluid above sediment in the cell to zero mark

4.5.1.3.3 Results

The results for the determination of formation factor using the resistivity method for the materials can be seen in Figure 4-15. A line of best fit has been applied to the data for the Indoor Tank material that has a gradient (and therefore a value of m) of 1.92, whilst a gradient of 1.82 has been determined for the HMC Stone Lane material and 1.26 for the ARG Test site material.

The formation factor of the materials was then calculated using:-

$$F = a\Omega^{-m} \qquad \textit{(Eq. 4-49)}$$

Using the values of porosity as determined in Section 4.5.1.2 and the relationship:-

$$\tau = F\Omega \qquad \textit{(Eq. 4-50)}$$

the tortuosity of the material has been calculated. These values can be seen in Table 4-15.

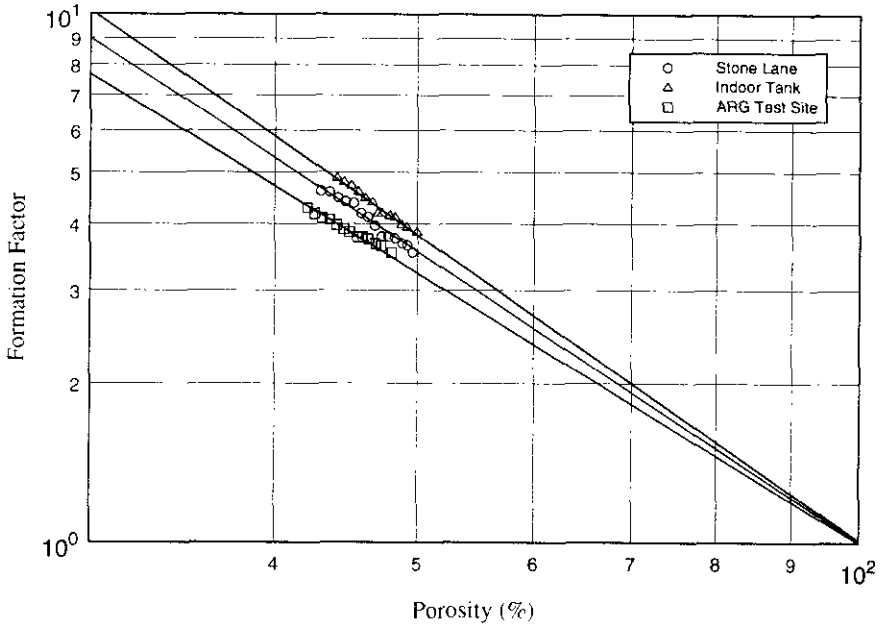

Figure 4-15. Plot of log Formation Factor against Log Porosity for the sediment samples under investigation. Measurements were taken over a porosity range of 40-50%.

Sample	Porosity (%)	Tortuosity
Indoor Tank	38.92±0.31	2.38±0.02
HMC Stone Lane	37.31±0.96	2.24±0.04
ARG Test Site	45.88±0.13	1.22±0.002

Table 4-15. Calculated values of tortuosity.

4.5.1.4 Elastic Moduli

A resonant column device was used to measure the shear, Young's modulus and frame loss coefficients of the cohesionless sediments. This device can accurately measure the dynamic moduli and frame loss coefficient of soils at a very low shear strain of the order 10^{-6}.

The quantities measured during the test are the resonant frequency, vibration amplitude, force or torque produced by the oscillator, the length and volume changes in the sample and the confining pressure at which the measurements are taken. From this data,

the Shear and Young's modulus, strain amplitude, damping and propagation velocity can be determined for both torsional and longitudinal vibrations.

Due to the nature of the apparatus it is unsuitable for very coarse materials such as those found at the ARG test site. Therefore, only the materials from the indoor tank and HMC Stone Lane Quarry were tested.

4.5.1.4.1 Equipment

The instrument used was a modified version of the Drnevich resonant column apparatus in which the sample under investigation is firmly attached at the base and is free to oscillate at the top (Figure 4-16).

The sample is prepared in a similar manner to the triaxial test where a cylindrical sample is placed within a rubber membrane to which a confining pressure can be applied. In the case of cohesionless materials a metal mould is used to form the cylindrical shape and the material carefully placed.

The instrument is designed so that both torsional and longitudinal motions can be induced by means of coil magnet drive mechanisms and the resultant movement is recorded by horizontal and vertically placed accelerometers attached at the top of the sample. A linear variable differential transformer (LVDT) is used to detect any length changes in the sample during testing. LVDT's are a common type of electromechanical transducer that can convert the rectilinear motion of an object to which it is coupled mechanically into a corresponding electrical signal. A schematic of the electronic components used in the test can be seen in Figure 4-17.

A signal generator is used to generate a sinusoidal voltage, which is amplified and is used to drive either the torsional or longitudinal coils. Accelerometers are used to record horizontal and vertical motion.

A set of calipers is needed for accurate measurement of the sample dimensions.

4.5.1.4.2 Procedure

For the cohesionless materials a sample mould was used to form the cylindrical sample shape used in the test. This gave a sample of approximately 78mm x 36mm.

The sample mould was positioned on the bottom end platen with a rubber membrane on the inside. The membrane is held in position with the aid of a vacuum pump. The cohesionless material under investigation is then carefully placed into the mould with any excess material tested for moisture content.

With the sample in place the top end platen containing the shear wave transducer, were carefully positioned, the split mould removed and the sample dimensions were measured using a pair of vernier capliers. The remaining portions of the apparatus were then positioned. Once the perspex outer casing was in place the chamber was filled with distilled water up to the top of the sample so that the electrical components were still above the water.

An initial reading was then taken from the LVDT. This measured an effective length of the sample so that changes in length and volume could be monitored with increasing effective confining pressure. A confining pressure of $10kN/m^2$ was then applied to the cell and the sample left for several hours in order for it to consolidate to the applied effective stress. Once this period had elapsed the specimen was ready for measurements to be undertaken.

A low confining pressure was used since the materials were sampled close to the surface and only small values of effective depth were of interest.

With the control box switched to the torsional setting, and the torsional charge amplifier on, a frequency of 10Hz was set on the signal generator and the plot on the X-Y oscilloscope noted. The X-Y plot on the oscilloscope shows the phase relationship between the driving force/torque and the resulting motion. When they are 90^o out of phase the sample is at its undamped resonant frequency and a vertical ellipse is observed on the scope. Using this method the resonant frequency can be established to approximately 0.1Hz.

The frequency from the generator was increased until a vertical ellipse was observed. At this point the driving voltage to the coils, the accelerometer output voltage as monitored on the digital volt meter, and the resonant frequency from the signal generator were all noted.

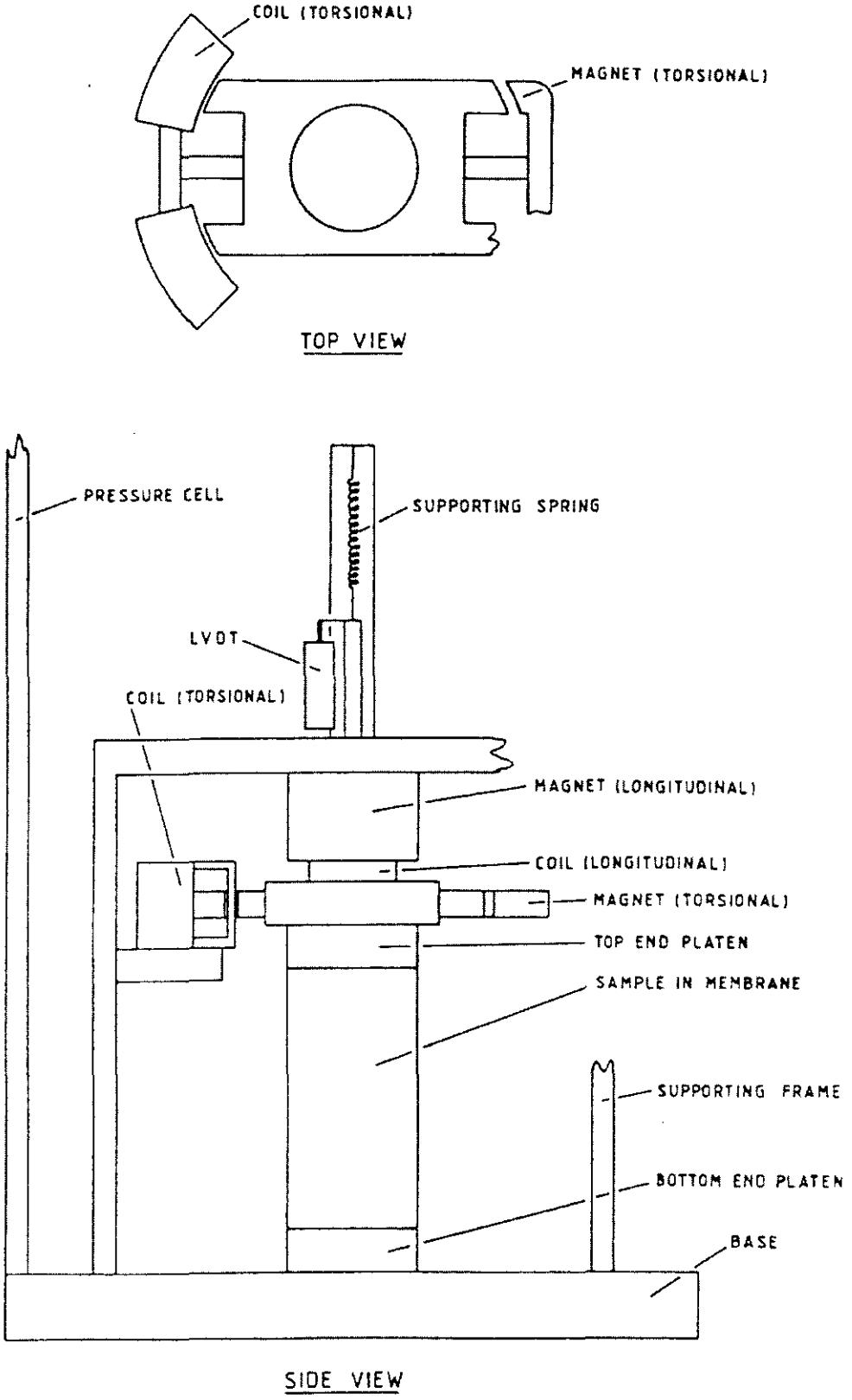

Figure 4-16. Schematic Diagram of the Resonant Column Apparatus

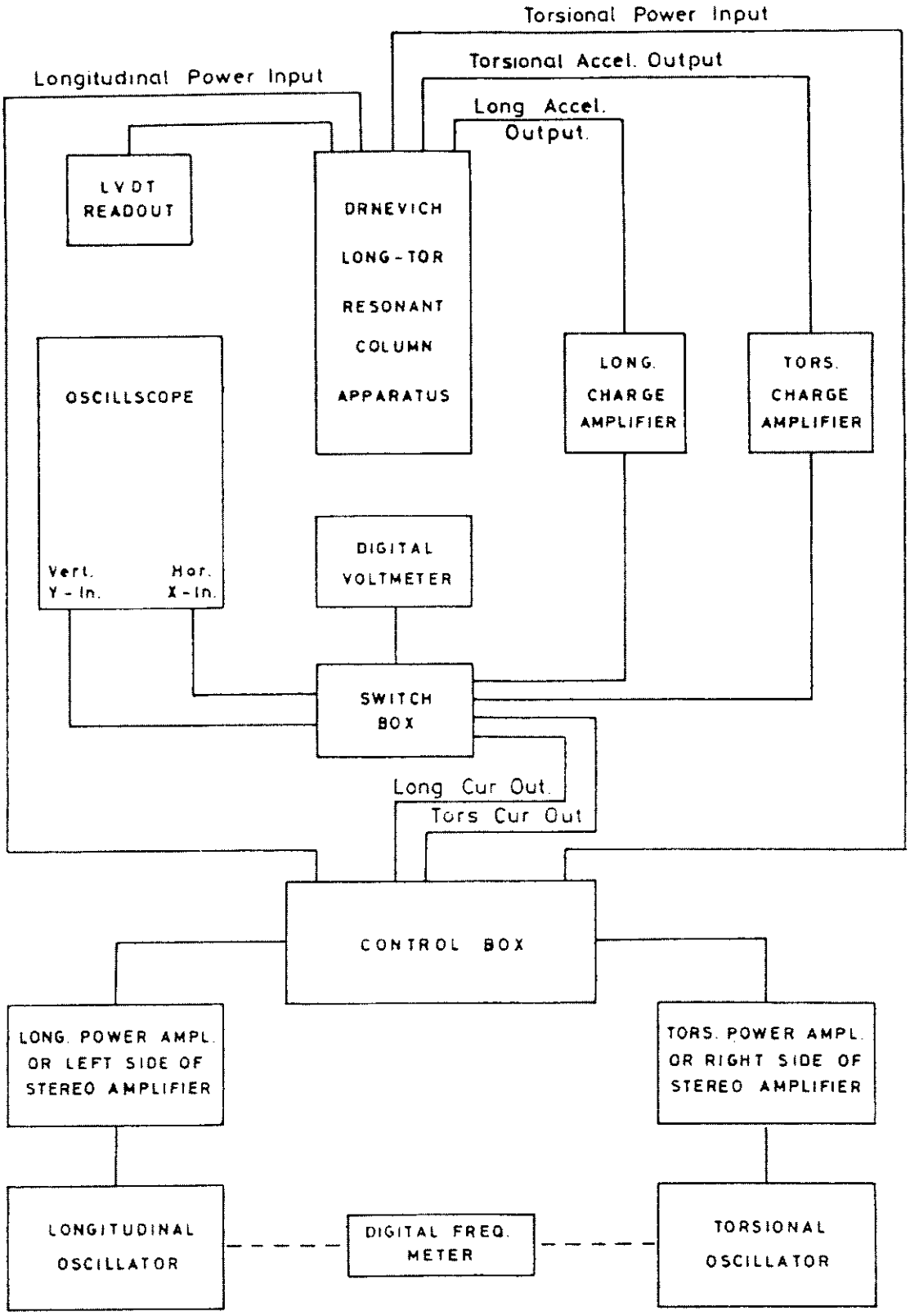

Figure 4-17. A schematic of the electronic components used in the resonant column test.

With this completed the control box was switched to the longitudinal setting and the longitudinal charge amplifier turned on. The process was then repeated, increasing the output frequency to the drive coils until again, a vertical ellipse was observed on the X-Y oscilloscope. Once more, the driving voltage to the coils, the accelerometer output voltage and the resonant frequency were all noted.

The input to the drive coils and the output from the longitudinal accelerometer was then viewed on a second oscilloscope. The control switch was then turned off and the oscilloscope manually triggered to hold the current plot. Measurements were taken of the amplitude of the first 5 cycles from the accelerometer after the input to the drive coils had been turned off.

These measurements were used for determination of the damping using the logarithmic decrement method.

The confining pressure in the chamber was then increased to 20kN/m^2 and the sample was again left for several hours to consolidate to the new confining pressure. The complete process was then repeated. Further measurements were taken at confining pressures of 30, 40, 50, 70, and 100kN/m^2.

At the end of the test cycles, the apparatus was dismantled and the sample was carefully removed, ensuring all the material was recovered. The material was then placed into a bowl, weighed and placed into an oven for 24hrs. This enabled the bulk density and moisture content to be determined.

Once all the measurements had been taken the shear modulus at each resonant frequency, f_n, could be calculated using:

$$\mu = \rho_b (2\pi L)^2 (f_T / F_T)^2 \qquad \textit{(Eq. 4-51)}$$

where

ρ_b = bulk density of the sediment sample

L = length of the sample

f_T = resonant frequency

F_T = dimensionless frequency factor that is obtained from the relationship

$$F(\tan F) = \frac{J}{\left\{ J_A - \left[\frac{T_s}{(2\pi f)^2} \right] \right\}} \qquad \textit{(Eq. 4-52)}$$

where:-

$$J = \frac{wr^2}{2} \qquad \textit{(Eq. 4-53)}$$

In these equations,

J_A = rotational inertia of the mass attached to the top of the specimen

r = radius of the specimen

w = weight of the sample

T_s = torsional spring constant attached to the top mass.

The longitudinal measurements allow the dynamic Young's Modulus of the material to be calculated by inserting E into equation 4-51 instead of G. Making use of the relations between the elastic moduli, outlined in Section 4.2.4, allows the determination of the Bulk Modulus of the samples and the P-wave velocity to be calculated. However, it must be noted that for materials where the Young's Modulus is three times greater than the Shear Modulus the theory is no longer valid, since the Poisson's Ratio (σ) becomes greater than 0.5.

4.5.1.4.3 Results

The results of the resonant column experiment can be found in Appendix B.

Figure 4-18 shows the variation in shear modulus and shear damping with effective depth for the Indoor Tank material, whilst Figure 4-19 shows the data for the HMC Stone Lane material. It can be seen that both materials show similar behaviours, showing an increase in shear moduli and a decrease in shear damping with increasing depth. They have a shear modulus of approximately 20MPa at depths close to the surface. Best-fit regressions have been applied to the shear modulus data.

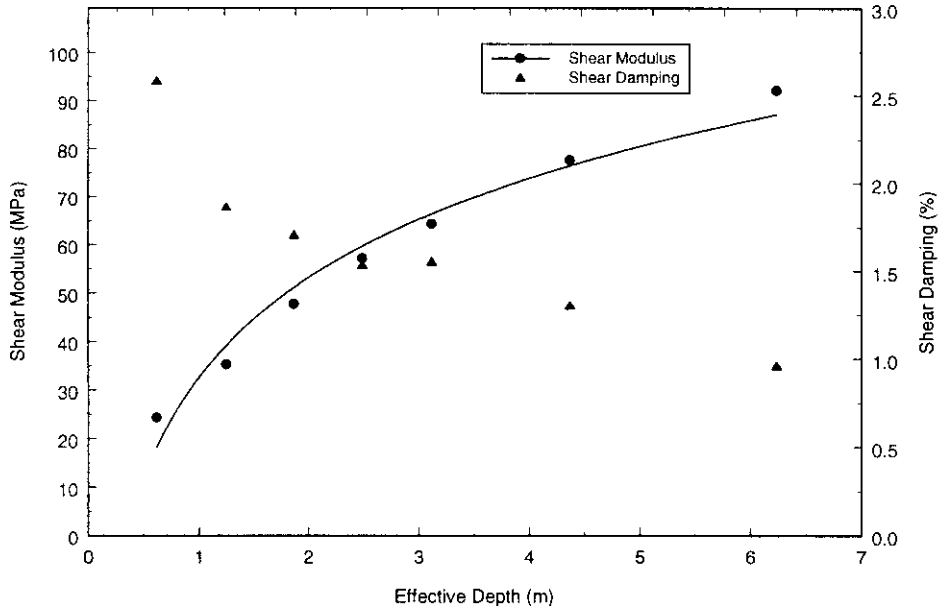

Figure 4-18. Change in Shear Modulus and Shear Damping with effective depth for the Indoor Tank material. Best fit regression has been applied to the modulus data.

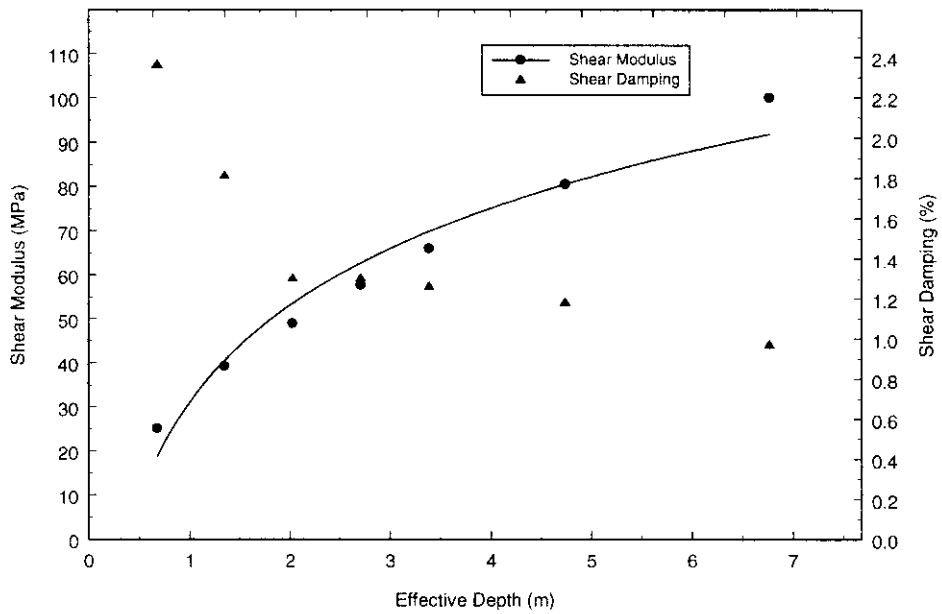

Figure 4-19. Change in shear modulus and shear damping with effective depth for the HMC Stone Lane material. Best fit regression has been applied to the modulus data.

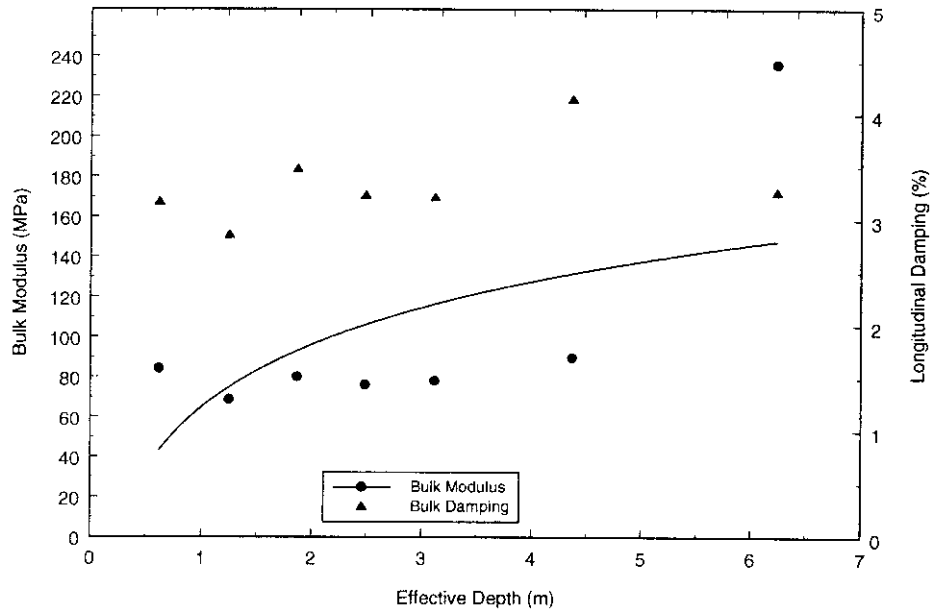

Figure 4-20. Change in bulk modulus and longitudinal damping with effective depth for the Indoor Tank material. Best-fit regression has been applied to the modulus data.

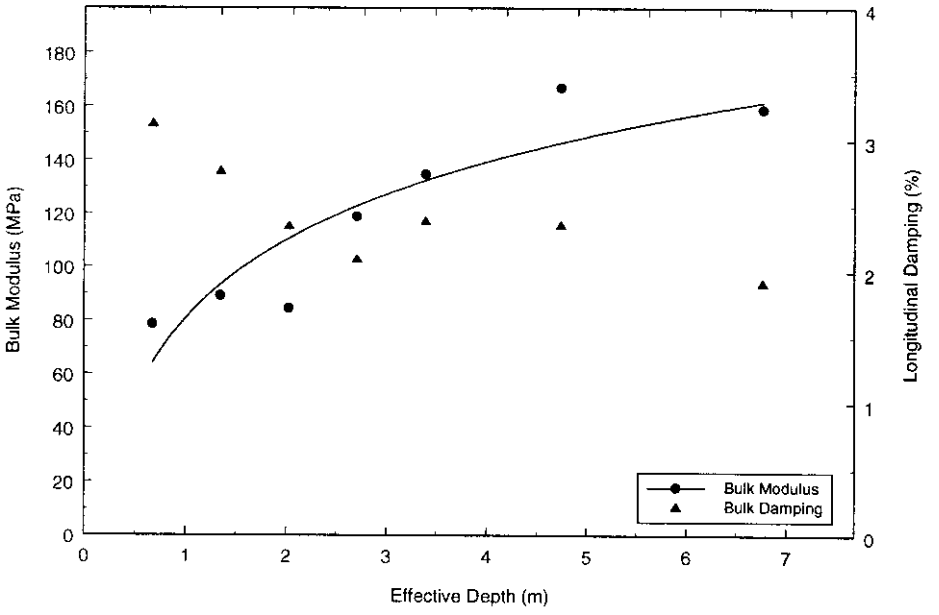

Figure 4-21. Change in bulk modulus and longitudinal damping with effective depth for the HMC Stone Lane material. Best-fit regression has been applied to the modulus data.

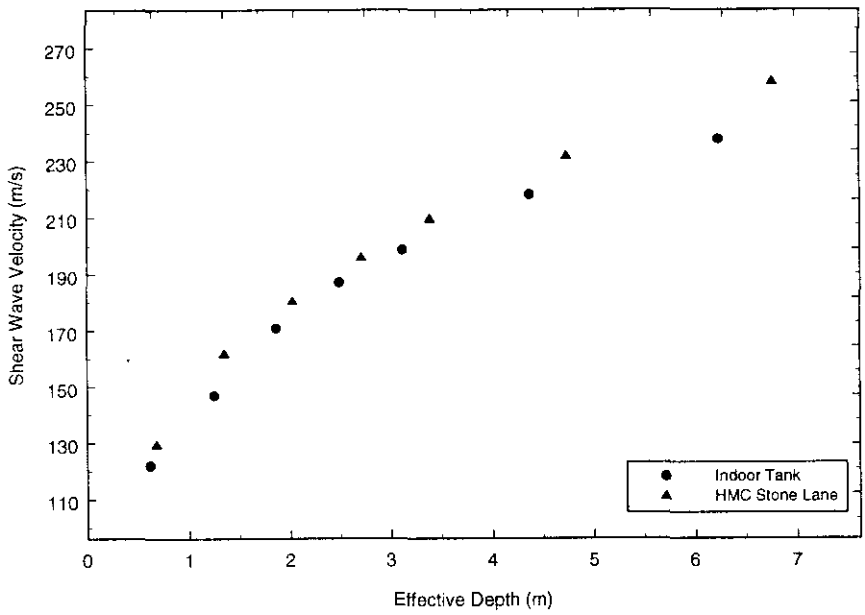

Figure 4-22. Change in shear wave velocity with effective depth for the cohesionless materials.

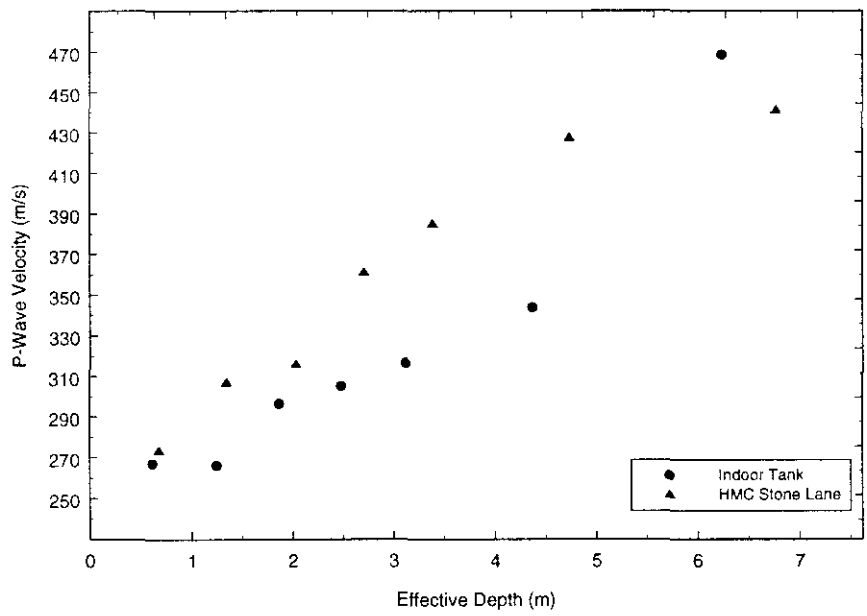

Figure 4-23. Change in P-wave velocity with effective depth for the cohesionless materials.

Knowledge of the shear modulus allows the determination of the shear wave velocity to be calculated. Figure 4-22 shows the variation in shear wave velocity with effective depth for both cohesionless materials. It can be seen that both materials exhibit similar shear wave profiles and have shear wave velocities typical of unconsolidated materials such as these, rising from approximately 130m/s close to the surface to 240m/s at a depth of 6.5m

Figure 4-20 shows the variation in bulk modulus and longitudinal damping with effective depth for the Indoor Tank material. The plot shows that there is little change in either of the two parameters up to an effective depth of 4.5m after which the bulk modulus of the material rises rapidly from 80MPa to 240Mpa at 6.2m. The data from HMC Stone Lane can be seen in Figure 4-21. This data shows a gradual increase in bulk modulus, whilst a gradual decrease in the longitudinal damping can be seen.

Figure 4-23 shows the variation in P-wave velocity with effective depth for both materials. For the Indoor Tank, the plot shows an increase in P-wave velocity with depth from approximately 270m/s at the surface to 350m/s at a depth of 4.5m. The velocity increases rapidly to 470m/s at a depth of 6m. This follows the trend seen in the bulk modulus from which the P-wave velocity is calculated. The velocity results show that at a depth of 0.5m, for example, the Poisson's Ratio of the material is 0.36, which is typical for a loose sand such as this.

Again the results for the HMC Stone Lane material, indicate wave speeds typical for this type of material. These range from roughly 270m/s at the surface and rise gradually with increasing depth to 450 m/s at a depth of 6.5m.

It can be seen in all the plots that there is some spread in the data. This is to be expected since the materials tested were disturbed samples. The results will be subject to the quality of sample emplacement into the mould, with any inhomogeneities in sample preparation showing in the results.

The spread is most noticeable in the plots showing calculated bulk modulus, since this is calculated from the measured shear and Young's modulus and calculated via inter-relationships.

4.5.2 Classification

4.5.2.1 Particle Size Analysis

As described in Section 4.3.1.1.1 the most common method used for the size analysis of large particles (sand and gravels) is dry sieving. The dry sieving technique for particle size analysis was undertaken upon the three cohesionless materials and was carried out in accordance with procedures to be found in BS 1377, 1990, Part 2.

The sieving method requires a weight of sample between 60 and 80g taken as a random sample from the original sample. To ensure that a random sample is taken the cone and quartering method was employed as outlined in BS 1377 Part 1. Material classification is based upon the Wentworth Scale.

4.5.2.1.1 ARG Test Site

Dry sieving of the material taken from the ARG test site led to the particle size distribution as seen in Figure 4-24, whilst Table 4-16 shows the statistical parameters calculated using data from Figure 4-25.

Statistical Parameter	Value
Median	-2.74
Mean	-2.68
Degree of Sorting	0.61
Kurtosis	0.21
Skewness	1.08

Table 4-16. Statistical Parameters for ARG test site material.

It can be seen from the particle size distribution curve that the material consists of a range of particle sizes with the median value being 6.7mm, indicating this to be a Medium GRAVEL. The distribution shows that nearly 68% of the material is of medium gravel sized, 30% being of fine gravel size and with approximately 2% being of sand sized particles.

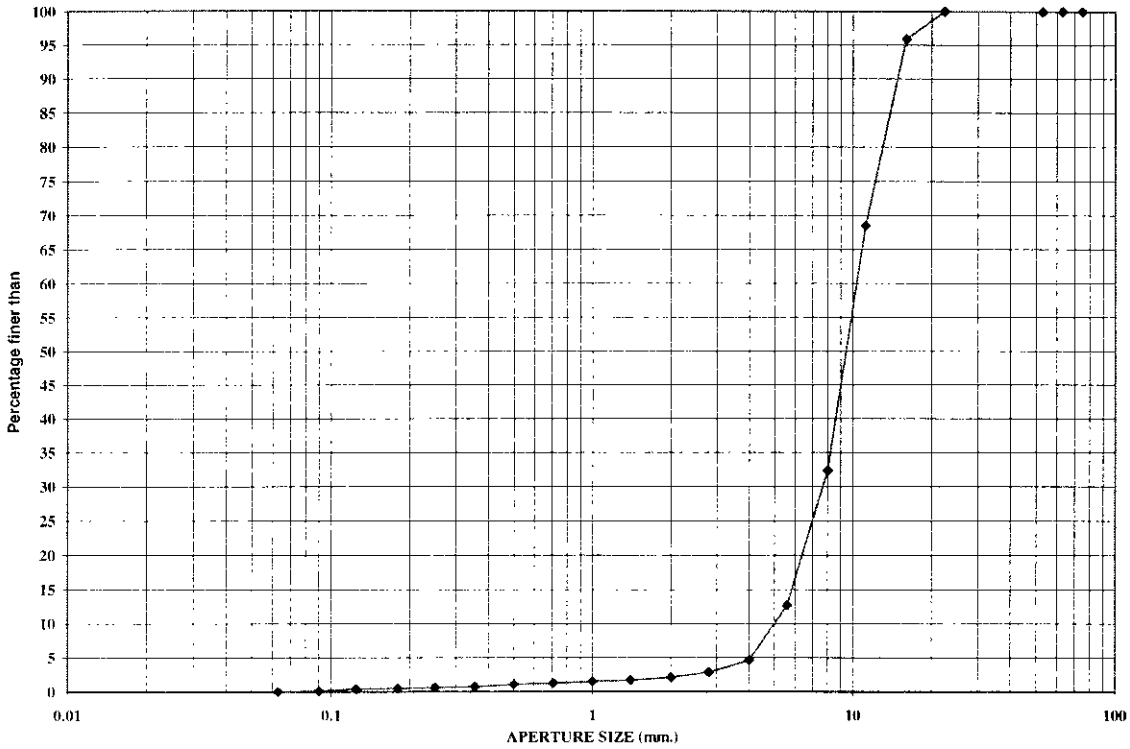

Figure 4-24. Particle size distribution of the ARG test site material.

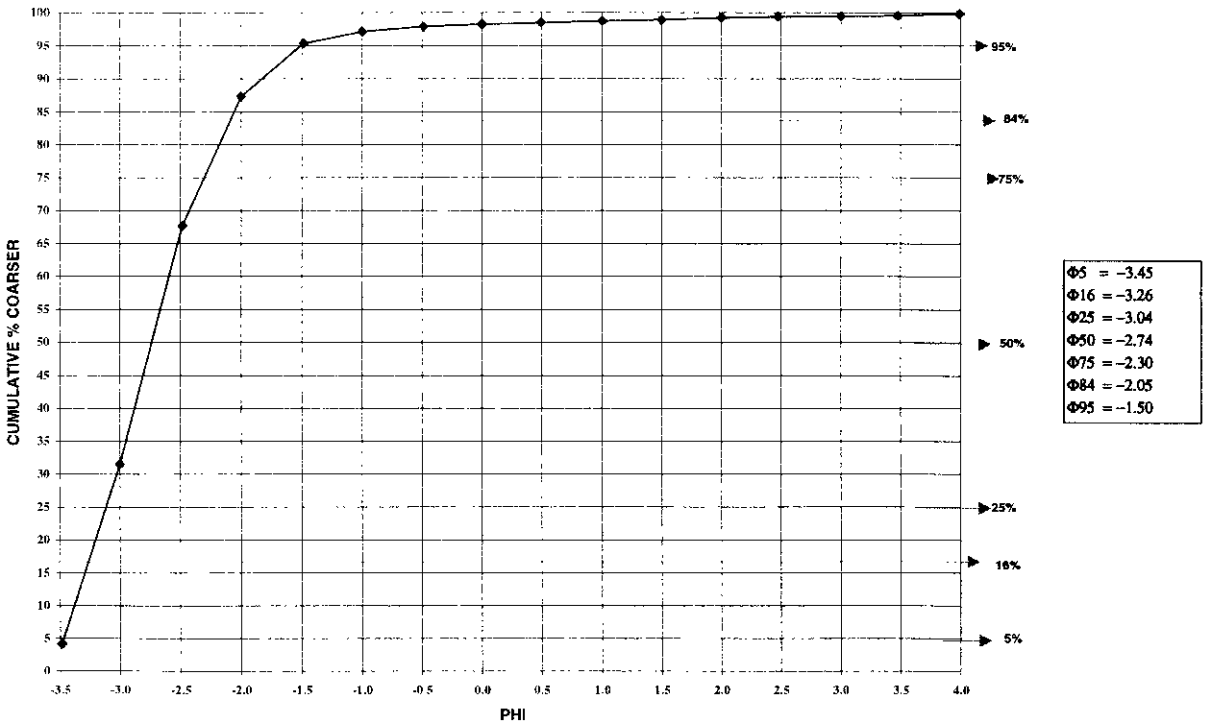

Figure 4-25. Percentage cumulative coarser than for the ARG test site material.

This shows the material to be relatively poorly graded and relatively well sorted. This is emphasised by a uniformity coefficient of 2.1, which is near but not close to 1.0. A uniformity coefficient of 1.0 indicates that a sediment is nearly perfectly sorted and is uniform, i.e. it contains only one type of material.

The standard deviation indicates the degree of scattering about the central tendency with lower the value the increased the degree of sorting. The degree of sorting calculated was 0.61, which indicates that the sediment has relatively good sorting, which is in agreement with the conclusions already drawn.

The skewness is a measure of the tendency of the data to spread on one side or another of the average. The skewness measure is zero for a symmetrical size distribution. The measured skewness of 0.21 shows that the materials is skewed slightly towards the finer particles but with a less peaked than normal distribution.

4.5.2.1.2 Indoor Tank

Dry sieving of the material taken from the Indoor Tank led to the particle size distribution as seen in Figure 4-26, whilst Table 4-17 shows the statistical parameters calculated using data from Figure 4-27.

Statistical Parameter	Value
Median	-0.42
Mean	-0.46
Degree of Sorting	0.34
Kurtosis	0.79
Skewness	-0.15

Table 4-17. Statistical Parameters for Indoor Tank material.

It can be seen from the particle size distribution curve that the material consists almost entirely of one grain size, the median value being 1.33mm, indicating this to be a Coarse SAND, since the curve extends over a very limited range. The distribution shows that 92% of the material is coarse sand sized, 3% is fine sand sized and approximately 5% is gravel sized particles.

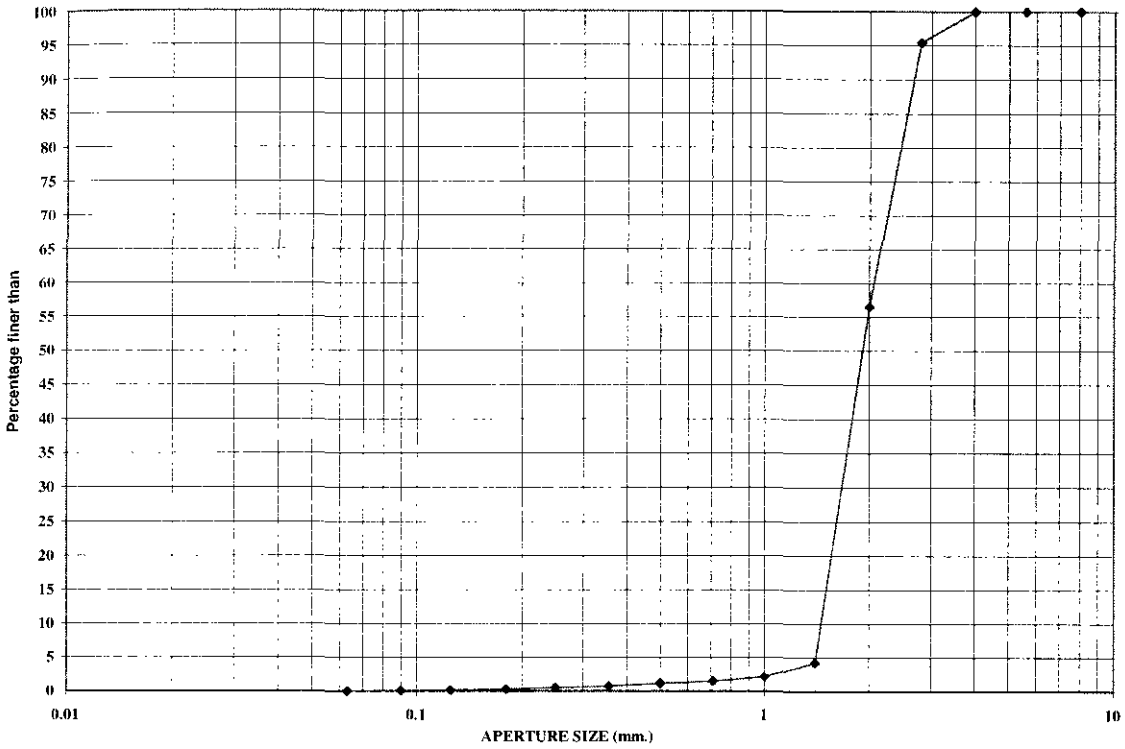

Figure 4-26. Particle size distribution of the Indoor Tank.

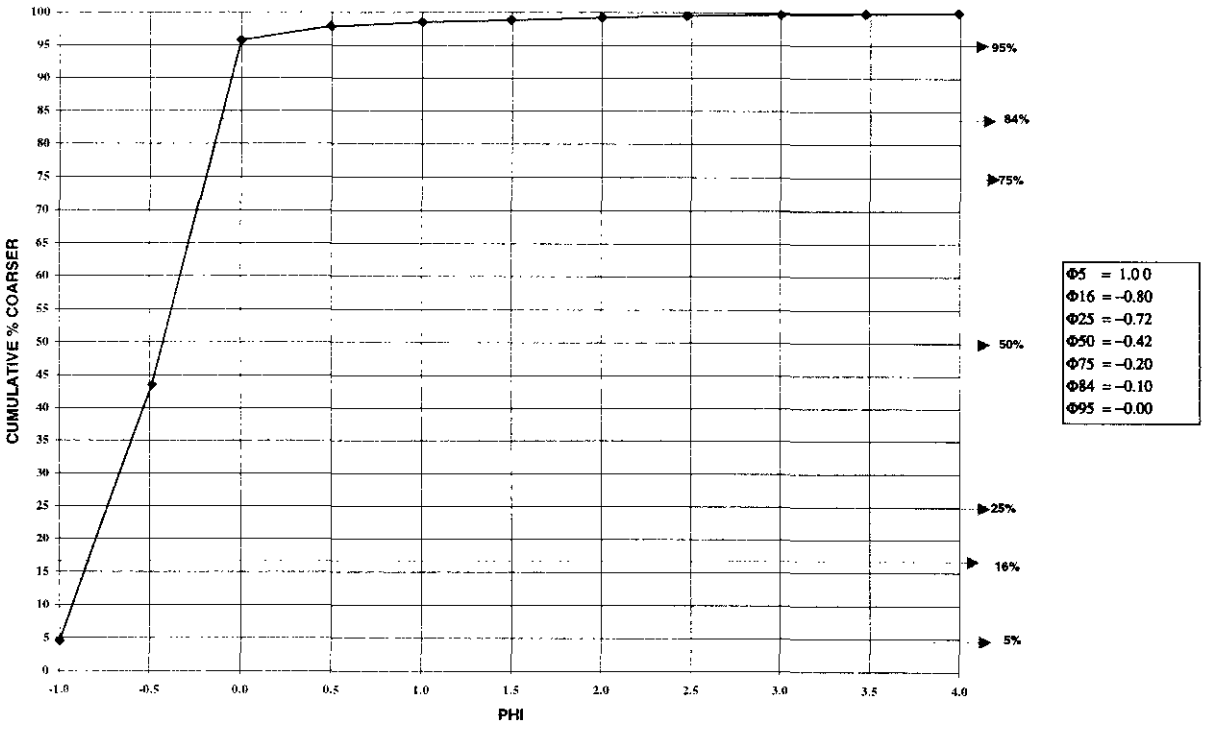

Figure 4-27. Percentage cumulative coarser than for the Indoor Tank.

This shows the material to be poorly graded but well sorted. This is emphasised by a uniformity coefficient of 1.3, which is very close to 1.0. The degree of sorting calculated was 0.34, which again indicates that the sediment has good sorting. The measured skewness of –0.15 shows that the material is skewed slightly towards the coarser particles but with a less peaked than normal distribution.

4.5.2.1.3 HMC Stone Lane

Dry sieving of the material taken from the Indoor Tank led to the particle size distribution as seen in Figure 4-28, whilst Table 4-18 shows the statistical parameters calculated using data from Figure 4-29.

Statistical Parameter	Value
Median	1.70
Mean	1.73
Degree of Sorting	0.68
Kurtosis	-0.08
Skewness	1.30

Table 4-18. Statistical Parameters for HMC Stone Lane Quarry material.

It can be seen from the particle size distribution curve that the material consists of a range of particle sizes with the median value being 0.31mm, indicating this to be a Medium SAND. The distribution shows that 61% of the material is medium sand sized, 30% being of fine sand size and with approximately 4% being of coarse sand sized particles.

The degree of sorting shows the material to be relatively poorly graded and relatively well sorted. This is emphasised by a uniformity coefficient of 1.95, which is near but not close to 1.0. The degree of sorting calculated was 0.68, which again indicates that the sediment has relatively good sorting. The measured skewness of 1.30 shows that the material is markedly skewed towards the finer particles but with a less peaked than normal distribution.

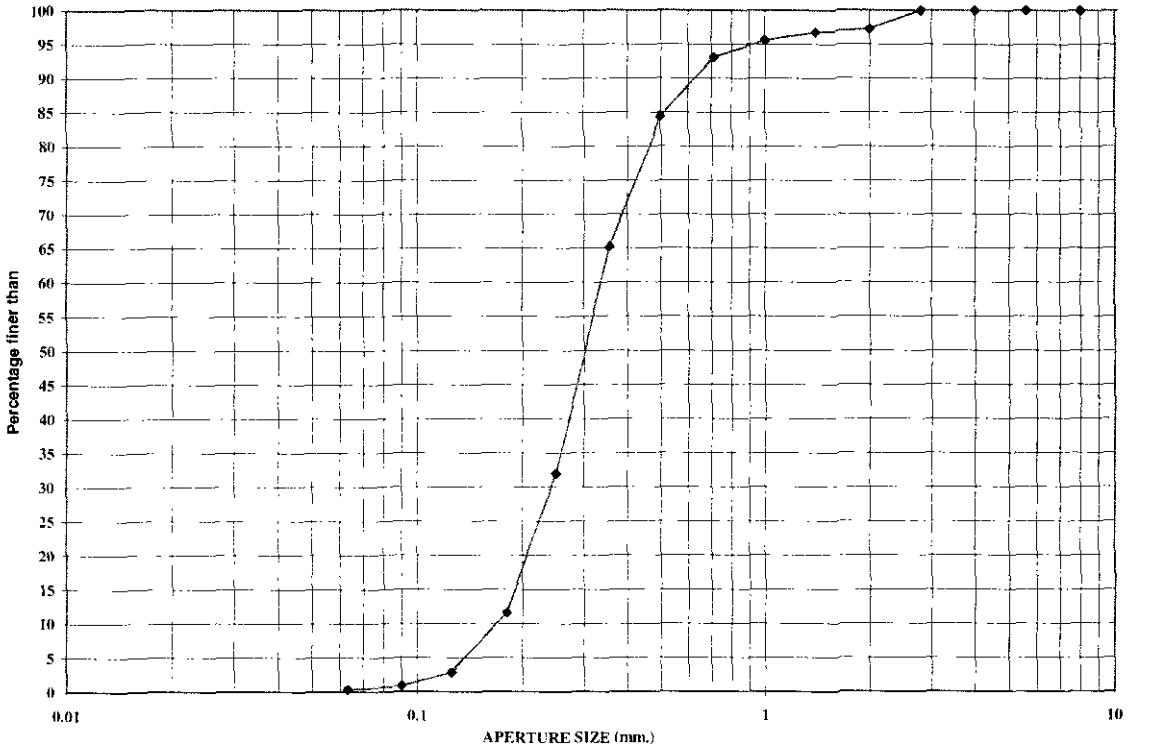

Figure 4-28. Particle size distribution of the Stone Lane Quarry material.

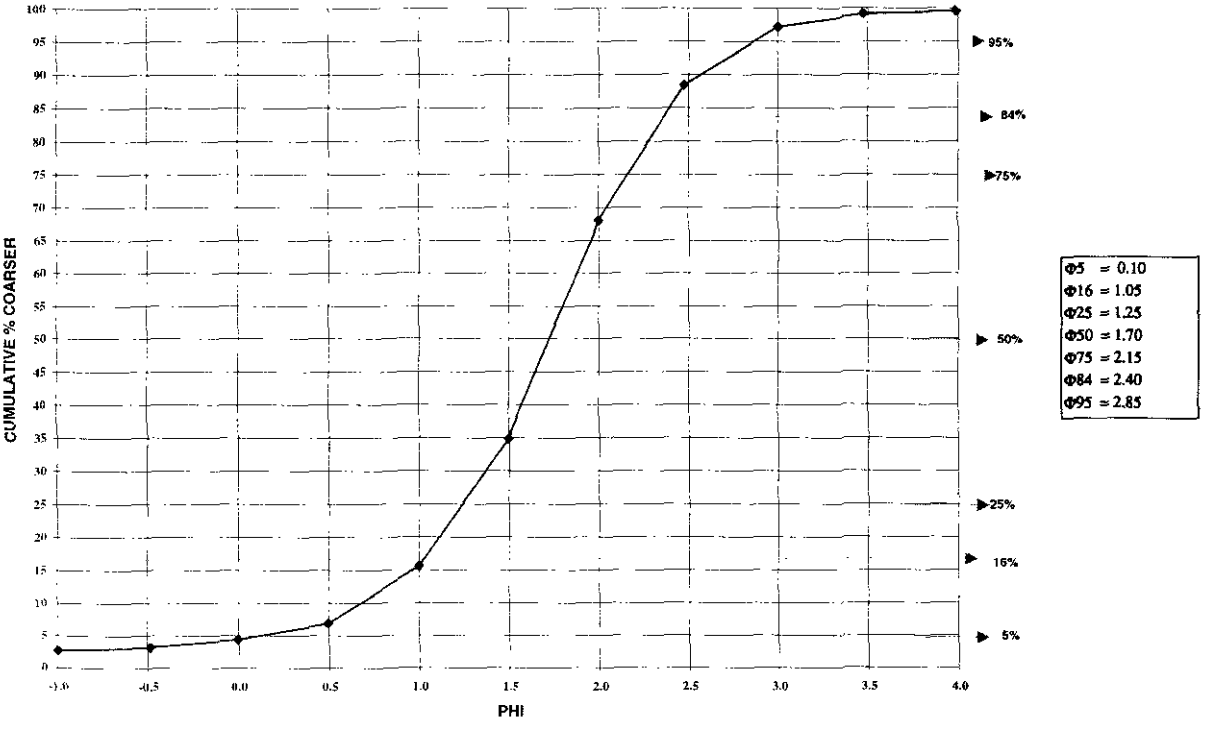

Figure 4-29. Percentage cumulative coarser than for the Stone Lane Quarry material.

4.5.3 Other Tests

4.5.3.1 Natural Sediment Properties

4.5.3.1.1 Natural Moisture Content

Throughout the experimental portion of the project, the moisture content of the material under investigation was taken whenever acoustic measurements were taken. The natural moisture content tests were carried out in accordance with procedures to be found in BS 1377, 1990, Part 2.

The following values are the moisture contents calculated during the laboratory work carried out at the University of Wales, Bangor.

The results of the natural moisture content determination can be seen in Table 4-19.

Sample	Moisture Content (%)	Particle Specific Gravity	Colour
ARG Test Site	2.03±0.37	- - - - - -	Greyish Black to Greyish White 10PB 2.5/4.6 D to 10Y 2.8/10 D
Indoor Tank	0.46±0.10	2.68±0.01	Yellowish Red 10R 4.3/6 D
HMC Stone Lane	2.30±0.05	2.65±0.01	Redish Yellow 5YR 7.5/14.4 D

Table 4-19. Natural Sediment properties of the cohesionless materials.

4.5.3.1.2 Particle Specific Gravity

The particle specific gravity tests were carried out in accordance with procedures to be found in BS 1377, 1990, Part 2. Tests were carried out in duplicate with the given value being an average of the two. Material from the ARG test site was not tested for specific gravity as the coarse nature of the material meant that the test bottles were unsuitable for use.

The results of the specific gravity determination can be seen in Table 4-19. The value of specific gravity measured for the indoor tank material of 2.68 is slightly higher than value of 2.65 (the value for quartz) that would have been expected. Meanwhile the value for the HMC Stone Lane material was exactly 2.65 as expected for a material of this nature.

4.5.3.1.3 Colour

The colour of the cohesionless materials was determined in the laboratory using the Munsell Colour Chart. Since the ARG test site material consists of a number of differing materials a range of colours has been given. These can be found in Table 4-19.

4.5.3.2 Shear Strength

In Section 4.4.2.3, a number of methods for the determination of shear strength were outlined. As stated, for most purposes the triaxial test is carried out for shear strength analysis. However, testing of cohesionless materials in the triaxial cell is extremely difficult due to problems with sample preparation, whilst the direct shear box is extremely well suited for analysis of these materials. Therefore, the direct shear test was used.

The direct shear test was carried out in accordance with procedures to be found in BS 1377, 1990, Part 7. The dimensions of the shear box used were 101mm x 101mm x 35mm. This meant that it was not possible to test the ARG test site material, since the diameter of the material was greater than one tenth the height the box (as specified in Section 4.2.1 of the British Standard).

The results of the direct shear test can be found in Appendix B which contains plots of shear stress against shear strain. From these plots the maximum shear stress was noted. Figure 4-30 and Figure 4-31 shows plots of normal stress against shear stress at failure for the materials under investigation. These plots allow the determination of effective shear strength and angle of internal friction.

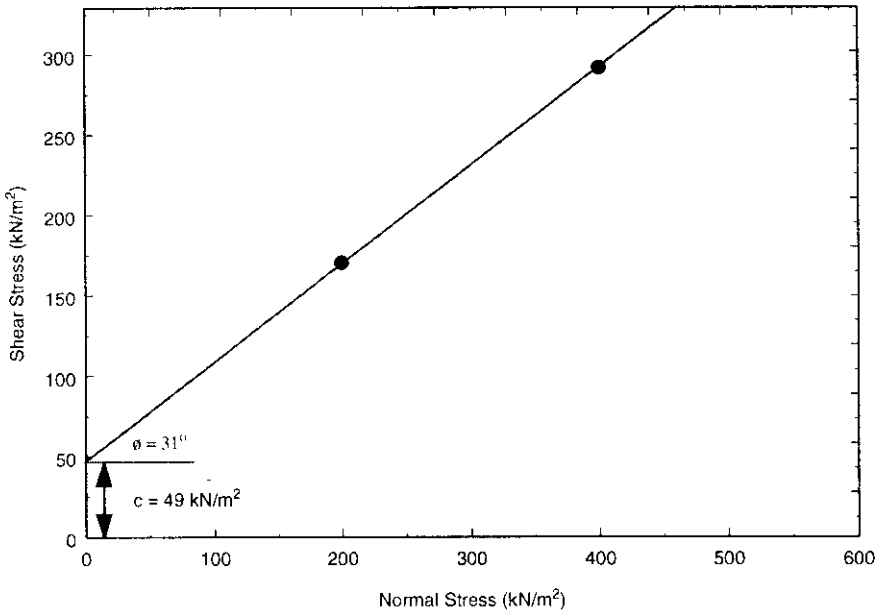

Figure 4-30. Plot of Normal Stress against Shear Stress at failure for the Indoor Tank Material.

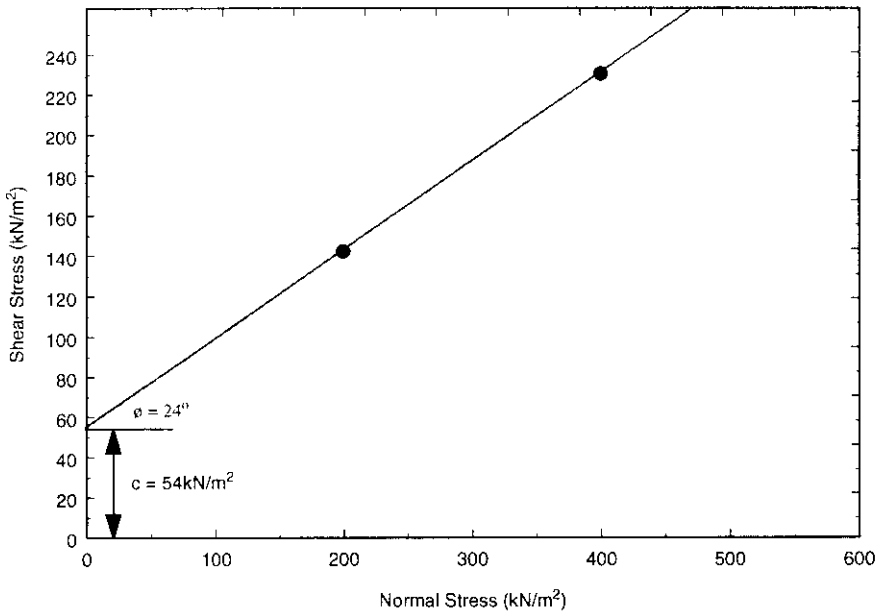

Figure 4-31. Plot of Normal Stress against Shear Stress at failure for the HMC Stone Lane Material.

As well as the determination of shear strength and angle of internal friction, the direct shear test enables the calculation of the bulk density and void ratio (the ratio of the volume of the voids to the volume of the solids) of the material under test. Table 4-20 shows the results of the direct shear tests for the cohesionless materials.

Sample	Shear Strength (kN/m^2)	Angle of Internal Friction (^{o})	Bulk Density (Mg/m^3)	Void Ratio
Indoor Tank	49	31	1.5402	0.74
HMC Stone Lane	54	24	1.2425	1.19

Table 4-20. Results of the direct shear tests for the cohesionless materials.

4.5.4 Conclusions

The classification of the cohesionless materials based upon the particle size analysis can be seen in Table 4-21.

Sample	Classification
ARG Test Site	Medium GRAVEL
Indoor Tank	Coarse SAND
HMC Stone Lane	Medium SAND

Table 4-21. Classification of the cohesionless materials.

The values of water permeability measured using the constant head permeameter were typical for the types of materials tested, although the value for the gravel of $4.92 \times 10^{-2} \pm 0.43 \times 10^{-2}$m/s is slightly lower than would have been expected. This may be due to the particle size distribution of the material being skewed towards the finer particles, with approximately 66% of the material being medium gravel sized particles and the remaining 33% being fine gravel or sand sized particles.

The value of permeability for the Indoor tank material of $6.76 \times 10^{-3} \pm 8.10 \times 10^{-5}$m/s is slightly higher than that of $2.22 \times 10^{-4} \pm 2.50 \times 10^{-6}$m/s for the HMC Stone Lane material, although both these values lie within the expected range for sands. The higher permeability of the tank sand is also expected since it has been classified as a Coarse SAND as opposed to the HMC Stone Lane material that has been classified as a Medium SAND.

Comparison of the value of permeability calculated using the Hazen formula (see Section 4.2.1.1) can be seen in Table 4-22.

Material	Constant Head Permeameter	Hazen Formula
ARG Test Site	$4.92 \times 10^{-2} \pm 0.43 \times 10^{-2}$ m/s	25×10^{-2} m/s
Indoor Tank	$6.76 \times 10^{-3} \pm 8.10 \times 10^{-5}$ m/s	25.6×10^{-3} m/s
HMC Stone Lane	$2.22 \times 10^{-4} \pm 2.50 \times 10^{-6}$ m/s	2.89×10^{-4} m/s

Table 4-22. Comparison of measured permeability with interpolated.

The values show that the Hazen formula gives an indication of the permeability, although it should be noted that the formula is only accurate for single sized sands.

Although the constant head permeameter will give a more accurate value for the permeability it also has several limitations. The results of the tests (See Appendix B) clearly show that differing results can be gained from the varying rates by which the sediment is placed into the cell. Uneven packing and distribution can lead to areas of high or low permeability. It may also lead to piping of the fluid between the soil and the side walls of the cell, or entrapment of air bubbles between the grains. The test is most suited for fine to medium sands and sediments having a medium permeability. It is not suitable for cohesive sediments as it relies on a sample hydraulic gradient of less than one. The nature of the permeating fluid can also affect the accuracy of the results and, for this reason, distilled water at a constant temperature of 20°C should be used.

The greatest limitation of the test is its inaccurate representation of actual in-situ conditions by the cell. Removal of the sample from the ground exerts great disturbance of the soil structure. In nearly all sediments there are variations between horizontal and vertical permeability due to the effects of areas of coarser and finer material within beds. The sediment mass will also contain secondary permeability such as joints and fissures which are completely ignored in the laboratory.

The values measured for the flow resistivity all appear smaller than published values, although the values appear appropriate for materials of this nature. It should be noted that the published values make no mention of the moisture content of the materials tested. The moisture content of the sample will greatly affect the measured flow resistivity, with increasing moisture content leading to high values of flow resistivity. It can be seen in Table 4-19 that the materials are all extremely dry, having a moisture content of less than 3%.

A comparison of the intrinsic permeability of the test materials as calculated using the constant head permeameter and the airflow rig can be seen in Table 4-23.

	Constant head permeameter	Airflow rig
ARG test site	$5.43x10^{-9} + 3.97x10^{-10} m^2$	$18.3x10^{-9} \pm 1.40x10^{-9}$ m^2
Indoor tank	$0.69x10^{-9} + 8.28x10^{-12} m^2$	$1.09x10^{-9} \pm 5.00x10^{-12}$ m^2
HMC Stone Lane	$2.26x10^{-9} + 2.55x10^{-11} m^2$	$0.92x10^{-9} \pm 8.90x10^{-11}$ m^2

Table 4-23. Comparison of intrinsic permeability calculated from constant head water permeability and air flow resistivity measurements.

These results show that for cohesionless materials a reasonable agreement can be obtained between values of the intrinsic permeability of a sample resulting from either of the two methods used.

The values of tortuosity calculated for the materials are within expected values. Comparisons of the measured values with those calculated using the Bruggeman equation (see Section 4.2.3.1) can be seen in Table 4-24. The calculated values use a value of one for n.

	Measured	Calculated
Indoor Tank	2.38±0.02	2.56±0.01
HMC Stone Lane	2.24±0.04	2.68±0.07
ARG Test Site	1.22±0.002	2.18±0.01

Table 4-24. Comparison of measured and calculated tortuosity.

It can be seen from Figure 4-15, the plot of formation factor against porosity, that the samples obey Archie's Law, since the results produce straight lines of constant gradient.

The values of m of 1.92 for the Indoor tank and 1.82 for the Stone Lane sample are slightly higher than would have been expected for sediments of similar nature. The value of m, usually varies between 1.5 for coarse material to approximately 2.0 for clay, and is generally lower for sediments with grains of spherical nature. However, experiments on natural sands have produced values between 1.3 and 1.7.

It is can be seen that the value for m of the Indoor Tank is slightly higher than that gained for the Stone Lane sample. This may have been expected since the cementation factor is dependent primarily upon the pore space shape and the paths between these pores,

i.e. tortuosity. Investigations show that the sediment grains of the Indoor Tank material show a higher degree of angularity than those from the Stone Lane material. The structure of the sediment would therefore produce a higher porosity (Figure 4-32a), hence conduction of the current through the sediment was less restricted due to the more open contact between the grains.

This can be seen in the results from the porosity determination that show the porosity of the Indoor Tank material was measured at 38.92% compared to 37.31% for the Stone Lane sample. Both these porosities are typical of dry sands (See Table 4-4).

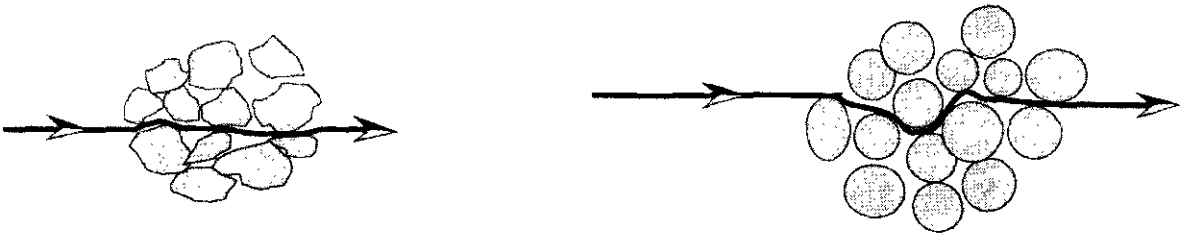

Figure 4-32. Effect of grain sphericity on porosity. (a) Angular grains will produce a greater porosity leading to greater conduction through the sediment. (b) Spherical sediment grains will reduce porosity and conduction.

The presence of the spherical sand grains in the HMC Stone Lane sample, will produce a more compact initial structure, with the grains interlocking to give a reduced porosity (See Figure 4-32b). This results in a greater tortuosity giving a more convoluted pore fluid path, reducing the conduction of the current and therefore giving a smaller cementation factor.

However, it can be seen in Table 4-24 that the measured tortuosity for the Stone Lane material is lower than that for the Indoor Tank material, whilst the trend is reversed for the calculated values. The Bruggeman relationship depends entirely upon porosity and the above argument relating porosity solely to tortuosity holds true, i.e. higher values of porosity lead to higher tortuosities. It takes no account of the pore shapes, which are considered by use of the Formation Factor as measured in the Jackson cell experiment since they are filled with the saturating fluid.

The value of 1.22 calculated for the ARG Test Site material is much less than that calculated for the two sands and is probably due to the coarser more rounded nature of the grains which is mirrored in the higher measured porosity. Comparison with the Bruggeman relationship shows a poor agreement.

The results for the determination of the elastic moduli results are typical for unconsolidated materials such as these. The results show that the materials exhibit similar properties, each having a shear modulus close to 10MPa near to the surface, resulting in a shear wave velocity of approximately 80m/s. The bulk modulus of the materials is close to 30MPa at the surface resulting in a P-wave velocity of 170m/s. This gives a Poisson's ratio of 0.36, which is typical for loose sands such as these.

The results of the natural sediment properties tests show that all the materials were extremely dry when tested, having measured moisture contents of less than 3%. This low moisture content is expressed in the colour notations for the Indoor Tank and Stone Lane since a light colour is typical of dry materials (although light colour frequently results from the preponderance of quartz that is the primary mineral of the two samples).

Since the ARG Test Site sample consists of a number of differing coloured minerals, including chert, there is little correlation between colour notation and moisture content, although since the materials are very permeable it is expected that it would have a low moisture content.

Since the two samples tested for specific particle density have been classified as sand it is not surprising that the specific gravity of the materials was measured close to 2.65, the value for quartz.

The values of shear strength and angle of internal friction determined using the direct shear test are indicative of very loose to loose materials. This classification is expected.

4.6 Results and Analysis of Consolidated Materials

4.6.1 Sample Preparation

In order to carry out the classification tests, approximately 200g of material was required from each sample point. This material underwent a pre-treatment prior to any testing.

This pre-treatment consisted of passing all the material through a Buchner Funnel to remove any salt from the sediment. Approximately 40g was then removed from the sample to be used to test for the organic matter content, whilst the remaining material was placed in a beaker of Hydrogen Peroxide to remove any organic matter remaining in the

sample. The removal of the organic matter was necessary, since if over 0.5% organic matter is present during the hydrometer analysis, it will give erroneous results as the settling rates of the material will be non-uniform.

No pre-treatment of the undisturbed material taken for permeability or shear strength determination was necessary.

The unconsolidated materials tested were taken from Horticultural Research International, Wellesbourne, Warwick. The site has been described in Section 4.1.3. The site consists of three individual soils that have been termed *Soil A*, *Soil B* and *Soil C* (See Figure 4-3).

4.6.2 Comparative Tests

4.6.2.1 Permeability

4.6.2.1.1 Water Permeability

The most widely used technique for the determination of the permeability of cohesive sediments is the falling head test. The test and its procedure is described in detail in BS 1377, 1990, Part 5.

However, the standard apparatus for the falling head test was unavailable at UCW, Bangor, where the soil testing was undertaken, so a modified falling head test was devised.

4.6.2.1.1.1 Equipment

The apparatus used in the experiment included a mercury manometer, a large glass flask, a steffi filter and filter paper and a vacuum pump. A schematic diagram showing the apparatus can be seen in Figure 4-33. The graph paper is placed inside the steffi filter and held in place using a piece of sellotape. This is used to determine the initial height of the sediment and to measure the fall in water head.

4.6.2.1.1.2 Procedure

With the apparatus set up as shown and the vacuum pump enabled, a small amount of the material under test, approximately 20g, was mixed with distilled water until a paste was formed. The paste was then poured into the steffi filter and the excess water allowed to drain into the glass flask. At this point the sample thickness (l) was read off the graph paper.

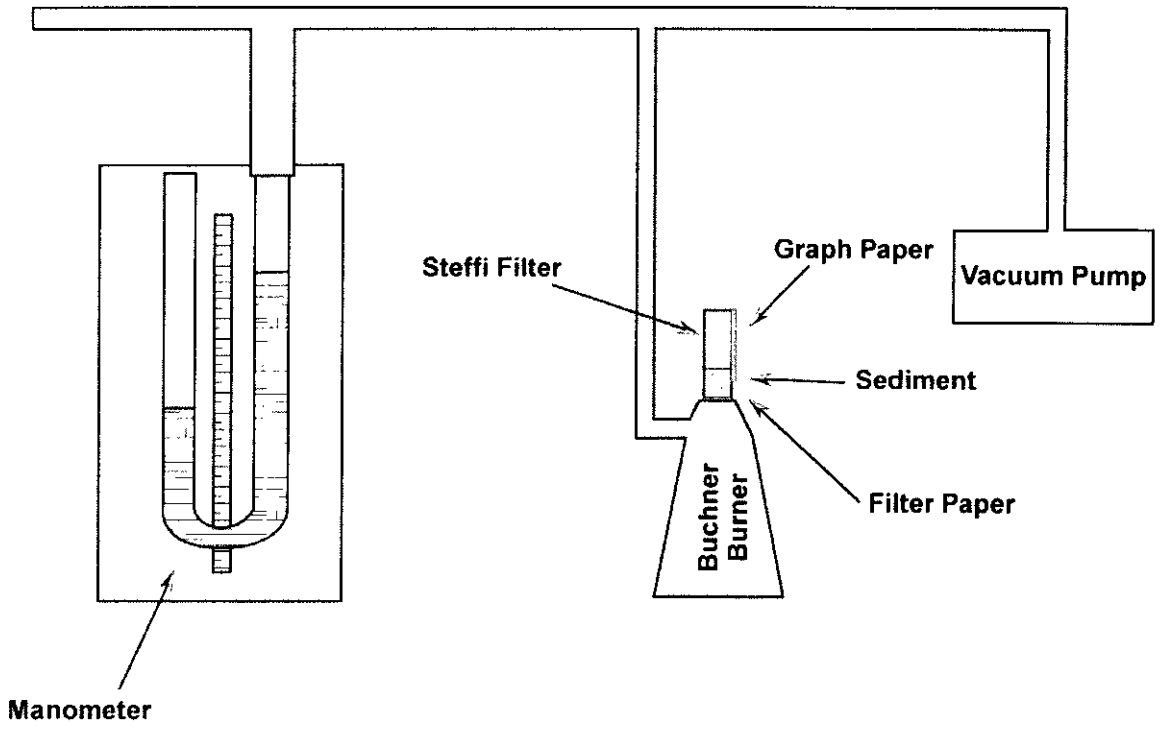

Figure 4-33. Schematic diagram of experiment for permeability determination of cohesive sediments.

Distilled water was then carefully poured into the steffi filter ensuring as little sample disturbance as possible. The height of water, time and level of mercury in the manometer were then noted. These measurements were then repeated over a period of time enabling an average permeability to be calculated.

The permeability (k) was then be calculated from:-

$$k = \frac{V}{A.t}.\frac{l}{h} \qquad \textit{(Eq. 4-54)}$$

where:-

k = Permeability (m/s)

V = Volume of water permeating over time (m^3)

A = Area of sample (m^2)

t = Time taken (s)

l = Thickness of sample (m)

h = Pressure head of mercury (multiplied by 13.59506 to convert to head of water)

4.6.2.1.1.3 Results

The results of the test can be found in Appendix B. A summary of the results showing the measured average permeability and the calculated intrinsic permeability can be found in Table 4-25.

Sample	Permeability (m/s)	Intrinsic Permeability (m^2)
Soil A	$4.93x10^{-10}\pm3.00x10^{-11}$	$5.03x10^{-17}\pm3.08x10^{-18}$
Soil B	$7.85x10^{-10}\pm1.79x10^{-10}$	$8.02x10^{-17}\pm1.83x10^{-17}$
Soil C	$4.47x10^{-10}\pm1.50x10^{-10}$	$4.57x10^{-17}\pm1.53x10^{-17}$

Table 4-25. Measured permeability and calculated intrinsic permeability of cohesive sediments

From the typical values of permeability shown in Table 4-2, it can be seen that all three materials can be classified as CLAY since they all show a permeability of approximately $5x10^{-10}$m/s.

4.6.2.2 Elastic Moduli

4.6.2.2.1 Equipment

A description of the resonant column apparatus used for the determination of shear modulus and frame loss coefficients can be found in Section 4.5.1.4.1.

4.6.2.2.2 *Procedure*

A similar procedure was used for the cohesive sediments as for the cohesionless materials, as described in Section 4.5.1.4.2.

The only difference between the two experiments was the method of sample preparation. As described in Section 4.1.4, the sampler for the resonant column test consisted of metal tubes, 38mm in diameter and between 175 and 250mm in length. The test material was extruded from the sample tubes into a split mould 76mm x 38mm and the end trimmed so that they were flat and parallel.

The sample was then weighed and its initial dimension measured using a pair of vernier calipers. Part of the waste material was then taken for moisture content determination.

The experiment was then undertaken using the procedures outlined in Section 4.5.1.4.2.

4.6.2.2.3 *Results*

The results of the resonant column experiment can be found in Appendix B.

Figure 4-34, Figure 4-35 and Figure 4-36 show the variation in shear modulus and shear damping with effective depth for the three soils from HRI, Wellesbourne. Best-fit regressions have been applied to the modulus data. It can be seen that for all three soils the shear modulus increases with increasing depth, while there is a decrease in the shear damping (although there is some spread in the damping data for Soil C).

The results from Soil A show that for very low effective depths (those less than 1m) the shear modulus is very small, being of the order of 4MPa. It then rises rapidly to 44MPa at 1.5m, which is similar to the shear modulus of Soil C at that depth. Comparing Soils B and C shows that, for these depths, μ is close to 40MPa for Soil C and roughly 60MPa for Soil B.

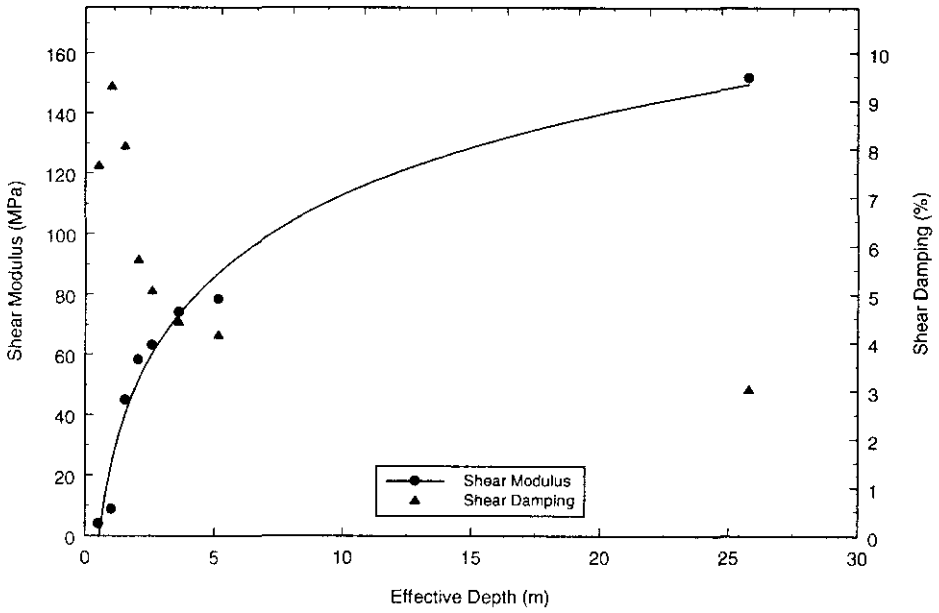

Figure 4-34. Change in shear modulus and shear damping with effective depth for Soil A. Best-fit regression has been applied to the modulus data.

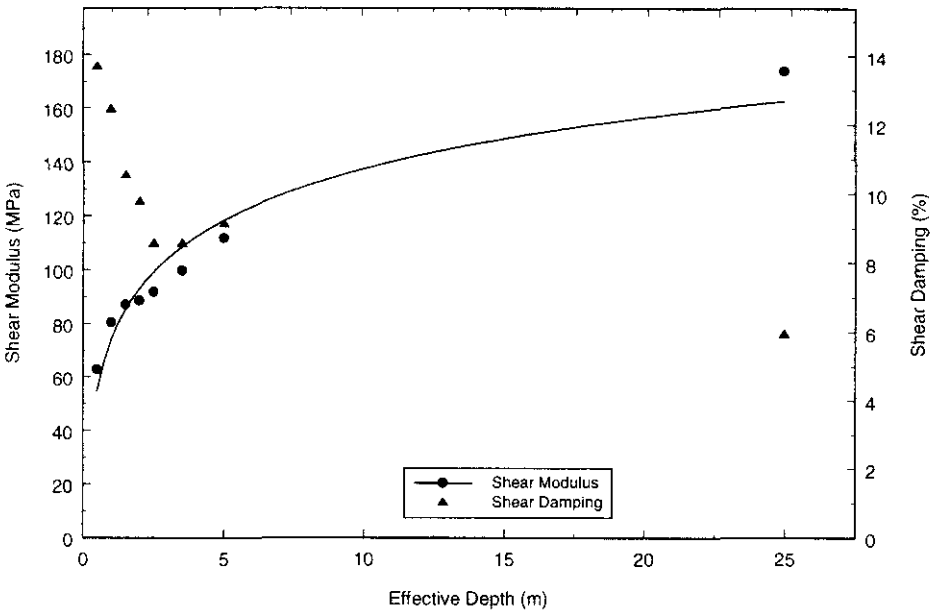

Figure 4-35. Change in shear modulus and shear damping with effective depth for Soil B. Best-fit regression has been applied to the modulus data.

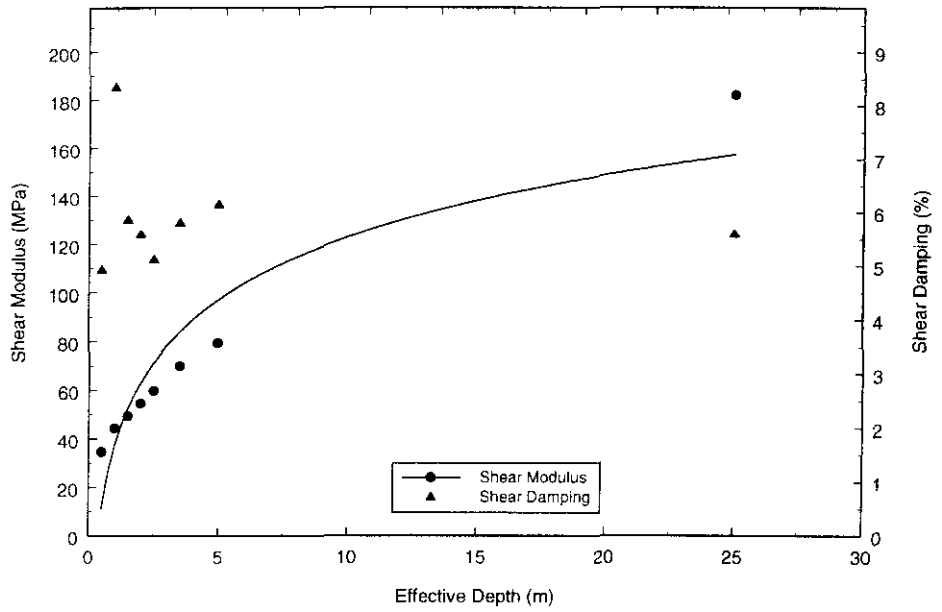

Figure 4-36. Change in shear modulus and shear damping with effective depth for Soil C. Best-fit regression has been applied to the modulus data.

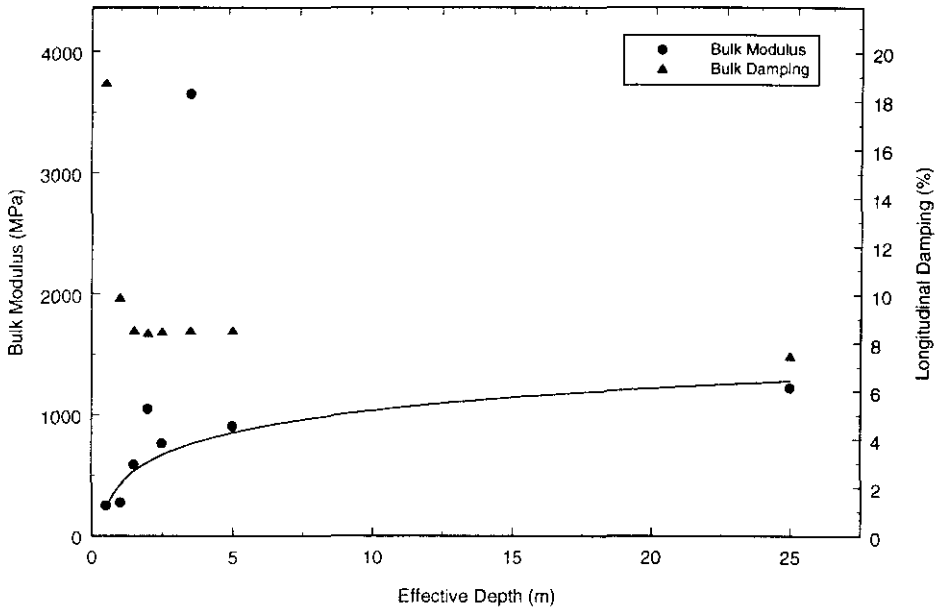

Figure 4-37. Change in Bulk modulus and longitudinal damping with effective depth for Soil B.

The variations in shear moduli are mirrored in Figure 4-38 which shows shear wave velocity with effective depth for all cohesionless materials. It can be seen that Soil A and C exhibit similar shear wave profiles (apart from the two lowest data points of Soil A) with Soil B having a slightly higher overall shear velocity. All the soils have shear wave velocities typical of consolidated materials such as these.

The bulk modulus was calculated from the measured values of shear and Young's moduli, using the relationship outlined in Section 4.2.4. For the relationships to be valid the measured values of Young's modulus cannot be three times greater than the Shear modulus. From the results of the experiments given in Appendix B it can be seen that for Soils A and C the bulk modulus could not be determined.

However this relationship is valid for the results of the Soil B and so bulk modulus was calculated. The results can be seen in Figure 4-37 which shows the variation in bulk modulus and longitudinal damping with effective depth. It can be seen from the plot that bulk modulus increases with increasing effective depth, although there is some spread in the data. These points have been ignored in the calculation of the best-fit data.

These two anomalous points can also be seen in the subsequent calculation of the P-wave velocity, the results of which can be seen in Figure 4-39. The plot shows an increase in P-wave velocity with increasing effective depth and that the P-wave velocity is roughly 400m/s at the surface (which is typical for an agricultural soil of this nature).

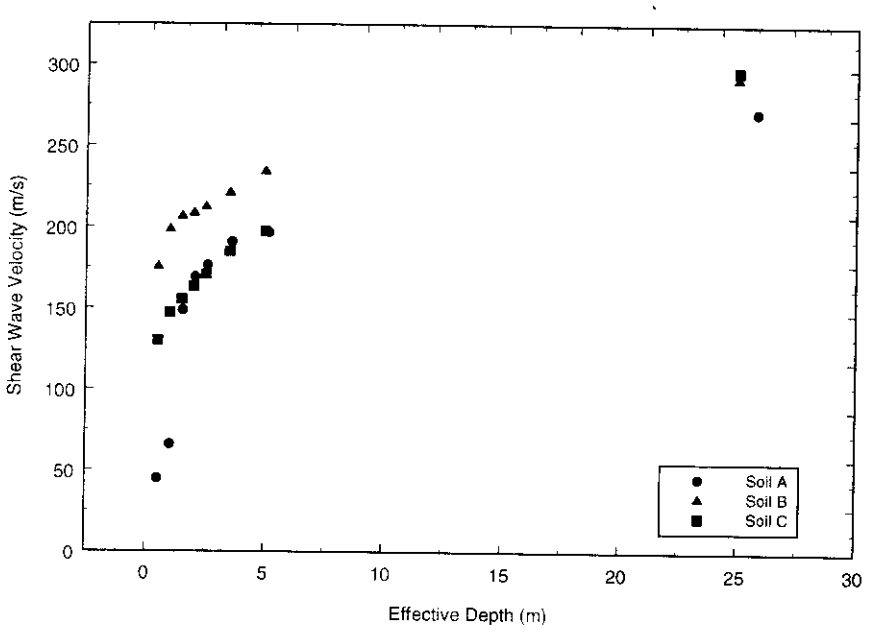

Figure 4-38. Change in shear wave velocity with effective depth for the cohesive materials.

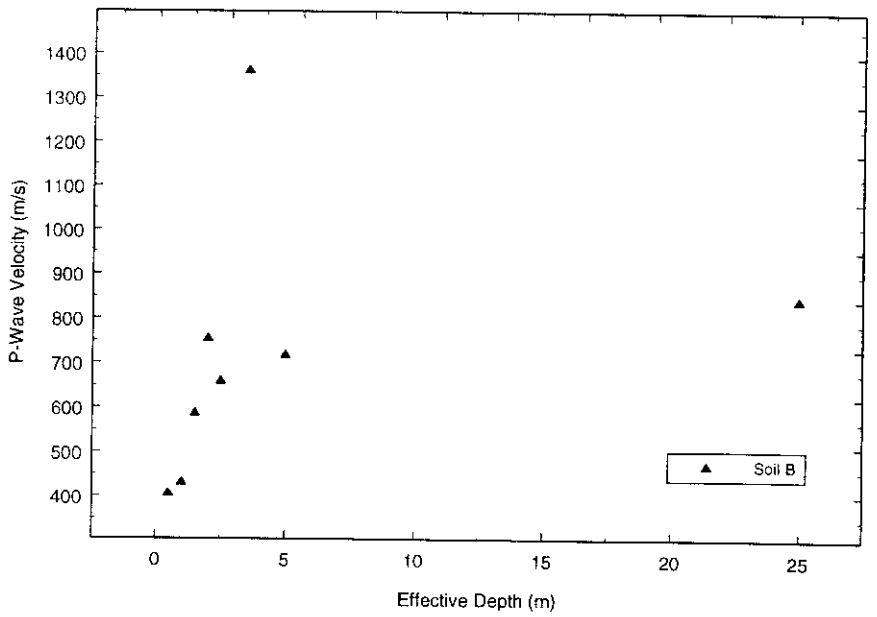

Figure 4-39. Change in P-wave velocity with effective depth for the Soil B.

4.6.3 Classification

4.6.3.1 Particle Size Analysis

The particle size analysis of the cohesive materials was undertaken using the hydrometer method. The analysis was carried out in accordance with procedures to be found in BS 1377, 1990, Part 2.

Hydrometer readings were reduced using standard procedures to give the normalised cumulative weight percent finer than, for the calculated particle diameter sizes. This data can be found in Appendix B and was used to plot the particle size distribution for the three sediments that can be seen in Figures 4-40, 4-41 and 4-42 respectively.

From these figures, the percentage of sand, silt and clay sized particles of each of the samples was determined and can be found in Table 4-26. This information was then used to classify the samples using triangular classification chart. Figure 4-43 shows the triangular sediment classification chart for the three soils.

Sample	Sand (%)	Silt (%)	Clay (%)	Classification
Soil A	79.0	9.0	12.0	Clayey Sand
Soil B	35.0	40.0	25.0	LOAM
Soil C	22.0	53.0	25.0	LOAM

Table 4-26. Results of the particle size analysis tests.

The results of the particle size analysis in Table 4-26 shows that Soil A is a poorly graded Clayey Sand, whilst Soils B and C have been classified as well graded LOAM since they have roughly equal distributions of sand, silt and clay sized particles.

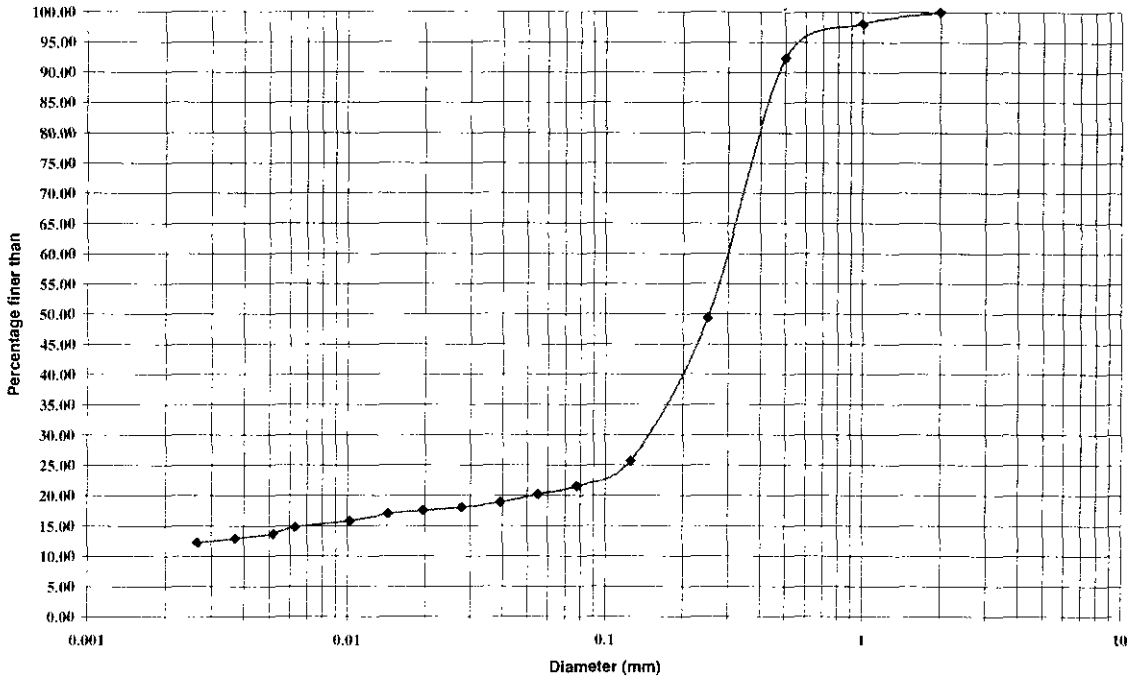

Figure 4-40. Particle size distribution of Soil A.

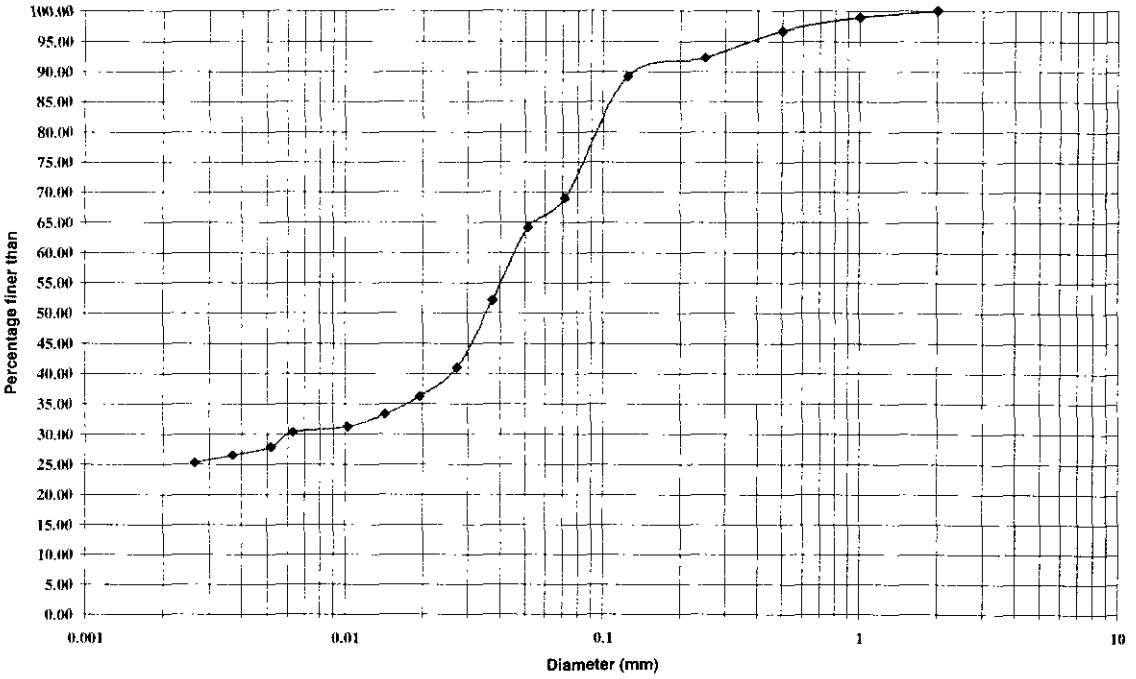

Figure 4-41. Particle size distribution of Soil B.

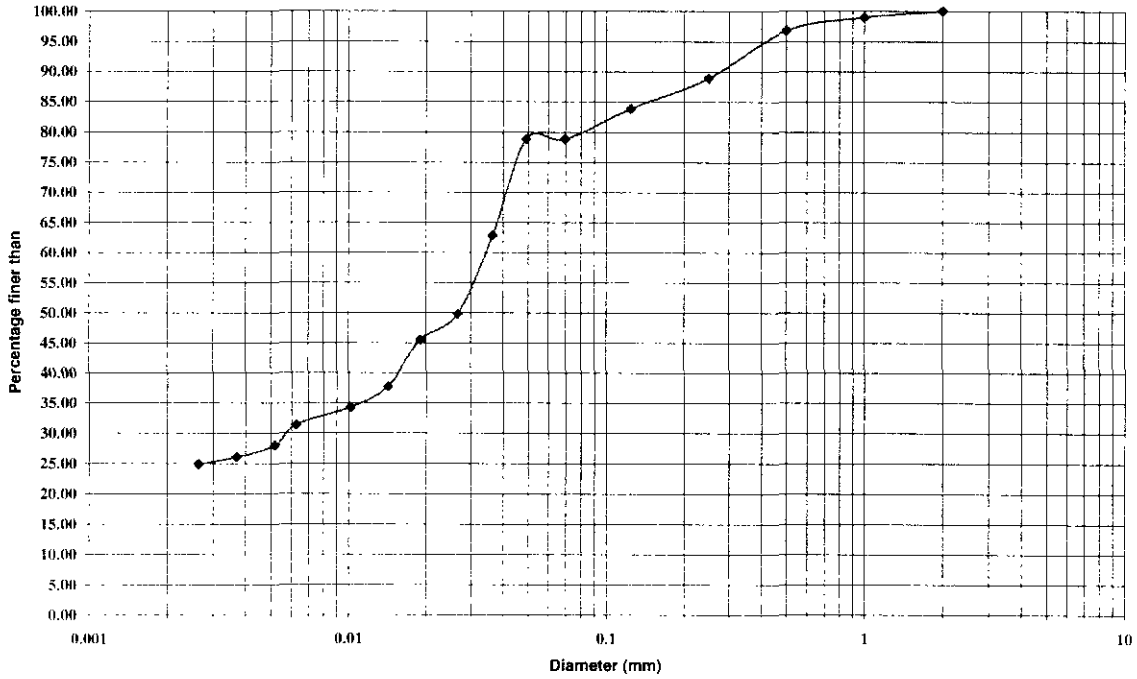

Figure 4-42. Particle size distribution of the Soil C.

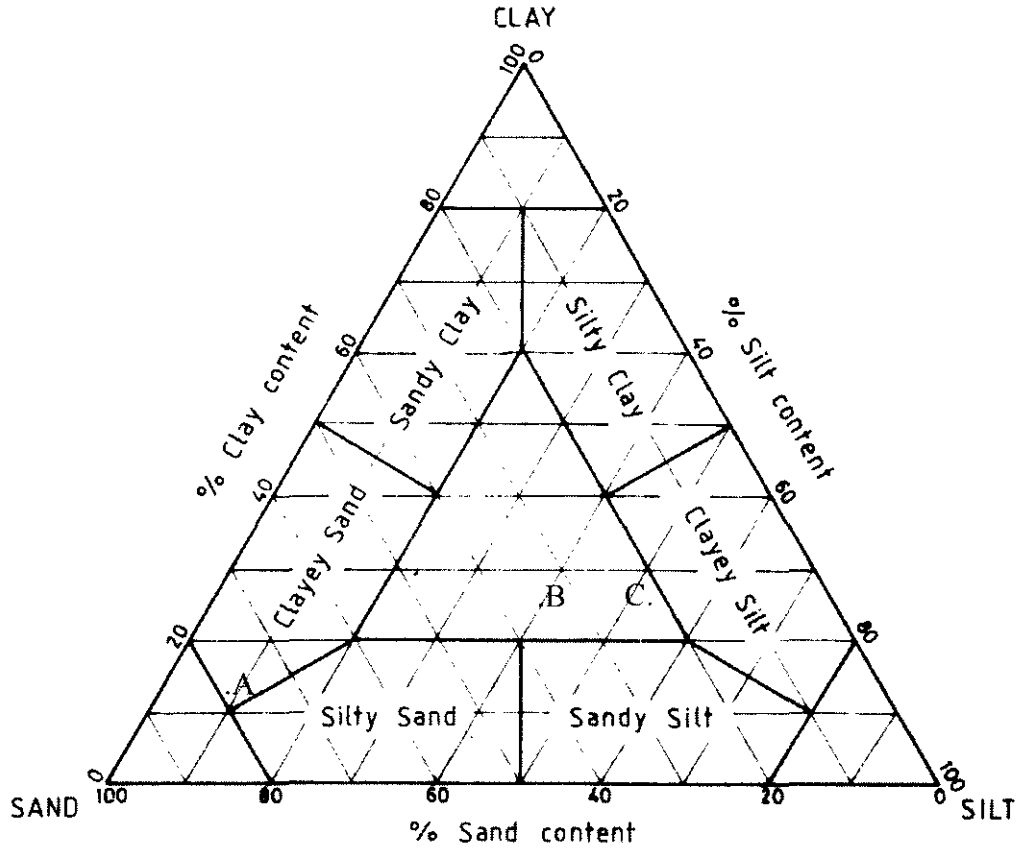

Figure 4-43. Triangular classification chart for the cohesive sediments. Soils are marked A, B and C.

4.6.3.2 Consistency

The consistency of the cohesive soils was determined using the Atterberg Limits. The Atterberg Limits tests were carried out in accordance with procedures to be found in BS 1377, 1990, Part 2.

Section 4.2.1 *Sample Preparation* of the British Standard (BS 1377, 1990, Part 2) states that *"With many clay soils it is permissable to remove by hand any coarse particles present, i.e. particles retained on a 425μm test sieve. Otherwise these particles shall be removed by wet sieving as specified in Section 4.2.4"*. This preparation was carried out on the three soils prior to testing.

The results of the index property tests can be found in Table 4-27, which gives the Liquid Limit, Plastic Limit, Plasticity Index and Liquidity Index for each of the samples. Also given in the table is the classification of the sediment, using Casagrande's plasticity chart as given in BS5930 and which can be seen in Figure 4-44.

Sample	Plastic Limit	Liquid Limit	Plasticity Index	Liquidity Index	Classification
Soil A	18.93	33.17	14.24	-0.21	CL
Soil B	15.03	22.43	6.40	-0.64	CL / ML
Soil C	13.88	17.71	3.83	-1.05	ML

Table 4-27. The Atterburg Limits of the cohesive materials

It can be seen from Figure 4-44 that Soil A and Soil B plot above the A-line and so are classified as clays. However, it can be seen that Soil B plots close to the A-line and could be classified as Silt. Soil C plots below the A-line and is classified as silt. It can also be seen that practically all of the samples plot close to each other, since the samples have a liquid limit of between 10% and 20% and have a plasticity index of between 3% and 15%. Since the samples exhibit similar results, they are further classified as having a low plasticity.

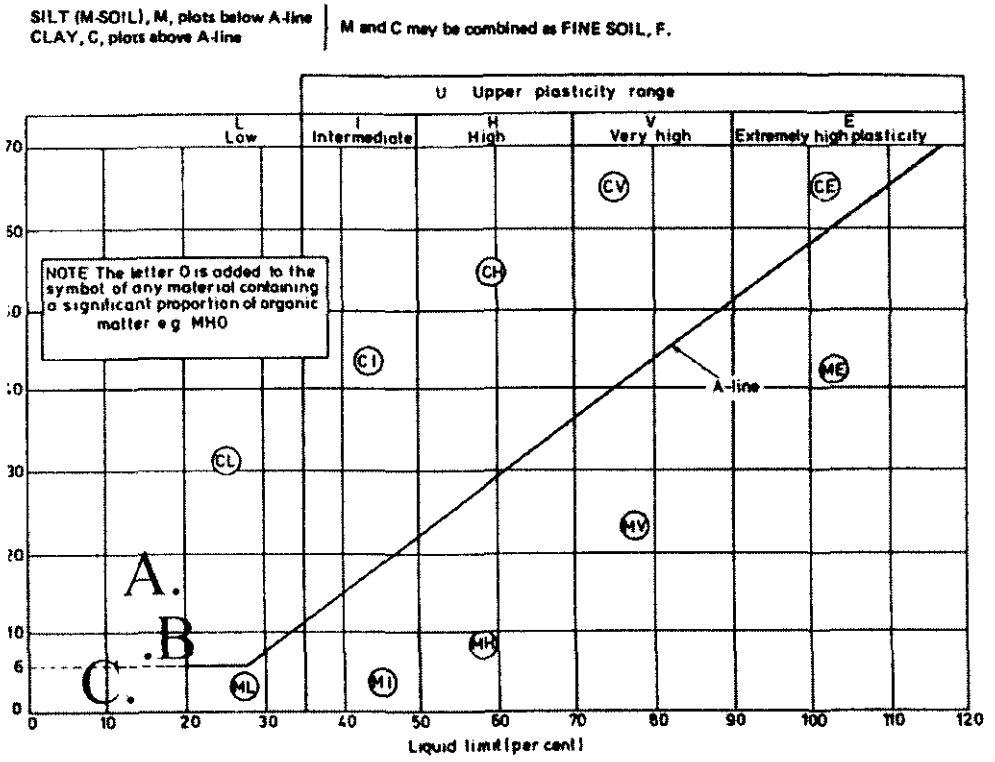

Figure 4-44. Plasticity chart for the cohesive materials. Soils are marked A, B and C.

4.6.4 Other Tests

4.6.4.1 Natural Sediment Properties

4.6.4.1.1 Natural Moisture Content

The natural moisture content tests were carried out in accordance with procedures to be found in BS 1377, 1990, Part 2. The results of the natural moisture content tests can be seen in Table 4-28.

Sample	Moisture Content (%)	Particle Specific Gravity	Colour
Soil A	14.21±1.05	2.65±0.01	Yellowish Brown 10YR 3/2 D
Soil B	10.53±0.35	2.64±0.01	Greyish Brown 2.5YR 4/4 D
Soil C	12.62±0.22	2.63±0.01	Brown 2.5YR 3/2 D

Table 4-28. Natural sediment properties of the cohesive materials.

4.6.4.1.2 Particle Specific Gravity

The specific gravity tests were carried out in accordance with procedures to be found in BS 1377, 1990, Part 2. Tests were carried out in duplicate with the given value being an average of the two.

The results of the specific gravity determination can be seen in Table 4-28. All three materials exhibit a particle specific gravity of approximately 2.65, a typical value for a general mineral soil (Freeze and Cherry, 1979).

4.6.4.1.3 Colour

The colour of the cohesionless materials was determined in the laboratory using the Munsell Colour Chart. The results can be found in Table 4-28.

4.6.4.1.4 Organic Matter Content

The organic matter content tests were carried out in accordance with procedures to be found in BS 1377, 1990, Part 4. The results of the organic matter content tests can be found in Table 4-29.

Sample	Organic Matter Content (%)
Soil A	1.51
Soil B	2.10
Soil C	2.28

Table 4-29. Organic matter content.

4.6.4.2 Shear Strength

The direct shear test was carried out in accordance with procedures to be found in BS 1377, 1990, Part 7.

The results of the direct shear test can be found in Appendix B which contains plots of shear stress against shear strain. From these the maximum shear stress was noted. Figure 4-45, Figure 4-46 and Figure 4-47 show plots of normal stress against shear stress at failure for the materials under investigation. These plots allow the determination of effective shear strength and angle of internal friction.

As well as the determination of shear strength and angle of internal friction, the direct shear tests enable the calculation of the bulk density and void ratio (the ratio of the volume of the voids to the volume of the solids) of the material under test. Table 4-30 shows the results of the direct shear tests for the cohesive materials.

Sample	Effective Shear Strength (kN/m^2)	Angle of Internal Friction (^{o})	Bulk Density (Mg/m^3)	Void Ratio
Soil A	79	27	0.801±0.028	2.77±0.14
Soil B	51	25	1.459±0.101	1.03±0.18
Soil C	56	25	1.501±0.078	0.96±0.09

Table 4-30. Results of the direct shear tests for the cohesive materials.

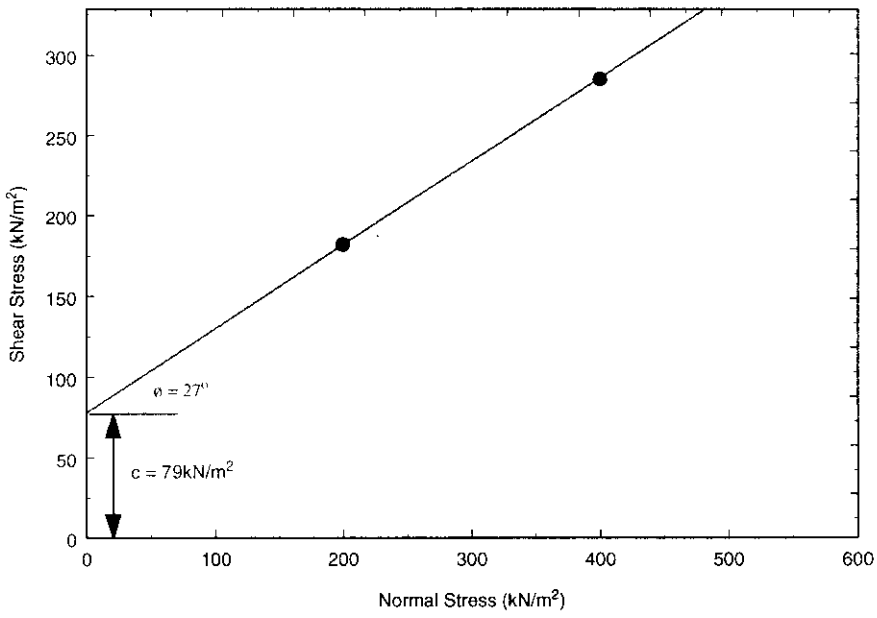

Figure 4-45. Plot of Normal Stress against Shear Stress at failure for Soil A.

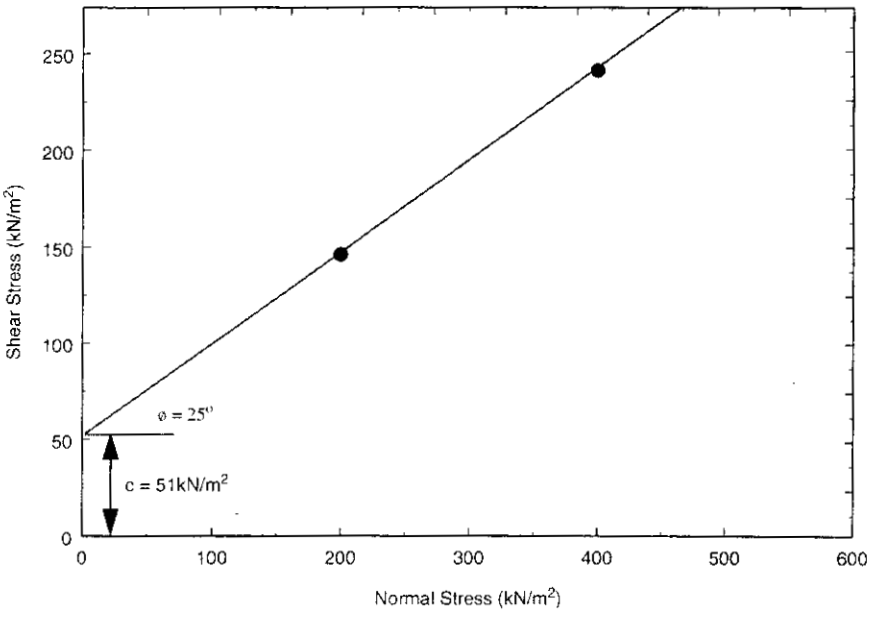

Figure 4-46. Plot of Normal Stress against Shear Stress at failure for Soil B.

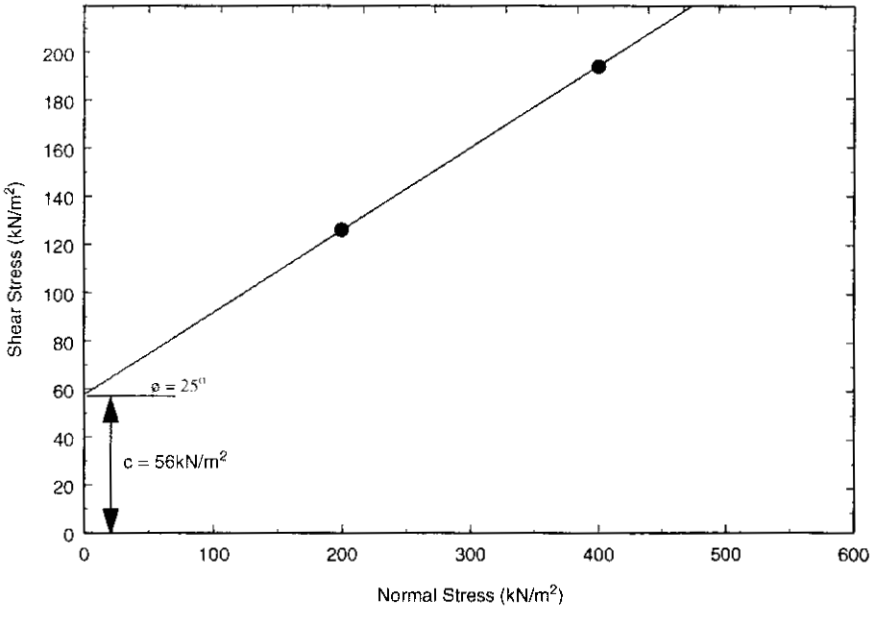

Figure 4-47. Plot of Normal Stress against Shear Stress at failure for Soil C.

4.6.5 Conclusions

It can be seen that many of the tests undertaken on the cohesionless sediments were not carried out upon the cohesive sediments from HRI, Wellesbourne, most noticeably direct measurements of tortuosity and flow resistivity. The main reason for this was the nature of the sediment itself. Since the test area was kept covered the ground retained little or no moisture and, as can be seen from the Atterburg Limits results, was very close to it plastic limit. This meant that the materials were extremely brittle and friable, so that collection of undisturbed samples was extremely difficult.

Measurements of tortuosity based upon Formation Factor were not appropriate since Archie's Law is not valid for sediments containing a significant percentage of clay. Clay provides conductive matrix, rendering a fundamental assumption invalid.

The measurement of flow resistivity requires an undisturbed sample of known size and shape. Any fissures in the specimen will allow flow additional to that through the material thus giving an incorrect value. These difficulties highlight the need for a non-invasive method of soil property determination for sediments of this nature.

The classification of the cohesive materials based upon the particle size analysis can be seen in Table 4-31.

Sample	Classification
Soil A	Clayey SAND
Soil B	LOAM
Soil C	LOAM

Table 4-31. Classification of the cohesive materials.

The values of water permeability measured using the modified falling head test, although smaller than expected, were reasonably typical for the types of materials tested. The lower than expected values may be due to the test procedure, although all the materials can be classed as being impermeable.

This trend can be seen in the value for the Soil A of $4.93 \times 10^{-10} \pm 3.00 \times 10^{-11}$m/s. This is slightly lower than would have been expected considering that the material consists of approximately 80% sand sized particles.

The value of permeability for the Soil B of $7.85x10^{-10}\pm1.79x10^{-10}$m/s is slightly higher than that of $4.47x10^{-10}\pm1.50x10^{-10}$m/s for Soil C but both these values lie within the expected range for clays. The higher permeability of the Soil B could be expected since it consists of approximately 13% more Sand sized particles.

Since the material was not suited to laboratory flow resistivity measurements and no in-situ permeameter was available, an approximation has been made using the relationships between intrinsic permeability calculated from the permeability tests and flow resistivity.

Table 4-32 shows calculated values of flow resistivity from the intrinsic permeability as measured using the modified falling head test.

	Intrinsic Permeability (from permeability test)	**Calculated Flow Resistivity (MKS Ralys)**
ARG test site	$5.03x10^{-17}\pm3.08x10^{-18}$	$3.60x10^{11}+x2.09x10^{10}$
Indoor tank	$8.02x10^{-17}\pm1.83x10^{-17}$	$2.26x10^{11}\pm4.24x10^{10}$
HMC Stone Lane	$4.57x10^{-17}\pm1.53x10^{-17}$	$3.96x10^{11}\pm9.93x10^{10}$

Table 4-32. Calculated values of flow resistivity from the intrinsic permeability as measured using the modified falling head test.

These results show that for cohesive materials the relationship between intrinsic permeability and flow resistivity is no longer valid. As stated in Section 4.2.1.1, the intrinsic permeability is really only applicable to inert particles such as sands and gravels. With clays, the chemical interaction between different fluids and the soil can be much more complex than described by viscosity and unit weight.

Tortuosity and porosity measurements were not taken for the three cohesive soils, however, an assessment can be made of the porosity (Ω) from the value of void ratio (e) calculated from the shear strength tests.

$$\Omega = \frac{e}{1+e} \qquad \textit{(Eq. 4-55)}$$

From the values of porosity, tortuosity can be assessed using the Bruggeman relationship. These results can be seen in Table 4-33.

Sample	Void Ratio	Porosity (%)	Porosity (%) (Res. Column)	Tortuosity
Soil A	2.77±0.14	73.47±0.95	23.76	1.36±0.02
Soil B	1.03±0.18	50.74±4.01	17.94	1.97±0.14
Soil C	0.96±0.09	48.98±2.24	12.43	2.04±0.09

Table 4-33. Calculated values of porosity from void and subsequent assessment of tortuosity using the Bruggeman relationship.

Table 4-4 and Table 4-5 all give values of porosities for Loam which range from 37.5% for loamy sand on plain to 55.2% for a loamy sand with roots. The values evaluated for Soils B and C appear typical. Soil A however, has an extremely high porosity of approximately 75%, which may be due to the high percentage of sand sized particles in the material. However, this value is more likely to be due to the nature of the material and the method of calculating the void ratio.

The void ratio is calculated from a determination of the bulk density of the material which is in-turn calculated from the mass of the soil in the known area of the shear test cell. The calculations rely upon the fact that all of the test cell is occupied by material. It is known that the materials from HRI are very friable and as such it is difficult to produce a perfect square to fill the test cell. It is therefore likely that voids were present in the test cell which were not allowed for in the bulk density determination and as such led to an abnormally high void ratio. Porosities for the three soils determined from the resonant column test provide more realistic values since a more accurate volume of soil is known.

The results of the elastic moduli determination highlight the difficulties of sample extraction and testing of materials such as those found at HRI, Wellesbourne. Namely, friable and fissured agricultural soils. This is highlighted by the results for Soils A and C, from which a bulk modulus calculation was not possible, since the measured value of shear modulus was over three times greater than the measured Young's modulus. This is especially so of Soil A.

It can be seen in the results and Figure 4-34 that for very shallow effective depths (less than 1m) the shear modulus is extremely small (approximately 4MPa). This value is most likely due to the presence of cracks in the specimen. At low confining pressures, such as those found close to the surface, these cracks are open. Thus, torsional motion induced in the sample will rotate about the cracks as opposed to homogeneous soil. At higher confining pressures these cracks will close. Torsion will be placed onto the soil

mass and an increase in the rigidity of the sample observed. This can be observed in Figure 4-34 where μ increases from 4MPa at 0.5m to 44MPa at 1.5m.

This shows the importance of the both the homogeneity of the sample and the accuracy of the experiment that a 1MPa change in shear modulus will result in a 50MPa change in bulk modulus and a resultant shift of 30m/s in the calculated P-wave velocity

The results of the Atterburg Limits test show that the three soils exhibit similar consistencies. However, it can be seen that Soil A has been classified as a CLAY of low plasticity, despite the fact it contained approximately 80% sand sized particles and has been classified as a Clayey SAND from the particle size analysis. This is due to the fact that the sample was passed through a 425μm sieve prior to testing as outlined in Section 4.6.3.2, thus reducing the sand content of the sample. Soils B and C plot very close to the A-line as would be expected for materials of this nature, having been classified as LOAM from the particle size analysis.

It can be seen in Table 4-27 that all three materials have a liquidity index of less than one. This means that they no longer exhibit permanent deformation and act as brittle solids, confirming the field description of the soils as being very friable and fissured. This value of liquidity index also confirms their classification as being of low plasticity.

None of the soils were classified as being organic since the organic matter content results show that all three materials contain less than approximately 2.5% organic matter.

The results of the natural sediment properties tests show that all the materials were dry when tested, having measured moisture contents of less than 15%. This moisture content is expected since, as described in Section 4.1.3 the site area was kept covered at all times. This low moisture content is expressed in the colour notations since a light colour is typical of dry materials.

The specific particle density measurements again show a similarity between the three soils. The values are close to the typical value of 2.65g/cm^3 that has been suggested to characterise the soil particle density of a general mineral soil (Freeze and Cherry, 1979).

Overall, the problems relating from sample disturbance and the nature of the sediments meant that problems were encountered whilst trying to measure the properties of the agricultural soils found at HRI, Wellesbourne. The problems help to promote the necessity of non-invasive methods of soil property deduction.

Sample	Void Ratio	Porosity (%)	Porosity (%) (Res. Column)	Tortuosity
Soil A	2.77±0.14	73.47±0.95	23.76	1.36±0.02
Soil B	1.03±0.18	50.74±4.01	17.94	1.97±0.14
Soil C	0.96±0.09	48.98±2.24	12.43	2.04±0.09

Table 4-33. Calculated values of porosity from void and subsequent assessment of tortuosity using the Bruggeman relationship.

Table 4-4 and Table 4-5 all give values of porosities for Loam which range from 37.5% for loamy sand on plain to 55.2% for a loamy sand with roots. The values evaluated for Soils B and C appear typical. Soil A however, has an extremely high porosity of approximately 75%, which may be due to the high percentage of sand sized particles in the material. However, this value is more likely to be due to the nature of the material and the method of calculating the void ratio.

The void ratio is calculated from a determination of the bulk density of the material which is in-turn calculated from the mass of the soil in the known area of the shear test cell. The calculations rely upon the fact that all of the test cell is occupied by material. It is known that the materials from HRI are very friable and as such it is difficult to produce a perfect square to fill the test cell. It is therefore likely that voids were present in the test cell which were not allowed for in the bulk density determination and as such led to an abnormally high void ratio. Porosities for the three soils determined from the resonant column test provide more realistic values since a more accurate volume of soil is known.

The results of the elastic moduli determination highlight the difficulties of sample extraction and testing of materials such as those found at HRI, Wellesbourne. Namely, friable and fissured agricultural soils. This is highlighted by the results for Soils A and C, from which a bulk modulus calculation was not possible, since the measured value of shear modulus was over three times greater than the measured Young's modulus. This is especially so of Soil A.

It can be seen in the results and Figure 4-34 that for very shallow effective depths (less than 1m) the shear modulus is extremely small (approximately 4MPa). This value is most likely due to the presence of cracks in the specimen. At low confining pressures, such as those found close to the surface, these cracks are open. Thus, torsional motion induced in the sample will rotate about the cracks as opposed to homogeneous soil. At higher confining pressures these cracks will close. Torsion will be placed onto the soil

mass and an increase in the rigidity of the sample observed. This can be observed in Figure 4-34 where μ increases from 4MPa at 0.5m to 44MPa at 1.5m.

This shows the importance of the both the homogeneity of the sample and the accuracy of the experiment that a 1MPa change in shear modulus will result in a 50MPa change in bulk modulus and a resultant shift of 30m/s in the calculated P-wave velocity

The results of the Atterburg Limits test show that the three soils exhibit similar consistencies. However, it can be seen that Soil A has been classified as a CLAY of low plasticity, despite the fact it contained approximately 80% sand sized particles and has been classified as a Clayey SAND from the particle size analysis. This is due to the fact that the sample was passed through a 425µm sieve prior to testing as outlined in Section 4.6.3.2, thus reducing the sand content of the sample. Soils B and C plot very close to the A-line as would be expected for materials of this nature, having been classified as LOAM from the particle size analysis.

It can be seen in Table 4-27 that all three materials have a liquidity index of less than one. This means that they no longer exhibit permanent deformation and act as brittle solids, confirming the field description of the soils as being very friable and fissured. This value of liquidity index also confirms their classification as being of low plasticity.

None of the soils were classified as being organic since the organic matter content results show that all three materials contain less than approximately 2.5% organic matter.

The results of the natural sediment properties tests show that all the materials were dry when tested, having measured moisture contents of less than 15%. This moisture content is expected since, as described in Section 4.1.3 the site area was kept covered at all times. This low moisture content is expressed in the colour notations since a light colour is typical of dry materials.

The specific particle density measurements again show a similarity between the three soils. The values are close to the typical value of 2.65g/cm^3 that has been suggested to characterise the soil particle density of a general mineral soil (Freeze and Cherry, 1979).

Overall, the problems relating from sample disturbance and the nature of the sediments meant that problems were encountered whilst trying to measure the properties of the agricultural soils found at HRI, Wellesbourne. The problems help to promote the necessity of non-invasive methods of soil property deduction.

Chapter 5

Design and Execution of Indoor Experiments

5 Experiments

The major portion of this study has concerned the exploitation of acoustic-to-seismic coupling in the determination of the bulk properties of soils. This has led to a variety of experiments.

The experiments undertaken can be sub-divided into two distinct categories; indoor and outdoor. These categories can be further sub-divided into those experiments directly investigating soil property determination and those concerned with the calibration of the equipment.

As stated previously, the main subject of the thesis is the exploitation of acoustic-to-seismic coupling in the determination of bulk properties of soils. As remarked in Chapter 1 (the review of previous work) several authors have undertaken small-scale or restricted studies of acoustic-to-seismic coupling. An important contribution of the present work was an in-depth experimental study into acoustic-to-seismic coupling. Field experiments have been designed to investigate:

1) The repeatability of the coupling.

2) The reliability of the technique.

3) The angle dependence of the coupling.

4) The acoustically induced wave types.

5) The accuracy of the available predictive models.

The reliability experiments led to further investigations into sensor response, namely the effect of ground-geophone coupling and the development of a different vibration sensor. The review revealed the limitations of the geophone sensor, which led to an investigation into the use of a Laser Doppler Vibrometer (LDV). The LDV is a non-

contact optical system for measuring the instantaneous velocity of moving surfaces. The system has a linear transfer function, and a real time analogue output proportional to velocity.

The indoor studies involved the use of a soil bin and measurement of the three Biot acoustic waves and the subsequent deduction of bulk soil properties. Study was also made of the use of microphones as detectors of Biot Type I wave.

5.1 Indoor Experiments

The indoor experiments undertaken include:

- Measurement of the three Biot acoustic waves and the subsequent deduction of bulk soil properties
- A study of geophone calibration, with particular emphasis on geophone-ground coupling.
- The use of a Laser Doppler Vibrometer (LDV) as a vibration sensor in acoustic-to-seismic coupling measurements.

The majority of the experiments undertaken as part of this study involved the use of the Labview programming language for the acquisition and partial analysis of the experimental data. A brief note on the fundamentals of FFT based signal analysis and measurement, with specific relation to Labview has been given in Appendix A for those unfamiliar with this subject.

5.1.1 Soil Tank

An opportunity arose to carry out measurements in a soil tank at the American National Centre for Physical Acoustics (NCPA), based at the University of Mississippi, USA. Based on this work, similar apparatus was designed and built at The Open University, where similar measurements were carried out.

accurate determination of the depth of burial can be made. For added accuracy, a length of "scalafix" was applied to the tube. This is a self-adhesive tape that has a graduated scale down to millimetres.

The inner design of the microphone is a "u-shaped" brass tube surrounded by a rubber sheath, to which the microphone element is attached. This second tube when inserted into the outer tube expands to give a flush fit. This ensures that as little sound as possible can pass directly down the tube to the element. A silicon seal is also placed around the copper end-plug as a further seal and to keep foreign debris from entering the probe. The microphone element is an AOI model ECM-1028A, ultra-miniature Electret condenser microphone.

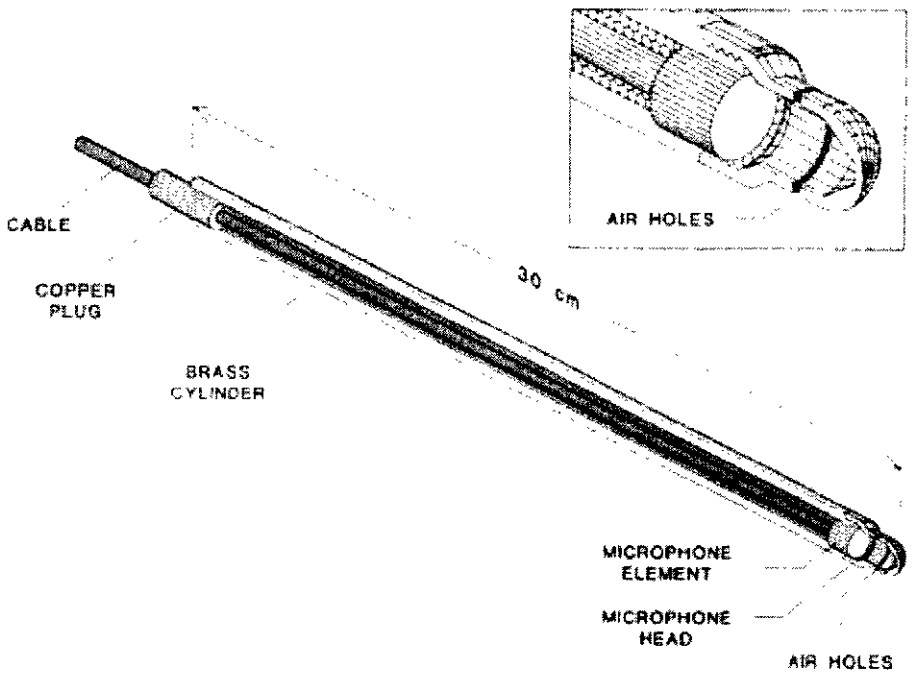

Figure 5-1. Diagram of probe microphone. Insert shows enlarged view of the nose cone and microphone element.

The nose cone is designed to have a resonant frequency greater than 5000Hz. All measurements were made well below this frequency. When designing the nose cone several important parameters need careful consideration. These are the inner volume of the noise cone and the number, diameter and length of air holes in the nose cone.

When an acoustic pressure fluctuation occurs at the nose, the mass of air in the small holes is accelerated, whilst the air in the inner volume is compressed. Together,

these components combine to function as an acoustic Helmholtz resonator (Beranek, 1986), with a resonant frequency

$$f_0 = \frac{1}{2\pi\sqrt{MC}} \qquad \textit{(Eq. 5-1)}$$

where M is the total acoustic mass of the air in the small holes and C is the acoustic compliance of the large inner volume. This can be rewritten to give

$$f_0 = \frac{\sqrt{nrc_0}}{2\sqrt{\pi(L+L')V}} \qquad \textit{(Eq. 5-2)}$$

where r is the radius of one hole, n is the number of holes, c_0 is the speed of sound in air, L is the length of an air hole, L' is an acoustic correction to the length and V is the volume of the nose cone cavity.

Before installation, all sensors were calibrated using techniques outlined in Section 5.1.2 to assess their useable bandwidth and sensitivity. The frequency response of the probe microphone was measured with several of the holes sealed, to allow for the effect of blocking of the holes in granular materials.

To ensure that all the sensors were as accurately positioned as possible a wooden former was made. This consisted of a crosspiece that rested on the rim of the container, with a centre-pole placed vertically in the centre of the tank. A second wooden former was then placed onto the wooden centre-pole, to be used as a template for the positioning of the sensors. This template was moved up the centre-pole as more sand was added, with the height from the rim checked with a ruler.

Sand was placed into the container in 10cm increments, manually levelled and lightly tamped. This was continued until there was approximately 21cm of soil in the container. At this point, the first of the vertical component geophones and microphones were added. More sand was added and additional sensors placed, in a staggered fashion, at 5cm intervals. The horizontal component geophones were positioned 10cm below the surface and spaced every 10cm. A total of ten vertical component geophones, five horizontal component geophones and ten microphones were buried (See Figure 5-2). Receiver placement was accurate to $\pm$ 0.2cm both horizontally and vertically.

Two separate sources were used. A loudspeaker that was suspended approximately 2m directly above the soil-surface and was driven using an H&H S150 professional power amplifier. The other source was a Ling Dynamic Systems Model V203 mechanical shaker, that was placed in contact with the surface of the soil. The mechanical shaker has a

circular base with a diameter of 7.5cm. This was driven using a Brüel and Kjær Type 2706 power amplifier.

The geophone signals were amplified using a Brüel and Kjær Type 2160 measuring amplifier. The microphones signals were first amplified using a purpose built battery pre-amp (this also acted as a microphone power supply), before amplification by the Brüel and Kjær measuring amplifier. The probe microphone also required a purpose built battery pre-amplifier before amplification by the Brüel and Kjær measuring amplifier.

At NCPA, again two separate source types are used. A loudspeaker, consisting of a Peavey Loudspeaker suspended about 2m directly above the soil surface. The other source was a mechanical shaker, Ling Dynamic Systems Model V203, placed in contact with the surface of the soil. The mechanical shaker has a circular base with a diameter of 7.5cm.

5.1.1.2 Choice of Source Signal

The selection of the input signal depends on many factors. The main parameters are:

- *Bandwidth*: the range of frequencies in which sufficient energy is present.
- *Signal Type*: continuous or transient. If continuous, periodic or random; periodic signals will repeat after a fixed duration, and therefore have a line spectrum, random signals are aperiodic and have a continuous spectrum.
- *Crest factor*: the ratio of the signal's peak amplitude to its RMS value. Since, to avoid overload, the power to a transducer is often limited by the peak amplitude, the mean output power of the signals with high crest factors will be lower than low crest factor signals, and hence resulting measurements will have a worse signal-to-noise ratio.
- *Estimation accuracy*: some signals permit more robust estimation techniques than others do.

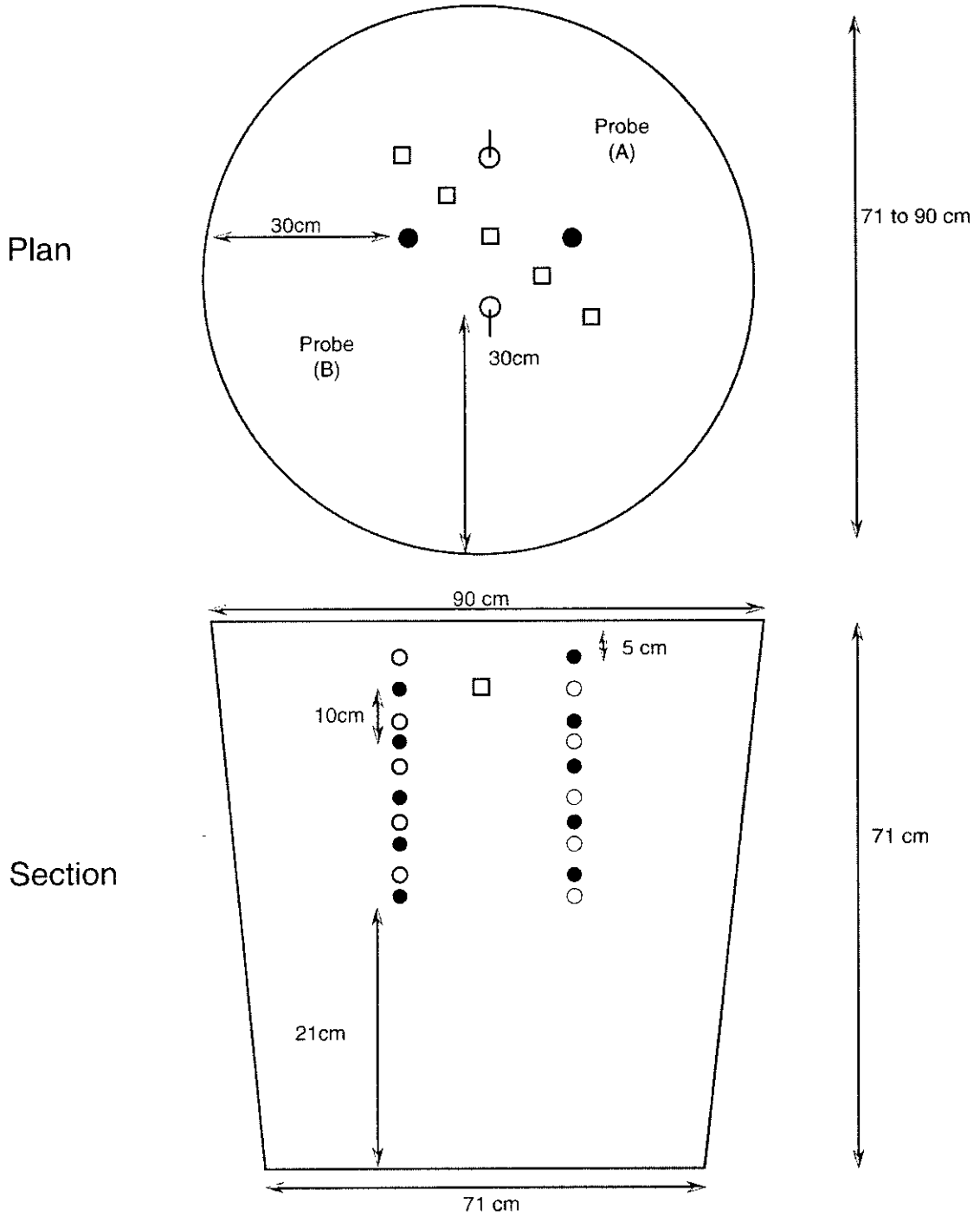

Figure 5-2. Schematic of the acoustic wave transmission experiment in soil tank at the OU. The Black Symbol (●) represents vertical component geophones, the symbol (□) represents the horizontal component geophones and the white symbols(○) represent microphones. The Probe microphone was inserted at two positions A and B.

	Bandwidth	Signal Type	Crest Factor	Accuracy
Sine	single frequency ⇒ slow analysis	Continuous, Periodic	3 dB	Good for non-linearity & noise. Allows time delay identification
Swept Sine	arbitrarily wide & flat response	Continuous, Aperiodic	3 dB	Good for non-linearity & noise. Allows time delay identification
Random "noise"	arbitrarily wide & flat response	Continuous, Aperiodic	11 dB	Good statistical characterisation, good estimates with non-linearities, poor SNR, slow due to need for averaging.
Impulse	wide, limited low frequencies	Transient. Can simulate impulse response	Very high (low energy)	Poor: high CF gives low SNR and excites non-linearities. Repeatability suspect. Allows time-delay identification & editing
Pseudo-random	arbitrarily wide & flat, low frequencies limited by period	Continuous, periodic	Arbitrary, depending on phase spectrum	Good for noise (synchronous averaging possible), poor for non-linearities, always excites them similarly.

Table 5-1. Properties of commonly used excitation signals

Pseudo-random signals appear locally random, but involve a fixed pattern that repeats each time after a fixed duration. This has three main advantages:

- If the duration is synchronised with the data collection window, then the line spacing of the (periodic) signal is identical to that of the sampled waveform, and therefore no windowing is required, and no frequency "leakage" occurs (Randall, 1987).
- Since the same signal repeats periodically, the measured data block can be averaged in the time domain, with the recording synchronised with the generated signal, to reduce the level of uncorrelated noise. This technique – called synchronous averaging – increases the signal-to-noise of the measurement, and can recover the signal even in the presence of considerable noise.
- Unlike excitation by random "noise", spectral averaging is not necessary to remove the effect of random fluctuations.

The maximum length sequence (MLS) is a special type of pseudo-random signal first proposed by Schroeder (1979) for use in room acoustics. It is a binary sequence, taking the values +1 and –1 in equal numbers, and therefore having the lowest possible crest factor of 0dB. The sequence is generated by an *n*-stage shift register (Chu, 1987), yielding a sequence length of $N = 2^n - 1$. Since the spectrum is flat (in a given range), the circular autocorrelation function $r(m)$ approximates to an impulse. This can be seen below:

$$r(m) = \frac{1}{N}\sum_{k=1}^{N} x(k)x(k+m) = 1 \qquad m \bmod N = 0 \qquad \text{(Eq. 5-3)}$$

$$= \frac{-1}{N+1} \qquad m \bmod N \neq 0$$

Since N is chosen to be high (typically 32767 for n=15), the value of $r(m)$ for $m \bmod N \neq 0$ is small. Therefore, this approximates a periodic unit pulse:

$$\delta'(\mathrm{m}) = 1 \qquad m \bmod N = 0 \qquad \text{(Eq. 5-4)}$$

$$= 0 \qquad m \bmod N \neq 0$$

where the dash signifies a periodic quantity.

This leads to the property that the periodic impulse response of the system under test can be approximated by cross-correlating the sampled response signal with the original

MLS sequence. Rife and Vanderkooy (1989) prove this rigorously, and described many properties and limitations of analysis with MLS.

Testing with MLS became popular when an efficient method of performing the cross-correlation was found using a fast Hadamard transform (Chu, 1990; Altrutz and Schroeder, 1983).

The advantages of this technique are

- The signal approximates to the same flat amplitude response as a delta pulse (-3dB at ½ the pulse generation frequency, and hence at the Nyquist frequency of the sampled signal).

- The crest factor is very much lower than a pulse (due to the erratic phase spectrum of the MLS). With a crest factor of 0dB, the maximum possible power is delivered to the transmitter, giving a limit to maximum amplitude. For an amplitude-limited system, the energy content of a MLS signal is a factor N higher than that of a single pulse. In consequence, the signal-to-noise ratio (SNR) is higher by $10\mathrm{Log}_{10}N$; for example, the SNR of an n=15 sequence is 45dB higher than a pulse of the same amplitude.

- This method is equivalent to testing with impulses, but offers a much higher SNR and reduced risk of exciting non-linearities. In particular, reflecting paths in the system can readily be identified, and edited in the time domain, if necessary.

- The impulse response is very long (up to N samples). Therefore, very reverberant environments can be measured, with remarkably little noise in the low amplitude "tails" of the response, and long duration records may be collected at a high bandwidth. Furthermore, if a Fourier transform is applied to the long time sequence, a very high-resolution frequency will be obtained without the necessity for zoom processing – the usual method with analysers that are typically limited to 2-8k sample transforms.

- Cross-correlation makes the resulting impulse response quite immune to noise: for example, a single noise transient in the response signal will have its energy spread evenly throughout all N samples in the impulse response. In addition, since each repetition of the MLS is identical, the signal may be synchronously averaged to reduce uncorrelated noise, increasing the SNR to $10\mathrm{Log}_{10}N_a$ (where N_a = number of averages) dB.

- Instead of driving a linear transducer, the digital output of the MLS can trigger, for example, spark gaps, or booms for use in oceanography (Birdsall, 1995). The cross-correlation algorithm effectively acts as a matched inverse filter, to compress the energy spread out over the N pulses back into a single pulse.

The disadvantages of MLS testing are:

- It is not good at estimation in the presence of any non-linearity in signals, since they are always excited in the same way. However, their presence is easily detected. Non-linearity shows up as a "fixed pattern" noise in the time-of-flight gap, or after the impulse response has decayed – that is regions where the impulse response should be zero show a noise signal that is the same each time the measurement is taken.

- The signal contains no energy at D.C. (0 Hz). This is not usually a problem in acoustic testing.

- The technique only applies to time-invariant systems. The same is true of all other signals, but the long duration of the MLS signal means that the time-scale over which the system must be time-invariant is longer, than an impulse for example.

- The statistical estimation techniques are not as well developed as for Gaussian noise, making error estimates of the resulting transfer more difficult. Rife and Vanderkooy (1989) have developed a limited method of deriving coherence from an MLS-derived impulse response.

- The duration of the sequence must be longer than the impulse response of the system otherwise "time-aliasing" will result (Rife and Vanderkooy, 1989). This is not usually a problem, due to the long durations possible (for example, an n=16 sequence measuring at 20kHz bandwidth lasts over 1s).

Continuous wave (CW) signals, like the maximum length sequence described above, offer a convenient method for calculating phase speed and attenuation over a range of frequencies in the soil tank. However, fluctuations in the data begin to appear at deeper depths. These fluctuations are probably due to signal reflections from the bottom and sides of the container. It was therefore decided to use the MLS for probe microphone measurements which were taken close to the surface whilst measurements at deeper depths were taken using five cycle tone bursts.

The MLS was produced using a propriety DAQcard by DRA Laboratories, called MLSSA. It is a P.C. based add-in card with software that performs as a single channel system analyser. The hardware produces the maximum-length sequence output signal, whilst the software performs the cross-correlation between the input and received signals. The card incorporates an anti-aliasing filter with programmable corner frequency, shape and gain. It has a measurement bandwidth of 1 – 40 kHz, with a sample clock, signal generation clock, and anti-aliasing filter automatically changing according to the bandwidth.

The five cycle tone bursts were generated using a National Instruments AT-MIO-16E-2 DAQcard controlled using a Labview program.

If an inversion for the material properties is to be determined, a measure of the wavenumber squared is required. The MLS measurement consists of a phase difference and relative magnitude of the signal at the appropriate sensor with respect to some sensor.

A time harmonic plane wave propagating in the x direction with a complex wave number $Re(k)+i\ Im(k)$ is written as,

$$e^{-\mathrm{Im}(k)x}e^{i(\mathrm{Re}(k)x-\omega t)} \qquad \textit{(Eq. 5-5)}$$

The real part of the wavenumber can be determined from the phase difference, $\Delta\Phi$, by,

$$\mathrm{Re}(k)=\frac{\Delta\Phi}{\Delta x} \qquad \textit{(Eq. 5-6)}$$

where Δx is the distance between receivers. The imaginary part of the wavenumber can be obtained from the relative magnitude, $\ln|A_2/A_1|$, by,

$$\mathrm{Im}(k)=-\frac{\ln|A_2/A_1|}{\Delta x} \qquad \textit{(Eq. 5-7)}$$

For the five cycle tone burst measurements, first break arrival time and peak-to-peak amplitudes were measured, (See Figure 5-3), from the signal received by the probe and the various geophones and microphones. Knowing the spatial separation between the sensors and the difference in arrival time the wave speed or $Re(k)$ may be determined by

$$\mathrm{Re}(k)=\frac{\omega}{c}=\frac{\omega\Delta t}{\Delta x} \qquad \textit{(Eq. 5-8)}$$

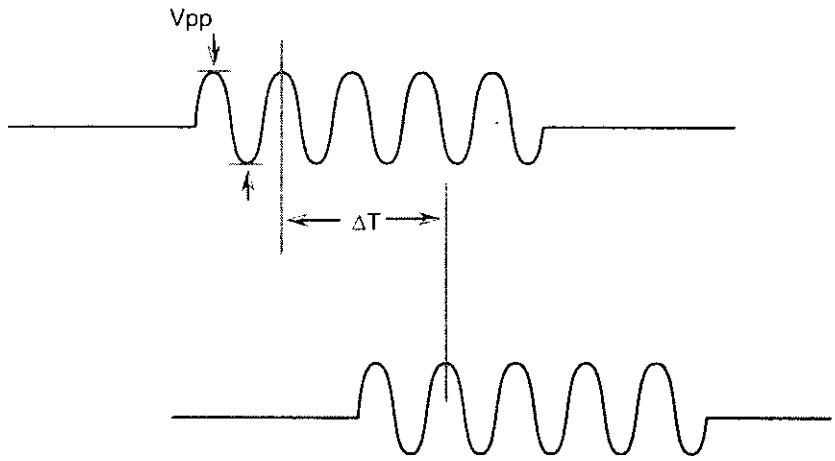

Figure 5-3. Procedure for the determination of transit time interval, Δt, and peak to peak voltage, Vpp, from the five-cycle tone bursts. The top signal is the transmitted signal with the received signal below.

At NCPA, source signals used were either swept sine or five cycle tone bursts. These signals were produced using a HP 3314A signal generator. The signal to the loudspeaker was amplified using a Techron 5515 power supply whereas the signal to the shaker was amplified using its own power oscillator.

5.1.1.3 Test Procedure

a) Mechanical Shaker Measurements

A mechanical source was used for the production of primarily Type I P-waves, with the transmitted signal received by the vertical component geophones and the microphones (Figure 5-2). Figure 5-4 shows the experimental set-up.

The source consists of a Ling Dynamic Systems Model V203, placed in contact with the surface of the soil. The mechanical shaker has a circular base with a diameter of 7.5cm. A circular footing such as this has been shown (Richart *et al.*, 1970) to produce a dilatational wave, shear wave and a Rayleigh wave. In order to obtain a signal at the receiver which is comprised of energy predominantly associated with the dilatational wave, it is necessary to move the source four times to place it directly over each column of receivers. This may cause some errors in the amplitude data due to the change in coupling between the source and the soil whenever it is moved.

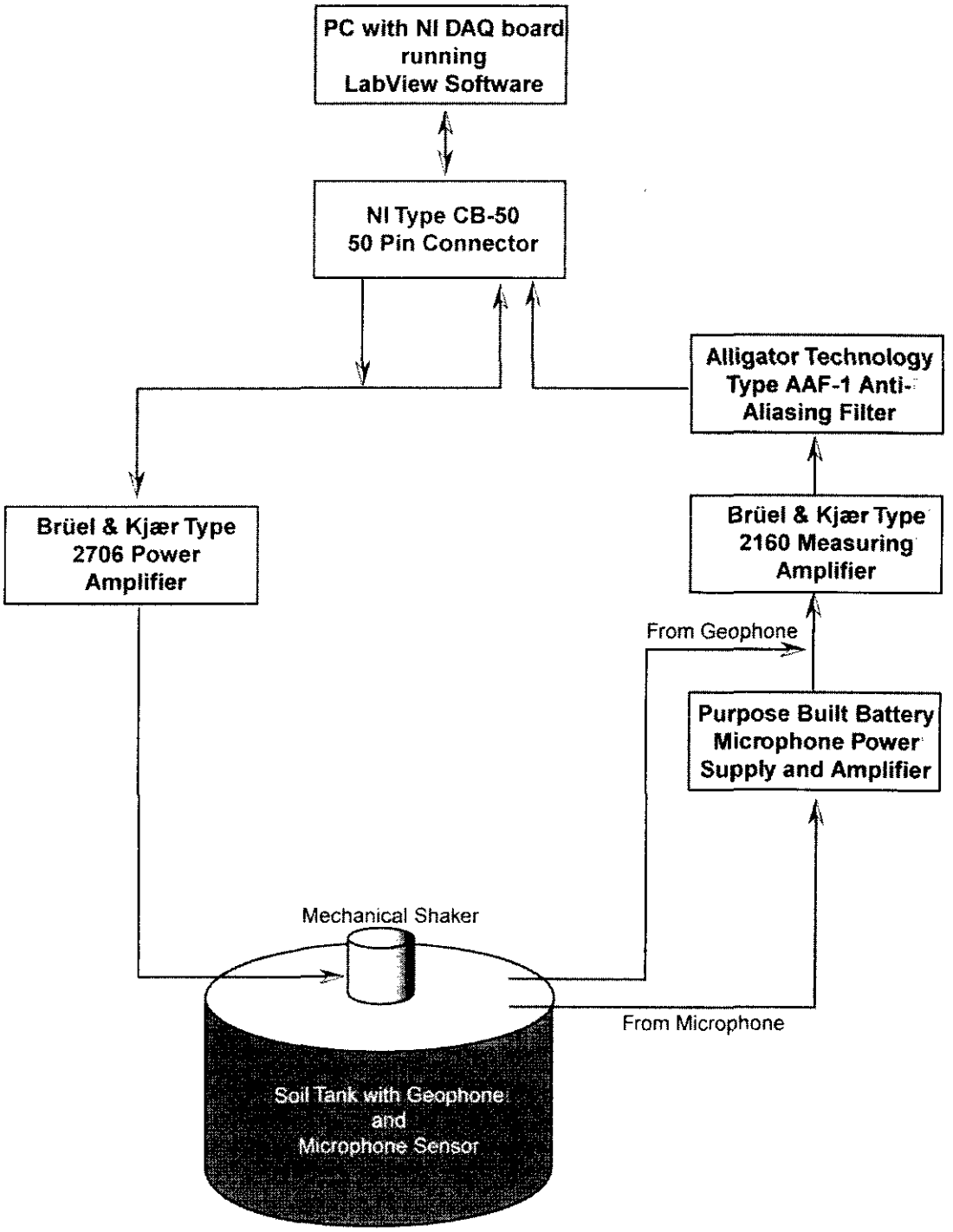

Figure 5-4. Experimental set-up for five-cycle tone burst experiment in soil tank

Based on previous work it appears that the shaker generates significantly more Type I than Type II dilatational wave energy. When a mechanical source is placed in contact with a porous material, the normal component of the solid and fluid displacements at the surface are in phase. Such in phase motion of material components is usually associated with the Type I dilatational wave at low frequencies. It has also been shown (Geertsam and Smit, 1961) that for the case of an elastic wave passing through an interface separating an impermeable elastic solid and a fluid-filled permeable porous material, that no second wave is generated at the interface.

Signal generation and data acquisition were undertaken on an IBM compatible PC using a National Instruments E-Series AT-MIO-16E-2 I/O acquisition board controlled using a purpose written Labview program (Figure 5-5 and Figure 5-6). The AT-MIO-16E-2 has eight differential inputs and two output channels, both having a 12 bits (1 in 4096) resolution.

The signal generation is controlled within the program from the "output section". The program reads a single cycle of sine, with arbitrary amplitude and offset, into a buffer that can be repeated *x* number of times. This was usually set at five, with the frequency of this sine wave either 500Hz, 750Hz, 1000Hz, 1250Hz or 1500Hz. The repetition of this pulse was set at 1 second, although this could be set at any value. This repetition every second allowed all the energy to have attenuated before the next burst was generated.

The five-cycle burst was then sent to the power amplifier that drives the shaker. This output also acts as the trigger for the signal acquisition. The output is plotted on Trace 1, the upper trace in Figure 5-6 and is used as a reference for the travel time determination. Since a 1 Vpp was used as the output signal, the input gain values were also set to $\pm$1Vpp.

This software programmable gain increases the overall flexibility of the board by matching the input signal ranges to those that the analogue-to-digital converter (ADC) can accommodate. With the proper gain setting, you can use the full resolution of the ADC to measure the input signal.

The scanrate for the acquisition was set as high as possible, to give as accurate a representation as possible of the sine wave. This ensured an accurate determination of Δt and Vpp. The maximum scanrate is controlled by both the maximum bandwidth of the analogue-to-digital converter on the board and, more importantly, by the settling time of the acquisition card.

With the shaker placed directly above a line of geophones, all connections made and the program running, the received signal from the shallowest sensor was amplified until it gives close to 1Vpp on Trace 2 on Figure 5-6. This required altering the gain on the Brüel and Kjær measuring amplifier and the variable gain on the Brüel and Kjær power amplifier. This amplification was fixed until all the geophones have been used, as any alteration affects the relative peak-to-peak amplitudes of the received signals.

Averaging was employed to increase the signal-to-noise ratio, with values of 50 to 100 used depending upon background levels.

Once the averaging was complete, the values of Δt and the peak-to-peak amplitude were determined using the method shown in Figure 5-3. The cursors were moved to the second peak on both Traces 1 and 2. The second peak was chosen since preliminary tests showed that the shaker exhibits a latency which gives the first output peak a variable amplitude, whilst at deeper depths the later peaks are altered due to reflections from the tank walls. The values of Δt and the peak-to-peak amplitude were read from the program.

Once the travel time and peak-to-peak amplitude for the sensor had been recorded the next geophone was connected and the processes repeated until the five sensors under the shaker were recorded. The program was then stopped and the shaker moved over the other line of geophones.

The same procedure was used for the microphone sensors. The Alligator Technologies Type AAF-1 anti-aliasing filter was used here as a low-pass filter to remove any high frequency components that may have distorted the acquired burst, and was set to a cut-off frequency of 5Khz.

It was not known whether the shaker would act as a point source for this set-up. If the shaker did behave as a point source then corrections for spherical spreading, based on the 1/r approximation, would need to be made. The condition for a source to act as a point source at angular frequency, ω, is $ka \ll 1$ (where $k = \omega/c$ is the wavenumber of the disturbance and a is the radius of the source). At a frequency of 1kHz, and assuming a speed of 250m/s (typical for sand), the ka for the shaker is 0.94. The condition for the far field is $kr \gg 1$, where r is the source to receiver distance. For a frequency of 1kHz and speed of 250m/s, kr=1.26 at the nearest receiver which is 0.05m away.

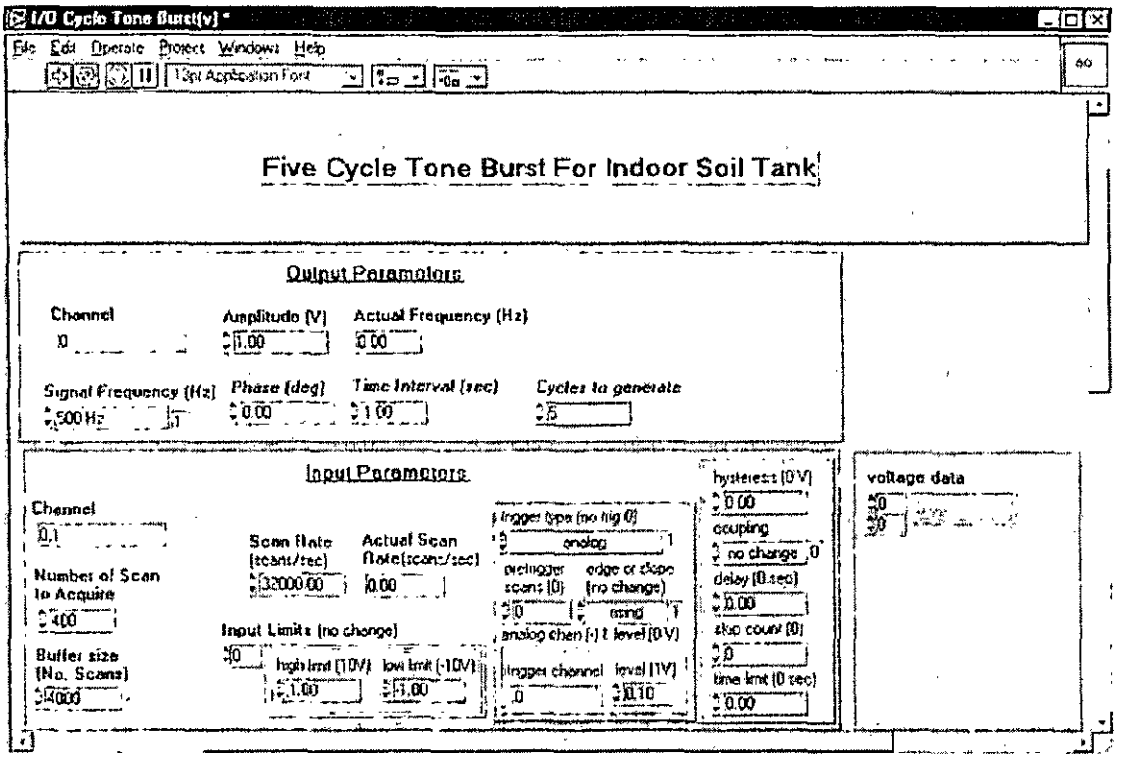

Figure 5-5. Hardware set-up for tank software

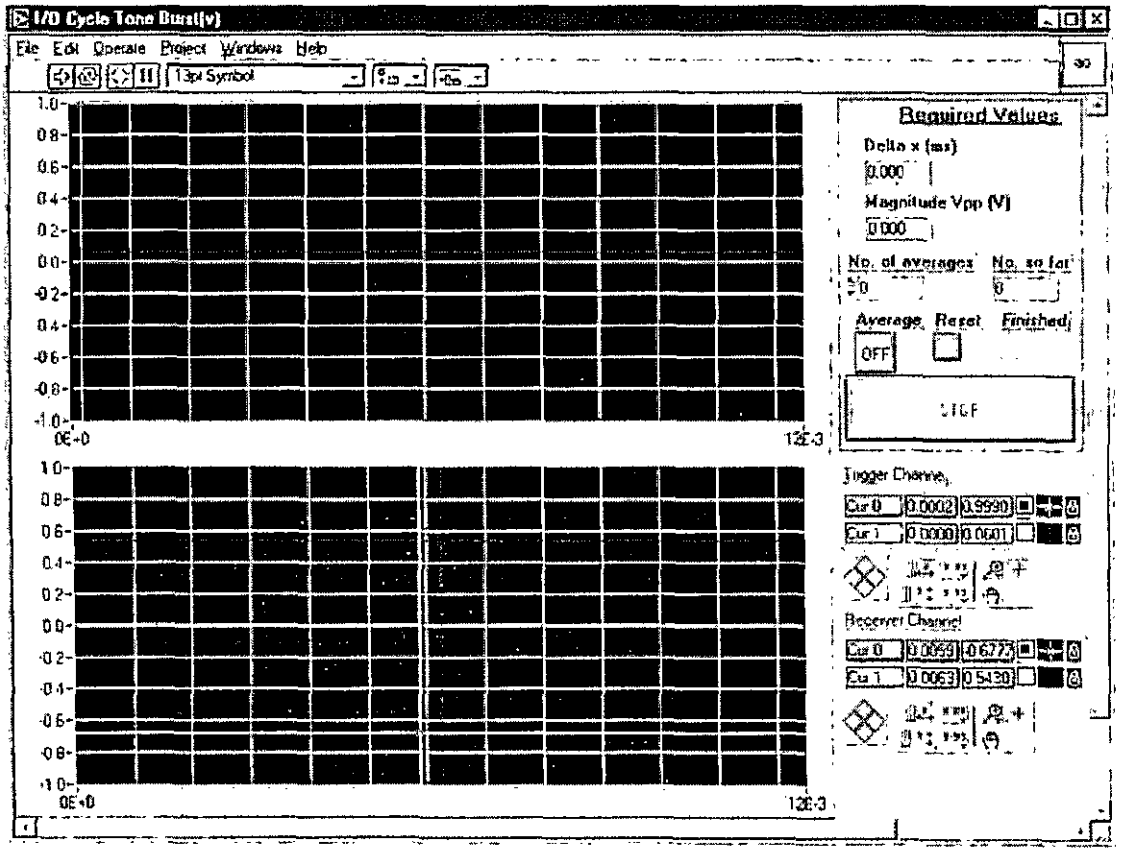

Figure 5-6. Determination of Δt and Vpp from five cycle tone bust.

In view of this, an experiment was designed to determine the directivity of the shaker. This experiment employs a similar method to that used to determine the directivity of loudspeakers.

A preliminary experiment was set-up as shown in Figure 5-7. This set-up was chosen so measurements would be taken at a set radius from the shaker with distances accurately measured using a rule and confirmed from arrival times. If the shaker were acting as a point source, then all the amplitudes at the same distance would be similar.

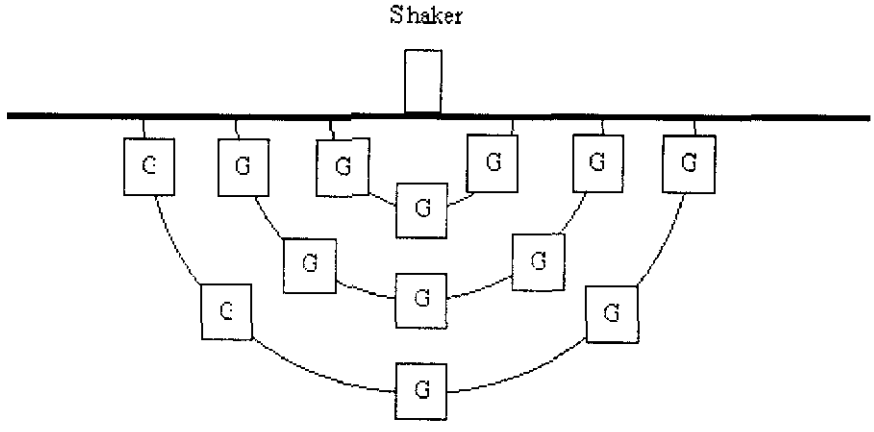

Figure 5-7. Geophone positioning in the determination of shaker directivity pattern.

Five-cycle tone bursts were generated using the shaker with the received transit times and amplitudes noted. This was achieved using the five-cycle tone burst program, described previously. However, initial results showed that for measurements taken close to grazing, the arrival times of the tone burst were very long compared to those close to normal incidence.

This difference was probably due to the shaker producing a dilatational wave, shear wave and a Rayleigh wave. It was thought that the geophones were reacting to the vertical component of the shear and Rayleigh wave which, having much slower velocities in the sand, produced the longer travel times.

A medium was therefore required that did not support shear waves, so that it could be assumed that the energy received by the sensor was the same. To this end, the sand was emptied from the tank and filled with water, as it is known that water does not support shear waves. Hydrophones were then used to record the transmitted signal.

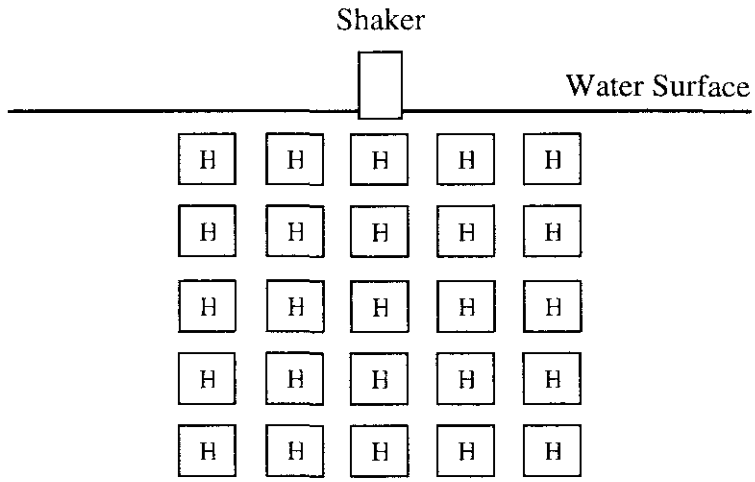

Figure 5-8. Hydrophone positioning in the determination of shaker directivity pattern.

The experiment was set-up as shown in Figure 5-8 with the shaker positioned at the water surface and a hydrophone accurately positioned in the water. The placing of the hydrophone was undertaken as accurately as possible using a steel rule to ensure that the hydrophone was subject to the same pressure field. The same hydrophone was used for all the measurements to eliminate the effect of differing hydrophone sensitivities.

The five-cycle tone burst program was then used to excite the shaker at a frequency of 3000Hz and the travel time and amplitude of the received hydrophone signal recorded. This frequency was chosen so that the transmitted signal would have the same wavelength as that received by the geophone in the sand (assuming a speed of sound in the sand of 250m/s and a speed of sound in water of 1500m/s).

The hydrophone was then moved to another position and the received signal amplitude recorded. Further measurements were taken with hydrophone positions shown in Figure 5-8.

The complete experiment was repeated at 4500Hz. Measurements were also attempted at frequencies of 6000Hz, 7500Hz and 9000Hz, however at these higher frequencies, reflections from the tank sides caused interference due to the higher sound speed in the water.

b) S-Wave measurements

The shear wave measurements used the same five cycle tone burst technique described above for the P-wave experiments, except here the geophones themselves are used as the source.

The first of the horizontal component geophones was connected to the Brüel and Kjær power amplifier. Care must be taken when using the geophones as sources, not to apply too high an input voltage, which may cause damage to the geophone coils. The voltage was increase until a faint click could be heard from the geophones. The gain on the measuring amplifier was then altered to give as close to the 1Vpp signal in a similar manner to the P-wave experiments.

All five horizontal component geophones are used in turn as a source, as this gave more points from which to determine the S-wave velocity and attenuation.

c) Loudspeaker measurements

The loudspeaker source was suspended approximately 2m directly above the soil surface in order to satisfy the assumption of a normal incidence plane wave. It is believed that this configuration provides preferential excitation of the Type II P-wave as a consequence of the following argument.

The loudspeaker emits a dilatational sound wave that impinges on the surface of the sand. The sand surface is composed of pores filled with air and the sand grains. The air just above the surface induces motion of the air within the pores due to their similar inertial characteristics. The solid grains, however, have a much higher density and are deformed only slightly. Therefore, the deformation induced into the sand by the impinging sound wave is one in which the motion is primarily that of the fluid component.

The probe microphone experiments consisted of measurements of the attenuation and phase shift between two positions in the sand. The source-signal (MLS), data acquisition and post processing were done using the MLSSA system. Two receivers were required, the probe microphone (described in Section 5.1.1.1) and a reference microphone. This reference microphone was a Brüel and Kjær Type 4191 condenser microphone, using a Type 2645 preamplifier.

The MLS produced using the MLSSA system was amplified using an H&H S150 professional power amplifier and was broadcast from the loudspeaker. The outputs from

the receivers were amplified using a Brüel and Kjær Type 2160 Measuring amplifier before being sampled back into the MLSSA system. A bandwidth of 3kHz was used with the signals being sampled at 9kHz.

The experiment was set-up as shown in Figure 5-9. Firstly, the probe microphone support was placed on the sand. This consisted of a retort stand and a Brüel and Kjær microphone holder. A reference measurement was taken with the probe and reference microphone co-located at the surface. This measurement was taken to normalise the probe pressure to a unit reference microphone pressure, since several non-simultaneous measurements are made. This procedure also removes the characteristic response of the loudspeaker and microphones (Beranek, 1986)

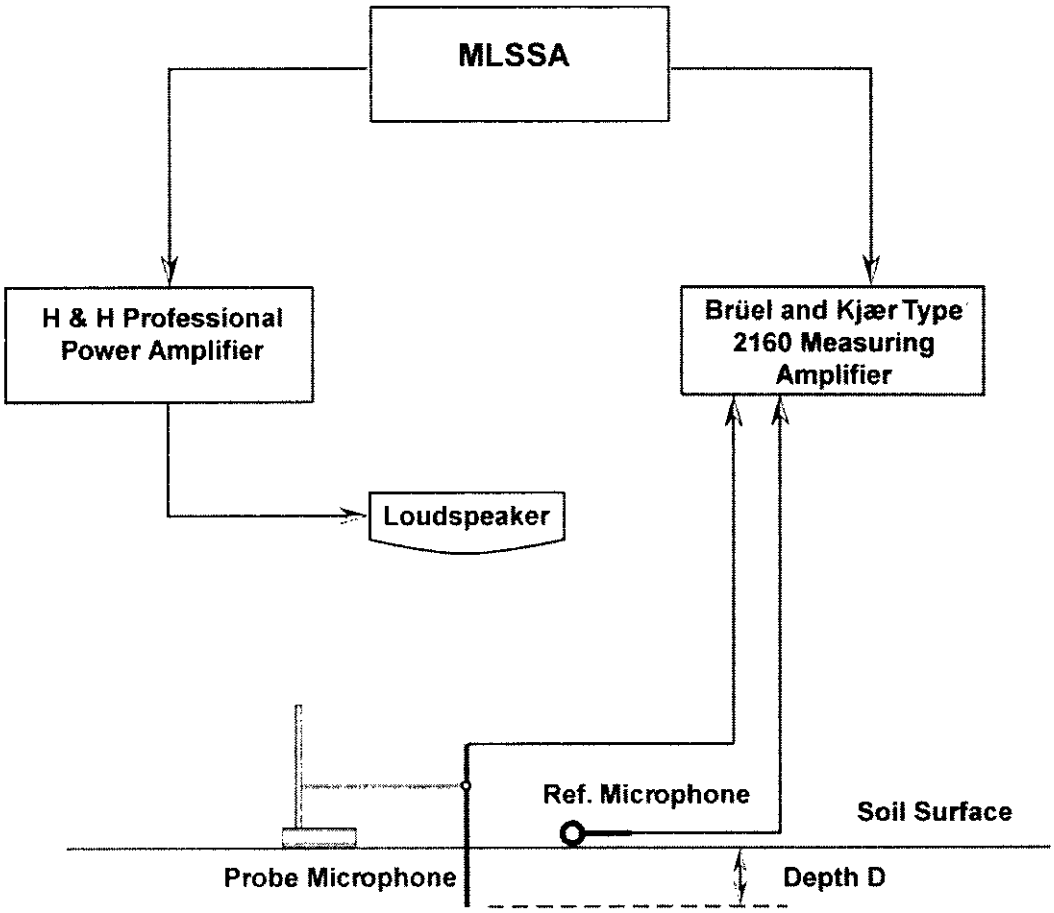

Figure 5-9. Experimental Set-up for probe microphone measurements.

The probe microphone was then placed in the microphone holder and gently inserted into the ground to a depth of 1cm. The reference microphone is left at the surface. Measurements were then taken to a depth of 30cm in 1cm steps. All time domain signals

were saved for subsequent analysis. A further set of data was taken at a different position in the tank (See Figure 5-2) to assess reproducibility.

The probe microphone measurements allow the calculation of tortuosity and effective flow resistivity through the use of real and imaginary components of the complex bulk propagation constant. The inversion process has been described in Chapter 3.

Attenuation and wave speed were also measured using the probe microphone and the loudspeaker in conjunction with the five cycle tone bursts to check the validity of the pulse transmission technique. The pulse technique was then used with the loudspeaker source and the in-situ geophones and microphones as receivers.

The data taken at NCPA was acquired using a swept sine signal. Measurements using the probe were taken every 0.5cm from a depth of 0.5cm to 7.5cm over a frequency range of 100Hz to 500Hz. The received signal was recorded and relative magnitude and phase difference data extracted using a digital oscilloscope.

5.1.2 Sensor Calibration

All sensors used throughout the project were calibrated. The calibrations were a mixture of "absolute calibrations" and "relative calibrations".

The terms "absolute calibration" and "relative calibration" are used to describe the degree of traceability of the particular calibration technique. In practice, all calibrations are relative to some established standard. In this report, we use the term "absolute calibration" to describe a technique which is traceable to something other than an identical sensor to the one being calibrated.

For example, geophone "*A*" and geophone "*B*" are exposed to the same sinusoidal vibration of peak displacement X_0 and frequency ω_0. A calibration of geophone "*A*" relative to "*B*" is done by noting the voltage output of "*A*" is e.g. 1.043 times the voltage output of geophone "*B*". Assuming "*B*" is known to have a sensitivity of 2.01 volts per *g*, the sensitivity of "*A*" is 1.043 times 2.01 or 2.096 volts per *g*. For what we would call an "absolute calibration" of either sensor "*A*" or "*B*", one could easily compute the maximum or RMS acceleration using the peak displacement X_0 and frequency ω_0. The peak acceleration is simply $(X_0\ \omega_0)^2$ m/s^2, so if sensor "*B*" generated 1volt peak where X_0 is

0.01m and ω_0=10rads/s the peak acceleration is 0.1mm/s^2 and the conversion to V/g or RMS values can be simply calculated.

The accuracy of the "absolute calibration" is tied to the precision of the value of peak displacement X_0 and frequency ω_0. These values can be far more accurate than the stability of the electronics from one sensor to the next.

5.1.2.1 Microphone Calibration

One of the oldest and most reliable devices for calibrating microphones is the pistonphone. A Brüel and Kjær Type 4228 pistonphone was used for the absolute calibration of the Brüel and Kjær microphones. The pistonphone has a rotating cam that drives a piston nearly sinusoidally, but with an exact displacement inside a small airtight cavity encompassing the microphone calibrated. The sound level produced by the pistonphone will vary with barometric pressure, and to a lesser degree, temperature and humidity. For the Brüel and Kjær pistonphone, if a microphone other than a Brüel and Kjær microphone is used, there is no guarantee that the sound levels generated will be in the specified range due to poor seals and a possible change in cavity volume.

The effect of barometric pressures on the acoustic pressure produced in the pistonphone can be seen by looking at how the pressure is produced. Starting with Boyle's law for ideal gases, it can be shown that for adiabatic conditions:

$$PV^{\gamma} = \text{Constant} \qquad \textit{(Eq. 5-9)}$$

where P is pressure, V is volume, γ is the ratio of specific heat at constant pressure to that at constant volume and is 1.402 for dry air at 0°C. For acoustic signals the small perturbations of pressure can be handled by taking the logarithm of equation 5.09 and examine the partial derivatives as seen in equation 5.10

$$\frac{\partial P}{P} + \gamma \frac{\partial V}{V} = 0 \qquad \textit{(Eq. 5-10)}$$

If we denote the acoustic pressure by $p=\partial P/\partial t$ and the acoustic volume velocity of the piston by $u=\partial V/\partial t$, then

$$p = -\gamma \frac{P}{V} u \qquad \textit{(Eq. 5-11)}$$

field" and "random-incidence" correction factors were ignored as all measurements for this project were well below the upper limit of the microphones used.

A similar method was used for calibration of the probe microphone. Again, a Brüel and Kjær microphone was placed 1.0m away from a loudspeaker and a reading taken. The probe microphone was then positioned in exactly the same position, ensuring that both microphones were subject to an identical sound field, and an another reading taken. The outputs of the two microphones were then compared using the Brüel and Kjær microphone as the reference.

Further measurements were taken with several of the air holes in the nose of the probe blocked.

5.1.2.2 Geophone Calibration

The calibration of the geophone sensors was carried out in order to gauge their sensitivity, to allow the conversion of their output (volts) to real world units (m/s) and to assess the bandwidth over which the sensor accurately reproduced vibration.

Anomalies and variations seen in outdoor experimental acoustic-to-seismic coupling ratio measurements led to an investigation into both the sensitivity and the reliability of the geophone sensors upon burial in the ground. To investigate all these parameters, two experiments were devised to test the amplitude and phase information of a vertical geophone over a selectable frequency range and the effect of geophone-ground coupling on these variables.

The first configuration used was a standard arrangement for geophone calibration (Figure 5-10), whilst the second configuration allowed the geophone ground coupling to be investigated (Figure 5-11).

In the first experiment, the geophone under investigation was bolted directly to the shaker. The shaker used was a Ling Dynamics Model 403. A TT*i* TGA1230 arbitrary wave generator was used to supply the input signal, which was in the form of a sine wave. The frequency of the sine wave was swept from 10Hz to 1000Hz in 10Hz steps. The amplitude of the sine wave was set by monitoring the RMS output from the Dantec Laser Doppler Vibrometer (LDV) on a Brüel & Kjær 2610 Measuring Amplifier, ensuring that there was always a constant velocity output of 0.63mm/s.

which clearly shows a negative change in volume causing a positive increase in pressure. Given a controlled cavity volume V and piston displacement u, the only variables in equation 5.11 are the barometric pressure and specific heat ratio.

Humidity and temperature changes have a nearly negligible effect on the generated pressure when compared to the effect of barometric pressure on the resulting sound level. The most significant changes on barometric pressure can be attributed to altitude when the pistonphone is used in various locations. Therefore, it was imperative to always note the barometric pressure so that corrections to the pistonphone sound level could be made.

The Brüel and Kjær pistonphone is designed to produce 124dB at sea level (1013mbars barometric pressure), the dB correction for the pistonphone output at a barometric pressure P_0 (measured in mbars) is

$$\Delta L_p = 20Log_{10}\frac{P_0}{1013}dB \qquad (Eq.\ 5\text{-}12)$$

The correction in equation 5.12 is the major correction for absolute pistonphone calibration.

The microphone cartridge under test was first connected to a Brüel and Kjær Type 2160 measuring amplifier. To facilitate direct reading of measured sound, vibration and voltage levels, the meter is supplied with interchangeable scales. Scales for sound measurements have a linear 30dB SPL range for reading of sound pressure level. The microphone was inserted into the pistonphone, which was then turned on and the sound pressure level measured on the amplifier.

The pistonphone has an output of 124dB and all the microphone cartridges tested gave a reading of 124$\pm$1dB. Once the absolute calibration of the Brüel and Kjær microphone had been undertaken, the remaining non- Brüel and Kjær microphones were calibrated.

This was achieved using the MLSSA system in the acoustic research group anechoic chamber at Silsoe. First, a Brüel and Kjær microphone was placed 1.0m away from a loudspeaker and a reading taken. The microphone to be calibrated was then positioned in exactly the same position, ensuring that both microphones were subject to an identical sound field, and an another reading taken. The outputs of the two microphones were then compared using the Brüel and Kjær microphone as the reference.

Additional correction factors which affect a microphone's response at very high frequencies (where the wavelength is smaller than the microphone aperture), such as "free-

field" and "random-incidence" correction factors were ignored as all measurements for this project were well below the upper limit of the microphones used.

A similar method was used for calibration of the probe microphone. Again, a Brüel and Kjær microphone was placed 1.0m away from a loudspeaker and a reading taken. The probe microphone was then positioned in exactly the same position, ensuring that both microphones were subject to an identical sound field, and an another reading taken. The outputs of the two microphones were then compared using the Brüel and Kjær microphone as the reference.

Further measurements were taken with several of the air holes in the nose of the probe blocked.

5.1.2.2 Geophone Calibration

The calibration of the geophone sensors was carried out in order to gauge their sensitivity, to allow the conversion of their output (volts) to real world units (m/s) and to assess the bandwidth over which the sensor accurately reproduced vibration.

Anomalies and variations seen in outdoor experimental acoustic-to-seismic coupling ratio measurements led to an investigation into both the sensitivity and the reliability of the geophone sensors upon burial in the ground. To investigate all these parameters, two experiments were devised to test the amplitude and phase information of a vertical geophone over a selectable frequency range and the effect of geophone-ground coupling on these variables.

The first configuration used was a standard arrangement for geophone calibration (Figure 5-10), whilst the second configuration allowed the geophone ground coupling to be investigated (Figure 5-11).

In the first experiment, the geophone under investigation was bolted directly to the shaker. The shaker used was a Ling Dynamics Model 403. A TT*i* TGA1230 arbitrary wave generator was used to supply the input signal, which was in the form of a sine wave. The frequency of the sine wave was swept from 10Hz to 1000Hz in 10Hz steps. The amplitude of the sine wave was set by monitoring the RMS output from the Dantec Laser Doppler Vibrometer (LDV) on a Brüel & Kjær 2610 Measuring Amplifier, ensuring that there was always a constant velocity output of 0.63mm/s.

The outputs from the geophone and Laser Doppler Vibrometer were sampled on an IBM compatible PC using a National Instruments E-Series AT-MIO-16E-2 acquisition board in conjunction with a SC-2040 add-on board.

The SC-2040 analogue input circuitry consists of eight channels with DIP-switch-programmable instrumentation amplifiers followed by buffered track-and-hold amplifiers. The instrumentation amplifiers fulfil two purposes. Firstly, they convert the differential input signals into single-ended signals referred to the SC-2040 analogue ground for input common-mode signal rejection. Secondly, they amplify input signals, resulting in an increase in measurement resolution and accuracy.

Gains for each channel can be selected independently with the separate DIP switches. Gains of 1, 10, 100, 200, 300, 500, 600, 700 and 800 can be used.

The track and hold amplifiers operate as simple buffers when in track mode, but freeze their outputs when placed into hold mode. Because all the track-and-hold amplifiers in each SC-2040 board enter hold mode at the same time, they implement simultaneous sampling of all channels. The simultaneous sampling is useful in preserving phase relations between channels.

The signals were analysed using Labview software. The program allowed the amplitude and phase of the geophone to be plotted at discrete frequencies, using the LDV output as a reference (See Figure 5-12). Averaging was employed to increase the signal-to-noise ratio of the measurements. A software bandpass filter was also used to reduce the effect of building vibration and higher frequencies.

In order to protect the equipment from unwanted background vibrations, experiments were conducted in an anechoic chamber with the experimental equipment placed on anti-vibration optical tables (AVOT's). One AVOT supports the shaker, whilst a second AVOT is used to support the Laser Doppler Vibrometer. Background noise was measured at 0.03mm/s and at predominately 7-8Hz. All instruments were controlled from outside the anechoic chamber. The shaker was shielded to reduce any magnetic fields and the measurement system was completed isolated from the drive system to minimise noise from ground loops.

The second experiment is similar to the first, except that a cylindrical metal box was bolted to the shaker; sand was placed in the box, and a geophone inserted in the sand. The shaker was then excited over a frequency range of 10Hz to 600Hz in 10Hz steps.

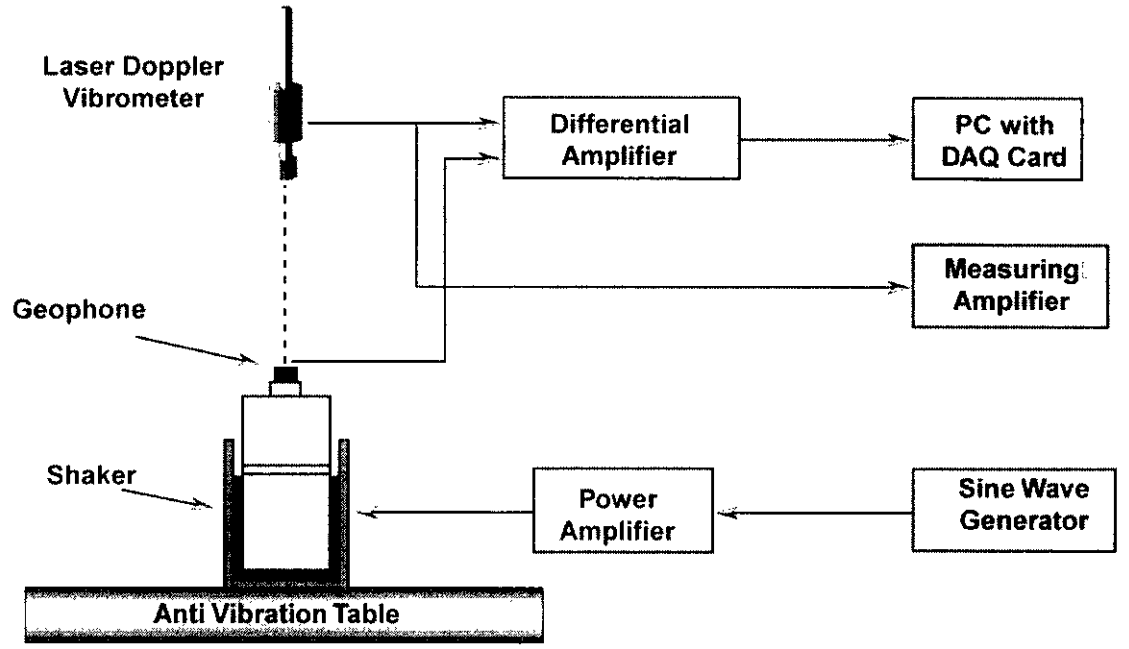

Figure 5-10. Instrumentation configuration for standard geophone calibration.

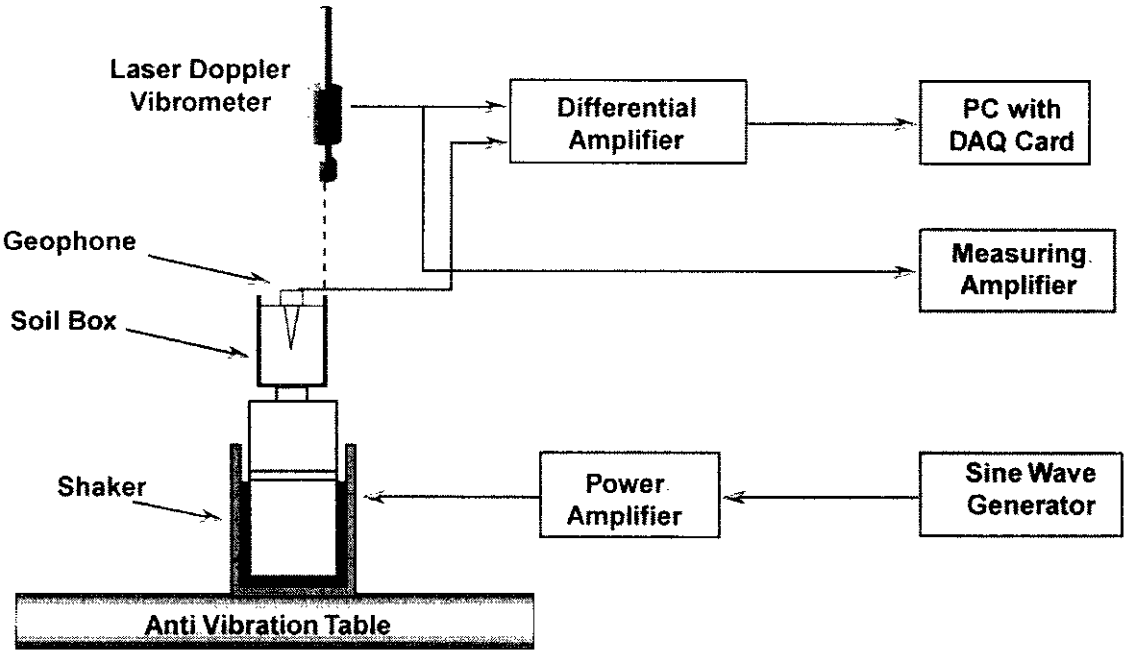

Figure 5-11. Instrumentation configuration for investigating geophone-ground coupling.

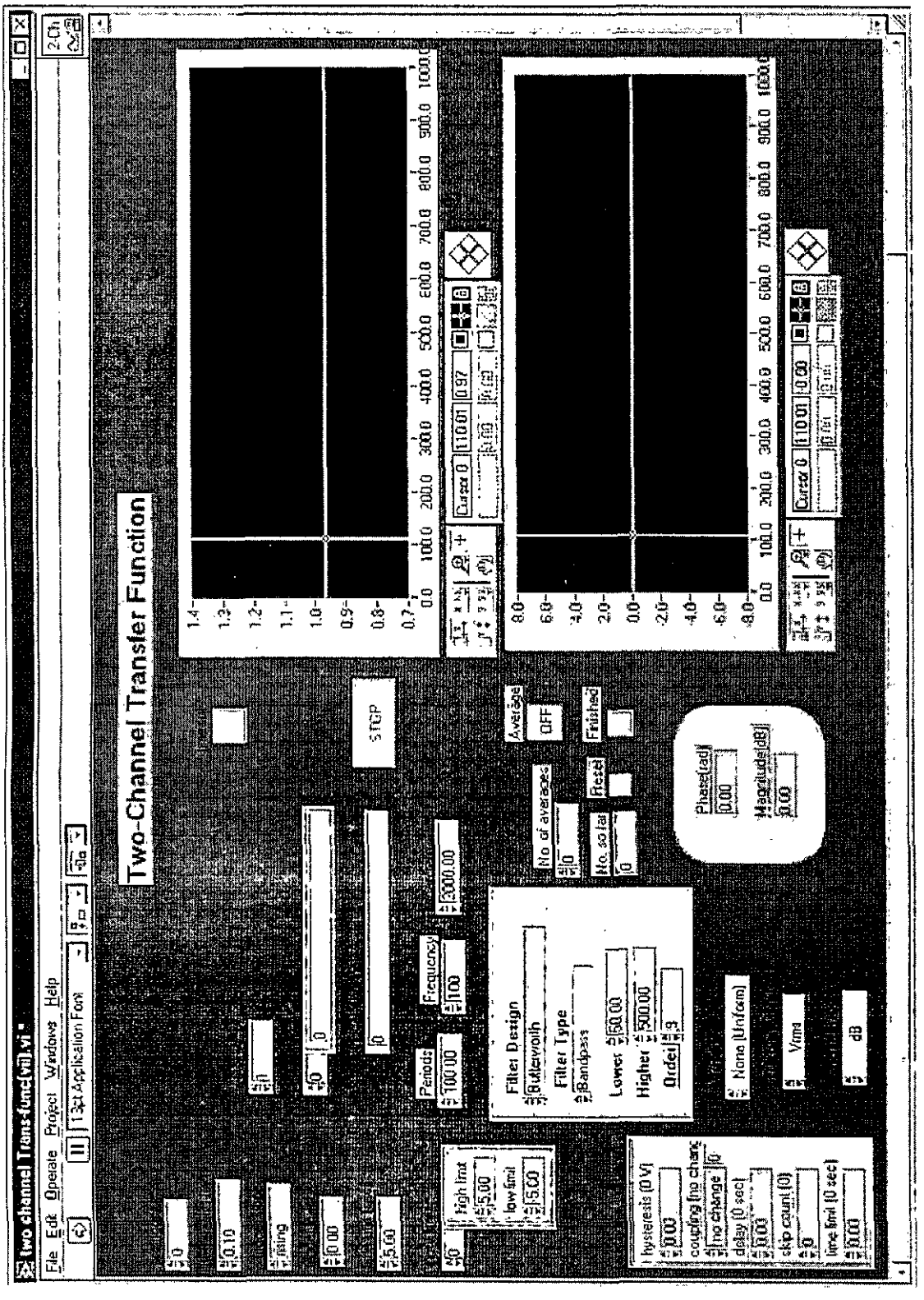

Figure 5-12. Two-channel transfer function determination for geophone calibration

5.1.3 The Use of a Laser Doppler Vibrometer in Acoustic-to-Seismic Coupling Measurements

The Laser Doppler Vibrometer (LDV) is a non-contact optical system for measuring the instantaneous velocity of moving surfaces. The system has a linear transfer function, and a real-time digital and analogue output proportional to velocity, which can be further analysed to give either displacement or acceleration information.

The LDV system used was a Dantec model 55x laser vibrometer. The system consists of a Uniphase Model 1125P laser, a Type 55N11 Frequency Shifter and a Type 55N21 Tracker. The laser is a single transverse mode, multi-longitudinal mode helium-neon laser, whose general specifications can be seen in Table 5-2.

Minimum output power(mW. TEM_{00},633nm)	10.0
Beam diameter(mm. TEM_{00}, $1/e^2$ points $\pm$3%)	0.81
Beam Divergence(mrad, TEM_{00}, $\pm$ 3%)	1.0
Min Polarisation ratio(P version)	500:1
Longitudinal mode spacing(MHz)	435

Table 5-2. Laser Specifications - Uniphase Model 1125P.

5.1.3.1 Principle of Operation

The laser beam is split into two beams, a reference beam and a measuring beam, which undergoes an optical frequency shift of 40MHz using a Bragg Cell.

A Doppler frequency shift (equation 5-13) is superimposed on the measuring beam by the velocity component of the measuring surface relative to the vibrometer's optical axis. The backscattered light is collected by the front lens and recombined with the reference beam. The combined beams are focused onto the optical detectors, which reproduce the Doppler signal shifted up by 40MHz, e.g.

For large vibrational Velocities (1.5m/s)
- Doppler signal is +/- 4.5MHz
- Detector output is from 40MHz +/- 4.5MHz

For small vibrational Velocities (10e-6m/s)
- Doppler signal is +/- 3Hz
- Detector output is from 40MHz +/- 3Hz

$$f = (2/\lambda)\sin(\theta/2)v = 2v/\lambda \qquad \text{(Eq. 5-13)}$$

where f = the Doppler frequency shift

λ = the laser beam wavelength(633nm)

θ = the angle between incoming and scattered beams (=180°)

v = velocity relative to the vibrometer's optical axis

The detector output is mixed with the 40MHz Bragg cell signal to produce sum and difference signals, the difference being the Doppler shift. For a vibrating object, the detector output will vary above and below 40MHz. For example 40MHz +/- 4.5Mhz for 1.5m/s velocity. The difference signal cannot discriminate between 35.5MHz and 44.5MHz; both will give a difference of 4.5MHz. In order to discriminate between the two and provide directional information, the detector output signal is electronically shifted up before being mixed with the 40MHz signal to produce the Doppler frequency. The size of the shift depends on the sensitivity range in use.

The Doppler frequency is fed into the frequency tracker which provides an analogue output of 1 to 10V proportional to the measuring surface velocity in each of the 7 ranges (only 6 of which are available to the LDV).

The working distance depends on the bandwidth and reflectivity of the measuring surface but the standard lens permits measurement between 1.2 and 20m. The LDV can measure vibration over a wide range of amplitudes in the frequency range from DC to 740KHz and has a dynamic range from 10^{-8} m/s to 1.5m/s for vibrational motion and from 10^{-8} m/s to 1.5m/s for translational motion.

5.1.3.2 Method of Operation

With the laser beam aimed at the measuring point, the beam is focussed using the focus ring. This can be attained by either viewing the focal spot through an attenuation filter or by making use of the speckle pattern which is composed of four small dots whose size is inversely proportional to the size of the focal spot. Once the beam has been focussed using this method, fine focussing can be achieved by observing the MONITOR OUT signal from the Doppler frequency tracker. At focus a clear 40 MHz square wave should be observed.

It is desirable that the probe beam samples a single speckle on diffusely reflecting surfaces. To improve heterodyne detection efficiency, the distance from the end of the LDV to the object should be an integral number of laser cavity lengths. When this length criteria is met, maximum coherence occurs between the reference and probe laser beams. If a poor signal-to-noise ratio is obtained it may be due to the LDV-to-object distance being midway between two integral cavity lengths. This can be checked by again observing the MONITOR OUT signal on an oscilloscope whilst varying the working distance through one half of a laser cavity laser length.

Several factors can influence the quality of the LDV output. Firstly, any movement of the LDV itself will translate to an overestimation of the velocity of the sample under test, since the optical path length changes between the reflecting surface and the photodiode inside the LDV unit. Induced motion in the LDV can be from background building vibration, or especially in acoustic-to-seismic coupling measurements, motion can be induced through acoustic pressure from the loudspeaker.

The acoustic pressure wave imparts a force on the LDV equal to the product of its mass and acceleration. Thus to minimise LDV motion, the LDV should be massive and rigid. It is important that the LDV is kept stationary, since the impedance of the LDV and its supports should be much greater than the same product for the ground so that the LDV response to atmospheric sound is much less than that of the ground.

As part of the experiments therefore, the LDV was firmly bolted to a high-speed camera stand. The stand was designed so that the laser could easily be moved vertically and horizontally, whilst still keeping its axis vertical and perpendicular to the material under test. The camera stand was placed upon an anti-vibration optical table to reduce the effect of building vibration.

The table used was an Ealing Electro-Optics Micro-g Series 62 Post Isolator System. The system consists of a stand onto which an aluminium plate breadboard was placed. Each stand is constructed of four heavy-duty steel vertical posts of 100mm square section. The support posts are fitted with pneumatic isolator units that provide the vibration isolation. A compressed air line with pressure of about 80psi was required to operate the system.

In addition, the maximum velocity amplitudes of the ground motion in the study were approximately 200μm/s over the frequency range of interest. The lowest velocity amplitude that the LDV can accurately measure is 1μm/s. It is proposed to resolve 5-

10μm/s in the measurements. Although the ground vibrations being measured are within the useful range of the LDV, all extraneous signals need to be kept to a minimum.

Secondly, it is important that sufficient reflected light reaches the photodetector. This can be enhanced by treating the surface under investigation with reflecting paint or using reflective tape.

5.1.3.3 Electronics

To begin using the laser the range on the Doppler frequency range on the tracker needs to be set to the mid range (0.1-1MHz or 33-333KHz). The range selected is indicated an LED on the tracker. If the frequency and amplitude of vibration are known then the velocity can be calculated and the optimum tracker range can be selected.

Doppler Frequency Range	Vibration Frequency Range	Calibration Factor mV/mm/s	Calibration Factor m/s/Volt
1.0 to 10.0 MHz	740 kHz	3.16	316.4 x 10-3
0.3 to 3.33 MHz	240 kHz	9.62	104.0x 10-3
0.1 to 1.00 MHz	74 kHz	31.6	31.64 x 10-3
33 to 333 kHz	24 kHz	96.2	10.40 x 10-3
10 to 100 kHz	7.4 kHz	316	3.164 x 10-3
3.0 to 33 kHz	2.4kHz	962	1.040 x 10-3

Table 5-3. Laser Doppler Vibrometer frequency ranges and calibration factors.

Using the frequency shift selector and the multiplier switch on the Frequency Shifter, the frequency shift is adjusted to the middle of the Doppler frequency range. For vibrational measurement, the multiplier can be turned in either direction. When the Doppler frequency is within the tracker range the green lock detector LED will be illuminated and the analogue output will be continuous.

If the tracker is out of range then the analogue output will be interspersed with straight lines where the tracker is at zero or full scale and the lock detector LED will flicker. Translational motion can also be measured but because the velocity is in one direction only, the sensitivity of each range is effectively doubled. For frequencies greater than 40 MHz (when the measuring surface moves towards the LDV) turn the multiplier clockwise. Similarly for frequencies, less than 40MHz turn the multiplier anticlockwise.

Instead of adjusting the frequency shift to the middle of the Tracker range, it should be adjusted to the lower end to make use of the full Tracker range.

Finally, the gain should be set to a minimum required to obtain a clear square wave. The red level indicator LED on the Tracker flashes when the gain is properly adjusted.

5.1.3.4 Measurements Using the LDV

A series of experiments were undertaken using an LDV to assess its suitability for the measurement of induced ground vibration as part of acoustic-to-seismic coupling investigations. LDV's have several advantages over more conventional vibration sensors, such as geophones, in that they have a flat amplitude and phase response and are non-invasive.

The experiments undertaken were designed to show the precision and reliability of vertical ground motion measured using an LDV. In the study, ground motion was excited with atmospheric acoustic sound with a continuous wave speaker source. Vertical particle velocities were measured with geophones and compared with the LDV system. Measurements were taken in an anechoic chamber.

The test materials used included the Indoor Tank sand, which was used in the soil tray, and the HMC Stone Lane sand that was used in the coupling experiments (See Chapter 4 for details).

The experimental configuration for the measurements can be seen in Figure 5-13.

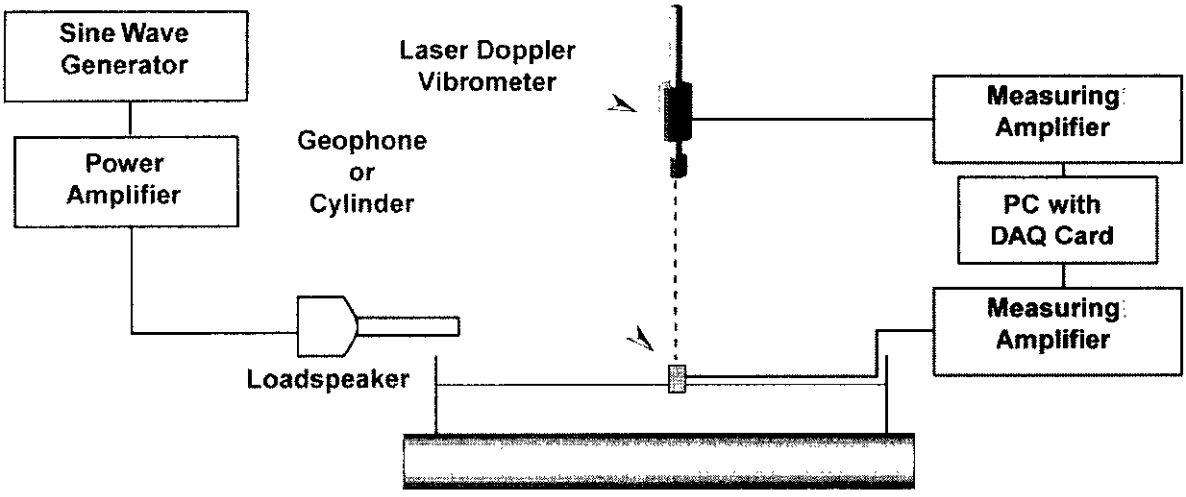

Figure 5-13. Instrumentation configuration for the LDV assessment measurements.

A TT*i* TGA1230 arbitrary wave generator was used to supply the input signal, which was in the form of a sine wave. The output was amplified using an H&H S150 professional power amplifier and was then broadcast using a 30W Tannoy loudspeaker. A 1m brass tube, 0.017m in diameter, was attached to the driver in an attempt to approximate the speaker to a point source. The frequency of the sine wave was swept from 100Hz to 750Hz in 20Hz steps.

Vertical particle velocities were measured using Mark Products L-40A-2, 100Hz, uncased geophones and a Dantec LDV system. Outputs from the sensors were amplified separately prior to recording, using Brüel and Kjær Type 2160 measuring amplifiers. The signals were recorded on an IBM compatible PC using a National Instruments E-Series AT-MIO-16E-2 I/O acquisition board controlled using a purpose written Labview program.

The program allowed the time domain output and resultant frequency spectrum of either sensor to be viewed and can be seen in Figure 5-14. Averaging was employed to increase the signal-to-noise ratio of the measurements. A software bandpass filter was also used to reduce the effect of low frequency building vibration and higher frequencies.

To evaluate the LDV system, the laser beam was focussed onto a geophone, positioned at the sand surface. To enhance laser reflection back to the photodetector, a piece of 3M reflective tape was applied to the geophone surface. Measurements of the response of the geophone and laser to a series of pure tones produced by the loudspeaker were made.

With the apparatus set-up and the laser reflecting at the geophone surface, a 100Hz tone was broadcast from the loudspeaker. The received signal from the geophone was then amplified and sampled on the PC. The time domain signal was transformed into the frequency domain using a Fast Fourier Transform and the peak frequency amplitude noted. Averaging was employed to enhance the signal-to-noise ratio.

The output from the laser was then viewed and again the peak frequency amplitude noted. The frequency was then increased by 20Hz and the procedure repeated, noting the peak frequency amplitude of the laser and geophone in further 20Hz steps up to 750Hz.

All measurements were repeated with a similar L-40A-2 geophone to test reproducibility. To compare the sensor outputs, they were both converted into particle velocities (m/s), having first corrected to remove the effect of the gain used on the amplifiers.

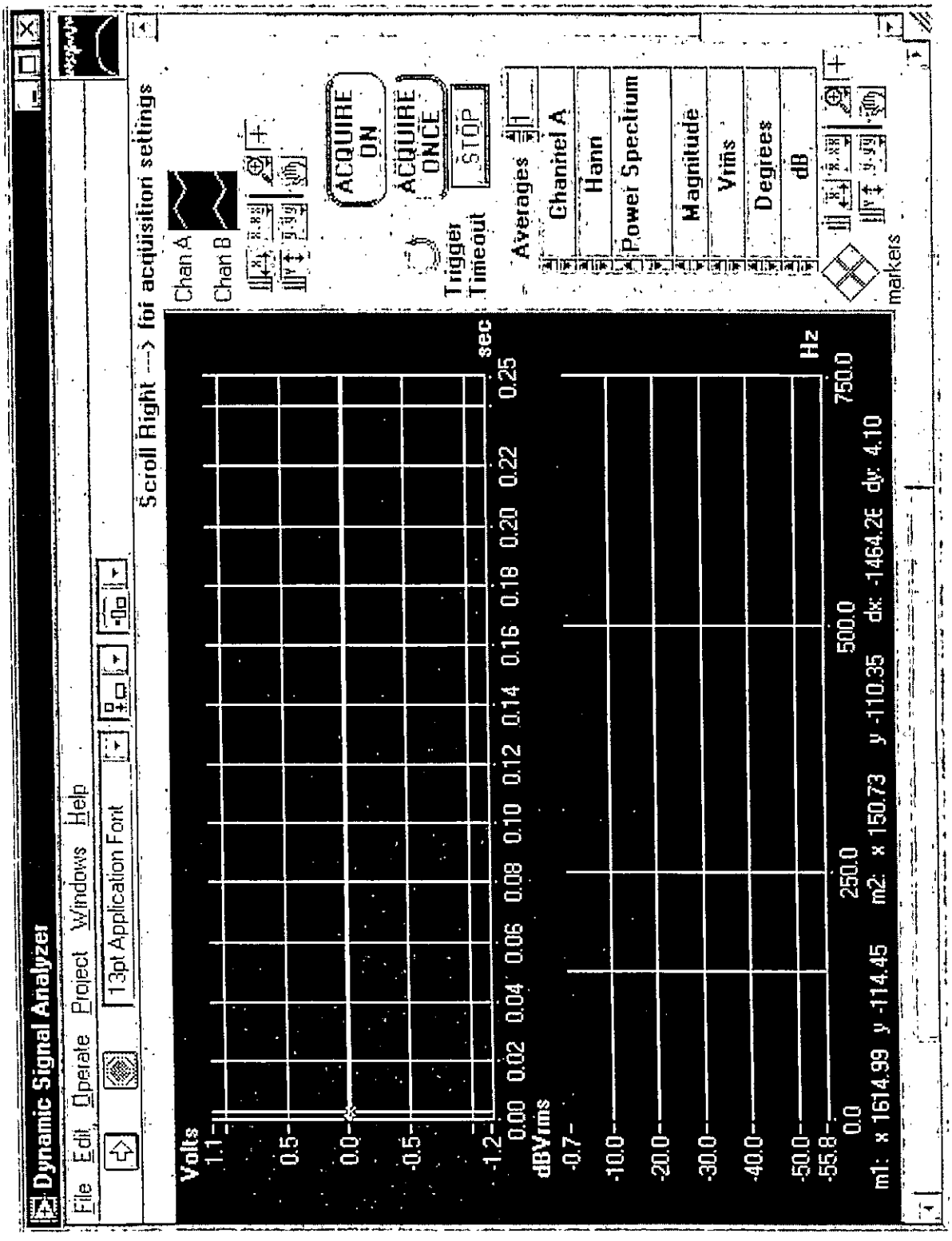

Figure 5-14. Dynamic spectrum analyser used for the LDV experiments.

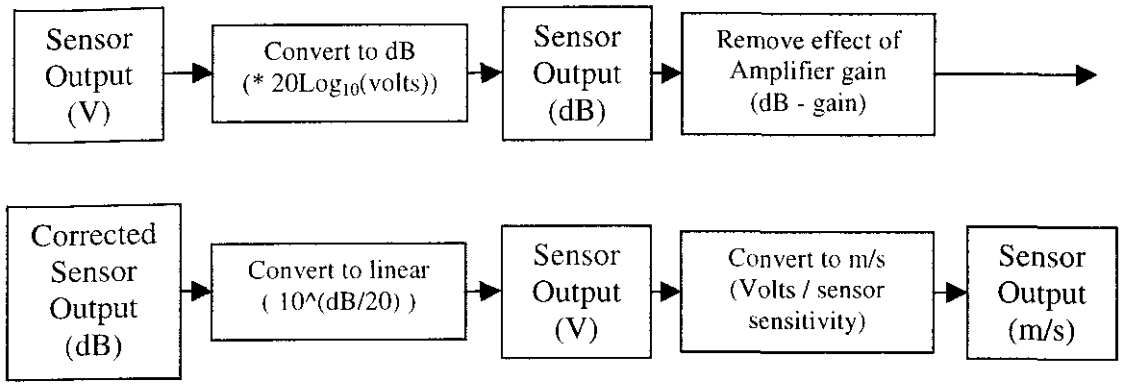

Figure 5-15. Conversion of the sensor output from volts to m/s. The conversion removes the effect of any intermediate amplifiers and the sensitivity of the sensor used.

The laser was then moved to a point approximately 0.05m away from the geophone and the response to pure tones noted. It was immediately noticeable that due to the nature of the sand, that it was very difficult to focus the laser (it became very problematical for the laser to attain an adequate lock).

To overcome the difficulty of obtaining sufficient back reflection from the sand to the photodetector, a cylinder with a flat top covered with reflecting tape was pushed into the sand. The laser beam was then reflected off the cylinder instead of the sand surface. The cylinder was manufactured from acrylic. This material was chosen as the most available material with a density close to that of the sand.

Three differing cylinders were made each having a different internal diameter. The dimensions of the three cylinders can be seen in Table 5-4.

Cylinder	**Dimensions (Height x Diameter)**
Cylinder 1	26.3mm x 48.5mm
Cylinder 2	24.8mm x 27.1mm
Cylinder 3	23.2mm x 12.1mm

Table 5-4. Internal diameters of the test cylinders.

In order to assess the effect of the cylinder, the geophone was positioned at the sand surface and the response to the continuous wave over the range 100Hz to 750Hz was noted. Cylinder 1 was then pushed into the sand surface and the geophone firmly attached to the top surface using double-sided tape. The experiment was then repeated, noting the

peak frequency amplitude for each test frequency. Repeat measurements were then undertaken using Cylinders' 2 and 3.

Comparisons of the three cylinder tests with the original geophone measurements indicated that Cylinder 3 showed the least effect upon the received signal. Once this had been ascertained, a further set of measurements was undertaken where the laser beam was focussed onto the cylinder top (onto which reflecting tape had been placed) and the response to the pure tones recorded.

Finally, an experiment similar to that described in Section 5.1.2.2 – Geophone Calibration, was undertaken to assess if any ground cylinder coupling was occurring. The apparatus was set-up as described Section 5.1.2.2. A TT*i* TGA1230 arbitrary wave generator was used to supply the input signal, which was in the form of a sine wave. The laser was focussed onto the soil box. The amplitude of the sine wave was set by monitoring the RMS output from the Dantec Laser Doppler Vibrometer (LDV) on a Brüel & Kjær 2610 Measuring Amplifier, ensuring that there was always a constant velocity output of 0.26mm/s.

Cylinder 3 was pushed into the sand and the laser beam focussed upon the top using the horizontal adjustment feature of the high-speed camera stand. The output from the laser was amplified using a Brüel and Kjær Type 2160 measuring amplifier and sampled on the PC using the same program described previously (Figure 5-14). The time domain signal was then transformed into the frequency domain and the peak frequency amplitude noted. Averaging was employed to enhance the signal-to-noise ratio.

The frequency of the sine wave was swept from 100Hz to 1000Hz in 25Hz steps with the peak frequency amplitude noted at each frequency. Since the laser was used as both the reference and vibration sensor, only amplitude measurements were taken.

peak frequency amplitude for each test frequency. Repeat measurements were then undertaken using Cylinders' 2 and 3.

Comparisons of the three cylinder tests with the original geophone measurements indicated that Cylinder 3 showed the least effect upon the received signal. Once this had been ascertained, a further set of measurements was undertaken where the laser beam was focussed onto the cylinder top (onto which reflecting tape had been placed) and the response to the pure tones recorded.

Finally, an experiment similar to that described in Section 5.1.2.2 – Geophone Calibration, was undertaken to assess if any ground cylinder coupling was occurring. The apparatus was set-up as described Section 5.1.2.2. A TT*i* TGA1230 arbitrary wave generator was used to supply the input signal, which was in the form of a sine wave. The laser was focussed onto the soil box. The amplitude of the sine wave was set by monitoring the RMS output from the Dantec Laser Doppler Vibrometer (LDV) on a Brüel & Kjær 2610 Measuring Amplifier, ensuring that there was always a constant velocity output of 0.26mm/s.

Cylinder 3 was pushed into the sand and the laser beam focussed upon the top using the horizontal adjustment feature of the high-speed camera stand. The output from the laser was amplified using a Brüel and Kjær Type 2160 measuring amplifier and sampled on the PC using the same program described previously (Figure 5-14). The time domain signal was then transformed into the frequency domain and the peak frequency amplitude noted. Averaging was employed to enhance the signal-to-noise ratio.

The frequency of the sine wave was swept from 100Hz to 1000Hz in 25Hz steps with the peak frequency amplitude noted at each frequency. Since the laser was used as both the reference and vibration sensor, only amplitude measurements were taken.

Chapter 6

Results and Analysis of Indoor Experiments

6 Indoor Experiments

6.1 Soil Tank

6.1.1 Loudspeaker Measurements

Loudspeaker measurements were undertaken in conjunction with a probe microphone, as it is believed that for this source the measured signal would be associated with the type II P-wave as outlined in Chapter 5. Measurements were taken at two positions in the tank to assess repeatability and the homogeneity of the tank material. Hence, the measurements can be inverted for tortuosity and flow resistivity using the rigid frame theory outlined in Chapter 4.

Probe microphone measurements were obtained in the soil tank at 1cm intervals down to a depth of 30cm over a frequency range of 1.5KHz using an MLS output signal. The results from one of the measurement positions have been given in the text, whilst the results from the second can be found in Appendix C.

The relative magnitude and phase difference between the sound pressure level measured by a reference microphone positioned at the soil surface and the sound pressure level measured by the probe microphone, at 2cm intervals down to 25cm are shown in Figure 6-1 and Figure 6-2. Figure 6-1 shows that the magnitude of the probe microphone signal decreases systematically with depth until approximately 15cm after which there is a decrease in the amount by which the magnitude drops. The phase of the probe microphone signal, as shown in Figure 6-2, appears to decrease systematically at the same rate over the whole depth range. It is noticeable that the change in both the magnitude and phase change per unit depth increases with increasing frequency.

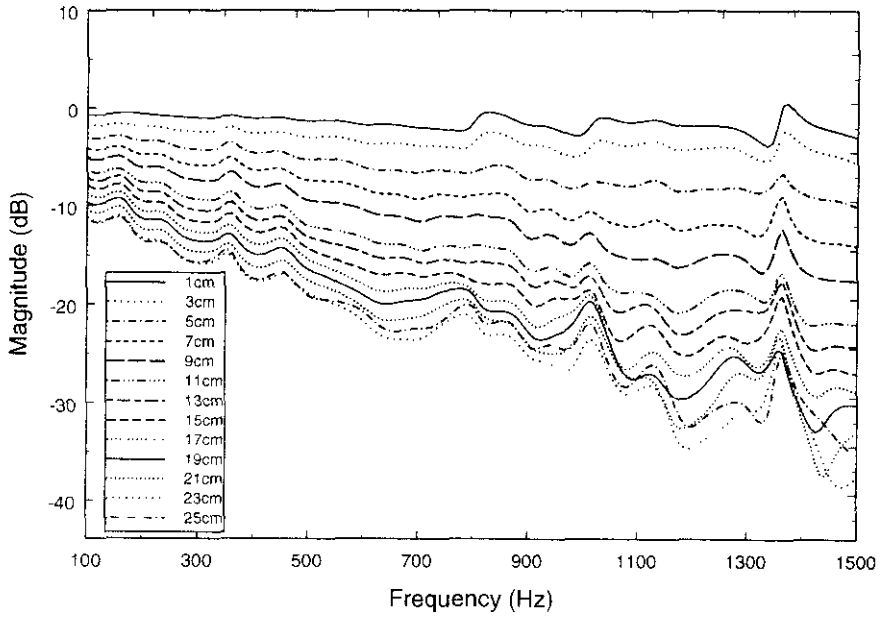

Figure 6-1. Measured relative magnitude between the probe microphone at various depths and a reference microphone situated at the sand surface.

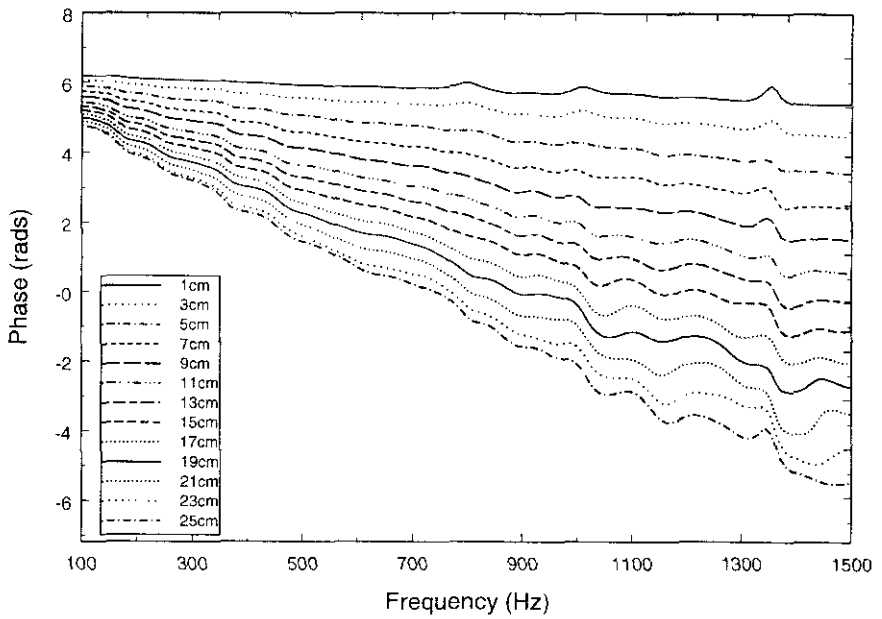

Figure 6-2. Measured phase difference between the probe microphone at various depths and a reference microphone situated at the sand surface.

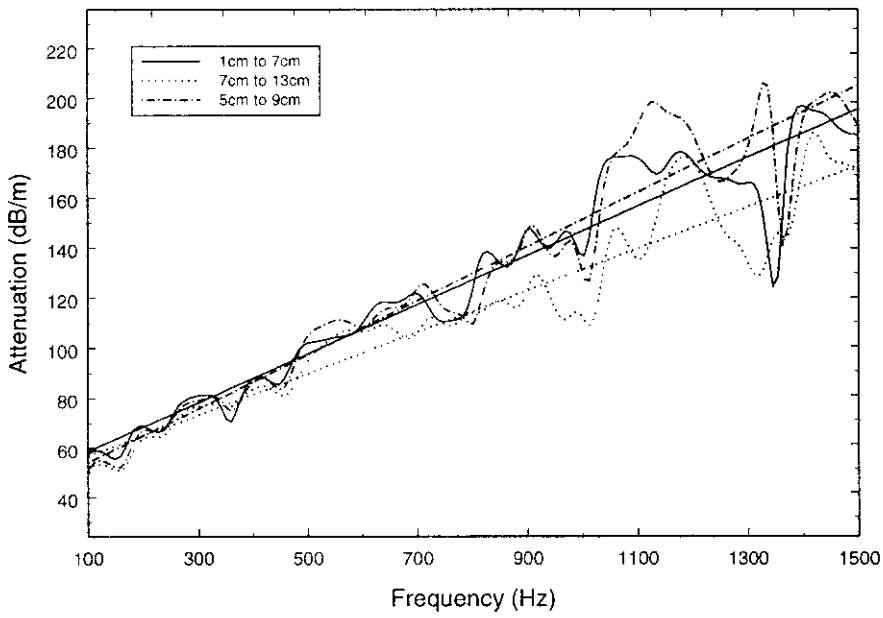

Figure 6-3. Calculated attenuation using the data in Figure 6-1 over three different depth intervals. Best-fit regression has been applied to the data.

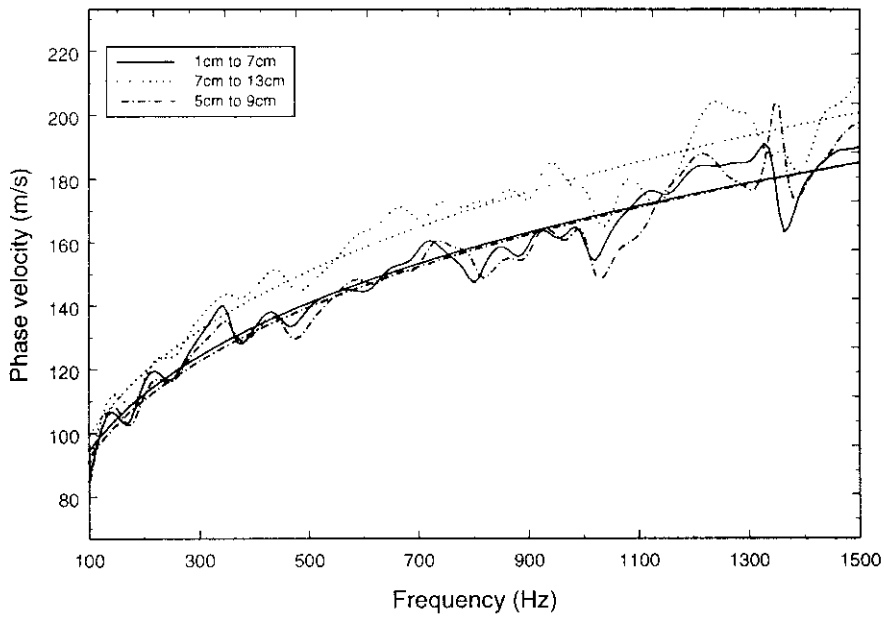

Figure 6-4. Calculated phase velocity using the data in Figure 6-2 over three different depth intervals. Best-fit regression has been applied to the data.

It can be seen from the plots that there are fluctuations in the data, especially at higher frequencies. These may be attributed to resonances in the container or the laboratory. However, these fluctuations in the signal have also been observed in outdoor measurements (See Chapter 8). This suggests that these fluctuations are not solely a consequence of performing this experiment indoors on a sample of finite size. The results suggest that the attenuation remains reasonably constant as a function of depth down to roughly 10-15cm, after which there is a decrease in the attenuation and that the phase speed increases with increasing frequency over the whole depth range. This indicates that down to a depth of approximately 15cm the Type II P-wave is predominant. There is then a zone of integration between the Type I and Type II waves.

However, the slight change in magnitude may be due to small scale layering in the tank that affects the magnitude and not the phase of the signal, which would indicate that the type II wave is present to much greater depths.

Calculations of attenuation and phase speed over the depth intervals of 1cm to 7cm, 7cm to 13cm and 5cm to 9cm are shown in Figure 6-3 and Figure 6-4 respectively. Best-fit regressions have been superimposed on the data. The values of attenuation (dB/m) calculated over three depth intervals and for frequencies of 500Hz, 750Hz, 1000Hz, 1250Hz and 1500Hz can be found in Table 6-1. The corresponding phase velocities can be found in Table 6-2.

	Depth Interval	**Frequency**				
		500Hz	**750Hz**	**1000Hz**	**1250Hz**	**1500Hz**
Position A	**1cm to 7cm**	98.0	122.5	147.0	171.6	196.1
	7cm to 13cm	89.7	110.3	130.9	151.6	172.2
	5cm to 9cm	97.2	124.1	151.1	178.0	204.9
Position B	**1cm to 7cm**	123.5	159.3	195.1	230.9	266.7
	7cm to 13cm	61.4	71.9	82.4	92.9	103.4
	5cm to 9cm	98.6	121.3	144.0	166.7	189.4

Table 6-1. Attenuation (dB/m) calculated from the data collected (Figure 6-1) with the probe microphone.

	Depth Interval	Frequency				
		500Hz	750Hz	1000Hz	1250Hz	1500Hz
Position A	**1cm to 7cm**	141.0	156.0	167.6	177.1	185.4
	7cm to 13cm	151.1	167.9	180.9	191.7	200.9
	5cm to 9cm	139.8	155.1	166.9	176.8	185.2
Position B	**1cm to 7cm**	114.0	128.9	138.7	147.7	155.5
	7cm to 13cm	202.8	209.3	220.0	217.7	220.8
	5cm to 9cm	127.2	142.9	155.2	164.5	174.4

Table 6-2. Phase velocity (m/s) calculated from the data collected (Figure 6-2) with the probe microphone.

Calculations of the attenuation and phase velocity were made from measurements of the real and imaginary parts of the bulk propagation constant ($Re(k_b)$ and $Im(k_b)$) as outlined in Section 3.1.1 of Chapter 3. Using these functions and using the theory outlined in Section 3.1 of the same chapter, it is possible to calculate the tortuosity (τ) and the flow resistivity (R_s). The constants required for the calculations can be found in Table 6-3.

Figure 6-5 shows the calculated flow resistivity for the three depth intervals, whilst Figure 6-6 shows the calculated tortuosity It appears from the plots that there is a frequency dependence to both parameters, with the flow resistivity increasing with increasing frequency and the tortuosity decreasing with increasing frequency. However, both these trends maybe suspect as this trend is not seen in the results gained in the loam soil measurements taken at NCPA, nor has it been reported elsewhere.

Parameter	Symbol	Value	Unit
Tortuosity	τ	--	--
Flow resistivity	R_s	--	
Adiabatic sound speed	C_o	343	m/s
Ratio of specific heats	γ	1.402	--
Density of air	P_0	1.21	kg/m^3
Prandtl Number	N_{pr}	0.75	--

Table 6-3. Parameters used for the determination of flow resistivity and tortuosity.

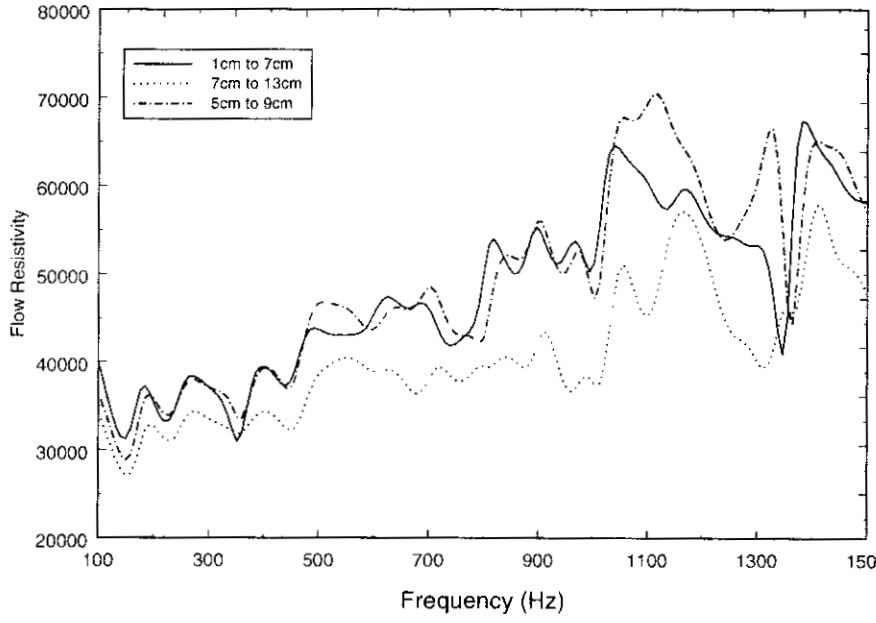

Figure 6-5. Calculated flow resistivity of the Tank Sand.

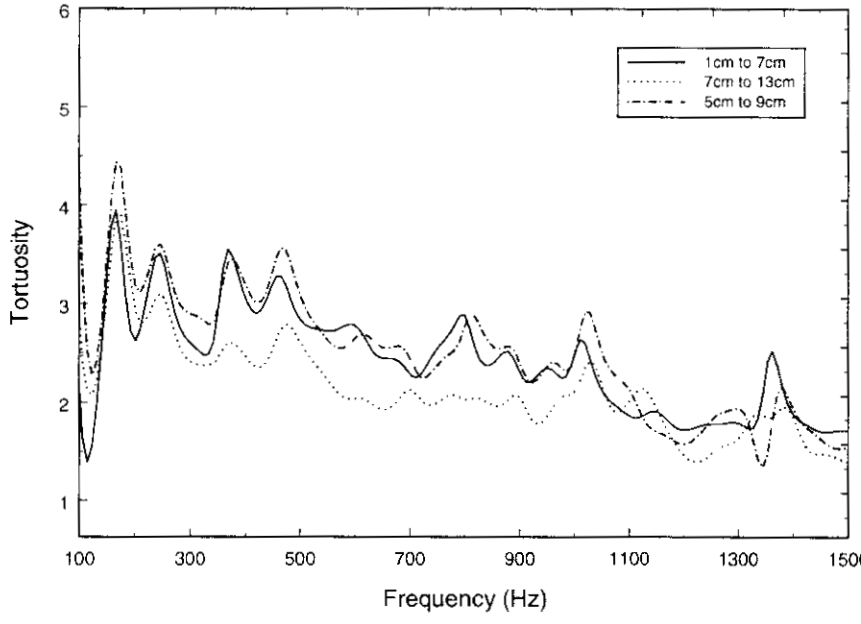

Figure 6-6. Calculated tortuosity of the Tank Sand.

The results for the two tank positions used can be seen in Table 6-4. Since any trends observed have been deemed to be suspect, the results given are a mean value for each depth interval. The frequency range over which the average value has been computed is governed by approximations in the algorithm. The approximations show that the flow resistivity is most sensitive at low frequencies whilst the tortuosity is most sensitive at the higher frequencies (Attenborough *pers. comm.*). Therefore, the flow resistivity has been calculated over the frequency range 100-750Hz, whilst the tortuosity is calculated between 750 and 1500Hz.

The results show that the sand has an average measured flow resistivity of approximately 40000MKS Rayls and an average tortuosity of 2.1. Both these values are typical of materials such as these.

	Depth Interval	**Tortuosity**	**Flow Resistivity (MKS Rayls)**
Position A	**1cm to 7cm**	2.1	39688
	7cm to 13cm	1.8	34968
	5cm to 9cm	2.1	39943
	Average	**2.0±0.2**	**38200±3232**
Position B	**1cm to 7cm**	2.9	62706
	7cm to 13cm	1.6	17516
	5cm to 9cm	2.6	46233
	Average	**2.3±0.6**	**42152±24636**

Table 6-4. Calculated values of tortuosity and effective flow resistivity from probe microphone measurements.

Measurements were also taken with the probe microphone with the loudspeaker at non-normal angles of incidence to ascertain whether there is any angle dependence to either flow resistivity or tortuosity. Measurements were taken with angles of incidence at 14°, 21° and 37°. The complete set of results can be found in Appendix C, whilst a summary can be found in Table 6-5.

The calculated values of flow resistivity in the tank sand are all approximately 45000MKS Rayls, a similar value to those calculated with the loudspeaker at normal incidence (see Table 6-4). The results of the tortuosity determination at the varying angles of incidence are also approximately the same, again showing that there appears to be no angle dependence to the parameters.

	Depth Interval	Tortuosity	Flow Resistivity (MKS Rayls)
Angle 1 (14°)	**1cm to 7cm**	1.6	49144
	7cm to 13cm	1.5	39475
	5cm to 9cm	1.4	45236
	Average	**1.5±0.1**	**44618±5143**
Angle 2 (21°)	**1cm to 7cm**	1.6	53332
	7cm to 13cm	1.3	44150
	5cm to 9cm	1.5	44954
	Average	**1.5±0.2**	**47479±5853**
Angle 3 (37°)	**1cm to 7cm**	1.2	50725
	7cm to 13cm	1.6	46987
	5cm to 9cm	1.4	45183
	Average	**1.4±0.2**	**47632±3093**

Table 6-5. Measured Tortuosity and Flow Resistivity for three differing angles of incidence.

However, comparison of the tortuosity of 2.2 calculated for normal incidence with that of roughly 1.5 calculated at non-normal incidence, shows that the values of τ are slightly different. However, from the repeatability of the values it is probable that the variation is due to disturbance of the soil structure.

Probe microphone measurements were also obtained in a soil tank at NCPA, Oxford, Mississippi. Here measurements were taken at 0.5cm intervals down to a depth of 7cm over a frequency range of 100Hz to 500Hz using a swept-sine output. The relative magnitude and phase difference between a reference microphone, placed at the soil surface near the probe, and the probe microphone, at 0.5cm intervals down to 7cm are shown in Figure 6-7 and Figure 6-8.

It can be seen that the magnitude decreases systematically down to 2.0cm, with the phase difference increasing systematically down to 2.0cm, with the change in both magnitude and phase difference increasing slightly with frequency. This suggests that both the attenuation and phase velocity increase with increasing frequency but remain constant with depth after approximately 2.0cm. This indicates that down to a depth of approximately 2cm the Type II P-wave is predominant. There is then a zone of integration between the Type I and Type II waves, after which the Type I wave is dominant.

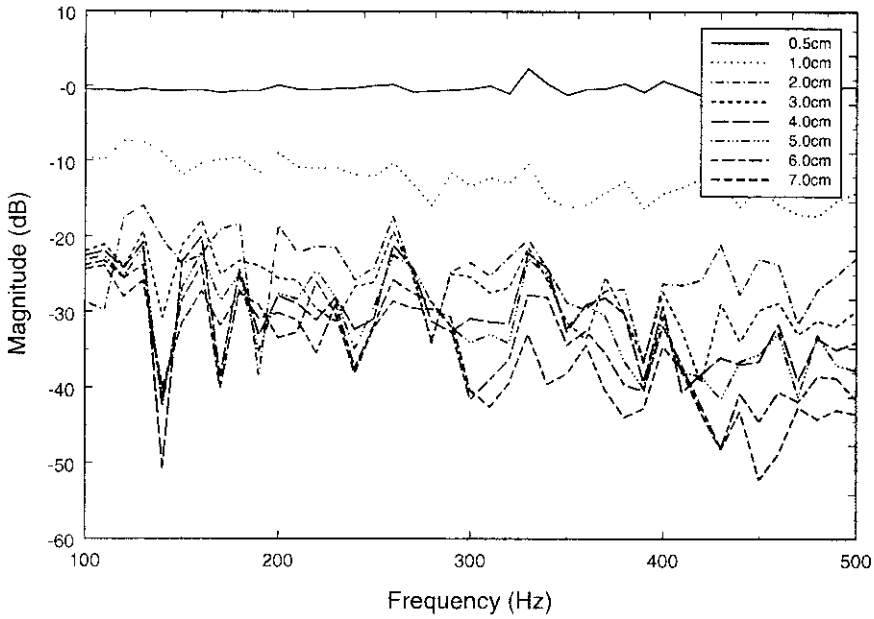

Figure 6-7. Measured relative magnitude between the probe microphone at various depths and a reference microphone situated at the loam surface.

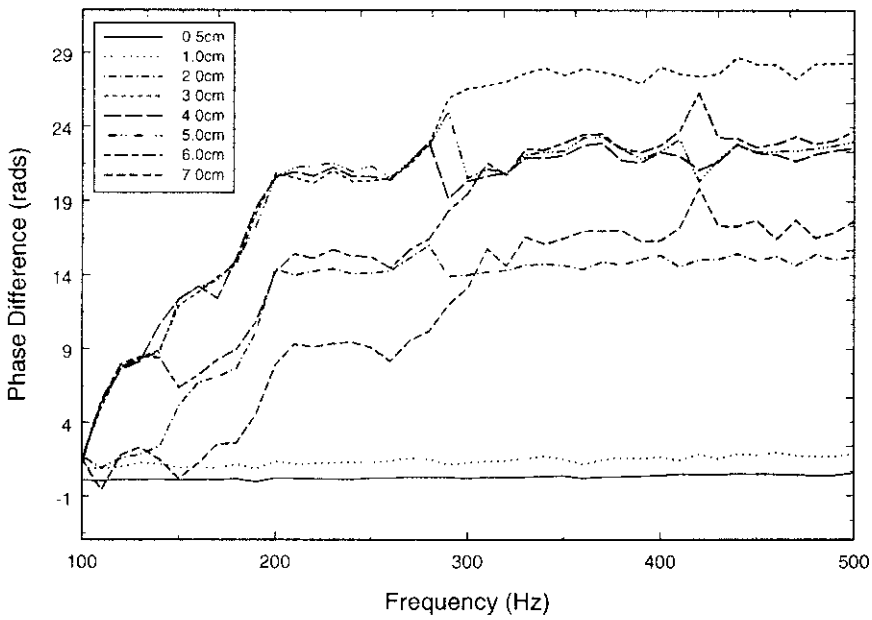

Figure 6-8. Measured phase difference between the probe microphone at various depths and a reference microphone situated at the loam surface.

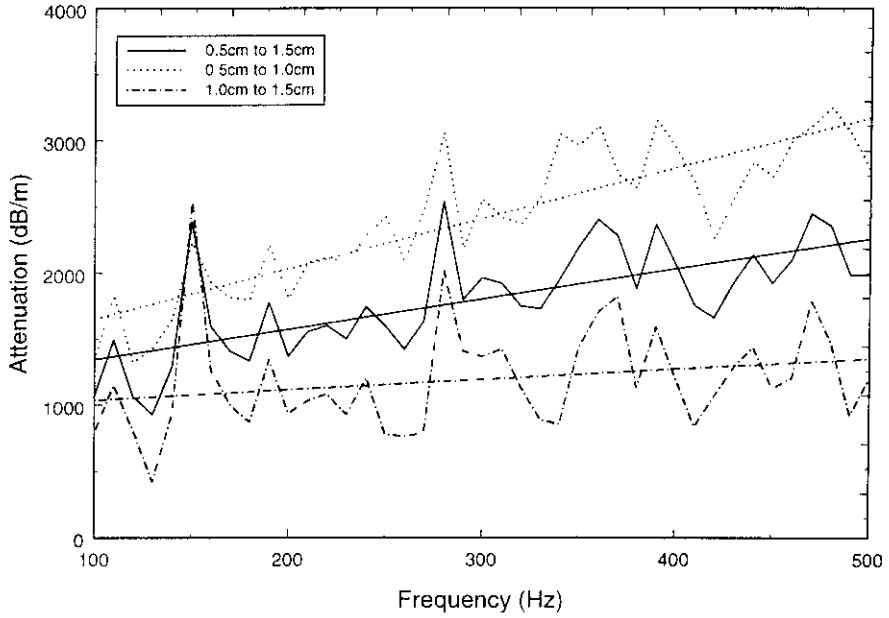

Figure 6-9. Calculated attenuation using the data in Figure 6-7 over three different depth intervals. Best-fit regression has been applied to the data.

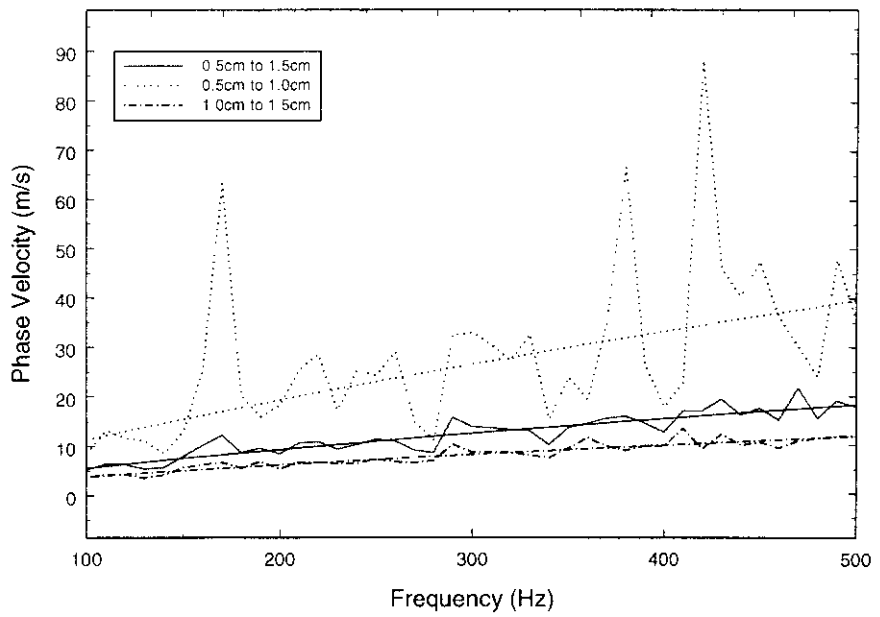

Figure 6-10. Calculated phase velocity using the data in Figure 6-8 over three different depth intervals. Best-fit regression has been applied to the data.

Calculations of attenuation and phase velocity over three depth intervals (0.5cm to 1.0cm, 0.5cm to 1.5cm and 1.0cm to 1.5cm) can be seen in Figure 6-9 and Figure 6-10 respectively. Best-fit linear regression lines are superimposed onto the data. The calculated attenuation over the three depth intervals and for frequencies of 100Hz, 250Hz and 500Hz are presented in Table 6-6, with corresponding phase speeds in Table 6-7.

Depth Interval	**Frequency**		
	100Hz	**250Hz**	**500Hz**
0.5cm to 1.0cm	5.6	11.1	18.5
0.5cm to 1.5cm	11.3	23.1	39.6
1.0cm to 1.5cm	3.8	7.4	12.1

Table 6-6. Attenuation (dB/m) calculated from the data collected (Figure 6-7) with the probe microphone.

Depth Interval	**Frequency**		
	100Hz	**250Hz**	**500Hz**
0.5cm to 1.0cm	1346.9	1655.1	1038.6
0.5cm to 1.5cm	1689.8	2224.6	1150.0
1.0cm to 1.5cm	2261.5	3173.7	1349.1

Table 6-7. Phase velocity (m/s) calculated from the data collected (Figure 6-8) with the probe microphone.

Calculations of phase velocity and attenuation over the three depth intervals show an increase with increasing frequency. The velocities calculated for each of the depth intervals are only slightly similar, with the 0.5cm to 1.0cm and 0.5cm to 1.5cm intervals showing most similarity, coupled with the higher degree of fit in the regression data. The attenuation data also shows a large span of values with again the 0.5cm to 1.0cm and 0.5cm to 1.5cm depth intervals showing the better regression fits.

It can be seen from the graphs that there are large fluctuations in the recorded data. It is likely that the most significant errors in the experiment were in the data collection, since it is extremely difficult to achieve an accurate depth positioning of the probe in this material. In addition, since the depth intervals over which the calculations are being made are very small, any errors in probe positioning will be greatly magnified. Some of the fluctuations in the data may be attributable to resonances of the container or the room.

Using the method outlined above and the theory detailed in Section 3.1 of Chapter 3, the tortuosity and flow resistivity of the test material has been determined. The results of which can be seen in Table 6-8.

Due to the large fluctuations in the data, calculations led to the values of $Im(k_b)$ being larger than $Re(k_b)$. Thus when $(kr^2\text{-}ki^2)$ is calculated in Equation 3-25, a negative value is returned. This makes an inversion for tortuosity impossible.

Depth Interval	Tortuosity	Flow Resistivity (MKS Rayls)
0.5cm to 1.5cm	---	6.85×10^6
0.5cm to 1.0cm	---	4.63×10^6
1.0cm to 1.5cm	---	6.86×10^6
Average	**---**	**6.11×10^6**

Table 6-8. Calculated values of tortuosity and flow resistivity from probe microphone measurements on NPCA loam.

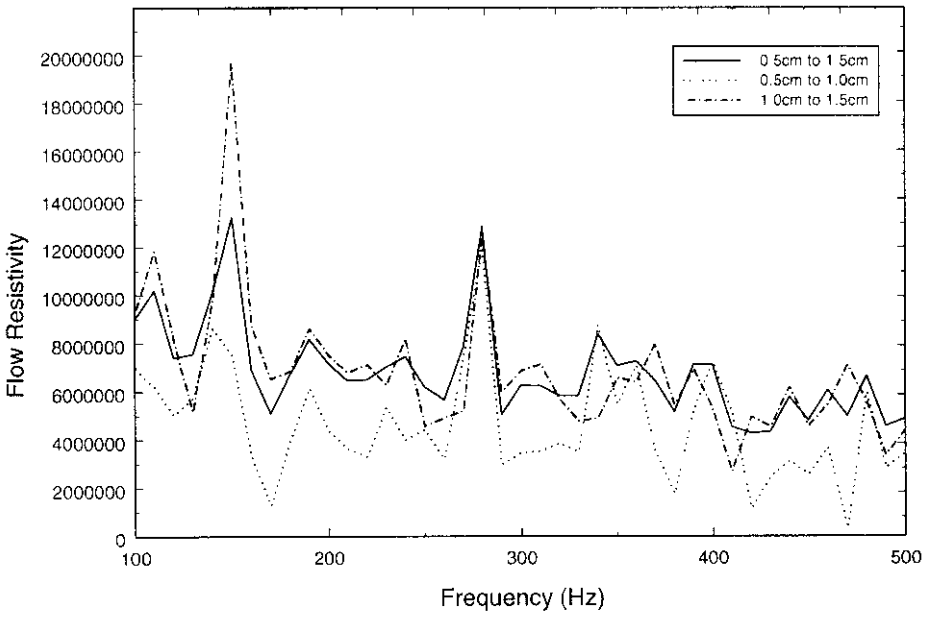

Figure 6-11. Calculated flow resistivity of the NCPA loam.

The in-situ geophones were used to measure the arrival times of five-cycle tone bursts emitted from the loudspeaker. These experiments have been described in Section 5.1.1.3 of Chapter 5. As described in this section three sequences of experiments were undertaken to assess the repeatability of the techniques.

Figure 6-12 shows the travel time versus receiver depth for the first sequence of experiments using a source signal of 500Hz. This plot shows the repeatability of the tests with calculated phase velocities of 246.3, 243.5 and 249.1m/s. The travel time versus receiver separation over the range of frequencies for Run 1 of the experiments is given in Figure 6-13. Linear regression was carried out upon the time of flight data with the resultant line of best-fit superimposed upon the data. The results of which can be seen in Table 6-9. The data shows that the measured wave velocity remains constant (within experimental error) over the frequency range.

Frequency (Hz)	**Phase velocity (m/s)**	**K_{ud} (elastic) (Pa)**
500	246.3±8.4	$8.81\text{x}10^{7}\pm6.21\text{x}10^{6}$
750	241.4±10.0	$8.37\text{x}10^{7}\pm7.24\text{x}10^{6}$
1000	243.3±7.9	$8.60\text{x}10^{7}\pm5.69\text{x}10^{6}$
1250	236.5±8.4	$8.11\text{x}10^{7}\pm5.96\text{x}10^{5}$
1500	234.5±9.3	$7.83\text{x}10^{7}\pm6.45\text{x}10^{6}$

Table 6-9. Measured values of phase velocity using the pulse transmission technique with vertical component geophone receivers. Also, the values of the material bulk modulus obtained by inversion.

Since the measured wave velocity remained constant with frequency and was greater than the velocity measured using the probe microphone (which had been attributed as the Type II P-wave), the wave measured was attributed to be the Type I P-wave. The measured velocities were therefore used in conjunction with values of shear modulus calculated in Section 6.1.2 to calculate the bulk modulus. This was achieved using the elastic theory outlined in Chapter 3.

Figure 6-14 shows the plots of vertical component amplitude against receiver depth for the three runs using a source signal of 500Hz. The data exhibits a reasonably high degree of scatter between subsequent experiments, although it can be seen that there is some repeatability. An attempt has been made to correct the geophone amplitudes for the differing sensitivities between the upper five and lower five geophones.

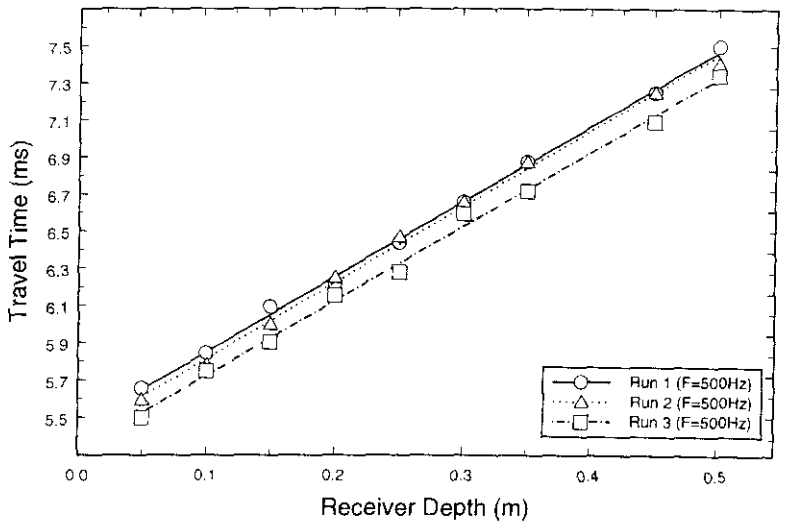

Figure 6-12. Travel time versus vertical component geophone depth for a source signal of 500Hz. Best-fit linear regressions are superimposed onto the data.

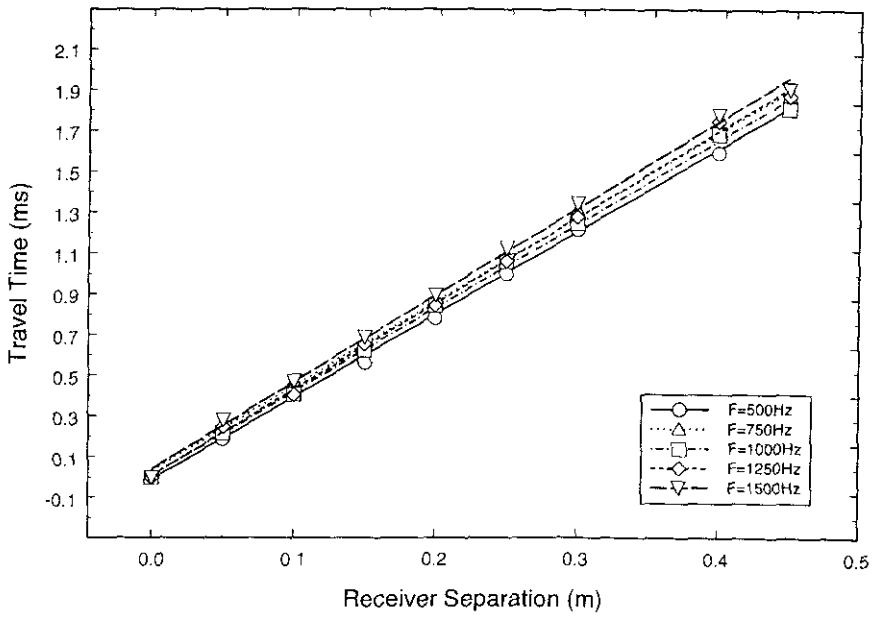

Figure 6-13. Transit time versus vertical component geophone separation for varying source frequencies. Best-fit linear regressions are superimposed onto the data.

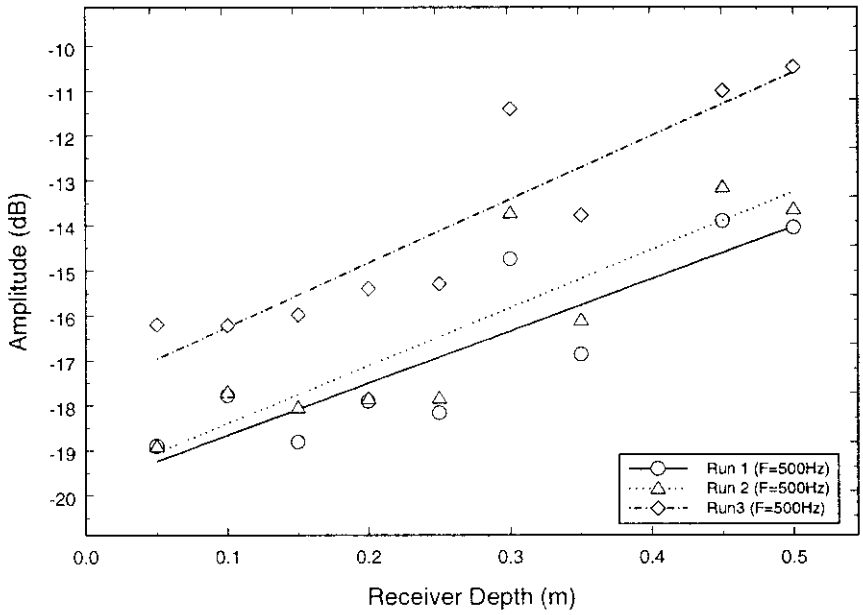

Figure 6-14. Vertical component geophone amplitude versus receiver depth for a source signal of 500Hz. Best-fit linear regressions for all geophones are shown.

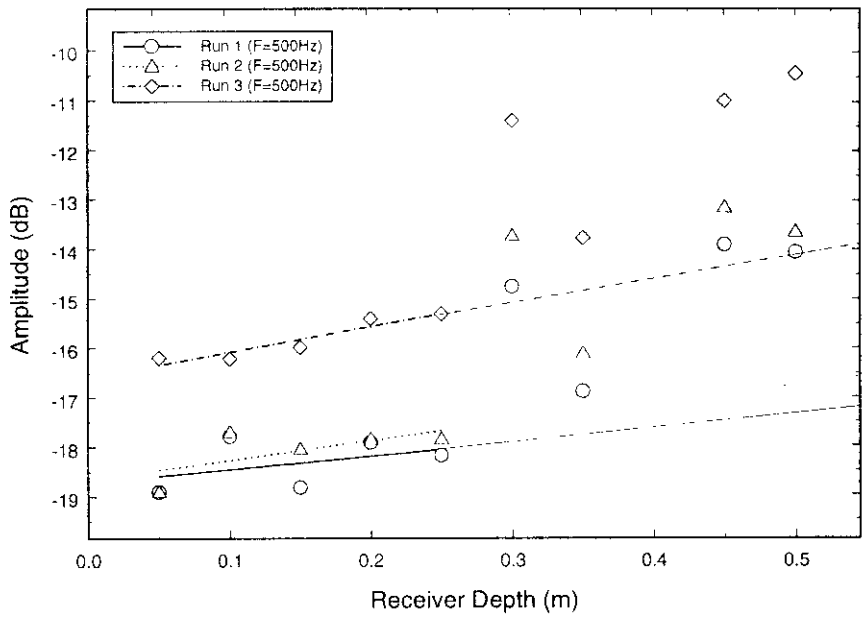

Figure 6-15. As above, except Best-fit linear regressions are shown for the top 5 geophones only.

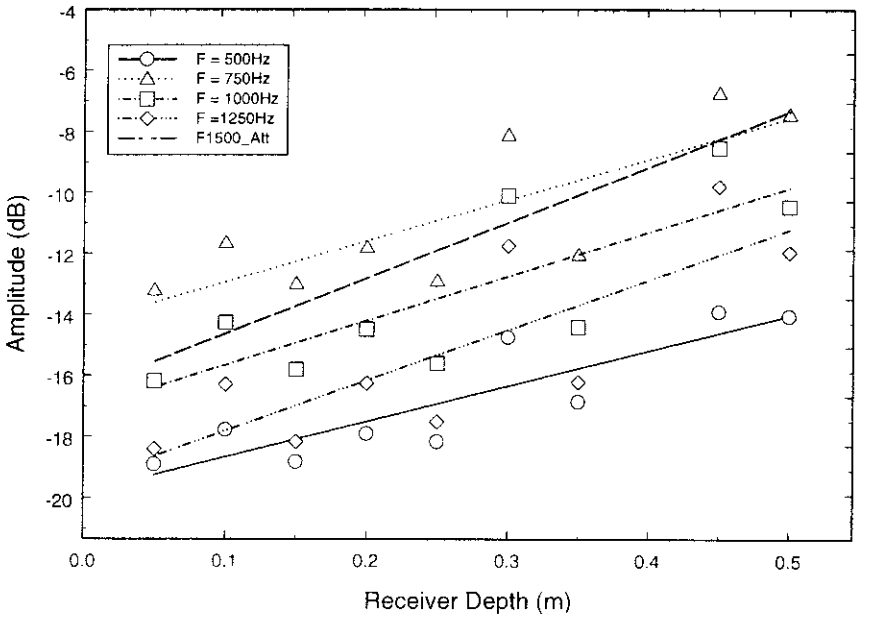

Figure 6-16. Vertical component geophone amplitude versus receiver depth for varying source frequencies. Best-fit linear regressions for all geophones are shown.

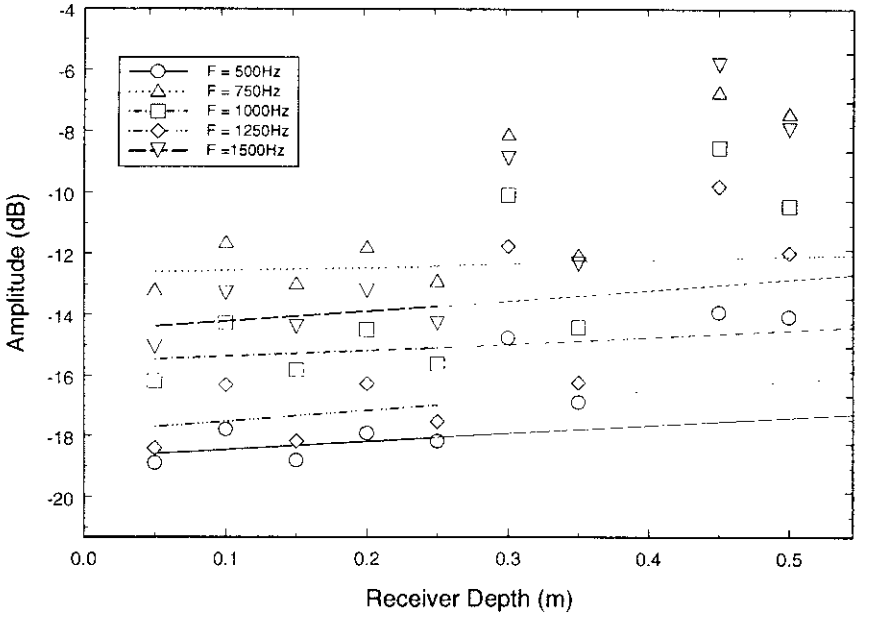

Figure 6-17. As above, except Best-fit linear regressions are shown for the top 5 geophones only.

The scatter in the data might be attributed to the variation in the coupling of the geophones or to non-uniformity of the sand packing.

In an attempt to overcome the differences between the geophones, Figure 6-15 again shows the geophone amplitude for each receiver, but the linear regression has only been applied to the upper five geophones. The results show a marked improvement in the linear regression over the previous plot. However, it is noticeable from both Figure 6-14 and Figure 6-15 that there is an increase in geophone amplitude with increasing depth. It is most likely therefore that the loudspeaker source is producing some resonance in the sand matrix, which cannot be accounted for.

Figure 6-16 and Figure 6-17 are similar plots to Figure 6-14 and Figure 6-15, in that they show the results for the range of frequencies from Run 1. Again, both plots show a high degree of scatter with the regressions for the upper five geophones showing a marked improvement over the results gained using all 10 geophones. Again, both plots show an increase in geophone amplitude with depth. It is therefore impossible to draw any conclusions from the experiments.

No attempt has been made to calculate the bulk modulus using the limiting case 1 outlined in Chapter 3, due to the high degree of uncertainty in the data.

The previous experiments were repeated using the loudspeaker source with the in-situ microphones as receivers. Figure 6-18 shows the travel time versus receiver depth for the first sequence of experiments using a source signal of 500Hz. This plot shows the repeatability of the tests with calculated phase velocities of 196.8, 200.2 and 205.4m/s. These values are much smaller than the phase velocities calculated using the in-situ geophones.

The travel time versus receiver separation over the range of frequencies for Run 1 of the experiments is given in Figure 6-19. Linear regression was carried out upon the time of flight data with the resulting line of best-fit superimposed upon the data. The results show a slight increase in phase velocity with increasing frequency, although this relationship may be suspect. The calculated values of phase velocity can be seen in Table 6-10.

It appears that the in-situ microphones are reacting to the Type-II P-wave and as such the bulk modulus cannot be calculated.

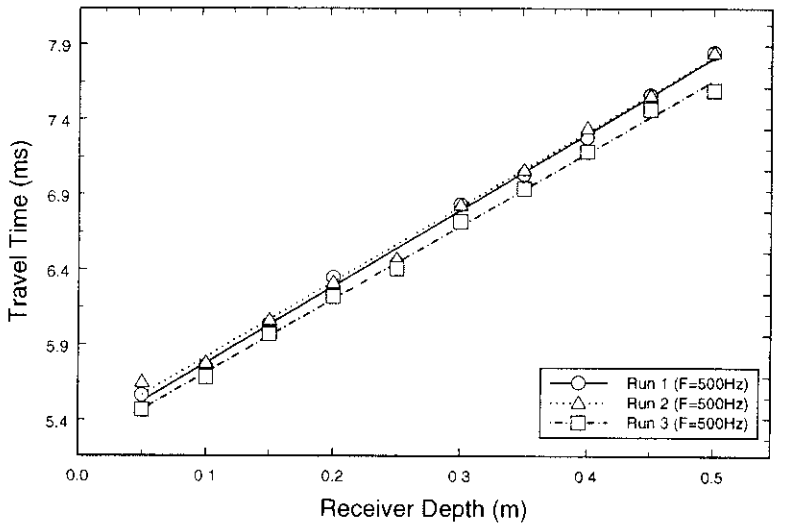

Figure 6-18. Travel time versus in-situ microphone depth for a source signal of 500Hz. Best-fit linear regressions are superimposed onto the data.

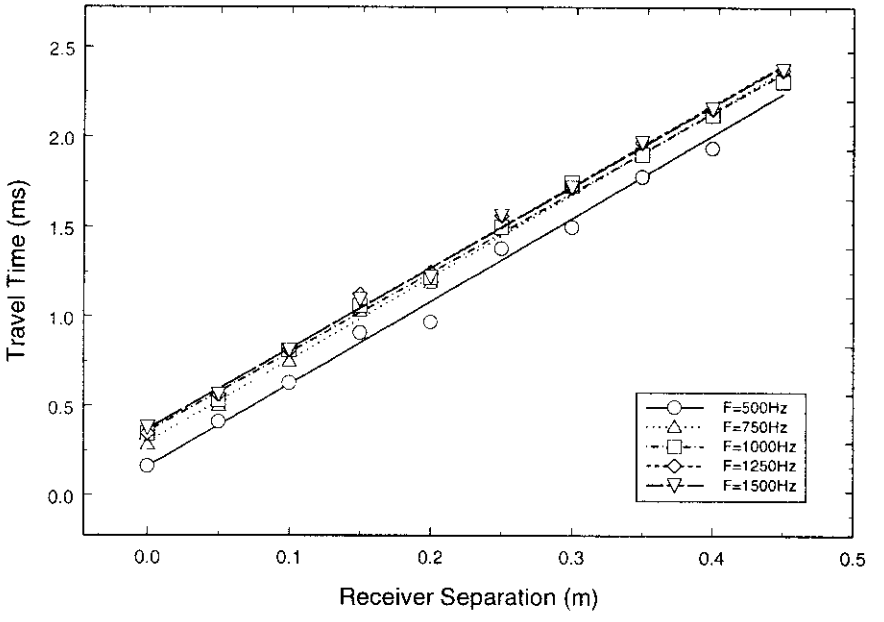

Figure 6-19. Transit time versus in-situ microphone separation for varying source frequencies. Best-fit linear regressions are superimposed onto the data.

Frequency (Hz)	Phase velocity (m/s)	Attenuation (dB/m)
500	198.8±10.2	57.7±6.8
750	208.2±7.7	70.7±7.8
1000	211.4±7.5	82.2±9.5
1250	215.7±6.5	89.9±11.0
1500	217.4±13.9	106.8±10.8

Table 6-10. Measured values of wave velocity and wave attenuation using the pulse transmission technique with in-situ microphone receivers.

Figure 6-20 shows a plot of in-situ microphone voltage amplitude against receiver depth for the three runs. The plot shows a high degree of repeatability between the three runs with measured attenuations of 57.7, 58.1 and 60.5dB/m. No correction has been made to attribute for the differences in sensor sensitivity.

The results of the in-situ microphone voltage amplitude against receiver depth for varying source frequencies can be seen in Figure 6-21 and the resultant calculated attenuation for each frequency can be found in Table 6-10. This shows that there is a significant increase in attenuation with increasing frequency.

Table 6-12 and Table 6-13 give a summary of the complete set of measurement taken using the loudspeaker source with the geophone and in-situ microphone receivers. The tables show the calculated phase velocities for each frequency and calculated attenuation together with the upper and lower limits set by the linear regression (using a 95% confidence limit).

The probe microphone was also used to measure the arrival times of five-cycle tone bursts emitted by the loudspeaker. The time interval and receiver separation, (see Figure 6-22) are measured with respect to a reference signal. In this case, the reference is the probe at 1cm depth. The calculated phase velocities are given in Table 6-11. These velocities are slightly larger than the velocities obtained using the MLS.

Frequency (Hz)	Measured Phase Velocity (m/s)	
	MLS Method	Tone Burst Method
500	144.0	183.3
750	159.4	192.4
1000	171.8	196.5
1250	181.9	205.1
1500	190.5	208.4

Table 6-11. Comparison of measured phase velocity using probe microphone. The output signal is either MLS or tone burst.

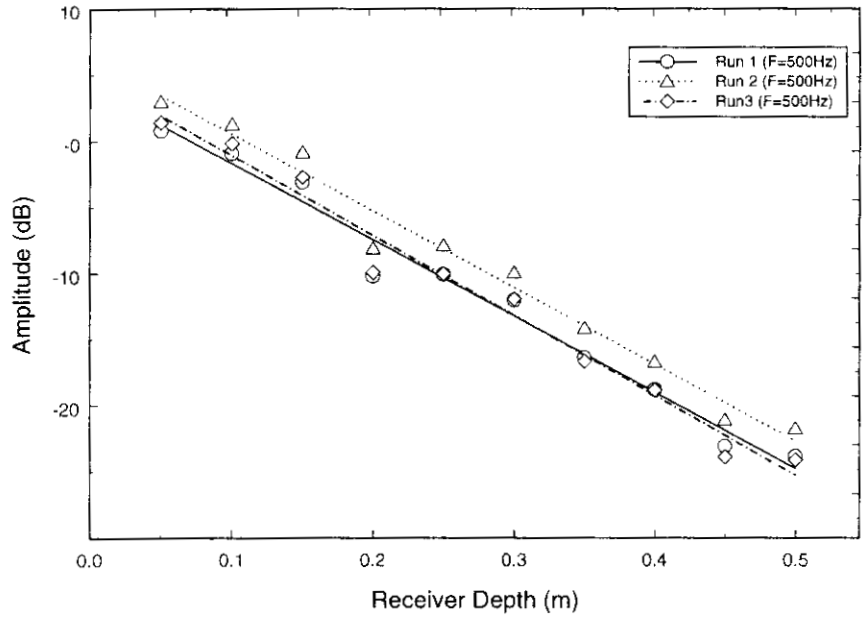

Figure 6-20. In-situ microphone amplitude versus receiver depth for a source signal of 500Hz. Best-fit linear regressions are superimposed on the data.

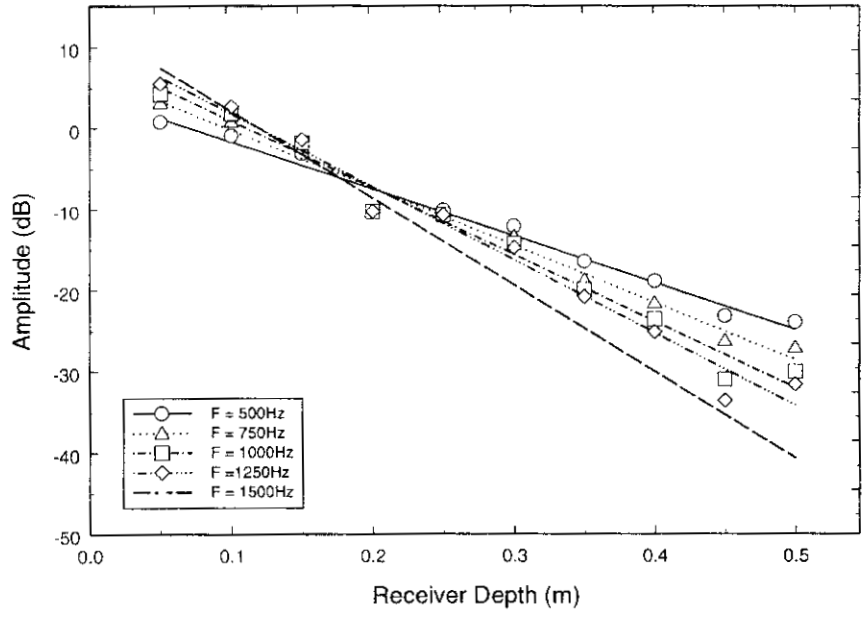

Figure 6-21. In-situ microphone amplitude versus receiver depth for varying source frequencies. Best-fit linear regressions are superimposed on the data.

Using the loudspeaker as a source, arrival times were measured from pulses down to much greater depths using the in-situ vertical component geophones and in-situ microphones. Figure 6-23 shows the arrival times versus receiver separation to the sensors for a 500Hz tone burst. The reference for the geophone and microphones is the corresponding receiver at 5cm depth. At shallow depths, less than 15cm, the measured phase velocity is the same for all sensors at around 190m/s. At deeper depths, the velocity as measured using the geophones increases to roughly 260m/s.

It appears from the measurements taken with the loudspeaker source that preferential excitation of the Type II P-wave occurs and that at depths up to approximately 15cm it is the dominant wave type in the material. This can be seen in the magnitude data taken with the probe microphone and from the results of the five-cycle tone burst travel times shown in Figure 6-23.

After this depth there is still considerable Type II energy in the sand, that is being received by both the probe microphone and in-situ microphones (since the Type II wave travels mostly in the fluid and the microphone is a pressure transducer this is to be expected) as well as Type I energy that is being received by the in-situ geophones.

This can be seen in the differing wave velocities measured by the microphones and geophones. It is most likely that the wave velocity measured by the in-situ microphones is greater than that measured by the probe microphone because the in-situ microphone wave velocity is calculated over a range of 0.50m as opposed to 0.30m.

It can also be seen that the attenuation measured by the probe microphone over the range 1-7cm where the Type II P-wave is dominant is 98dB/m as opposed to an attenuation of 60dB measured using the in-situ microphones. Again, this may be due to the depth range over which the calculations are made. A calculation of the attenuation from probe microphone measurements over the complete 30cm range shows a value of 69dB/m. This value show a reasonable agreement with that measured using the in-situ microphones.

This result is markedly different than that found previously (Hickey and Sabatier, 1996). Figure 6-24 shows the published results of this work. Hickey showed that in a similar manner to the above results that at shallow depths, again less than 15cm, the type II wave was dominant and was detected by all three receivers. However, below this depth the type I wave became the more dominant wave type and was detected by the geophone, as expected, but also by both microphones.

Phase Velocity Determination Summary Table Using Loudspeaker Source						
Frequency	**Receiver**	**Upper Vel**	**Vel**	**Lower Vel**	**R^2**	**Std Error**
500	Geophone	255.4	**246.3**	237.9	0.9984	0.026
500	Geophone	254.9	**243.5**	233.0	0.9975	0.034
500	Geophone	262.9	**249.1**	236.6	0.9965	0.039
500	Microphone	207.0	**196.8**	187.6	0.9964	0.049
500	Microphone	210.9	**200.2**	190.5	0.9961	0.050
500	Microphone	213.5	**205.4**	197.8	0.9978	0.037
750	Geophone	252.3	**241.4**	231.3	0.9977	0.033
750	Geophone	246.1	**236.1**	226.8	0.9950	0.046
750	Geophone	269.5	**252.5**	237.4	0.9950	0.046
750	Microphone	215.9	**208.2**	201.0	09960	0.036
750	Microphone	209.3	**203.4**	197.8	0.9988	0.027
750	Microphone	216.3	**209.3**	202.8	0.9985	0.030
1000	Geophone	251.7	**243.3**	235.4	0.9986	0.025
1000	Geophone	247.3	**237.5**	228.5	0.9980	0.031
1000	Geophone	264.7	**251.0**	238.6	0.9966	0.038
1000	Microphone	219.5	**211.4**	203.9	0.9980	0.034
1000	Microphone	217.6	**210.3**	203.5	0.9983	0.032
1000	Microphone	226.2	**218.7**	211.6	0.9983	0.030
1250	Geophone	245.5	**236.5**	228.1	0.9983	0.029
1250	Geophone	250.2	**239.2**	229.0	0.9976	0.034
1250	Geophone	261.3	**249.1**	238.0	0.9973	0.034
1250	Microphone	222.5	**215.7**	209.2	0.9986	0.028
1250	Microphone	226.7	**217.9**	209.6	0.9977	0.035
1250	Microphone	225.8	**216.7**	208.4	0.9976	0.037
1500	Geophone	244.6	**234.5**	225.1	0.9979	0.032
1500	Geophone	247.5	**237.5**	228.3	0.9980	0.031
1500	Geophone	262.9	**248.0**	234.6	0.9960	0.042
1500	Microphone	233.4	**217.4**	203.5	0.993	0.062
1500	Microphone	231.1	**222.3**	214.2	0.9978	0.034
1500	Microphone	222.8	**215.3**	208.4	0.9983	0.030

Table 6-12. Summary of phase velocities determination using a loudspeaker source. Results are for vertical component geophones and in-situ microphones.

Wave Attenuation(dB/m) Determination Summary Table						
Frequency	**Receiver**	**Upper Att**	**Att**	**Lower Att**	**R^2**	**Std Error**
500	Geophone	****	****	****	0.7739	1.025
500	Geophone	****	****	****	0.7767	1.131
500	Geophone	****	****	****	0.8296	1.053
500	Microphone	-64.5	-57.7	-50.9	0.9794	1.343
500	Microphone	-65.1	-58.1	-51.0	0.9785	1.382
500	Microphone	-67.8	-60.5	-53.1	0.9783	1.446
750	Geophone	****	****	****	0.6401	1.653
750	Geophone	****	****	****	0.6580	1.631
750	Geophone	****	****	****	0.6580	1.631
750	Microphone	-78.5	-70.7	-62.9	0.982	1.537
750	Microphone	-78.0	-70.1	-62.2	0.9812	1.558
750	Microphone	-80.2	-71.4	-62.5	0.9773	1.745
1000	Geophone	****	****	****	0.6183	1.877
1000	Geophone	****	****	****	0.6983	1.780
1000	Geophone	****	****	****	0.6735	1.723
1000	Microphone	-91.7	-82.2	-72.7	0.9803	1.874
1000	Microphone	-92.1	-83.3	-74.6	0.9837	1.723
1000	Microphone	-91.3	-83.1	-74.9	0.9855	1.617
1250	Geophone	****	****	****	0.6455	2.005
1250	Geophone	****	****	****	0.7307	1.806
1250	Geophone	****	****	****	0.7199	1.653
1250	Microphone	-100.9	-89.9	-78.8	0.9778	2.175
1250	Microphone	-101.3	-91.2	-81.2	0.9822	1.973
1250	Microphone	-101.3	-92.1	-82.8	0.9851	1.820
1500	Geophone	****	****	****	0.7235	1.852
1500	Geophone	****	****	****	0.7284	1.831
1500	Geophone	****	****	****	0.7320	1.565
1500	Microphone	-117.6	-106.8	-96.0	0.9849	2.126
1500	Microphone	-133.2	-117.9	-102.6	0.9752	3.018
1500	Microphone	-105.5	-95.7	-86.0	0.9846	1.921
Wave Attenuation(dB/m) Determination Using Upper Five Geophones						
Frequency	Receiver	Upper Att	Att	Lower Att	R^2	Std Error
500.0	Geophone	8.2	****	****	0.1684	0.5429
500.0	Geophone	4.5	****	****	0.4219	0.4250
500.0	Geophone		****	****	0.8812	0.1740
750.0	Geophone	15.8	****	****	0.0099	0.8327
750	Geophone	10.1	****	****	0.5561	0.1876
750	Geophone	1.4	****	****	0.5561	0.1876
1000	Geophone	17.5	****	****	0.0300	0.9664
1000	Geophone	13.2	****	****	0.0905	0.7964
1000	Geophone	3.7	****	****	0.4797	0.3922
1250	Geophone	18.9	****	****	0.0798	1.1183
1250	Geophone	13.4	****	****	0.1197	0.8378
1250	Geophone	0.5	****	****	0.8065	0.2250
1500	Geophone	13.9	****	****	0.1094	0.8557
1500	Geophone	14.8	****	****	0.0927	0.8961
1500	Geophone	0.9	****	****	0.7064	0.3040

Table 6-13. Summary of attenuation determination using a loudspeaker source. Results are for in-situ microphones only.

**** indicates where a positive value for attenuation was measured

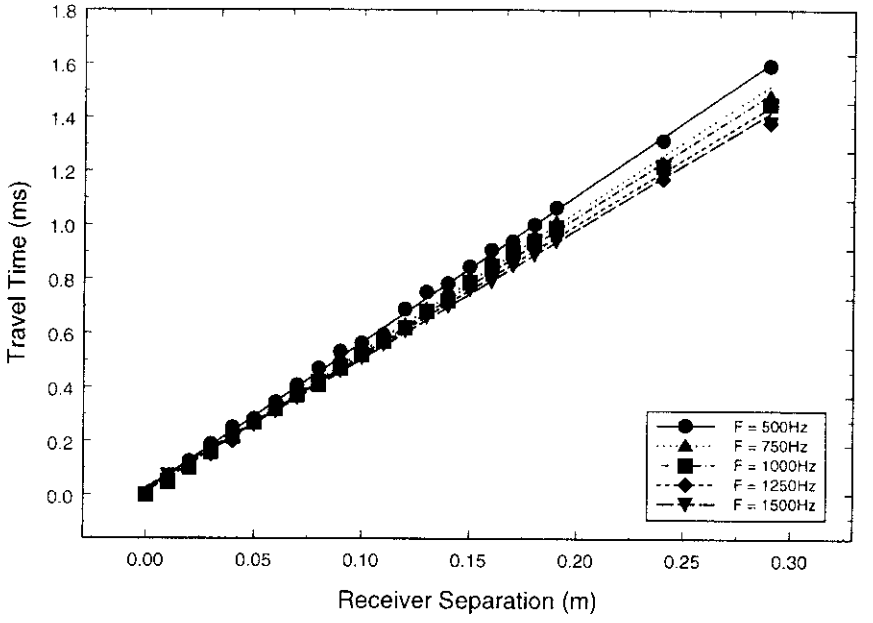

Figure 6-22. Travel time versus receiver separation measured by the probe microphone. Best-fit regressions have been applied to the data.

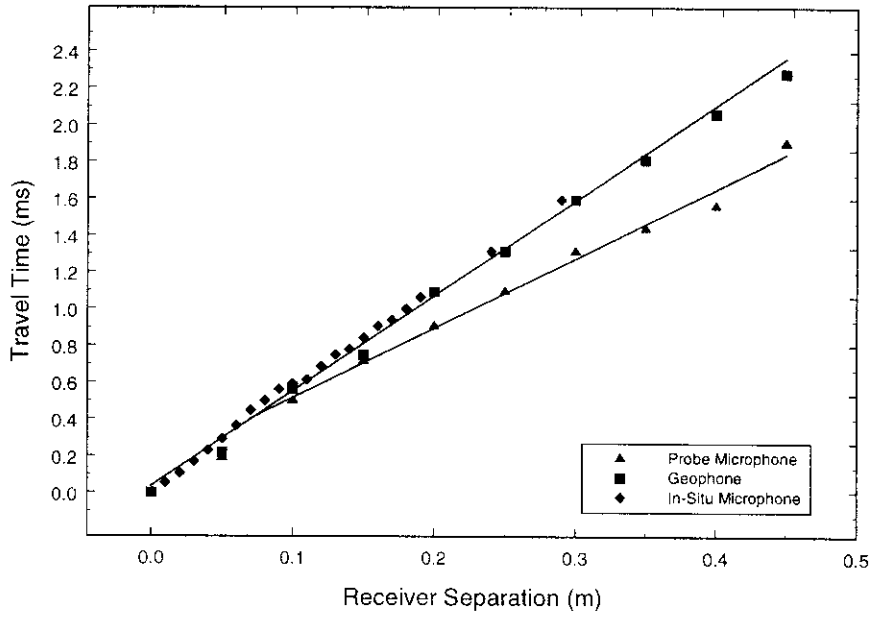

Figure 6-23. Response of Geophone, In-situ Microphone and Probe Microphone to a 500Hz five-cycle tone burst.

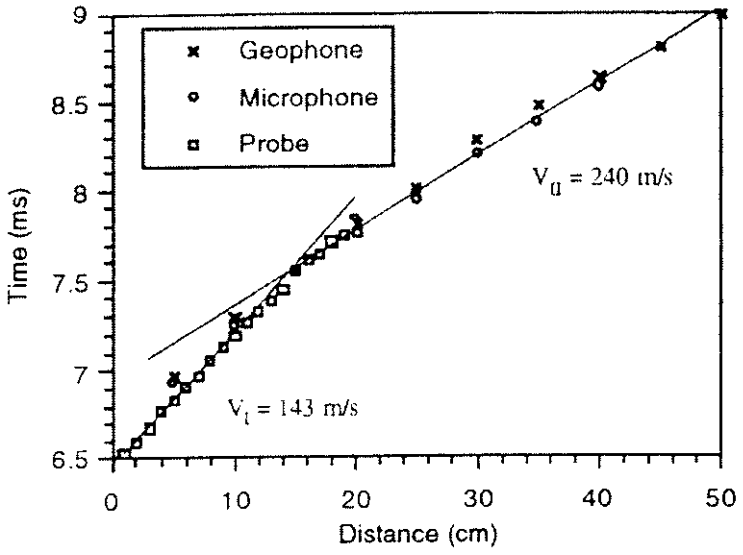

Figure 6-24. Travel time versus depth measured by pulse transmission. A loudspeaker source at a frequency of 1kHz is used and probe microphone, in-situ geophone and in-situ microphone are used as receivers (Hickey and Sabatier, 1996).

6.1.2 Shear Wave Measurements

Shear wave velocities were measured using the technique outlined in Section 5.1.1.3 of Chapter 5. As described in this section three sequences of experiments were undertaken in order to test the repeatability of the techniques.

Each geophone in turn was used as a source and the others as receivers. Figure 6-25 shows the travel time versus receiver separation for the first sequence of experiments. Here, a source signal of 500Hz is shown. The plot shows the repeatability of the procedure, although some scatter is seen in *Run 3* of the sequence. Fewer data are collected at larger offsets due to attenuation of the signal. The time offset between frequencies is a consequence of taking measurements between the electronic trigger and the second peak of the tone burst.

The travel times versus offset between many source/receiver combinations over a range of frequencies are shown in Figure 6-26. Linear regression was carried out upon the time of flight of data with the resulting line superimposed on the data. A summary of the phase velocities for *Run 1* is presented in Table 6-14. The shear wave velocity is approximately 70 m/s and shows no variation with frequency other than that due to experimental error.

Frequency (Hz)	**Phase velocity (m/s)**	**Attenuation (dB/m)**	μ_m **(Pa)**	μ_m **(elastic) (Pa)**
500	70.3±2.1	27.8±7.4	$8.10\times10^{6}\pm5.22\times10^{5}$	$8.06\times10^{6}\pm4.88\times10^{5}$
750	72.1±2.5	39.9±6.0	$8.52\times10^{6}\pm6.20\times10^{5}$	$8.47\times10^{6}\pm5.98\times10^{5}$
1000	69.5±2.2	44.4±8.2	$7.90\times10^{6}\pm5.21\times10^{5}$	$7.87\times10^{6}\pm5.06\times10^{5}$
1250	68.1±2.1	57.6±4.8	$7.58\times10^{6}\pm4.84\times10^{5}$	$7.56\times10^{6}\pm4.73\times10^{5}$

Table 6-14. Measured values of shear wave velocity and shear wave attenuation obtained from pulse transmission by means of Equation 3-9.

Figure 6-27 shows the plots of the horizontal component geophone voltage amplitude against receiver separation for the three runs. This shows the relative repeatability of the experiments. The voltage amplitude has been corrected for spherical spreading, although the recorded amplitude has not been corrected for the sensitivity of the geophone as source or receiver. The scatter in the data might be attributed to the variation in coupling of the geophones or to non-uniformity of the sand pack.

Figure 6-28 shows the results from *Run 1*. The plot gives the horizontal component geophone voltage versus receiver separation for varying source frequencies. Linear regression was carried out upon the amplitude data with the resulting line superimposed on the data. The calculated attenuation can be seen in Table 6-14. It can be seen that the attenuation increases with frequency.

Table 6-14 also shows calculations of the material shear modulus using two approaches. The first approach is to use the $Re(k_b^2)$ method as outlined in Chapter 3. The second approach neglects the attenuation $(Im(k_b))$ and inverts directly using the phase velocity. Both approaches produce identical results. This is because $Im(k_b)$ is substantially smaller than $Re(k_b)$.

Figure 6-29 and Figure 6-30 show the results of the tank experiment carried out at NCPA on the crushed loam described in Chapter 4.

Linear regression was carried out on the time of flight and amplitude data with the resulting line superimposed on the data. Phase velocity and attenuation determined from the slopes are presented in Table 6-15. The shear wave velocity is approximately 73m/s and shows no variation with frequency other than that due to experimental error. The attenuation appears to increase with increasing frequency, although the scatter in the data may make this assumption suspect.

Table 6-15 also shows the values of shear modulus calculated using the two methods outlined above.

Frequency (Hz)	**Phase velocity (m/s)**	**Attenuation (dB/m)**	**μ_m (Pa)**	**μ_m (elastic) (Pa)**
500	74.1±7.7	8.32±7.3	$8.06\times10^6\pm4.99\times10^5$	$7.29\times10^6\pm1.59\times10^6$
750	73.0±6.5	14.3±5.3	$8.48\times10^6\pm6.04\times10^5$	$7.08\times10^6\pm1.32\times10^6$
1000	73.6±5.8	28.3±6.3	$7.88\times10^6\pm5.13\times10^5$	$7.19\times10^6\pm1.18\times10^6$
1250	72.6±5.1	33.7±7.2	$7.57\times10^6\pm4.79\times10^5$	$7.00\times10^6\pm1.02\times10^6$

Table 6-15. Measured values of shear wave velocity and shear wave attenuation using the pulse transmission technique. Also the values of the material shear modulus obtained by inversion.

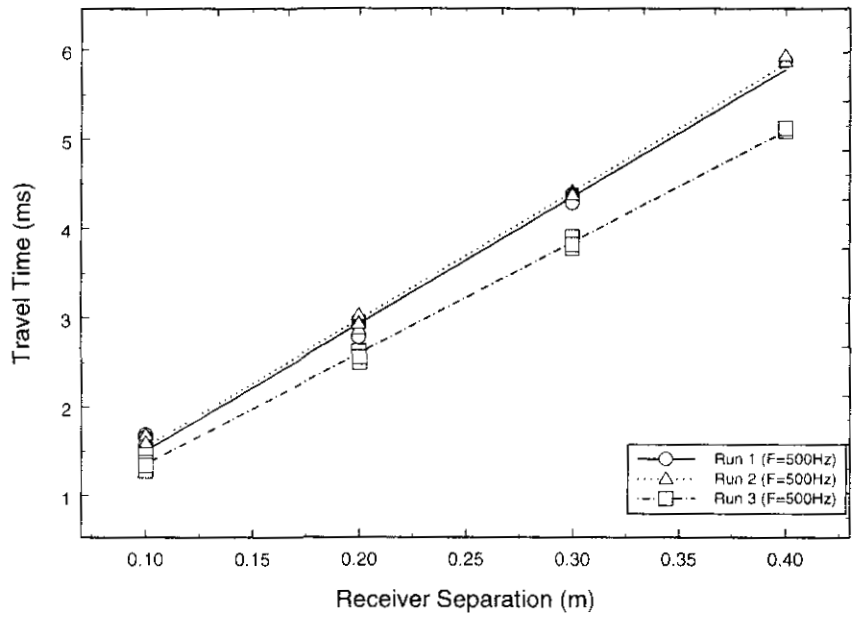

Figure 6-25. Transit time versus horizontal component geophone separation for a source signal of 500Hz. Best-fit linear regressions are superimposed onto the data.

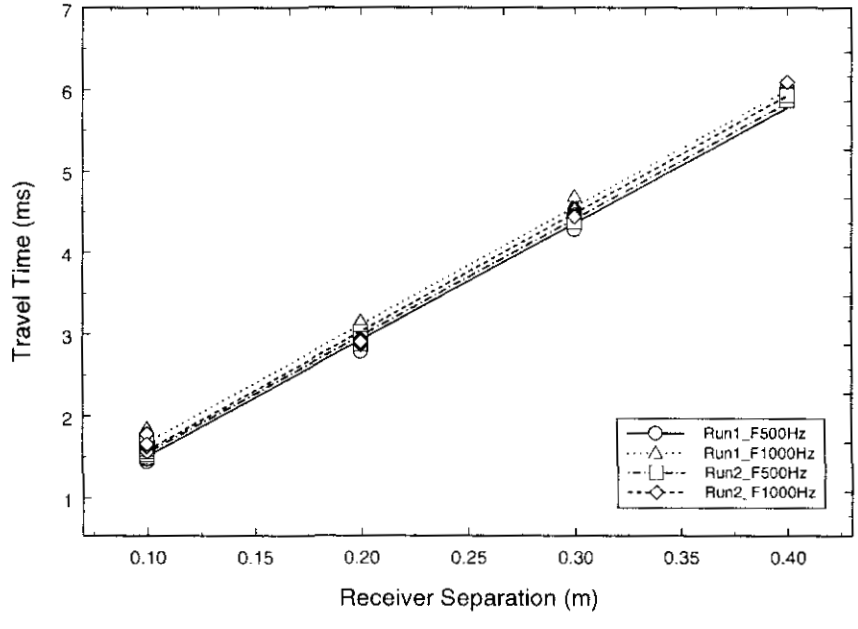

Figure 6-26. Run 1. Transit time versus horizontal component geophone separation for varying source frequencies. Best-fit linear regressions are superimposed onto the data.

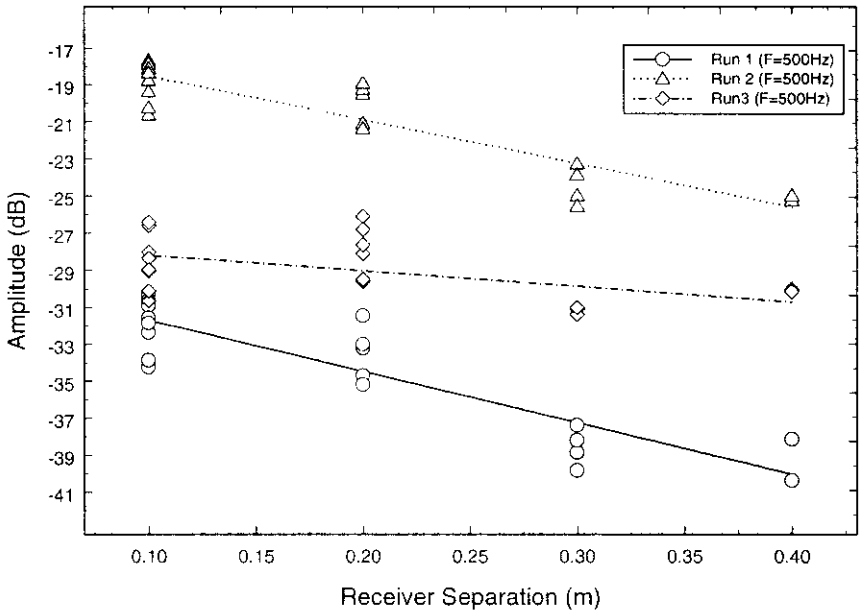

Figure 6-27. Horizontal component geophone amplitude (dB) versus receiver separation for a source signal of 500Hz.

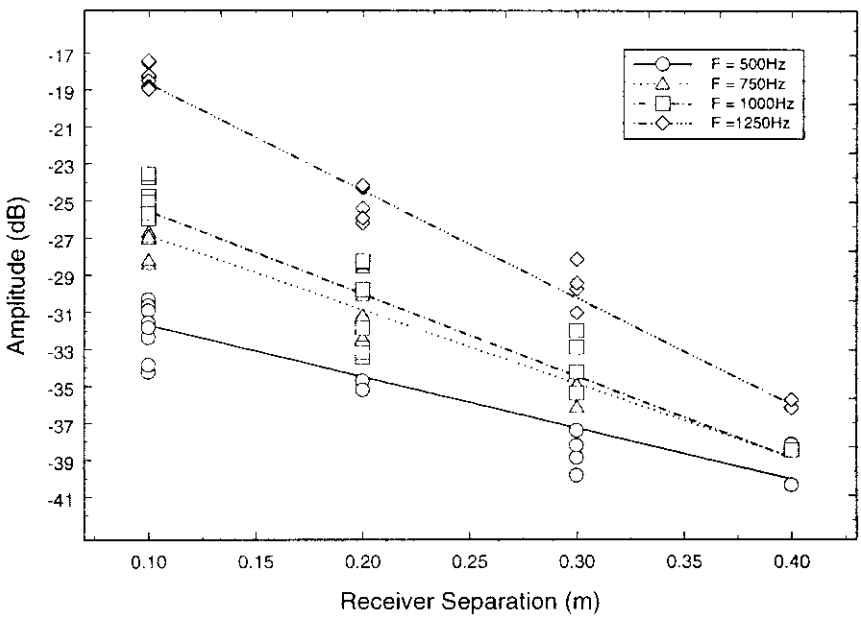

Figure 6-28. Run 1. Horizontal component geophone amplitude versus receiver separation for varying source frequencies.

Table 6-16 shows a summary of the complete set of shear wave experiments taken in the first set, as well as the results of the data taken at NCPA. The table shows the calculated phase velocity for each frequency, and the upper and lower limits set by the linear regression (using a 95% confidence limit). The table also shows the R^2 value and standard error of the linear regression.

Also shown in the table are the results for the shear wave attenuation, including similar limits and statistical data from the linear regression calculation.

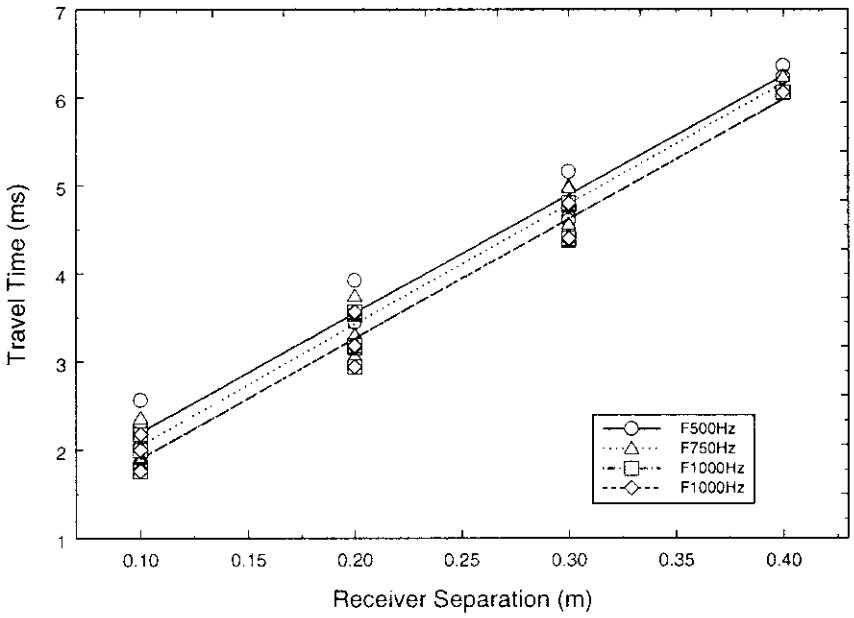

Figure 6-29. Transit time versus horizontal component geophone separation for varying source frequencies. Best-fit linear regressions are superimposed onto the data.

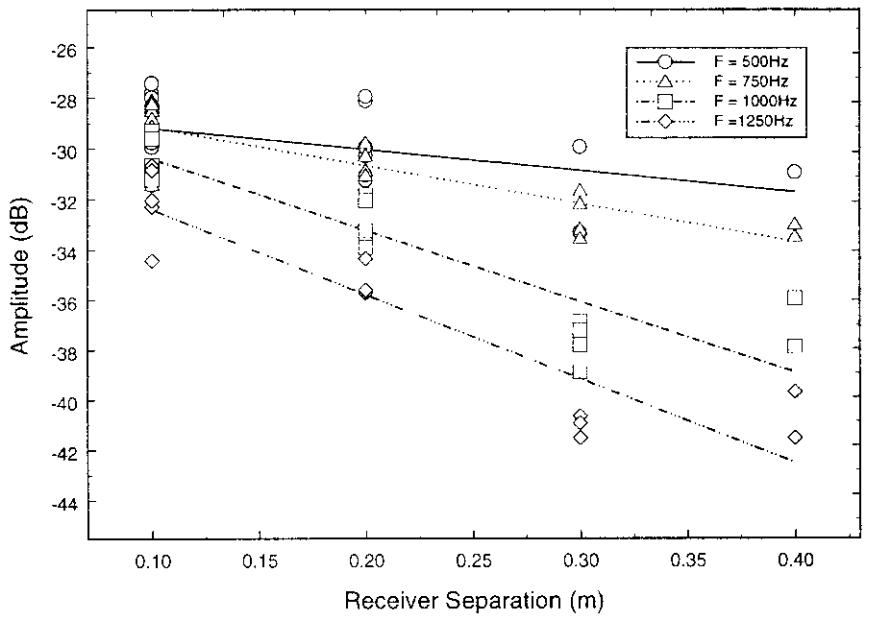

Figure 6-30. Horizontal component geophone amplitude for versus receiver separation for varying source frequencies.

OU Indoor Tank – Shear Wave Analysis							
Phase Velocity Determination							
Frequency (Hz)	**Source**	**Receiver**	**Upper Vs (m/s)**	**Vs (m/s)**	**Lower Vs (m/s)**	**R^2**	**Std Error**
500	Geophone	Geophone	72.4	70.3	68.3	0.9965	0.0884
500	Geophone	Geophone	71.7	70.0	68.5	0.9979	0.0695
500	Geophone	Geophone	82.2	80.4	78.7	0.9980	0.0583
750	Geophone	Geophone	74.6	72.1	69.7	0.9952	0.1013
750	Geophone	Geophone	74.8	72.3	70.0	0.9956	0.0966
750	Geophone	Geophone	82.2	80.1	78.2	0.9975	0.0665
1000	Geophone	Geophone	71.7	69.5	67.4	0.9960	0.0956
1000	Geophone	Geophone	71.7	69.0	66.5	0.9943	0.1161
1000	Geophone	Geophone	81.9	79.6	77.5	0.9969	0.0739
1250	Geophone	Geophone	70.2	68.1	66.1	0.9964	0.0929
1250	Geophone	Geophone	72.4	69.8	67.3	0.9946	0.1113
1250	Geophone	Geophone	81.2	79.4	77.7	0.9980	0.0598
Attenuation Determination							
Frequency (Hz)	**Source**	**Receiver**	**Upper Att. (dB/m)**	**Att. (dB/m)**	**Lower Att. (dB/m)**	**R^2**	**Std Error**
500	Geophone	Geophone	35.2	27.8	20.4	0.7765	1.5705
500	Geophone	Geophone	29.8	23.6	17.3	0.7791	1.3227
500	Geophone	Geophone	15.4	8.4	1.3	0.2550	1.5066
750	Geophone	Geophone	45.9	39.9	33.9	0.9163	1.2706
750	Geophone	Geophone	44.5	39.6	34.6	0.9389	1.0634
750	Geophone	Geophone	23.2	16.1	8.9	0.9712	0.5009
1000	Geophone	Geophone	52.6	44.4	36.2	0.8769	1.7529
1000	Geophone	Geophone	64.1	53.8	43.6	0.8715	2.1790
1000	Geophone	Geophone	29.7	25.0	20.3	0.9454	0.6402
1250	Geophone	Geophone	62.4	57.6	52.8	0.9728	1.0157
1250	Geophone	Geophone	61.7	55.8	49.9	0.9560	1.2627
1250	Geophone	Geophone	38.3	34.3	30.4	0.9488	0.8405
NCPA – Shear Wave Analysis							
Phase Velocity Determination							
Frequency (Hz)	**Source**	**Receiver**	**Upper Vs (m/s)**	**Vs (m/s)**	**Lower Vs (m/s)**	**R^2**	**Std Error**
500	Geophone	Geophone	81.8	74.1	67.8	0.9652	0.2698
750	Geophone	Geophone	79.5	73.0	67.5	0.9737	0.2371
1000	Geophone	Geophone	79.4	73.6	68.5	0.9793	0.2129
1250	Geophone	Geophone	77.7	72.6	68.1	0.9826	0.1934
Attenuation Determination							
Frequency (Hz)	**Source**	**Receiver**	**Upper Att. (dB/m)**	**Att. (dB/m)**	**Lower Att. (dB/m)**	**R^2**	**Std Error**
500	Geophone	Geophone	15.6	8.3	1.0	0.2429	1.5477
750	Geophone	Geophone	19.6	14.3	10.3	0.7198	0.9822
1000	Geophone	Geophone	34.5	28.3	22.0	0.8328	1.3343
1250	Geophone	Geophone	40.1	33.7	26.5	0.8455	1.5165

Table 6-16. Summary of the Result of first series of shear wave experiment in the OU Indoor Tank and data taken at NCPA.

6.1.3 Mechanical Shaker Measurements

6.1.3.1 Shaker Directivity

As described in Chapter 5, before any of the shaker measurements could be analysed the directivity of the shaker needed to be calculated. This would then confirm whether the shaker was acting like a point source and if the amplitude measurements required any correction for spherical spreading.

Measurements were taken in the water tank at 3000Hz (this equates to 500Hz in the sand) and the results of the experiments can be seen in Figure 6-31 and Figure 6-32. Figure 6-31 shows the directivity pattern for the shaker at 3000Hz, whilst Figure 6-32 shows the amplitude recorded at the hydrophone positions normal to the shaker. Also shown in Figure 6-32 are the predicted values of amplitude for a point source.

Figure 6-33 and Figure 6-34 show the results of the experiment using a source signal of 4500Hz (this equates to 750Hz in the sand).

It can be seen from Figure 6-31 and Figure 6-33 that the source shows a reasonable approximation to a point source with the presence of spherical wave fronts clearly seen up to about 6-8cm. Consequently, it can be assumed that the mechanical shaker is acting as a point source at the frequencies used and therefore the vertical component geophone amplitude data should be corrected for the effect of spherical spreading.

The result can be seen in more clearly in Figure 6-32 and Figure 6-34, which shows the measured amplitude normal to the shaker and the predicted values of amplitude assuming 1/r attenuation. Although the fit is not exact, a reasonable agreement between the measured and predicted values can be seen. The agreement is superior at higher frequencies.

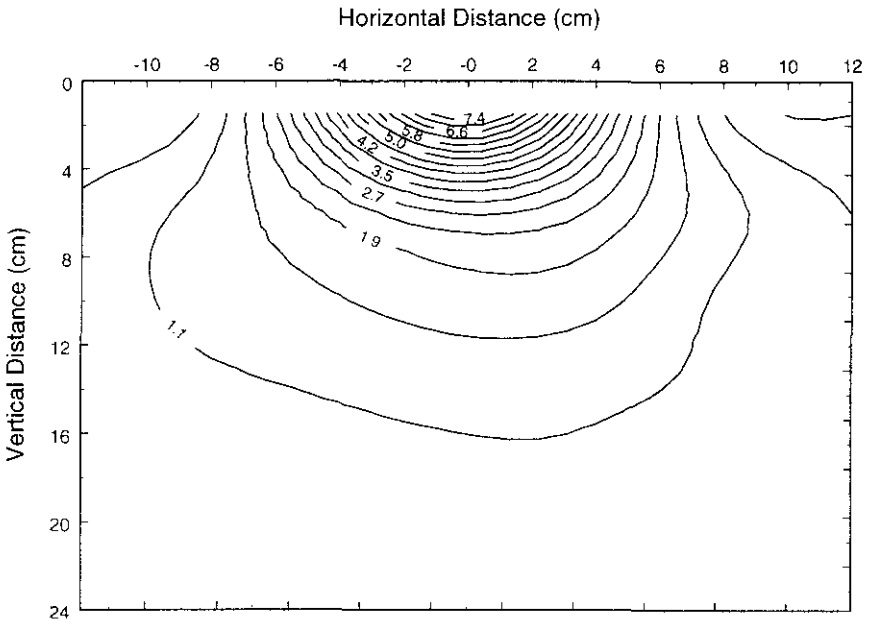

Figure 6-31. Directivity pattern of the mechanical shaker at 3000Hz.

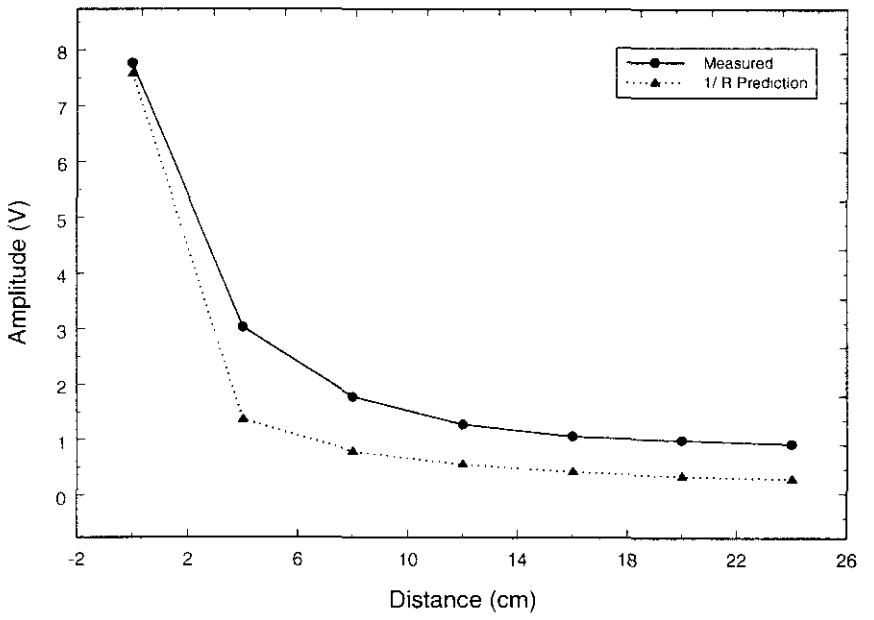

Figure 6-32. Amplitude against distance normal to the shaker. A plot of predicted 1/R amplitude is shown. Measurements taken at 3000Hz.

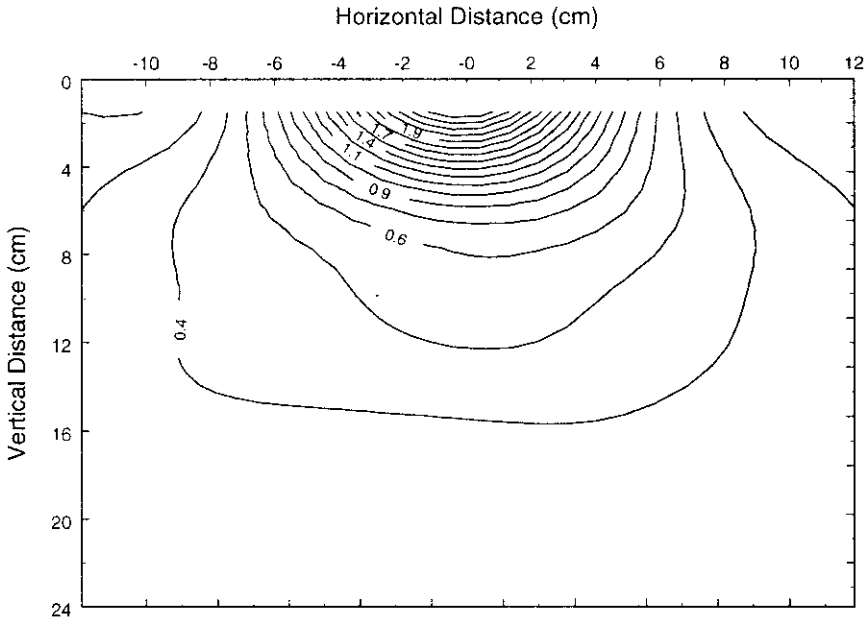

Figure 6-33. Directivity pattern of the mechanical shaker at 4500kHz.

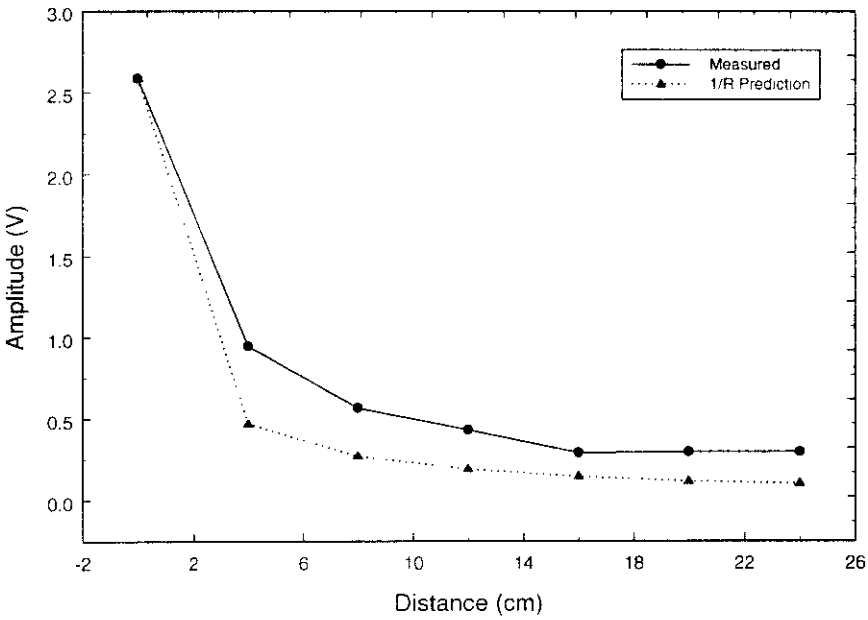

Figure 6-34. Amplitude against distance normal to the shaker. A plot of predicted 1/R amplitude is shown. Measurements taken at 4500kHz.

6.1.3.2 Measurements

The mechanical shaker was used for the measurement of the Type I P-wave. It was assumed that since the mechanical shaker was in direct contact with the material surface it would produce preferential excitement of the type I P-wave. The technique has been outlined in Section 5.1.1.3 of Chapter 5. As described in this section three sequences of experiments were undertaken in order to test the repeatability of the techniques.

Figure 6-35 shows the travel time versus receiver depth for the first sequence of experiments. Here, a source signal of 500Hz is shown. The plot shows the repeatability of the procedure showing wave velocities of 249.1, 261.3 and 268.7, although some scatter is seen in *Run 1* of the sequence. The time offset between frequencies is a consequence of taking measurements between the electronic trigger and the second peak of the tone burst.

The travel times versus offset between many source/receiver combinations over a range of frequencies are shown in Figure 6-36. Linear regression was carried out upon the time of flight of data with the resulting line superimposed in the data. A summary of the phase velocities for *Run 1* is presented in Table 6-17. The wave velocity is approximately 246m/s and shows no variation with frequency other than that due to experimental error.

Figure 6-37 shows the plots of the vertical component geophone voltage amplitude against receiver depth for the three runs. The data exhibits a high degree of scatter between subsequent experiments. The voltage amplitude has been corrected for spherical spreading, and an attempt has been made to correct for the differing sensitivities of the upper five geophones and the lower five geophones. The scatter in the data might be attributed to the variation in coupling of the geophones or to non-uniformity of the sand pack, but is most likely to be some factor due to the sensitivity.

The scatter may also be due to the fact that the shaker needs to be moved between columns of receivers, thus changing the coupling to the material. It can be seen that the attenuation decreases with increasing frequency, although the scatter in the data makes this hypothesis uncertain.

It seems likely, however, that in a similar manner to the loudspeaker source, the shaker is producing some resonances in the tank, which result in false wave amplitudes being recorded by the geophones. The tank was designed with sloping sides in the hope of minimising this problem. However, this didn't seem to work.

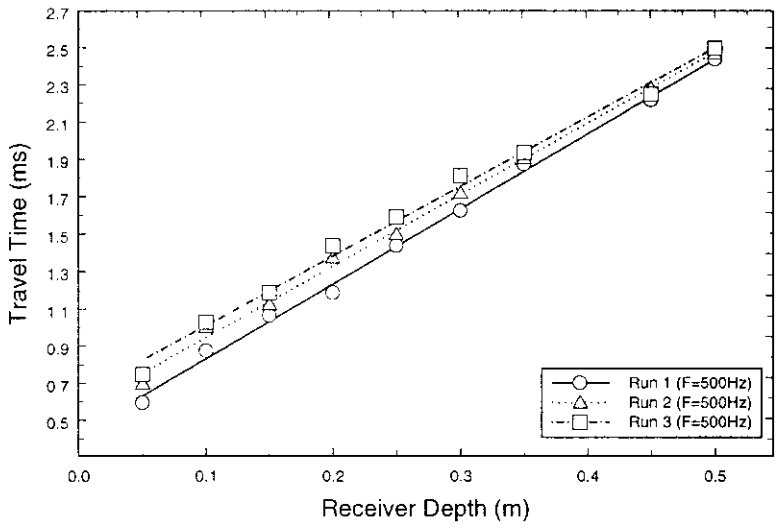

Figure 6-35. Travel time versus vertical component geophone depth for a source signal of 500Hz. Best-fit linear regressions are superimposed onto the data.

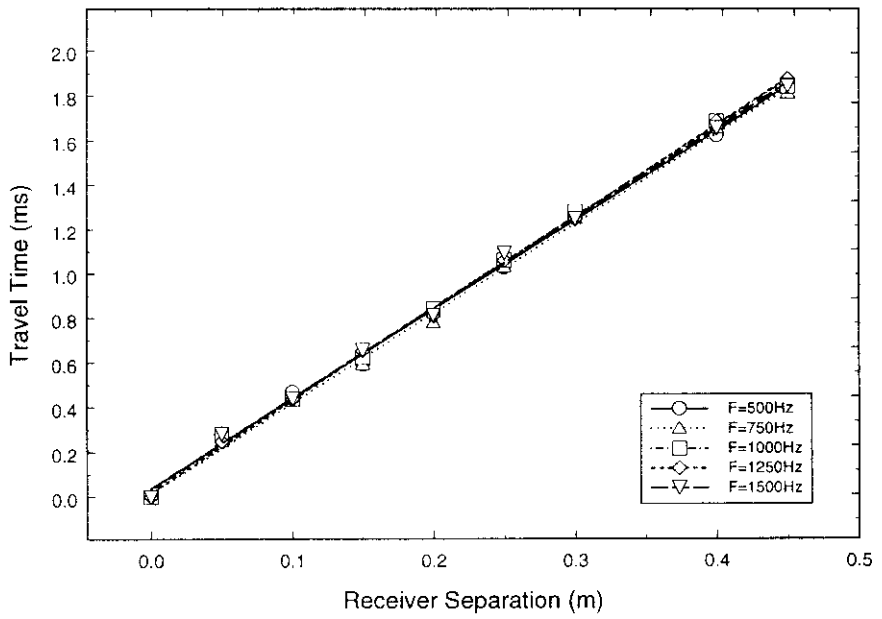

Figure 6-36. Run 1. Transit time versus vertical component geophone separation for varying source frequencies. Best-fit linear regressions are superimposed onto the data.

Frequency (Hz)	Phase velocity (m/s)	Attenuation (dB/m)	Attenuation (dB/m) (Top 5)	K_{ud} (Pa)	K_{ud} (elastic) (Pa)
500	249.1±12.1	6.8±7.9	17.6±26.8	$10.4\times10^{7}\pm 3.19\times10^{7}$	$9.04\times10^{7}\pm 9.41\times10^{6}$
750	247.4±9.9	-1.4±10.6	16.7±4.6	$10.1\times10^{7}\pm 9.96\times10^{6}$	$8.85\times10^{7}\pm 8.19\times10^{6}$
1000	244.4±9.3	-10.4±10.6	5.9±15.8	$9.74\times10^{7}\pm 8.90\times10^{6}$	$8.69\times10^{7}\pm 7.21\times10^{6}$
1250	241.8±6.6	-14.7±12.6	8.0±17.3	$9.54\times10^{7}\pm 6.06\times10^{5}$	$8.52\times10^{7}\pm 4.64\times10^{5}$
1500	247.3±10.7	-18.3±11.3	0.8±17.2	$9.97\times10^{7}\pm 9.32\times10^{6}$	$8.84\times10^{7}\pm 8.02\times10^{6}$

Table 6-17. Measured values of phase velocity and attenuation using the pulse transmission technique with vertical component geophone receivers. Also, the values of the material bulk modulus obtained by inversion.

Figure 6-38 shows the same three test runs, however, this time linear regression was only undertaken on the upper receivers. This plot shows some degree of repeatability between the experiments, showing that the scatter in the data is most likely due to in-situ geophone sensitivity.

Figure 6-39 shows the data from *Run 1* showing the results of wave attenuation over the frequency range of the experiment. Again, large scatter in the data makes analysis difficult. In a similar manner to Figure 6-38, Figure 6-40 shows the linear regression data for the upper geophones. This shows a decrease in attenuation with increasing frequency although due to the high degree of scatter in the data such a trend is suspect.

Since it is assumed that the shaker produced primarily Type-I P-wave energy, a calculation for bulk modulus can be made. Table 6-17 shows the calculations of the material bulk modulus using two approaches. The first approach is to use the $Re(k_b^2)$ method as outlined in Chapter 2. The second approach neglects the attenuation $(Im(k_b))$ and inverts directly using the phase velocity.

The approach using $Re(k_b^2)$ produces consistently larger values of K_{ud} with the differences larger at lower frequencies. The attenuation $(Im(k_b))$ is significant when compared to $Re(k_b)$ and reduced the measured value of $Re(k_b^2)$. However, since the measured attenuations are suspect, so this trend may also be suspect.

However, all the values of K_{ud} obtained by the two inversion schemes shown in Table 6-17 are within an order of magnitude.

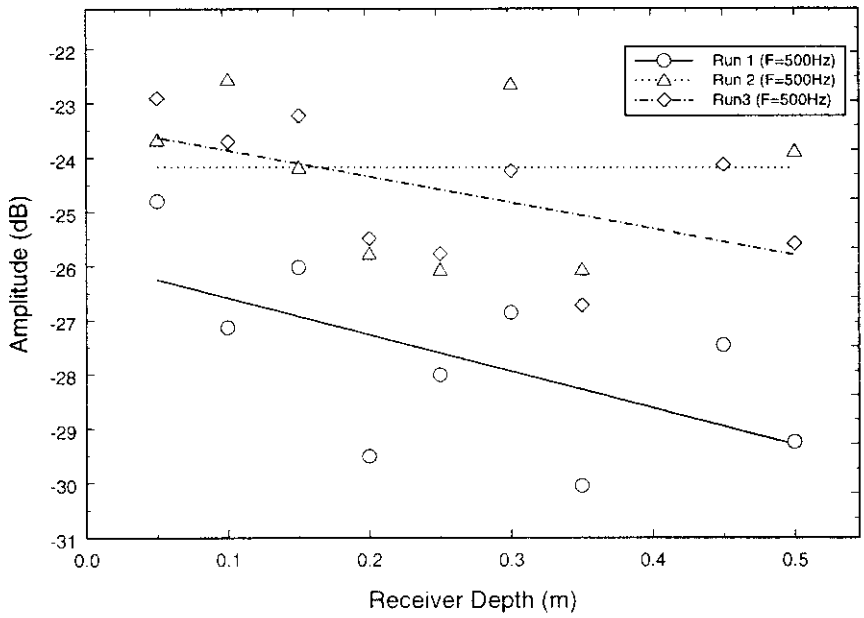

Figure 6-37. Vertical component geophone amplitude versus receiver depth for a source signal of 500Hz. Best-fit linear regressions for all geophones are shown.

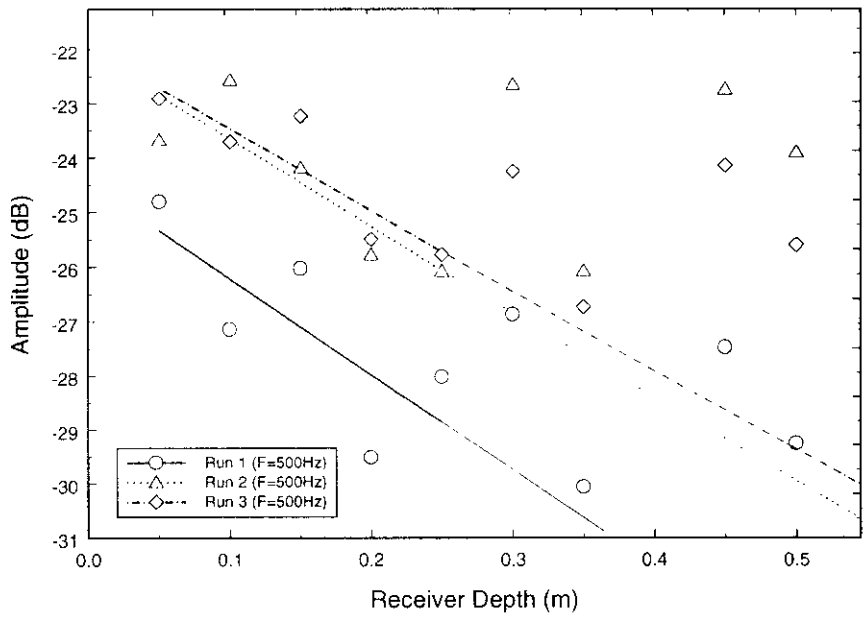

Figure 6-38. As above, except Best-fit linear regressions are shown for the top 5 geophones only.

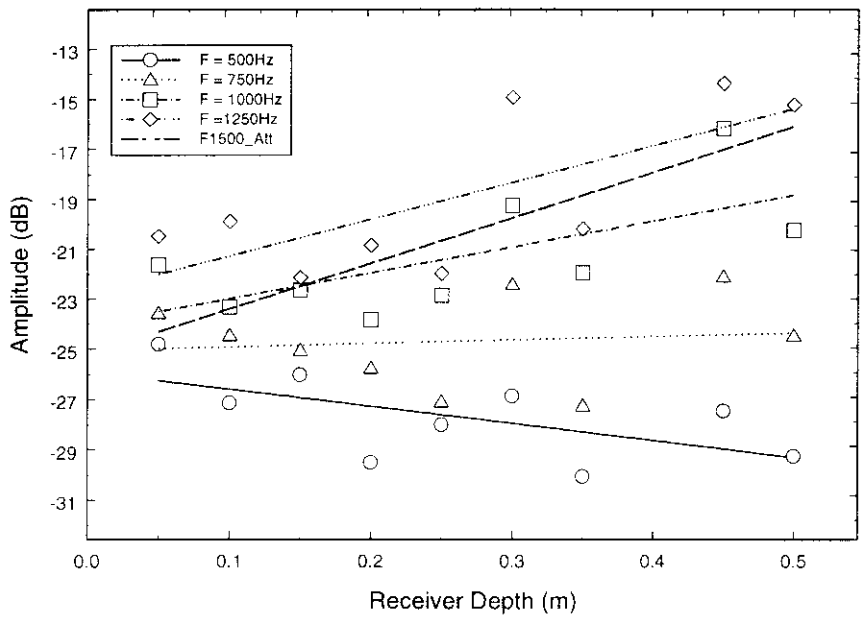

Figure 6-39. Vertical component geophone amplitude versus receiver depth for varying source frequencies. Best-fit linear regressions for all geophones are shown.

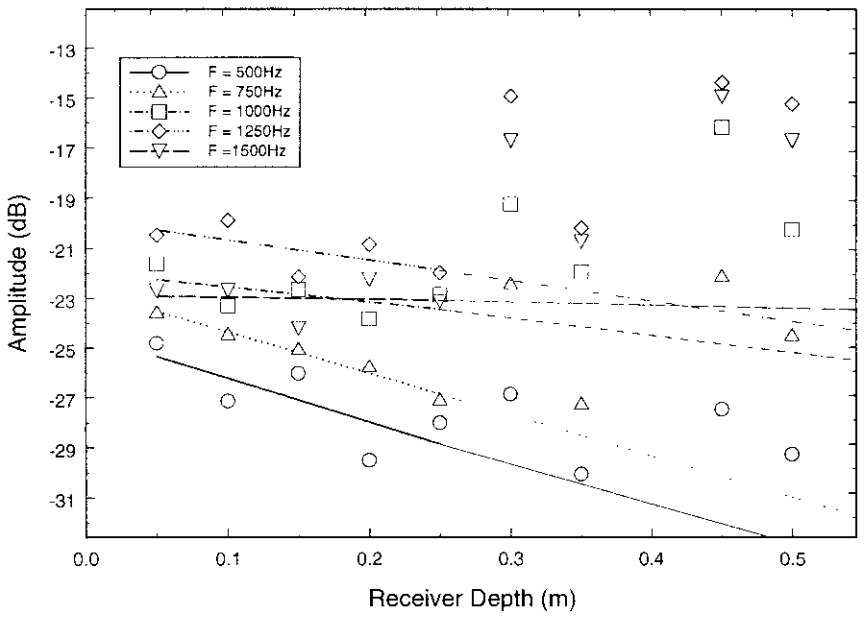

Figure 6-40. As above, except Best-fit linear regressions are shown for the top 5 geophones only.

As well as the vertical component geophones, in-situ microphones were used to receive the signal from the mechanical shaker, the results from which can be seen in Table 6-18.

Frequency (Hz)	Phase velocity (m/s)	Attenuation (dB/m)
500	221.4±14.4	18.2±8.8
750	216.9±9.5	1.3±10.0
1000	224.9±10.2	-0.8±10.6
1250	221.1±10.9	0±7.7
1500	222.1±10.0	1.7±9.3

Table 6-18. Measured values of wave velocity and wave attenuation using the pulse transmission technique with in-situ microphone receivers.

Figure 6-41 shows measured travel time versus in-situ microphone depth for a source signal of 500Hz. Best-fit linear regressions are superimposed onto the data. The results show a reasonable reproducibility with calculated phase velocities of 221.4, 214.2 and 214.8m/s. The lower phase velocities measured by the microphones, makes the assumption that the shaker produces predominantly type-I P-wave energy suspect. Therefore, bulk modulus was not calculated using the in-situ microphone data.

The travel times versus offset between many source/receiver combinations over a range of frequencies are shown in Figure 6-42. Linear regression was carried out upon the time of flight of data with the resulting line superimposed in the data. A summary of the phase velocities for *Run 1* are presented in Table 6-18. The wave velocity is approximately 221m/s and shows a slight increase with frequency, although this trend may be due simply to experimental error.

Figure 6-43 shows the plots of the in-situ microphone voltage amplitude against receiver depth for the three runs. This shows that there is little repeatability between the experiments. The voltage amplitude has been corrected for spherical spreading, although the recorded amplitude has not been corrected for the sensitivity of the microphone as a receiver. The probable causes of the scatter in the data have been discussed previously.

The results of the in-situ microphone voltage amplitude against receiver depth for varying source frequencies can be seen in Figure 6-44. This again shows the large amount of scatter in the microphone amplitude data which can also be seen the calculated values of attenuation shown in Table 6-18.

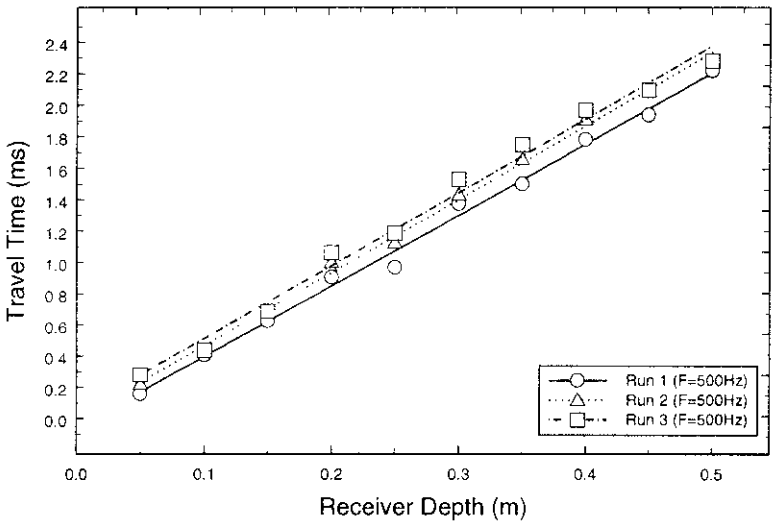

Figure 6-41. Travel time versus in-situ microphone depth for a source signal of 500Hz. Best-fit linear regressions are superimposed onto the data.

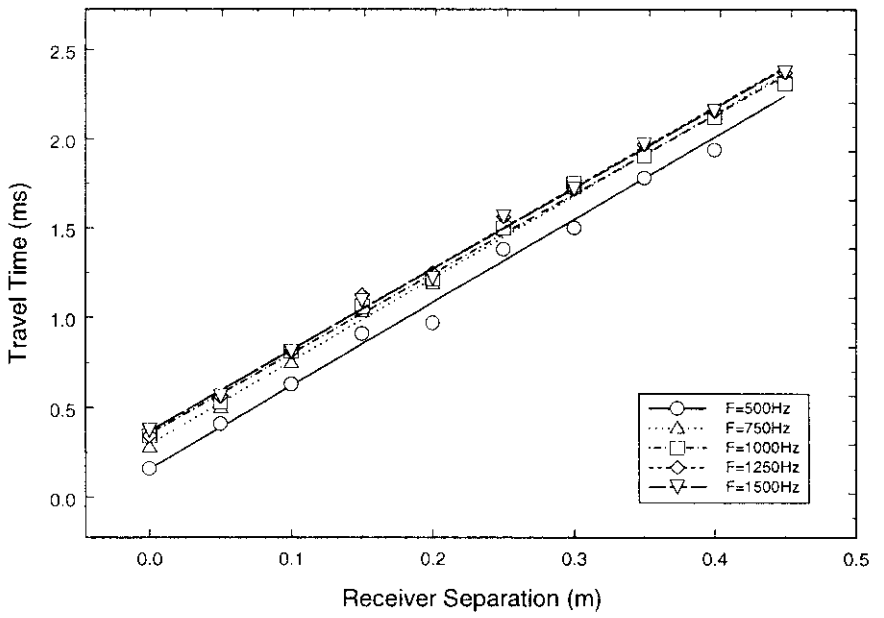

Figure 6-42. Run 1. Transit time versus in-situ microphone separation for varying source frequencies. Best-fit linear regressions are superimposed onto the data.

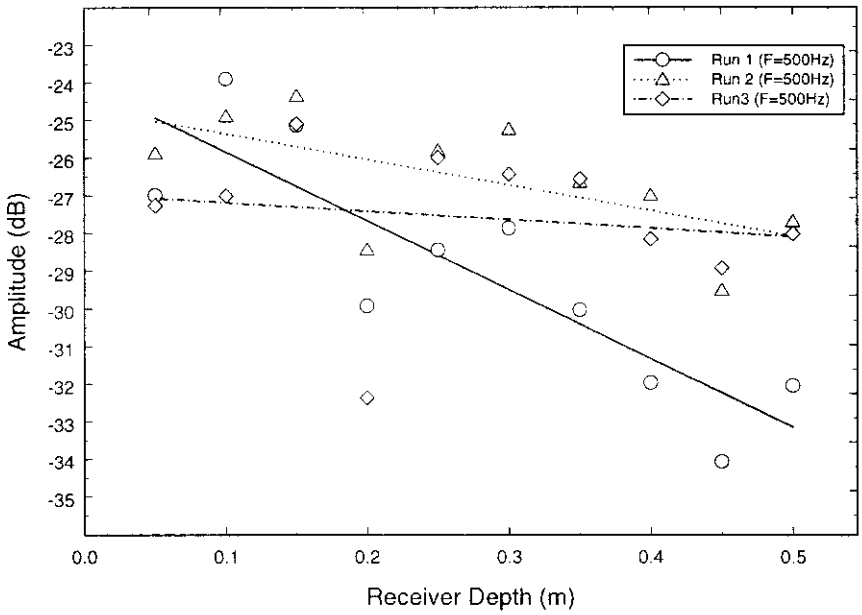

Figure 6-43. In-situ microphone amplitude versus receiver depth for a source signal of 500Hz. Best-fit linear regressions are superimposed on the data.

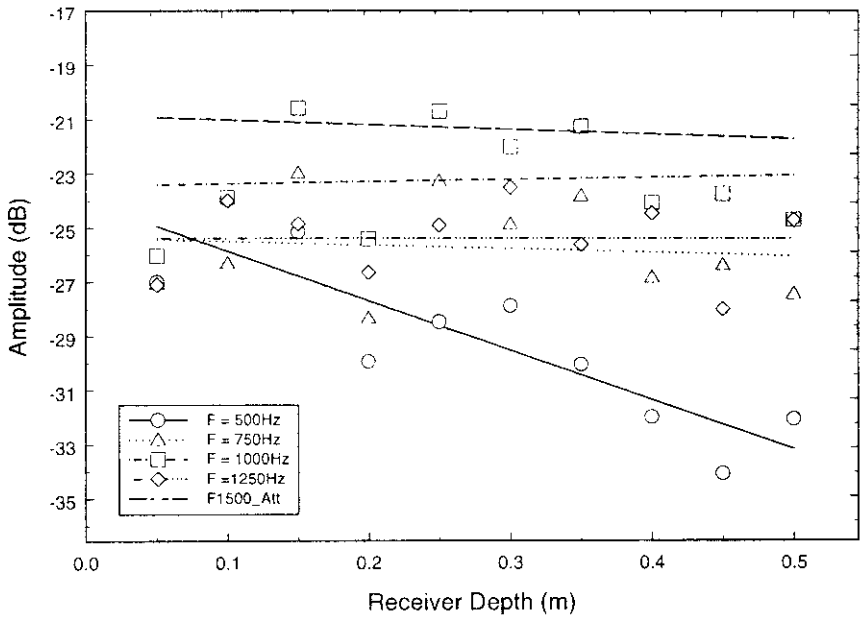

Figure 6-44. In-situ microphone amplitude versus receiver depth for varying source frequencies.

Table 6-20 and Table 6-21 show a summary of the complete set of experiments taken with the mechanical shaker. The tables show the calculated phase velocity for each frequency and calculated attenuation together with the upper and lower limits set by the linear regression (using a 95% confidence limit). The table also shows the R^2 value and standard error of the linear regression.

The time of flight data taken with the mechanical shaker at NCPA can be seen in Figure 6-45, which shows geophone data, whilst Figure 6-46 shows the microphone data.

The data shows that the P-wave velocity measured using the geophones is approximately 159m/s, whilst it is approximately 167m/s measured using the microphones. Both plots show there is no variation in phase velocity with frequency.

Figure 6-47 and Figure 6-48 show voltage amplitude versus receiver depth for the vertical component geophones and in-situ microphones respectively. It can be seen that there is a large amount of scatter in the geophone data, though the microphone data appears more reliable. The results from the microphone data suggest that attenuation appears to decrease with increasing frequency, although the scatter in the data may make this assumption suspect.

A summary of the data taken at NCPA using the mechanical shaker can be seen in Table 6-19.

P-Wave Velocity Determination Using Mechanical Shaker Source						
Frequency	**Receiver**	**Upper Vel**	**Vel**	**Lower Vel**	**R^2**	**Std Error**
500	Geophone	176.2	**166.5**	157.9	0.9955	0.065
500	Microphone	180.9	**172.0**	164.0	0.9964	0.056
750	Geophone	169.3	**158.0**	148.2	0.9934	0.083
750	Microphone	180.2	**170.4**	161.6	0.0000	0.000
1000	Geophone	164.3	**158.0**	152.1	0.9978	0.048
1000	Microphone	172.9	**166.2**	160.0	0.9977	0.046
1500	Geophone	158.9	**152.8**	147.1	0.9978	0.050
1500	Microphone	169.4	**159.6**	150.9	0.9950	0.071
P-Wave Attenuation(dB/m) Determination Using Mechanical Shaker Source						
Frequency	**Receiver**	**Upper Att**	**Att**	**Lower Att**	**R^2**	**Std Error**
500	Geophone	11.0	**5.1**	-0.8	0.3326	1.1632
500	Microphone	61.2	**41.5**	21.7	0.7455	3.8924
750	Geophone	9.7	**3.9**	-2.0	0.2241	1.1512
750	Microphone	56.6	**36.6**	16.5	0.0000	0.0000
1000	Geophone	4.8	**-2.2**	-9.1	0.0612	1.3685
1000	Microphone	51.1	**32.8**	14.4	0.6794	3.6161
1500	Geophone	-0.1	**-15.1**	-30.1	0.6772	2.0712
1500	Microphone	49.8	**29.6**	9.4	0.5873	3.9846

Table 6-19. Summary of mechanical shaker experiments taken at NCPA.

Phase Velocity Determination Using Mechanical Shaker Source						
Frequency	**Receiver**	**Upper Vel**	**Vel**	**Lower Vel**	**R^2**	**Std Error**
500	Geophone	261.2	**249.1**	238.0	0.9973	0.0342
500	Geophone	275.3	**261.3**	248.7	0.9968	0.0358
500	Geophone	289.6	**268.7**	250.6	0.9935	0.0494
500	Microphone	235.8	**221.4**	208.7	0.9944	0.0544
500	Microphone	224.1	**214.2**	205.2	0.9971	0.0405
500	Microphone	233.7	**214.8**	198.7	0.9902	0.0742
750	Geophone	257.3	**247.4**	238.2	0.9981	0.0286
750	Geophone	274.8	**258.2**	243.5	0.9955	0.0430
750	Geophone	266.1	**256.9**	248.3	0.9985	0.0247
750	Microphone	226.4	**216.9**	208.2	0.9974	0.0380
750	Microphone	229.5	**219.6**	210.6	0.9972	0.0386
750	Microphone	231.4	**218.9**	207.7	0.9956	0.0485
1000	Geophone	253.7	**244.4**	235.7	0.9983	0.0277
1000	Geophone	255.7	**247.8**	240.4	0.9988	0.0229
1000	Geophone	271.3	**253.8**	238.4	0.9948	0.0467
1000	Microphone	235.1	**224.9**	215.5	0.9972	0.0380
1000	Microphone	227.3	**218.7**	210.7	0.9979	0.0340
1000	Microphone	231.7	**221.4**	212.1	0.9971	0.0393
1250	Geophone	248.4	**241.8**	235.6	0.9991	0.0200
1250	Geophone	250.7	**241.0**	232.1	0.9981	0.0294
1250	Geophone	270.1	**257.2**	245.4	0.9971	0.0343
1250	Microphone	232.0	**221.1**	211.2	0.9967	0.0418
1250	Microphone	228.3	**220.0**	212.3	0.9980	0.0326
1250	Microphone	234.2	**225.5**	217.3	0.9979	0.0327
1500	Geophone	258.0	**247.3**	237.4	0.9978	0.0310
1500	Geophone	250.8	**241.4**	232.7	0.9982	0.0286
1500	Geophone	256.6	**250.3**	244.2	0.9992	0.0182
1500	Microphone	232.1	**222.1**	212.8	0.9972	0.0385
1500	Microphone	228.1	**219.6**	211.7	0.9979	0.0335
1500	Microphone	238.3	**229.6**	221.5	0.9980	0.0313

Table 6-20. Summary of phase velocity determination using mechanical shaker source. Results are for vertical component geophones and in-situ microphones.

Wave Attenuation(dB/m) Determination Using Mechanical Shaker Source						
Frequency	**Receiver**	**Upper Att**	**Att**	**Lower Att**	**R^2**	**Std Error**
500	Geophone	14.7	**6.8**	-1.2	0.3662	1.462
500	Geophone	8.6	**0.1**	****	0.0001	1.563
500	Geophone	11.0	**4.8**	-1.4	0.3259	1.141
500	Microphone	27.0	**18.2**	****	0.7446	1.716
500	Microphone	13.7	**6.8**	-0.1	0.9712	0.698
500	Microphone	13.0	**2.2**	****	0.0283	2.111
750	Geophone	9.2	**-1.4**	****	0.0132	1.944
750	Geophone	3.4	****	****	0.0684	1.748
750	Geophone	6.6	**-2.9**	****	0.0684	1.748
750	Microphone	11.3	**1.3**	****	0.0113	1.966
750	Microphone	7.8	**-0.7**	****	0.0044	1.678
750	Microphone	13.2	**1.7**	****	0.0140	2.264
1000	Geophone	0.2	****	****	0.4345	1.948
1000	Geophone	2.0	****	****	0.3505	2.053
1000	Geophone	3.3	****	****	0.2862	2.109
1000	Microphone	9.8	**-0.8**	****	0.0039	2.088
1000	Microphone	9.7	**1.3**	****	0.0150	1.652
1000	Microphone	14.4	**3.3**	****	0.0557	2.183
1250	Geophone	-2.1	****	****	0.5195	2.326
1250	Geophone	-0.4	****	****	0.4600	2.089
1250	Geophone	-1.3	****	****	0.4978	2.126
1250	Microphone	7.7	**0.0**	****	2E-07	1.525
1250	Microphone	11.1	**1.5**	****	0.0151	1.905
1250	Microphone	20.3	**7.3**	****	0.1765	2.547
1500	Geophone	-7.0	****	****	0.6772	2.071
1500	Geophone	-0.7	****	****	0.4771	1.845
1500	Geophone	-7.3	****	****	0.6748	2.192
1500	Microphone	11.0	**1.7**	****	0.0218	1.824
1500	Microphone	10.3	**1.8**	****	0.0278	1.676
1500	Microphone	23.5	**10.6**	-2.3	0.3097	2.540
Wave Attenuation(dB/m) Determination Using Upper Geophones						
500.0	Geophone	-44.4	**-17.6**	9.3	0.5915	1.3339
500.0	Geophone	-33.3	**-16.0**	1.3	0.7436	0.8592
500.0	Geophone	-28.5	**-15.0**	-1.6	0.8088	0.6678
750.0	Geophone	-21.3	**-16.7**	-12.1	0.9781	0.2280
750.0	Geophone	-24.3	**-11.3**	1.7	0.7482	0.8479
750	Geophone	-33.1	**-16.0**	1.1	0.7482	0.8479
1000	Geophone	-21.7	**-5.9**	9.8	0.3242	0.7827
1000	Geophone	-22.4	**-11.1**	0.1	0.7681	0.5589
1000	Geophone	-42.0	**-11.4**	19.3	0.3178	1.5224
1250	Geophone	-25.3	**-8.0**	9.3	0.4184	0.8587
1250	Geophone	-14.2	**-8.6**	-3.0	0.8892	0.2780
1250	Geophone	-30.2	**-8.4**	13.4	0.3347	1.0827
1500	Geophone	-18.0	**-0.8**	16.4	0.0075	0.8544
1500	Geophone	-13.3	**-1.1**	11.1	0.0247	0.6062
1500	Geophone	-26.7	**0.4**	27.5	0.0006	1.3462

Table 6-21. Summary of P-wave attenuation determination using mechanical shaker source. Results are for vertical component geophones and in-situ microphones.

**** indicates where a positive value for attenuation was measured

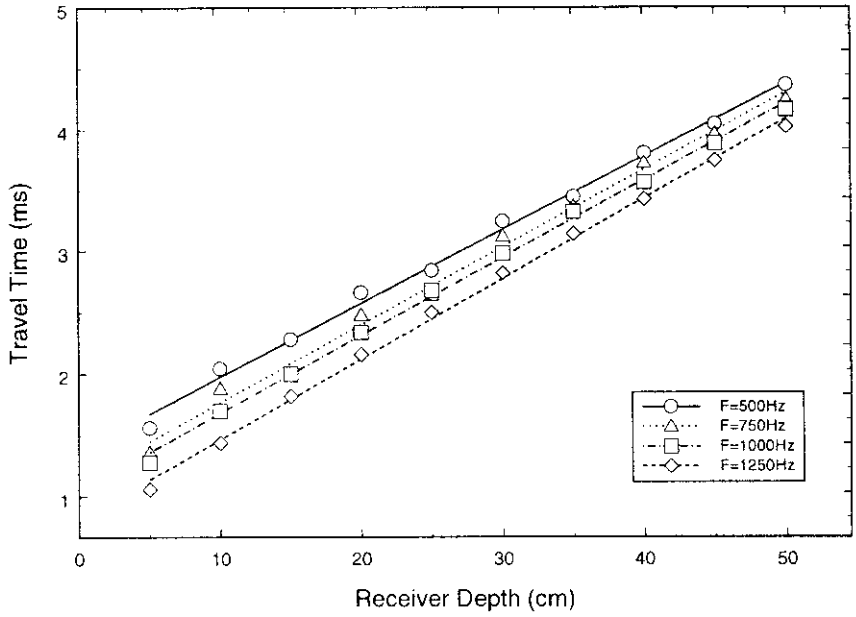

Figure 6-45. Transit time versus vertical component geophone depth for varying source frequencies. Best-fit linear regressions are superimposed onto the data.

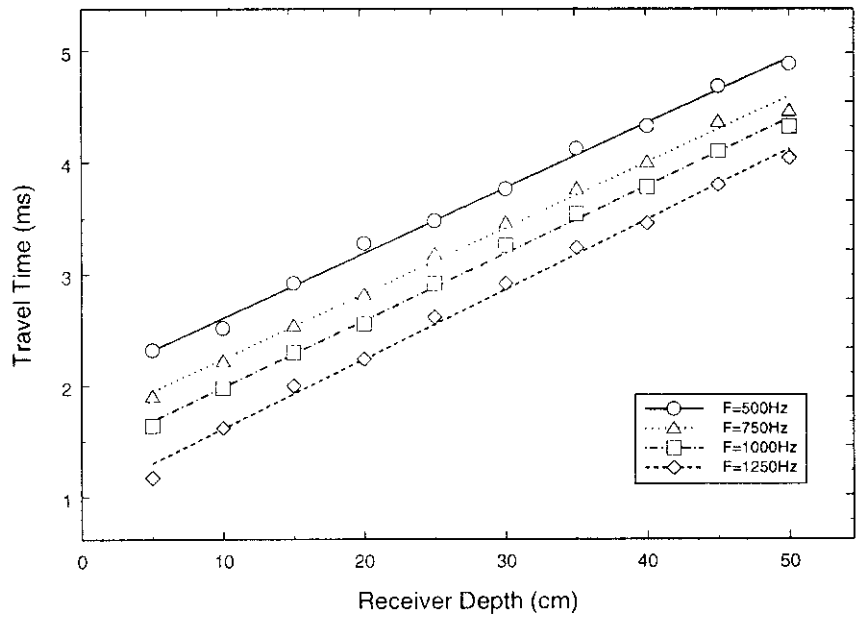

Figure 6-46. Transit time versus in-situ microphone depth for varying source frequencies. Best-fit linear regressions are superimposed onto the data.

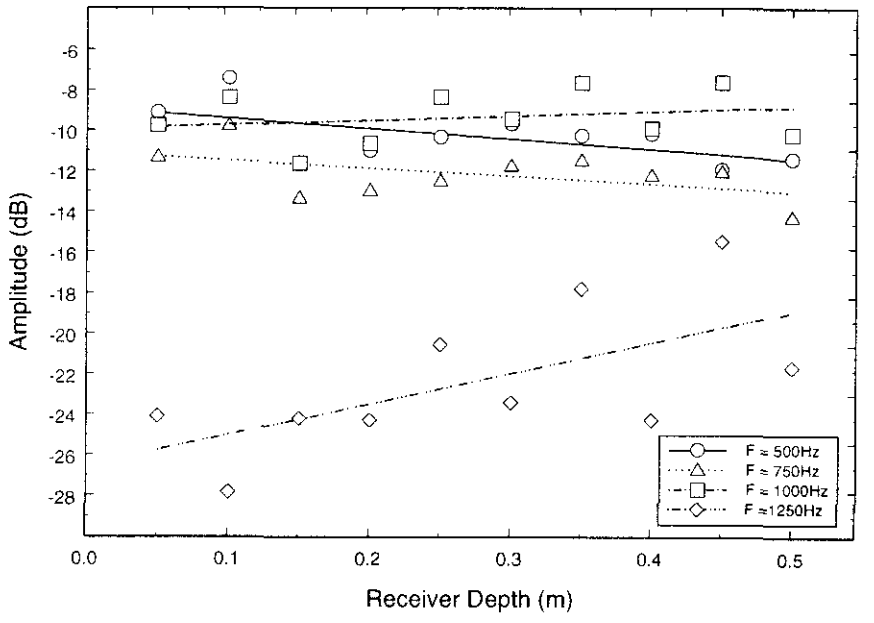

Figure 6-47. Vertical component geophone amplitude versus receiver depth for varying source frequencies.

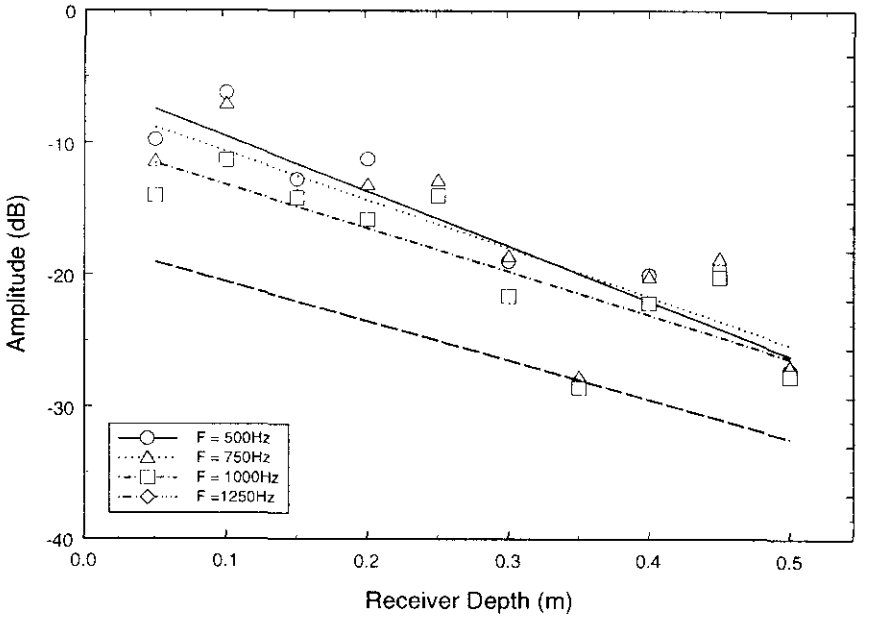

Figure 6-48. In-situ microphone amplitude versus receiver depth for varying source frequencies.

From the calculated phase velocities in the loam it appears that both the geophones and microphones are excited by the type I P-wave. As such, it was possible to calculate the bulk modulus of the material using the inversion techniques described previously. However, again, with the attenuation data from the geophones showing large scatter, no attempt was made to calculate K_{ud} using the $Re(k_b^2)$ method. The results can be seen in Table 6-22.

Frequency (Hz)	Geophone	Microphone	
	K_{ud} (elastic) (Pa)	K_{ud} (Pa)	K_{ud} (elastic) (Pa)
500Hz	$2.71 \times 10^7 \pm 2.29 \times 10^6$	$3.93 \times 10^7 \pm 9.52 \times 10^6$	$2.96 \times 10^7 \pm 2.05 \times 10^6$
750Hz	$2.37 \times 10^7 \pm 3.16 \times 10^6$	$3.38 \times 10^7 \pm 6.44 \times 10^6$	$2.91 \times 10^7 \pm 2.81 \times 10^6$
1000Hz	$2.36 \times 10^7 \pm 1.13 \times 10^6$	$3.35 \times 10^7 \pm 3.26 \times 10^6$	$2.71 \times 10^7 \pm 1.45 \times 10^6$
1500Hz	$2.17 \times 10^7 \pm 1.17 \times 10^6$	$3.11 \times 10^7 \pm 2.85 \times 10^6$	$2.45 \times 10^7 \pm 2.92 \times 10^6$

Table 6-22. Calculated values of the bulk modulus of the NCPA material.

It can be seen from the data taken in the Indoor Tank at the Open University, that the microphones exhibit a slower phase velocity than that calculated from the vertical component geophones for the same frequency. Figure 6-49 shows the travel times for both the geophones and in-situ microphones over the range of test frequencies.

The difference between the two is larger than could be attributed to experimental error alone. This difference was not seen in the data taken at NCPA, although here only 1 set of data was taken. This difference was also not observed in measurements taken by Hickey and Sabatier (1996) in a similar material to that used at the OU. Their measurements, seen in Figure 6-51, showed that since the graph shows only one slope, this was indicative of the presence of only one wave. They concluded from this that the microphone receivers were as good as geophones for the detection of the type I wave.

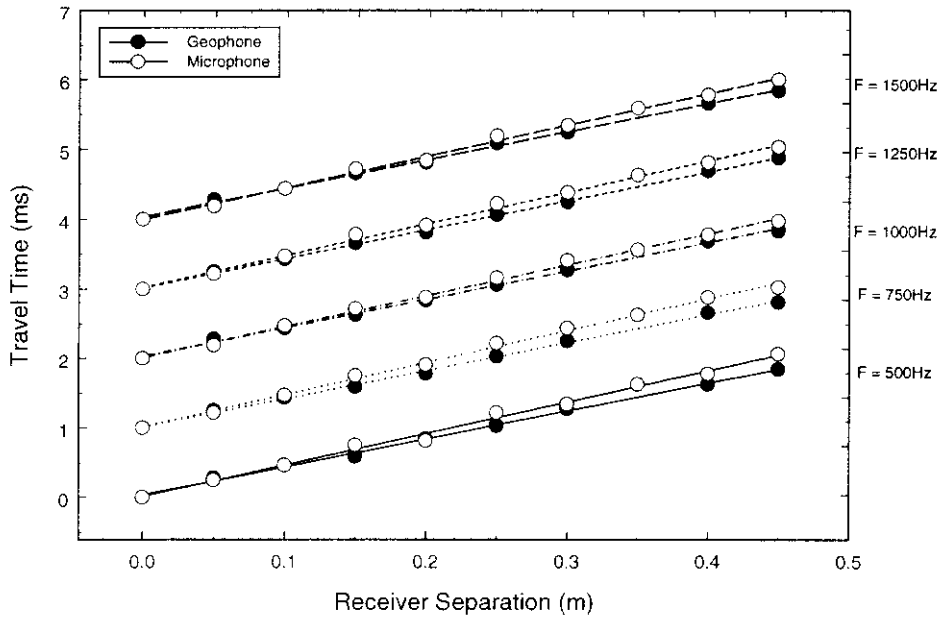

Figure 6-49. Travel time versus receiver separation measured using the geophone and in-situ microphones. Data was taken at Open University.

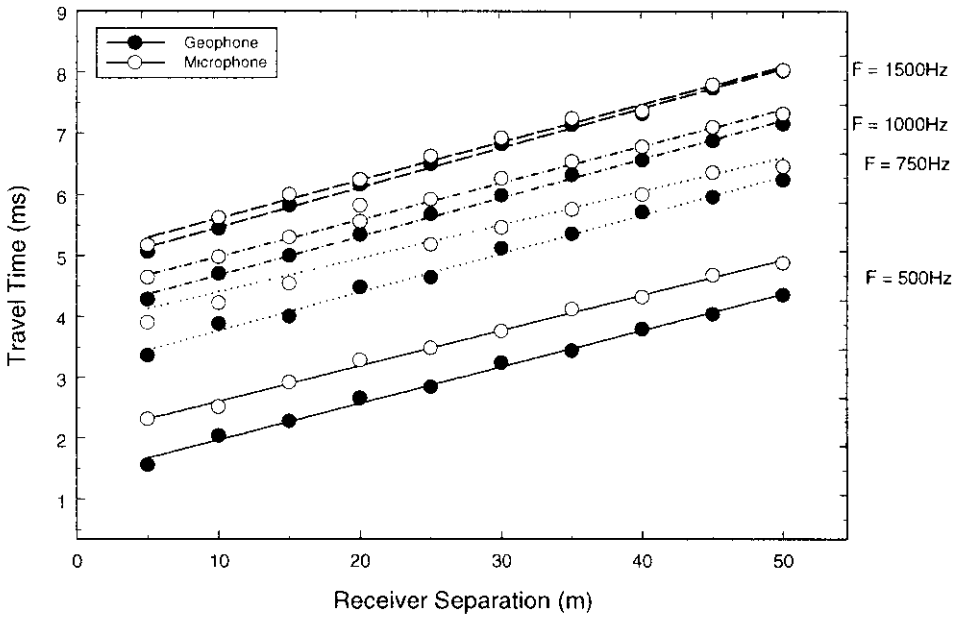

Figure 6-50. Travel time versus receiver separation measured using the geophone and in-situ microphones. Data was taken at NCPA.

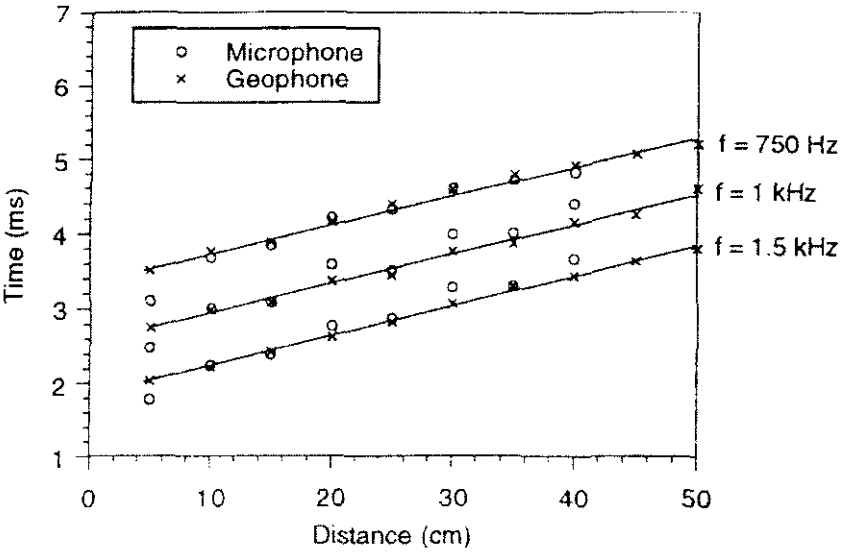

Figure 6-51. Travel-time versus receiver depth measured by pulse transmission. In-situ microphones and geophones are used as receivers (Hickey and Sabatier, 1996).

6.1.4 Comparisons with dual wave theory

Using the values for parameters measured in the above experiments, the Biot theory was used to calculate phase velocities, attenuations and ratio of solid to fluid displacement of different propagation modes. This was achieved using the "*Porovel*" computer program.

Parameter	Value	Unit
Air		
Density	1.21	Kg/m^3
Sound speed (c_0)	343	m/s
Material Properties		
Flow resistivity	17000	MKS Rayls
Porosity	0.38	
Pore shape factor	0.5	
Grain shape factor ratio	1.0	
Type I wave velocity	242	m/s
Type II wave velocity	112	m/s
Layer Depth	0.5	M
Solid grain density	2650	Kg/m^3
Frame bulk modulus	$8.0x10^7$	Pa

Table 6-23. Input parameters for the numerical predictions

The prediction for the fluid / solid displacement of the type II wave shown in Figure 6-54 is very large supporting the assumption of a rigid frame. Comparison of the predicted phase velocity shows good agreement between the measured values and the theory. However, the predicted attenuation is much smaller than that measured.

The predictions for the Type I P-wave and for the S-wave show that the predicted phase velocity shows very little dispersion and that the attenuation increases linearly with frequency.

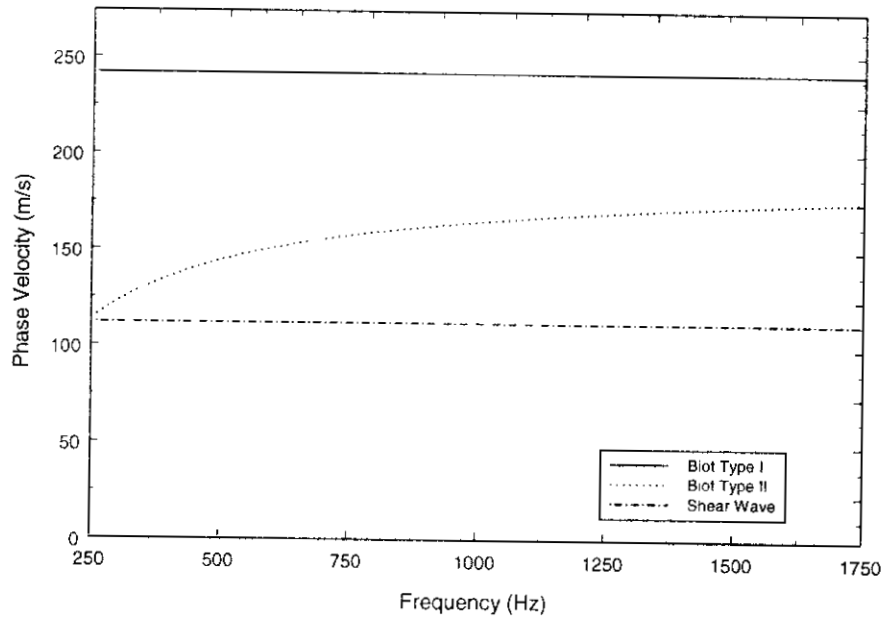

Figure 6-52. Predictions of phase velocity by the Biot theory for the three types of waves in an air filled sand.

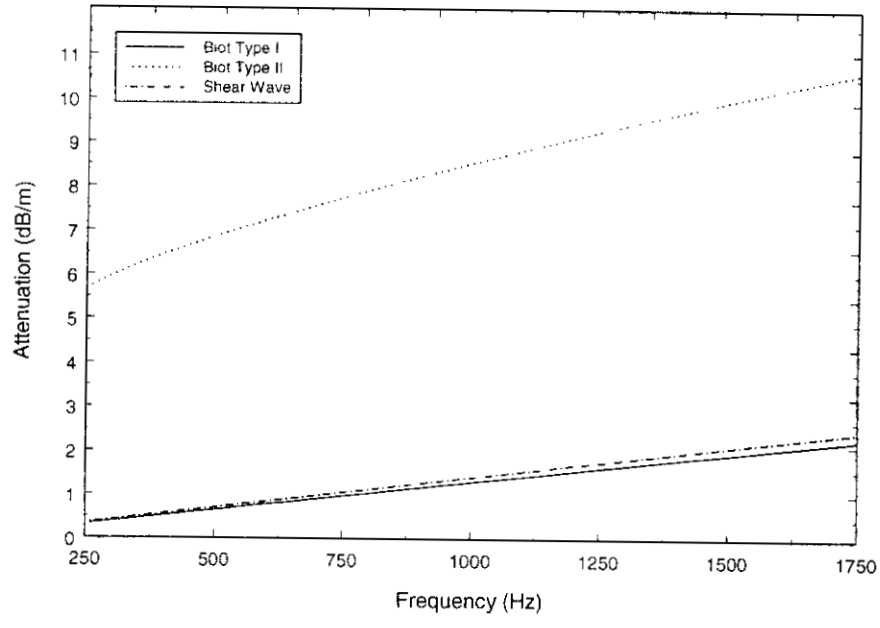

Figure 6-53. Predictions of attenuation by the Biot theory for the three types of waves in an air filled sand.

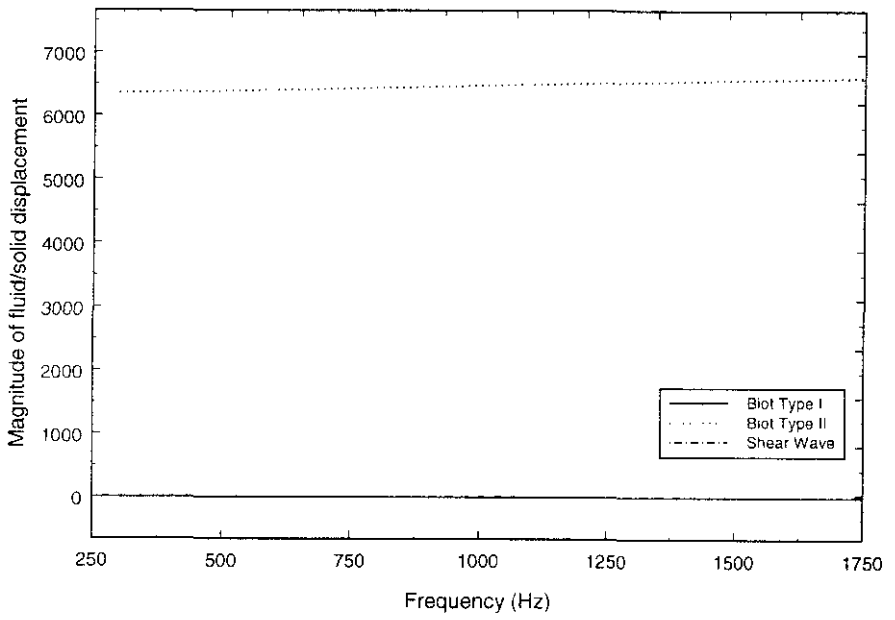

Figure 6-54. Magnitude of the fluid/solid displacement amplitude predicted by the Biot theory for the three waves in an air-filled sand.

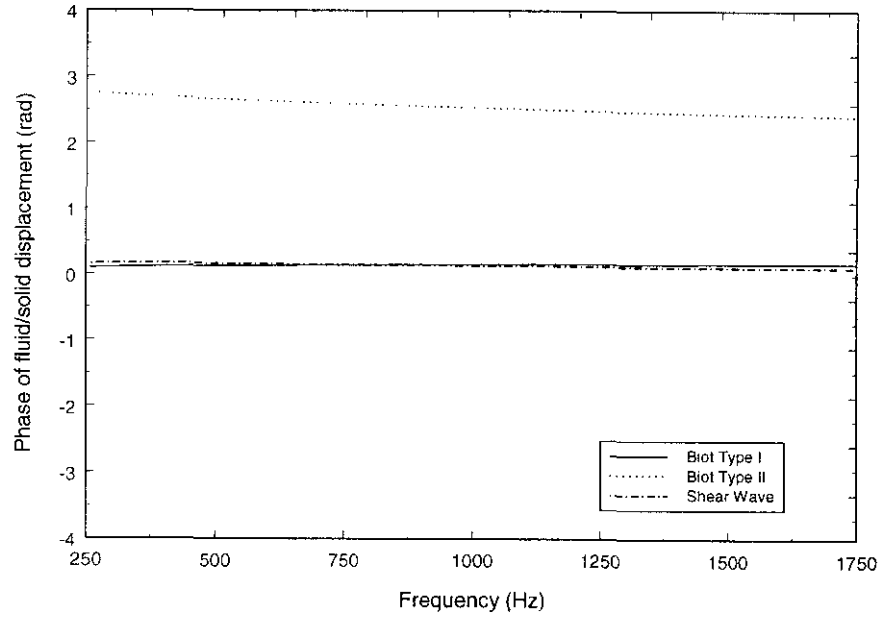

Figure 6-55. Phase of the fluid/solid displacement amplitude predicted by the Biot theory for the three waves in an air-filled sand. Phase is in radians.

6.1.5 Conclusions

Measurements have been made of the two dilatational and one shear wave predicted by porous elastic theory in an unconsolidated air-filled sand and a crushed loam. Measurements were taken using a loudspeaker source and a mechanical shaker. It was hoped that the loudspeaker would provide selective excitation of the type II P-wave and this has been shown correct.

Probe microphone measurements were obtained using an MLS signal in the sand in the frequency range 100-1500Hz and using a swept sine in the loam in a frequency range of 100-500Hz. From these measurements, values for the tortuosity and flow resistivity of the materials were determined using a rigid frame limit. A comparison of the mechanically and acoustically derived sediment properties for each of the sediments can be seen in Table 6-24.

Material	Flow Resistivity		Tortuosity	
	Flow Rig	Probe Microphone	Jackson Cell	Probe Microphone
Tank Sand	16545 ± 726	38200±3232	2.38±0.02	2.0±0.3
NCPA Loam	419855±264044	6110000	-----	-----

Table 6-24. Comparison of mechanically and acoustically derived sediment properties.

It can be seen that for the sand there is good agreement between the values derived for the tortuosity, but that agreement is poorer for the flow resistivity. However, it has been stated (Sabatier *et al.*, 1996) that the ratio of acoustically determined flow resistivity and that measured using the standard flow rig is between 2.0 and 2.3 for sands. This would give an increased accuracy in the agreement. The modifications made to the air-flow rig may alter the measured flow resistivity slightly.

However, the results for the loam soil tested at NCPA, highlight the limitations of the probe microphone in very fine materials that have a high flow resistivity. The high attenuation of the type II wave meant that tortuosity could not be calculated and the predicted value of R_s of over 6×10^6MKS Rayls is over 10 times greater than the value measured using the air flow rig.

Investigations into the angle dependence of the measurements showed that the flow resistivity and tortuosity appear independent of angle of incidence. This is in agreement with previous work (Moore and Attenborough, 1992).

Measurements using the in-situ receivers and the loudspeaker source again showed that type II P-wave is the dominant wave type in the both the solid structure and the pores, down to a depth of roughly 15cm. After which there appears a transition where the dominant energy in the solid structure is the type I P-wave. This is shown in the travel times calculated using the in-situ geophones. However, the type II energy is still present in the pores as measured using the probe microphone and in-situ microphones.

This is a markedly different result to that published previously (Hickey and Sabatier, 1996) who showed that for a fine grained sand that the type II wave was dominant down to 15-20cm after which all the receivers reacted only to the type I P-wave.

The results of the attenuation determinations showed that the microphones gave reasonable results, but that it appears that the loudspeaker was producing resonances in the soil structure which were giving false results by the geophones.

For the sand, a shear wave phase velocity of 70m/s was measured over the frequency range with an increase in attenuation seen with increasing frequency. This trend is in agreement with that shown by the predictions. Predictions of shear modulus using both theoretical techniques produced similar results. Table 6-25 shows the comparison of the mechanically and acoustically derived values of shear modulus. The resonant column data (described in Chapter 4) has been used to give a value for μ at 0.50m, since the acoustically derived values are taken as an average over this depth. The results show good agreement between the two values.

Indoor Tank		**Resonant Column (at an effective depth of 0.50m)**
Frequency (Hz)	μ_m **(Pa)**	μ_m **(Pa)**
500	$8.10\times10^6\pm5.22\times10^5$	11.85×10^6
750	$8.52\times10^6\pm6.20\times10^5$	
1000	$7.90\times10^6\pm5.21\times10^5$	
1250	$7.58\times10^6\pm4.84\times10^5$	

Table 6-25. Comparison of mechanical and acoustically derived values of shear modulus.

Similar values of s-wave velocity were measured in the NCPA loam although the measured attenuation was less. Again, predictions of shear modulus using both theoretical techniques produced similar results.

Using the mechanical shaker, a P-wave phase velocity of 252m/s was measured using the geophone over the complete frequency range and is in agreement with the predictions. The data showed a decrease in attenuation with increasing frequency. Although the scatter in the data made this trend suspect. This trend was not shown by the predictions, which show an increase in attenuation with increasing frequency.

Predictions of bulk modulus based on the "elastic" method and a limit of the dual wave theory produced slightly differing results. The dual wave limit does not incorporate the proper attenuation mechanisms and values determined for K_{ud} are larger. Predictions using the dual wave theory, together with values of K_{ud} inverted by way of the "elastic" method, produces phase velocities similar to those measured.

Indoor Tank			**Resonant Column (at an effective depth of 0.50m)**
Frequency (Hz)	**K_{ud} (Pa)**	**K_{ud} (elastic) (Pa)**	**K_{ud}**
500	$10.4\text{x}10^7 \pm 3.19\text{x}10^7$	$9.04\text{x}10^7 \pm 9.41\text{x}10^6$	$33.40\text{x}10^6$
750	$10.1\text{x}10^7 \pm 9.96\text{x}10^6$	$8.85\text{x}10^7 \pm 8.19\text{x}10^6$	
1000	$9.74\text{x}10^7 \pm 8.90\text{x}10^6$	$8.69\text{x}10^7 \pm 7.21\text{x}10^6$	
1250	$9.54\text{x}10^7 \pm 6.06\text{x}10^5$	$8.52\text{x}10^7 \pm 4.64\text{x}10^5$	
1500	$9.97\text{x}10^7 \pm 9.32\text{x}10^6$	$8.84\text{x}10^7 \pm 8.02\text{x}10^6$	

Table 6-26. Comparison of mechanical and acoustically derived values of bulk modulus.

Table 6-26 shows the comparison of the mechanically and acoustically derived values of bulk modulus. The resonant column data (described in Chapter 4) has been used to give a value for K_{ud} at 0.50m, since the acoustically derived values are taken as an average over this depth. The results show a reasonable agreement between the two values.

From the shaker results in the sand, it appears that the shaker produces primarily type-I P-wave energy as expected for this type of source. This energy is clearly measured by the in-situ geophones. However, the microphones appear to detect the type-II P-wave energy.

This pattern is opposite in the high flow resistivity loam, where the microphones produce similar results as the geophones. This may be a useful phenomenon since, in

general, microphones have a higher frequency response and can be built with smaller physical dimensions than geophones.

From the tank measurements undertaken at both the Open University and at NCPA it can be concluded that:

1) Probe microphones can be used to give estimations of soil tortuosity and flow resistivity using a rigid frame limit over a wide range of sediments. Care must be taken in very high flow resistivity materials where high type-II P-wave attenuation occurs and in fine grained materials which may block the holes in the probe end.

2) There is a need for speaker angle correction to be used in calculating the tortuosity with no correction necessary for the flow resistivity.

3) It appears that the "elastic" method is suitable for the determination of frame shear modulus and undrained bulk modulus.

4) The measurement of the wave attenuation requires improvement.

5) The use of the measured attenuation required further theoretical implementation.

6) Type-II P-wave has been observed to greater depths than previously published in sands.

7) There is a limiting value of flow resistivity above which microphones can be used to detect type-I P-wave.

6.2 *Sensor Calibration*

6.2.1 Microphone Calibration

A number of microphones were used during the course of the project. For the outdoors acoustic-to-seismic coupling experiments Brüel and Kjær Type 4165 ½" microphone cartridges were used. Prior to measurements being taken these were tested using the Brüel and Kjær Pistonphone using the method outlined in Section 5.1.2.1 of Chapter 5.

One of the Brüel and Kjær microphones was then used as a reference microphone for the calibration of the non-standard microphones used in the indoor tank and as part of the probe microphone.

Figure 6-56 shows an example calibration chart for one of the electret microphones used in the indoor tank experiments. The plot shows both the variation in output (V/Pa) and phase with frequency. The experiments in the tank were undertaken over a frequency range of 500Hz to 2000Hz. It can be seen from the plots that both the phase and output amplitude are relatively flat over the frequency range.

Figure 6-57 shows the measured calibration chart for the probe microphone used in both the indoor tank and for outdoors experiments. The plot shows the frequency response of the probe microphone as the number of air holes in the nose cone as sealed. It can be seen that up to approximately 1500Hz the microphone behaves in a similar manner whether no holes or five holes have been blocked.

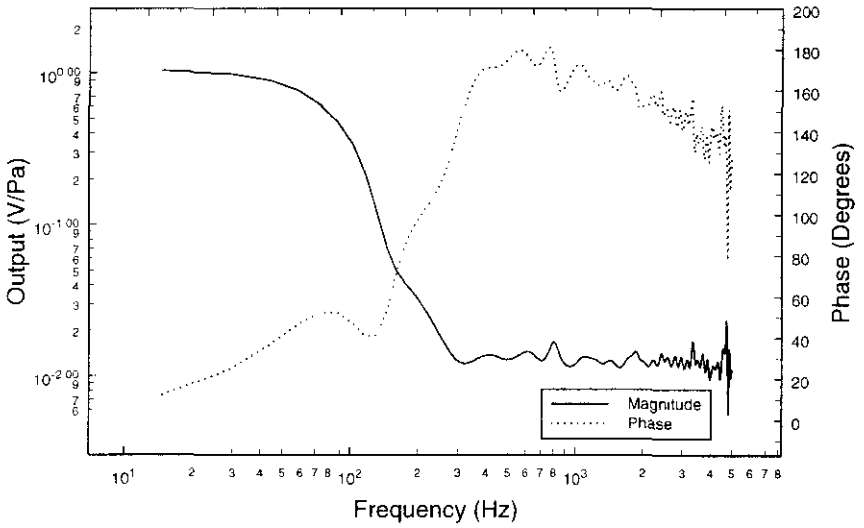

Figure 6-56. Example calibration chart for the electret microphones used in the Indoor Tank.

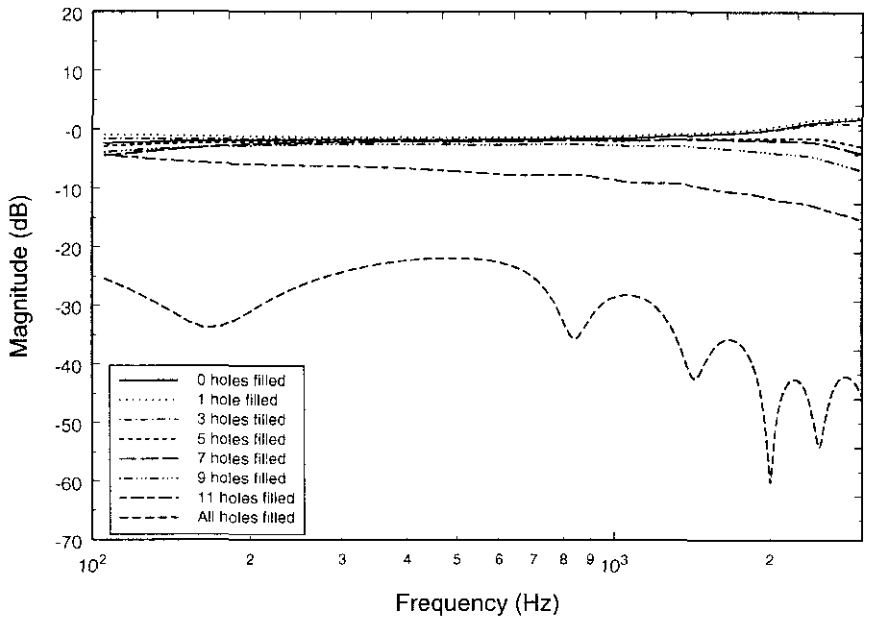

Figure 6-57. Frequency response of the probe microphone as the number of air holes in the nose cone are sealed.

6.2.2 Geophone Calibration

All the geophones used in both the indoor tank and outdoors acoustic-to-seismic coupling experiments were calibrated to gauge their sensitivity and to assess their reliable bandwidth. The geophones were calibrated using the techniques described in Section 5.1.2.2 of Chapter 5.

This calibration was especially important for the analysis of the data taken in the indoor tank, since two differing types of geophone were used. The five upper vertical component geophones consisted of Mark Products L-40A-2, 100 Hertz uncased geophones, whilst the lower five vertical component geophones consisted of Mark Products UM-2, 10 Hertz uncased geophones.

Figure 6-58 shows an example calibration chart for one of the Mark Products L-40A-2, 100 Hertz uncased geophones. It can be seen that the output sensitivity and phase are relatively flat in the region of interest in the tank. Figure 6-59, shows an example calibration chart for one of the Mark Products UM-2, 10 Hertz uncased geophones. The chart shows that the geophone has a flat amplitude and phase response until 1000Hz, after which sharp fluctuations appear in the output. This, shows that the geophones may prove unreliable at the higher testing frequencies used in the tank.

A similar trend is seen in the calibration chart for one of the horizontal component geophones, seen in Figure 6-60.

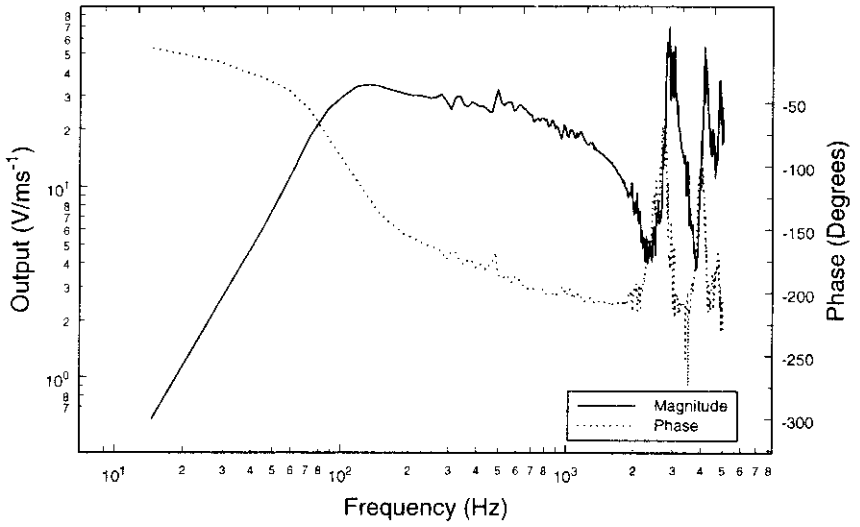

Figure 6-58. Example calibration chart for a vertical component geophone from the top of the Indoor Tank.

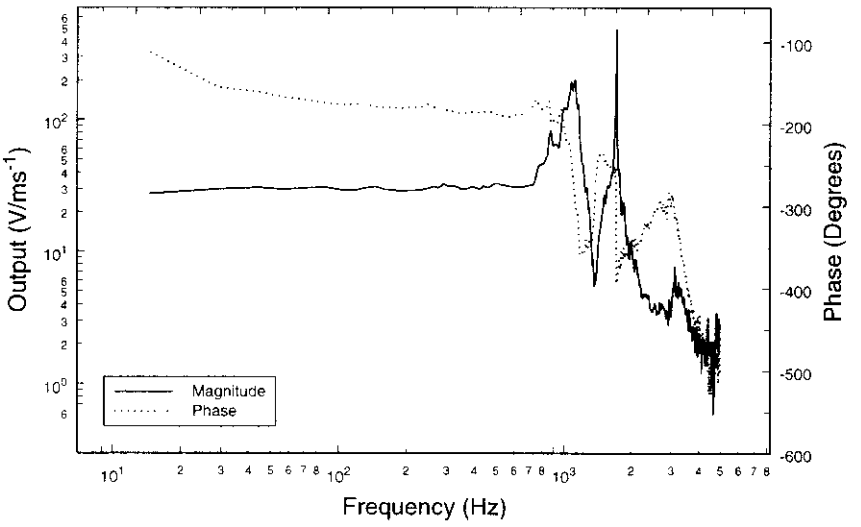

Figure 6-59. Example calibration chart for a vertical component geophone from the bottom of the Indoor Tank.

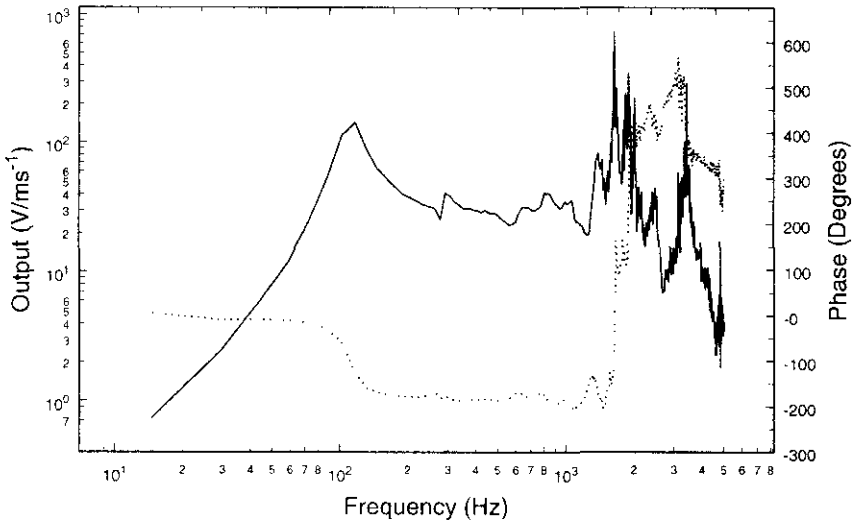

Figure 6-60. Example calibration chart for a horizontal component geophone from the bottom of the Indoor Tank.

As part of the geophone calibration, an investigation was made into the effect of geophone-ground coupling. This investigation consisted of comparing the geophone output and phase with varying frequency when firmly clamped to a mechanical shaker to that measured when the geophone was buried in the ground. The technique has been described in Section 5.1.2.2 of Chapter 5

Figure 6-61 shows the results of the standard geophone calibration using the configuration described in Section 5.1.2.2. The plot shows both amplitude and phase response of the sensor up to 1000Hz. Both the magnitude and phase show reasonable linearity over the experimental bandwidth.

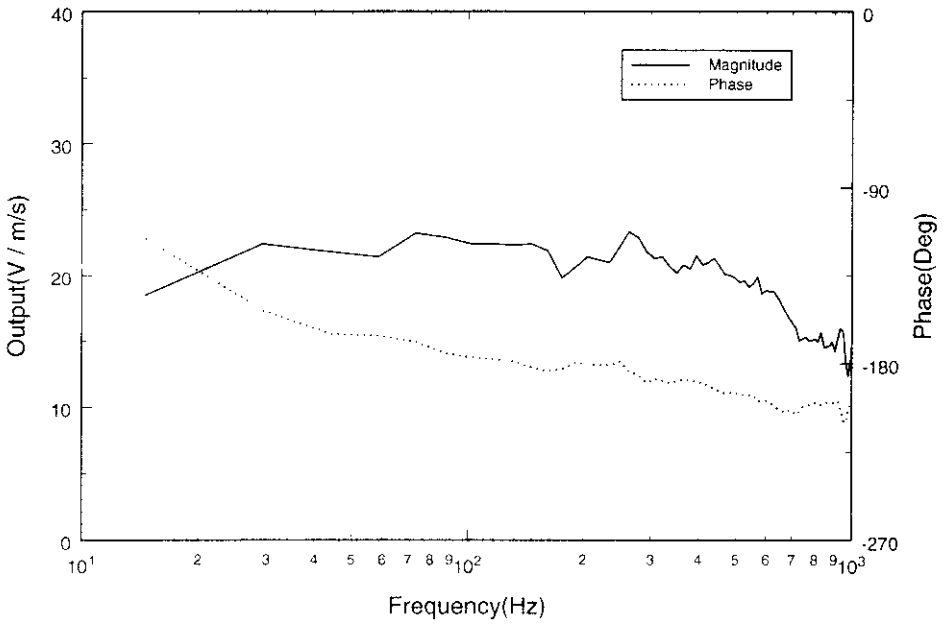

Figure 6-61. Example calibration chart for a vertical component geophone used in the outdoor experiments.

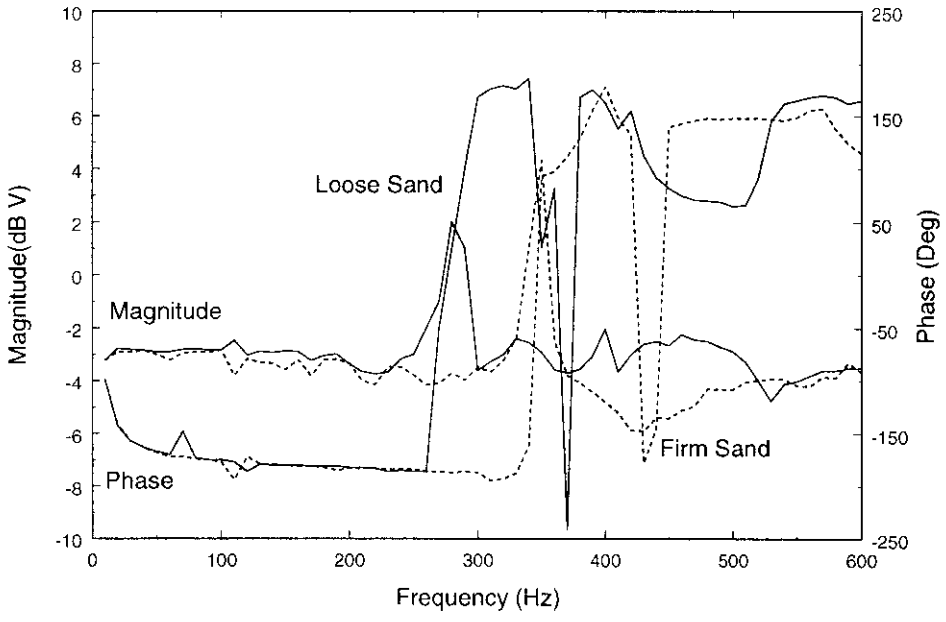

Figure 6-62. Geophone calibration chart using the sand box. Experiments were undertaken using the same geophone as used in Figure 6-61.

Figure 6-62 shows the amplitude and phase response for the Sensor (30Hz) geophone when it had been planted in the sand and driven by the shaker. The figure shows the results of two experiments, the first where the sand was loosely poured into the box and the second where the sand was introduced into the box in 5cm layers, which were compacted before more sand was introduced.

The results for both soil compactions show marked similarities. For the loose data the coupling resonance occurs at 280Hz, where there is a peak in the amplitude and a rapid change in the phase. At low frequencies, the amplitude is flat. At about 220Hz the amplitude starts to increase gradually reaching a peak nearly 5dB larger than seen at low frequencies. Moreover, the phase is linear from the low frequencies all the way to the coupling resonant frequency. There are other fluctuations seen at higher frequencies, although are possibly due to the finite size of the soil box. A similar result is seen for the data collected using compacted sand. However, here the value of coupling resonant frequency is shifted to a higher frequency: 360Hz.

A further experiment involved an investigation into how the position of the geophone in the ground altered the response. Figure 6-63 shows the response of the geophone in the loose sand, with the geophone spike buried to the base and secondly with the whole geophone buried in the ground. This plot shows that there is a small decrease in the magnitude of the coupling resonant frequency brought about by burial.

From these results it was believed that resonant coupling frequency was therefore dependent upon soil compaction and was geophone independent. The theory was tested by undertaking the calibration using a Mark Products L-40-A2 geophone which has a natural frequency of 100Hz. Figure 6-64 shows the plot of this test. It can be seen that the coupling resonant frequency is almost identical for both geophones, confirming that the coupling resonant frequency magnitude does not depend on the geophone.

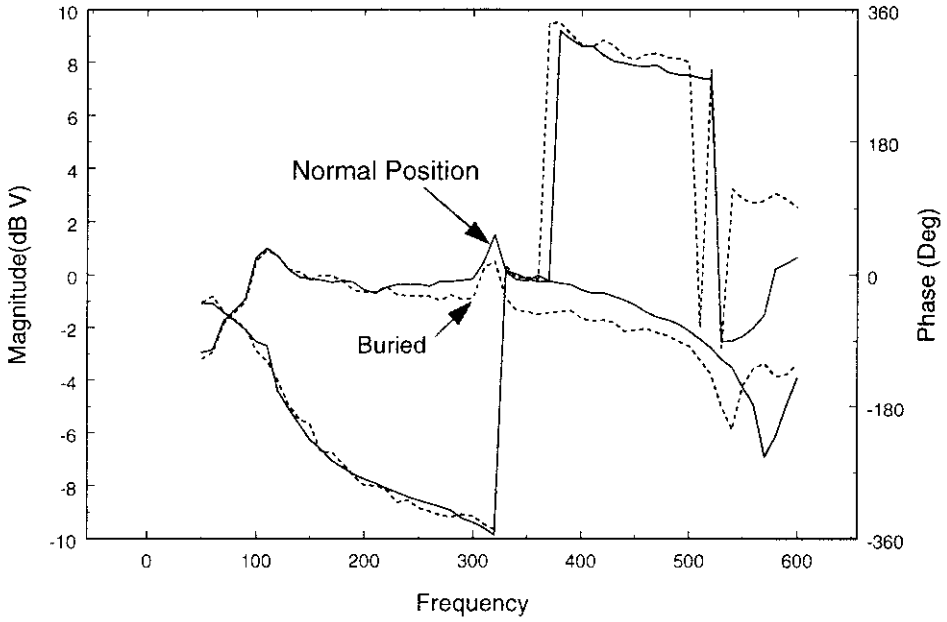

Figure 6-63. Geophone calibration chart using the sand box. Experiments were undertaken using the same geophone as used in Figure 6-61.

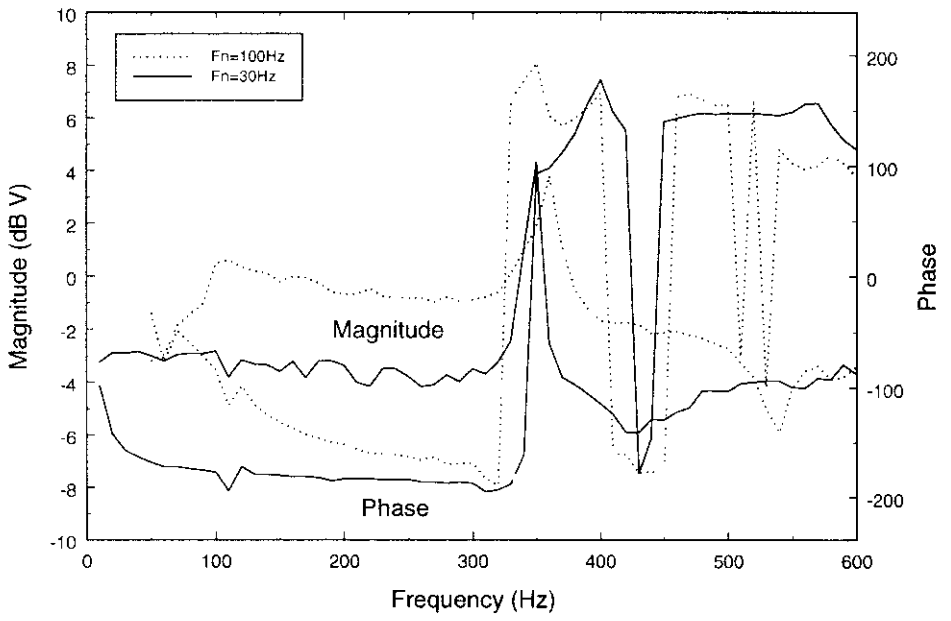

Figure 6-64. Geophone calibration chart using the sand box. This shows the comparison between geophones of differing natural frequencies.

6.2.3 The Use of Laser Doppler Vibrometer in Acoustic-to-Seismic Coupling Measurements

The results of the initial experiment can be seen in Figure 6-65. This shows the response of the geophone situated at the ground surface to the acoustic source over a frequency range of 100Hz to 750Hz. The plot also shows the response of the LDV when focused on the top of the geophone.

The plot shows that it is possible to use the LDV system for measurements of ground velocity excited by atmospheric sound sources when the LDV probe beam reflects from the geophone. To be more useful, it would be desirable for the LDV system to work when the laser beam is reflected from the ground surface, rather than the reflective tape on the geophone top.

Figure 6-66 shows the response of the LDV to a 300Hz tone. Here the LDV has been focussed directly onto the sand surface. The upper plot, which is the time domain signal, shows a large noise component that is mirrored in the frequency spectrum below. The poor response of the LDV is probably due to scattering of the laser beam from the grains. The use of the plastic cylinders, proposed to overcome this problem can be seen in Figure 6-67. In the upper plot, a sine wave can be clearly seen with very little noise content, and the subsequent frequency spectrum shown in the lower plot shows a strong peak at 300Hz, well above the background levels.

The second series of experiments was undertaken to assess the effect of using the cylinders to enhance the LDV signal as seen in Figure 6-67. The results of this assessment can be seen in Figure 6-68. The figure shows the response of the geophone positioned at the ground surface to the atmospheric sound source. The three remaining plots are the response of the geophone whilst attached to each of the cylinders that had been inserted into the sand.

It can be seen from the figure that the response of each of the three cylinders shows a reasonable agreement to that of the geophone without the presence of the cylinders. The agreement is improved at lower frequencies (less than roughly 400Hz), with greater variation at the high frequencies. Of the three cylinders tested in appears that Cylinder 3 has least effect on the geophone response, since the response of the geophone only and the geophone coupled to Cylinder 3 shows the most agreement over the frequency range used.

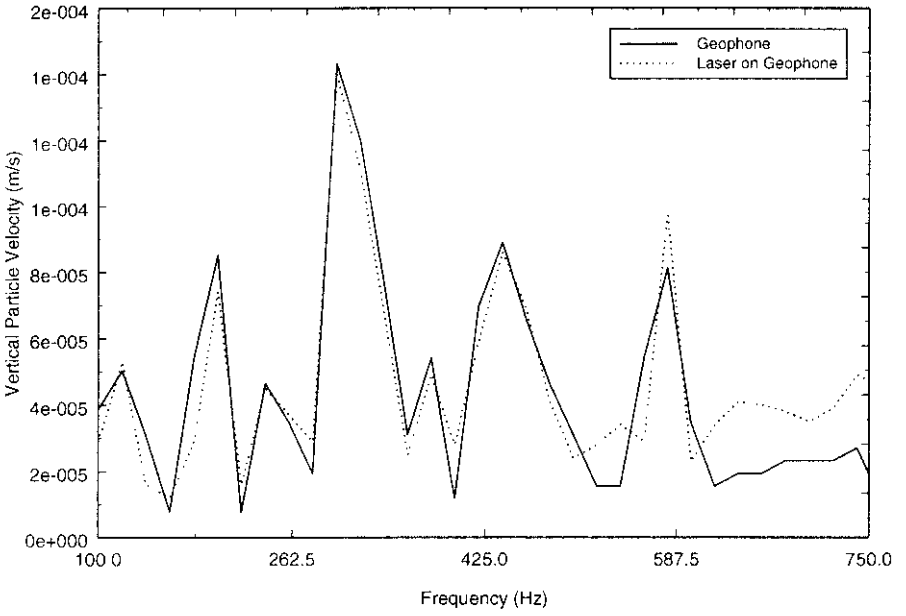

Figure 6-65. Geophone and LDV response to a series of pure tones. Here the geophone is positioned at the ground surface, with the laser focussed onto the geophone top.

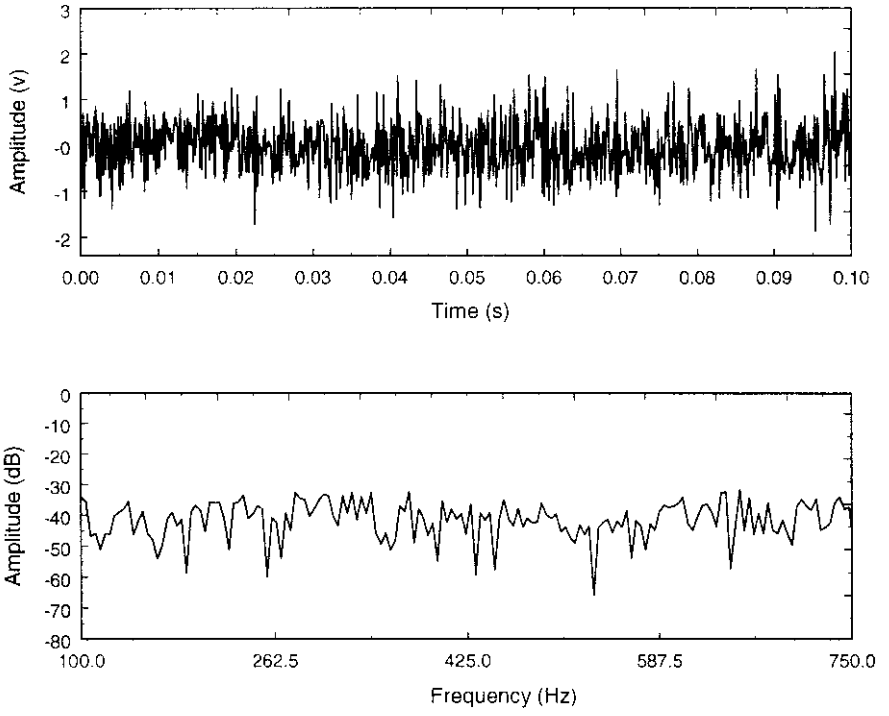

Figure 6-66. LDV response to a 300Hz pure tone. Here the LDV is focussed directly onto the ground surface.

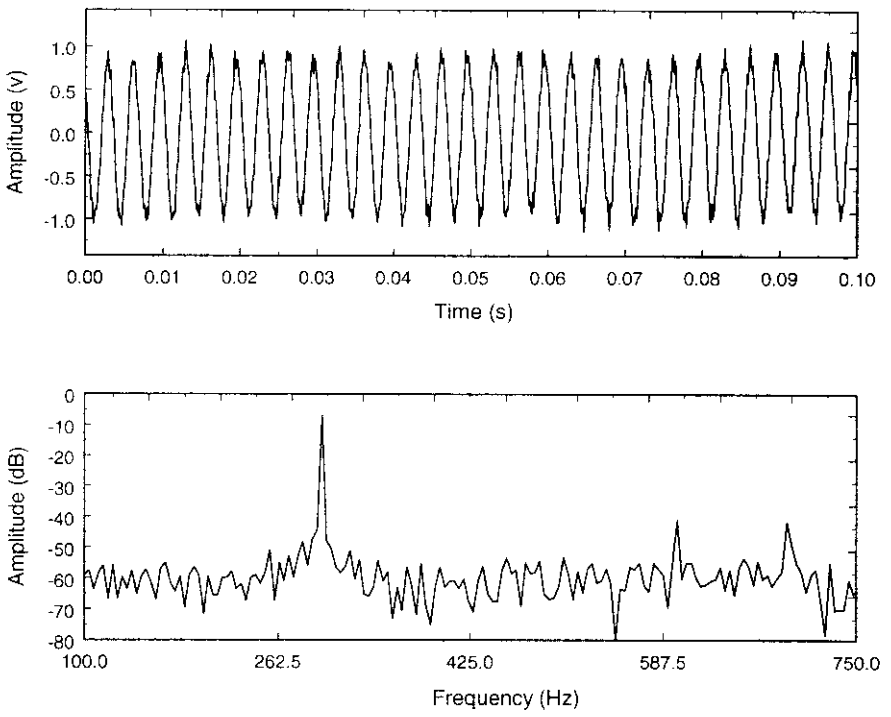

Figure 6-67. LDV response to a 300Hz pure tone. Here the LDV is focussed onto a plastic cylinder.

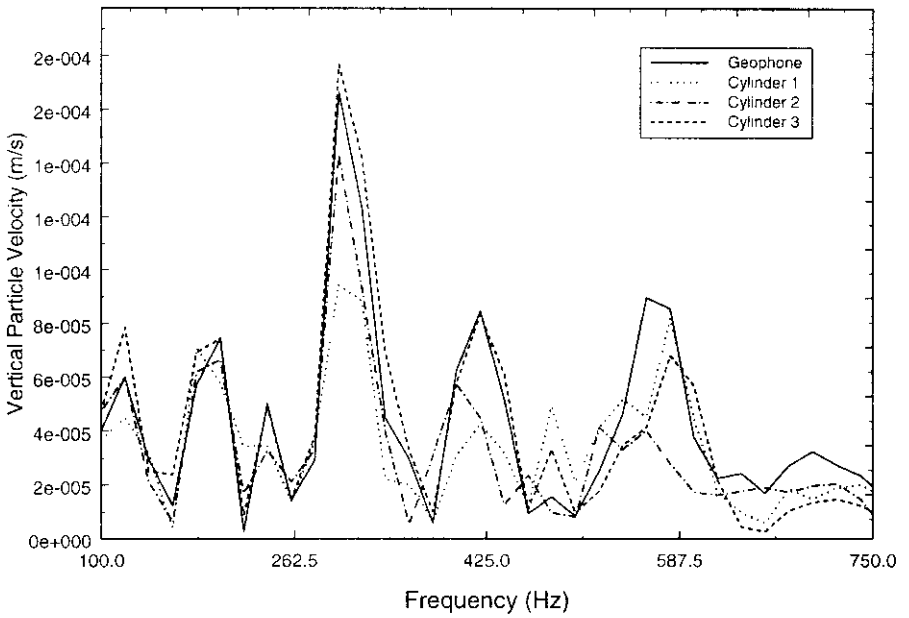

Figure 6-68. Response of the geophone to a range of pure tones, whilst positioned at the ground surface and the response whilst attached to Cylinders 1 to 3 buried in the ground.

Chapter 7

Design and Execution of Outdoor Experiments

7 Experiments

A significant portion of this study involved the undertaking of outdoor measurements in the study of acoustic-to-seismic coupling. Experiments were undertaken at three different locations; all having markedly different soils (see Chapter 4 for details of the locations, as well as detailed sedimentological descriptions). The measurements included:

- Seismic refraction surveying
- Acoustic-to-seismic coupling ratio
- In-situ geophone calibration
- Acoustically induced seismic surface waves

The bulk of experiments were undertaken at the Open University Acoustic Research Group test area and at the Hepworth Minerals and Chemicals, Stone Lane Quarry, Heath and Reach, Bedfordshire. Finally, a case study was undertaken at Horticultural Research International, Wellesbourne, Warwickshire utilising the experimental procedures and data acquisition systems which had been tested at the two main investigation sites.

The majority of the experiments undertaken at each of the sites were the same, although a number of differing set-ups were used. As such, a detailed experimental explanation has been given in the section describing measurements taken at Acoustic Research Group test area. For the remaining test areas, experimental descriptions refer to this section, except to describe any differing configurations used.

7.1.1 Seismic Refraction Surveying

The seismic refraction surveying method utilises seismic energy that returns to the surface after travelling through the ground along refracted ray paths. The normal technique involves recording the compressional (P-wave) waves travelling both directly and through surface layers and refracted along underlying layers of high seismic velocity.

The objective of the shallow refraction survey is two-fold. Firstly, to obtain the P-wave and S-wave velocities for the differing ground layers in the ground and secondly to determine the thickness' of these layers.

7.1.1.1 Principles of Seismic Refraction Surveying

The general assumption relating to the ray path geometries considered below is that the substrata are composed of a series of layers separated by plane or possibly dipping interfaces. Additionally, it is assumed that seismic velocities are uniform within each layer, that layer velocities increase with depth, and that ray paths are restricted to a vertical plane containing the profile line (i.e. that there is no component of cross-dip).

A seismic wave propagating from a source at the surface will travel through a medium until it strikes a boundary. At a critical angle of incidence I_c, to this boundary, such that the angle of incidence R in the lower medium is 90^o to the normal, some of the initial energy will be propagated along the boundary in the lower medium.

The refracted energy will travel in a waveform and is called the "head wave". In travelling along the boundary, the head wave creates secondary sources of vibration, which cause waves to be refracted back into the upper medium. These waves are recorded by receivers set at a distance away from the source. As well as waves travelling down through the upper medium, a direct wave is produced which travels through the upper medium just below the surface.

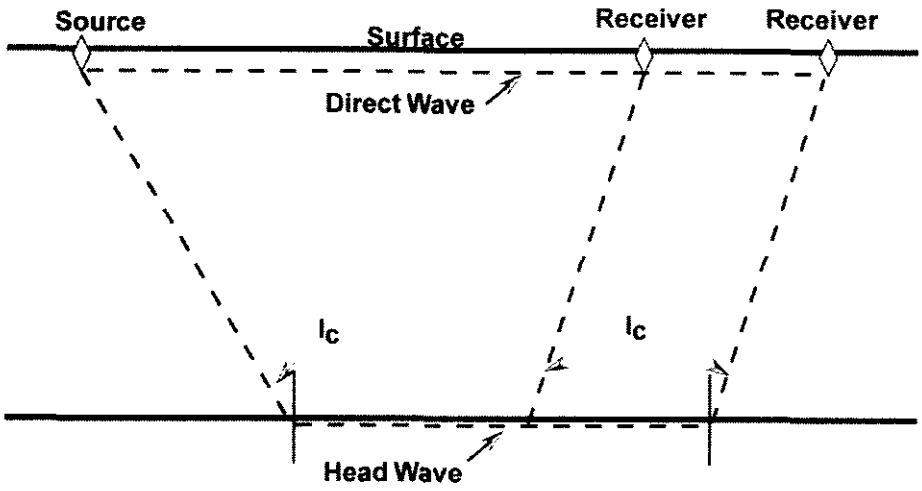

Figure 7-1. The principles of seismic refraction surveying

Not all of the initial energy will strike the boundary at the critical angle of incidence. This energy may either by reflected back to the surface or be refracted through the lower layer and through subsequent deeper layers, until it strikes a boundary at the critical angle of incidence and is refracted back to the surface or is attenuated by the sub-surface material.

7.1.1.2 Seismic sources

The source should ideally provide a pulse of duration of no more than a few milliseconds, have a large amplitude and should be safe, cheap and repeatable. On land, explosives are still quite commonly used in refraction work involving surface ranges greater than 50-100m, corresponding to depths of investigation of over 10m or so. They give a good source pulse of high frequency and amplitude. However, for smaller surveys or those in built-up areas, other surface sources needed to be used.

These can include drop-weights in which a weight of about 10kg strikes the surface coupling plate after falling some 3-4m. Drop weights, are often used in site investigation surveys for depths up to about 10m. A sledgehammer with an enthusiastic operator can give comparable seismic energy.

7.1.1.3 Seismic detectors

The ground motion detector most commonly used in land surveys is the geophone. This is an electromechanical transducer commonly of the moving-coil type shown in Figure 7-2.

In the geophone, a cylindrical coil is suspended from a spring support in the field of a permanent magnet that is attached to the instrument casing. The magnet has a cylindrical pole piece inside the coil and an annular pole piece surrounding the coil. The suspended coil represents an oscillatory system with a resonance frequency determined by the mass of the coil and the stiffness of its spring suspension.

The geophone is fixed into the ground by the use of a spike base. With the passage of a seismic wave, there is a relative motion between the suspended coil and the fixed magnet. Movement of the coil in the magnetic field generates a voltage across the terminals of the coil.

The oscillatory motion of the coil is inherently damped because the current flowing in the coil induces a magnetic field that interacts with the field of the magnet to oppose the motion of the coil. The amount of this damping can be altered by connecting a shunt resistor across the coil terminals to control the amount of current flowing in the coil.

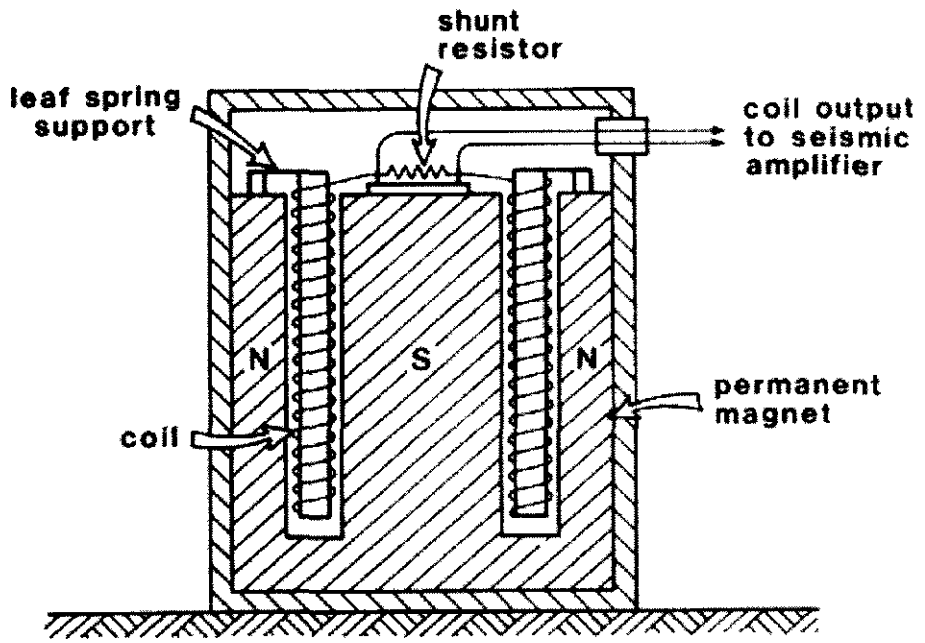

Figure 7-2. Simplified sectional view of a typical moving-coil geophone

Ideally, the output waveform of the geophone closely mirrors the ground motion and this is arranged by careful determination of the amount of damping. Too little damping results in an oscillatory output at the resonant frequency, whilst overdamping leads to a reduction of sensitivity.

Damping is typically arranged to be about 0.7 of the critical value at which oscillation would just fail to occur for an impulsive mechanical input such as a sharp tap. With this amount of damping the frequency, response of the geophone is effectively flat above the resonant frequency. The effects of differing amounts of damping on the frequency and phase response of a geophone are shown below in Figure 7-3.

To ensure that the geophone models the seismic waveform accurately, the geophone should have a flat frequency response and minimal phase distortion within the frequency range of interest. Therefore, geophones should be used which have a resonant frequency well below the lowest frequency of interest.

Above the resonant frequency, the output of the geophone is proportional to the velocity of the coil. The sensitivity of the geophone, measured in output volts per unit of velocity, is determined by the number of windings in the coil and the strength of the magnetic field.

Moving coil geophones are sensitive only to the component of ground motion along the axis of the coil. Vertically travelling P-waves are therefore best detected by geophones with an upright coil, as illustrated in Figure 7-2. The optimal recording of seismic phases that involve mainly horizontal ground motions, such as horizontally polarised shear waves, require geophones in which the coil is mounted and constrained to move horizontally.

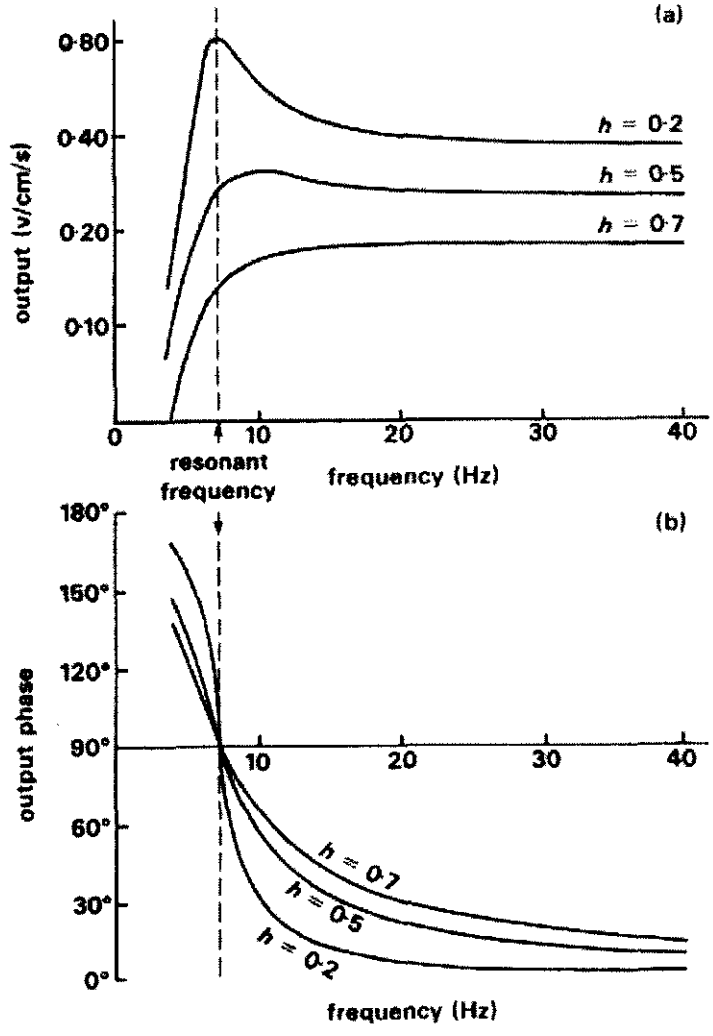

Figure 7-3. Amplitude and phase responses of a geophone with a resonant frequency of 7Hz, for different damping factors, h. Output phase is expressed relative to input phase (Telford et al., 1976).

7.1.1.4 Calculations

A) Horizontal Boundary

For a simple two-layer case, where there is a horizontal boundary, the true velocity of each layer and the depth to the boundary, H, can be calculated from travel times measured between source and receivers in the field. Plotting travel time (t) against distance (x), for the field data, the velocities can be calculated from the corresponding direct and head wave gradients (see Figure 7-4). The critical angle of incidence can be calculated using an extension of Snell's law of optics, such that: -

$$\frac{Sin\ I}{Sin\ \mathrm{R}} = \frac{\text{Sin angle of incidence in medium 1}}{\text{Sin angle of incidence in medium 2}} = \frac{v_1}{v_2} \qquad \textit{(Eq. 7-1)}$$

If $v_2 > v_1$, then $R > I$.

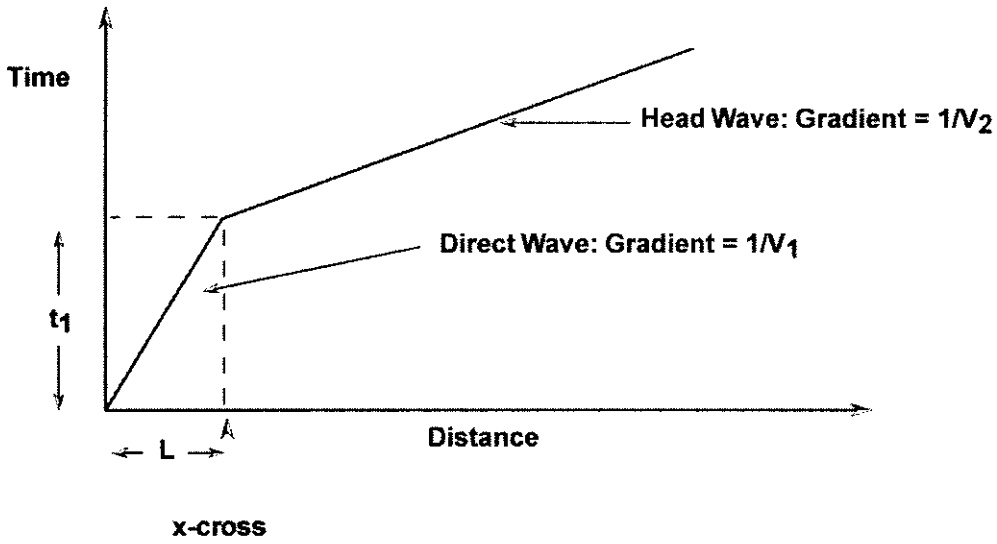

Figure 7-4. Time – distance graph for seismic refraction surveying.

i) Velocity of the upper layer

$$\textit{Gradient of the direct wave} = \frac{1}{v_1} \qquad \textit{(Eq. 7-2)}$$

$$\textit{Velocity of upper layer} = \frac{1}{Gradient} \qquad \textit{(Eq. 7-3)}$$

ii) Velocity of the lower layer

$$\textit{Gradient of the head wave} = \frac{1}{v_2} \qquad \textit{(Eq. 7-4)}$$

$$\textit{Velocity of the lower layer} = \frac{1}{Gradient} \qquad \textit{(Eq. 7-5)}$$

iii) Angle of incidence

From Snell's law

$$\frac{Sin\ I}{Sin\ \mathrm{R}} = \frac{\text{Sin angle of incidence in medium 1}}{\text{Sin angle of incidence in medium 2}} = \frac{v_1}{v_2} \qquad \textit{(Eq. 7-6)}$$

For critical refraction: - $I = I_c$

$R = 90^{\circ}$

Hence: - $$\frac{v_1}{v_2} = Sin\ I_c \qquad \textit{(Eq. 7-7)}$$

$$I_c = Sin^{-1}\left[\frac{v_1}{v_2}\right] \qquad \textit{(Eq. 7-8)}$$

iv) Depth to Boundary

There are several methods that can be utilised to calculate the depth to the refracting boundary below each shot point, h (such as the Intercept Time and Break Point methods listed below). All the techniques make use of the time-distance graph.

i) Intercept time method

$$t_i = 2h\sqrt{\frac{1}{v_1^2} - \frac{1}{v_2^2}} \qquad \textit{(Eq. 7-9)}$$

where: -

t_i = head wave intercept time (See Figure 7-4)

v_1 and v_2 are the layer velocities

ii) Break Point Method

$$L = 2h\sqrt{\frac{v_2 + v_1}{v_2 - v_1}} \qquad \textit{(Eq. 7-10)}$$

$$L = \frac{C2 - C1}{M1 - M2} \qquad \textit{(Eq. 7-11)}$$

where: -

L = crossover distance (See Figure 7-4)

$C1,M1$ = direct wave intercept, gradient

$C2,M2$ = head wave intercept, gradient

v_1 and v_2 are the layer velocities

B) Inclined Boundary

For seismic refraction at an inclined boundary, the same principles apply as indicated for a horizontal boundary. To identify an inclined refractor it is necessary to repeat the experiment with the source and receiver positions reversed. The resultant combined time-distance graph will be asymmetrical as shown below.

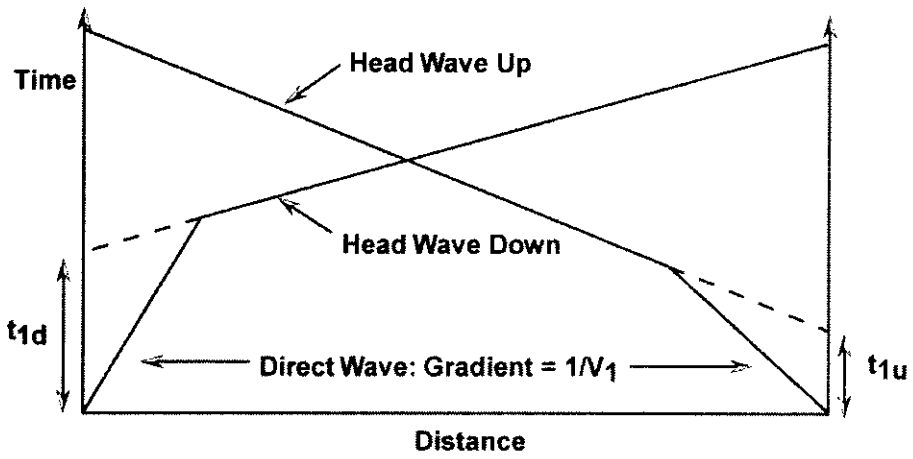

Figure 7-5. Time-distance graph for an inclined boundary.

The direction of the slope can be judged from this graph, such that the intercept of the head wave for the refraction data in the down slope direction will be less than that in the up slope direction. The apparent surface velocity down slope, determined from the corresponding head wave gradient, will be less than the apparent surface velocity up slope. The velocity in the upper layer, together with the corresponding up and down slope

velocities in the lower, can be determined from the time-distance graph. The angle of dip of the inclined boundary can also be determined.

i) Velocity of upper medium

$$v_{1down} = \frac{1}{Gradient(d)} \qquad (Eq.\ 7\text{-}12)$$

$$v_{1up} = \frac{1}{Gradient(u)} \qquad (Eq.\ 7\text{-}13)$$

$$v_{1mean} = Mean(v_{1down} + v_{1up}) \qquad (Eq.\ 7\text{-}14)$$

ii) Angle of critical incidence

$$I_c = 0.5\left[Sin^{-1}\left[\frac{v_1}{v_{down}}\right] + Sin^{-1}\left[\frac{v_1}{v_{up}}\right]\right] \qquad (Eq.\ 7\text{-}15)$$

iii) Dip of interface

$$a = 0.5\left[Sin^{-1}\left[\frac{v_1}{v_{down}}\right] - Sin^{-1}\left[\frac{v_1}{v_{up}}\right]\right] \qquad (Eq.\ 7\text{-}16)$$

iv) True velocity of lower medium

$$v_2 = \frac{v_1}{Sin\, I_c} \qquad (Eq.\ 7\text{-}17)$$

v) Depth at down slope shot point

$$h = \frac{t_{id} \times v_1}{2 \times \text{Cos}\, I_c} \qquad \textit{(Eq. 7-18)}$$

where: -

t_{id} = Down slope head wave intercept (See Figure 7-5)

v) Depth at up slope shot point

$$h = \frac{t_{iu} \times v_1}{2 \times \text{Cos}\, I_c} \qquad \textit{(Eq. 7-19)}$$

where: -

t_{iu} = Up slope head wave intercept (See Figure 7-5)

7.1.1.5 Field Techniques

The spacing of the detectors along a seismic refraction line is determined by the detail in which one wishes to examine the refracting horizon, since a depth estimate can in principle be made at each geophone position. A general rule of thumb for planning a seismic survey is that the spread length (i.e. the length of line from shot to last geophone on line) should be about eight times the depth of interest.

For a small-scale refraction survey of a construction site to locate the water table, or rockhead, recordings out to an offset distance of about 100m normally suffice. The geophones are connected via a multicore cable to a portable 12- or 24-channel seismic recorder.

The seismic P-wave impulse can be generated by a vertical hammer blow on a metal plate. Horizontal polarised shear waves (SH) can be generated by placing a wooden plank on the ground and loading it (usually with a vehicle) to produce good coupling between the plank and the sediment. A hammer blow is made to either end of the plank thus producing a 180° phase reversal on the shear wave. A second method with which to produce this phase reversal is to reverse the polarity setting on the acquisition system.

This reversal is made in order to aid the identification of the S-wave. Displaying polarisations of the normal and reversed SH waves (Figure 7-6), then inverting the reversed and adding the resultant, can aid the identification of the S-wave onset.

More information concerning the technique and interpretation of seismic refraction methods can be found in Griffiths and King (1988) and Kearey and Brooks (1992).

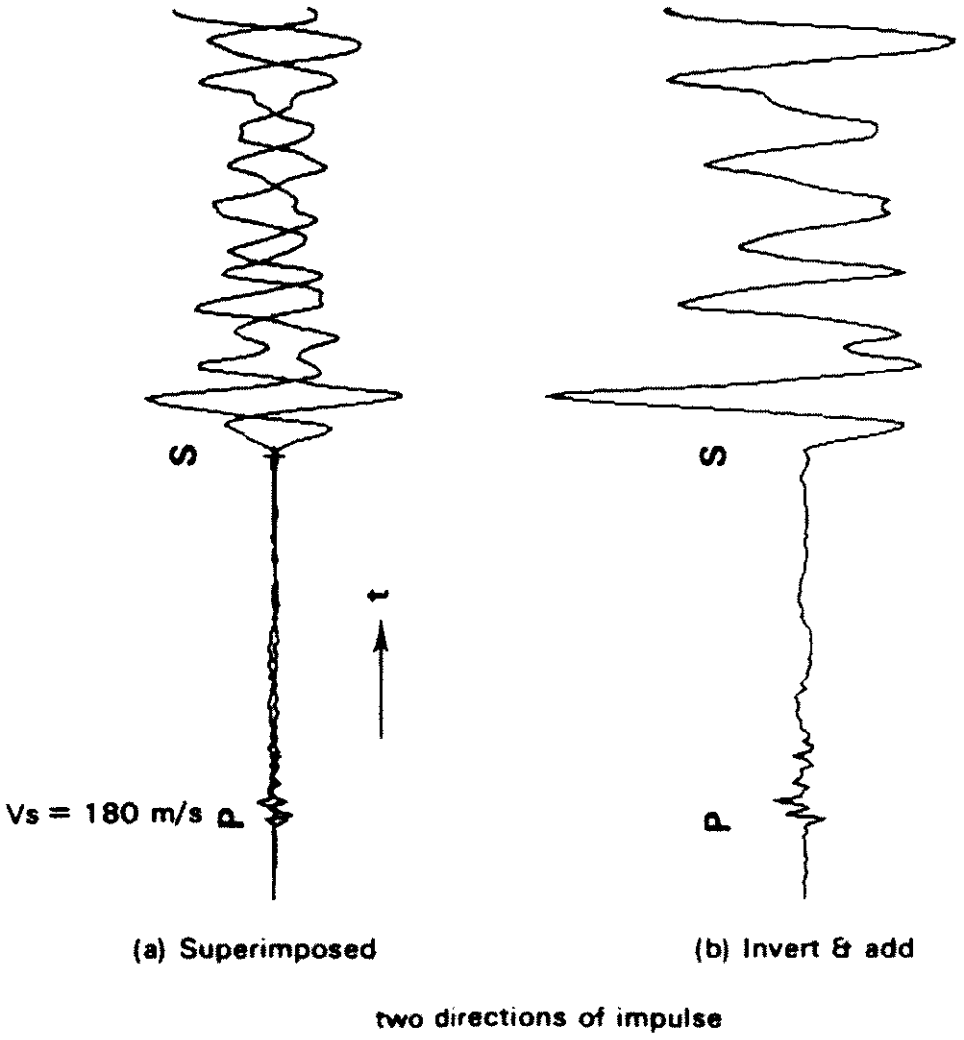

Figure 7-6. The identification of shear wave arrivals by (a) the combined display of the reversed impulse and (b) the addition of waveforms after inverting the reversed impulse.

Seismic refraction surveys taken during the course of the project were all based upon standard techniques. Signal acquisition was accomplished using an IBM compatible PC containing a National Instruments E-Series AT-MIO-16E-2 acquisition card in conjunction with a SC-2040 add-on board. The SC-2040 was used as a differential amplifier for the

geophone signals. The acquisition was controlled using a purpose written Labview program.

The geophone sensors used were manufactured by Western Atlas, developed by HGS Sensors Operations. The vertical component sensors were Type SM-4/U-B, having a natural frequency of 10Hz and installed in a PE-3/C land case. The horizontal component sensors were Type SM-6/H-B, having a natural frequency of 10Hz and installed in a HPE land case. In total four vertical and four horizontal geophones were available for use. A Mark Products L-40A-2, 100 Hertz uncased geophone was used as a trigger source.

The source employed was a sledgehammer striking a metal plate for the excitation of P-wave waves, whilst S-waves were excited by striking either end of a wooden plank, suitably weighted to ensure adequate coupling to the ground. A different configuration for S-wave excitation was employed where specified.

The acquisition program retrieves the specified amount of data from one or more analogue input channels when a hardware analogue trigger occurs. This is a timed acquisition, meaning that a hardware clock is used to control the acquisition rate for fast and accurate timing. It is also a buffered acquisition, meaning that the data are stored in an intermediate memory buffer after they are acquired from the DAQ board. The acquisition "front-end" can be seen in Figure 7-7.

A small-scale seismic refraction survey was undertaken at the Acoustics Research Group field site at the Open University. As stated in Chapter 4, the test area consists of an area 3.5m x 3.0m x 2.0m of pea-gravel. Since the area has been specially prepared one of the objectives of the refraction survey was unnecessary, since there were no layers to be discerned (the material being homogeneous). Therefore, the objective of the survey was to determine the P-wave and S-wave velocity of the gravel. Since this was the only aim of the survey, the receiver separation was not an important consideration.

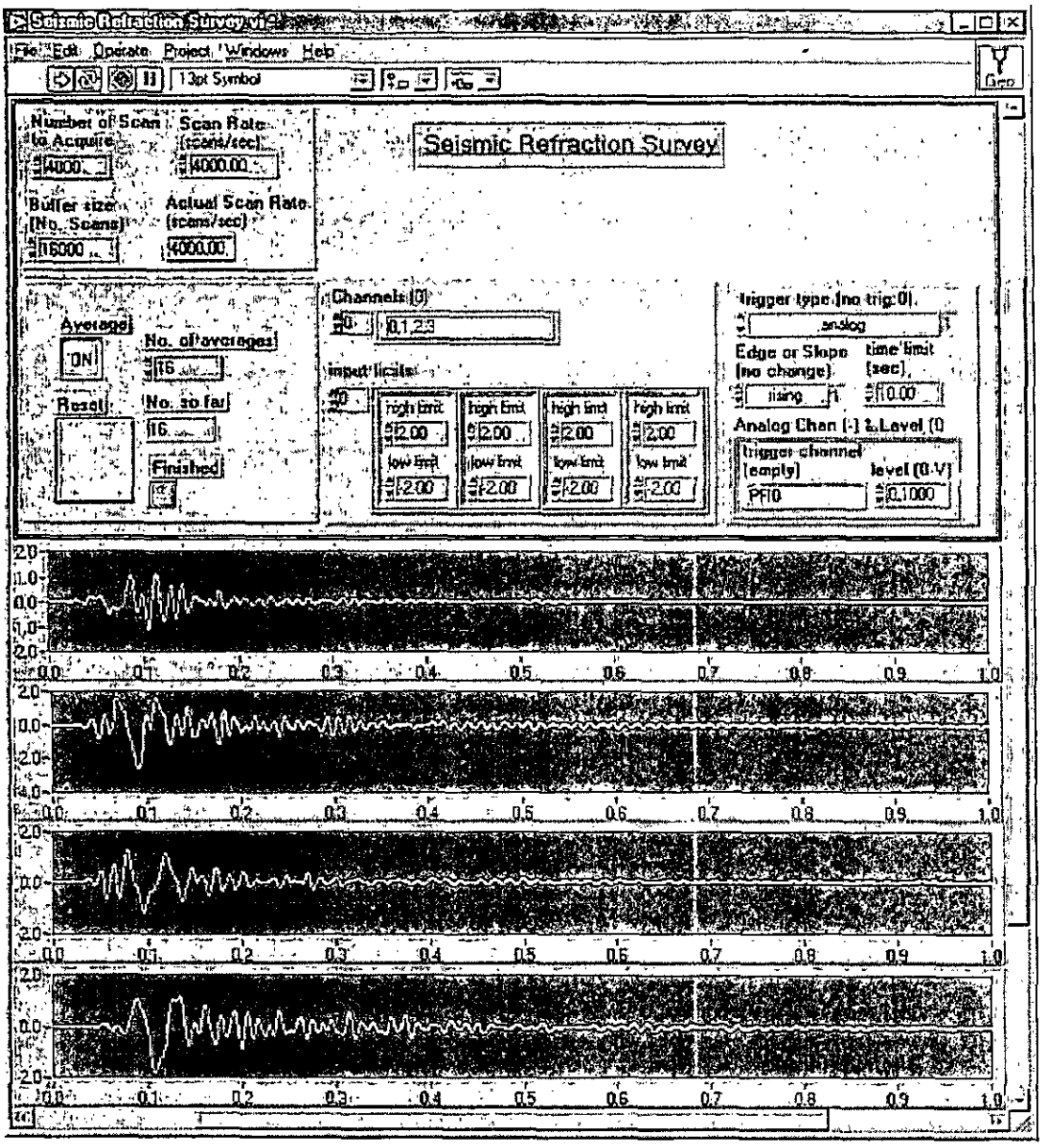

Figure 7-7. Seismic Data Acquisition Program.

For the P-wave velocity determination, four geophones were used. A small metal plate ($15cm^2$) was placed approximately 0.50m from one edge of the gravel. A tape measure was then laid out to ensure accurate positioning of the geophones and the first sensor positioned 1.0m away from the plate. Further geophones were added at 0.50m separation. The trigger geophone was positioned next to the plate.

With all connections made and ambient noise at a minimum the acquisition program was run and an initial hammer blow was made on the metal plate. This initial blow was made so that adequate gain could be set on the SC-2040 and that the input gain values could be set in the program. Further blows were made to ensure these parameters were optimally set.

Once the gain levels had been satisfactorily set, the number of averages to acquire was set to sixteen, and sixteen blows of the hammer made onto the metal plate. A few seconds were left between each strike of the hammer to allow acquisition and averaging of the data to be made. Once the acquisition was completed, the collected data was saved to file for subsequent analysis.

The first part of the analysis was the picking of the first arrival times enabling the time-distance graph was to be plotted. Initially, a second Labview program was used (See Figure 7-8) to pick the arrival times. The program "first-break" reads in the scanned data and attempts to pick the first-arrival times automatically. This is accomplished by looking for changes in the standard deviation of the recorded voltage.

The principle behind the program is that when the first arrival occurs there will be a sudden change in the gradient of the trace. This results in an increase in the standard deviation. By looking at the standard deviation over a number of sample points and the neighbouring same number of points, if there is a large change in the value then this point is taken as the time of the first arrival. An allowable error is input into the system to allow for noise on the trace.

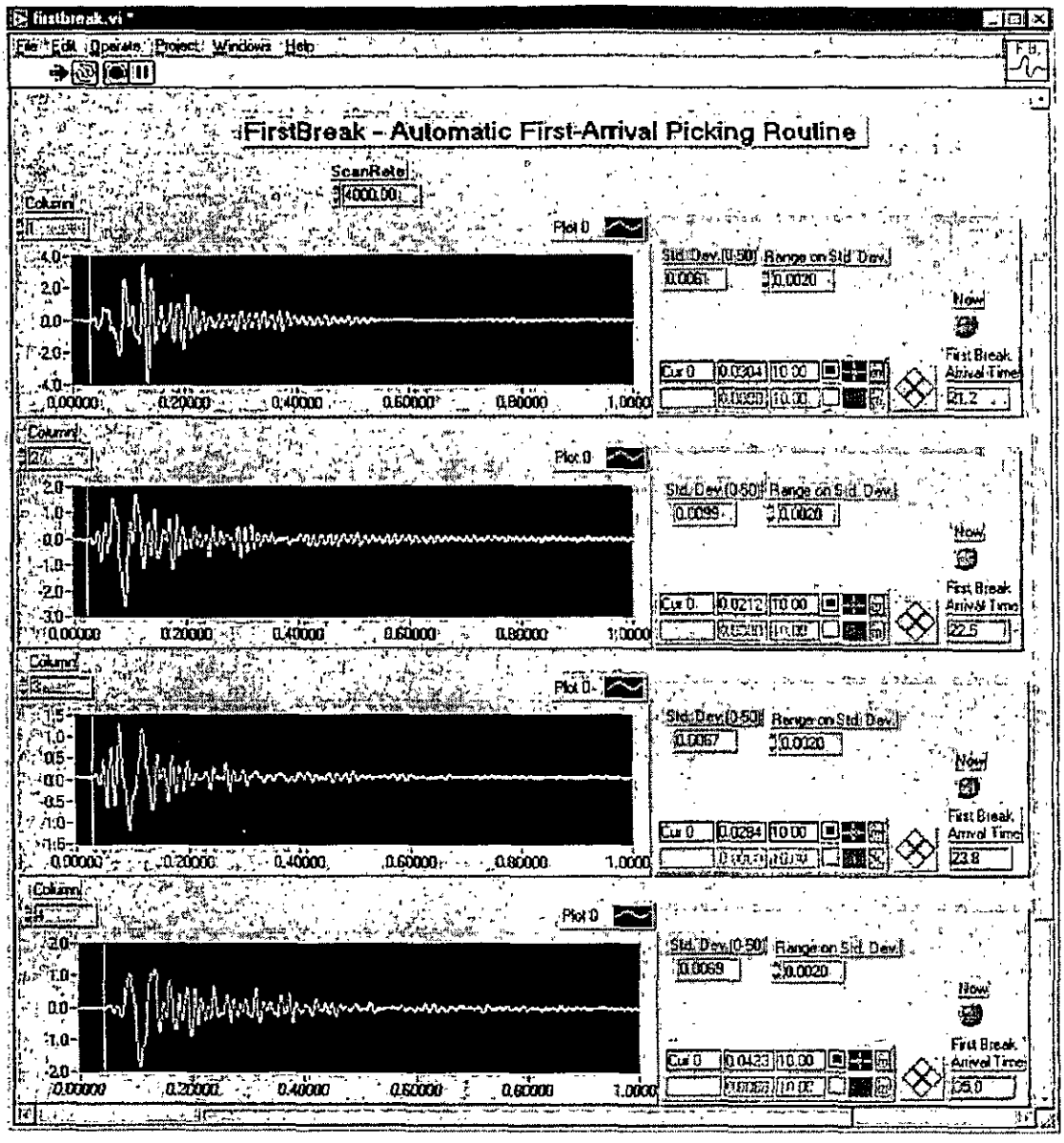

Figure 7-8. Automatic picking of first-break arrival times using Labview.

The input parameters for the program are the scanrate at which the data was collected (for the travel-time determination) and the allowable error on the standard deviation. The program initially calculates the standard deviation of the first 50 points of data - (a). This period is before any arrivals occur and the traces can therefore be assumed to be having flat amplitudes. It then takes the next 10 points - (c) and again calculates the voltage standard deviation. This value of standard deviation (c) is then compared against the value of the first 50 points - (a) plus the allowable error - (b).

If the value is less, then the program takes the next 10 points and the process is repeated until it calculates a value over 10 points which is greater than the (a) + (b). The starting point of these 10 points is then taken as the first-break arrival time.

Although this method works satisfactorily and usually picks the correct arrival time, under conditions of high background noise, it was found that the first-arrival travel times could be more accurately and speedily determined manually. Manual picking was accomplished using *Matlab*. Here a "wiggle trace" was programmed. The wiggle trace is a standard graph type in seismic interpretation used to aid identification of seismic events. An example of the wiggle trace can be seen in Figure 7-9.

The *Matlab* function "GINPUT" allows the manual picking of the arrival times. The cursor can be positioned using a mouse (or by using, the Arrow Keys on some systems). Data points are entered by pressing a mouse button or any key on the keyboard except carriage return, which terminates the input before N points are entered. The plot can be enhanced using the "ZOOM" function.

Once the first-break arrival times have been picked, they can be plotted as time-distance, with velocities calculated using techniques described in Section 7.1.1.4.

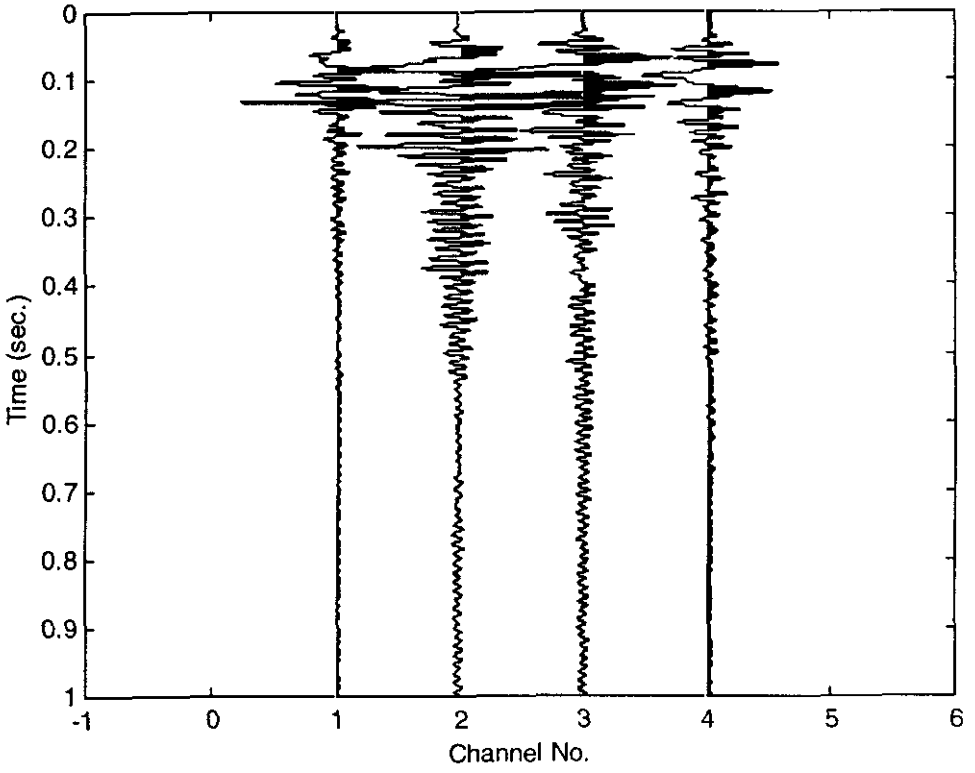

Figure 7-9. Example of "wiggle trace" plotted using Matlab.

Shear Wave velocities were also investigated at the site. A 6' scaffold plank was laid on the ground and a Land Rover driven onto it as a kentlidge. The trigger geophone was positioned at the end of the plank and the geophones positioned perpendicular to the plank, aligned with the centre. The first horizontal component geophone was placed 1.0m from the plank with the remaining geophones placed at 0.5m intervals.

With background noise at a minimum and gain levels set, hammer blows were made to the end of the plank and the resultant averaged signals recorded. The operator then moved to the other end of the plank together with the trigger geophone and further blows made.

Analysis of the data showed that the results were unsatisfactory for subsequent analysis. This may have been due to poor coupling of the plank to the ground or that the plank was very close to the edge of the pit. Due to this problem, the shear wave velocity of the gravel was determined using the shear wave measurement technique used in the indoor soil tank (see Section 5.1.1.3).

A line of four horizontal component geophones was laid out close to the centre of the pit, with an end geophone used as the source. Five-cycle tone bursts were used as a source signal, broadcast by the first geophone with travel times to the subsequent geophones recorded. Geophones were laid 0.10m apart. Each geophone was subsequently used as a source in turn.

The procedure was repeated in a second position in the pit to test homogeneity.

7.1.2 Acoustic-to-Seismic Coupling Ratio

The aim of acoustic-to-seismic coupling ratio measurements undertaken at the ARG test site was to establish and test the procedure and acquisition of data. In addition, since it was known that the ground was homogeneous, a series of experiments was devised to investigate the reliability and repeatability of the technique. Measurements were also taken to determine if there was any angle dependence on the received signals.

The experimental configuration can be seen in Figure 7-11. The loudspeaker used was a 30W Tannoy that was driven using an H&H S150 professional power amplifier. A 1m brass tube, 0.017m in diameter, was attached to the driver in an attempt to approximate the speaker to a point source.

Vertical particle velocities were measured using Western Atlas Type SM-4/U-B geophones, having a natural frequency of 10Hz and installed in a PE-3/C land case. Sound pressures were measured using Brüel and Kjær Type 4191 condenser microphones, using Type 2645 preamplifiers.

Outputs from the sensors were amplified prior to recording, using a Brüel and Kjær Type 2160 measuring amplifier. The amplifier is furnished with two alternative AC coupled signal inputs - a direct input which accepts standard Brüel and Kjær coaxial plugs used for the geophones, and a preamplifier input that accepts the 7-pin plug of Brüel and Kjær microphone preamplifiers. Varying levels of gain can be used from –30 to +100dB selectable in 10 ± 0.05dB steps.

The amplifier also has three filter settings, a linear 2Hz to 200kHz, 22.4Hz high pass and an "A" weighting network. In all the measurements the 22.4Hz high pass filter was used. This has a low frequency attenuation slope of 18dB/octave and was useful in limiting the influence of unwanted low frequency environmental disturbance.

The MLSSA system, described previously, was used for the source signal and for subsequent data acquisition. An output signal bandwidth of 3kHz was used with the received impulse response sampled at a scanrate at 9kHz. A schematic of the data recording system used in the measurements can be seen in Figure 7-10.

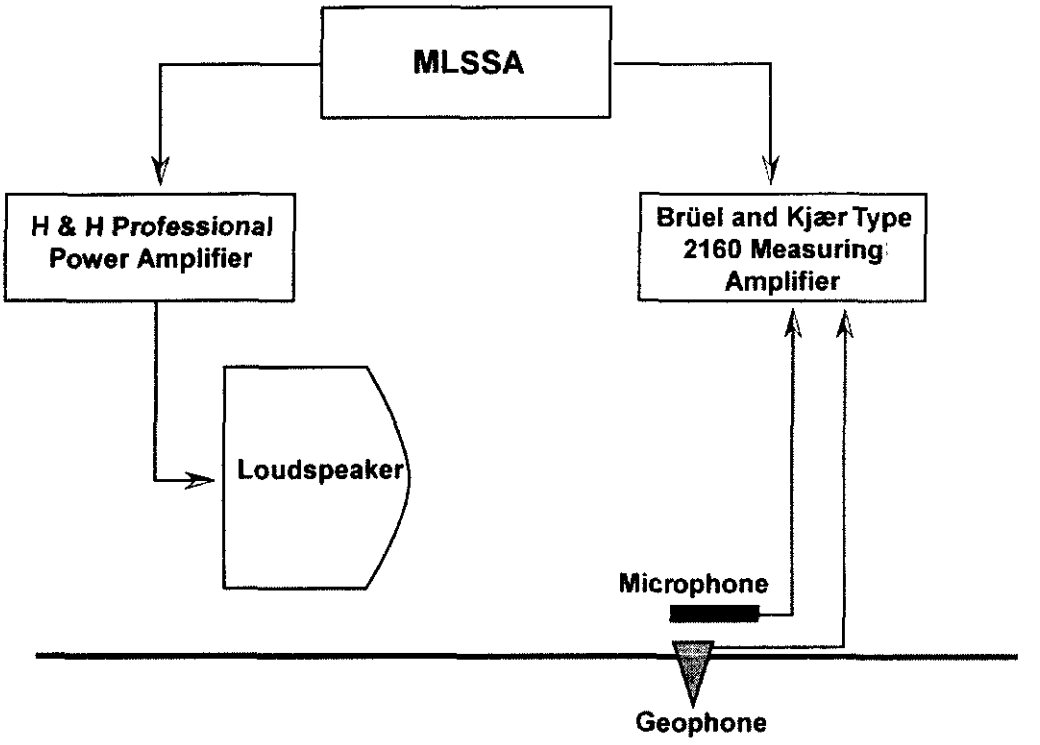

Figure 7-10. Data recording system for acoustic-to-seismic coupling measurements.

Before any measurements were taken, time was spent to avoid direct mechanical transfer of energy between the loudspeaker and the ground.

Firstly, the Tannoy was laid directly on the ground. Impulses were then generated on the outer casing of the Tannoy and the resulting acoustic and seismic waves were measured. The microphone provided a time scale to permit the separation of a seismic wave generated mechanically at the source and an acoustically coupled wave. The Tannoy was then supported by two retort stands and clamped in place and the effect on the received signals noted. Thick elastic bands were then used to suspend the speaker from the retort clamps and finally both retort stands were placed on a 6cm thick piece of felt.

All the solutions reduced the measured signals to below the ambient seismic noise level. Subsequent measurements were taken with the Tannoy supported from elastic bands, which were connected to the retort stands.

The geophone response to a 3kHz MLS generated by the speaker was also noted as the de-coupling was applied. This allowed the effectiveness of the de-coupling as a function of frequency to be observed. It also showed that there were no resonant frequencies in the isolation system that would selectively pass low frequency energy to the earth and geophone.

Initial experiments were conducted using the experimental set-up seen in Figure 7-11. The loudspeaker was set-up as described above, at a height of 0.15m. The geophone was then positioned at a range of 1.0m and pushed firmly into the gravel until it was flush with the surface. The microphone was then placed in a microphone holder and positioned 0.05m directly above.

The geophone was then connected to MLSSA, via the measuring amplifier. The MLSSA system allows MLS noise to be broadcast without data acquisition and this was completed first so that the levels on the amplifier could be modified until a reasonable scale-deflection was achieved.

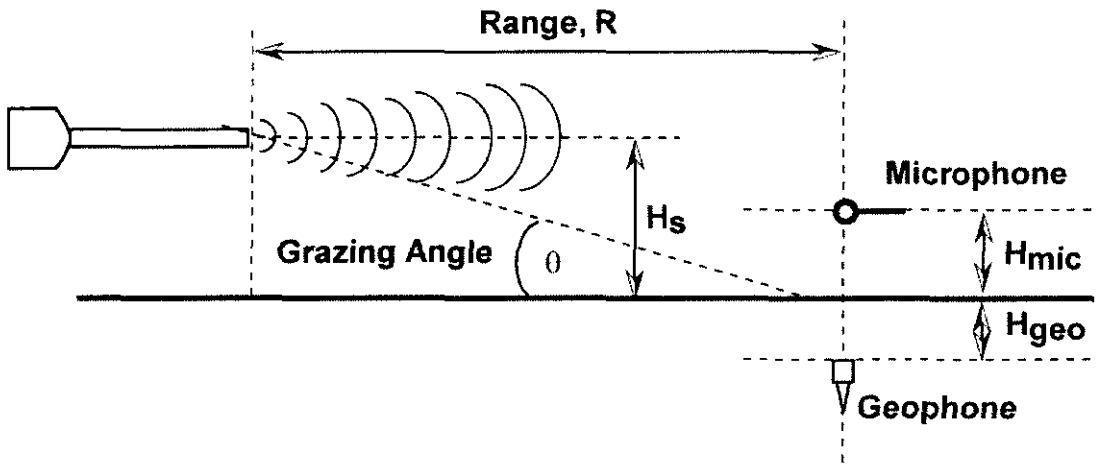

Figure 7-11. Experimental Set-up for acoustic-to-seismic coupling ratio measurements

Background levels of vibration were observed on the measuring amplifier until background environmental noise was seen to be a minimum. The number of averages was set and a reading taken. This number was usually set at 16, using the "GO Average" command.

The pre-averaging MLSSA routine was also used when levels of background noise were high. Pre-averaging of 16 MLS periods can result in a 12dB signal-to-noise ratio improvement.

The difference between the GO Average command and pre-averaging is that the former averages the impulse response, not the raw data, after the cross-correlation operation and is therefore inherently slower than pre-averaging which averages the raw data before cross-correlation in real time. By combining pre-averaging and Go Average command it is possible to achieve very long averaging times with a minimum of computational overhead, that is, only slightly slower than real time operation. For example, by selecting 16 pre-average cycles and 10 Go Average you can obtain the same signal-to-noise ratio as doing 160 pre-averages with only a small computational time penalty.

Once a geophone measurement had been taken the microphone was connected into the circuit and the procedure repeated. All time domain signals are saved for later analysis.

Further measurements were taken with increasing source heights of 0.20m, 0.30m, 0.40m, 0.50m and 0.75m to assess if there was any angle dependence on the recorded sensor responses. The source was then set back to 0.15m and all source heights repeated. Both receivers were left untouched throughout.

Once this set of experiments had been completed, all the equipment was moved 20cm to one-side and a set of measurements taken parallel to the original readings. Measurements were also taken at ranges of 1.5m 2.0m 2.5m and 3.0m. All these measurements were undertaken in an attempt to assess the repeatability of the experiments and the reliability of the technique.

The whole examination was then repeated as described above, however, once a complete set of source heights had been recorded the geophone was removed and replaced in the same position. This was performed to test the influence of the geophone ground coupling on the recorded signal and ultimately its effect on the acoustic-to-seismic coupling ratio spectra.

7.1.3 In-situ Sensor Calibration

The vertical component geophone sensors used in the experiments underwent in-situ calibration to assess their useable bandwidth and to assess their sensitivity once buried.

The earth-geophone coupling was investigated by dropping a small steel ballbearing onto the geophone case and recording the geophone signal. From each measurement, the ping frequency f_0' was obtained from the geophone response by zero crossing measurements (See Figure 7-12), whilst the damping coefficient (γ_d) was obtained from a line fit to the logarithmic plot of amplitude versus time. The influence of the geophone internal coil was neglected.

The coupling resonant frequency f_0 was then calculated from the experimental values of the ping frequency (f_0') and the damping coefficient (γ_d) by using the following relationships:

$$\eta_d = \frac{2\gamma_d}{\omega_0} \qquad \textit{(Eq. 7-20)}$$

and

$$(\omega_0')^2 = \omega_0^2\left(1 - \frac{\eta_d^{\,2}}{4}\right) \qquad \textit{(Eq. 7-21)}$$

Rearranging gives:

$$(\omega_0) = \sqrt{(\omega_0')^2 + \gamma_d^{\,2}} \qquad \textit{(Eq. 7-22)}$$

This working follows that undertaken by Hoover and O'Brien (1980), although it can be noted that in their paper Equation 7-22 is incorrectly given.

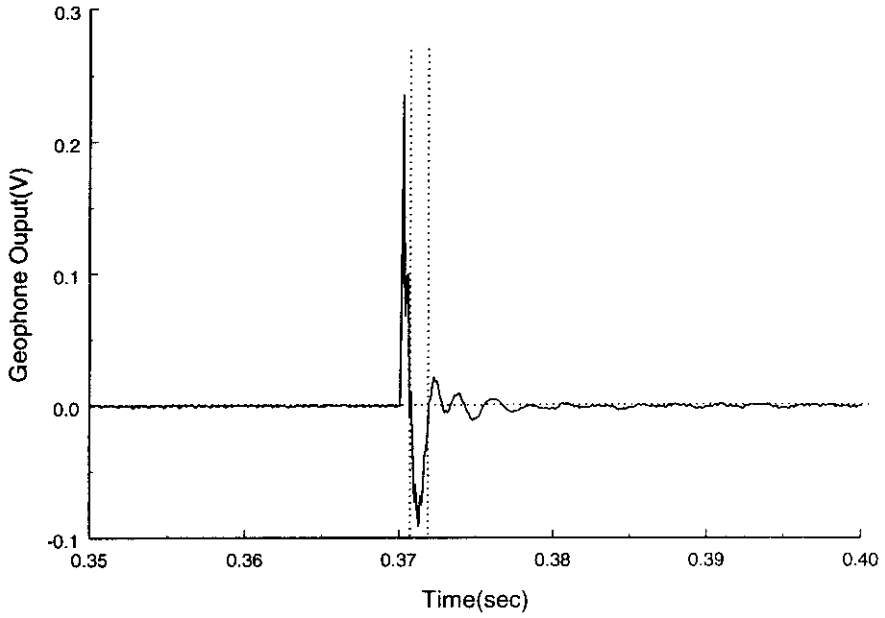

*Figure 7-12. Determination of "ping" frequency from zero-crossing measurements. The zero axis is crossed twice per period - once downwards and once upwards. The period of the oscillation is twice the time between zero crossing. The "ping" frequency is then 1/period. Here: Zero crossing = 1.3e-3sec. Frequency = 1/(1.3e-3)*2 = 385Hz*

In a modification of the "pinging" technique, an assessment of the in-situ sensitivity of the geophone was determined by using the laws of conservation of momentum. The initial height from which the ball bearing is dropped was not known. However, the output voltage of the geophone and the time interval Δt between bounces could be measured accurately, allowing the impact velocity v of the ballbearing to be determined from: -

$$v = g\,\Delta t / 2 \qquad \textit{(Eq. 7-23)}$$

where g = 9.8m/s^2. The law of conservation of momentum for the collision between the ballbearing (of mass m^{bb} and velocity v^{bb}) and the geophone (with mass m^{geo} and velocity V^{geo}) is

$$m^{bb}v_1{}^{bb} = m^{geo}v_2{}^{geo} - m^{bb}v_2{}^{bb} \qquad \textit{(Eq. 7-24)}$$

where the subscripts 1 and 2 refer to before and after the impact; the geophone is initially at rest (v_1^{geo}=0). Rearranging gives:

$$v_2^{geo}=(v_1^{bb}+v_2^{bb})m^{bb} / m^{geo} \qquad (Eq.\ 7\text{-}25)$$

The masses m^{geo} and m^{bb} were determined by weighing. These values were used to determine v_2^{geo} from Eq. 7-25. The sensitivity was calculated over a number of bounces to find an average value for the geophone sensitivity. This is an adaptation of a technique used by Albert (1993).

This method for geophone sensitivity relies on the assumption that only the geophone is accelerated by the ballbearing. In practice, some portion of the surrounding soil will also be accelerated, so the effective mass (m^{eff}) is $m^{eff}=m^{geo}+m^{soil}$, and the calculated geophone sensitivities should be decreased. The value of m^{eff} depends on how firmly the geophone is planted into the ground and on the soil properties. For these reasons, it is very difficult to determine an accurate value of m^{eff}.

The results, therefore, give an indication of the variability between geophones and their coupling to the soil, and act as confirmation that the amplitude measurements are within the accuracy of the "pinging".

Geophone "pinging" measurements in the field were undertaken to quantify the coupling resonant frequency and the sensitivity of the geophones used in the acoustic-to-seismic coupling ratio measurements. A ballbearing was dropped through a steel pipe, 15cm long, held vertically above the geophone and allowed to bounce a number of times. A schematic of the experiment can be seen in Figure 7-13.

Signal acquisition is accomplished using an IBM compatible PC containing a National Instruments E-Series AT-MIO-16E-2 acquisition board in conjunction with a SC-2040 add-on board. The SC-2040 is used here as a differential amplifier for the geophone signal. The ballbearing was placed into the tube and held in-place by the magnetic field produced by powering the solenoid. It was important when setting up the tube that it was held vertical so that the subsequent bounces of the ballbearing didn't hit the side of the tube, which would give a false indication of the recorded amplitudes. When the current to the solenoid was turned off the ballbearing fell and the current drop triggered the acquisition. The geophone signal was displayed and recorded using purpose-built Labview software.

A Brüel and Kjær pistonphone was used for microphone calibration.

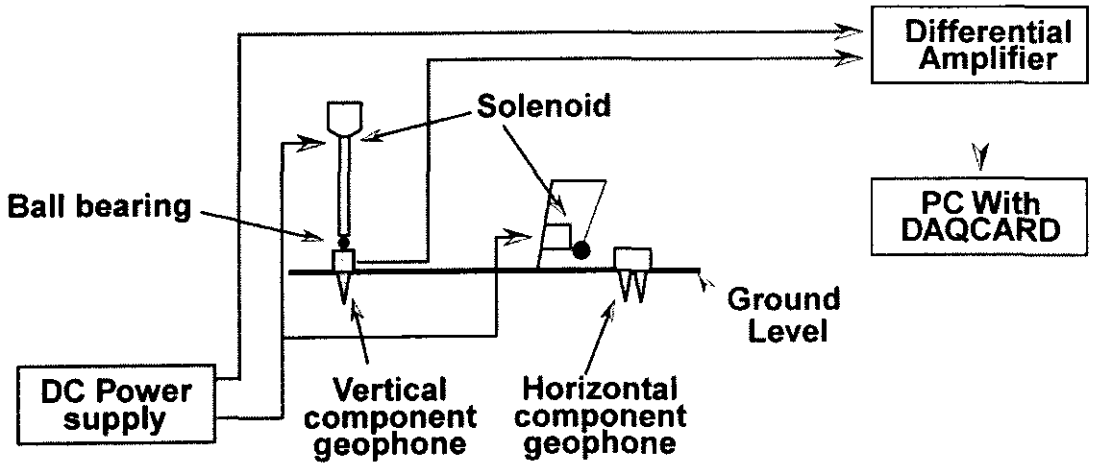

Figure 7-13. Experimental Set-up for geophone "Ping" tests.

7.1.4 Probe Microphone

Probe microphone measurements were taken at the test site. Experiments were undertaken in a similar manner to that used in the indoor soil tank.

The source-signal (MLS), data acquisition and post processing were accomplished using the MLSSA system. Two receivers were used, the probe microphone and a reference microphone. This reference was a Brüel and Kjær Type 4191 condenser microphone, using a Type 2645 preamplifier.

The MLS produced was amplified using an H&H S150 professional power amplifier and broadcast from a loudspeaker. The outputs from the receivers were amplified using a Brüel and Kjær Type 2160 Measuring amplifier before being sampled back into the MLSSA system. The probe was also amplified using a purpose built battery power supply/preamplifier. A bandwidth of 3kHz was used with the signals being sampled at 9kHz by MLSSA.

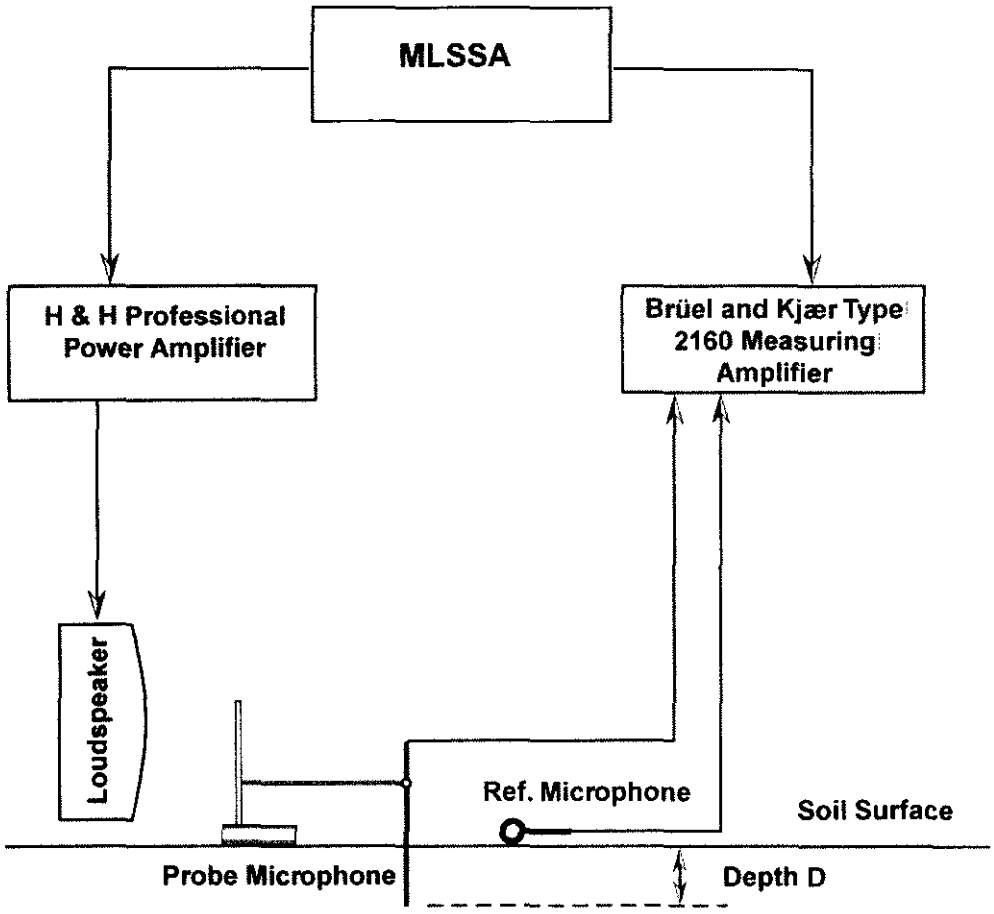

Figure 7-14. Probe microphone set-up

Firstly, the probe microphone support was placed on the gravel. This consisted of a retort stand and a Brüel and Kjær microphone holder. A reference measurement was taken with the probe and reference microphone collocated at the surface. Data was taken at a range of 2.0m from the loudspeaker.

The probe microphone was then placed in the microphone holder and gently inserted into the ground until its was buried to 1cm. The reference microphone is left untouched. Measurements were then taken with the probe down to 0.14m in 0.01m steps. All time domain signals were saved for subsequent analysis.

Burial of the probe and accurate depth determination of the probe was hampered by the coarse nature of the gravel. It was found extremely difficult to hand push the probe further than 0.14m into the gravel. The gravel proved too unstable to allow a hole to be pre-drilled with a soil auger.

7.1.5 Meteorological Data

During the acoustic-to-seismic coupling measurements, temperature and wind speed data was collected using a Dantec 54N-60 Flowmaster precision anemometer. These values were used to confirm similar meteorological conditions during subsequent measurements.

The instrument calibration was referred to air at 101kPa, 20°C and 20% relative humidity (*rH*). If maximum accuracy is needed or if the measuring conditions deviate considerably from those during calibration, the actual values for pressure and humidity can be entered into the instrument. However, this level of accuracy was not required and no further calibration was carried out.

The transducer was mounted on a retort stand approximately 0.75m above the ground surface close to the gravel pit. The wind-direction is determined and the transducer oriented perpendicular to the flow and with the marks on the shank pointing towards the flow.

7.2 Stone Lane Quarry, Heath and Reach

Measurements were undertaken at the Hepworth Minerals and Chemicals (HMC), Stone Lane Quarry, Heath and Reach, Bedfordshire. A description of the site and the in-situ material can be found in Chapter 4. Briefly, the site consists of a large depth of sand. The test area was an area of $20m^2$ of sand that was not used for extraction and so remained undisturbed during the period of investigation.

7.2.1 Seismic Refraction Surveying

A seismic refraction survey was carried out at the site to deduce the P-wave and S-wave velocity, and to determine whether there were any layers in the sand.

The P-wave survey was carried out in a similar manner to that described in Section 7.1.1.6. However, for this investigation the first sensor was positioned 4.0m away from the

plate. The three remaining geophones were added at 1.00m intervals. Sixteen averages were taken. Once the acquisition had been completed, geophones were moved to a distance of 7.0m, 8.0m, 9.0m and 10.0m, to increase the spread length and therefore the depth of investigation.

On completion, the process was repeated with the shot point moved to the other end of the survey line for reverse shooting.

The S-wave survey was carried out using the standard procedure. An 8" scaffold plank was laid on the ground and a Land Rover driven onto it as a kentledge. The trigger geophone was positioned at the end of the plank and the geophones positioned perpendicular to the plank, aligned with the centre. The first horizontal component geophone was placed 4.0m from the plank with the remaining geophones placed at 1.0m intervals.

With background noise at a minimum and gain levels set, hammer blows were made to the end of the plank and the resultant averaged signals recorded. The operator then moved to the other end of the plank together with the trigger geophone and further blows made. Once this process had been completed, further measurements were taken with the geophones at 7.0m, 8.0m, 9.0m and 10.0m from the plank. All signals were saved for subsequent analysis as outlined in Section 7.1.1.5.

7.2.2 Acoustic-to-Seismic Coupling Ratio

A similar set of acoustic-to-seismic coupling experiments to those undertaken at the ARG test site were carried out here. For the majority of the experiments, the same apparatus was used. A schematic of the test apparatus is shown in Figure 7-10, whilst the experimental set-up can be seen in Figure 7-11.

Initial experiments taken at the quarry produced some anomalous results on the geophone response. Figure 7-15 shows an example of a geophone response that includes the spurious signal content. Further investigations showed that the anomaly only appeared on the geophone response and was not seen in the microphone data.

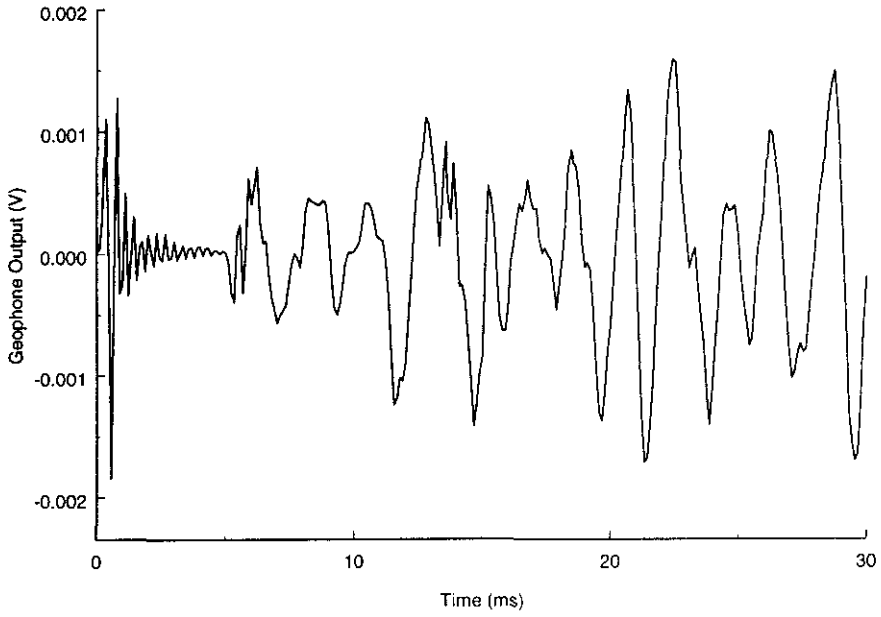

Figure 7-15. Geophone Response that includes spurious signal component at 0ms.

No mains power supply was available at the Stone Lane, the equipment was powered by a portable power supply. It was also seen that this anomaly only appeared on records taken using the portable power supply.

Several weeks of investigations showed that the problem related to electrostatic interference with stray electric fields. By surrounding the geophone with a conducting lining the interference seen on the geophone response was reduced to almost zero. To accomplish the shielding, the positive pin of the geophone was potted with silicon rubber to seal it, and then the geophone was sprayed with nickel screening compound. This is an electro-conductive coating based on nickel and designed for EMI/RFI shielding.

By surrounding the geophone with a conducting lining, the external electric field redistributes the free electrons in the conductor, leaving a net positive charge on the outer surface in some regions and a net negative charge in other (See Figure 7-16). This charge distribution causes an additional electric field such that the total field at every point inside the geophone is zero, in accordance with Gauss's law. Such a set-up is often called a Faraday cage.

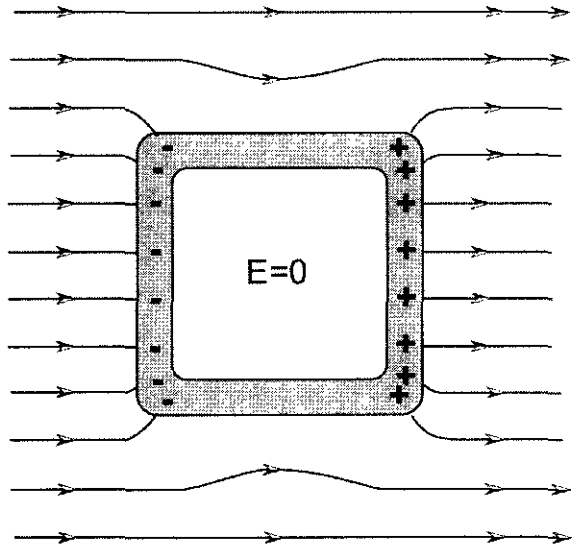

Figure 7-16. A geophone (with electrostatic shielding) in a uniform electric field. The field pushes electrons toward the left, leaving a net negative charge on the left side and a positive charge on the right side. The total electric field at every point inside the geophone is zero.

In addition to the conductive lining modification, the twin-core geophone cable was replaced by co-axial cable.

Once the problems with the geophones had been resolved, measurements followed those taken at the ARG. The Tannoy was set at height of 0.15m, whilst a vertical component geophone was placed at a range of 1.0m. The microphone was then positioned at a height of 0.05m directly above the geophone. Measurements were taken at further source heights of 0.30m, 0.40m, 0.50m and 0.75m. After data had been collected at all the source heights, the geophone was removed and replaced in the same position. Determinations of the coupling were then repeated for all source heights. On completion of this data collection, the experimental set-up was moved to an area 20cm parallel to the original position and all the measurements repeated.

Due to the increased area available at the quarry, longer-range measurements were possible. However, the Tannoy source was not suitable for these measurements due to its lack of power output. For long-range experiments, a purpose built loudspeaker was designed (dubbed "OU-1"). It was designed to have a strong output at low frequencies to match the measurement requirements, i.e. in the 100Hz to 500Hz range. It was based around a 12" Precision driver.

Loudspeaker design is a balance of compromises involving enclosure size, low frequency cut-off, and transient response. The speaker enclosure was designed using "Perfect Box" CAD program. This is a shareware program written by Warren A Merkel, which allows the modelling of loudspeaker enclosures on a PC. The program only considers low frequency drivers in multi-way systems (or the only driver in a full-range system). The numerical model used is based around the use of the Theile/Small (or T/S) parameters.

Again, before any measurements were taken, time was spent to avoid direct mechanical transfer of energy between the loudspeaker "OU-1" and the ground. Firstly, the loudspeaker was laid directly on the ground. Impulses were then generated on the outer casing of the speaker enclosure and the resulting acoustic and seismic waves were measured. The microphone provided a time scale to permit the separation of a seismic wave generated mechanically at the source and an acoustically coupled wave.

The speaker was then placed on an articulated loudspeaker stand that reduced the measured signals to below the ambient seismic noise level, without the need for further improvements. The stand is adjustable to allow differing source heights to be used. The geophone response to an MLS generated by the speaker was also noted as the de-coupling was applied. This allowed the effectiveness of the de-coupling as a function of frequency to be observed. It also showed that there were no resonant frequencies in the isolation system that would selectively pass low frequency energy to the earth and geophone.

The loudspeaker was then set-up at a height of 0.75m and a vertical component geophone placed at a range of 3.0m. The microphone was placed directly above the geophone at a height of 0.05m. At this time, data was also taken using a horizontal component geophone. The horizontal component sensors used were Western Atlas Type SM-6/H-B, having a natural frequency of 10Hz and installed in a HPE land case.

Further measurements were taken with both vertical and horizontal component geophones using a source height of 1.5m before the apparatus was moved approximately 20cm parallel to the original test area and the experiments repeated. Data was also taken using a range of 6.0m and 9.0m.

As part of the suite of experiments to assess the influence of the effect of geophone ground coupling on the received sensor response, a number of readings were taken using the vertical component geophone inserted into the ground in various attitudes. These can be seen in Figure 7-17.

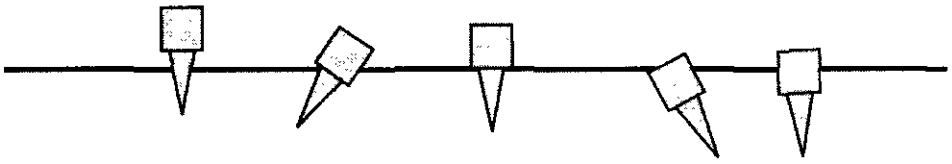

Figure 7-17. Variation in geophone position.

7.2.3 In-situ Sensor Calibration

The vertical component geophones underwent in-situ calibration as described in Section 7.1.3. A method was also devised for assessing the in-situ bandwidth of the horizontal component geophones used (a schematic can be seen in Figure 7-13) based upon the method used for the vertical component geophones.

The experiments consisted of a small metal tripod, to which a small weight was attached via a piece of string. A solenoid was also attached to the tripod. With current applied to the solenoid, the weight was held in place. When the current to the solenoid was switched off, the weight was released. The current drop also acted as the trigger for the acquisition.

A Brüel and Kjær pistonphone was used for microphone calibration.

7.2.4 Probe Microphone

Probe microphone measurements were taken at Stone Lane. Experiments were undertaken in a similar manner to that used in the indoor soil tank (See Chapter 5). The equipment used was the same as that used at the ARG test site, as described in Section 7.1.4 and set-up as shown in Figure 7-14.

Measurements were taken with the probe down to 0.16m in 0.01m steps with all time domain signals saved for subsequent analysis. The fine nature of the sand proved to be a difficulty, as it tended to block the air holes in the nose of the probe. The sand proved too unstable to allow a hole to be pre-drilled with a soil auger.

7.2.5 Meteorological Data

Meteorological data was again taken concurrently with the acoustic-to-seismic coupling ratio measurements. These were taken as described in Section 7.1.5.

7.3 Horticultural Research International, Wellesbourne

Measurements were undertaken at Horticultural Research International, Wellesbourne, Warwickshire. A description of the site and the in-situ material can be found in Chapter 4. Briefly, the site consists of a specially prepared experimental plot that was being used by HRI as part of a seed emergence monitoring experiment. The site consisted of an artificial seedbed 6m wide by 26m length with three different soil types in 2-m wide bands.

7.3.1 Seismic Refraction Surveying

Small-scale refraction surveys were undertaken on all three soil-beds at the HRI test site. The P-wave survey was undertaken using the standard procedures as outlined in Section 7.1.1.6. Three vertical component geophones were used throughout, with a fourth used as the trigger signal. The first receiver was placed at 1.5m with the remaining geophones placed at 0.5m offsets. Measurements were repeated with geophones positioned at 0.5m intervals up to an offset of 5.5m. The process was then repeated by reversing the scanline for reverse-shooting.

Due to the limited width of the three soil-beds, it proved impossible to use the scaffold plank previously used for the shear wave survey. The use of a shorter plank was precluded due to a lack of suitable kentledge. Therefore, to evaluate the S-wave velocity of the soils, measurements were taken based upon the technique used in the indoor soil tank (see Section 4.1.1.3). A line of four horizontal component geophones was laid out close to the centre of the each soil-bed, with an end geophone used as the source. Five-cycle tone

bursts were used as a source signal, broadcast by the first geophone with travel times to the subsequent geophones recorded. Geophones were laid 0.10m apart. Each geophone was subsequently used as a source in turn.

The procedure was repeated in a second position in the soil to test homogeneity.

7.3.2 Acoustic-to-Seismic Coupling Ratio

Identical acoustic-to-seismic coupling ratio measurements were carried out on all three soil-beds using the procedures outlined in Section 7.1.2. Short-range measurements were taken at a range of 1.0m and 2.0m with the Tannoy speaker, using source heights of 0.15m, 0.30m and 0.45m. Data was taken using both vertical and horizontal component geophones, with a microphone set at a height of 0.05m

Longer-range measurements were taken using the "OU-1" loudspeaker at 2.0m and 3.0m. The source was set at a height of 0.45m and 0.68m, using the same sensor configuration.

7.3.3 In-situ Sensor Calibration

In-situ calibration of both the vertical and horizontal component geophone sensors used in the acoustic-to-seismic coupling measurements was undertaken using the methods outlined in Section 7.1.3 and 7.2.3, using the set-up shown in Figure 7-13.

A Brüel and Kjær pistonphone was used for microphone calibration.

7.3.4 Probe Microphone

Probe microphone measurements were undertaken on the three soil-beds using a similar experimental configuration to that described in Section 7.1.4. The "OU-1" loudspeaker was set-up at a height of 0.68m whilst the probe microphone was placed at a range of 2.0m. Since the in-situ materials were consolidated and friable, a special preparation

procedure was used to ensure that an acoustic seal existed around the perimeter of the probe microphones entry into the soil.

A cylindrical soil auger of the same diameter as the probe was then slowly inserted into the ground. The depth of penetration was regularly checked by carefully removing the auger and inserting the probe into the pre-drilled hole. Once the correct depth had been achieved, the probe was inserted into the ground. To ensure the acoustic seal, the soil which had been removed by the auger was crushed and placed around the probe.

7.3.5 Meteorological Data

Although HRI had a permanent weather station at the site recording wind speed, direction and waterfall levels, separate meteorological data was taken throughout the test period.

Data was collected using a Gill Instruments R3 omnidirectional sonic anemometer. The anemometer uses time-of-flight measurements between three transducers to evaluate windspeed, wind direction and either speed of sound or sonic temperature. Sonic temperature closely approximates the virtual temperature of the air, although for true temperature values the humidity of the air must be known. The humidity of the air was not known during the experiments and therefore only virtual temperatures were recorded.

The basic time-of-flight operating principle is physically fundamental and provides vector measurements of air velocity dependent mainly on the dimensions and geometry of the transducer array. A pair of transducers act alternatively as transmitters and receivers, sending pulses of high frequency ultrasound between themselves. The times of flight in each direction, t_1 and t_2, are measured. If c_0 is the speed of sound, L is the distance between transducers and there is an air flow v along the line of the transducers, the following relationships are readily derived.

$$t_1 = L / (c_0 + v) \qquad \textit{(Eq. 7-26)}$$

$$t_2 = L / (c_0 - v) \qquad \textit{(Eq. 7-27)}$$

By inverting and subtracting, v is solved explicitly: -

$$v = 0.5L \, (1 / t_1 - 1 / t_2) \qquad \textit{(Eq. 7-28)}$$

This wind vector derivation is not affected by c_0 or any other parameters such as temperature or contaminant content. Conversely, c_0 is obtained by inverting and adding

$$c_0 = 0.5L\,(1/t_1 + 1/t_2) \qquad (Eq.\ 7\text{-}29)$$

v represents the vector component of air flow resolved along the line of the pair of transducers. By arranging three pairs of transducers in different orientations, the direction and magnitude of the incident airflow may be unambiguously derived. The transducer pairs do not have to conform to cartesian axes. For optimum undisturbed airflow a non-orthogonal arrangement is employed.

The use of the three transducers in the derivation of the sonic temperature has the following advantages.

1) Noise reduction due to averaging over three axes.

2) Reduction of errors caused by wind shadowing on a single measurement axis in specific wind directions.

3) Cancellation of measurement errors caused by the anemometer head bending. However stiff the head assembly is made, some bending is inevitable in strong winds.

4) Improved correlation between the velocity and temperature measurements, since both are derived from the same set of six transit times.

5) Simpler implementation, because crosswind correction can be carried out without complicated vector algebra or trigonometric functions.

A correction is applied to the anemometer output to calibrate out the effect of the transducers and head framework. The anemometer then gives the UVW orthogonal components of the wind direction and the sonic temperature, sampled at a rate of 100Hz.

From the four outputs, the speed of sound in air can be calculated from the value of sonic temperature from: -

$$Ts_1 = c_0^2 / 403 \qquad (Eq.\ 7\text{-}30)$$

whilst windspeed and direction are calculated from the values of *UVW*. The values of *UVW* and *T* can also allow a number of other meteorological parameters to be calculated including longitudinal, transversal and vertical turbulence intensities; friction velocity and drag coefficient.

A full description of the principles of sonic thermometry can be found in Kaimal and Gaynor (1991).

The four analogue outputs, *UVW* and *T*, were recorded using a Sony DAT recorder. This has eight differential input/outputs, each of which has a software selectable gain setting. The DAT has an overall bandwidth of 44kHz, which is divided over the eight channels. The anemometer was set-up at the start of the experiments and as each measurement was taken a digital marker was placed on the DAT tape. This marker was used in the subsequent analysis to differentiate between the measurements.

The meteorological data was analysed using a purpose written Labview program to calculate the wind speed, direction, temperature and turbulence parameters (See Figure 7-18) from recorded values of *UVW* and *T*.

7.3.6 Acoustically induced Surface Waves

Shear wave velocity is an important soil property for the evaluation of dynamic behaviour of soils as well as static deformation of the ground. Most of the field tests currently conducted for determining v_s-profiles require boreholes, which are by their very nature invasive.

According to elastic theory there is a direct link between shear wave velocity and Rayleigh wave velocity. The determination of v_s-profiles from Rayleigh wave methods is promising and attractive, since the field measurements can be performed just by placing sensors on the ground surface. To determine v_s-profiles, the Rayleigh wave method requires both measurement of the relationship between phase velocity and wavelength, called the dispersion curve, and the inverse analysis of the measured curve.

An experimental investigation was made into the measurement of acoustically induced seismic surface waves. The basic procedures adopted in Rayleigh wave investigations involve:

a) the generation of predominantly vertical ground motions using a point source of energy, as either a transient impulse or a continuous wave

b) measurement of ground surface motions using geophones placed in a line with is co-linear with the source

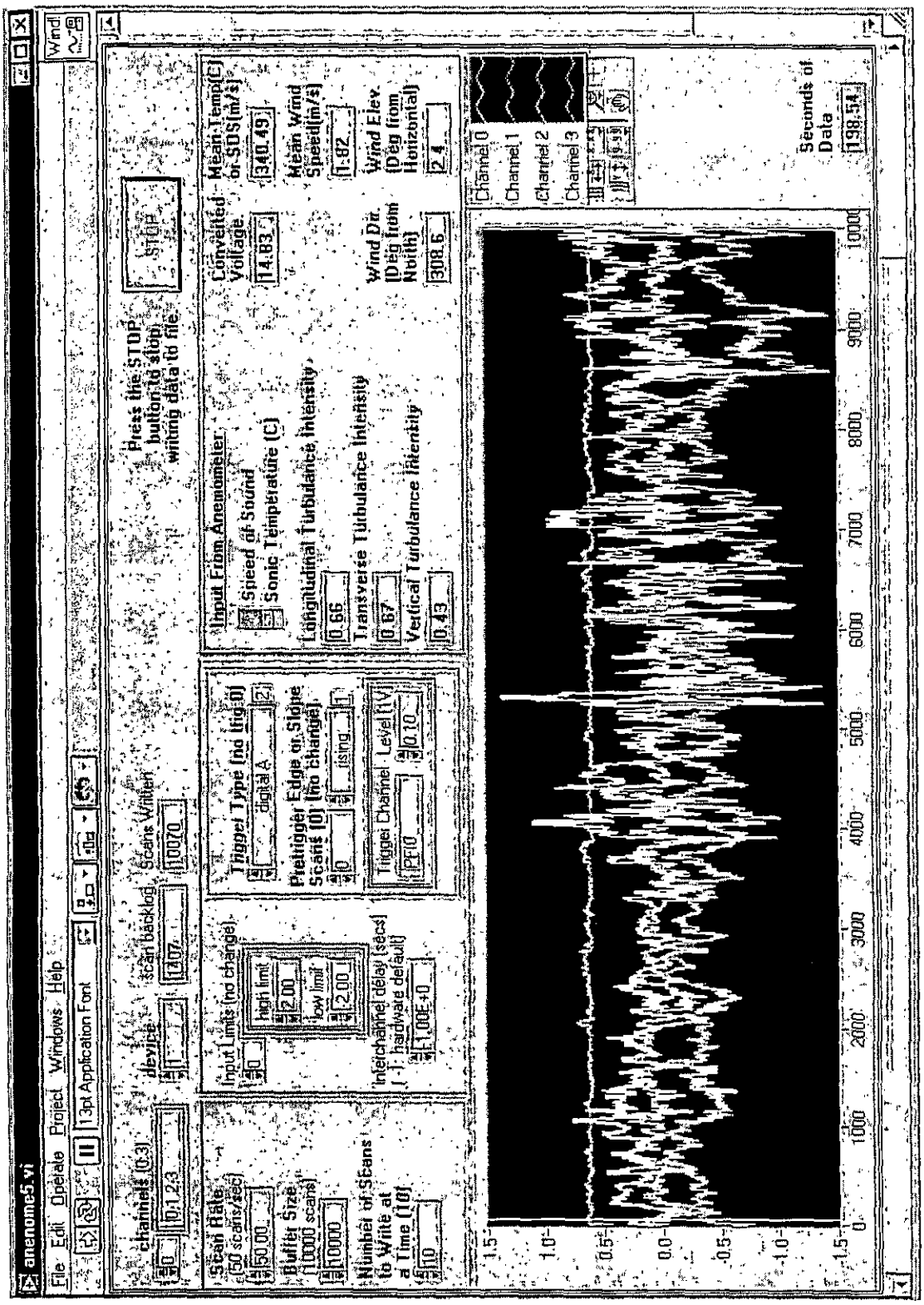

Figure 7-18. Analysis of meteorological data taken using the anemometer

c) the recording of ground surface motions with an oscilloscope, spectrum analyser or seismogram

d) use of spectral analysis of the data to produce a dispersion curve, showing the variation of Rayleigh wave velocity with wavelength

In seismic investigations, there are two forms of surface wave source in use: impact sources, such as a hammer or drop weight, which produce a transient impulse, and vibrators that produce continuous waves. The choice of source affects the details of the way in which the field data are acquired and subsequent data processing. Impact sources have been frequently used in North America (Stokoe and Nazauan, 1985; Addo and Robertson, 1992) with the data being processed using the Spectral Analysis of Surface Waves (SASW) method. Vibrator sources have been widely adopted in the UK (Abbiss, 1981; Matthews, 1993; Butcher and Tam, 1994) and Japan (Tokimatsu *et al.*, 1991) with the Continuous Surface Wave (CSW) method.

Of the two approaches to surface wave testing, SASW appears to be more attractive due to the simplicity and cheapness of the sources. However, the restricted lack of control over the frequencies generated by impulse-type sources imposes a serious limitation on the SASW method. The use of a source capable of producing mono-frequencies, such as a loudspeaker, overcomes this problem. Also, since the loudspeaker can produce pure tones, unwanted noise is easily filtered from the data. For this reason, experiments on acoustically induced seismic surface waves were undertaken using the continuous surface wave method. The system consisted of a loudspeaker source, two pairs of geophones sensors, an amplifier and an acquisition board. Figure 7-19 shows a schematic diagram of the test system.

A TT*i* TGA1230 arbitrary wave generator was used to supply the input signal that was amplified using an H&H S150 professional power amplifier before being broadcast by OU-1 loudspeaker. A series of pure tones with frequencies of 100Hz to 500Hz, in 10Hz steps, were used as the output signal. Signal acquisition was accomplished using an IBM compatible PC containing a National Instruments E-Series AT-MIO-16E-2 acquisition card in conjunction with a SC-2040 add-on board. The SC-2040 was used for both amplification of the geophone signals and to preserve interchannel phase relationships. This is especially important for the subsequent spectral analysis. The acquisition and field analysis was undertaken using a purpose written Labview program (Figure 7-21) based upon previous work (Tokimatsu *et al.*, 1991).

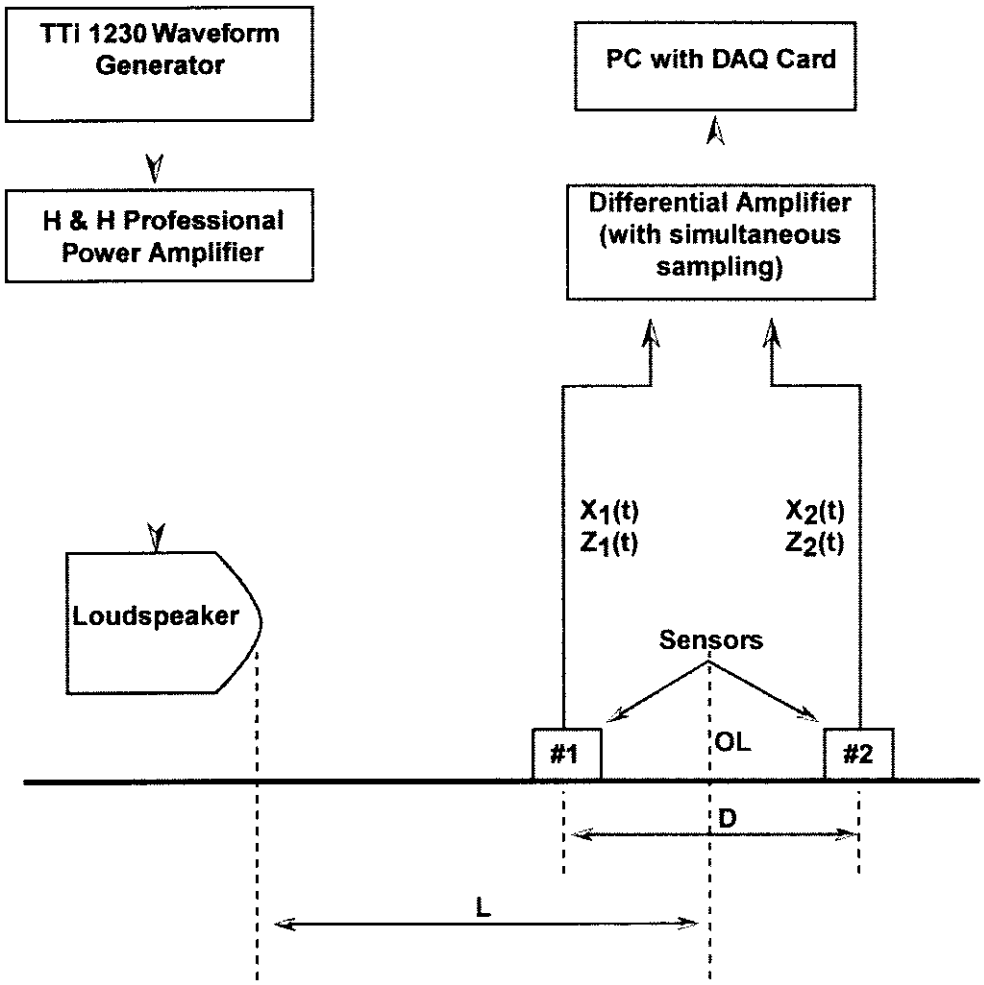

Figure 7-19. Schematic diagram of the test system.

Both vertical and horizontal component geophones were used as ground motion sensors. The geophone sensors used were manufactured by Western Atlas, developed by HGS Sensors Operations. The vertical component sensors were Type SM-4/U-B, having a natural frequency of 10Hz and installed in a PE-3/C land case. The horizontal component sensors were Type SM-6/H-B, having a natural frequency of 10Hz and installed in a HPE land case.

As shown in Figure 7-19 a point was selected on the ground surface under which the Rayleigh wave profile is to be made. The loudspeaker was positioned at a horizontal distance L from the point. The two pairs of sensors (#1 and #2) were then positioned in line with the loudspeaker and the point and symmetrically about the centre line at a distance D.

The spacing of the geophones is important consideration in the experiment. The distances D, between the pairs of sensors, and L, between source and mid-point of the

sensors are essential factors in the survey design. Heisey *et al.* (1982) suggested due to limitations of recording equipment and the attenuative properties of the ground, D should be $\lambda/3<D>2\lambda$ where λ is the wavelength of the surface wave under consideration. Based on a more comprehensive study of Rayleigh wave propagation and particle orbits (Tokimatsu *et al.*, 1991) recommended the following empirical rules

$$\lambda/4 \leq L \qquad \textit{(Eq. 7-31)}$$

And

$$\lambda/16 \leq D < \lambda \qquad \textit{(Eq. 7-32)}$$

Based on these recommendations L was set at 2.0m and D at 30cm.

It has been shown that the particle orbit of Rayleigh waves in any place in the ground is elliptical in the vertical plane containing the direction of propagation, as shown in Figure 7-20. In an ideal case, the horizontal particle motion is either behind or ahead the vertical motion by 90° in phase. This means that the orbit is either prograde or retrograde elliptical and that the major and minor axes of the ellipse correspond to the vertical and horizontal axes.

The characteristics of particle orbits may vary depending upon the mode and wavelength of Rayleigh wave as well as the soil profile underground. Thus, such information can be used to identify which mode of Rayleigh wave is predominant and whether or not the measured motions are Rayleigh waves. This is the reason that the radial motions are measured in conjunction with the vertical motions.

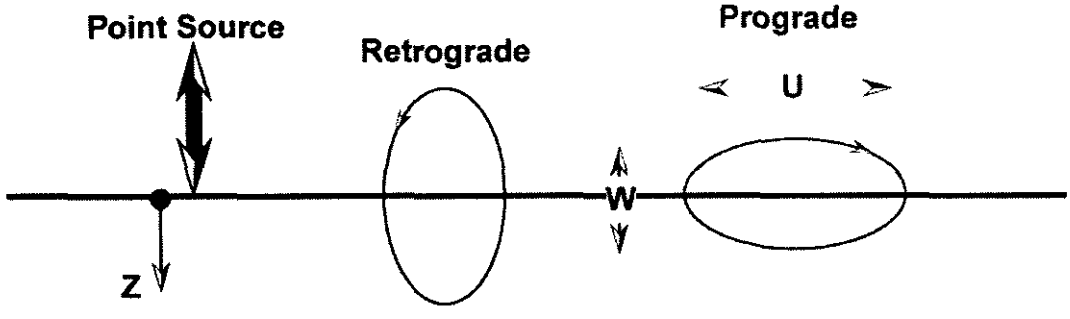

Figure 7-20. Particle orbits of the Rayleigh wave.

The waveform generator was used to output a pure tone of frequency, f_i, which was amplified and broadcast by the loudspeaker. The analogue motions measured with the sensors were amplified and digitised by the AT-MIO-16E-2 acquisition card. The digitised motions in the time domain are defined as $z_1(t)$, $z_2(t)$, $x_1(t)$ and $x_2(t)$ in which z and x indicate vertical and horizontal motions, and the subscripts *1* and *2* correspond to the sensor number. The A/D conversion and the following spectrum analysis was made for 2048 digitised points at equal time intervals.

The recorded signals were first transformed from the time domain to the frequency domain $S_{z1}(f)$, $S_{z2}(f)$, $S_{x1}(f)$ and $S_{x1}(f)$, by Fast Fourier Transform. The cross power spectrum between the two vertical motions is given by

$$G_{z1z2}(f) = S_{z1}^{*}(f)S_{z2}(f) \qquad \textit{(Eq. 7-33)}$$

where * indicates the complex conjugate. The phase lag of the motions between the two observed points, ϕ_i, at frequency f_i, was determined from: -

$$\phi_i = -tan^{-1}(Q_{z1z2}(f_i) / K_{z1z2}(f_i)) \qquad \textit{(Eq. 7-34)}$$

where K is the real part of G and Q is the imaginary part of G. Where the amplitude of the vertical motions is significantly less than the horizontal motions, the computation of phase lag may be made using horizontal motions. The time lag of motions between two observed points, Δt, is then given by: -

$$\Delta t = \phi_i / 2\pi f_i \qquad \textit{(Eq. 7-35)}$$

The phase velocity, c_i, can then be calculated from: -

$$c_i = D / \Delta t \qquad \textit{(Eq. 7-36)}$$

By noting $c = f\lambda$, the corresponding wavelength, λ, is readily determined.

The particle orbit at each observed point can be obtained by plotting its horizontal and vertical motions on a x-z plane. The amplitude ratio between horizontal and vertical motions, u/w, (See Figure 7-20) may be given by

$$(u/w)_{in} = sign[Q_{xnzn}(f_i)]\frac{|S_{xn}(f_i)|}{|S_{zn}(f_i)|} \qquad \textit{(Eq. 7-37)}$$

where n indicates sensor number. Positive values of u/w indicate that the particle orbit is prograde, while negative values correspond to retrograde. Large absolute values mean the horizontal motions prevail, while small absolute values indicate dominance of vertical motions.

The particle velocity, the particle orbits and amplitude ratios were calculated and displayed by the program (Figure 7-21). These values together with the raw recorded motions are saved for later analysis.

Time constraints at the test area meant that surface wave measurements were only made on Soil A.

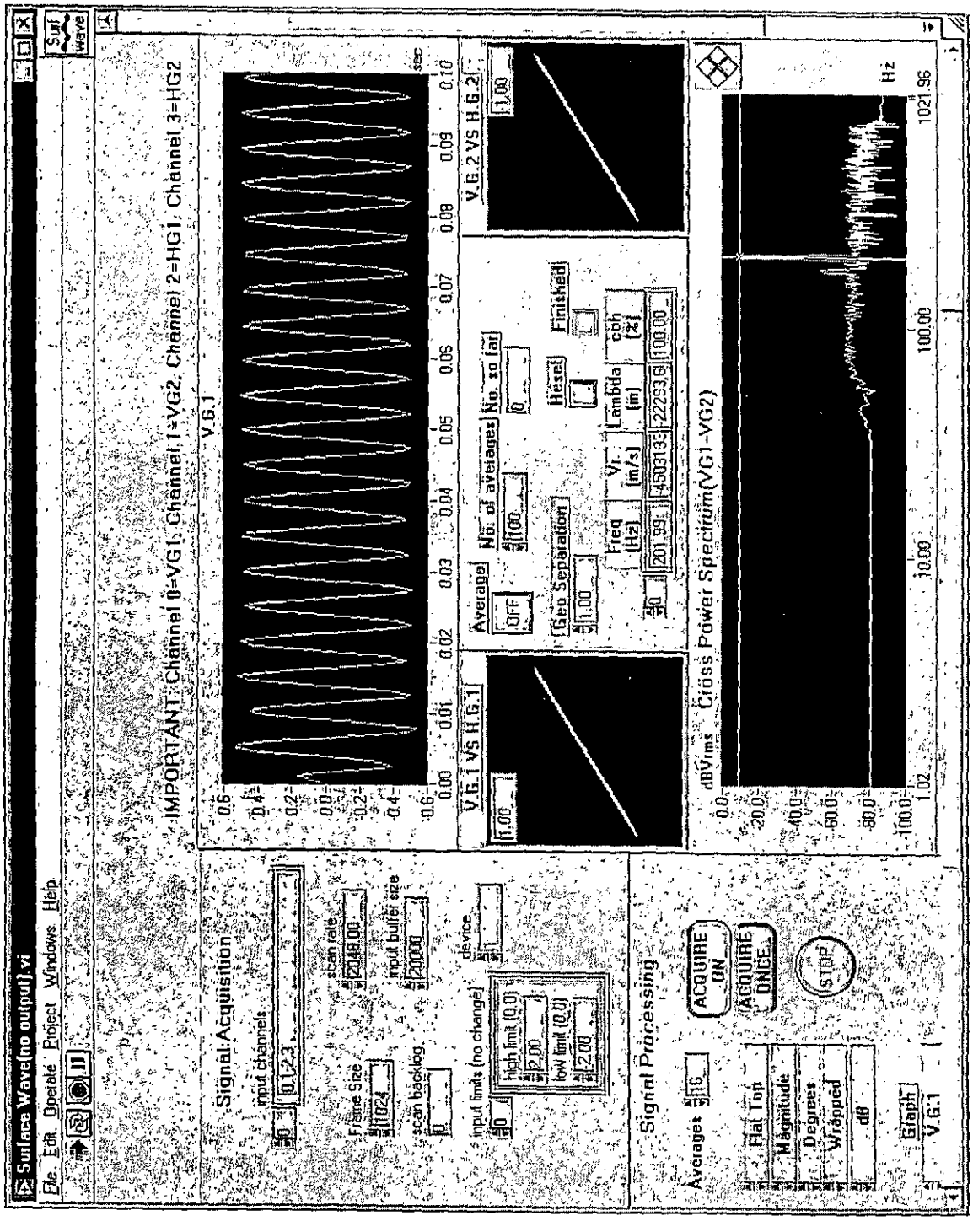

Figure 7-21. Signal acquisition and field processing for acoustically induced surface waves.

Chapter 8

Results and Analysis of Outdoor Experiments

8 Outdoor Experiments

8.1 Acoustic Research Group Test Site

8.1.1 Seismic Refraction Survey

The majority of seismic refraction surveys are undertaken to determine ground layering and the seismic wave velocities of the layers. Since the test site had been purposely built, it was assumed that there would not be any multiple layers present; i.e. there was only 1 continuous layer of gravel. Therefore, the main purpose of the investigation was the determination of the seismic P- and S-wave velocities.

A P-wave survey was carried out at the site using the standard seismic refraction technique outlined in Chapter 7 and the subsequent seismogram can be found in Appendix D. From the seismogram, first arrival picking was carried out to produce the travel time-distance plot seen in Figure 8-1. The plot shows that all the points lie upon a single line confirming the lack of layering at the site. The P-wave velocity was then calculated from the gradient of the line and is given in Table 8-1.

	Layer 1
v_p	314 m/s
v_s	110 m/s
(v_p/v_s)	0.35

Table 8-1. Layer properties at the ARG Test Site determined from the seismic refraction survey.

A shear wave survey was also carried out at the site, again using the standard technique outlined in Chapter 7.

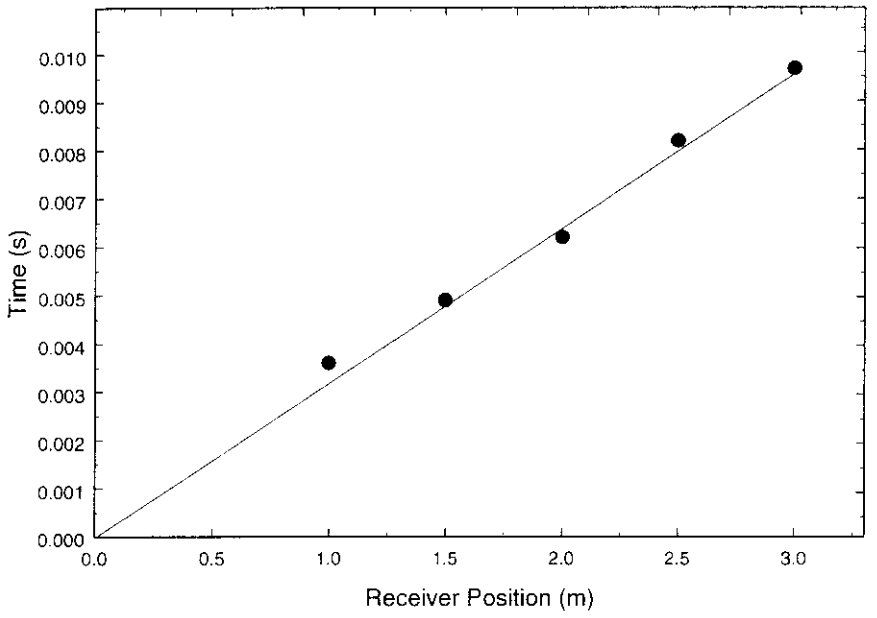

Figure 8-1. Travel Time versus vertical component geophone position.

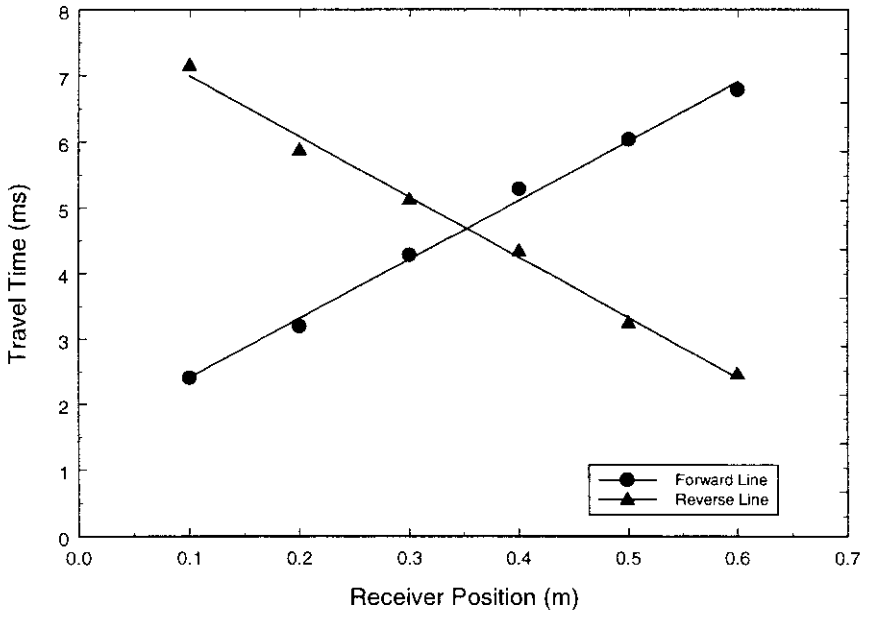

Figure 8-2. Travel Time versus horizontal component geophone position.

Due to poor coupling of the source to the gravel, the resultant seismogram from the S-wave survey showed that considerable P-wave energy had been produced. It therefore proved extremely difficult to ascertain the onset of the shear wave. Therefore, the shear wave velocity in the gravel was determined by the technique used in the Indoor Tank.

A line of four horizontal component geophones was laid out close to the centre of the pit. An end geophone was then driven using a 500Hz five-cycle tone burst with the travel time to each further geophone noted. The experiment was repeated and the subsequent traveltime-distance plot can be seen in Figure 8-2 with the calculated mean shear wave velocity given in Table 8-1.

Table 8-1 also gives the shear/compressional wave velocity ratio for the gravel. The calculated value of 0.35 can be compared with Figure 8-3. This shows the numerical relationship between the shear/compressional wave velocity ratio and one of the Lamé constants, the Poisson's Ratio. Relevant values for typical materials have been superimposed on the plot.

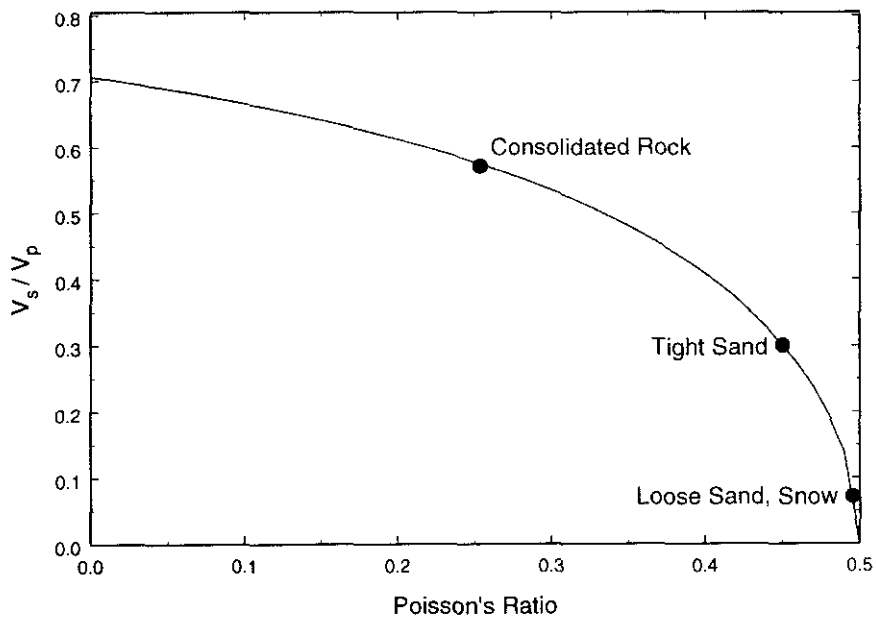

Figure 8-3. Shear-compressional velocity ratio versus Poisson's Ratio (values for the materials given have been taken from Hoover and O'Brien (1980).

The resultant Poisson's ratio for the gravel of 0.35 appears close to the value of tight sand and is a slightly higher than would be expected for a loose sand, although the value is not unreasonable for a material such as this.

8.1.2 Acoustic-to-Seismic Coupling

Measurements of acoustic-to-seismic coupling ratio were made at the site. Initial investigations were made to show reproducibility of the technique. As part of this, tests were made at varying ranges and source heights close to the centre of the pit at a position *A*. The tests were then repeated after approximately 30 minutes, during which time no changes were made to the sensors.

Figure 8-4 shows the acoustic-to-seismic coupling ratio measured at a range of 1.0m with a source height of 0.15m, the microphone at a height of 0.05m and the geophone flush with the ground surface. The plot shows variation in the recorded acoustic-to-seismic coupling spectra with time. The measurements were made approximately 30 minutes apart, during which time no changes were made to the experimental set-up. It can be clearly seen that there is very little difference between the two plots.

Figure 8-5 shows a similar plot to Figure 8-4. Here the source height was 0.75m; again, the agreement between the two results is very good. The purpose of these initial experiments helps to show that the coupling can be reproduced with adequate agreement.

Figure 8-6 and Figure 8-7 give the results for all source heights used with Figure 8-7 being the results of the tests taken approximately 30 minutes after the first. It can be seen from Figure 8-6 that there appears to be a variation in acoustic-to-seismic coupling ratio with source height. The main dip in the spectra, seen at nearly 480Hz at a source height of 0.15m, reduces in both magnitude and frequency with increasing source height. Whereas, at a source height of 0.75m the dip has reduced to roughly 450Hz and decreased in magnitude by approximately 15dB. This trend can also be seen in Figure 8-7.

A similar set of tests was undertaken 0.20m parallel to the initial experiments at a position *B*. Figure 8-8 and Figure 8-9 show the results of tests taken at source heights of 0.15m and 0.75m. Both show satisfactory reproducibility between measurements. Figure 8-10 and Figure 8-11 show the results for all the varying source heights and it again can be seen that there is a shift towards the lower frequencies of the major peaks and dips with increasing source height.

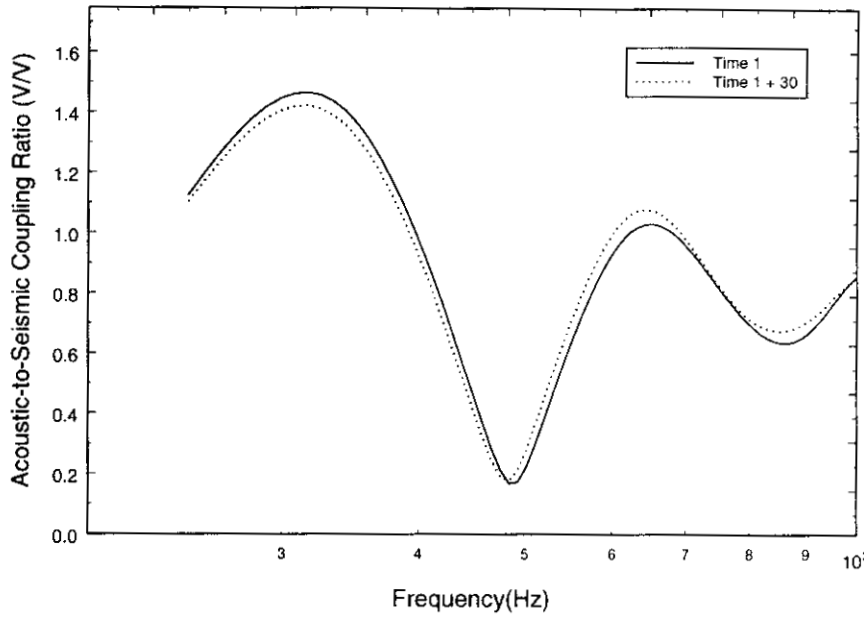

Figure 8-4. Variation in acoustic-to-seismic coupling ratio with time. Measurements are 30mins apart and the sensors were not removed. R=1.0m Hs=0.15m (Position A).

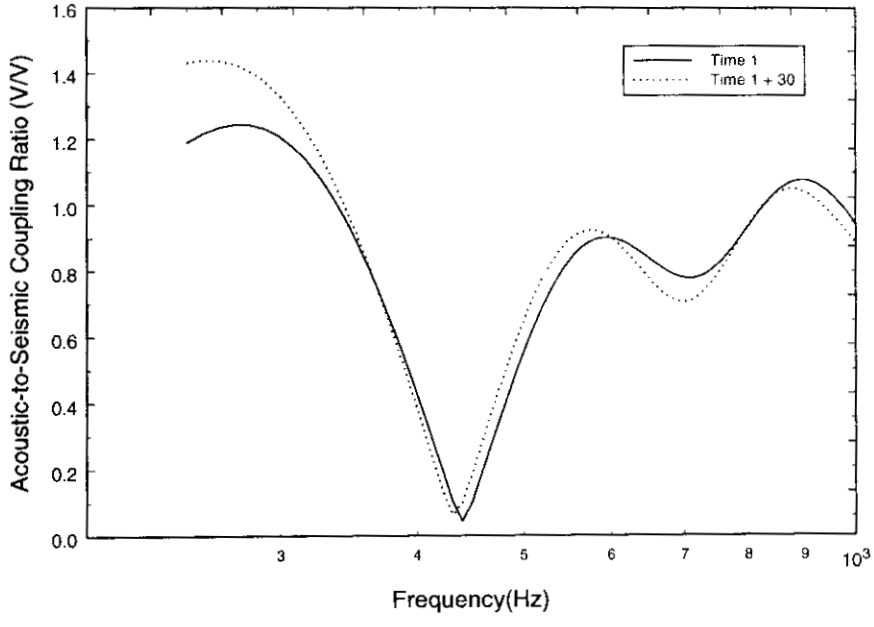

Figure 8-5. Variation in acoustic-to-seismic coupling ratio with time. Measurements are 30mins apart and the sensors were not removed. R=1.0m Hs=0.75m (Position A).

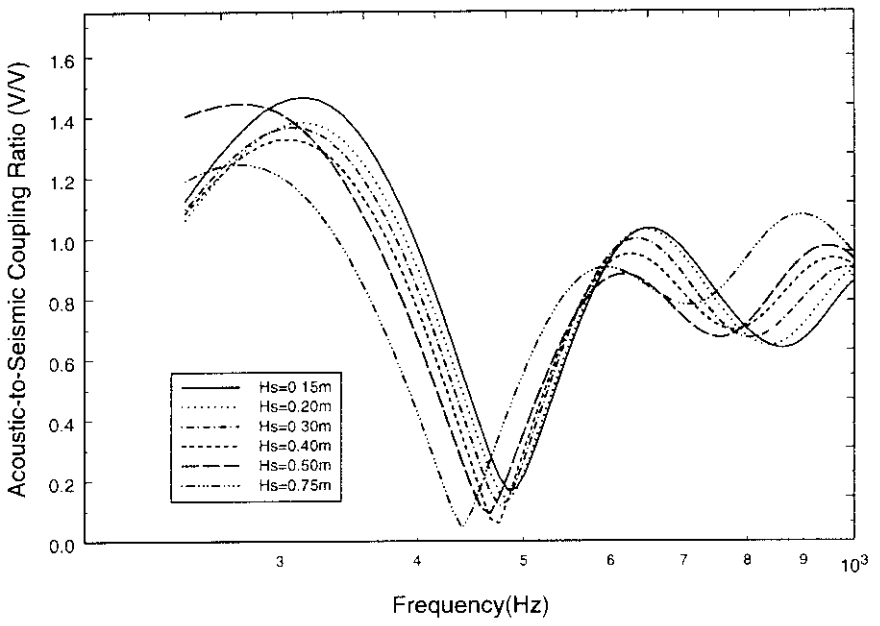

Figure 8-6. Variation in acoustic-to-seismic coupling ratio with varying source height. Data taken at time T1 (Position A).

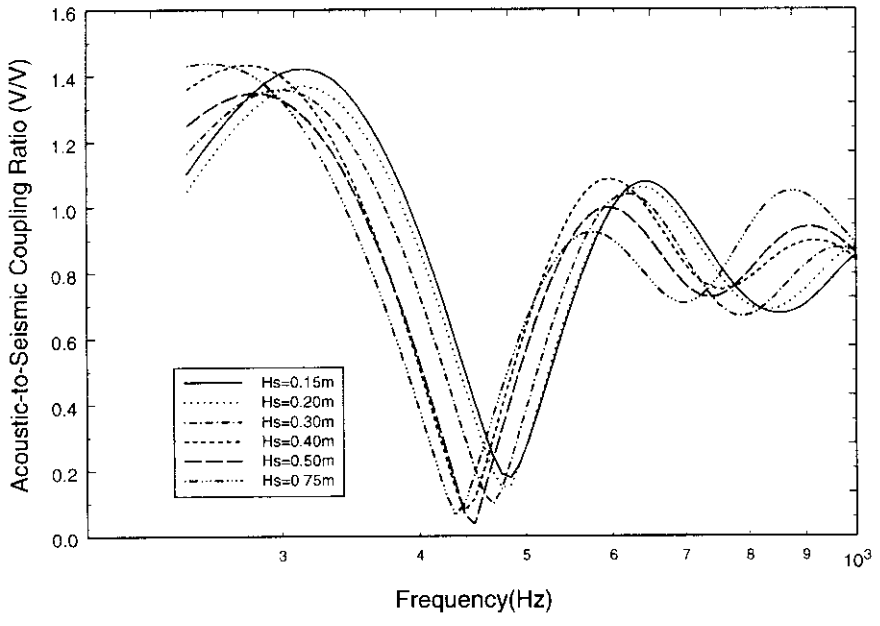

Figure 8-7. Variation in acoustic-to-seismic coupling ratio with varying source height. Data taken at T1+30 minutes (Position A).

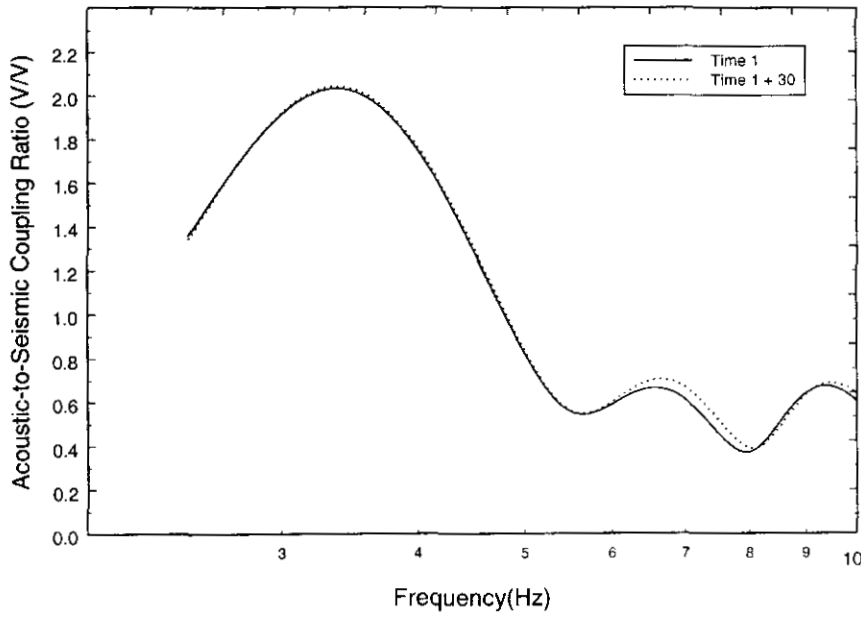

Figure 8-8. Variation in acoustic-to-seismic coupling ratio with time. Measurements are 30mins apart and the sensors were not removed. R=1.0m Hs=0.15m (Position B).

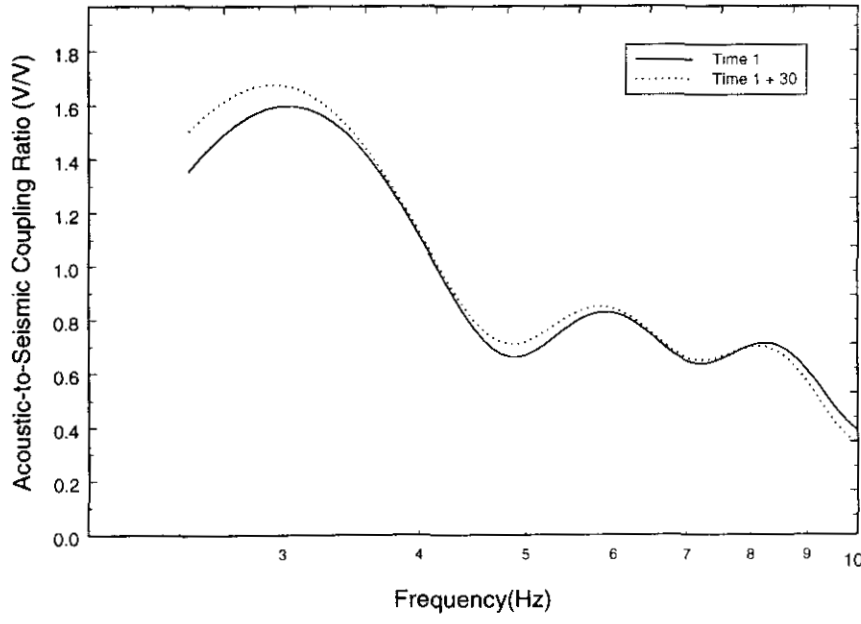

Figure 8-9. Variation in acoustic-to-seismic coupling ratio with time. Measurements are 30mins apart and the sensors were not removed. R=1.0m Hs=0.75m (Position B).

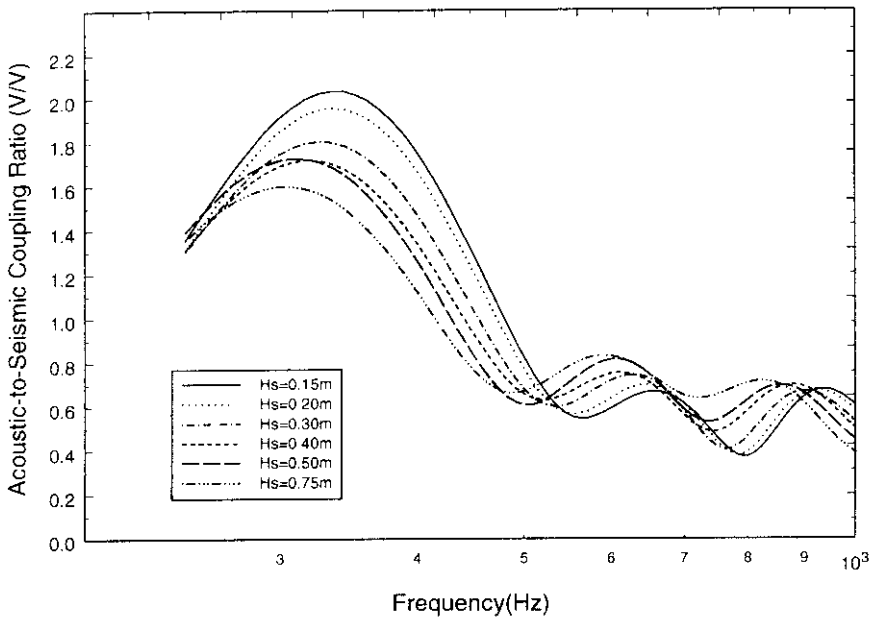

Figure 8-10. Variation in acoustic-to-seismic coupling ratio with varying source height. Data taken at time T1 (Position B).

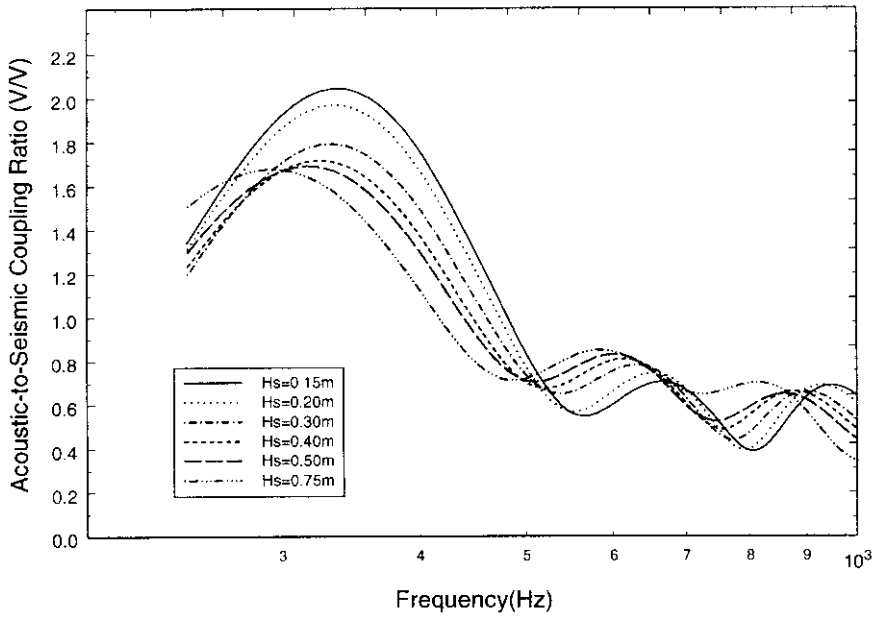

Figure 8-11. Variation in acoustic-to-seismic coupling ratio with varying source height. Data taken at T1+30 minutes (Position B).

Meteorological data taken concurrently with all these measurements can be found in Table D-1 in Appendix D.

Data taken at a range of 2m and 3m showing the variation in acoustic-to-seismic coupling ratio with varying source heights has been given in Appendix D. From all these plots, it has been shown that the acoustic-to-seismic coupling ratio is reproducible between measurements taken in the same position and that there is an angle dependence to the acoustic-to-seismic coupling ratio.

It can be noted, however, that there are differences in the position and magnitude of the extrema in the plots between position *A* and *B*, 0.20m away. Comparing Figure 8-4 and Figure 8-8 measurements taken with a source height of 0.15m, it can be seen that both plots exhibit a maximum in the coupling spectra at roughly 350Hz and have a magnitude of approximately 5dB. However, the data taken at position *A* shows a deep minimum at 500Hz with a reduction in magnitude of close to 20dB, whereas the minimum at Position B is closer to 550Hz and is only 10dB lower than the maxima. Further extrema also exhibit differing magnitudes.

It appears therefore that these differences at the higher frequencies are due to changes in the near surface soil properties. However, in order to validate this assumption further measurements were taken. These measurements were a repeat of the previous set, but whereas in the initial experiments no changes were made to the sensors, now the geophone was removed and replaced in the same position.

Figure 8-12 and Figure 8-13 shows the variation in the acoustic-to-seismic coupling ratio with time. Here, the geophone was removed and replaced in the same position between measurements. Both plots show that up to approximately 500Hz the agreement between the two measurements is superior to that above this frequency where the agreement is less tolerable. Figure 8-14 and Figure 8-15 again shows the variation in the coupling ratio with source height.

It is now appears that it is the positioning of the geophone that is affecting the higher frequency response of the acoustic-to-seismic coupling. Figure 8-16 gives the separate outputs from the geophone and microphone. It is clear that there is very little difference between the two microphone responses and that there are large differences between the two geophone responses at frequencies greater than 500Hz.

Meteorological data taken concurrently with this second set of measurements can be found in Table D-2 in Appendix D.

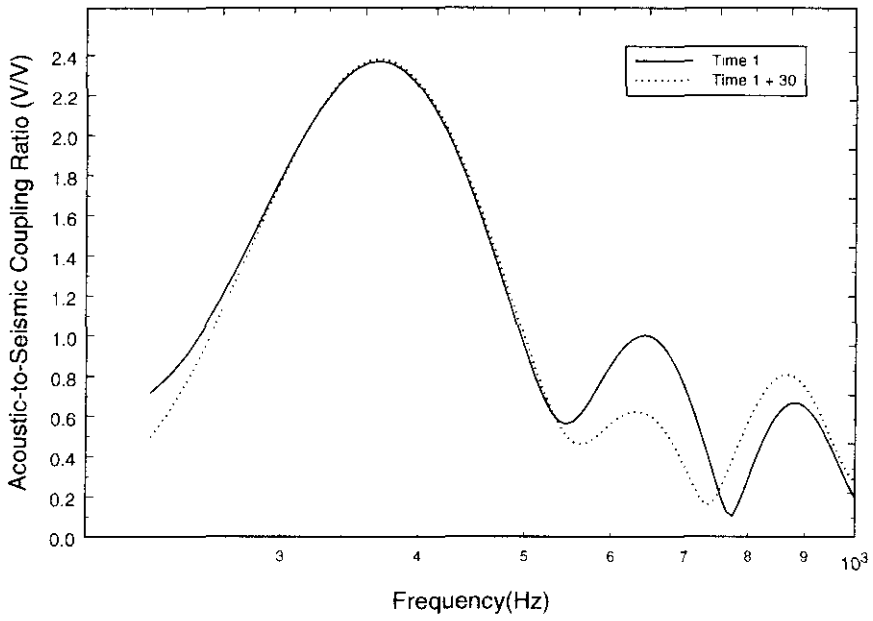

Figure 8-12. Variation in acoustic-to-seismic coupling ratio with time. Measurements are 30mins apart and the sensors were removed. R=1.0m Hs=0.15m (Position A).

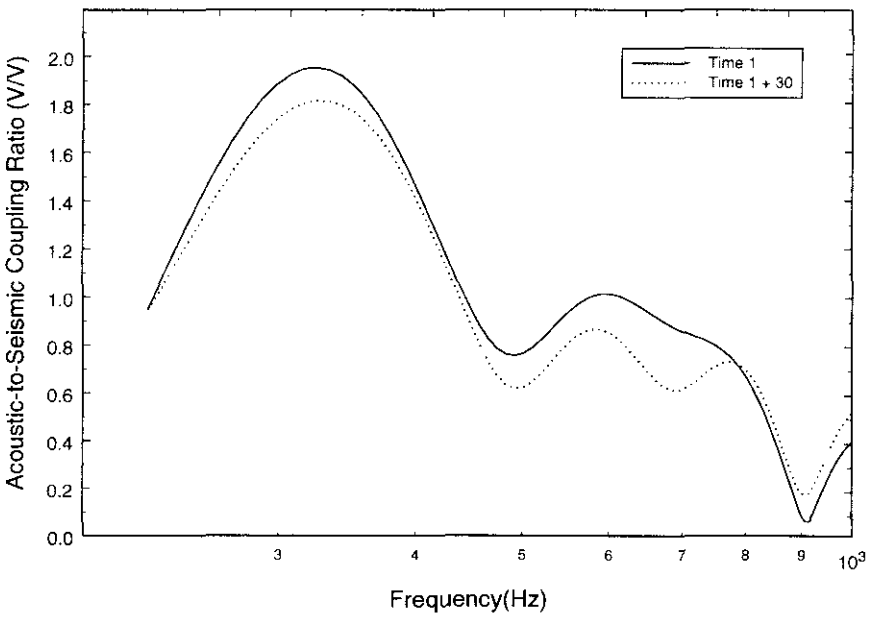

Figure 8-13. Variation in acoustic-to-seismic coupling ratio with time. Measurements are 30mins apart and the sensors were removed. R=1.0m Hs=0.75m (Position A).

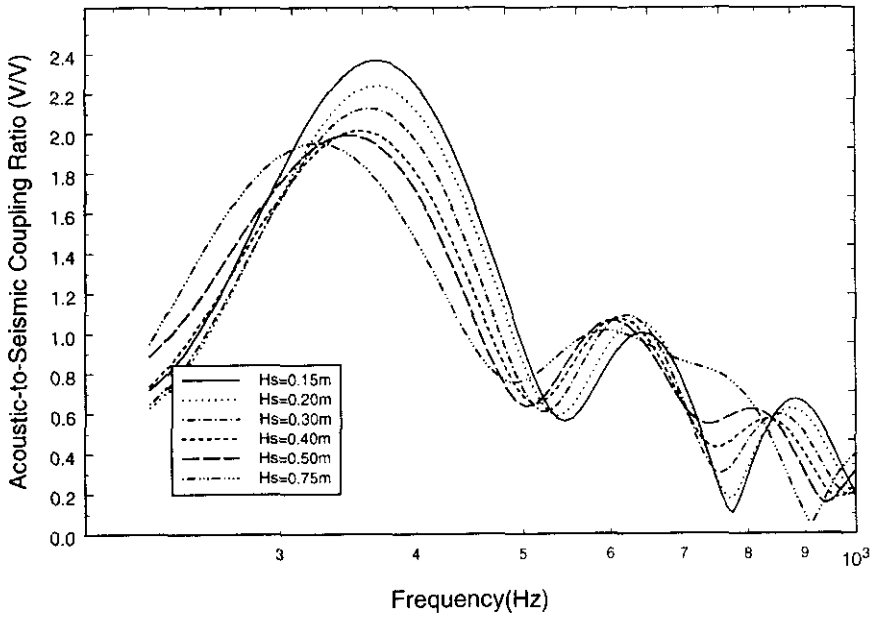

Figure 8-14. Variation in acoustic-to-seismic coupling ratio with varying source height. Data taken at time T1 (Position A).

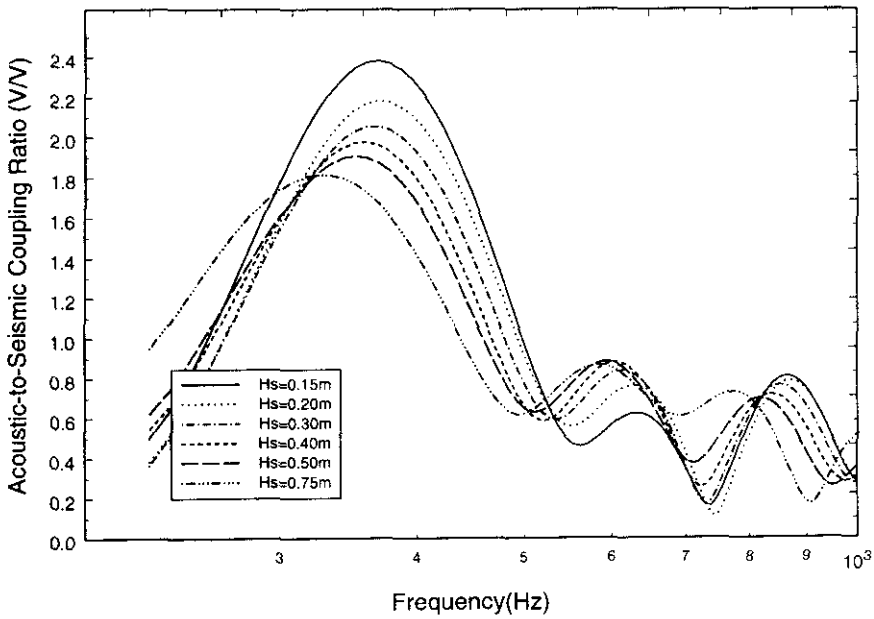

Figure 8-15. Variation in acoustic-to-seismic coupling ratio with varying source height. Data taken at T1+30 minutes (Position A).

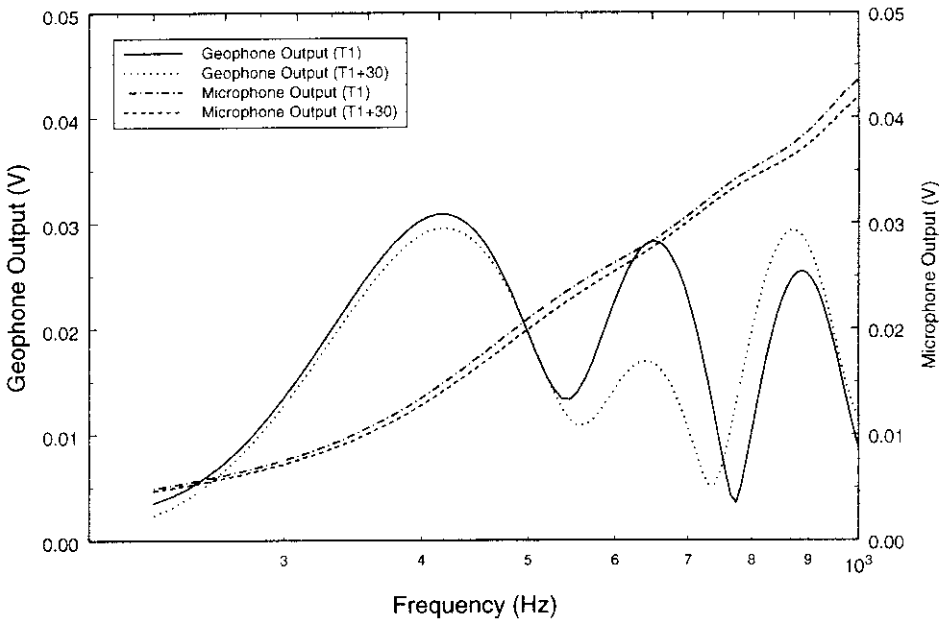

Figure 8-16. Geophone and microphone outputs at T1 and T1+30.

This gives a clear indication that the positioning of the geophone sensor into the ground has a marked effect on the received signal. These findings led to the indoor investigation into the effect of the geophone ground coupling that has been described in Chapter 5 together with results and analysis in Chapter 6.

This investigation has shown that there is a range of frequencies over which a geophone sensor will accurately follow ground motion, bounded at the lower end by the natural resonant frequency of the sensor and at the upper end by a coupling resonant frequency. This coupling resonant frequency has been shown to be dependent upon soil compaction and to be independent of geophone natural frequency.

Section 6.1.3 of Chapter 6 outlines an in-situ method of determining this coupling resonant frequency, known as geophone "pinging".

8.1.3 Sensor Calibration

Geophone "pinging" measurements in the field were undertaken to quantify the coupling resonant frequency and the sensitivity of the geophones used in the acoustic-to-seismic coupling ratio measurements. The earth-geophone coupling was investigated by dropping a small steel ballbearing onto the geophone case and recording the geophone signal. Figure 8-17 gives an example plot of the geophone output being excited by the ballbearing.

The main use of this test is the determination of the coupling resonant frequency. This is calculated using Equation 7.22 of Chapter 7. In order to use this equation the damping coefficient (γ_d) and the ping frequency (f_o') are need. As described in Chapter 7, γ_d is calculated from a line fit to the logarithmic plot of amplitude versus time, whilst f_o' is obtained from zero-crossing measurements.

Table 8-2 gives the calculated ping frequency and subsequent coupling frequency from the example measurements given in Figure 8-17.

Ping No.	Ping Frequency (Hz)	Damping Coefficient (sec^{-1})	Coupling Frequency (Hz)
1	454	414	420
2	454	465	471
3	500	524	528
4	416	575	579
5	454	510	515
6	454	502	505
7	454	490	495
8	416	432	437
9	416	560	564
		Mean	**501**
		Standard Deviation	**53**

Table 8-2. Determination of coupling resonant frequency from geophone "pinging" experiments.

Figure 8-17 shows the response of the geophone to the falling ballbearing, whilst Figure 8-18 shows the response of a single ballbearing drop. This plot is used to determine the ping frequency (f_0') from the zero crossing measurement (as shown on the plot) and the amplitudes used to determine the damping coefficient (γ_d). The amplitudes used are shown in the figure and plotted in Figure 8-19.

8.1.3 Sensor Calibration

Geophone "pinging" measurements in the field were undertaken to quantify the coupling resonant frequency and the sensitivity of the geophones used in the acoustic-to-seismic coupling ratio measurements. The earth-geophone coupling was investigated by dropping a small steel ballbearing onto the geophone case and recording the geophone signal. Figure 8-17 gives an example plot of the geophone output being excited by the ballbearing.

The main use of this test is the determination of the coupling resonant frequency. This is calculated using Equation 7.22 of Chapter 7. In order to use this equation the damping coefficient (γ_d) and the ping frequency (f_o') are need. As described in Chapter 7, γ_d is calculated from a line fit to the logarithmic plot of amplitude versus time, whilst f_o' is obtained from zero-crossing measurements.

Table 8-2 gives the calculated ping frequency and subsequent coupling frequency from the example measurements given in Figure 8-17.

Ping No.	Ping Frequency (Hz)	Damping Coefficient (sec^{-1})	Coupling Frequency (Hz)
1	454	414	420
2	454	465	471
3	500	524	528
4	416	575	579
5	454	510	515
6	454	502	505
7	454	490	495
8	416	432	437
9	416	560	564
		Mean	**501**
		Standard Deviation	**53**

Table 8-2. Determination of coupling resonant frequency from geophone "pinging" experiments.

Figure 8-17 shows the response of the geophone to the falling ballbearing, whilst Figure 8-18 shows the response of a single ballbearing drop. This plot is used to determine the ping frequency (f_0') from the zero crossing measurement (as shown on the plot) and the amplitudes used to determine the damping coefficient (γ_d). The amplitudes used are shown in the figure and plotted in Figure 8-19.

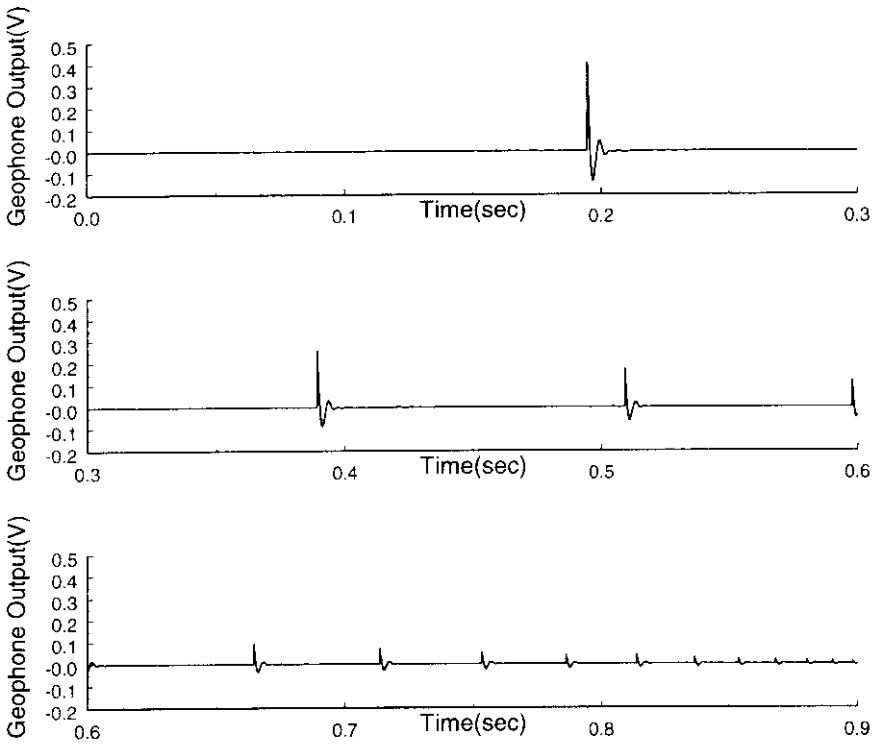

Figure 8-17. The response of the geophone used in the acoustic-to-seismic coupling ratio measurement shown in Figure 8-20, to the falling ballbearing.

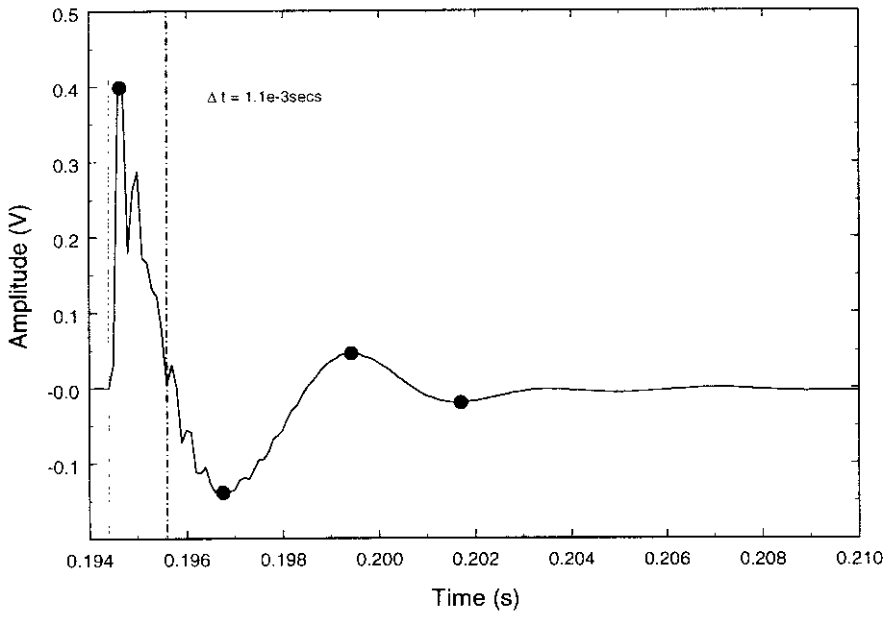

Figure 8-18. Response of the geophone to a single ballbearing drop. Δt is used to determine f_0' whilst the absolute amplitudes are used to determine γ (see Figure 8-19).

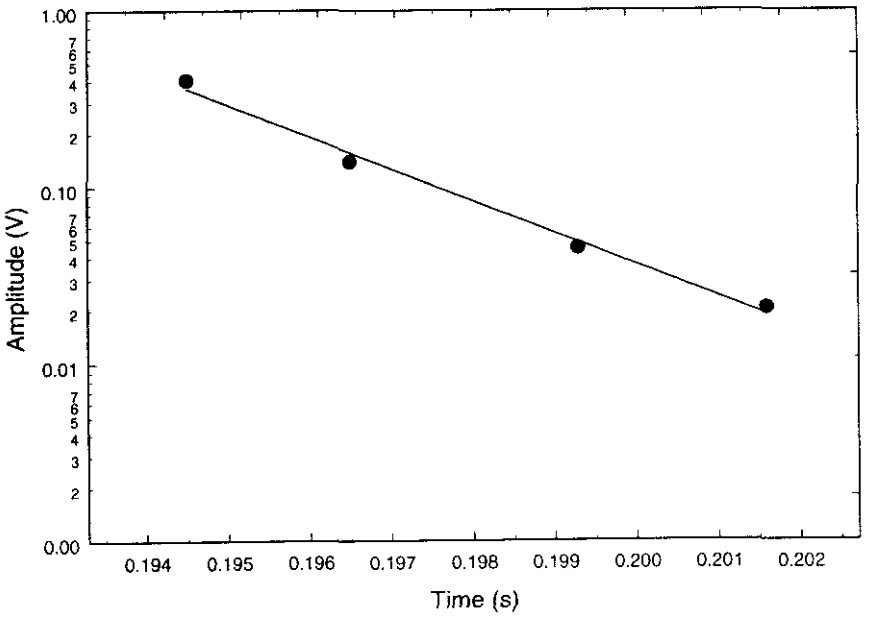

Figure 8-19. Determination of damping coefficient (γ_d) for "ping" number 1. γ_d is determined from the line fit from the plot of absolute amplitude against time.

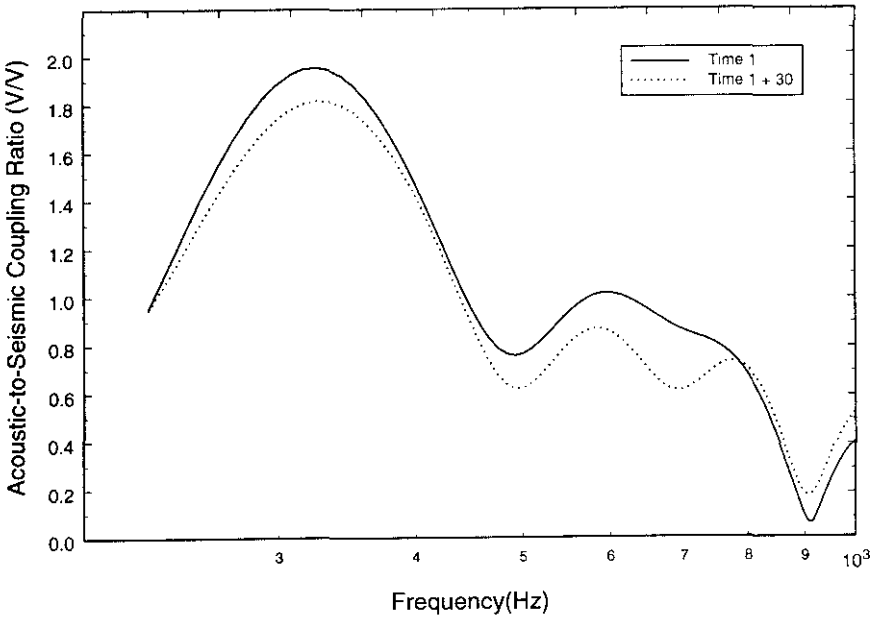

Figure 8-20. Acoustic-to-seismic coupling ratio measurement from which the geophone-ground coupling has been determined.

The geophone "ping" data shows that in this case the coupling resonant frequency of the geophone is 501Hz with a standard deviation of 53Hz. The plot of acoustic-to-seismic coupling ratio from which the geophone data was taken is shown in Figure 8-20. The two measurements in the plot show reasonable agreement until roughly 500Hz, after which there is some divergence. This appears to corroborate the results of the geophone test.

A secondary function of the "pinging" test was to assess the in-situ sensitivity of geophone sensor. As discussed in Chapter 7, the calculated sensitivity gives an indication of the variability between geophones and their coupling to the soil, and act as confirmation that the amplitude measurements are within the accuracy of the "pinging".

Using the conservation of momentum method outlined in Chapter 7 and the example data above (Figure 8-17), Table 8-3 gives the calculated in-situ geophone sensitivity and the ratio of geophone velocity after impact to the velocity determined from geophone output voltage times the manufacturers stated sensitivity.

Peak	T1 (sec)	T2 (sec)	T3 (sec)	ΔT (sec)	v1(bb) (m/s)	ΔT (sec)	v2(bb) (m/s)	v2(Geo) (m/s)	Amplitude	Calculated Sensivitity (V / m/s)	Manufacturer Sensivitity (V / m/s)	v2(Geo)	Ratio
2	0.1956	0.4099	0.5314	0.2143	1.0508	0.1215	0.5958	0.0098	0.2341	23.9	20.0	0.0117	1.1959
3	0.4099	0.5314	0.6081	0.1215	0.5958	0.0767	0.3761	0.0058	0.1487	25.7	20.0	0.0074	1.2869
4	0.5314	0.6081	0.6574	0.0767	0.3761	0.0493	0.2417	0.0037	0.0948	25.8	20.0	0.0047	1.2900
5	0.6081	0.6574	0.6961	0.0493	0.2417	0.0387	0.1898	0.0026	0.0593	23.1	20.0	0.0030	1.1568
6	0.6574	0.6961	0.7236	0.0387	0.1898	0.0275	0.1348	0.0019	0.0533	27.6	20.0	0.0027	1.3822
7	0.6961	0.7236	0.7432	0.0275	0.1348	0.0196	0.0961	0.0014	0.0375	27.3	20.0	0.0019	1.3673
8	0.7236	0.7432	0.7528	0.0196	0.0961	0.0096	0.0471	0.0009	0.0179	21.1	20.0	0.0009	1.0534
9	0.7432	0.7528	0.7612	0.0096	0.0471	0.0084	0.0412	0.0005	0.0141	26.9	20.0	0.0007	1.3447
10	0.7528	0.7612	0.7668	0.0084	0.0412	0.0056	0.0275	0.0004	0.0095	23.2	20.0	0.0005	1.1616
												Average	**1.2488**
												Std Dev	**0.1125**

Table 8-3. Example calculation of geophone sensitivity using conservation of momentum method.

It can be seen from the table that for this measurement, the calculated sensitivity of the geophone is 1.25 times greater than that given by the manufacturer. As previously stated due to the inherent nature of the test, this value is not an exact calibration, but provides a guide to the error in magnitude that may appear in the geophone signal.

Figure 8-21 shows the effect of geophone sensitivity on the magnitude of a prediction of acoustic-to-seismic coupling ratio. The plot shows an example measurements taken at the ARG test site (range =1.5m Hs=0.15). The manufacturers sensitivity of 20 V/m/s was taken as 1, with the subsequent plots showing sensitivities at 0.75, 1.25 and 1.5

times this value. The plot shows that small changes in geophone sensitivity will produce noticeable differences in the reduced magnitude and that for this case the measured geophone sensitivity enabled the closest fit with the porous elastic model to be found.

With the previous plots of acoustic-to-seismic coupling ratio given in Section 8.1.2, no attempt has been made to reduce the data to "real world" units. At that stage the plots were designed solely to show trends in the data and the reproducibility of the technique, before any attempt was made to model the data.

Figure 8-22 to Figure 8-24, are examples of acoustic-to-seismic coupling spectra taken at the ARG test site with the effect of amplifier gains and both geophone and microphone sensitivities taken into account. The geophone coupling resonant frequency and sensitivity were calculated from geophone "pinging" tests, with the microphone sensitivity determined using a Brüel and Kjær pistonphone.

The plots also show computer predictions made using the full spherical wave poro-elastic wave model with the FFLAGS program. Parameters used to describe the ground are given in Table 8-4. It can be seen from the figures that a moderate agreement has been found between the measured and predicted values of acoustic-to-seismic coupling ratio in all three plots over the whole frequency range.

If however, the coupling resonant frequency (f_0) of the geophone is taken into account then the agreement between the data and the prediction becomes more tolerable. For example, Figure 8-22, shows data taken at a range of 1.5m and a source height of 0.15m. For this measurement the FFLAGS predictions shows a reasonable agreement up to roughly 480Hz after which there is a noticeable difference in the magnitude between the two plots. However, by noting that the coupling resonant frequency for this measurement was calculated at 522Hz, then the standard of the prediction rises considerably.

This pattern confirms the results of the indoor geophone ground coupling investigation which showed that at frequencies higher than the geophone coupling resonant frequency, the geophone produces amplitude magnifications.

It is noticeable from Table 8-4 that little alteration of the ground parameters was required between each prediction, showing the ground in the test area to be relatively homogeneous, as would have been expected. A result of note is that the value of shear wave velocity used in the predictions is 1.5 times greater than that measured in the seismic refraction survey, this may be due to local variations in the material.

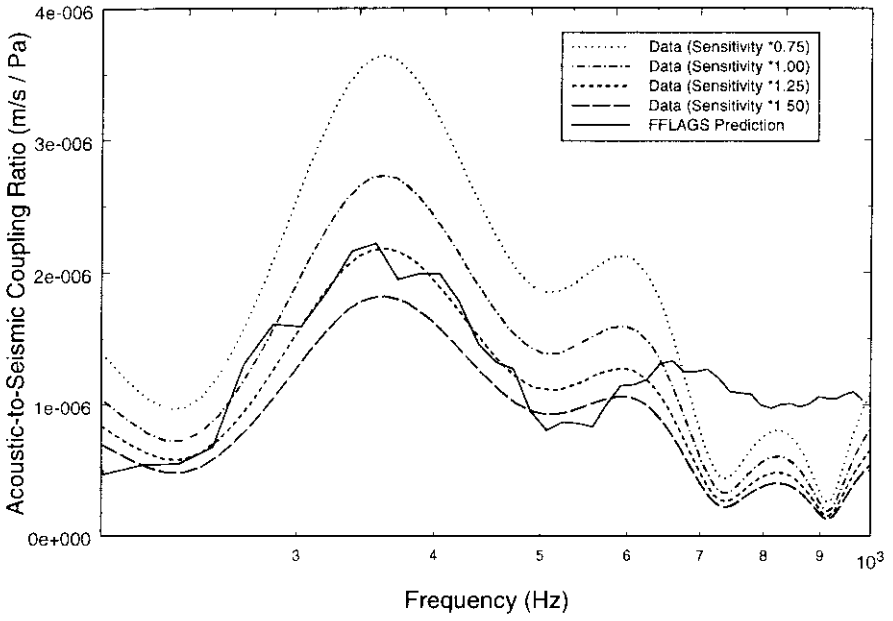

Figure 8-21. The effect of geophone sensitivity on a reduced measurement of acoustic-to-seismic coupling ratio.

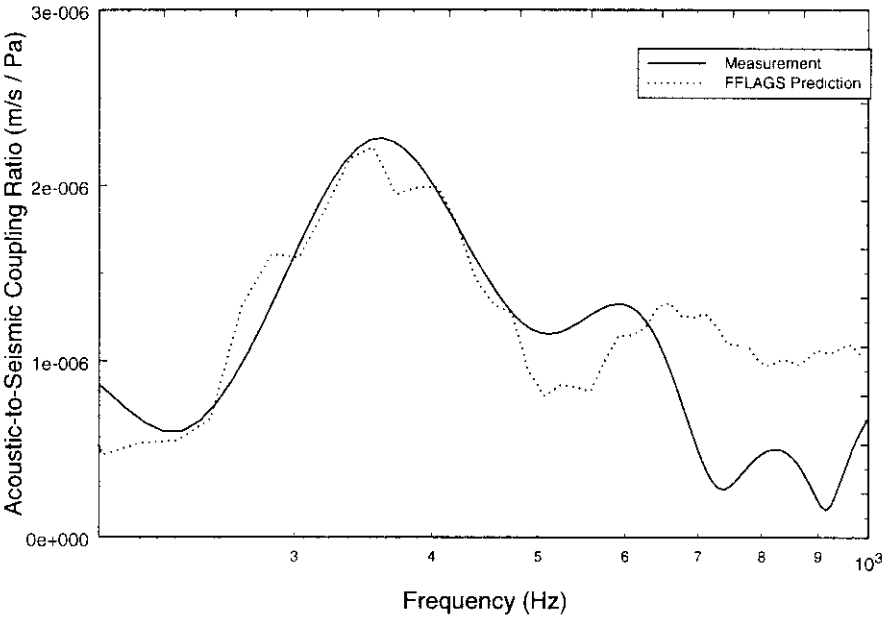

Figure 8-22. Measured acoustic-to-seismic coupling ratio and FFLAGS prediction taken at the ARG test site (Range=1.5, Hs=0.15m and f_0=522Hz).

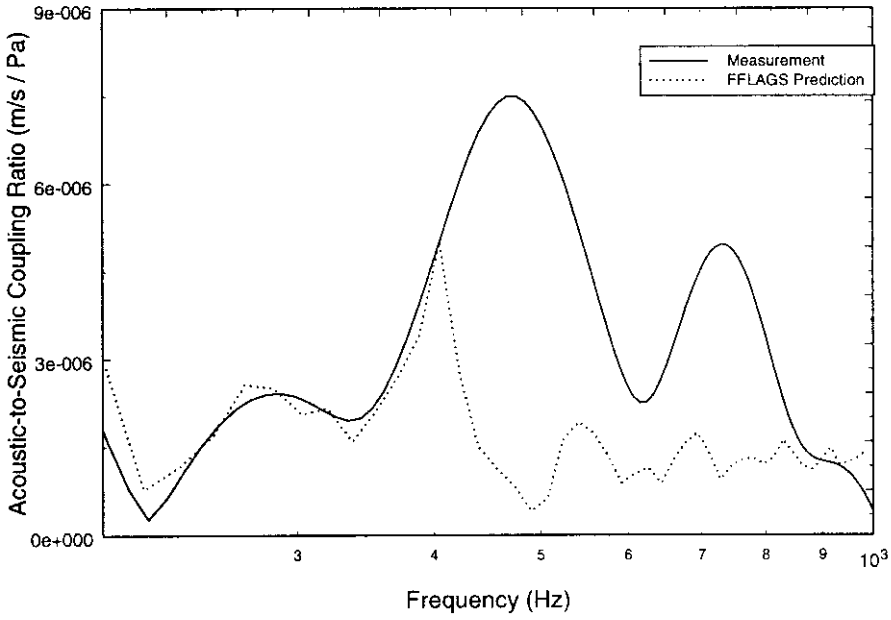

Figure 8-23. Measured acoustic-to-seismic coupling ratio and FFLAGS prediction taken at the ARG test site (Range=2.0m, Hs=0.15m and f_0=446Hz).

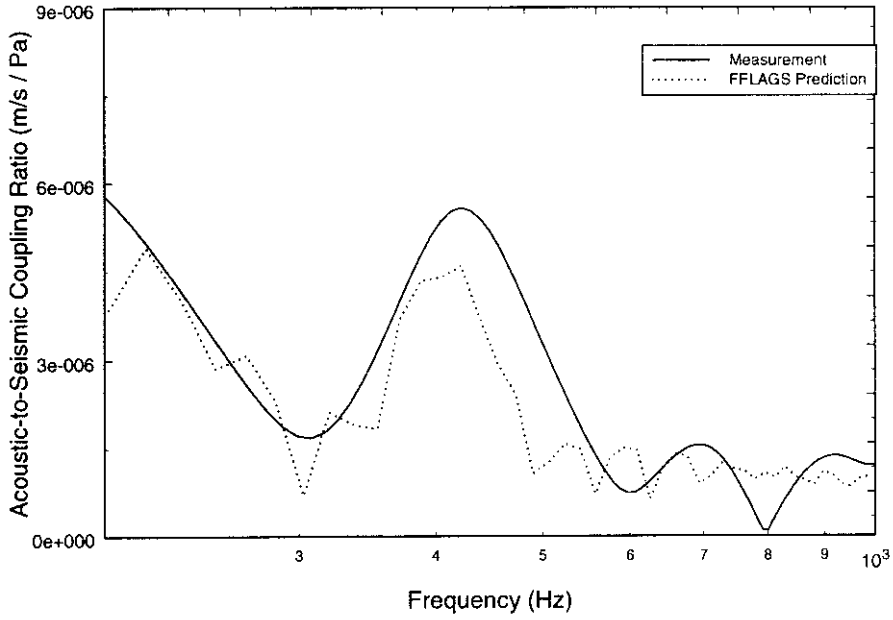

Figure 8-24. Measured acoustic-to-seismic coupling ratio and FFLAGS prediction taken at the ARG test site (Range=2.5m, Hs=0.15m and f_0=492Hz).

	Layer		Substrate
P-wave speed (m/s)	R=1.5m	325	650
	R=2.0m	315	
	R=2.5m	315	
S-wave speed (m/s)	R=1.5m	165	330
	R=2.0m	165	
	R=2.5m	130	
Flow resistivity (Pa sm^{-2})	2000		36000000
Porosity	0.46		0.0046
Grain shape factor	0.5		0.5
Soil density (kg/m^3)	1700.0		2650.0
Layer thickness (m)	3.0		∞
Attenuation (v_p)	0.02		0.02
Attenuation (v_s)	0.01		0.01
Dynamic viscosity of air (Nsm^{-2})	1.81×10^{-5}		
Microphone height (m)	0.05		
Geophone depth (m)	-0.05		
Frequency range (Hz)	150 – 1000		
Speed of sound in air	344.0		
Coupling Resonant Frequency (Hz)	R=1.5m	522	
	R=2.0m	446	
	R=2.5m	492	
Geophone Sensitivity (measured) (V / m/s)	R=1.5m	28	
	R=2.0m	24	
	R=2.5m	25	
Microphone Sensitivity (measured) (V / Pa)	R=1.5m	13.4e-3	
	R=2.0m	13.4e-3	
	R=2.5m	13.4e-3	

Table 8-4. Parameters used to predict the acoustic-to-seismic coupling ratio measurements taken at the ARG test site.

Figures D-10 to D-13 in Appendix D show comparisons between acoustic-to-seismic coupling ratio measurements and predictions taken at a range of 2.0m with a source height of 0.20, 0.30, 0.40 and 0.50m. Table D-5 gives a list of the parameters needed to fit the FFLAGS prediction to the measurement. It can be seen from the table that little or no alterations, except for changes in source height, in the parameters were needed to fit the data.

Reasonable agreements have been found for all the plots. It can be seen however, that in none of the figures could the large peak at approximately 450Hz be predicted. This may be due to the peak being close to the calculated coupling resonant frequency of the geophone which may have produced some magnitude amplification in this region.

It can also be noted from the figures that with increasing source height the agreement between the prediction and data becomes less tolerable. It appears that model is predicting a greater change in acoustic-to-seismic coupling ratio with grazing angle than can be seen in the measurements.

8.1.4 Probe Microphone

Loudspeaker measurements were undertaken in conjunction with a probe microphone, using the same method as that used in the indoor tank. Measurements were taken at three grazing angles. For each grazing angle, data was collected at two positions (A and B) to assess variations in ground conditions.

Probe microphone measurements were obtained at 1cm intervals down to a depth of 14cm over a frequency range of 500Hz using an MLS output signal. Burial of the probe and accurate depth determination of the probe was hampered by the coarse nature of the gravel. The example plots of the reduced data, following the method described in Chapter 5, for Position A at a grazing angle of 19° can be found in Appendix D.

It can be seen from the plots that the magnitude of the signal from the probe microphone decreases systematically with depth over the complete range of investigation, although there is a noticeable dip in the magnitude at around 250Hz. The relative phase of the signal from the probe microphone also appears to decrease systematically at the same rate over the whole depth range. There are small variations in the change in phase that are most likely due to inaccurate depth determination of the probe. However, the dip seen in the magnitude data does not appear in the phase data. It is noticeable that the change in both the magnitude and phase change per unit depth increases with increasing frequency.

This data indicated that down to a depth of approximately 14cm the Type II P-wave is predominant.

Calculations of attenuation and phase speed over the depth intervals of 1cm to 5cm, 3cm to 5cm and 2cm to 4cm have been calculated with best-fit regressions applied to the data. The values of attenuation (dB/m) calculated over three depth intervals and for frequencies of 100Hz, 200Hz, 300Hz, 400Hz and 500Hz can be found in Table 8-5. The given values are based upon data taken at a grazing angle of 19°. The corresponding phase velocities can be found in Table 8-6.

	Depth Interval	Frequency				
		100Hz	200Hz	300Hz	400Hz	500Hz
Position A	1cm to 5m	14.8	14.5	14.0	13.6	13.2
	3cm to 5m	17.0	19.0	21.1	23.1	25.1
	2cm to 4cm	14.4	14.8	15.3	15.8	16.3

Table 8-5. Attenuation (dB/m) calculated from the data taken at a grazing angle of 19° with the probe microphone.

	Depth Interval	Frequency				
		100Hz	200Hz	300Hz	400Hz	500Hz
Position A	1cm to 5m	146.75	206.35	241.2	265.95	285.1
	3cm to 5m	111.15	167.8	200.95	224.5	242.75
	2cm to 4cm	178.5	236.35	270.15	294.15	312.75

Table 8-6. Phase velocity (m/s) calculated from the data taken at a grazing angle of 19° with the probe microphone.

The values gained for the phase velocity given in Table 8-6 show an increase with frequency systematic of the Biot Type II wave and as such the measured wave type is assumed to be the Biot Type II wave.

Calculations of attenuation and phase velocity were made from measurements of the real and imaginary parts of the bulk propagation constant ($Re(k_b)$ and $Im(k_b)$) as outlined in Section 3.1.1 of Chapter 3. Using these functions and using the theory outlined in Section 3.1 of the same chapter, the tortuosity (τ) and the flow resistivity (R_s) have been calculated. Table 8-7 shows the calculations of τ and R_s for all the measurements taken at the site.

Grazing Angle	Depth Interval	Tortuosity	Flow Resistivity (MKS Rayls)
19° (Position A)	1cm to 5cm	1.4	1709
	3cm to 5cm	1.5	2995
	2cm to 4cm	1.3	1639
	Average	**1.4±0.1**	**2114±475**
19° (Position B)		1.3±0.1	1570±428
34° (Position A)		1.7±0.2	2798±206
34° (Position B)		1.6±0.1	2599±351
12° (Position A)		1.4±0.1	2087±986
12° (Position A)		1.2±0.2	1358±654
	Overall Average	**1.4±0.2**	**2088±517**

Table 8-7. Calculated values of tortuosity and effective flow resistivity from probe microphone measurements.

Table 8-8 shows a comparison of physically measured and acoustically deduced soil properties using the probe microphone for the ARG test site.

	Physical Measurement		Probe Microphone	
	Tortuosity	**Flow Resistivity (MKS Rayls)**	**Tortuosity**	**Flow Resistivity (MKS Rayls)**
ARG Gravel	1.22±0.002	999±68	1.4±0.1	1924±473

Table 8-8. Comparison of physically measured and acoustically deduced soil properties for the ARG test site.

The results show reasonable agreement has been found for both soil properties between that physically measured and that deduced from the probe microphone measurements. In a similar manner to the results gained in the Indoor Tank (described in Chapter 6), the acoustically deduced flow resistivity is approximately twice that measured using the airflow rig.

8.1.5 Conclusions

The main aims behind the experiments undertaken at the ARG test site appear to have been completed satisfactorily. Initial measurements were undertaken to show the reliability of the technique as a whole and it has been shown that with small changes in time (approximately 30mins) and with consistent meteorological conditions there is a strong repeatability of acoustic-to-seismic coupling ratio measurements.

It was hoped to show whether there was any angle dependence on the coupling spectra and it does appear that there is a slight dependence of the source height on the recorded spectra.

Further studies into the reliability of the technique showed that removal and re-positioning of the geophone between measurements has a great effect on the shape of the coupling especially at high frequencies. Indoor measurements have shown that there is a range of frequencies over which a geophone sensor will accurately follow ground motion, bounded at the lower end by the natural resonant frequency of the sensor and at the upper end by a coupling resonant frequency.

An experiment has been devised for a field determination of the coupling resonant frequency. This measurement also allows an assessment of the in-situ sensitivity of the geophone. Results from the geophone "pinging" tests show that a reasonable approximation can be gained for the coupling resonant frequency that is consistent with coupling ratio measurements and predictions.

The probe microphone measurement technique that had been reliably used in the Indoor Soil Tank proved to give acceptable results. The data shows the same fluctuations seen indoors and again there appears to be no angle dependence to either the calculated tortuosity or flow resistivity. Comparisons of the acoustically and mechanically derived values of tortuosity and flow resistivity show a reasonable agreement.

From the measurements taken at the site a number of material properties have been determined using acoustic techniques and these can be seen in Table 8-9. The table shows that overall a reasonable agreement has been found between the soil properties measured using more standard techniques and those derived from acoustic measurements.

The amount of priori information concerning the site helped in matching the predictions of acoustic-to-seismic coupling ratio to the measurements. This was especially true of the ground layering and thickness of the layer.

Soil Parameter	Directly Measured	Acoustically Derived
Number of Layers	1	1
Layer Thickness (m)	3.0	3.0
Flow Resistivity (mks rayls)	999±68	1924±473
Permeability (m/s)	$5.31\text{x}10^{-2} \pm 0.39\text{x}10^{-2}$	$9.20\text{x}10^{-2} \pm 1.82\text{x}10^{-2}$
Porosity (%)	45.88±0.13	50.0
Bulk Modulus (MPa)	---	132.30
Shear Modulus (MPa)	---	39.97
Soil Density (kg/m^3)	1634	1700
Tortuosity	1.22±0.002	1.4±0.1

Table 8-9. Soil Properties determined from acoustic experiments undertaken at the ARG test site.

One major drawback of this site was the limited area of the test material. The finite size of the soil pit governed the frequency range of the measurements. Time windowing was applied to the sensor responses to ensure that any reflections from the pit walls were removed.

This time windowing leads to a reduction in the accuracy of the low frequency information. Since in MLSSA the system transfer function is computed by applying an FFT to the impulse response, the displayed frequency resolution is given by the sample rate divided by the FFT size. However, the true frequency resolution of a measurement is at best equal to $1/T$, where T is the length of the impulse response segment used in the FFT calculation. Thus, the data falling below the $1/T$ should be treated as suspect and has been ignored.

To overcome this problem, measurements were taken at the Stone Lane Quarry, Heath and Reach. This site, described in Chapter 4, consists of a large expanse of undisturbed sand. The large area of sand available overcame the problem of wall reflections, allowing longer time windows to be taken which gave an increased frequency resolution.

8.2 Stone Lane Quarry, Heath and Reach

8.2.1 Seismic Refraction Survey

A P-wave survey was carried out using the standard seismic refraction technique outlined in Chapter 7 and the subsequent seismogram can be found in Appendix E. From the seismogram first arrival picking was carried out to produce the travel time-distance plot seen in Figure 8-25.

From the plot for the forward shot it can be seen that there are two distinct portions of the graph, indicating that there are two layers present. The P-wave velocities have been calculated from the gradient of each line and are given in Table 8-10. The plot of the reverse shot also shows the two distinct portions again suggesting the presence of more than one layer. Again, P-wave velocities have been calculated and are given in Table 8-10.

Analysis of the time-distance plots show that two layers exist and that the boundary between the upper and lower layer is parallel to the ground surface, i.e. there is no dip to the interface. This is confirmed by the results of the S-wave survey which are shown in Figure 8-26.

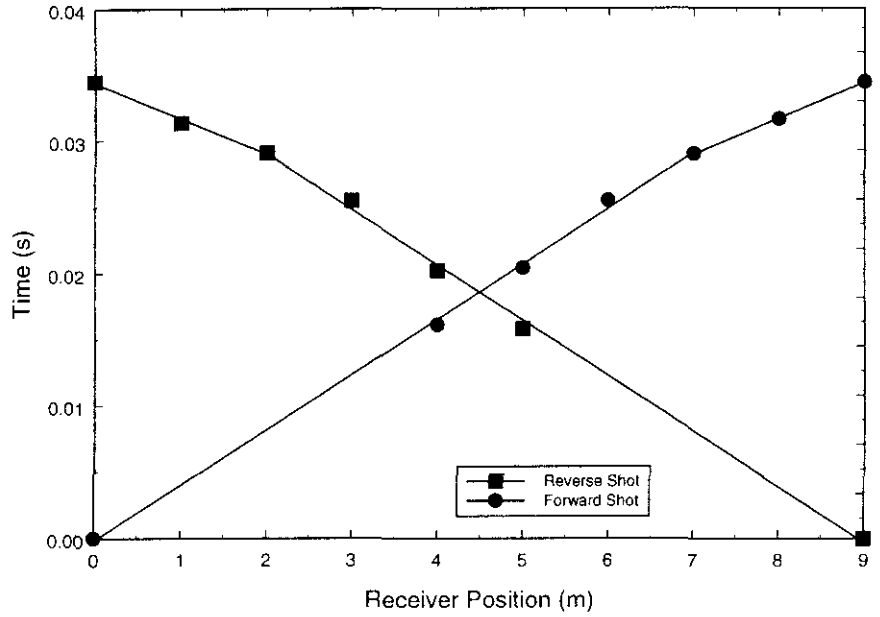

Figure 8-25. Travel Time versus vertical component geophone position.

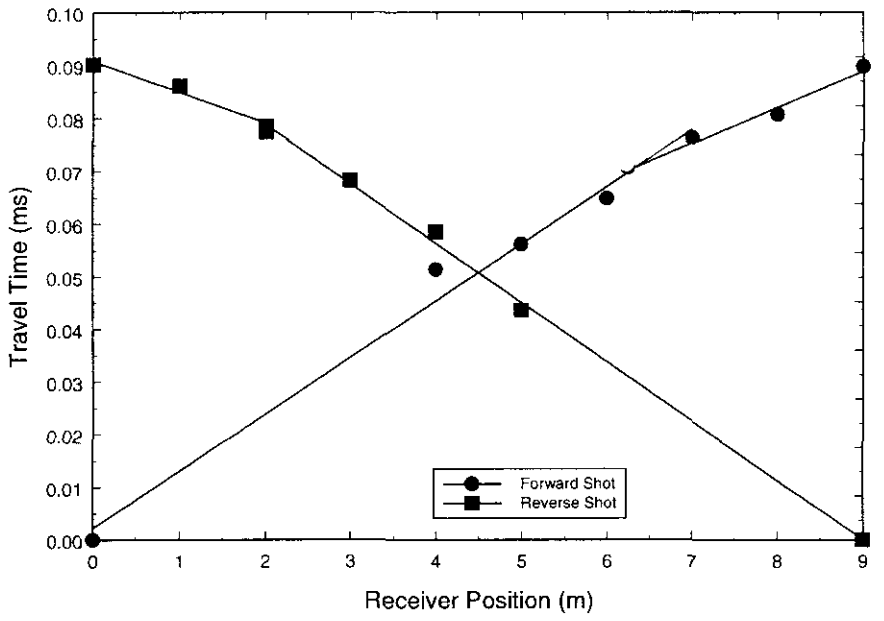

Figure 8-26. Travel Time versus horizontal component geophone position.

	Layer 1	Layer 2
v_p (m/s)	239	370
v_s (m/s)	91	157
v_s/v_p	0.38	0.42
H_{down} (m)	1.28	--
H_{up} (m)	1.28	--
a (°)	0	--

Table 8-10. Layer properties at Stone Lane Quarry determined from the seismic refraction survey.

Comparison of the calculated shear/compressional wave velocity ratio of 0.38 with Figure 8-3 shows this value to be slightly greater than value of 0.30 given by Hoover and O'Brien (1980) to be indicative of a tight sand. However, the calculated shear/compressional wave velocity ratio does appear satisfactory.

8.2.2 Acoustic-to-Seismic Coupling

In a similar manner to the experiments undertaken at the ARG test site, a number of initial experiments were undertaken at the quarry to determine the repeatability and reliability of acoustic-to-seismic coupling ratio measurements. For all measurements, in-situ calibrations were carried out. A Brüel and Kjær pistonphone was used for the microphones, whilst the geophone "ping" tests were undertaken on both the vertical and horizontal component geophones.

Having already proved that the measurements were repeatable with time and without removing the geophone, the measurements undertaken at Stone Lane focussed on the effect of geophone implantation.

Figure 8-27 shows the acoustic-to-seismic coupling ratio at a range of 1m and with a source height of 0.15m. The measurements were taken approximately 30 minutes apart during which time the geophone was removed and replaced in the same position. It can be seen that although there is reasonable agreement between the two plots up to approximately 350Hz. At higher frequencies, the agreement becomes less tolerable and after roughly 600Hz the two measurements differ greatly.

Figure 8-28 shows the acoustic-to-seismic coupling ratio at a range of 1m and with a source height of 0.75m. A similar trend in the agreements described above can be seen.

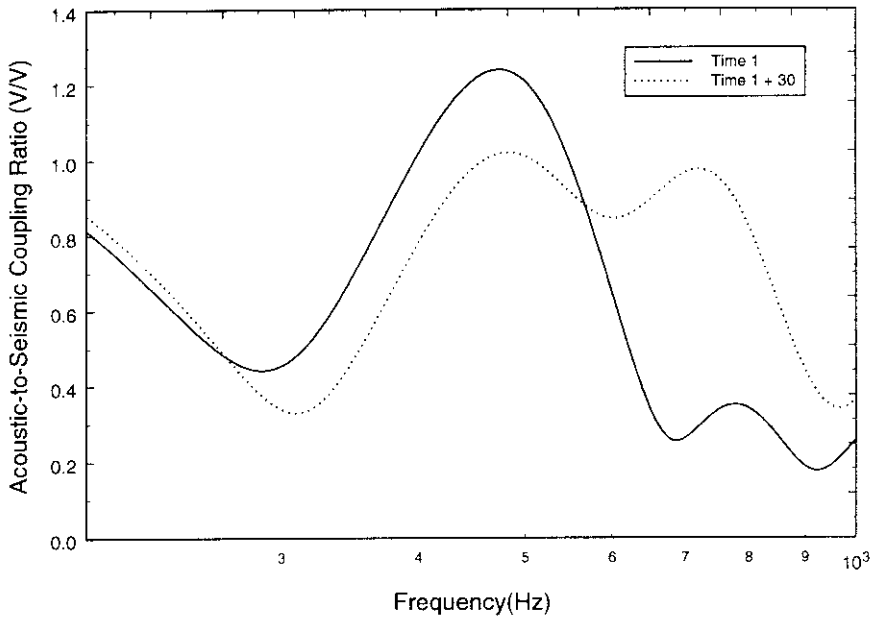

Figure 8-27. Variation in acoustic-to-seismic coupling ratio with time. Measurements are 30mins apart and the sensors were removed. R=1.0m Hs=0.15m (Position A).

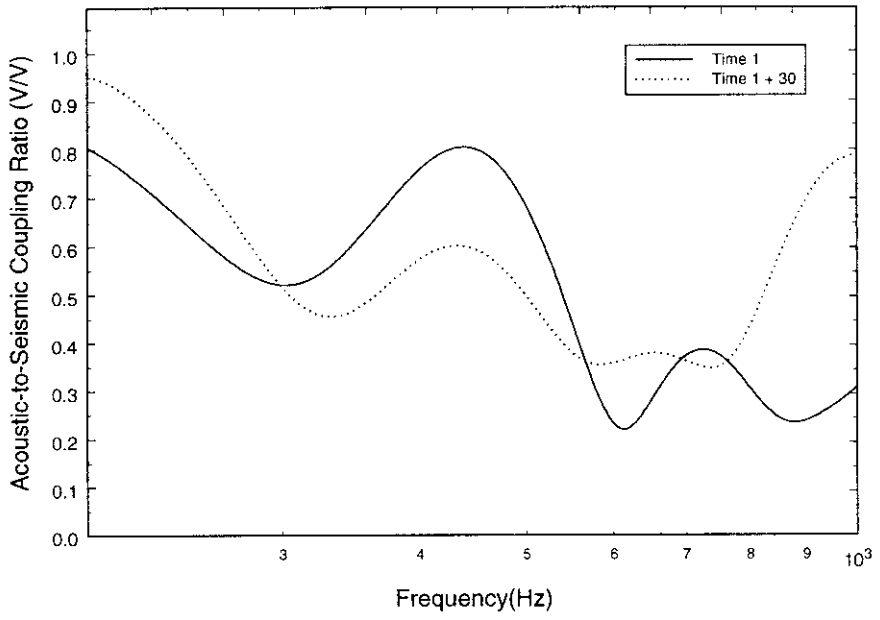

Figure 8-28. Variation in acoustic-to-seismic coupling ratio with time. Measurements are 30mins apart and the sensors were removed. R=1.0m Hs=0.75m (Position A).

Figure 8-29 shows the variation in acoustic-to-seismic coupling ratio at a range of 1m with varying source heights. The sensors were not moved between each measurement. The results appear to show the same angle dependence seen in the measurements taken at the ARG test site. Figure 8-30 shows the variation in acoustic-to-seismic coupling ratio measurements taken approximately 30 minutes after those shown in Figure 8-29.

Between the measurements, the geophone was removed and replaced in the same position. It can be seen that the agreement between the two figures is satisfactory up to frequencies of 350Hz, after which there is considerable divergence in the measurements. From the data shown in Figure 8-30, the clear variation of coupling ratio with source height seen in Figure 8-29 is less pronounced due to fluctuations in the data.

Meteorological data taken concurrently with all these measurements can be found in Table E-1 in Appendix E.

Examination of the separate geophone and microphone signals (see Figure 8-31) reveals that the two microphone signals show almost identical frequency spectra over the whole range of interest. Meanwhile the geophone signals show a reasonable agreement up to 350Hz after which there is a strong divergence between the spectra.

Again, it appears that the measured geophone signal has a strong effect on the recorded acoustic-to-seismic coupling spectra. For all the data shown, in-situ calibrations were undertaken and the data is given in Table 8-11.

Figure	Ping Frequency (Hz)	Damping Coefficient (sec^{-1})	Coupling Frequency (Hz)	Sensitivity (V/ms^{-1})
Figure 8-29	385	576	396	29.1
Figure 8-30	414	600	425	29.7

Table 8-11. In-situ geophone calibration data, for the measurements shown in Figure 8-29 and Figure 8-30.

Comparison of the data in Table 8-11 with the measurements given in Figure 8-29 and Figure 8-30 supports the description given previously, that up to these frequencies the two measurements are consistent with each other, where after the coupling resonant frequency the two measurements show a strong divergence.

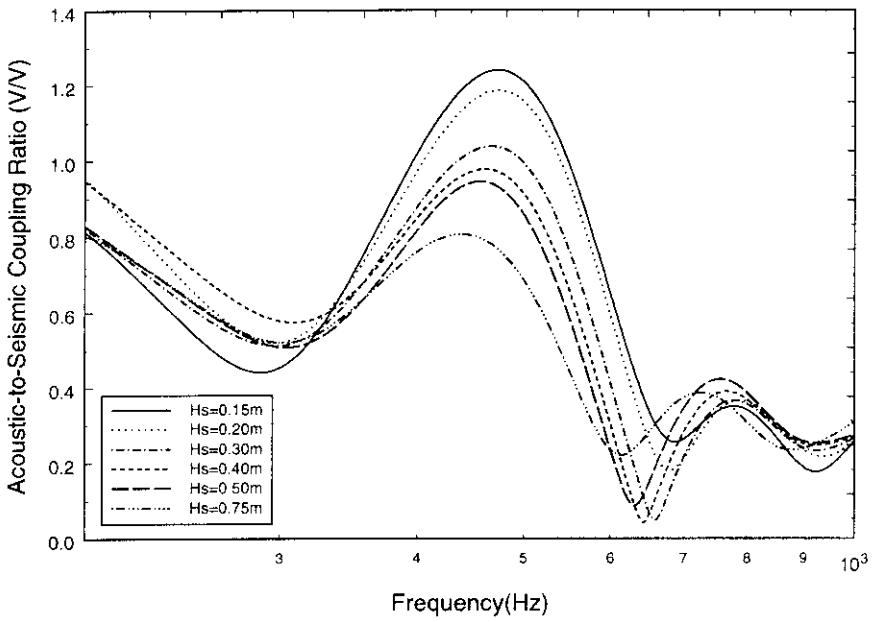

Figure 8-29. Variation in acoustic-to-seismic coupling ratio with varying source height. Data taken at time T1 with no removal of geophone sensor between measurements.

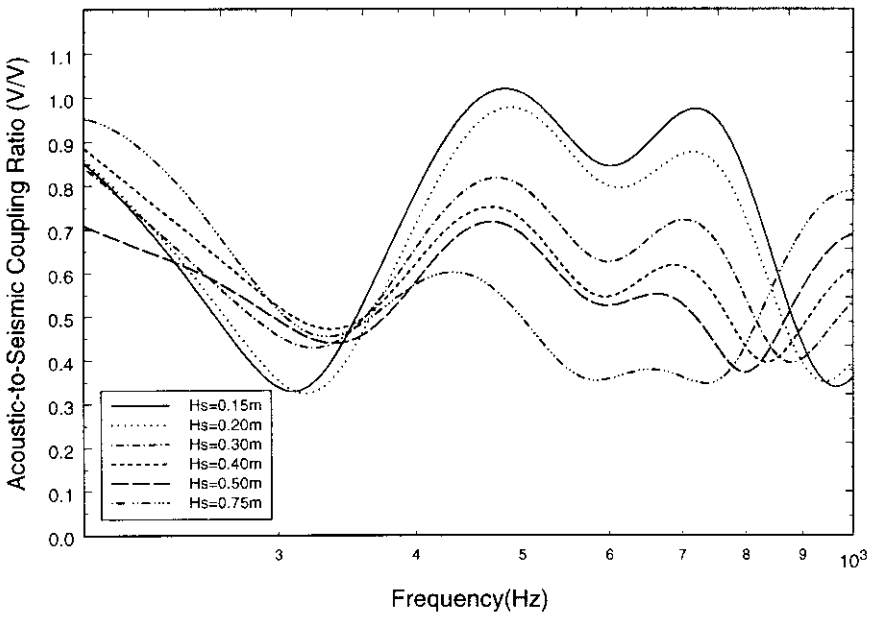

Figure 8-30. Variation in acoustic-to-seismic coupling ratio with varying source height. Data taken at T1+30 minutes and the geophone sensor was re-positioned.

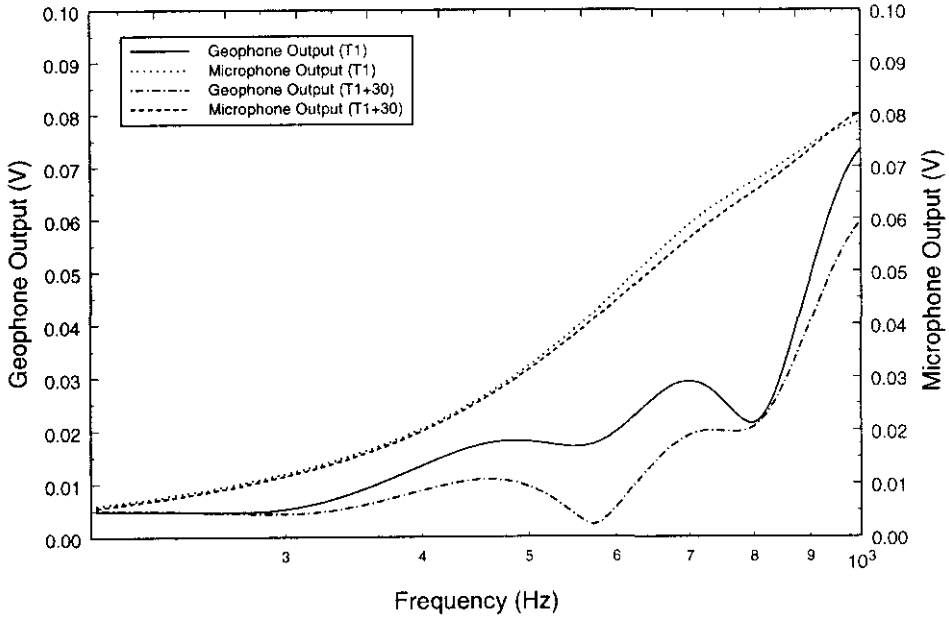

Figure 8-31. Geophone and microphone outputs at T1 and T1+30 (Acoustic-to-Seismic coupling ratio data shown in Figure 8-27).

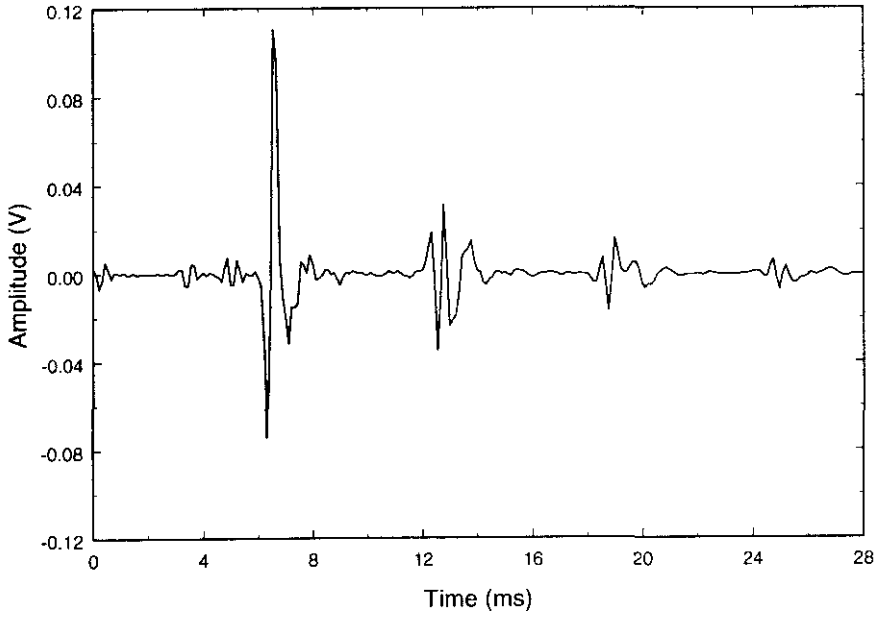

Figure 8-32. Example microphone response, showing the reflections due to the presence of the brass tube.

The trends observed and described for the set of measurements given can be seen throughout the whole of the measurements taken at the quarry. Further examples of data taken have been given in Appendix E. The meteorological data taken concurrently with all these measurements is shown in Table E-2 of Appendix E.

As noted in Section 8.1.5, a major drawback of the ARG test site was the limited size of the test area. This led to time-windowing of the impulse response, which in turn led to a reduction in the frequency resolution. A similar time windowing problem arises through the use of the point source loudspeaker. The point source consisted of a 30W Tannoy loudspeaker onto which a 1m brass tube has been attached.

The presence of the tube produces reflections in the output signal, as the signal is reflected from the mouth of the tube back down the tube. It then hits the front of the loudspeaker and returns up the tube. This results in an extra path length of 2m that approximates to a time delay of roughly 6ms. This phenomenon can be seen in Figure 8-32 which shows an example microphone response. The initial impulse can clearly be seen in the plot as the major event at roughly 6ms. The next main event on the trace is then the reflection due to the presence on the tube. This appears a further 6ms after the first arrival.

Since, the time cut-off at the ARG test site was approximately 6ms due to the size of the test area this loudspeaker reflection was not of great importance. However, at Stone Lane where there was a larger expanse of material there was an opportunity to increase the frequency resolution of the measurements.

Several attempts were made to rectify this problem. A simple solution to the problem was to increase the length of the brass tube used. A simple doubling of the length to 2m increased the time interval between the reflections to 12ms, which would be sufficient time to record all the differing wave arrivals at the geophone. However, the practicality of taking a 2m long tube into the field was not appropriate.

This problem was overcome by using a length of coiled pipe. Due to the thin walls of the coiled pipe, it was necessary to place the pipe inside a small box to reduce the radiation of energy from the pipe and reduce resonance set up in the coil. However, the presence of the box introduced fresh reflections into the impulse response. The effects of these were diminished by using a piece of straight pipe out from the box.

This configuration provided an adequate solution to increase the time interval between the reflections. However, the major disadvantage of this method was the fact that

due to the relatively low power of the Tannoy loudspeaker, once the output impulse had travelled through the 2m of the coil and 1m of straight brass tube, little energy remained. This reduced the useful range of the loudspeaker for acoustic-to-seismic coupling ratio measurements from 4m to less than 1m, where near-field effects became an issue.

Since a mechanical solution could not be found, a software solution was investigated. The methods included use of the complex cepstrum and time-domain filtering.

The cepstrum belongs to the area of homomorphic signal processing. Cepstral analysis is the name given to a range of techniques all involving functions that can be considered as a "spectrum of a logarithmic spectrum". It was first introduced by Bogart *et al.* (1963). It was found that the logarithm of the power spectrum of a signal containing an echo had an additive periodic component due to this echo and thus the Fourier transform of the log-power spectrum should exhibit a peak at the echo delay. It was proposed at the time as a better alternative to the autocorrelation function for the detection of echoes in seismic signals.

The distinctive feature of the cepstrum is not that it is a spectrum of a spectrum, but rather the logarithmic conversion of the original spectrum. The autocorrelation function is the inverse Fourier transform of the power spectrum and can also be considered a "spectrum of a spectrum". The most commonly used definition of the cepstrum nowadays is as the "inverse Fourier transform of the logarithmic power spectrum" which differs from the auto-correlation only by virtue of the logarithmic conversion of the spectrum. Randall (1987) illustrates some of the situations where the cepstrum gives advantages over the auto-correlation function.

Cepstra derived from power spectra are now known as "power cepstra". Similarly, cepstra derived from complex spectra, and thus using phase as well as log amplitude information at each frequency, are known as "complex cepstra". For this reason, the complex cepstra operation is reversible back to the time domain (Randall, 1987).

The main issue of the implementation of the cepstrum is the unwrapping of the phase information. The values of phase must be given as modulo of 2π. If the phase is unwrapped incorrectly then any filtering in the cepstrum domain cannot be effectively achieved and the inverse transform yields incorrect results.

For the microphone data, the cepstrum analysis appears to work satisfactorily as the convoluted signals are not overlapping, however, this is not the case for the geophone data

and the cepstrum did not work as envisaged. For this case, it appears that the cepstrum is not very suitable as a deconvolution process.

As such, simple time-domain filtering was tried. This method involves the filtering of the time domain response of the appropriate sensor; this is achieved using windowing techniques. Again, for the microphone data, an adequate solution was found, since (see Figure 8-32) the output pulse received at the microphone has decayed before the reflection appears.

Unfortunately, this is not the case for the geophone data where the reflection due to the pipe is masked in the Rayleigh wavetrain. Applying the same filter size to the geophone data caused large distortions in the geophone spectrum.

Since no adequate solution could be found to overcome the problem, to take measurements at longer ranges a standard loudspeaker was used. A loudspeaker was designed and constructed to give a strong output in the frequency range 100-500Hz.

A number of initial experiments were undertaken again to assess the effect of geophone positioning on the recorded acoustic-to-seismic coupling spectra. Figure 8-33 shows the acoustic-to-seismic coupling ratio measured at the quarry at a range of 5.0m with a source height 0.75m. Three differing geophone positions are shown. For each subsequent measurement, the geophone was pushed further into the sand. The individual positions are given in the legend of the figure.

The plots clearly show that the differing geophone implantation depths have a significant influence on the coupling spectra. At the lower frequencies, less than 300Hz, all three geophone positions give almost identical results, whilst at the higher frequencies large differences become noticeable. This is especially noticeable by the fact that the large peak at 400Hz seen in the spectrum from Position 1 is greatly reduced in the subsequent plots.

The coupling resonant frequency and geophone sensitivity derived from geophone "pinging" for each of the three geophone positions are also given in Table 8-12. The results given in the table show that the further the geophone is pushed into the ground, there is an increase in the coupling frequency and the damping. The increasing sensitivity of the geophone also highlights the enhanced coupling between the geophone and the sand.

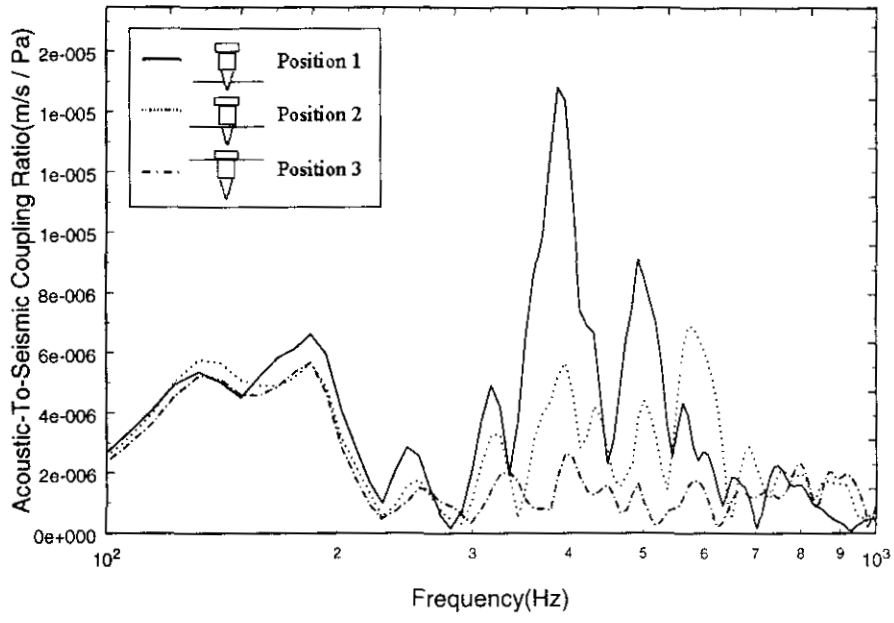

Figure 8-33. Variation in acoustic-to-seismic coupling ratio with differing geophone position (Range=5.0m, Hs=0.75m).

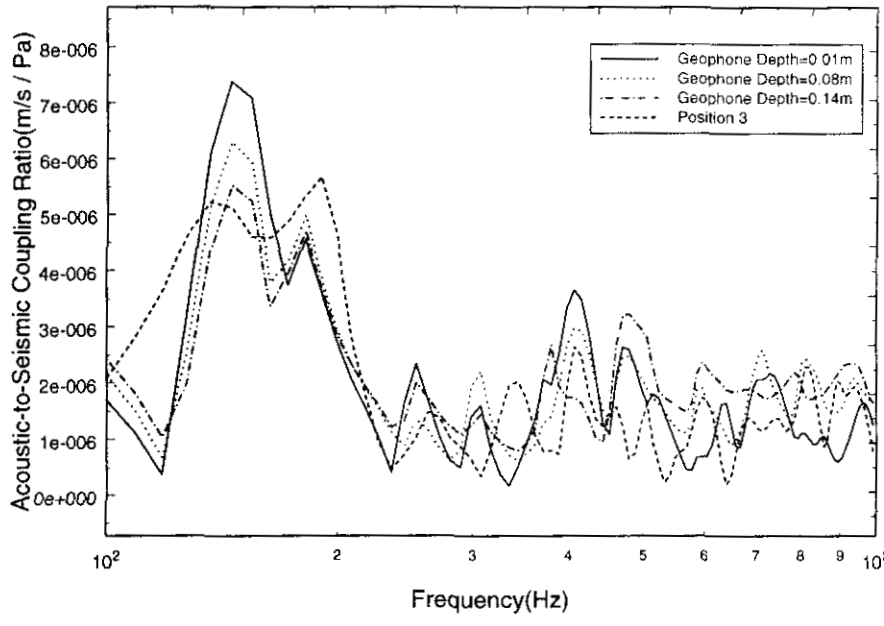

Figure 8-34. Comparison of acoustic-to-seismic coupling ratio data and the effect of differing geophone depth on the FFLAGS prediction.

Geophone Position	Ping Frequency (Hz)	Damping Coefficient (sec^{-1})	Coupling Frequency (Hz)	Sensitivity (V/ms^{-1})
1	357	600	370	20.2
2	385	678	400	23.6
3	414	764	431	28.0

Table 8-12. The coupling resonant frequency and geophone sensitivity derived from geophone "pinging" for each of the three geophone positions shown in Figure 8-33.

Predictions using FFLAGS showed that the coupling spectra for Positions 1 and 2 could not be fitted to any reasonable standard, whilst the coupling spectra from Position 3 gave the most accurate agreement. This can be seen in Figure 8-34 that shows the FFLAGS prediction and the data for geophone Position 3. The plot also shows that the variation in coupling ratio observed in Figure 8-33 cannot be predicted by simply altering the geophone depth in the model.

The parameters used to model the ground in Figure 8-34 are given in Table 8-13.

	Layer 1	Layer 2	Substrate
P-wave speed (m/s)	240	380	760
S-wave speed (m/s)	80	130	260
Flow resistivity ($Pa\ sm^{-2}$)	40000	40000	360000
Porosity	0.38	0.38	0.027
Grain shape factor	0.5	0.5	0.5
Soil density (kg/m^3)	1650.0	1650.0	2700
Layer thickness (m)	0.60	1.0	∞
Attenuation (v_p)	0.02	0.02	
Attenuation (v_s)	0.01	0.01	
Dynamic viscosity of air (Nsm^{-2})	1.81×10^{-5}		
Range (m)	5.0		
Source Height (m)	0.75		
Microphone height (m)	0.05		
Geophone depth (m)	-0.01		
	-0.08		
	-0.14		
Frequency range (Hz)	100 – 1000		
Speed of sound in air	344.0		

Table 8-13. Parameters used to predict the acoustic-to-seismic coupling ratio measurements taken at a range of 3m at Stone Lane Quarry and shown in Figure 8-34.

Again, these results provide more evidence for the marked effect that the geophone ground coupling has on the acoustic-to-seismic coupling ratio spectra. As more of the geophone comes into contact with the ground, from Position 1 to 3, the coupling becomes stronger. This can be seen in the increasing coupling resonant frequency of the geophone with increasing penetration into the ground.

As the effects of the variation in geophone depth in the measurements cannot be predicted at the higher frequencies, but can be modelled adequately at the lower frequencies, it appears that the measurements are suspect and the model is behaving correctly.

Acoustic-to-seismic coupling ratio experiments were also taken at the quarry using the standard configuration. It was thought that the layering in the ground and the more natural in-situ conditions than found at the ARG test site, would provide a useful environment to provide further validation of the technique. It would also serve to test the accuracy of the FFLAGS model for predicting the measured spectra in more complex situations.

Measurements undertaken at a range of 3.0m and for source heights of 0.75m and 1.5m can be seen in Figure 8-35 and Figure 8-36. The figures show the recorded coupling spectra and the FFLAGS prediction. Parameters used to predict the acoustic-to-seismic coupling ratio measurements taken at a range of 3m at Stone Lane Quarry are given in Table 8-14.

Figure 8-35 gives the measurement and prediction for the source height of 0.75m. From the figure, it can be seen that reasonable agreement has been achieved by the model. There are a number of minor peaks in the measurement that have not been predicted by the model, though these are likely to be due to small-scale layering in the ground that have not been located using the seismic refraction method.

From Table 8-14 it can be seen that the phase velocities used in the FFLAGS model are very close to those determined from the seismic refraction investigation. However, the major difference between the two is the value of layer depth. From the seismic refraction data, a layer depth of 1.28m was calculated whilst the depth of the second layer could not be determined due to the spread length being too short.

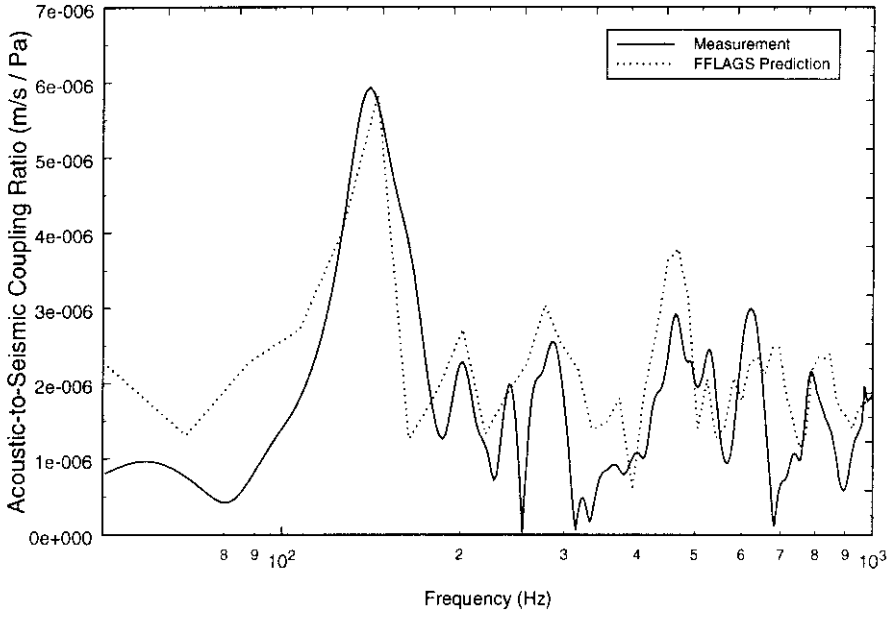

Figure 8-35. Measured acoustic-to-seismic coupling ratio and FFLAGS prediction taken at HMC Stone Lane (Range=3.0m, Hs=0.75m and f_0=387Hz).

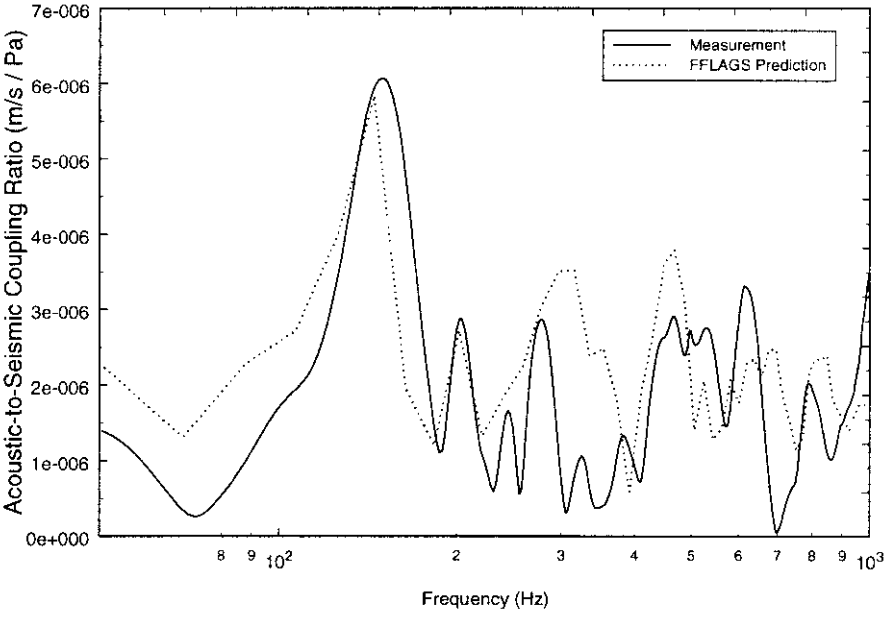

Figure 8-36. Measured acoustic-to-seismic coupling ratio and FFLAGS prediction taken at HMC Stone Lane (Range=3.0m, Hs=1.50m and f_0=387Hz).

		Layer 1	Layer 2	Substrate
P-wave speed (m/s)	(Hs=0.75)	240	375	750
	(Hs=1.50)	250	390	750
S-wave speed (m/s)	(Hs=0.75)	90	160	320
	(Hs=1.50)	85	170	320
Flow Resistivity ((Pa sm^{-2})	(Hs=0.75)	40000	40000	3600000
	(Hs=1.50)	40000	40000	3600000
Porosity	(Hs=0.75)	0.36	0.36	0.036
	(Hs=1.50)	0.36	0.36	0.036
Grain shape factor		0.5	0.5	0.5
Soil density (kg/m^3)		1500.0	1500.0	2700
Layer thickness (m)	(Hs=0.75)	0.95	0.85	∞
	(Hs=1.50)	0.90	0.90	∞
Attenuation (v_p)		0.02	0.02	0.04
Attenuation (v_s)		0.01	0.01	0.02
Dynamic viscosity of air (Nsm^{-2})		1.81×10^{-5}		
Microphone height (m)		0.05		
Geophone depth (m)		-0.05		
Frequency range (Hz)		100 – 1000		
Speed of sound in air		344.0		
Coupling Resonant Frequency (Hz)		387		
Geophone Sensitivity (V / m/s) (measured)		29.0		
Microphone Sensitivity (V / Pa) (measured)		$13.4e^{-3}$		

Table 8-14. Parameters used to predict the acoustic-to-seismic coupling ratio measurements taken at a range of 3m at Stone Lane Quarry.

The FFLAGS model used a layer depth of 0.95m for the upper layer and 0.85m for the lower layer. This depth difference may be due to errors in the travel time determination in the seismic method, which would produce errors in the subsequent calculations. It is less likely to be errors in the FFLAGS prediction, since very small changes in layer depth, e.g. 0.10m, will produce noticeable changes in the resultant coupling spectrum.

However, although the acoustic-to-seismic coupling measurements were taken along the same positional line as the seismic refraction survey, the depth determination for each method are determined for differing positions. The depth determined from the seismic method is directly under the shot point, whereas, the depth determined from the acoustic-to-seismic coupling is below the measurement position. It may be therefore, that the difference may simply be due to actual variations in the layer depth.

Figure 8-36 shows the data and subsequent FFLAGS prediction taken at a range of 3m and using a source height of 1.5m, where again a reasonable agreement can be seen between the two plots.

As with the previous plot there are a number of minor peaks in the measurement that have not been predicted which have been attributed to the possible presence of a number of unknown layers. The layer depth used in the prediction are very close to those used to predict the data shown in Figure 8-35. Variations of 0.05m between the predictions appear to support the assumption that the depth determination from the seismic survey may be in error.

The meteorological data taken concurrently with all these measurements taken using the loudspeaker are shown in Table E-3 of Appendix E. Further examples of data and the subsequent FFLAGS predictions taken at ranges of 6.0m and 9.0m have been given in Appendix E. The predictions for these longer ranges show little variation in the soil parameters used in the FFLAGS model providing further corroboration of the parameters used to predict the data shown in Figure 8-35 and Figure 8-36.

A number of experiments were undertaken at the quarry, using both vertical and horizontal component geophones. Integrating the output from the co-located vertical and horizontal geophones provided a picture of the particle motion caused by the incident air-wave. Figure 8-37 shows the motion when the loudspeaker was 3m from the sensors and at a height of 0.75m. The initial sand particle motion starting 0.009 seconds after the shot is down and away from the source as expected. Within 0.07 seconds the motion becomes elliptical retrograde with both components about equal in size.

After several retrograde loops, the motion switches back to prograde, then back again. It remains mostly retrograde and gradually flattens out to horizontal by 0.040 seconds.

Classically, elliptical particle motion is associated with surface waves in seismology and there is evidence of this motion in the measurements taken. The initial vertical motion is caused by the force applied to the surface from the passage of the air-wave. The prograde and retrograde motions arise from the surface waves coupled to the air-wave travelling in the shallow ground.

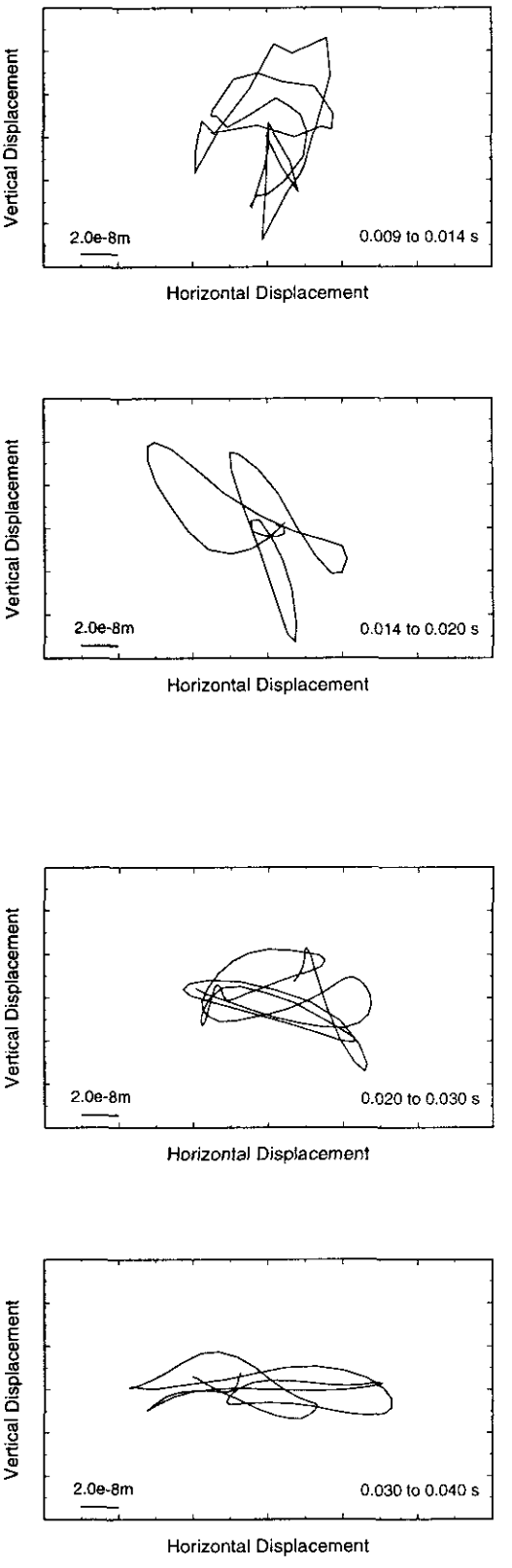

Figure 8-37. Particle diagrams from Stone Lane Quarry. Source height of 0.75m and a range of 3.0m. Each segment shows successive time intervals starting 0.009 seconds after the start of the output.

It appears from the experiments taken at the quarry, utilising both vertical and horizontal component geophones, that the presence of acoustically induced surface waves can be measured. In order to exploit the surface waves produced, a more systematic and detailed investigation must be carried out. A surface wave experiment using the Spectral Analysis of Surface Waves (SASW) method has been undertaken at the HRI, Wellesbourne site and is detailed in Section 8.3.4.

8.2.3 Probe Microphone

A series of probe microphone measurements were taken at the site. Measurements were taken at differing angles of grazing over a period of time and at two positions (A and B) for each range. Table 8-17 shows a set of results for measurements taken at a grazing angle of 19°. The figures showing an example set of data (taken at Position A) can be found in Appendix E.

It can be seen from these plots that the magnitude of the signal decreases systematically down to 8cm after which there appears little decrease with increasing depth. These are slight variations in the rate of decrease, though these are likely to be due to inaccuracies in depth determination of the probe.

As in previous measurements, it is noticeable that the change in both the magnitude and phase change per unit depth increases with increasing frequency. This indicates that down to a depth of approximately 8cm the Type II P-wave is predominant.

Calculations of attenuation and phase speed versus the depth intervals 1cm to 7cm, 3cm to 7cm and 2cm to 4cm have been made, with best–fit regressions applied to the data. The values of attenuation in dB/m and for frequencies of 100Hz, 200Hz, 300Hz, 400Hz and 500Hz can be found in Table 8-15, with the corresponding values of phase velocity given in Table 8-16.

	Depth Interval	Frequency				
		100Hz	200Hz	300Hz	400Hz	500Hz
Position A	1cm to 7m	207.0	244.8	282.6	320.4	358.2
	3cm to 7m	190.9	220.8	250.8	280.4	310.2
	2cm to 4cm	198.6	250.8	303.0	355.3	407.5

Table 8-15. Attenuation (dB/m) calculated from the data taken at a grazing angle of 19° with the probe microphone.

The measured values of attenuation are much greater than those measured at the ARG test site as would be expected, since the gravel at the ARG test has a greater flow resistivity and porosity than that of the fine sand found at the quarry. The values are closer to the attenuation measured in the Indoor Tank sand, since the two materials are of similar composition.

	Depth Interval	Frequency				
		100Hz	200Hz	300Hz	400Hz	500Hz
Position A	**1cm to 7m**	105.7	139.1	158.6	175.5	182.2
	3cm to 7m	92.5	117.6	132.3	142.7	150.8
	2cm to 4cm	211.2	246.9	267.8	282.6	294.1

Table 8-16. Phase velocity (m/s) calculated from the data taken at a grazing angle of 19° with the probe microphone.

The values gained for the phase velocity given in Table 8-16 show an increase with frequency, indicating that the measured wave type is Biot Type-II wave. It can be noted from this table that the phase velocity measured over the depth interval 2cm to 4cm is greater than the P-wave velocity measured using the seismic refraction method.

It has previously been stated that, under certain conditions it is possible for the Type-II wave to have a greater velocity than the Type-I wave. However, these conditions usually apply at much higher frequencies, e.g. 10's of kHz. Numerical predictions made using the *porovel* computer program used in Chapter 6, proved that in this case the Type-II wave could not have a greater velocity than the Type-I wave.

It is most likely that in the instance the anomaly is due to an incorrect depth determination of the probe, since an error in depth determination of 10% will reduce the calculated velocities by approximately 25%. This would reduce the Type-II wave velocity below the measured value for Type-I wave.

This result highlights the need for extreme care is depth determination of the probe as small errors can cause anomalies such as those observed here. It also highlights the difficulties of using the probe microphone technique in unconsolidated materials.

Using the technique described previously, the measurements of the real and imaginary parts of the bulk propagation constant have been used to determine the tortuosity (τ) and flow resistivity (σ). These results for all the measurements taken at the quarry can be seen in Table 8-17.

Angle of Grazing	Depth Interval	Tortuosity	Flow Resistivity (MKS Rayls)
9° (Position A)	**1cm to 7cm**	2.8	40888
	3cm to 7cm	4.0	43068
	2cm to 4cm	1.1	16020
	Average	**2.6±1.5**	**33325±17305**
9° (Position B)		2.4±0.6	39369±12083
19° (Position A)		3.0±0.8	46812±16513
19° (Position B)		2.4±0.5	38236±9562
6° (Position A)		2.1±0.2	30651±9342
6° (Position B)		2.6±0.9	37512±11055
	Overall Average	**2.5±0.8**	**37651±12643**

Table 8-17. Calculated values of tortuosity and effective flow resistivity from probe microphone measurements.

Table 8-18 shows a comparison of physically measured and acoustically deduced soil properties using the probe microphone for the ARG test site. The results show a reasonable agreement for both the tortuosity and flow resistivity between the physical measured and acoustically deduced values. Again, as seen with the Indoor tank and the ARG test site results, the acoustically deduced value of flow resistivity is approximately twice that measured using the airflow rig.

	Physical Measurement		Probe Microphone	
	Tortuosity	**Flow Resistivity (MKS Rayls)**	**Tortuosity**	**Flow Resistivity (MKS Rayls)**
HMS Sand	2.24±0.04	19838±515	2.5±0.8	37651±12643

Table 8-18. Comparison of physically measured and acoustically deduced soil properties for the HMC Stone Lane Quarry.

8.2.4 Conclusions

Experiments undertaken at HMC Stone Lane Quarry have again highlighted the effect of geophone-ground coupling on the measurement of acoustic-to-seismic coupling ratio and the data taken using the point source does appear to show that there is a slight dependence of the source height on the recorded spectra.

The problem of removing the reflections caused by the presence of the brass tube, which has been used to approximate the Tannoy source to a point source, has been investigated although no completely satisfactory solution could be found using either a hardware or software solution.

The long-range experiments have shown that low frequency layer resonances have been cut-off by the time-windowing necessary with the use of the Tannoy source. However, the point source experiments have proved extremely useful due to the increased accuracy in the source height determination that can be achieved using this speaker.

The predictions using the FFLAGS model have given reasonable agreement for all the long-range measurements with predicted P- and S-wave velocities being very close to those value found from the seismic refraction survey. However, noticeable differences were found in the layer depth determination, with a difference of 0.30m found between the values determined using the two techniques.

The repeatability of the values gained from the predictions suggests that the error in layer depth may be in the seismic refraction method, although the difference may be due to actual layering changes at the site. It can also be noted that using the refraction technique the second layer depth could not be determined, however, the FFLAGS model does allow this layer depth to be determined.

Analysis of measurements using co-located vertical and horizontal component geophones have shown that the presence of retrograde elliptical motion, which has been taken to indicate the existence of acoustically induced surface waves. The exploitation of surface waves for soil stiffness profiles has already been made in seismic exploration. The presence of acoustically induced surface waves at the site leads to the belief that the techniques developed for seismic exploration can be utilised in acoustic exploration. A more systematic measurement of acoustically induced surface waves has been made at HRI, Wellesbourne and is described in Section 8.3.4.

The probe microphone measurement technique that had been reliably used in the Indoor Soil Tank proved to give acceptable results. The data shows the same fluctuations seen indoors and again there appears to be no angle dependence to either the calculated tortuosity or flow resistivity. Comparisons of the acoustically and mechanically derived values of tortuosity and flow resistivity show reasonable agreement.

From the measurements taken at the site, a number of material properties have been determined using acoustic techniques and these can be seen in Table 8-19 and Table 8-20. The table also shows the values of the parameters measured using standard techniques.

Soil Parameter		Directly Measured	Acoustically Derived
Number of Layers		2	2
Layer Thickness (m)	1	1.28	0.90
	2	---	0.85
Flow Resistivity (mks rayls)	1	19838±515	40000
	2	---	40000
Permeability (m/s)	1	$6.76\times10^{-3} \pm 8.10\times10^{-5}$	4.42×10^{-3}
	2	---	4.42×10^{-3}
Porosity (%)	1	36.0	36.0
	2	---	36.0
Bulk Modulus (MPa)	1	46.74	81.22
	2	---	167.89
Shear Modulus (MPa)	1	5.62	13.37
	2	---	40.84
Soil Density (kg/m^3)	1	1505.3	1500
	2	---	1700

Table 8-19. Soil Properties determined from acoustic-to-seismic coupling experiments undertaken at the HMC Stone Lane Quarry site.

Soil Parameter	Directly Measured	Acoustically Derived
Flow Resistivity (mks rayls)	19838±515	37651±12643
Permeability (m/s)	$6.76\times10^{-3} \pm 8.10\times10^{-5}$	$4.70\times10^{3}\pm1.18\times10^{3}$
Tortuosity	2.24±0.04	2.5±0.8

Table 8-20. Soil Properties determined from probe microphone experiments undertaken at the HMC Stone Lane Quarry site.

Both tables show a good correlation between the values of soil properties deduced from the acoustic measurements and the values gained from the standard testing procedures. However, it can be seen from Table 8-19 that the values derived using the resonant column apparatus of bulk and shear moduli are approximately half the size of the values derived from the acoustic-to-seismic coupling measurements. This is possibly due to the derivation of each value.

The value derived from the acoustic-to-seismic coupling measurements is based upon the relationship between p- and s-wave velocity and the elastic moduli. The

velocities are an average over the whole layer depth of 0.90m, whereas the values derived from the resonant column test have been calculated from the line of best-fit of the plot of moduli against depth. The value given here is based upon a depth of 0.45m (half the layer depth).

From the measurements undertaken at ARG test site and at HMC Stone Lane Quarry, it appears that under controlled conditions acoustic measurements, which include acoustic-to-seismic coupling ratio and probe microphone experiments, can be used with a reasonable degree of reliability for the determination of soil properties.

The experimental techniques developed at the two sites should allow measurements to be taken in agricultural soils that will result in accurate and reliable soil property determination. This has been attempted in three agricultural soils found at Horticultural Research International, Wellesbourne and will be reported in Section 8.3.

8.3 Horticultural Research International, Wellesbourne

The site at HRI, Wellesbourne has been described in Section 4.1.3 of Chapter 4. Briefly, the site consisted of an artificial seedbed 6m wide by 26m length with three different soil types A, B and C in 2-m wide bands. As part of the HRI experiments, the area is permanently covered. This fact coupled with the dry summer of 1999 meant that at the time of the experiments the soils were very stiff and friable. Obtaining samples for laboratory measurement proved extremely difficult. As the material was very hard, it proved exceptionally problematical to remove and once removed the friability of the material meant that it invariably disintegrated.

It was envisaged that this was a situation where the use of a non-invasive method of soil property determination would be extremely useful.

8.3.1 Seismic Refraction Survey

A P-wave survey was carried out on all three soils present at the site using the standard seismic refraction technique outlined in Chapter 7. The subsequent seismograms can be found in Appendix F. From the seismograms, first arrival picking was carried out to

produce the traveltime-distance plots seen in Figure 8-38, Figure 8-40 and Figure 8-42 for Soil A, B and C respectively.

From Figure 8-38, the forward shot in Soil A, it can be seen that there are two distinct portions of the graph, indicating that there are two layers present. The plot of the reverse shot also shows the two distinct portions again suggesting the presence of more than one layer. Subsequent calculations of P-wave velocity are given in Table 8-21.

Analysis of the time-distance plots show that two layers exist and that the boundary between the upper and lower layer is not parallel to the ground surface, but that a small degree of dip is present.

	Layer 1	**Layer 2**
v_p (m/s)	189	450
v_s (m/s)	111	266 (assumed)
v_s/v_p	0.59	0.59 (assumed)
H_{down} (m)	0.47	--
H_{up} (m)	0.41	--
a (°)	-0.2	--

Table 8-21. Layer properties of Soil A determined from the seismic refraction survey.

Due to the constraints of the site, outlined in Chapter 4 and 7, the undertaking of a standard shear wave survey was not possible. The shear wave velocity of the upper layer was therefore determined using the technique developed in the Indoor tank and used at the ARG test site (Section 8.1.1).

A line of seven horizontal component geophones was laid out close to the centre of the pit. An end geophone was then driven using a 500Hz five-cycle tone burst with the travel time to each further geophone noted. Two experiments were undertaken and the subsequent traveltime-distance plot can be seen in Figure 8-39 with the calculated mean shear wave velocity given in Table 8-21.

The same technique was used to determine the shear wave velocity in Soil B and C. The results of these experiments can be seen in Figure 8-41 and Figure 8-43 respectively.

Comparison of the calculated shear/compressional wave velocity ratio of 0.59 with Figure 8-3 shows this value to be roughly the figure given for consolidated rock. This value appears very high for an agricultural soil, although the in-situ condition of the soil at the site makes this value more plausible.

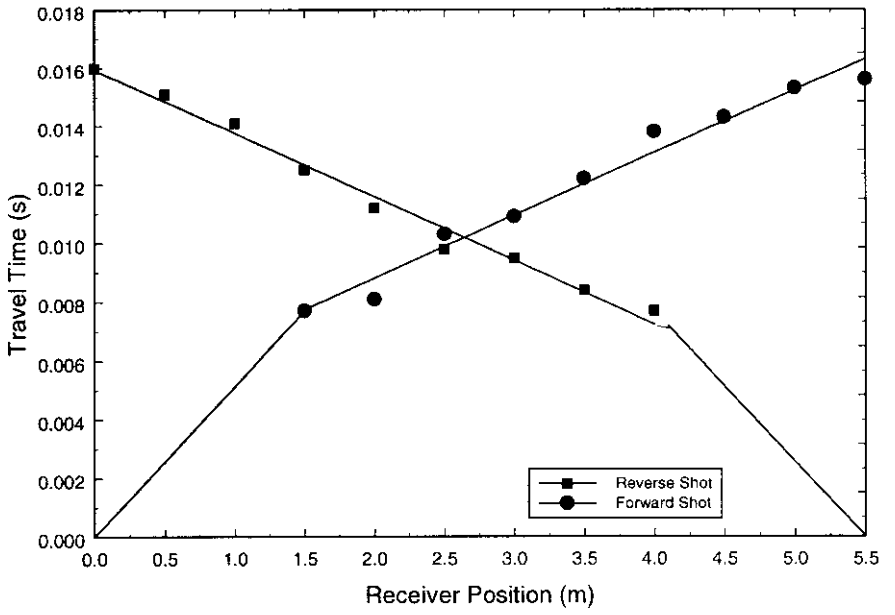

Figure 8-38. Travel Time versus vertical component geophone position for Soil A.

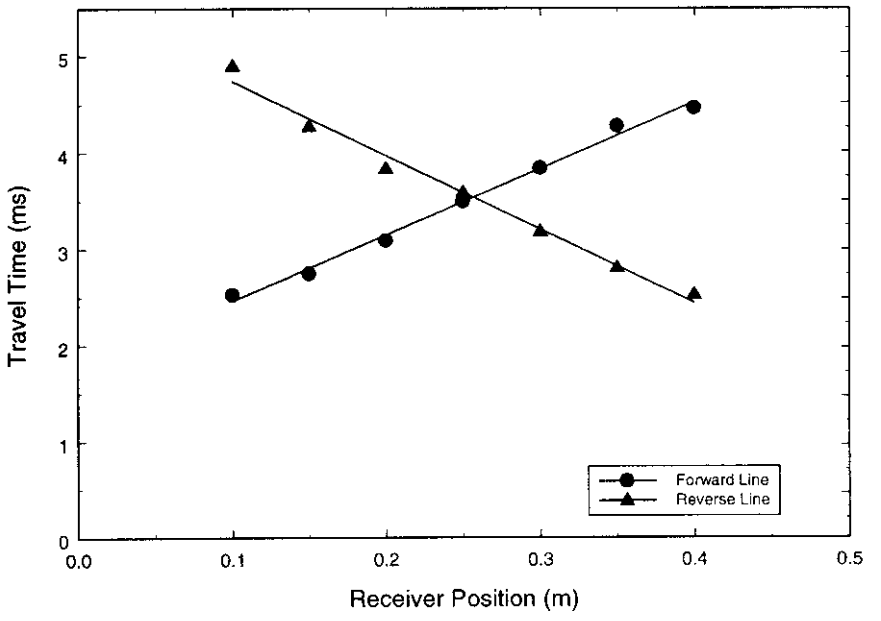

Figure 8-39. Travel Time versus horizontal component geophone position for Soil A.

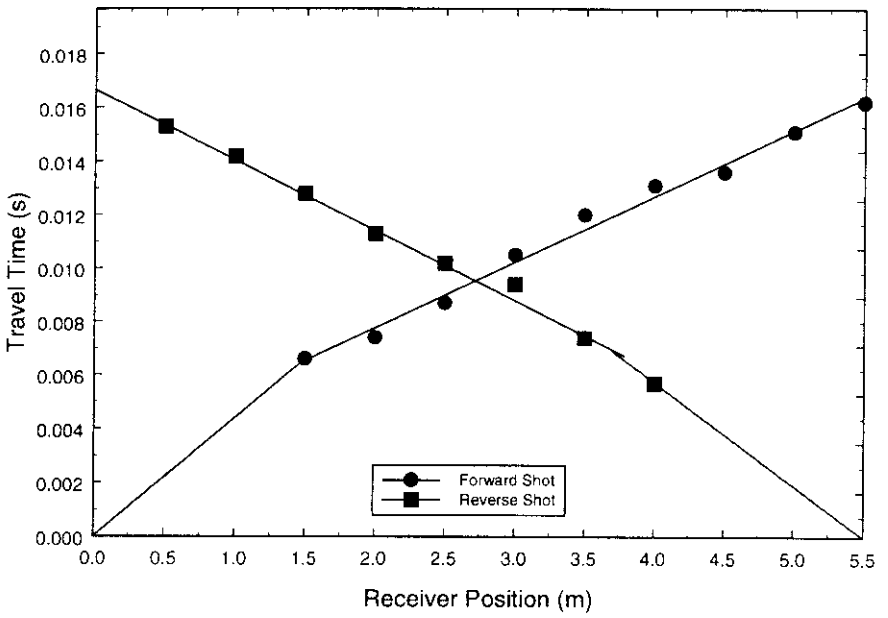

Figure 8-40. Travel Time versus vertical component geophone position for Soil B.

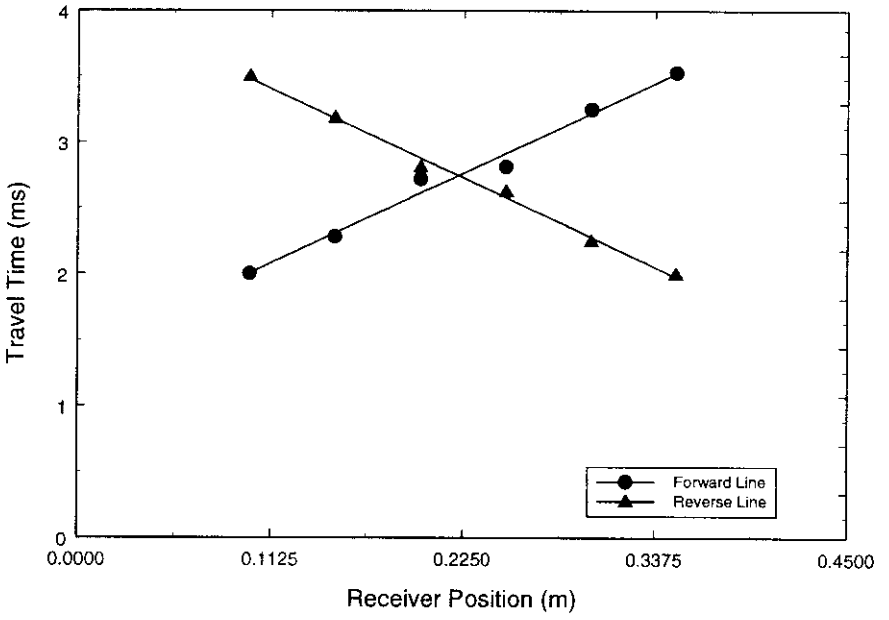

Figure 8-41. Travel Time versus horizontal component geophone position Soil B.

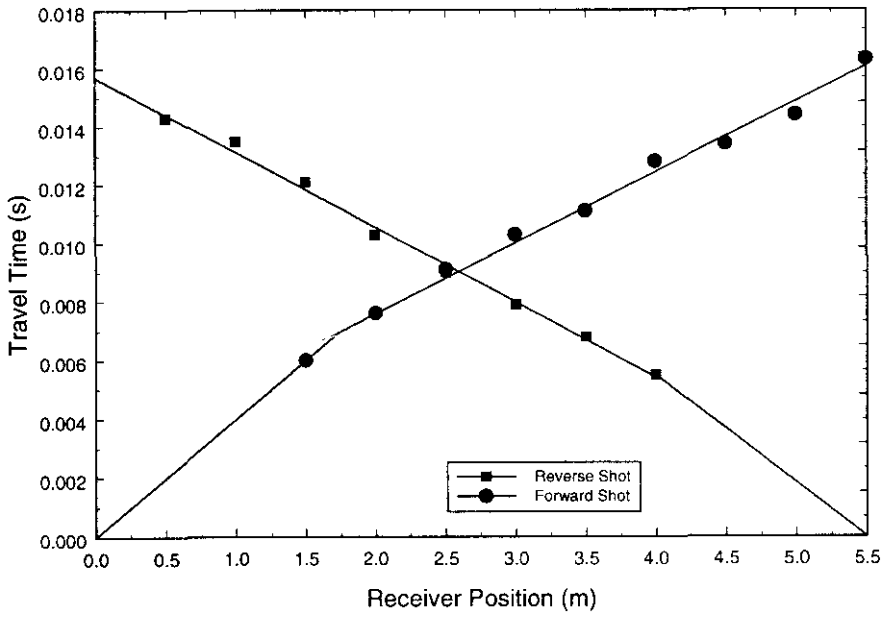

Figure 8-42. Travel Time versus vertical component geophone position for Soil C.

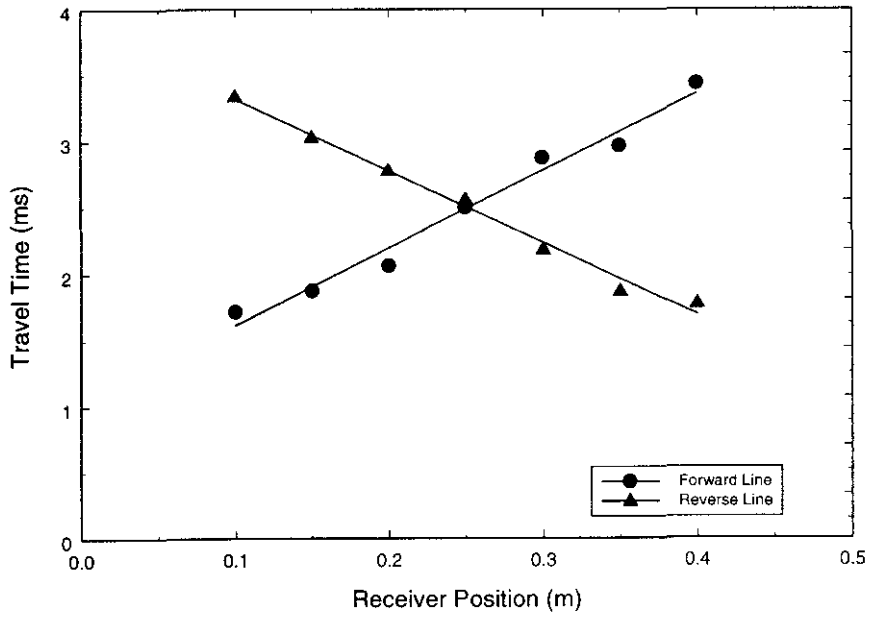

Figure 8-43. Travel Time versus horizontal component geophone position Soil C.

With the site permanently covered and the moisture content of the material low, the upper level of the soils at the time of the study were very stiff and this may explain the high shear/compressional wave velocity ratio.

Due to the configuration of the shear wave experiment, the s-wave velocity of the lower layer could not be determined. Therefore, the shear wave velocity of the lower layer, has been calculated using the P-wave velocity and the shear/compressional wave velocity ratio of the upper layer. It is believed that this will provide an indicative value.

Calculations have also been made for the two remaining soils at the site. From the time-distance graphs, it again appears that there are two layers present in each soil. Calculations of P and S-wave velocities and layer depths for Soil B are given in Table 8-22, whilst the calculation for Soil C can be found in Table 8-23.

	Layer 1	**Layer 2**
v_p (m/s)	245	393
v_s (m/s)	145	232 (assumed)
v_s/v_p	0.59	0.59 (assumed)
H_{down} (m)	0.45	--
H_{up} (m)	0.35	--
a (°)	-1.5	--

Table 8-22. Layer properties of Soil B determined from the seismic refraction survey.

	Layer 1	**Layer 2**
v_p (m/s)	261	400
v_s (m/s)	154	236 (assumed)
v_s/v_p	0.59	0.59 (assumed)
H_{down} (m)	0.47	--
H_{up} (m)	0.27	--
a (°)	-1.5	--

Table 8-23. Layer properties of Soil C determined from the seismic refraction survey.

8.3.2 Acoustic-to-Seismic Coupling Ratio

Acoustic-to-seismic coupling ratio measurements were undertaken on the three soils present at the site. For each measurement, concurrent meteorological data was taken and this has been given in Appendix F. In addition, in-situ sensor calibrations were undertaken to determine the sensitivities of the sensors used.

Geophone sensors were calibrated using the geophone "pinging" technique detailed previously, whilst the microphones were calibrated using a Brüel and Kjær pistonphone.

Example measurements of the acoustic-to-seismic coupling ratio in Soil A, together with the FFLAGS prediction have been given in Figure 8-44 and Figure 8-45. The plots show data taken using the loudspeaker at a range of 2.0m and 3.0m and with a source height of 0.45m. The parameters used to describe the ground in the model have been given in Table 8-24

		Layer 1	Layer 2	Substrate
P-wave speed (m/s)	(R=2.0m)	180	470	900
	(R=3.0m)	190	460	900
S-wave speed (m/s)	(R=2.0m)	110	280	600
	(R=3.0m)	110	290	600
Flow Resistivity ((Pa sm^{-2})	(R=2.0m)	450000	450000	3600000
	(R=3.0m)	450000	450000	3600000
Porosity	(R=2.0m)	0.23	0.23	0.036
	(R=3.0m)	0.23	0.23	0.036
Grain shape factor		0.5	0.5	0.5
Soil density (kg/m^3)		2000	2200	2650
Layer thickness (m)	(R=2.0m)	0.55	2.00	∞
	(R=3.0m)	0.60	2.00	∞
Attenuation (v_p)		0.04	0.04	0.04
Attenuation (v_s)		0.02	0.02	0.02
Dynamic viscosity of air (Nsm^{-2})		1.81×10^{-5}		
Microphone height (m)		0.05		
Geophone depth (m)		-0.05		
Frequency range (Hz)		100 – 1000		
Speed of sound in air		344.0		
Coupling Resonant Frequency (Hz)	(R=2.0m)	802		
	(R=3.0m)	898		
Geophone Sensitivity (V / m/s) (measured)	(R=2.0m)	23.0		
	(R=3.0m)	22.0		
Microphone Sensitivity (V / Pa) (measured)	(R=2.0m)	$13.4e^{-3}$		
	(R=3.0m)	$13.4e^{-3}$		

Table 8-24. Parameters used to predict the acoustic-to-seismic coupling ratio measurements taken in Soil A at HRI, Wellesbourne (source height=0.45m and range=2.0m, 3.0m).

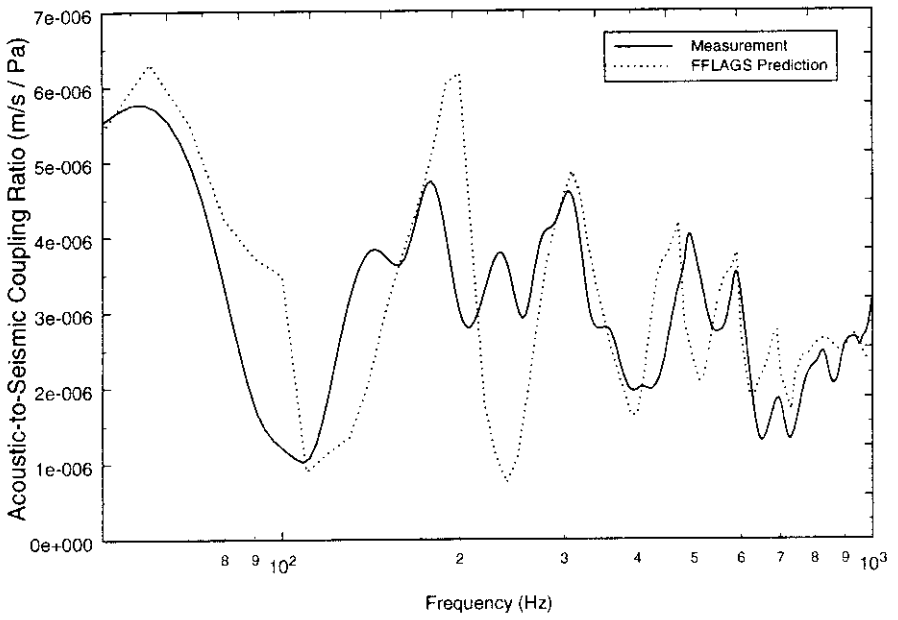

Figure 8-44. Measured acoustic-to-seismic coupling ratio and FFLAGS prediction taken at HRI for Soil A (Range=2.0m, Hs=0.45m and f_0=802Hz).

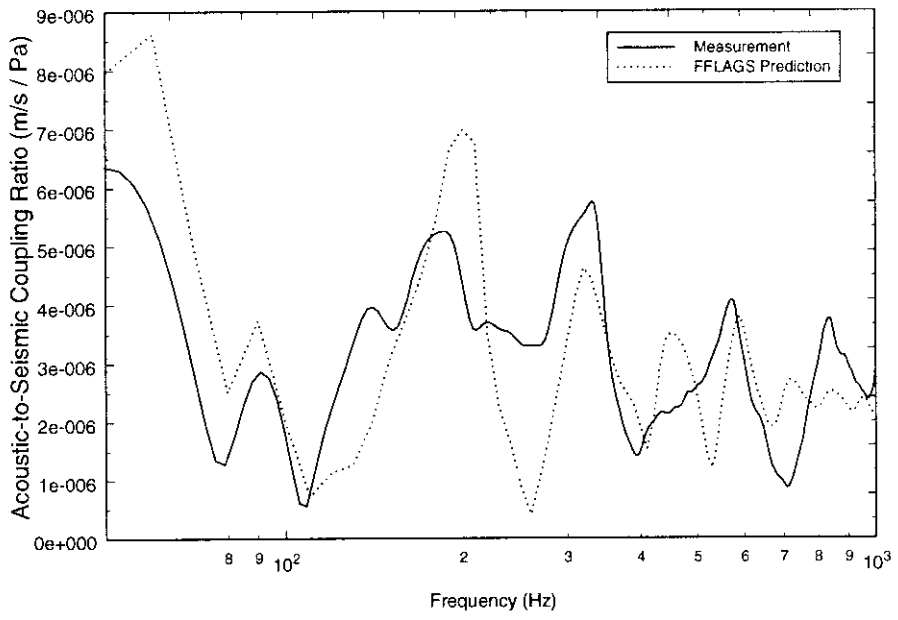

Figure 8-45. Measured acoustic-to-seismic coupling ratio and FFLAGS prediction taken at HRI for Soil A (Range=3.0m, Hs=0.45m and f_0=898Hz).

It can be seen from the two plots that a satisfactory agreement has been achieved between the data and predicted values, with the frequencies of all major and some minor peaks found.

The extremely well compacted ground encountered at the site has enabled extremely good coupling between the geophone and the ground. This has resulted in a coupling resonant frequency, for the two measurements shown, of approximately 850Hz. It is likely that the higher coupling resonant frequency seen in the figures, results in the predictions matching the data to much higher frequencies than previously seen at either the ARG test site or at HMC Stone Lane Quarry. There are still a number of small minor peaks in both figures that have not been predicted, though it is likely that these are due to minor layering which has not be identified.

Further example data together with FFLAGS predictions can be found in Appendix F. The data given in the appendix was taken using the loudspeaker at a range of 2.0m and 3.0m and with a source height of 0.68m. The predicted soil properties for this data are shown in Table F-1 and are in agreement with the corresponding values given in Table 8-24.

The values of wave velocities given in Table 8-24 show good agreement with those values derived using the seismic refraction method. Some difference is seen however, between the depth of the upper layer derived using the two techniques. The depth of the upper layer is approximately 15cm deeper using the acoustic-to-seismic coupling measurements and is deeper than the known value.

The value of porosity used in the model was taken from the porosity calculated from the resonant column experiment, whilst the value of flow resistivity was based upon previously reported values that have been given in Chapter 4. All the values used to model the data are indicative of a material such as Soil A.

Example measurements of the acoustic-to-seismic coupling ratio in Soil B, together with the FFLAGS prediction have been given in Figure 8-46 and Figure 8-47. The plots show data taken using the loudspeaker at a range of 2.0m and 3.0m and with a source height of 0.45m. The plots show a satisfactory agreement has been achieved between the measured coupling ratio and the predicted values.

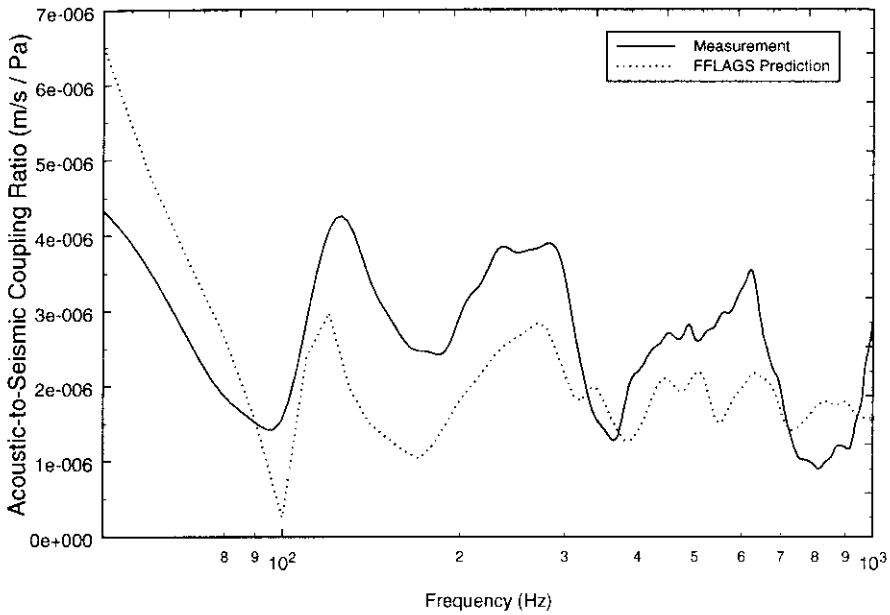

Figure 8-46. Measured acoustic-to-seismic coupling ratio and FFLAGS prediction taken at HRI for Soil A (Range=2.0m, Hs=0.45m and f_0=763Hz).

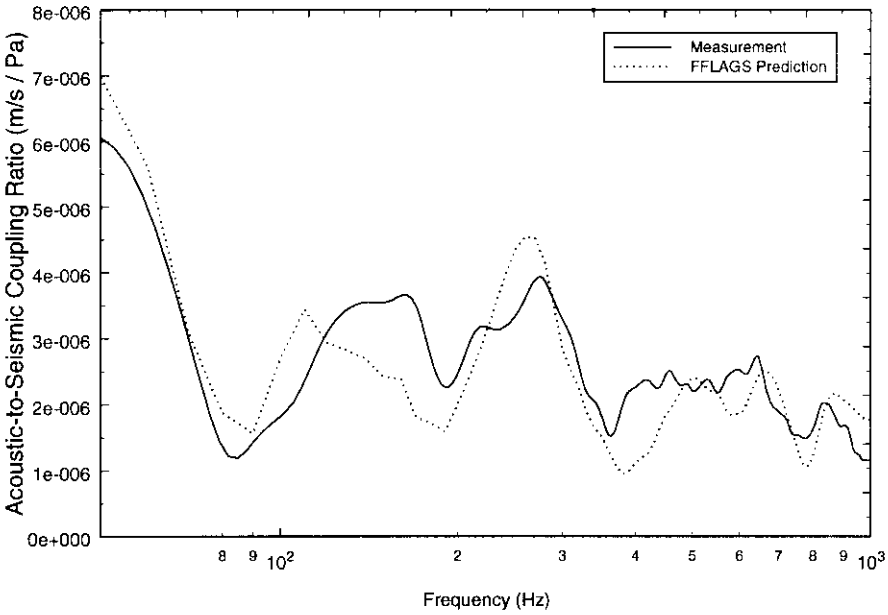

Figure 8-47. Measured acoustic-to-seismic coupling ratio and FFLAGS prediction taken at HRI for Soil A (Range=3.0m, Hs=0.45m and f_0=872Hz).

The parameters used to describe the ground in the model have been given in Table 8-25. The values of wave velocities given in Table 8-25 show good agreement with those values derived using the seismic refraction method. Some difference is again seen however between the depth of the upper layer derived using the two techniques.

		Layer 1	Layer 2	Substrate
P-wave speed (m/s)	(R=2.0m)	265.0	390.0	900.0
	(R=3.0m)	255.0	400.0	900.0
S-wave speed (m/s)	(R=2.0m)	145.0	230.0	600.0
	(R=3.0m)	150.0	230.0	600.0
Flow Resistivity ((Pa sm^{-2})	(R=2.0m)	475000	475000	3600000
	(R=3.0m)	475000	475000	3600000
Porosity	(R=2.0m)	0.18	0.18	0.036
	(R=3.0m)	0.18	0.18	0.036
Grain shape factor		0.5	0.5	0.5
Soil density (kg/m^3)		2000	2200	2650
Layer thickness (m)	(R=2.0m)	0.60	1.40	∞
	(R=3.0m)	0.58	1.50	∞
Attenuation (v_p)		0.02	0.02	0.04
Attenuation (v_s)		0.01	0.01	0.02
Dynamic viscosity of air (Nsm^{-2})		$1.81x10^{-5}$		
Microphone height (m)		0.05		
Geophone depth (m)		-0.05		
Frequency range (Hz)		100 – 1000		
Speed of sound in air		344.0		
Coupling Resonant Frequency (Hz)	(R=2.0m)	763		
	(R=3.0m)	882		
Geophone Sensitivity (V / m/s) (measured)	(R=2.0m)	24.6		
	(R=3.0m)	25.1		
Microphone Sensitivity (V / Pa) (measured)	(R=2.0m)	$13.4e^{-3}$		
	(R=3.0m)	$13.4e^{-3}$		

Table 8-25. Parameters used to predict the acoustic-to-seismic coupling ratio measurements taken in Soil B at HRI, Wellesbourne (source height=0.45m and range=2.0m, 3.0m).

Porosities were again taken from the resonant column tests, with the flow resistivity taken from indicative values in Table 4-4 of Chapter 4

The small magnitude difference seen in Figure 8-46 is most likely due to a differing geophone sensitivity, rather than a large variation in flow resistivity or porosity (the two

main controls on coupling magnitude), since the same values of flow resistivity and porosity were used in Figure 8-47 where the magnitude agreement is good. For all the measurements the data was reduced using the value of geophone sensitivity derived from geophone "pinging" experiments

As stated when describing the "pinging" experiment, the in-situ sensitivity calculated gives an indication of the actual sensitivity of the geophone. It acts as confirmation that the amplitude measurements are within the accuracy of the "pinging". The difference between the measurement and prediction shown are small enough to be assumed to be errors in geophone sensitivity.

Further example data together with FFLAGS predictions can be found in Appendix F. The data given in the appendix was taken using the loudspeaker at a range of 2.0m and 3.0m and with a source height of 0.68m. The predicted soil properties for this data are shown in Table F-2 and are in agreement with the corresponding values given in Table 8-25.

Example measurements of the acoustic-to-seismic coupling ratio in Soil C, together with the FFLAGS prediction have been given in Figure 8-48 and Figure 8-49. The plots show data taken using the loudspeaker at a range of 2.0m and 3.0m and with a source height of 0.45m. The parameters used to describe the ground in the model have been given in Table 8-26.

It can be seen from Figure 8-48 that a fair agreement has been found between the measured and predicted values of acoustic-to-seismic coupling ratio. However, variations can be seen between the two plots at the higher frequencies. The agreement is less close in Figure 8-49. It can be seen from this data that the major peak at approximately 200Hz is not predicted, with the nearest predicted peak being some 80Hz higher. This result is also seen in Figure F-12, the measurement at 3.0m and a source height of 0.68m

It can be seen from Table 8-26 that for this measurement the coupling resonant frequency of the geophone was 505Hz. This value is approximately 250Hz lower than the value calculated for the measurement taken at a range of 2.0m. As stated previously, the material at the site at the time of the measurements was highly compacted and friable, containing many fissures. It is believed that for the measurements taken at 3.0m that the geophone was positioned in the ground, at the point where a fissure unseen from the surface was located. This may explain the relatively low coupling frequency and the unpredictable major peak in the data.

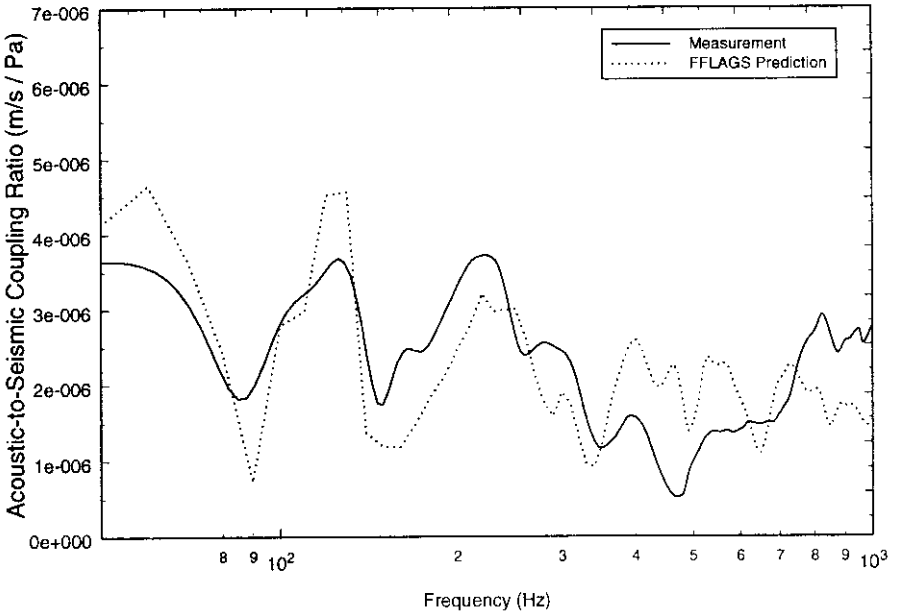

Figure 8-48. Measured acoustic-to-seismic coupling ratio and FFLAGS prediction taken at HRI for Soil C (Range=2.0m, Hs=0.45m and f_0=744Hz).

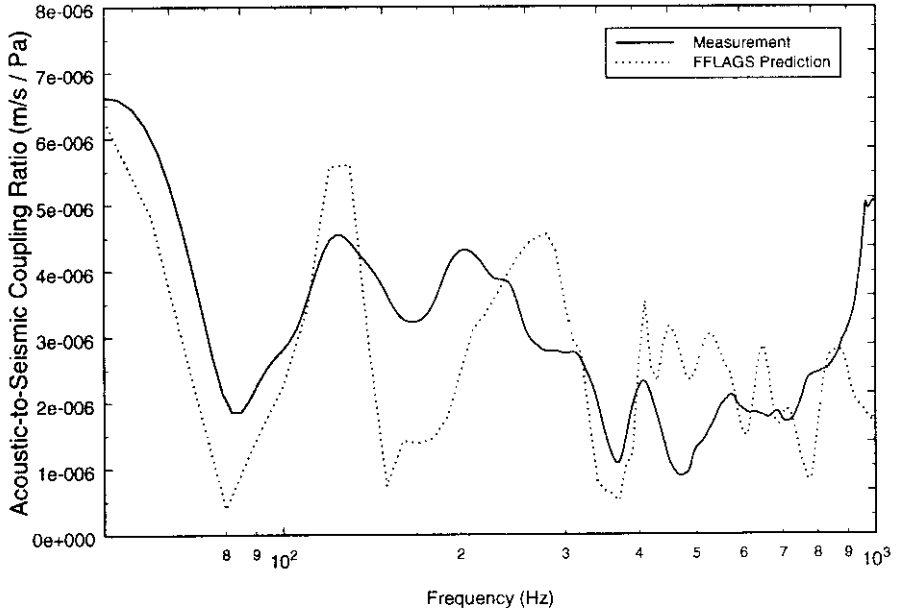

Figure 8-49. Measured acoustic-to-seismic coupling ratio and FFLAGS prediction taken at HRI for Soil C (Range=3.0m, Hs=0.45m and f_0=505Hz).

		Layer 1	Layer 2	Substrate
P-wave speed (m/s)	(R=2.0m)	255.0	390.0	900.0
	(R=3.0m)	245.0	380.0	900.0
S-wave speed (m/s)	(R=2.0m)	140.0	230.0	600.0
	(R=3.0m)	145.0	225.0	600.0
Flow Resistivity ((Pa sm^{-2})	(R=2.0m)	500000	500000	3600000
	(R=3.0m)	500000	500000	3600000
Porosity	(R=2.0m)	0.12	0.12	0.036
	(R=3.0m)	0.12	0.12	0.036
Grain shape factor		0.5	0.5	0.5
Soil density (kg/m^3)		2000	2200	2650
Layer thickness (m)	(R=2.0m)	0.55	1.50	∞
	(R=3.0m)	0.55	1.45	∞
Attenuation (v_p)		0.02	0.02	0.04
Attenuation (v_s)		0.01	0.01	0.02
Dynamic viscosity of air (Nsm^{-2})		$1.81x10^{-5}$		
Microphone height (m)		0.05		
Geophone depth (m)		-0.05		
Frequency range (Hz)		100 – 1000		
Speed of sound in air		344.0		
Coupling Resonant Frequency (Hz)	(R=2.0m)	744		
	(R=3.0m)	505		
Geophone Sensitivity (V / m/s) (measured)	(R=2.0m)	33.0		
	(R=3.0m)	25.6		
Microphone Sensitivity (V / Pa) (measured)	(R=2.0m)	$13.4e^{-3}$		
	(R=3.0m)	$13.4e^{-3}$		

Table 8-26. Parameters used to predict the acoustic-to-seismic coupling ratio measurements taken in Soil C at HRI, Wellesbourne (source height=0.45m and range=2.0m, 3.0m).

The values of wave velocities given in Table 8-26 show good agreement with those values derived using the seismic refraction method, whilst again difference is seen between the depth of the upper layer derived using the two techniques.

Further example data together with FFLAGS predictions can be found in Appendix F. The data given in the appendix was taken using the loudspeaker at a range of 2.0m and 3.0m and with a source height of 0.68m. The predicted soil properties for this data are shown in Table F-2 and are in agreement with the corresponding values given in Table 8-26.

8.3.3 Probe Microphone

Probe microphone measurements were undertaken on each of the three soils at the site. Measurements were taken using the loudspeaker at a grazing angle of 19° and at two positions in order to assess homogeneity.

Analysis of the probe microphone measurements taken at the site showed that the Type-II wave was highly attenuated and did not appear to propagate further than 1-2cm into the ground. This can be observed in Figure 8-50 and Figure 8-51 which show the relative magnitude and phase difference between the probe microphone at various depths and a reference microphone situated at the surface of Soil B.

From Figure 8-50 it can be seen that the magnitude difference between the measurement taken with the probe at 1cm depth to 2cm is relatively small, whereas there is a considerably larger difference in magnitude between 2cm and 3cm depth. This is mirrored in the results for the phase difference shown in Figure 8-51.

The figures show that the change in both magnitude and phase difference increases slightly with frequency between 1cm and 2cm measurements, although the deeper measurements do not appear to follow this behaviour. This suggests that the attenuation and phase velocity increase with increasing frequency but remain constant with depth after approximately 2.0cm. This indicates that down to a depth of approximately 1-2cm the Type II P-wave is predominant. After which, the Type-I wave is dominant.

It appears therefore, that the Type-II wave is the dominant wave down to depth of 1 to 2cm. Since, measurements were taken at these depths is it difficult to analyse the data based upon the assumption of predominance of Type-II wave energy. Also, calculations based on a 1cm depth interval are much more susceptible to errors in probe depth determination, thus increasing the errors in the subsequent calculations.

Similar results were produced for the measurements taken in Soil A and Soil C with the Type-II wave energy dissipating within 1 to 2cm.

These results are comparable to those gained for the loam measured at NCPA and described in Chapter 6. This loam was similar in nature to the in-situ materials found at HRI. It appears that for the materials found at HRI (well compacted and having a high flow resistivity) that the probe microphone technique is not suitable for the determination of flow resistivity and tortuosity.

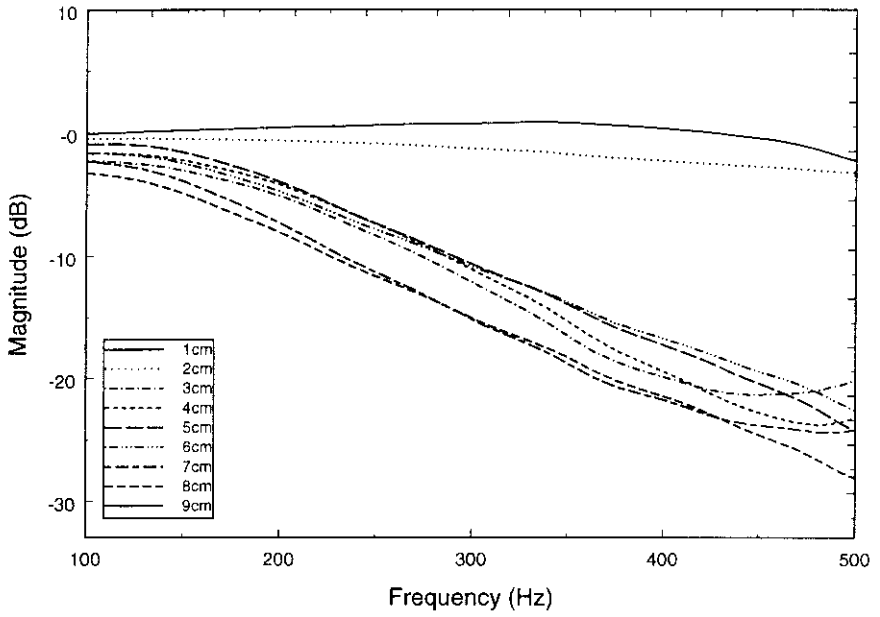

Figure 8-50. Measured relative magnitude between the probe microphone at various depths and a reference microphone situated at the surface of Soil B.

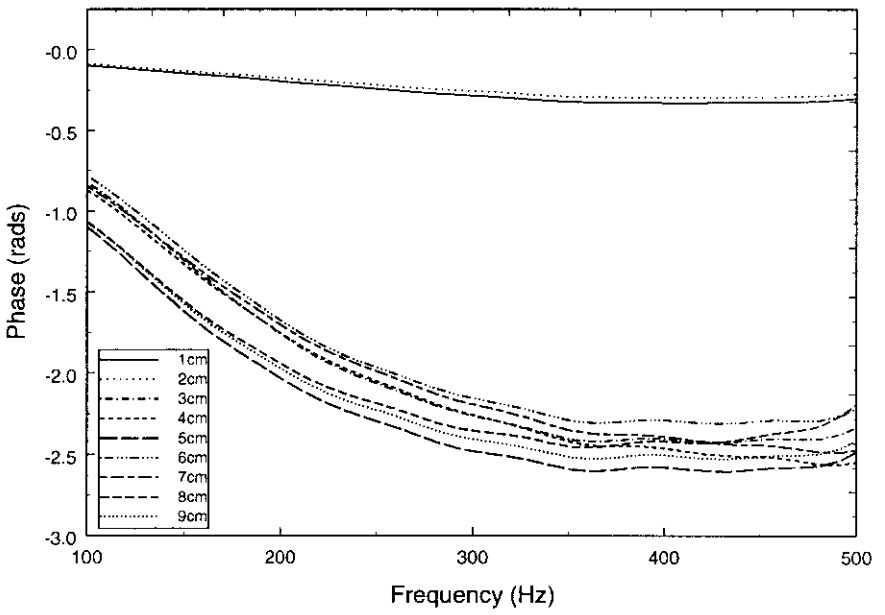

Figure 8-51. Measured phase difference between the probe microphone at various depths and a reference microphone situated at the surface of Soil B.

8.3.4 Acoustically Induced Surface Waves

Initial experiments undertaken at HMC Stone Lane Quarry using co-located vertical and horizontal component geophones showed that the presence of acoustically induced surface waves could be measured. In order to exploit the acoustically-induced surface waves produced a more systematic and detailed investigation was carried out at HRI, Wellesbourne.

Measurements were undertaken on Soil A using the technique outlined in Section 7.3.6 and using the experimental configuration shown in Figure 7-19. The output signal was a pure tone sine wave, which was swept over the range 100Hz to 500Hz in 5Hz steps. Analysis of the data showed that for the majority of frequencies the most dominant wave type was a body wave, and that selective excitation of surface waves was not widespread. The selection of when surface waves were dominant was based upon the shape of the particle orbit. The frequencies at which surface waves were dominant were picked for later analysis.

Figure 8-52 shows the results of the surface wave investigation in which the measured wavelength is plotted against (a) phase velocity and (b) *u/w*. Generally, the longer the wavelength the larger becomes the phase velocity as shown in Figure 8-52a for wavelength longer that 0.30m. In this wavelength range, the Rayleigh wave can be considered to be normally dispersive in which the fundamental mode is generally dominant. However, this trend is reversed for the shortest wavelengths, probably reflecting higher modes of Rayleigh waves. It is known (Tokimatsu *et al.*, 1991), that the presence of stiff layers near the ground surface tend to induce higher modes of Rayleigh waves, which is considered to be the main cause of the above mentioned trend.

Analysis of the particle orbit where the Rayleigh wave is seen to dominate shows that for the majority of wavelengths the particle motion is retrograde (although it can be seen that there are a number of frequencies at which the particle orbit is prograde). This is shown in Figure 8-52b. The difference in the pattern of particle orbits probably reflects small differences in the variation of soil stiffness with depth.

The conversion of the field dispersion curve to a shear modulus-depth relationship was undertaken using the wavelength-depth technique, outlined in Chapter 3. Figure 8-53 shows the calculated shear modulus-depth profile. The depth was determined using the $\lambda / z = 3$ relationship suggested by Gazetas (1982).

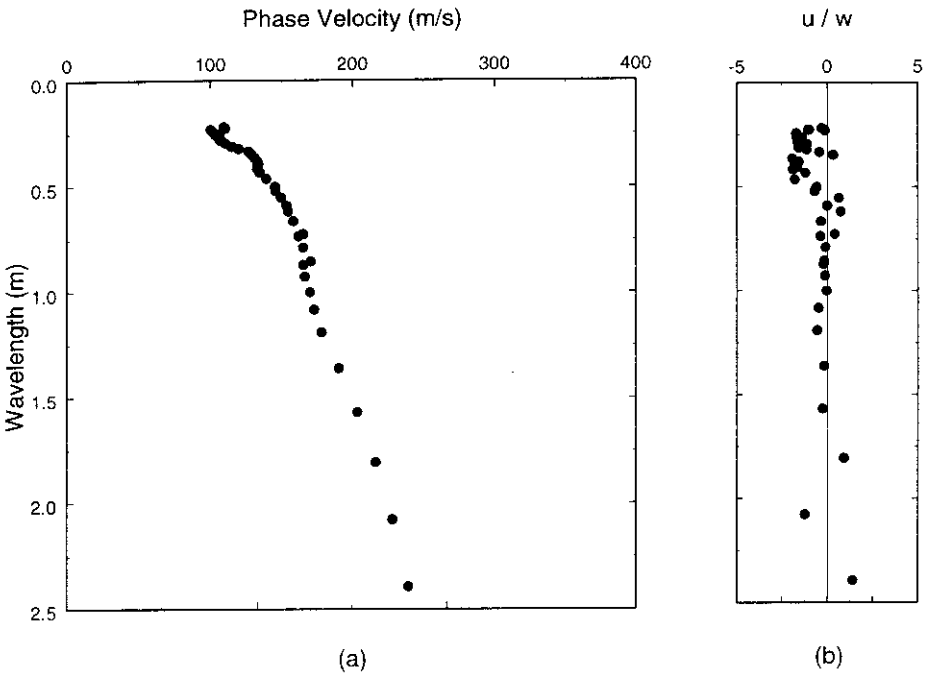

Figure 8-52. Observed dispersion curve and u/w for Soil A.

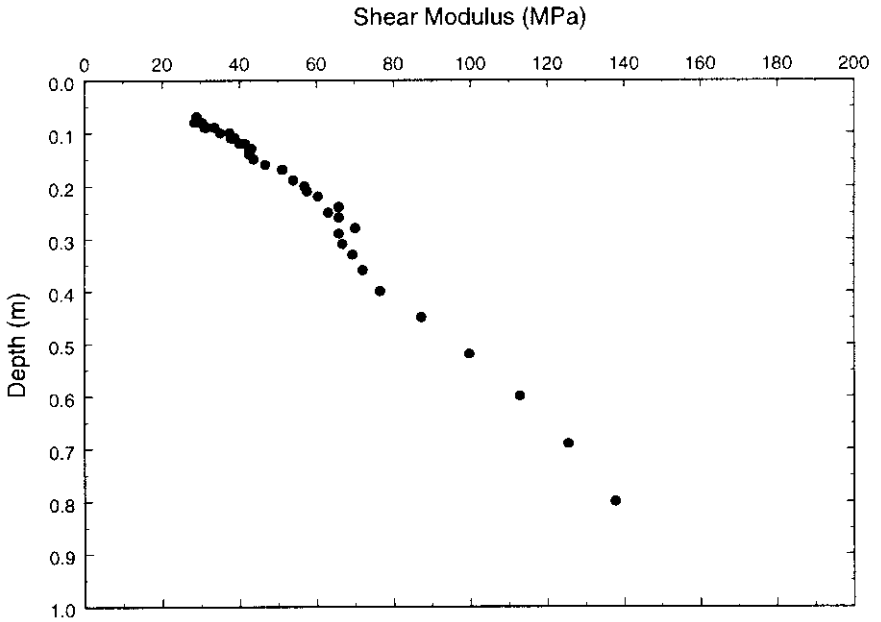

Figure 8-53. Calculated shear modulus-depth profile for Soil A.

It can be seen from the figure that there is a change in the profile close to 0.30m, which may indicate the boundary between the upper and lower soil layers found using the seismic refraction and acoustic-to-seismic coupling ratio measurements

8.3.5 *Conclusions*

Experiments were undertaken at HRI, Wellesbourne, in order to assess the suitability of the measurement techniques and soil deduction algorithms developed for the determination of the bulk properties of near-surface soils.

Experiments consisted of acoustic-to-seismic coupling ratio measurements and probe microphone measurements. As stated previously, at the time of the experiments the soils were extremely well consolidated and extremely friable. It proved exceptionally problematical to obtain undisturbed samples, since once removed the friability of the material meant that it invariably disintegrated. Therefore, obtaining samples for laboratory measurement proved extremely difficult. This meant that standard laboratory tests such as the airflow test to measure flow resistivity could not be carried out, since an adequate test sample could not be extracted.

It was envisaged that this was a situation where the use of a non-invasive method of soil property determination would be extremely useful.

The well compacted nature of the ground, and its consequently high flow resistivity meant that the probe microphone measurement technique proved unsuitable. This was due to the fact that the Type-II Biot wave, which forms the basis of the measurement technique, was highly attenuated and only dominant in the top 1 to 2cm of the soils.

Acoustic-to-seismic coupling ratio measurements, however, produced reasonable results. The well compacted nature of the soils increased the overall bandwidth of the geophones with measured coupling resonant frequencies for the sensors being approximately 700-1000Hz. These values are some 300-400Hz high than those previously seen in the unconsolidated materials found at the ARG test site and at HMC Stone Lane Quarry.

The increased reliable bandwidth of the geophones is reflected in the increased agreement between the measurements and the FFLAGS predictions to the higher frequencies, which improves the accuracy of the predicted values.

From the measurements taken at the site a number of material properties have been determined using acoustic techniques for the three soils. These can be seen in Table 8-27, Table 8-28 and Table 8-29 which give the results for Soil A, Soil B and Soil C respectively. The table also shows parameters measured using standard techniques.

Soil Parameter		Directly Measured	Acoustically Derived
Number of Layers		2	2
Layer Thickness (m)	1	0.20-0.40	0.55
	2	---	2.00
Flow Resistivity (mks rayls)	1	---	450000
	2	---	450000
Porosity (%)	1	0.23	0.23
	2	---	0.23
Bulk Modulus (MPa)	1	---	36.2
	2	---	237.4
Shear Modulus (MPa)	1	6.46	24.2
	2	---	178.7
Soil Density (kg/m^3)	1	2033.6	2000
	2	---	2200

Table 8-27. Soil Properties determined from acoustic-to-seismic coupling experiments undertaken on Soil A at HRI.

Soil Parameter		Directly Measured	Acoustically Derived
Number of Layers		2	2
Layer Thickness (m)	1	0.20-0.40	0.59
	2	---	1.45
Flow Resistivity (mks rayls)	1	---	475000
	2	---	475000
Porosity (%)	1	0.18	0.18
	2	---	0.18
Bulk Modulus (MPa)	1	102.9	77.2
	2	---	188.1
Shear Modulus (MPa)	1	40.8	43.5
	2	---	116.4
Soil Density (kg/m^3)	1	2040.2	2000
	2	---	2200

Table 8-28. Soil Properties determined from acoustic-to-seismic coupling experiments undertaken on Soil B at HRI.

Due to the nature of the ground, few standard tests were able to be undertaken. However, the tables show a good correlation between the values of soil properties deduced from the

acoustic measurements and the values gained from the standard testing procedures that were undertaken.

It can be seen from Table 8-27 and Table 8-29 that the values derived using the resonant column apparatus for shear moduli are approximately a third of the value derived from the acoustic-to-seismic coupling measurements. This is possibly due to the derivation of each value and the reliability of the resonant column data for these two soils.

Soil Parameter		Directly Measured	Acoustically Derived
Number of Layers		2	2
Layer Thickness (m)	1	0.20-0.40	0.55
	2	---	1.50
Flow Resistivity (mks rayls)	1	---	500000
	2	---	500000
Porosity (%)	1	0.12	0.12
	2	---	0.12
Bulk Modulus (MPa)	1	---	68.9
	2	---	170.9
Shear Modulus (MPa)	1	14.94	42.1
	2	---	116.4
Soil Density (kg/m^3)	1	2036.9	2000
	2	---	2200

Table 8-29. Soil Properties determined from acoustic-to-seismic coupling experiments undertaken on Soil C at HRI.

The value derived from the acoustic-to-seismic coupling measurements is based upon the relationship between p- and s-wave velocity and the elastic moduli. The velocities are an average over the whole layer depth of 0.55m, whereas the values derived from the resonant column test have been calculated from the line of best-fit of the plot of moduli against depth. The value given here is based upon a depth of 0.30m (half the layer depth).

It can also be noted from the results of the resonant column test, given in Chapter 4, that for Soil A and Soil C, the bulk modulus could not be calculated, since the measured values of Young's modulus was three times greater than the shear modulus. This discrepancy may be due to errors in the experiment that would produce an incorrect value of shear modulus. It is likely that the errors in the resonant column experiment were due to unseen discontinuities in the test sample.

Comparison of the values of bulk and shear moduli for Soil B determined using the resonant column test and the values determined from the acoustic-to-seismic coupling measurements show a reasonable agreement.

Some differences can be seen between the measured and acoustically deduced layer depths. A comparison of the measured layer depth with the values derived from the seismic refraction survey and the acoustic-to-seismic coupling ratio measurements can be seen in Table 8-30.

Soil	Layer Depth (m)		
	Physical Measurement	Seismic Refraction Survey	Acoustic-to-Seismic Coupling
A	0.20 - 0.40	0.41 - 0.47	0.55 - 0.60
B	0.20 - 0.40	0.35 - 0.45	0.58 – 0.60
C	0.20 - 0.40	0.27 – 0.47	0.55

Table 8-30. A comparison of the measured layer depth with the values derived from the seismic refraction survey and the acoustic-to-seismic coupling ratio measurements.

At the time of construction of the experimental site, it is believed that the three soils were between 0.20 and 0.40m deep (Finch-Savage, *pers. comm.*). Calculations based upon the seismic refraction survey gave the layer depths to be close to these values. However, the values determined from the acoustic-to-seismic coupling measurements indicate that the soils are some 0.10 to 0.15m deeper. Due to the sensitivity of the FFLAGS predictions to the layer depth, it is believed that the variation in layer depth seen must be a physical phenomenon and that the layer depth reported (Finch-Savage, *pers. comm.*) may be in error. However, as the author was not present at the time of construction of the site, this cannot be substantiated.

Since flow resistivity measurements could not be taken on the three soils and the probe microphone measurements did not prove successful, values of flow resistivity used in the predictions were based upon previously published values. The values used however, produced results which suggested that they were probably indicative of the actual values.

The surface wave measurements have shown the difficulty of selective excitation of acoustically induced surface waves. Changes in the input frequency of 10Hz can produce vastly differing particle orbits at the sensors. However, the results show that reasonable results can be gained using the Spectral Analysis of Surface Waves (SASW) method that has been modified for use with an acoustic source.

The results gained for the variation of shear modulus with depth show a tolerable agreement for the results achieved with the resonant column test. Values of shear modulus, calculated using the SASW technique, close to the surface are roughly 20-30MPa. This is a similar value to that derived from the acoustic-to-seismic coupling ratio measurements. Shear modulus calculated from the resonant column test is close to 10MPa at the surface. However, as discussed previously, there is some doubt over the calculated value of the elastic moduli at small effective stresses.

The accuracy in the inversion of the field dispersion curve may be enhanced using more sophisticated techniques than the wavelength-depth method. This can include the use of Haskell-Thompson matrix techniques or finite element approaches.

The advantages of the SASW method over the acoustic-to-seismic coupling determination of the shear modulus-depth profile, is that in the acoustic-to-seismic coupling ratio technique the shear modulus is calculated over the whole of the ground layer, whereas in the SASW method a continuous profile can be gained. The increment of profile is governed by the input signal increment.

The maximum depth of investigation of a Rayleigh wave survey depends on the lowest frequency generated by the source and the stiffness of the ground. The nature of the investigations undertaken as part of this project means that only the upper 2-3m of the ground is of interest. This means that for most materials frequencies of 50Hz and greater are required, well within the range of loudspeakers.

Overall, the site highlighted the advantages and disadvantages of the measurement techniques developed. The site showed the limitations of the probe microphone technique in high flow resistivity, highly compacted materials where the Type-II wave is extremely attenuated.

However, the site did highlight the advantages of non-invasive soil property determination techniques where removal of undisturbed samples of the in-situ material proves difficult. The acoustic-to-seismic coupling measurements proved successful in determining the ground layer structure and the seismic wave velocities, which were subsequently used for the determination of elastic moduli. The measurements also gave reasonable values for the structural properties of the materials, namely the porosity and flow resistivity.

Chapter 9

Conclusions and Recommendations for Further Work

9 Conclusions

An investigation has been made into whether the phenomenon of acoustic-to-seismic coupling can be exploited for the determination of soil properties. Theoretical models have been examined that allow the prediction of acoustically induced ground motion. A number of different experimental techniques based upon the measurements of induced wave types in the ground have been developed which allow the deduction of the bulk properties of near surface sediments.

Although the project concentrated primarily upon the development of experimental techniques from which soil properties could be determined, four models have been examined that can be used for the prediction of acoustically induced ground motion. These ranged from simplistic models based on plane waves and non-porous elastic layer resonances to full-wave propagation in layered porous and elastic solids.

Comparisons with previously published data show that those models based upon full-wave propagation give a more accurate description of the acoustic-to-seismic coupling ratio. Additionally, it has been shown that both full-wave propagation models based either upon elastic porous media or upon elastic media predict the same values of extrema in the coupling spectrum.

The magnitude of the coupling ratio predicted by the porous elastic model has been found to be dependent upon the ground parameters (porosity and flow resistivity) and upon the value of attenuation of the compressional and shear waves. Alteration of the value of attenuation input into either model allows agreement in the magnitude of the coupling ratio between the two models.

It has been concluded that the model based upon poroelastic theory is the more complete model. Using predictions of excess attenuation, it has been shown that the porous elastic theory can be used above rigid porous and elastic grounds as well as porous elastic media. Although the elastic theory can be used to model porous elastic ground, it

obviously cannot be used in rigid porous grounds, as by definition the two are mutually exclusive. Therefore, predictions of acoustically induced ground motion used throughout the project have used poroelastic theory.

Numerical comparisons of predictions of spherical wave and plane wave approximations of the porous elastic model show that close to the air-ground boundary predictions of acoustic-to-seismic coupling ratio are significantly different. The major differences are seen at lower frequencies, below 150Hz, where peaks in the coupling ratio, most likely attributed to the presence of acoustically induced interface waves, are not predicted by the plane wave solution.

Since part of the experimental portion of the project was the measurement of acoustically induced surface waves, the full spherical wave solution of the poroelastic model has been used. This has been achieved through use of the FFLAGS computer program, which is based upon a global matrix Fast Field method.

The poroelastic model of acoustic and seismic wave propagation predicts the existence of two dilatational waves (referred to as Type-I and Type-II P-wave) and one rotational wave, or S-wave. The Type-I P-wave and the S-wave are most sensitive to the macroscopic elastic properties of the frame, such as the bulk and shear moduli. The Type-II wave is most sensitive to the structural properties of the frame, such as the permeability and tortuosity.

Measurements of the three waves predicted by poroelastic theory have been made under laboratory conditions on two artificial soils. A loudspeaker source has been used for the preferential excitation of the Type II P-wave. A specially constructed probe microphone has allowed the measurement of the Type-II wave from which the flow resistivity and tortuosity of the material may be determined using a rigid frame model

However, care must be taken in very high flow resistivity materials where high type-II P-wave attenuations occur and in fine grained materials which may block the holes in the probe end. The probe microphone measurements also showed that there is a need for speaker angle correction to be used in calculating the tortuosity, although no correction is necessary for the calculation of flow resistivity.

Preferential excitement of the Type-I P-wave has been accomplished using a mechanical shaker, whilst deduction of elastic moduli has been made from signals received at buried geophones. Measurements using a loudspeaker source in conjunction with the geophone receivers have shown a reasonable agreement for values of the elastic moduli.

It has also been shown that in a high flow resistivity soil, microphone signals include Type-I P-wave energy and that the acoustically deduced soil properties are consistent with mechanically derived values.

A systematic investigation of outdoors measurement of the acoustic-to-seismic coupling ratio has been made. From the measurements, it has been found that the geophone-ground coupling has a great effect upon the measured coupling ratio. Studies of geophone ground coupling have shown that there is a bandwidth over which the geophone accurately follows the ground motion, whose lower end is the natural frequency of the geophone and whose upper limit is the coupling resonant frequency.

The coupling resonant frequency is independent of the natural frequency of the geophone but has been shown to be dependent upon the compaction of the soil into which the geophone is coupled. In-situ calibration methods have been developed to overcome this problem. Geophone "pinging" allows the determination of the coupling resonant frequency as well as giving an indication of the in-situ sensitivity of the geophone. This sensitivity is required for the conversion of the geophone output to real world units before a comparison of the data with a prediction can be made

In an effort to overcome this problem of sensor coupling with the ground, the use of a Laser Doppler Vibrometer has been proposed to provide a completely non-invasive method of measuring motion in soils. This technique has been previously shown to work in consolidated soils. Measurements in unconsolidated soils have shown that poor specular reflection is achieved, resulting in an inaccurate measurement of the induced ground motion.

A solution to this difficulty has been suggested using small cylinders that can be pushed into the ground. The cylinders used have a density similar to the density of the soil into which they are placed. This appears to reduce the effect of the coupling resonant frequency seen in the geophone sensors. The flat surface of the cylinder can be treated to provide a specularly reflective surface.

Measurements of acoustic-to-seismic coupling ratio have been made in several controlled environments. Through the use of the in-situ geophone calibration technique and prior knowledge of the ground properties, good agreement has been found between the measurements and theoretical predictions, using a modified Biot-Stoll formulation in a global matrix FFP calculation (FFLAGS). The model can be used to predict values of flow resistivity, porosity, bulk and shear moduli and layer depths.

Having developed procedures that exploit acoustic-to-seismic coupling data and models to determine soil properties, an investigation was undertaken to measure the soil properties of well compacted, friable agricultural soils where more standard investigation techniques have proved unsuitable.

The results from the site showed that the acoustic-to-seismic coupling ratio measurements provided reasonable values for the properties of the three soils. The site highlights a disadvantage of the probe microphone technique in that, as the soil was well compacted and had such a high flow resistivity, the Type-II wave energy had attenuated within the top 1 to 2cm.

Acoustically induced surface waves were seen in measurements taken in an unconsolidated sand. A more thorough investigation into the measurement of surface waves was undertaken based upon the Spectral Analysis of Surface Waves. The results gave a shear modulus-depth profile that was comparable with values gained from the resonant column experiment undertaken in the laboratory

The advantages of the SASW method over the acoustic-to-seismic coupling determination of the shear modulus-depth profile, is that in the acoustic-to-seismic coupling ratio technique the shear modulus is calculated over the whole of the ground layer, whereas in the SASW method a continuous profile can be gained. The increment of profile is governed by the input signal increment.

The maximum depth of investigation of a Rayleigh wave survey depends on the lowest frequency generated by the source and the stiffness of the ground. The nature of the investigations undertaken as part of this project means that only the upper 2-3m of the ground is of interest. This means that for most materials frequencies of 50Hz and greater are required, well within the range of loudspeakers.

9.1 Recommendations for Further Work

From this research, there are a number of areas where further investigation must be undertaken if acoustic-to-seismic coupling measurements are to be used as a standard technique for the determination of soil properties.

The study made of the theoretical models highlighted the similarity between the prediction of acoustic-to-seismic coupling ratio made using elastic and poroelastic models.

It appears that the influence of the pores, introduced into the poroelastic theory, does not appear to have as great an impact on the coupling ratio as previously thought.

It would appear therefore that a thorough numerical investigation needs to be made to compare and contrast the two models. Predictions shown in Chapter 2 suggest that the greatest divergence between the two models occurs at short ranges (less than 5m) and with shallow grazing angles. A numerical search should be undertaken to highlight further source and receiver configurations, ground properties and ground layer profiles where the two models diverge.

From the Indoor tank experiments, it is clear that the measurement of the wave attenuation requires further improvement and that the use of the measured attenuation required further theoretical implementation. From the probe microphone measurements it appears that the Vertical Seismic Profiling (VSP) technique used widely in seismic investigations could be modified for use with the probe microphone. The VSP technique is predominantly used in borehole geophysics to assess the ground properties ahead of the drill-bit and to assess the anisotropy of the ground.

Although it has been shown that acoustic-to-seismic coupling ratio measurements can be used with reasonable confidence to determine soil properties, the range of materials tested was limited. It would therefore be necessary to undertake measurements in more typical agricultural soils before the technique could be used in a more widespread manner.

This also applies to the measurements of the acoustically induced surface waves. A more thorough investigation is necessary to distinguish the most effective distances between the loudspeaker and the geophones and between the geophones themselves. Of prime importance to the use of acoustically induced surface waves, is the need for a numerical model for the prediction of surface waves in porous elastic media.

References

Abbiss, C. P. (1981). "Shear wave measurements of the ground." Geotechnique **31**(1): 91-104.

Abramowitz, M. and I. A. Stegun (1970). Handbook of Mathematical Functions. Dover, NY.

Addo, K. and P. K. Robertson (1992). "Shear Wave velocity using Rayleigh waves." Canadian Geotechnical Journal **29**(4): 558-568.

Aki, K. and P. G. Richards (1980). Quantative Seismology: theory and methods. San Francisco, W.N. Freeman & Co.

Albert, D. G. (1993a). Attenuation of outdoor sound propagation levels by a snow cover, US Army Corps of Engineers. Cold Regions Research & Engineering Laboratory.

Albert, D. G. (1993b). "A comparison between wave propagation in water-saturated and air-saturated porous materials." Journal of Applied Physics **73**(1): 28-36.

Albert, D. G. and J. A. Orcutt (1989). "Observations of low-frequency acoustic-to-seismic coupling in the summer and winter." Journal of the Acoustical Society of America **86**(1): 352-359.

Allard, J. F. (1993). Propagation of sound in porous media. London, Elsevier Applied Science.

Alpan, B. (1962). "An experimental method for determining the air permeability of partly saturated soils." Soil Science **94**(4): 263-269.

Altrutz, H. and M. R. Schroeder (1983). A fast Hadamard transform method for the evaluation of measurements using pseudorandom test signals. 11th Congress Acoustics, Paris, France.

Antmann, H. S. (1970). Oblique incidence of coupling of acoustic energy. Phase I: Acoustic propagation through air-earth interface. New York, EDO Corporation.

Archie, G. E. (1942). "The electrical resistivity log as an aid in determining reservoir characteristics." American Institute of Mining and Metallurgic Engineering **146**: 54-62.

Arnott, P. W. and J. M. Sabatier (1990). "Laser doppler vibrometer measurements of acoustic-to-seismic coupling." Applied Acoustics **30**: 279-291.

Asten, M. W. (1977). "Theory and practice of geophone calibration in-situ using a modified step method." IEEE Transactions of Geoscience Electronics **GE-15**(4).

Attenborough, K. (1982). "Acoustical characteristics of porous materials." Physics reports **82**(3): 179-227.

Attenborough, K. (1983). "Acoustical characteristics of rigid fibrous absorbents and granular materials." Journal of the Acoustical Society of America **73**: 785-799.

Attenborough, K. (1985). "Acoustic impedance models for outdoor ground surfaces." Journal of Sound and Vision **99**(4): 521-544.

Attenborough, K. (1986). Acoustic-to-seismic coupling at porous ground surfaces. Ocean Seismo-Acoustics. T. Akal and J. M. Berkson. New York, Plenum.

Attenborough, K. (1987). "On the acoustic slow wave in air filled granular media." Journal of the Acoustical Society of America **81**: 93-102.

Attenborough, K. (1993). "Models for the acoustical properties of air-saturated granular material." Acta Acoustica **1**: 312-226.

Attenborough, K. and Y. Chen (1990). "Surface waves at an interface between air and an air-filled poroelastic ground." Journal of the Acoustical Society of America **87**(3): 1010-1016.

Attenborough, K., J. M. Sabatier, H. E. Bass and L.N. Bolen (1986). "The acoustic transfer function at the surface of a layered poroelastic soil." Journal of the Acoustical Society of America **79**(5): 1353-1358.

Attenborough, K., S. Taherzadeh, H. E. Bass, X. Di, R. Raspet, G. R. Becker, A. Güdesen, A. Chrestman, G. A. Daigle, A. L'Esperance, Y. Gabillet, Y. L. Li, M. J. White, P. Naz, J. M. Noble and H. A. J. M. van Hoof (1995). "Benchmark cases for outdoor sound propagation models." Journal of the Acoustical Society of America **97**(1): 173-191.

Atterburg, A. (1911). "Uber die physikalishe Bodenuntersuchung und uber die plastimitat der tone." Internationale Mitteilurgen fur Bodenkunde **1**: 10-43.

Avery, B. W. and C. L. Bascombe (1982). Soil Survey Laboratory Methods. Soil Survey. Harpenden.

Bardet, J. P. and H. Sayed (1993). "Velocity and attenuation of compressional waves in nearly saturated soils." Soil Dynamics and Earthquake Engineering **12**: 391-401.

Bass, H. E. and L. N. Bolen (1984). Coupling of airborne sound into the earth. Oxford, MS., Physical Acoustics Research Group, University of Mississippi.

Bass, H. E., L. N. Bolen, D. Cress, J. Lundian and M. Flohr (1980). "Coupling of airborne sound into the earth: Frequency dependence." Journal of the Acoustical Society of America **67**(5): 1502-1506.

Beranek, L. L. (1947). "Acoustical properties of homogeneous, isotropic rigid tiles and flexible blankets." Journal of the Acoustical Society of America **19**: 556-568.

Beranek, L. L. (1986). Acoustics. New York, Am. Inst. Physics.

Berryman, J. G. (1980). "Confirmation of Biot's theory." Applied Physics Letters **37**: 382-384.

Berryman, J. G. (1981). "Elastic wave propagation in fluid-saturated porous media." Journal of the Acoustical Society of America **69**: 416-424.

Biot, M. A. (1941). "General theory of three-dimensional consolidation." Journal of Applied Physics **12**: 155-164.

Biot, M. A. (1956a). "Theory of elastic waves in a fluid saturated porous solid. I Low-frequency range." Journal of the Acoustical Society of America **28**: 168-178.

Biot, M. A. (1956b). "Theory of elastic waves in a fluid-saturated porous solid. II High-frequency range." Journal of the Acoustical Society of America **28**: 168-178.

Biot, M. A. (1962a). "Generalised theory of acoustic propagation in porous dissipative media." Journal of the Acoustical Society of America **34**: 1254-1262.

Biot, M. A. (1962b). "Mechanics of deformation and acoustic propagation in porous dissipative media." Journal of Applied Physics **33**: 1482-1498.

Birdsall, T. G. (1995). Signals and signal processing for acoustic monitoring of ocean processess. Proceedings of IEEE International Conference on Acoustics, Speech and Signal Processing, Detroit, MI, USA.

Bogart, B. P., M. J. R. Healy and J. W. Tukey (1963). The quefrency alanysis of time series for echos: Cepstrum, pseudo-autocovariance, cross-cepstrum and sapha cracking. Symposium on time series analysis, New York, Wiley.

Bolen, L. N. and H. E. Bass (1981). "Effects of ground cover on the propagation of sound through the atmosphere." Journal of the Acoustical Society of America **69**: 950-954.

Bolton, J. S. (1984). Cepstral techniques in the measurement of acoustic reflection coefficients, with applications to the determination of acoustic properties of elastic porous materials. *University of Southampton*, UK.

Bolton, J. S. and E. Gold (1984). "The application of cepstral techniques to the measurement of transfer functions and acoustical reflection coefficients." Journal of Sound and Vibration **93**(2): 217-233.

Bouchard, G. and D. B. Bogg (1985). "Experimental measurement of scattered surface waves using a laser doppler technique." Journal of the Acoustical Society of America **77**(3): 1003-1009.

Brandt, H. (1955). "A study of the speed of sound in porous granular media." Journal of Applied Mechanics **22**: 479-486.

Brown, R. J. S. (1980). "Connection between formation factor for electrical and fluid-solid coupling factor in Biot's equations for acoustics wave in fluid-fitted porous media." Geophysics **45**: 152-159.

Brutsaert, W. (1964). "The propagation of elastic waves in unconsolidated unsaturated granular materials." Journal of Geophysical Research **69**(2): 243-257.

Butcher, A. P. and A. S. W. Tam (1994). An example of the use of Rayleigh waves to detect the depth of a shallow landfill. 30th Conference of the Engineering Group of the Geological Society, Modern geophysics in engineering geology, Leige.

Casagrande, A. (1947). "Classification and identification of soils." Proceedings of the American Society of Civil Engineers **73**.

Champoux, Y. and M. R. Stinson (1992). "On acoustical models for sound propagation in rigid frame porous materials and the influence of shape factors." Journal of the Acoustical Society of America **92**(2): 1120-1131.

Childs, E. C. (1969). An introduction to the physical basis of soil water phenomena. London, J. Wiley and Sons Ltd.

Chu, W. T. (1987). A deterministic broad-band signal for acoustical measurements. Internoise 87.

Chu, W. T. (1990). "Impulse-response and reverberation-decay measurements made by using a periodic pseudorandom sequence." Applied Acoustics **29**: 193-205.

Cook, J. C. and J. J. Wormser (1973). "Semi-remote acoustic, electric and thermal sensing of small buried nonmetallic objects." Transactions of IEEE Geoscience Electronics **GE-11**: 135-152.

Crowley, F. A. (1985). Acoustic forecast for shuttle launches at Vandenburg, AFB. AIAA Meeting. Shuttle Environment and Operations II, Houston, Texas.

Crowley, F. A. and J. I. Blaney (1987). Surface disturbances produced by low-level, subsonic aircraft. Weston, Massachusetts, US Air Force Geophysics Laboratory.

Crowley, F. A. and H. A. Ossing (1969). On the application of air-coupled seismic waves, US Air Force Cambridge Research Labs, Mass.

Cruz, V. d. l. and T. J. T. Spanos (1985). "Seismic wave propagation in a porous medium." Geophysics **50**: 1556-1565.

Cruz, V. d. l. and T. J. T. Spanos (1989a). "Seismic boundary conditions for porous media." Journal of Geophysical Research **94**(B3): 3025-29.

Cruz, V. d. l. and T. J. T. Spanos (1989b). "Thermomechnical coupling during seismic wave propagation in a porous medium." Journal of Geophysical Research **94**(B1): 367-442.

Darcy, H. (1856). Les fountaines publiques de la ville de Dijon. Paris.

Delaney, M. E. and E. N. Bazley (1970). "Acoustical properties of fibrous materials." Applied Acoustics **3**: 105-115.

Dutta, N. C. (1980). "Theoretical analysis of observed second bulk compressional wave in a fluid-saturated porous solid at ultrasonic frequencies." Applied Physics Letters **37**: 898-900.

Embleton, T. F. W., J. E. Piercy and N. Olsen. (1976). "Outdoor sound propagation over ground of finite impedence." Journal of the Acoustical Society of America **59**: 267-277.

Espanosa, A. and W. Sierra (1967) "Seismic waves generated by sonic booms: a geoacoustical problem." Journal of the Acoustical Society of America **44**(4): 1074-1081.

Ewing, W. M., W. S. Jardetzky and F. Press (1957). Elastic waves in layered media. New York, McGraw-Hill Book Company.

Eyers, J. E. (1992). Lithostratigraphy of the Lower Greensand and Gault Clay(Lower Cretaceous) of the Bedfordshire Province, England. Department of Earth Sciences. Milton Keynes, Open University.

Fail, J. P., G. Grau and M. Lavergne. (1962). "Couplage de sismographs avec le sol." Geophysical Prospecting **10**: 142-147.

Flohr, M. D. and D. H. Cress (1979). Acoustic-to-seismic coupling: Properties and applications to seismic sensors. Vicksburg, MS., Waterways Experimental Station.

Folk, R. L. and A. A. Ward (1966). "A review of grain-size parameters." Sedimentology **6**: 73-93.

Freeze, R. A. and J. A. Cherry (1979). Groundwater. Englewood Cliffs, N.J., Prentice Hall.

Frenkel, J. (1944). "On the theory of seismic and seismoelectric phenomena in moist soils." Journal of Physics, U.S.S.R. **8**: 230.

Gazetas, G. (1982). "Vibrational characteristics of soil with variable deposits." Journal of numerical analytical methods in geomechanics **6**: 1-20.

Geertsma, J. and D. C. Smit (1961). "Some aspects of elastic wave propagation in fluid-saturated porous solids." Geophysics **26**: 169-181.

Goforth, T. T. and J. A. MacDonald (1970). "A physical interpretation of seismic waves induced by sonic booms." Journal of Geophysical Research **75**: 5087-5092.

Grant, F. S. and G. F. West (1965). Interpretation Theory in Applied Geophysics. New-York, McGraw-Hill.

Greenspan, M. (1959). "Rotational relaxation in nitrogen, oxygen, and air." Journal of the Acoustical Society of America **31**: 155-160.

Griffiths, D. H. and R. F. King (1988). Applied Geophysics for Geologists and Engineers. Oxford, Pergammon Press.

Grover, R. L. (1955). "Simplified air permeameters for soil in place." Soil Science Society of America Proceedings **19**: 414-418.

Harrop, N. D. (1994). An investigation into the rate of regression and instability of the boulder clay cliffs of Porth Neigwl, Gwynedd. School of Ocean Sciences. Bangor, University College of North Wales.

Hastrup, O. F. (1980). Some bottom-reflection loss anomalies near grazing and their effect on propagation in shallow water. Bottom-interacting ocean acoustics.

Heller, L. W. and R. A. Weiss (1967). Ground Transmission from surface sources. Symposium on wave propagation and dynamic properties of earth materials, University of New Mexico.

Heisey, J. S. (1982). Moduli of pavement systems from spectral analysis of surface waves. Washington DC.

Hickey, C. J. (1990). Numerical calculations of seismic wave propagation in porous media, University of Alberta.

Hickey, C. J. and J. M. Sabatier (1996). Determination of bulk elastic properties of soils using acoustic techniques. 2nd Symposium on Agroacoustics, National Centre for Physical Acoustics, Oxford, MS.

Hillel, D. (1982). Introduction to Soil Physics. London, Academic Press.

Hole, L. R., A. M. Kaynia and C. Madhus. (1998). Measurement and simulation of low frequency impulse noise and ground vibration from air blasts.

Hoof, H. V. (1986). Measurements in seismic boxes.

Hoof, H. V. and K. Doorman (1983). Coupling of airborne sound in a sandy soil, Laboratory for electronic developments for the armed forces.

Hoover, G. M. and J. T. O'Brien (1980). "The influence of the planted geophone on seismic land data." Geophysics **45**(8): 1239-1253.

Hovem, J. H. and G. D. Ingram (1979). "Viscous attenuation of sound in sediments." Journal of the Acoustical Society of America **66**(6): 1840.

Hudson, D. E. (1984). Strong motion accelerograph systems - problems and prospects. 8th Conference on Earthquake Engineering II.

Hunt, C. W. and M. Worthington (1999). Seismoelectric downhole survey techniques. Current research in shallow geophysics, BGS, Keyworth, Nottingham, UK.

Inman, D. L. (1952). "Measures for describing the size distribution of sediments." Journal of Sediment Petrology **22**: 125-145.

Institution, B. S. (1981). "Code of practice for site investigations." **BS 5930**.

Institution, B. S. (1990). "Methods of test for soils for civil engineering purposes. General requirements and sample preparation." **BS 1377 (Part 1)**.

Institution, B. S. (1990). "Methods of test for soils for civil engineering purposes. Classification tests. Methods of test for classifying soils and for determining their basic physical properties." **BS 1377 (Part 2)**.

Institution, B. S. (1990). "Methods of test for soils for civil engineering purposes. Chemical and electro-chemical tests. Methods of test for chemical substances." **BS 1377 (Part 3)**.

Institution, B. S. (1990). "Methods of test for soils for civil engineering purposes. Compressibility, permeability and durability tests." **BS 1377 (Part 5)**.

Institution, B. S. (1990). "Methods of test for soils for civil engineering purposes. Consolidation and permeability tests in hydraulic cells and with pore pressure measurement." **BS 1377 (Part 7)**.

Institution, B. S. (1990). "Methods of test for soils for civil engineering purposes. Shear strength tests (effective stress). Methods of test for determining the effective shear strength." **BS 1377 (Part 8)**.

Jardetsky, W. S. and F. Press (1952). "Rayleigh wave coupling to atmospheric compression wave." Bulletin of the Seismological Society of America **42**: 135-144.

Johnson, D. L. and T. J. Plona (1982). "Acoustic slow waves and the consolidation transition." Journal of the Acoustical Society of America **72**(2): 556-565.

Kaimal, J. C. and J. E. Gaynor (1991). "Another look at sonic thermometry." Boundary Layer Meteorology **56**: 401-410.

Kearey, P. and M. Brooks (1992). An Introduction to Geophysical Exploration. Oxford, Blackwell Scientific Publications.

Kirkham, D. (1947). "Field methods of determination of air permeability of soils in its undisturbed state." Soil Science Society of America Proceedings **11**: 93-99.

Kohnke, H. (1968). Soil Physics. New York, McGraw-Hill Book Co.

Krohn, C. E. (1984). "Geophone ground coupling." Geophysics **49**(6): 722-731.

Lamar, A. (1970). "Geophone-ground coupling." Geophysical Prospecting **18**: 300-319.

Leclaire, P. (1994). "Observation of two longitudinal and two transverse waves in a frozen porous medium." Journal of the Acoustical Society of America **97**(4): 2052-2055.

Liu, H. P. and L. Peselnick (1986). "Improved phase-ellipse method for in-situ geophone calibration." Geophysical Prospecting **34**: 537-544.

Loudon, A. G. (1952). "The computation of permeability from simple soil tests." Geotechnique **2**.

Low, A. J. (1954). "Study of soil structure in the field and laboratory." Journal of Soil Science **5**(1): 57-74.

MacArthur, A. (1985). "Geophone frequency calibration and laser verification." Geophysics **50**(1): 49-55.

Martens, M. J. M., L. A. M. v. d. Heijden, H. H. J. Walthaus and W. J. J. M. van Wens (1985). "Classification of soils based on acoustic impedence, air flow resistivity and other physical soil parameters." Journal of the Acoustical Society of America **78**(3): 970-980.

Massey, G. A. (1967). study of vibration measurements by laser methods, NASA.

Matthews, M. C., V. S. Hope and C. R. I. Clayton (1996). "The use of surface waves in the determination of ground stiffness profiles." Proceedings of the Institute of Civil Engineers. Geotechnical Engineering: 84-95.

Matthews, M. C. (1993). Mass compressibility of fractured chalk, University of Surrey.

McCarty, V. M. and I. Dalius (1971). "Frequency shift in air-coupled surface waves originated by a rocket launch." Journal of Geophysical Research **76**: 7027-7034.

Miles, J. W. (1960). "On the response of an elastic half space to a moving blast wave." Journal of Applied Mechanics **27**: 710-716.

Miller, G. F. and H. Pursey (1954). "The field and radiation impedence of mechanical radiators on the free surface of a semi-infinite isotropic solid." Proceedings of the Royal Society (London) **223**: 521-540.

Montcourt, C. (1995). Propagating shocks and moving loads on the ground - Two dimensional theoretical solutions, Norweigan Geotechnical Institute.

Mooney, H. M. and R. A. Kaasa (1962). "Air wave in engineering seismology." Geophysical Prospecting **10**: 84-91.

Moore, H. M. and K. Attenborough (1992). "Acoustic determination of air-filled porosity and relative air permeability of soils." Journal of Soil Science **43**: 211-228.

Nishizawa, O., T. Satoh, X. Lei and Y. Kuwahara (1998). "Detection of shear wave in ultrasonic range by using a laser doppler vibrometer." Review of Scientific Instruments **69**(6).

Nishizawa, O., T. Satoh and X. Lei (1997). "Laboratory studies of seismic wave propagation in homogeneous media using a laser doppler vibrometer." Bulletin of the Seismological Society of America **87**(4): 809-823.

Norris, A. N. (1985). "Low-frequency dispersion and attenuation in partially saturated rocks." Journal of the Acoustical Society of America **77**: 2012-2023.

Ogushwitz, P. R. (1985a). "Application of the Biot theory i) Low porosity materials." Journal of the Acoustical Society of America **77**(2): 429-440.

Ogushwitz, P. R. (1985b). "Application of the Biot theory ii) Suspensions." Journal of the Acoustical Society of America **77**(2): 441-452.

Ogushwitz, P. R. (1985c). "Application of the Biot theory iii) Wave speed versus depth in marine sediments." Journal of the Acoustical Society of America **77**(2): 453-464.

Omata, S. (1983). "Ground couplings and measurement frequency range of vibration transducers." Journal of the Acoustical Society of America **73**(6): 2187-2192.

Peck, L. (1987). Acoustic seismic coupling under winter conditions. 114th meeting of Acoustic Society America.

Plona, T. J. (1980). "Observation of the second bulk dilatational wave in a porous medium at ultrasonic frequencies." Applied Physics Letters **36**: 259-261.

Press, F. and M. Ewing (1951). "Ground roll coupling to atmospheric compressional waves." Geophysics **16**(1-4): 416-430.

Randall, R. B. (1987). Frequency Analysis. Denmark, Brüel and Kjær.

Richart, F. E., J. R. Hall and R. D. Woods (1970). Vibration of soils and foundations. New Jersey, Prentice Hall inc.

Rife, D. and J. Vanderkooy (1989). "Transfer function measurements with maximum length sequences." Journal of Audio Engineering Society **37**: 419-444.

Ringrose-Voase, A. J. (1991). "Micromorphology of soil-structure: description, quantification, application." Austrian Journal of Soil Research **29**: 777-813.

Rosin, G. S. (1973). "Oscillations induced in porous materials with an elastic matrix by sound waves at normal incidence." Soviet Physics-Acoustics **19**: 60-64.

Sabatier, J. M., H. E. Bass, L. M. Bolen and K. Attenborough (1986a). "Acoustically induced seismic waves." Journal of the Acoustical Society of America **80**: 646-649.

Sabatier, J. M., H. E. Bass, L. M. Bolen, K. Attenborough and V. S. S. S. Sastry (1986b). "The interaction of airborne sound with the porous ground: The theoretical formulation." Journal of the Acoustical Society of America **79**: 1345-1352.

Sabatier, J. M., H. E. Bass and G. R. Elliot (1986c). "On the location of frequencies of maximum acoustic-to-seismic coupling." Journal of the Acoustical Society of America **80**(4): 1200-1202.

Sabatier, J. M., H. Hess, W. P. Arnott, K. Attenborough and M. J. M. Rompkins (1990). "In-situ measurements of soil physical properties by acoustical techniques." Soil Science Society of America **54**: 68-72.

Sabatier, J. M., D. C. Sokol, C. K. Frederickson, M. J. M. Rompkins, E. H. Grissinger and J. C. Shipps (1996). "Probe microphone instrumentation for determining soil physical properties: Testing in model porous materials." Soil Technology **8**: 259-274.

Santos, J. E., J. Douglas, J. M. Corbero and O. M. Lovera (1990). "A model for wave propagation in a porous medium saturated by a two-phase fluid." Journal of the Acoustical Society of America **87**(4): 1439-1448.

Schmidt, H. (1986). SAFARI: Seismo-Acoustic Fast Field Algorithm for Range Independent Environments, Users Guide. San Bartolomeo, Italy, SACLANT Undersea Research Centre.

Schmidt, H. (1988). OASES: Ocean Acoustics and Seismic Exploration Synthesis (application and upgrade notes), Massachusetts Institute of Technology.

Schroeder, M. R. (1979). "Integrated-impulse method measuring sound decay without using impulses." Journal of the Acoustical Society of America **66**(2): 497-500.

Sens, P. N., C. Scala and M. H. Cohen (1981). "A self-similar model for sedimentary rocks with application to the dielectric constant of fused glass beads." Geophysics **46**: 781-794.

Shephard-Thorn, E. R., P. M. Harris, D. E. Highley and M. H. Thornton (1986). Outline study of the Lower Greensand of parts of Southern England. Keyworth, Nottingham, UK, British Geological Survey.

Sheriff, R. E. and L.P.Geldert (1982). Exploration Seismology Vol. 1: History, Theory and Data Acquisition. Cambridge, Cambridge University Press.

Siddharthan, R., Z. Zafir and G. Norris (1993). "Moving load response of a layered soil. I: Formulation." Journal of Engineering Mechanics, ASCE **19**: 2052-2071.

Sides, D. J., K. Attenborough and K. A. Mulholland (1971). "Application of a generalised acoustic propagation theory in fibrous absorbents." Journal of Sound and Vibration **19**(1): 49-64.

Smith, G. N. (1994). Elements of Soil Mechanics. Oxford, BSP Professional Books.

Stinson, M. R. (1991). "The propagation of plane sound waves in narrow and wide circular tubes and generalisation to uniform tubes of arbitrary cross-sectional shape." Journal of the Acoustical Society of America **89**(1): 550-558.

Stinson, M. R. and G. A. Daigle (1988). "Electronic system for the measurement of flow resistance." Journal of the Acoustical Society of America **83**(6): 2422-2428.

Stokoe, K. H. and S. Nazauan (1985). Use of Rayleigh waves in liquefaction studies. Measurement and use of shear wave velocity. New York: 1-17.

Stoll, R. D. (1974). Acoustic waves in saturated sediments. Physics of sound in marine sediments. L. Hampton. New York, Plenum.

Stoll, R. D. (1977). "Acoustic waves in ocean sediments." Geophysics **42**: 715-725.

Stoll, R. D. (1980). "Theoretical aspects of sound transmission in sediments." Journal of the Acoustical Society of America **68**(5): 1341-1350.

Stoll, R. D. and G. M. Bryan (1970). "Wave attenuation in saturated sediments." Journal of the Acoustical Society of America **47**: 1440-1447.

Taherzadeh, S. (1997). Sound propagation in inhomogenous media. Engineering Mechanics. Milton Keynes, The Open University.

Telford, W. M., R. E. Sheriff, L. P. Geldert and D. A. Keys (1976). Applied Geophysics. Cambridge, Cambridge University Press.

Tokimatsu, K., S. Kuwayama, S. Tumara and Y. Miyadera (1991). "Vs determination from steady state Rayleigh wave method." Soil and Foundations **31**(2): 153-163.

Tooms, S. (1990). Acoustic propagation near porous and elastic boundaries. Engineering Mechanics. Milton Keynes, The Open University.

Tooms, S. and K. Attenborough (1989). "An acoustic propagation model allowing multiple layered poroelastic ground surface." Proceedings of I.O.A. **11**(5): 223-229.

Tooms, S., S. Taherzadeh and K. Attenborough (1993). "Sound propagating in a refracting fluid above a layered fluid saturated porous elastic material." Journal of the Acoustical Society of America **93**(1): 173-181.

Washburn, H. and H. Wiley (1941). "The effect of the placement of a seismometer on its response characteristics." Geophysics **6**: 116-131.

Whitfield, W. A. D. (1974). "The soils of the National Vegetable Research Station, Wellesbourne." Report of the National Vegetable Research Station for 1973: 21-30.

Whitman, R. L., L. J. Laub and W. J. Bates (1968). "Acoustic surface displacement measurements on a wedge-shaped transducer using an optical probe technique." IEEE Transactions on Sonics and Ultrasonics **SU-15**(3): 186-189.

Wolf, A. (1944). "The equation of motion of a geophone on the surface of an elastic earth." Geophysics **9**: 29-35.

Zwikker, C. and C. W. Kosten (1949). Sound Absorbing Materials. New York, Elsevier.

Appendix A

A Brief Note on the Fundamentals of FFT-Based Signal Analysis and Measurement, with specific relation to Labview.

A Introduction

The Fast Fourier Transform (FFT) and the power spectrum in Labview are powerful tools for analysing and measuring signals from plug-in data acquisition (DAQ) boards. For example, you can effectively acquire time-domain signals, measure the frequency content, and convert the results to real-world units and displays as shown on traditional bench-top spectrum and network analysers. By using plug-in DAQ boards, you can build a lower cost measurement system as well as avoid the communication overhead of working with a stand-alone instrument. Plus, you have the flexibility of configuring your measurement processing to meet your needs.

To perform FFT-based measurement, however, you need to understand the fundamental issues and computations involved. This brief note describes some of the basic signal analysis computations, discusses antialiasing and acquisition front ends for FFT-based signal analysis, explains how to use windows correctly, explains some computations performed on the spectrum, and shows you how to use FFT-based functions for network measurement.

The basic functions in labview for FFT-based signal analysis are the FFT, the Power Spectrum, and the Cross Power Spectrum. Using these functions as building blocks, you can create additional measurement functions such as transfer, impulse response, coherence, amplitude spectrum, and phase spectrum function.

FFTs and the power spectrum are useful for measuring the frequency content of stationary or transient signals. FFTs produce the average frequency content of a signal over the entire time that the signal was acquired. For this reason, you should use FFTs for stationary signal analysis or in cases where you need only the average energy at each frequency line. For measuring frequency information that is changing over time, use joint time-frequency functions such as the Gabor Spectrogram.

This note also describes other issues critical to FFT-based measurement such as the characteristics of your signal acquisition front end, the necessity of using windows, the effect of using windows on your measurement, and measuring noise versus discrete frequency components.

A.1 Basic Signal Analysis Computations

The basic computations for analysing signals include converting from a two-sided power spectrum to a single-sided power spectrum, adjusting frequency resolution and graphing the spectrum, using the FFT, and converting power and amplitude into logarithmic units.

The power spectrum in Labview returns an array containing the two-sided power spectrum of a time-domain signal. The array values are proportional to amplitude squared of each frequency component making up the time-domain signal. A plot of the two-sided power spectrum shows negative and positive frequency components at a height

$$\frac{Ak^2}{4}$$

where A*k* is the peak amplitude of the sinusoidal component at frequency *k*. The DC component has a height of A_0^2 where A_0 is the amplitude of the DC component in the signal.

Figure 1 shows the power spectrum result from a time-domain signal consisting of a 3Vrms sine wave a t 128 Hz, a 3Vrms sine wave at 256Hz, and a DC component of 2 V DC. A 3Vrms sine wave has a peak voltage of 3.0 $\sqrt{2}$ or about 4.2426 V. The power spectrum is computed from the basic FFT function. You will see the exact formula in the Computations Using the FFT section later in this note.

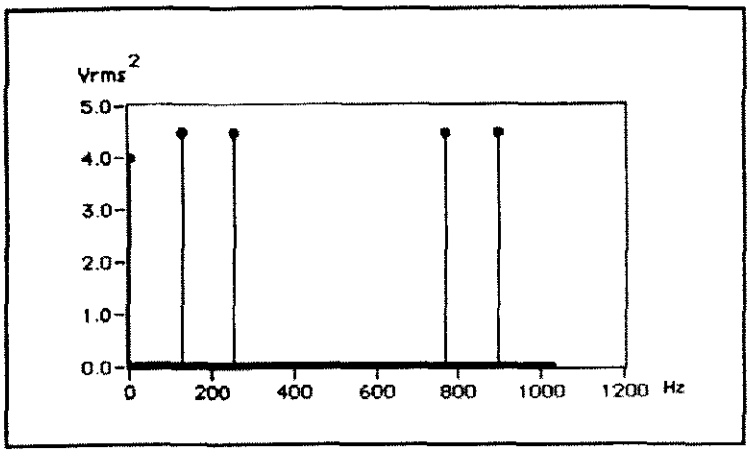

Figure 1. The Two-Sided Power Spectrum of a Signal

A.2 Converting from a Two-Sided Power Spectrum to a Single-Sided Power Spectrum

Most real-world frequency analysis instruments display only the positive half of the frequency spectrum because the spectrum of a real-world signal is symmetrical around DC. Thus, the negative frequency information is redundant. The two-sided results from the analysis functions in Labview, include the positive half of the spectrum followed by the negative half of the spectrum, as shown in Figure 1.

In a two-sided spectrum, for each frequency other than DC, half of the energy is displayed at the positive frequency, and half of the energy is displayed at the negative frequency. Therefore, to convert from a two-sided spectrum to a single-sided spectrum, discard the second half of the array and multiply every frequency point except for DC by two. (This equation assumes that N, the number of points, is even).

$$G_{AA}(i) = S_{AA}(i),\ i = 0\ (DC)$$

$$G_{AA}(i) = 2*S_{AA}(i),\ i = 1 \text{ to } N/2 - 1$$

where $S_{AA}(i)$ is the two-sided power spectrum, $G_{AA}(i)$ is the single-sided power spectrum, and N is the length of the two-sided power spectrum. The remainder of the two-sided power spectrum S_{AA}, (N/2 through N -1),is discarded.

The non-DC values in the single-sided spectrum are then at a height of

$$\frac{A_k^2}{2}$$

This is equivalent to:

$$\left(\frac{A_k}{\sqrt{2}}\right)^2$$

where

$$\frac{A_k}{\sqrt{2}}$$

is the root mean square (rms) amplitude of the sinusoidal component at frequency k. Thus, the units of a power spectrum are often referred to as quantity squared rms, where quantity is the unit of the time-domain signal. For example, the single-sided power spectrum of a voltage waveform will be in volts squared rms.

Figure 2 shows the single-sided spectrum of the signal whose two-sided spectrum is shown in Figure 1.

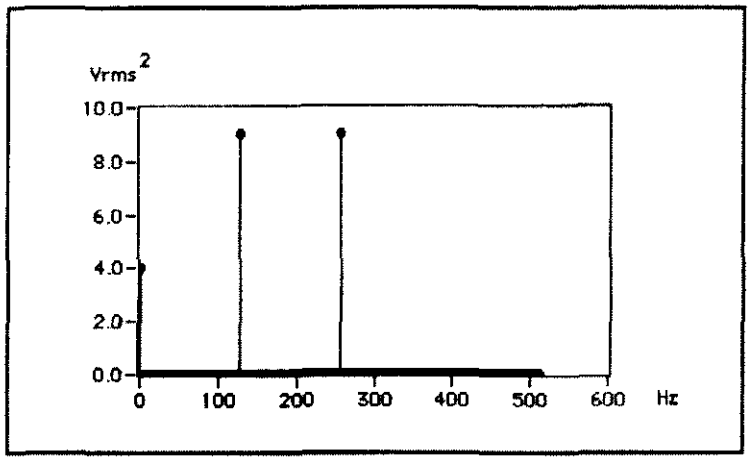

Figure 2. The Single-Sided Power Spectrum of the Signal Shown in Figure 1

A.3 Adjusting Frequency Resolution and Graphing the Spectrum

Figures 1 and 2 show power versus frequency for a time-domain signal. The frequency range and resolution on the x-axis of a spectrum plot depend on the sampling rate and the number of points acquired. The number of frequency points or lines in Figure 2 equals

$$N / 2$$

where N is the number of points in the acquired time-domain signal. The first frequency line is at 0 Hz, that is, DC. The last frequency line is at

$$\frac{Fs}{2} - \frac{Fs}{N}$$

where Fs is the frequency at which the acquired time-domain signal was sampled. The frequency lines occur at Δf intervals where

$$\Delta F = \frac{Fs}{N}$$

Frequency lines can also be referred to as frequency bins or FFT bins because you can think of an FFT as a set of parallel filters of bandwidth Δf centred at each frequency increment from

$$\text{DC to } \frac{Fs}{2} - \frac{Fs}{N}$$

Alternatively you can compute Δf as

$$\Delta f = \frac{1}{N * \Delta t}$$

where Δt is the sampling period. Thus N * Δt is the length of the time record containing the acquired time-domain signal. The signal in Figures 1 and 2 contains 1,024 points sampled at 1.024 kHz, to yield f = 1 Hz, and a frequency range from DC to 511 Hz.

The computations for the frequency axis demonstrate that your sampling frequency determines the frequency range or bandwidth of your spectrum, and that for a given sampling frequency, the number of points acquired in the time-domain signal record determine your resolution frequency. To increase your frequency resolution for a given frequency range, increase the number of points acquired at the same sampling frequency. For example, acquiring 2,048 points at 1.024 kHz would have yielded Δf = 0.5 Hz with

frequency range 0 to 511.5 Hz. Alternatively, if the sampling rate had been 10.24 kHz with 1,024 points, Δf would have been 10 Hz with frequency range from 0 to 5.11 kHz.

A.4 Computations Using the FFT

The power spectrum shows power as the mean squared amplitude at each frequency line, but includes no phase information. Because the power spectrum loses phase information, you may want to use the FFT to view both the frequency and the phase information of a signal.

The phase information the FFT yields is the phase relative to the start of the time-domain signal. For this reason, you must trigger from the same point in the signal to obtain consistent phase readings. A sine wave will show a phase of -90° at the sine wave frequency. A cosine will show a 0° phase. In many cases, your concern is the relative phases between components, or the phase difference between two signals acquired simultaneously. You can view the phase difference between two signals by using some of the advanced FFT functions described in the FFT-Based Network Measurement section of this note.

The FFT in Labview returns a two-sided spectrum in complex form (real and imaginary parts), which you must scale and convert to polar form to obtain magnitude and phase. The frequency axis is identical to that of the two-sided power spectrum. The amplitude of the FFT is related to the number of points in the time-domain signal. Use the following equation to compute the amplitude and phase versus frequency from the FFT.

$$\text{Amplitude spectrum in quantity peak} = \frac{\text{Magnitude[FFT(A)]}}{N}$$

$$= \frac{\left\{[\text{real[FFT(A)]}]^2 + [\text{Imag[FFT(A)]}]^2\right\}^{1/2}}{N}$$

$$\text{Phase spectrum in radians} = \text{Phase[FFT(A)]} = \text{arctangent}\frac{(\text{Imag[FFT(A)]})}{(\text{Real[FFT(A)]})}$$

where arctangent function here returns the value of phase between $-\pi$ and $+\pi$, a full range of 2πradians. Using the rectangular to polar conversion function to convert the complex array.

$$\frac{\text{FFT(A)}}{\text{N}}$$

to its magnitude (r) and phase (ø) is equivalent to using the preceding formulas.

The two-sided amplitude spectrum actually shows half of the peak amplitude at the positive and negative frequencies. To convert to the single-sided form, multiply each frequency other than DC by two, and discard the second half of the array. The units of the single-sided amplitude spectrum are then in quantity peak and give the peak amplitude of each sinusoidal component making up the time-domain signal. For the single-sided phase spectrum, simply discard the second half of the array.

To view the amplitude spectrum in volts (or another quantity) rms, divide the non-DC components by the square root of 2 after converting the spectrum to the single-sided form. Because the non-DC components were multiplied by two to convert from two-sided to single-sided form, you can calculate the rms amplitude spectrum directly from the two-sided amplitude spectrum by multiplying the non-DC components by the square root of two and discarding the second half of the array. The following equations show the entire computation from a two-sided FFT to a single-sided amplitude spectrum.

$$\text{Amplitude spectrum in VMS} = 2^{1/2} * \frac{\text{Magnitude[FFT(A)]}}{N} \quad \text{For i = 1 to (N/2)-1}$$

$$= \frac{\text{Magnitude[FFT(A)]}}{N} \qquad \text{For i = 0(DC)}$$

where i is the frequency line number(index array) of the FFT of A. The magnitude in volts rms gives the rms voltage of each sinusoidal component of the time-domain signal. To view the phase spectrum in degrees, use the following equation.

$$\text{Phase spectrum in degrees} = \frac{180}{\pi} * \text{Phase FFT(A)}$$

The amplitude spectrum is closely related to the power spectrum. You can compute the single-sided power spectrum by squaring the single-sided rms amplitude spectrum. Conversely, you can compute the amplitude spectrum by taking the square root of the

power spectrum. In Labview, the two-sided power spectrum is actually computed from the FFT as follows.

$$\text{Power Spectrum } S_{AA}(f) = \frac{FFT(A) * FFT^{*}(A)}{N}$$

where FFT * (A) denotes the complex conjugate of FFT(A). To form the complex conjugate, the imaginary part of FFT(A) is negated.

Be aware that the speed of the power spectrum and the FFT computation depend on the number of points acquired. If N is a power of 2, Labview uses the efficient FFT algorithm. Otherwise, Labview actually uses the discrete Fourier transform (DFT), which takes considerably longer. Typical bench-top instruments use FFTs of 1,024 and 2,048 points.

So far, you have looked at display units of volts peak, volts rms, and volts rms squared, which is equivalent to mean-square volts. In some spectrum displays, the rms qualifier is dropped for Vrms, in which case V implies Vrms, and V 2 implies Vrms 2, or mean-square volts.

A.5 Converting to Logarithmic Units

Most often, amplitude or power spectrums are shown in the logarithmic unit decibel (dB). Using this unit of measure, it is easy to view wide dynamic ranges; that is, it is easy to see small signal components in the presence of large ones. The decibel is a unit of ratio and is computed as follows.

$$\text{Power in dB} = 10\,\text{Log}_{10}\frac{\text{Measured Power}}{\text{Reference Power}}$$

Use the following equation to compute the ratio in decibels from amplitude values.

$$\text{Amplitude in dB} = 20\,\text{Log}_{10}\frac{\text{Measured Amplitude}}{\text{Reference Amplitude}}$$

When using amplitude or power as the amplitude-squared of the same signal, the resultant decibel level will be exactly the same. Multiplying the decibel ratio by two is equivalent to having a squared ratio. Therefore, you obtain the same decibel level and display regardless of whether you use the amplitude or power spectrum.

As shown in the preceding equations for power and amplitude, you must supply a reference for a measure in decibels. This reference then corresponds to the 0 dB level. Several conventions are used. A common convention is to use the reference 1 Vrms for amplitude or 1 Vrms squared for power, yielding a unit in dBV or dBVrms. In this case, 1 Vrms corresponds to 0 dB. Another common form of dB is dBm, which corresponds to a reference of 1 mW into a load of 50Ω for radio frequencies where 0 dB is 0.22 Vrms, or 600Ω for audio frequencies where 0 dB is 0.78 Vrms.

A.6 Antialiasing and Acquisition Front Ends for FFT-Based Signal Analysis

FFT-based measurement requires digitisation of a continuous signal. According to the Nyquist Criterion, the sampling frequency, Fs , must be at least twice the maximum frequency component in the signal. If this criterion is violated, a phenomenon known as aliasing occurs. Figure 3 shows an adequately sampled signal and an undersampled signal. In the undersampled case, the result is an aliased signal that appears to be at a lower frequency than the actual signal.

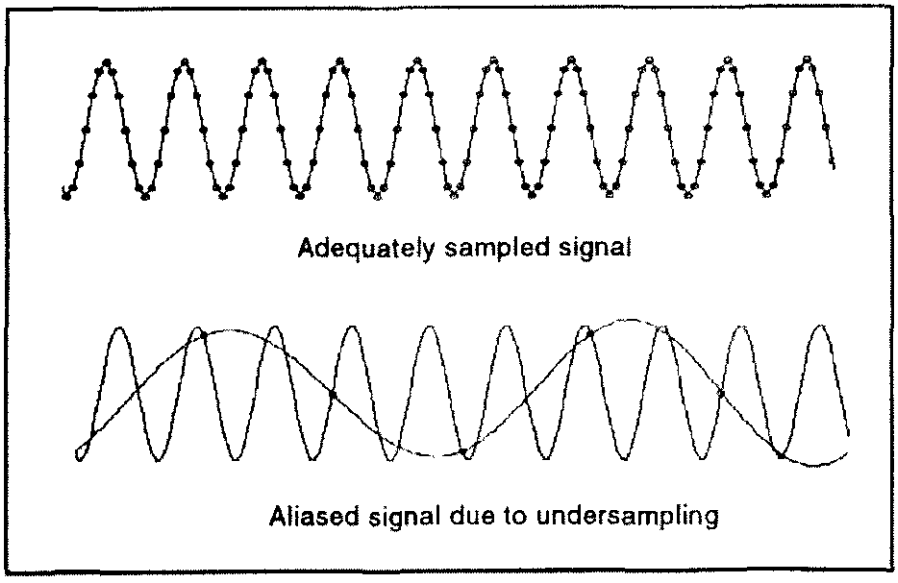

Figure 3. Adequate and Inadequate Signal Sampling

When the Nyquist Criterion is violated, frequency components above half the sampling frequency appear as frequency components below half the sampling frequency.

$F_s/2 < f_0 < F_s$

Appear as the frequency $F_s - f_0$

Figure 4, show the alias frequencies that appear when the signal with real components 25, 70, 160 and 510Hz is sampled at 100Hz. Alias frequencies occur at 10, 30 and 40 Hz.

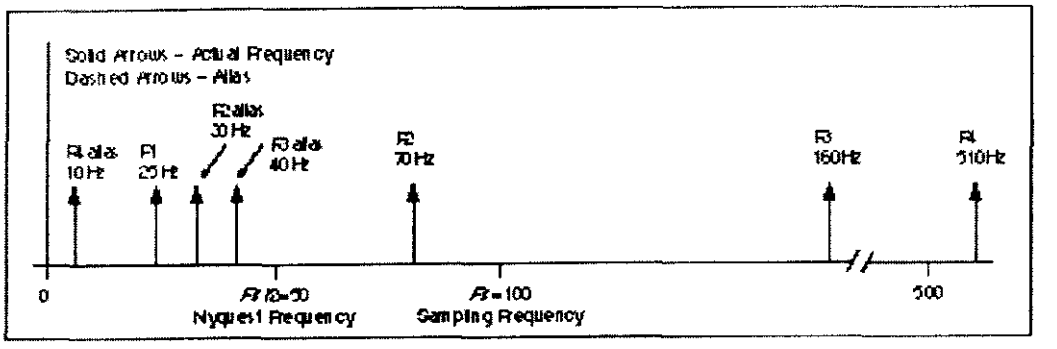

Figure 4. Alias Frequencies Resulting from Sampling a Signal at 100 Hz That Contains Frequency Components Greater than or Equal to 50 Hz

Before a signal is digitised, you can prevent aliasing by using antialiasing filters to attenuate the frequency components at and above half the sampling frequency to a level below the dynamic range of the digitizer (analog-to-digital converter). For example, if the digitizer has a full-scale range of 80dB, frequency components at and above half the sampling frequency must be attenuated to 80dB below full scale.

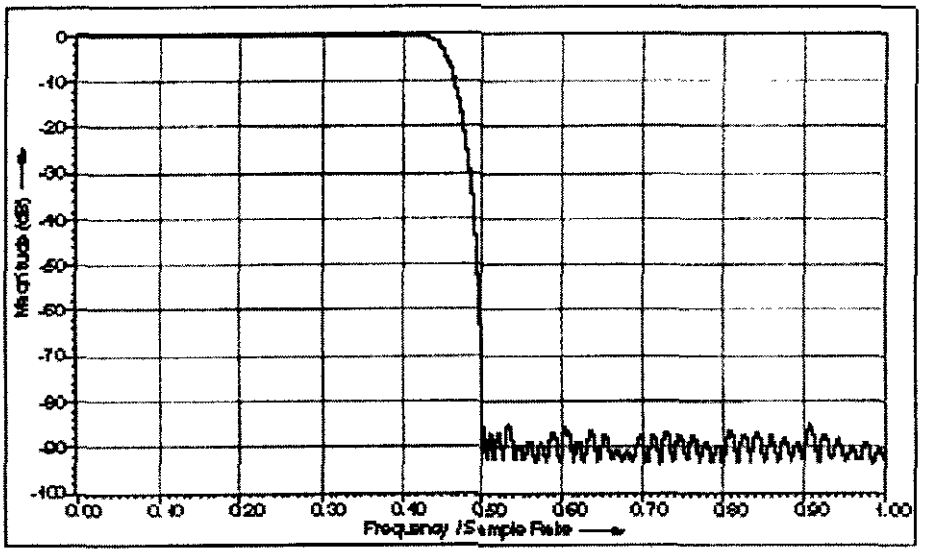

Figure 5. Bandwidth of the AT-A2150 Input Versus Frequency, Normalized to Sampling Rate

These higher frequency components, then, will not interfere with the measurement. If you know that the frequency bandwidth of the signal being measured is lower than half of the sampling frequency, you can choose not to use an antialiasing filter. Figure 5 shows the input bandwidth of the National Instruments AT-A2150 board, which has antialiasing filters, and how an input signal at or above half of the sampling frequency will be severely attenuated.

A.7 Limitations of the Acquisition Front End

In addition to reducing frequency components above half of the sampling frequency, the acquisition front end you are using will introduce some bandwidth limitations below half of the sampling frequency. To eliminate signals at or above half of the sampling rate to less than the measurement range, antialiasing filters start to attenuate frequencies at some point below half the sampling rate. Because these filters attenuate the highest frequency portion of your spectrum, you may want to limit your plot to the bandwidth you consider valid for your measurement.

For example, in the case of the AT-A2150 sample shown in Figure 5, amplitude flatness is maintained to within ± 0.025 dB, at up to 0.416 of the sampling frequency, and then the input gain starts to attenuate. The -3 dB point (or half-power bandwidth) of the input occurs at 0.45 of the input spectrum. Therefore, instead of showing the input spectrum all the way out to half the sampling frequency, you may want to show only 0.416 or 0.45 of the input spectrum. To do this, multiply the number of points acquired by 0.416 or 0.45, respectively, to compute the number of frequency lines to display.

The characteristics of your signal acquisition front end affect your measurement. The National Instruments AT-A2150 board is an excellent acquisition front end for performing FFT-based signal analysis measurements. This board use delta-sigma modulation technology, which yields excellent amplitude flatness, high-performance antialiasing filters, and wide dynamic range as shown in Figure 5. The input channels are also simultaneously sampled for good multichannel measurement performance.

At a sampling frequency of 51.2 kHz, this board can perform frequency measurements in the range of DC to 23 kHz (the -3 dB bandwidth). Amplitude flatness is ±0.025 dB maximum (±0.01 dB typical) from DC to 21.3 kHz. This frequency range excludes the

NB-A2100, which is limited to a 20 kHz ±0.025 dB bandwidth and 21.6 kHz -3dB bandwidth with its maximum sampling rate of 48 kHz.

A.8 Calculating the Measurement Bandwidth or Number of Lines for a Given Sampling Frequency

The AT-A2150 dynamic signal acquisition board has antialiasing filters built into the digitisation process. In addition, the cutoff filter frequency scales with the sampling rate to meet the Nyquist criterion as shown in Figure 5. The very fast cutoff of the antialiasing filters on the board means that the number of useful frequency lines in a 1,024-point FFT-based spectrum is 425 lines for ±0.025 dB amplitude flatness and 460 lines for -3 dB amplitude flatness.

To calculate the measurement bandwidth for a given sampling frequency, multiply the sampling frequency by 0.416 for the ±0.025 dB flatness, and by 0.45 for the -3 dB bandwidth. Also, the larger the FFT, the larger the number of frequency lines. A 2,048-point FFT will yield twice the number of lines listed above. Contrast this with typical benchtop instruments, which have 400 or 800 useful lines for a 1,024- point or 2,048-point FFT, respectively, and a flatness of ±0.025 dB.

A.9 Dynamic Range Specifications

The signal-to-noise ratio (SNR) of the AT-A2150 is 93 dB. SNR is defined as

$$SNR = 10Log_{10}\left(\frac{V_s^2}{V_n^2}\right)dB$$

where V_s and V_n are the rms amplitudes of the signal and noise, respectively. A bandwidth is usually given for SNR. In this case, the bandwidth is the frequency range of the board input, which is related to the sampling rate as shown in Figure 5. The 93 dB SNR means that you can detect the frequency components of a signal that is up to 93 dB below the full-scale range of the board. This is possible because the total input noise level caused by the acquisition front end is 93 dB below the full-scale input range of the board.

If the signal you are monitoring is a narrowband signal (that is, the signal energy is concentrated in a narrow band of frequencies), you will probably be able to detect an even lower level signal than 93 dB. This is possible because the noise energy of the board is spread out over the entire input frequency range. Narrowband versus broadband levels are discussed in the Computing Noise Level and Power Spectral Density section later.

The spurious-free dynamic range of the dynamic signal acquisition board is 85 dB. Besides input noise, the acquisition front end may introduce spurious frequencies into a measured spectrum because of harmonic or intermodulation distortion, among other things. This 85dB level indicates that any such spurious frequencies will be at least 85 dB below the full-scale input range of the board.

The signal to total harmonic distortion (THD) plus noise ratio, which excludes intermodulation distortion, is 90 dB. THD is a measure of the amount of distortion introduced into a signal because of the nonlinear behaviour of the acquisition front end. This harmonic distortion shows up as harmonic energy added to the spectrum for each of the discrete frequency components present in the input signal.

The wide dynamic range specifications of these boards is largely due to the 16-bit resolution A/D converters (ADCs). Figure 6 shows a typical spectrum plot of the AT-A2150 dynamic range with a full-scale 997-Hz signal applied. You can see that the harmonics of the 997-Hz input signal, the noise floor, and any other spurious frequencies are well below 90 dB. In contrast, dynamic range specifications for benchtop instruments typically range from 70 to 80 dB using 12-bit and 13-bit ADC technology.

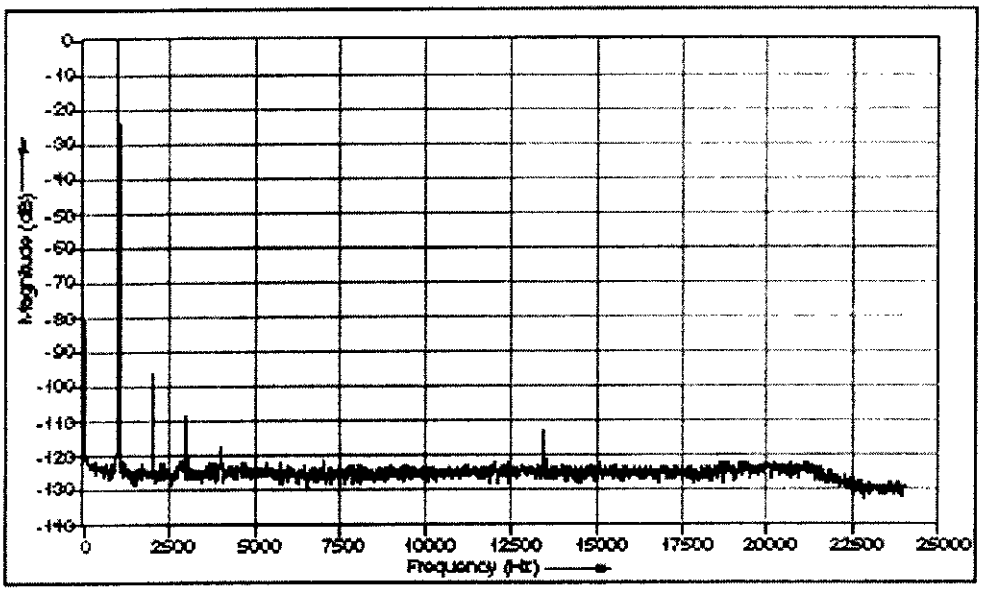

Figure 6. AT-A2150 Spectrum Plot with a 997-Hz Input at Full Scale (Full Scale = 0 dB)

A.10 Using Windows Correctly

As mentioned in the Introduction, using windows correctly is critical to FFT-based measurement. This section describes the problem of spectral leakage, the characteristics of windows, some strategies for choosing windows, and the importance of scaling windows.

A.10.1 Spectral Leakage

For an accurate spectral measurement, it is not sufficient to use proper signal acquisition techniques to have a nicely scaled, single-sided spectrum. You will probably still encounter spectral leakage. Spectral leakage is the result of an assumption in the FFT algorithm that the time record is exactly repeated throughout all time, and that signals contained in a time record are thus periodic at intervals corresponding to the length of the time record. If the time record has a noninteger number of cycles, then this assumption is violated and spectral leakage occurs. Another way of looking at this case is that the noninteger cycle frequency component of the signal does not correspond exactly to one of the spectrum frequency lines.

There are only two cases in which you can guarantee that an integer number of cycles will always be acquired. One case is if you are sampling synchronously with respect to the signal you are measuring and can therefore deliberately take an integral number of cycles.

The second case is if you are capturing a transient signal that fits entirely into your time record. In most cases, however, you are measuring an unknown signal that is stationary; that is, the signal is present before, during, and after the acquisition. In this case, you cannot guarantee that you are sampling an integral number of cycles. Spectral leakage distorts your measurement in such a way that energy from a given frequency component is spread over adjacent frequency lines or bins. You can use windows to minimise the effects of performing an FFT over a nonintegral number of cycles.

Figure 7 shows the effects of three different windows–none (Uniform), Hann, and Flat Top–when an integral number of cycles have been acquired, in this case, 256 cycles in a 1,024-point record. Notice that the windows have a main lobe around the frequency of interest. This main lobe is a frequency domain characteristic of windows. The Uniform window has the narrowest lobe, and the Hann and Flat Top windows introduce some spreading. The Flat Top window has a broader main lobe than the others. For an integral number of cycles, all windows yield the same peak amplitude reading and have excellent amplitude accuracy.

Figure 7 also shows the values at frequency lines of 254 Hz through 258 Hz for each window. The amplitude error at 256 Hz is 0 dB for each window. The graph shows the spectrum values between 240 and 272 Hz. The actual values in the resultant spectrum array for each window at 254 through 258 Hz are shown below the graph. Δf is 1 Hz.

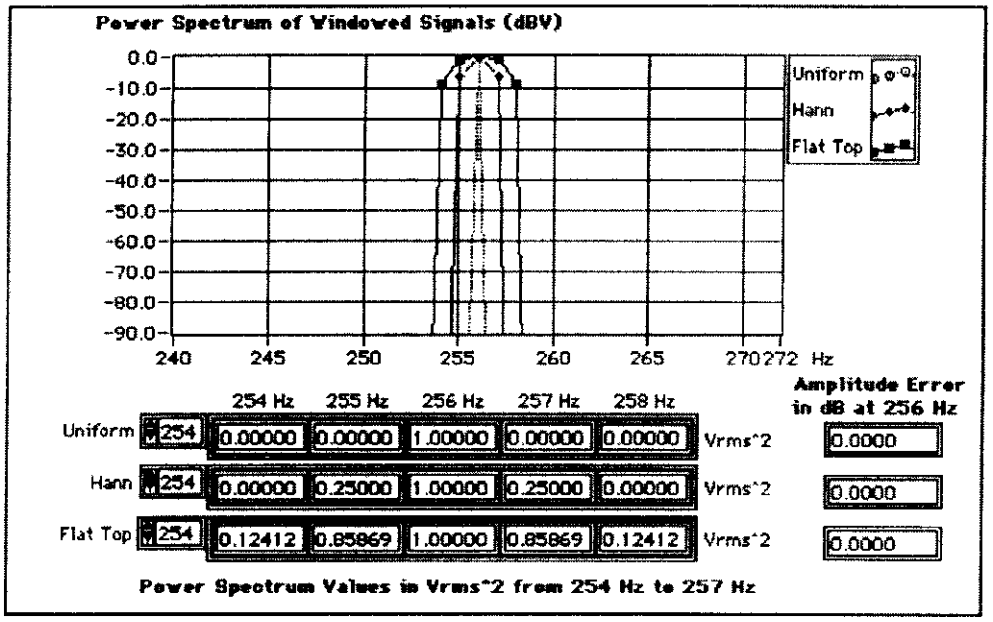

Figure 7. Power Spectrum of a 1 Vrms Signal at 256 Hz with Three Windows–Uniform, Hann, and Flat Top

Figure 8 shows the leakage effects when you acquire 256.5 cycles. Notice that at a nonintegral number of cycles, the Hann and Flat Top windows introduce much less spectral leakage than the Uniform window. Also, the amplitude error is better with the Hann and Flat Top windows. The Flat Top window demonstrates very good amplitude accuracy, but also has a wider spread and higher side lobes than the Hann window. Values at frequency lines of 254 Hz through 258 Hz for each window are shown. The amplitude error in decibels at 256 Hz is also shown for each window.

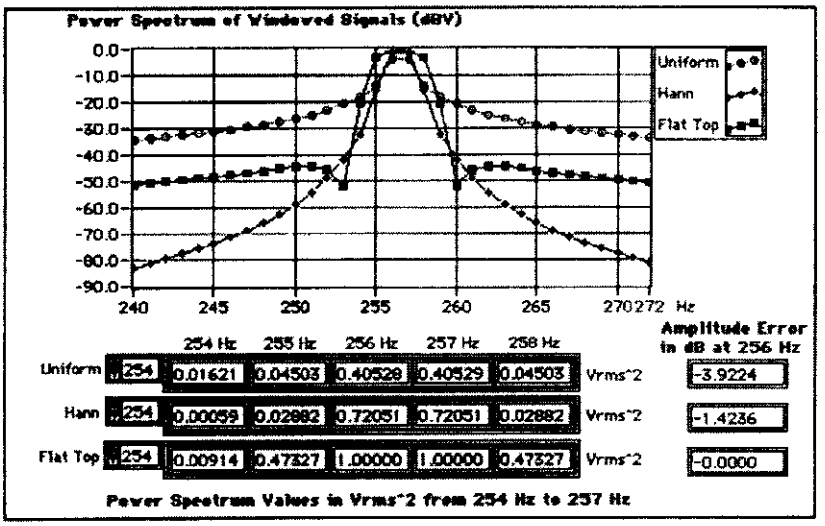

Figure 8. Power Spectrum of a 1 Vrms Signal at 256.5 Hz with Three Windows Uniform, Hann, and Flat Top

In addition to causing amplitude accuracy errors, spectral leakage can obscure adjacent frequency peaks. Figure 9 shows the spectrum for two close frequency components when no window is used and when a Hann window is used.

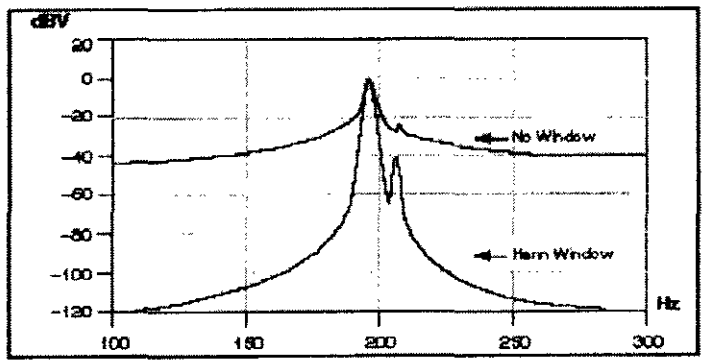

Figure 9. Spectral Leakage Obscuring Adjacent Frequency Components

A.10.2 Window Characteristics

To understand how a given window affects the frequency spectrum, you need to understand more about the frequency characteristics of windows. The windowing of the input data is equivalent to convolving the spectrum of the original signal with the spectrum of the window as shown in Figure 10. Even if you use no window, the signal is convolved with a rectangular-shaped window of uniform height, by the nature of taking a snapshot in time of the input signal. This convolution has a sinc function characteristic spectrum. For this reason, no window is often called the Uniform or Rectangular window because there is still a windowing effect.

An actual plot of a window shows that the frequency characteristic of a window is a continuous spectrum with a main lobe and several side lobes. The main lobe is centred at each frequency component of the time-domain signal, and the side lobes approach zero at

$$\Delta f = \frac{Fs}{N}$$

intervals on either side of the main lobe.

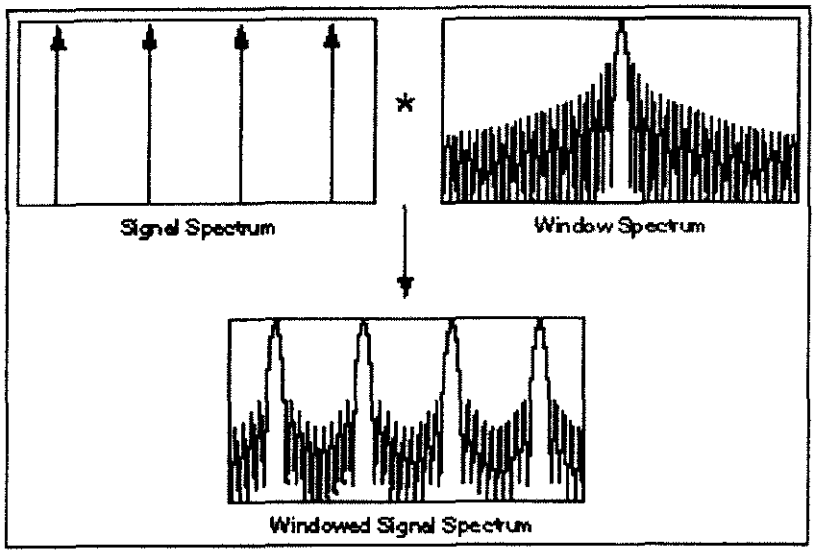

Figure 10. Frequency Characteristics of a Windowed Spectrum

An FFT produces a discrete frequency spectrum. The continuous, periodic frequency spectrum is sampled by the FFT, just as the time-domain signal was sampled by the ADC. What appears in each frequency line of the FFT is the value of the continuous convolved spectrum at each FFT frequency line. This is sometimes referred to as the picket-fence effect, because the FFT result is analogous to viewing the continuous windowed spectrum through a picket fence with slits at intervals corresponding to the frequency lines.

If the frequency components of the original signal match a frequency line exactly, as is the case when you acquire an integral number of cycles, you see only the main lobe of the spectrum. Side lobes do not appear because the spectrum of the window approaches zero at Δf intervals on either side of the main lobe. This case is shown in Figure 7.

If a time record does not contain an integral number of cycles, the continuous spectrum of the window is shifted from the main lobe centre at a fraction of • f corresponding to the difference between the frequency component and the FFT line frequencies. This shift causes the side lobes to appear in the spectrum. In addition, there will be some amplitude error at the frequency peak as shown in Figure 8 because the main lobe is sampled off centre (the spectrum will be smeared).

Figure 11 shows the frequency spectrum characteristics of a window in more detail. The side lobe characteristics of the window directly affect the extent to which adjacent frequency components bias (leak into) adjacent frequency bins. The side lobe response of a

strong sinusoidal signal can overpower the main lobe response of a nearby weak sinusoidal signal.

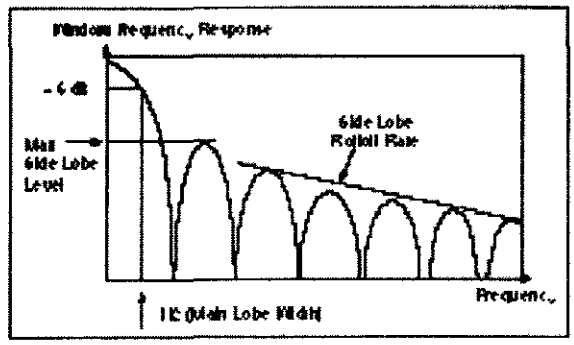

Figure 11. Frequency Response of a Window

Another important characteristic of window spectra is main lobe width. The frequency resolution of the windowed signal is limited by the width of the main lobe of the window spectrum. Therefore, the ability to distinguish two closely spaced frequency components increases as the main lobe of the window narrows. As the main lobe narrows and spectral resolution improves, the window energy spreads into its side lobes, and spectral leakage worsens. In general, then, there is a trade off between leakage suppression and spectral resolution.

A.10.3 Defining Window Characteristics

To simplify choosing a window, you need to define various characteristics so that you can make comparisons between windows. The spectrum of a typical window is shown in Figure 11. To characterise the main lobe shape, the -3 dB and -6 dB main lobe width are defined to be the width of the main lobe (in FFT bins or frequency lines) where the window response becomes 0.707 (-3 dB) and 0.5 (-6 dB), respectively, of the main lobe peak gain.

To characterise the side lobes of the window, the maximum side lobe level and side lobe roll-off rate are defined. The maximum side lobe level is the level in decibels relative to the main lobe peak gain, of the maximum side lobe. The side lobe rolloff rate is the

asymptotic decay rate, in decibels per decade of frequency, of the peaks of the side lobes. Table 1 lists the characteristics of several window functions and their effects on spectral leakage and resolution.

Window	-3dB Main Lode width (bins)	-6dB Main Lode width (bins)	Maximum Side Lobe Level(dB)	Side Lobe Rolloff rate (dB/decade)
Uniform	0.88	1.21	-13	20
Hanning	1.44	2.00	-32	60
Hamming	1.30	1.81	-43	20
Blackman-Harris	1.66	1.81	-71	20
Exact Blackman	1.52	2.13	-67	20
Blackman	1.68	2.35	-58	60
Flat Top	2.94	3.56	-44	20

*Table A-1. **Characteristics of Window Functions***

A.10.4 Strategies for Choosing Windows

Each window has its own characteristics, and different windows are used for different applications. To choose a spectral window, you must guess the signal frequency content. If the signal contains strong interfering frequency components distant from the frequency of interest, choose a window with a high side lobe roll-off rate. If there are strong interfering signals near the frequency of interest, choose a window with a low maximum side lobe level.

If the frequency of interest contains two or more signals very near to each other, spectral resolution is important. In this case, it is best to choose a window with a very narrow main lobe. If the amplitude accuracy of a single frequency component is more important than the exact location of the component in a given frequency bin, choose a window with a wide main lobe. If the signal spectrum is rather flat or broadband in frequency content, then use the Uniform window (no window). In general, the Hann window is satisfactory in 95% of cases. It has good frequency resolution as well as reduced spectral leakage.

The Flat Top window has good amplitude accuracy, but because it has a wide main lobe, it has poor frequency resolution and more spectral leakage. The Flat Top window has a lower maximum side lobe level than the Hann window, but the Hann window has a faster roll off-rate. If you do not know the nature of the signal but you want to apply a window, start with the Hann window. Figures 7 and 8 contrast the characteristics of the Hann, Flat Top, and Uniform windows.

If you are analysing transient signals such as impact and response signals, it is better not to use the spectral windows because these windows attenuate important information at the beginning of the sample block. Instead, use the Force and Exponential windows. A Force window is useful in analysing shock stimuli because it removes stray signals at the end of the signal. The Exponential window is useful for analysing transient response signals because it dampens the end of the signal, ensuring that the signal fully decays by the end of the sample block.

Selecting a window function is not a simple task. In fact, there is no universal approach for doing so. However, Table 2 can help you in your initial choice. Always compare the performance of different window functions to find the best one for your application. You can find more information about windows in the references at the end of this note.

A.10.5 Signal Content	**Window**
Sine wave or combination of sine waves	Hanning
Sine wave(amplitude accuracy is important)	Flat Top
Narrow-band random signal(vibration data)	Hanning
Broad-band random(white noise)	Uniform
Closely spaced sine waves	Uniform, Hamming
Excitation signals(Hammer blows)	Force
Response signals	Exponential
Unknown content	Hann

Table A-2. ***Initial Window Choice based on signal content***

A.10.6 Scaling Windows

Windows are useful in reducing spectral leakage when using the FFT for spectral analysis. However, because windows are multiplied with the acquired time-domain signal, they introduce distortion effects of their own. The windows in the Labview analysis libraries change the overall amplitude of the signal. The windows used to produce the plots in

Figures 7 and 8 were scaled by dividing the windowed array by the coherent gain of the window. As a result, each window yields the same spectrum amplitude result within its accuracy constraints.

You can think of an FFT as a set of parallel filters, each • f in bandwidth. Because of the spreading effect of a window, each window increases the effective bandwidth of an FFT bin by an amount known as the equivalent noise-power bandwidth of the window. The power of a given frequency peak is computed by adding the adjacent frequency bins around a peak, and will be inflated by the bandwidth of the window. You must take this inflation into account when you perform computations based on the spectrum. Some sample computations are presented in the next section, Computations on the Spectrum.

The scaling factor (or coherent gain), the noise power bandwidth, and the worst-case peak amplitude accuracy caused by off-centre components are listed for several popular windows in Table 3.

Window	Scaling Factor (coherent gain)	Noise Power Bandwidth	Worst-case Amplitude error (dB)
Uniform	1.00	1.0	3.92
Hanning	0.50	1.50	1.42
Hamming	0.54	1.36	1.78
Blackman-Harris	0.42	1.71	1.13
Blackman	0.43	1.73	1.10
Flat Top	0.28	2.97	<0.01

*Table A-3. **Correction factors and worst-case amplitude errors for Windows***

A.11 Computations on the Spectrum

When you have the amplitude or power spectrum, you can compute several useful characteristics of your input signal such as power and frequency, noise level, and power spectral density.

A.11.1 Estimating Power and Frequency

The preceding windowing examples demonstrate that if you have a frequency component in between two frequency lines, it will appear as energy spread among adjacent frequency lines with reduced amplitude. The actual peak is between the two frequency lines. In Figure 8, the amplitude error at 256.5 Hz is due to the fact that the window is sampled at ±0.5 Hz around the centre of its main lobe, rather than at the centre where the amplitude error would be 0. This is the picket-fence effect explained previously in the Window Characteristics section.

You can estimate the actual frequency of a discrete frequency component to a greater resolution than the Δf given by the FFT by performing a weighted average of the frequencies around a detected peak in the power spectrum.

$$\text{Estimated Frequency} = \frac{\sum_{i=j-3}^{j+3}\left(Power(i)\times i\times \Delta f\right)}{\sum_{i=j-3}^{j+3}\left(Power(i)\right)}$$

where j is the array index of the apparent peak of the frequency of interest, and

$$\Delta f = \frac{Fs}{N}$$

The span j ±3 is reasonable, because it represents a spread wider than the main lobes of the windows listed in Table 3.

Similarly, you can estimate the power in $Vrms^2$ of a given peak discrete frequency component by summing the power in the bins around the peak (computing the area under the peak)

$$\text{Estimated Power} = \frac{\sum_{i=j-3}^{j+3}\left(Power(i)\right)}{\text{noise power bandwidth of window}}$$

Notice that this method is valid only for a spectrum made up of discrete frequency components. It is not valid for a continuous spectrum. Also, if two or more frequency peaks are within six lines of each other, they will contribute to inflating the estimated powers and skewing the actual frequencies. You can reduce this effect by decreasing the number of lines spanned by the preceding computations. If two peaks are that close, they are probably already interfering with one another because of spectral leakage.

Similarly, if you want the total power in a given frequency range, sum the power in each bin that composes the frequency range and divide by the noise power bandwidth of the windows.

A.11.2 Computing Noise Level and Power Spectral Density

The measurement of noise levels depends on the bandwidth of the measurement. When looking at the noise floor of a power spectrum, you are looking at the narrow-band noise level in each FFT bin. Thus the noise floor of a given power spectrum depends on the Δf of the spectrum, which is in turn controlled by the sampling rate and number of points. In other words, the noise level at each frequency line reads as if it were measured through a Δf Hz filter centred at that frequency line. Therefore, for a given sampling rate, doubling the number of points acquired will reduce the noise power appearing in each bin by 3 dB. Discrete frequency components theoretically have zero bandwidth and therefore do not scale with the number of points or frequency range of the FFT.

To compute the SNR, compare the peak power in the frequencies of interest to the broadband noise level. Compute the broadband noise level in $Vrms^2$ by summing all of the power spectrum bins, excluding any peaks and the DC component, and dividing the sum by the equivalent noise bandwidth of the window. For example, in Figure 6 the noise floor appears to be more than 120 dB below full scale, even though the AT-A2150 dynamic range is only 93 dB. If you were to sum all the bins excluding DC, and any harmonic or other peak components, and divide by the noise power bandwidth of the window you used, the noise power level compared to full scale would be around -93 dB from full scale.

Because of noise-level scaling with Δf, spectra for noise measurement are often displayed in a normalised format called power or amplitude spectral density. This normalises the power or amplitude spectrum to the spectrum that would be measured by a 1-Hz-wide square filter, a convention for noise-level measurements. The level at each frequency line then reads as if it were measured through a 1-Hz filter centred at that frequency line. Power spectral density is computed as:

$$\text{Power Spectral Density} = \frac{\text{Power Spectrum (in Vrms}^2\text{)}}{\Delta f \times \text{noise power bandwidth of window}}$$

The units are then in $\frac{Vrms^2}{Hz}$ or $\frac{Volts^2}{Hz}$

Amplitude spectral density is computed as:

$$\text{Amplitude spectral density} = \frac{\text{Amplitude Spectrum (in Vrms)}}{(\Delta f \times \text{noise power bandwidth of window})^{1/2}}$$

The units are then in Vrms per root Hz or Volts per root Hz.

The Spectral density format is appropriate for random or noise signals, but inappropriate for discrete frequency components because the latter theoretically have zero bandwidth.

A.12 FFT-Based Network Measurement

When you understand how to handle computations with the FFT and power spectrums, and you understand the influence of windows on your spectrum, you can compute several FFT-based functions that are extremely useful for network analysis. These include the transfer, impulse, and coherence functions, which are discussed in the Frequency Response and Network Analysis section of this note. Chirp signals and broadband noise signals are discussed in the Signal Sources for Frequency Response Measurement section.

A.12.1 The Cross Power Spectrum

One additional building block in Labview is the cross power spectrum. The cross power spectrum is not typically used as a direct measurement, but is an important building block for other measurements.

The two-sided cross power spectrum of two time-domain signals A and B is computed as:

$$\text{Cross Power Spectrum } S_{AB}(f) = \frac{\text{FFT(B)} \times \text{FFT}^*(A)}{N^2}$$

The cross power spectrum is in two-sided complex form. To convert to magnitude and phase, use the rectangular-to- polar conversion functions in Labview. To convert to a single-sided form, use the same method as in converting the power spectrum to a single-sided form shown in the Converting from a Two-Sided Power Spectrum to a Single-Sided

Power Spectrum section of this note. The units of the single-sided form are in volts (or other quantity) rms squared.

The power spectrum is equivalent to the cross power spectrum when signals A and B are the same signal. Therefore, the power spectrum is often referred to as the auto power spectrum or the auto spectrum. The single-sided cross power spectrum yields the product of the rms amplitudes of the two signals, A and B, and the phase difference between the two signals.

When you know how to use these basic blocks, you can compute other useful functions.

A.12.2 Frequency Response and Network Analysis

Three useful functions for characterising the frequency response of a network are the transfer, impulse response, and coherence functions.

The frequency response of a network is measured by applying a stimulus to the network as shown in Figure 12 and computing the transfer function from the stimulus and response signals.

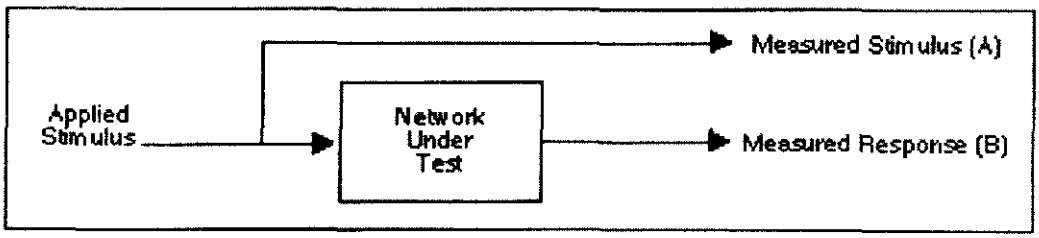

Figure 12. Configuration for Network Analysis

A.12.3 The Transfer Function

The transfer function gives the gain and phase versus frequency of a network, and is typically computed as

$$\text{Transfer Function H(f)} = \frac{\text{Cross Power Spectrum (Stimulus, Repsonse)}}{\text{Power Spectrum (Stimulus)}} = \frac{S_{AB}(f)}{S_{AA}(f)}$$

where A is the stimulus signal and B is the response signal.

The transfer function is in two-sided complex form. To convert to the frequency response gain (magnitude) and the frequency response phase, use the rectangular-to-polar conversion function. To convert to single-sided form, simply discard the second half of the array.

You may want to take several transfer function readings and then average them. To do so, average the cross power spectrum, $S_{AB}(f)$, by summing it in the complex form, then dividing by the number of averages, before converting it to magnitude and phase, and so forth. The power spectrum, $S_{AA}(f)$, is already in real form and is averaged normally.

A.12.4 The Impulse Response Function

The impulse response function of a network is the time-domain representation of the transfer function of the network. It is the output time-domain signal generated when an impulse is applied to the input at time t = 0.

To compute the impulse response of the network, take the inverse FFT of the two-sided complete transfer function given previously in The Transfer Function section.

$$\text{Impulse Response (f)} = \text{Inverse FFT (Transfer Function H(f))} = \text{Inverse FFT}\left(\frac{S_{AB}(f)}{S_{AA}(f)}\right)$$

The result is a time-domain function. To average multiple readings, take the inverse FFT of the averaged transfer function.

A.12.5 The Coherence Function

The coherence function is often used in conjunction with the transfer function as an indication of the quality of the transfer function measurement and indicates how much of the response energy is correlated to the stimulus energy. If there is some other signal

present in the response, either from excessive noise or from some other signal, the quality of the network response measurement will be poor. You can use the coherence function to identify both excessive noise and causality, that is, identify which of the multiple signal sources are contributing to the response signal. The Coherence Function is computed as:

$$\text{Coherence Function (f)} = \frac{[\text{Magnitude}(\text{Average } S_{AB}(f)]^2}{\text{Average } S_{AA}(f) - \text{Averaged } S_{BB}(f)}$$

The result is a value between zero and one versus frequency. A zero for a given frequency line indicates no correlation between the response and the stimulus signal. A one for a given frequency line indicates that the response energy is 100% due to the stimulus signal; in other words, there is no interference at that frequency.

For a valid result, the coherence function requires an average of two or more readings of the stimulus and response signals. For only one reading, it will register unity at all frequencies. To average the cross power spectrum, $S_{AB}(f)$, average it in the complex form, then convert to magnitude and phase as was described for the transfer function. The auto power spectra, $S_{AA}(f)$and $S_{BB}(f)$, are already in real form and you average them normally.

A.13 Signal Sources for Frequency Response Measurements

To achieve a good frequency response measurement, significant stimulus energy must be present in the frequency range of interest. Two common signals used are the chirp signal and a broadband noise signal. The chirp signal is a sinusoid swept from a start frequency to a stop frequency, thus generating energy across a given frequency range. White and pseudo-random noise have flat broadband frequency spectra–that is, energy is present at all frequencies.

It is best not to use windows when analysing frequency response signals. If you are generating a chirp stimulus signal at the same rate you are acquiring the response, you can match your acquisition frame size to match the length of the chirp. No window is generally the best choice for a broadband signal source. Because some stimulus signals are not constant in frequency across the time record, applying a window may obscure important portions of your transient response.

A.14 Conclusion

There are many issues to consider when analysing and measuring signals from plug-in DAQ boards. Unfortunately, it is easy to make incorrect spectral measurements. Understanding the basic computations involved in FFT-based measurement, knowing how to prevent antialiasing, properly scaling and converting to different units, being able to choose and use windows correctly, and learning how to use FFT-based functions for network measurement are all critical to the success of your analysis and measurement tasks. Being equipped with this knowledge and being able to use the tools discussed in this application note will bring you more success with your individual application.

Appendix B

Soil Properties

B Contents

Appendix B covers the results from the laboratory tests undertaken on the materials used through the project. It includes:

1) ARG Test Site
    i) Constant head permeameter
    ii) Particle size distribution
    iii) Flow Resistivity
2) OU Indoor Tank
    i) Constant head permeameter
    ii) Particle size distribution
    iii) Shear Box
    iv) Flow resistivity
    v) Resonant Column
3) HMC Stone Lane Quarry
    i) Constant head permeameter
    ii) Particle size distribution
    iii) Shear Box
    iv) Flow resistivity
    v) Resonant Column
4) NCPA Indoor Tank
    i) Flow Resistivity
5) HRI, Wellesbourne
    a) Soil A
        i) Falling head permeameter
        ii) Particle size distribution

iii) Shear Box

iv) Resonant column

b) Soil B

i) Falling head permeameter

ii) Particle size distribution

iii) Shear Box

iv) Resonant column

c) Soil C

i) Falling head permeameter

ii) Particle size distribution

iii) Shear Box

iv) Resonant column

Constant Head Permeameter

DIAMETER OF SAMPLE			8.89 cms.
CROSS SECTIONAL AREA			62.072 $cms.^2$
OVERALL LENGTH OF SAMPLE BETWEEN TOP & BOTTOM NIPPLE POINTS			20.00 cms.
LENGTH BETWEEN ANY TWO NIPPLE POINTS			10.00 cms.
TEST 1			
MANOMETER READINGS			
BOTTOM 23.3	MIDDLE 23.40		TOP 23.50
DIFF. IN HEAD BETWEEN TOP AND BOTTOM		(T/B)	0.20 cms.
DIFF. IN HEAD BETWEEN TOP AND MIDDLE		(T/M)	0.10 cms.
DIFF. IN HEAD BETWEEN MIDDLE AND BOTTOM		(M/B)	0.10 cms.
VOLUME OF WATER FLOWING IN THIS TIME			150.0 mls.
DURATION OF TEST			60 sec.
VOLUME OF WATER / TIME			2.50 mls.
PERMEABILITY (BOTTOM / MIDDLE)	(lower)		4.0276 cms./sec.
PERMEABILITY (MIDDLE / TOP)	(upper)		4.0276 cms./sec.
PERMEABILITY (BOTTOM / TOP)	(overall)		4.0276 cm/sec.
TEST 2			
MANOMETER READINGS			
BOTTOM 32.80	MIDDLE 33.10		TOP 33.50
DIFF. IN HEAD BETWEEN TOP AND BOTTOM		(T/B)	0.70 cms.
DIFF. IN HEAD BETWEEN TOP AND MIDDLE		(T/M)	0.40 cms.
DIFF. IN HEAD BETWEEN MIDDLE AND BOTTOM		(M/B)	0.30 cms.
VOLUME OF WATER FLOWING IN THIS TIME			570.0 mls.
DURATION OF TEST			60 sec.
VOLUME OF WATER / TIME			9.50 mls.
PERMEABILITY (BOTTOM / MIDDLE)	(lower)		5.10 cms./sec.
PERMEABILITY (MIDDLE / TOP)	(upper)		3.8262 cms./sec.
PERMEABILITY (BOTTOM / TOP)	(overall)		4.3728 cm/sec.
TEST 3			
MANOMETER READINGS			
BOTTOM 52.30	MIDDLE 52.600		TOP 52.90
DIFF. IN HEAD BETWEEN TOP AND BOTTOM		(T/B)	0.6 cms.
DIFF. IN HEAD BETWEEN TOP AND MIDDLE		(T/M)	0.3 cms.
DIFF. IN HEAD BETWEEN MIDDLE AND BOTTOM		(M/B)	0.3 cms.
VOLUME OF WATER FLOWING IN THIS TIME			710 mls.
DURATION OF TEST			60 sec.
VOLUME OF WATER / TIME			11.83 mls.
PERMEABILITY (BOTTOM / MIDDLE)	(lower)		6.3547 cms./sec.
PERMEABILITY (MIDDLE / TOP)	(upper)		6.3547 cms./sec.
PERMEABILITY (BOTTOM / TOP)	(overall)		6.3547 cm/sec.

MEAN OVERALL PERMEABILITY (k)	4.9184 cms./sec.

DIAMETER OF SAMPLE			8.89 cms.
CROSS SECTIONAL AREA			62.072 $cms.^2$
OVERALL LENGTH OF SAMPLE BETWEEN TOP & BOTTOM NIPPLE POINTS			20.00 cms.
LENGTH BETWEEN ANY TWO NIPPLE POINTS			10.00 cms.
TEST 1			
MANOMETER READINGS			
BOTTOM 24	MIDDLE 24.10		TOP 24.20
DIFF. IN HEAD BETWEEN TOP AND BOTTOM		(T/B)	0.20 cms.
DIFF. IN HEAD BETWEEN TOP AND MIDDLE		(T/M)	0.10 cms.
DIFF. IN HEAD BETWEEN MIDDLE AND BOTTOM		(M/B)	0.10 cms.
VOLUME OF WATER FLOWING IN THIS TIME			210.0 mls.
DURATION OF TEST			60 sec.
VOLUME OF WATER / TIME			3.50 mls.
PERMEABILITY (BOTTOM / MIDDLE)	(lower)		5.6386 cms./sec.
PERMEABILITY (MIDDLE / TOP)	(upper)		5.6386 cms./sec.
PERMEABILITY (BOTTOM / TOP)	(overall)		5.6386 cm/sec.
TEST 2			
MANOMETER READINGS			
BOTTOM 29.70	MIDDLE 29.90		TOP 30.10
DIFF. IN HEAD BETWEEN TOP AND BOTTOM		(T/B)	0.40 cms.
DIFF. IN HEAD BETWEEN TOP AND MIDDLE		(T/M)	0.20 cms.
DIFF. IN HEAD BETWEEN MIDDLE AND BOTTOM		(M/B)	0.20 cms.
VOLUME OF WATER FLOWING IN THIS TIME			400.0 mls.
DURATION OF TEST			60 sec.
VOLUME OF WATER / TIME			6.67 mls.
PERMEABILITY (BOTTOM / MIDDLE)	(lower)		5.37 cms./sec.
PERMEABILITY (MIDDLE / TOP)	(upper)		5.3701 cms./sec.
PERMEABILITY (BOTTOM / TOP)	(overall)		5.3701 cm/sec.
TEST 3			
MANOMETER READINGS			
BOTTOM 49.70	MIDDLE 50.000		TOP 50.30
DIFF. IN HEAD BETWEEN TOP AND BOTTOM		(T/B)	0.6 cms.
DIFF. IN HEAD BETWEEN TOP AND MIDDLE		(T/M)	0.3 cms.
DIFF. IN HEAD BETWEEN MIDDLE AND BOTTOM		(M/B)	0.3 cms.
VOLUME OF WATER FLOWING IN THIS TIME			680 mls.
DURATION OF TEST			60 sec.
VOLUME OF WATER / TIME			11.33 mls.
PERMEABILITY (BOTTOM / MIDDLE)	(lower)		6.0862 cms./sec.
PERMEABILITY (MIDDLE / TOP)	(upper)		6.0862 cms./sec.
PERMEABILITY (BOTTOM / TOP)	(overall)		6.0862 cm/sec.

MEAN OVERALL PERMEABILITY (k)	5.6983 cms./sec.

Particle Size Distribution

B.S.Sieve Number	Aperture mm	Phi Value	Cumulative Weight	Weight Retained	Weight Percent	Cumulative % Finer	Cumulative % Coarser
	75.00	-6.2		0.00	0.000	100.00	0.000
	63.00	-6.0		0.00	0.000	100.00	0.000
	53.00	-5.7		0.00	0.000	100.00	0.000
	22.40	-4.5		0.00	0.000	100.00	0.000
	16.00	-4.0		0.00	0.000	100.00	0.000
	11.20	-3.5	10.36	10.36	4.096	95.90	4.096
	8.00	-3.0	79.74	69.38	27.434	68.47	31.530
	5.60	-2.5	171.16	91.42	36.149	32.32	67.679
	4.00	-2.0	220.83	49.67	19.640	12.68	87.319
6	2.80	-1.5	241.17	20.34	8.043	4.64	95.362
8	2.00	-1.0	245.68	4.51	1.783	2.85	97.145
12	1.40	-0.5	247.57	1.89	0.747	2.11	97.892
16	1.00	0.0	248.51	0.94	0.372	1.74	98.264
22	0.71	0.5	249.09	0.58	0.229	1.51	98.493
30	0.50	1.0	249.70	0.61	0.241	1.27	98.735
44	0.355	1.5	250.14	0.44	0.174	1.09	98.909
60	0.250	2.0	250.98	0.84	0.332	0.76	99.241
85	0.180	2.5	251.34	0.36	0.142	0.62	99.383
120	0.125	3.0	251.58	0.24	0.095	0.52	99.478
170	0.090	3.5	251.82	0.24	0.095	0.43	99.573
240	0.063	4.0	252.53	0.71	0.281	0.15	99.854
		PAN	252.90	0.37	0.146	0.00	100.000

Total weight of sample =	252.90	Grams
Weight of sample =	253.19	Grams
Sieving gain / loss =	-0.11%	

%	PHI
F5	**-3.45**
F16	**-3.26**
F25	**-3.04**
F50	**-2.74**
F75	**-2.30**
F84	**-2.05**
F95	**-1.50**

MEDIAN DIAMETER =	**-2.74**
MEAN DIAMETER =	***-2.66***
GRAPHIC MEAN =	**-2.68**
STANDARD DEVIATION =	**0.61**
INCLUSIVE STANDARD DEVIATION =	**0.60**
PRIMARY SKEWNESS =	**0.14**
SECONDARY SKEWNESS =	**0.44**
INCLUSIVE GRAPHIC SKEWNESS =	**0.21**
GRAPHIC KURTOSIS =	**1.08**

AIR FLOW RIG TEST			SAMPLE TAKEN FROM ARG Test Site, OU.						Test Date: 15/07/97	
Material:		GRAVEL	NOTES: Sample depth of 11cm							
Area (A) cm^2		28.58								
Depth (L)		6								
1	2	3	4	5	7	8	9	10		
LFE.	LFE.	Sample	Sample	LFE	Sample	Resistivity	Resistivity	Resistivity		
Pressure		pressure		volume	velocity					
Drop		drop		flow						
mmH_20	Volts	mmH_20	Volts	cu.cm/sec	cm/sec	cgs Rayls	MKS Ralys	$N.Sec/m^4$		
0.204	1.020	0.026	0.013	11.4607	0.4010	6.3584	1059.7266	1.0597		
0.307	1.537	0.040	0.020	17.2697	0.6043	6.4917	1081.9491	1.0819		
0.398	1.988	0.050	0.025	22.3372	0.7816	6.2737	1045.6177	1.0456		
0.497	2.486	0.066	0.033	27.9327	0.9774	6.6224	1103.7295	1.1037		
0.595	2.974	0.076	0.038	33.4159	1.1692	6.3745	1062.4098	1.0624		
0.693	3.466	0.090	0.045	38.9440	1.3626	6.4772	1079.5272	1.0795		
0.796	3.979	0.098	0.049	44.7080	1.5643	6.1436	1023.9352	1.0239		
0.894	4.472	0.116	0.058	50.2474	1.7581	6.4703	1078.3905	1.0784		
0.996	4.981	0.130	0.065	55.9665	1.9582	6.5103	1085.0428	1.0850		
1.544	0.772	0.192	0.096	86.7419	3.0351	6.2038	1033.9605	1.0340		
2.020	1.010	0.262	0.131	113.4836	3.9707	6.4707	1078.4496	1.0784		
2.528	1.294	0.342	0.171	142.0230	4.9693	6.7492	1124.8616	1.1249		
3.016	1.508	0.424	0.212	169.4389	5.9286	7.0135	1168.9189	1.1689		
3.526	1.763	0.522	0.261	198.0907	6.9311	7.3857	1230.9433	1.2309		
3.996	1.998	0.616	0.308	224.4953	7.8550	7.6905	1281.7553	1.2818		
4.488	2.244	0.716	0.358	252.1358	8.8221	7.9591	1326.5089	1.3265		
				Average Flow Resistivity with a sample velocity range of 0.7 - 5.0cm/sec						**1071.592**

AIR FLOW RIG TEST			SAMPLE TAKEN FROM ARG Test Site, OU.						Test Date: 15/08/98	
Material:		GRAVEL	NOTES: Sample depth of 11cm							
Area (A) cm^2		28.58								
Depth (L)		11								
1	2	3	4	5	7	8	9	10		
LFE.	LFE.	Sample	Sample	LFE	Sample	Resistivity	Resistivity	Resistivity		
Pressure		pressure		volume	velocity					
Drop		drop		flow						
mmH_20	Volts	mmH_20	Volts	cu.cm/sec	cm/sec	cgs Rayls	MKS Ralys	$N.Sec/m^4$		
0.197	0.985	0.038	0.019	11.0675	0.3872	9.6231	874.8312	0.8748		
0.302	1.509	0.060	0.030	16.9551	0.5933	9.9182	901.6565	0.9017		
0.4	2.000	0.080	0.040	22.4720	0.7863	9.9777	907.0651	0.9071		
0.498	2.489	0.096	0.048	27.9664	0.9785	9.6209	874.6310	0.8746		
0.593	2.963	0.110	0.055	33.2923	1.1649	9.2604	841.8585	0.8419		
0.696	3.478	0.138	0.069	39.0788	1.3673	9.8974	899.7629	0.8998		
0.792	3.958	0.156	0.078	44.4721	1.5561	9.8315	893.7729	0.8938		
0.89	4.452	0.184	0.092	50.0227	1.7503	10.3094	937.2186	0.9372		
0.988	4.940	0.206	0.103	55.5058	1.9421	10.4019	945.6253	0.9456		
1.526	0.463	0.314	0.157	85.7307	2.9997	10.2654	933.2188	0.9332		
2.018	1.009	0.440	0.220	113.3712	3.9668	10.8776	988.8722	0.9889		
2.53	1.265	0.578	0.289	143.1354	5.0082	11.3178	1028.8949	1.0289		
3.032	1.516	0.730	0.365	170.3378	5.9600	12.0114	1091.9482	1.0919		
3.526	1.763	0.886	0.443	198.0907	6.9311	12.5358	1139.6194	1.1396		
4.01	2.005	1.052	0.526	225.2818	7.8825	13.0880	1189.8161	1.1898		
4.512	2.256	1.238	0.619	253.4842	8.8693	13.6884	1244.3999	1.2444		
				Average Flow Resistivity with a sample velocity range of 0.7 - 5.0cm/sec						**925.092**

Constant Head Permeameter

DIAMETER OF SAMPLE			6.89 cms.
CROSS SECTIONAL AREA			62.072 $cms.^2$
OVERALL LENGTH OF SAMPLE BETWEEN TOP & BOTTOM NIPPLE POINTS			20.00 cms.
LENGTH BETWEEN ANY TWO NIPPLE POINTS			10.00 cms.
TEST 1			
MANOMETER READINGS			
BOTTOM 36.1	MIDDLE 38.00		TOP 40.00
DIFF. IN HEAD BETWEEN TOP AND BOTTOM		(T/B)	3.90 cms.
DIFF. IN HEAD BETWEEN TOP AND MIDDLE		(T/M)	2.00 cms.
DIFF. IN HEAD BETWEEN MIDDLE AND BOTTOM		(M/B)	1.90 cms.
VOLUME OF WATER FLOWING IN THIS TIME			460.0 mls.
DURATION OF TEST			60 sec.
VOLUME OF WATER / TIME			7.67 mls.
PERMEABILITY (BOTTOM / MIDDLE)	(lower)		0.6501 cms./sec.
PERMEABILITY (MIDDLE / TOP)	(upper)		0.6176 cms./sec.
PERMEABILITY (BOTTOM / TOP)	(overall)		0.6334 cm/sec.
TEST 2			
MANOMETER READINGS			
BOTTOM 49.10	MIDDLE 51.70		TOP 53.90
DIFF. IN HEAD BETWEEN TOP AND BOTTOM		(T/B)	4.80 cms.
DIFF. IN HEAD BETWEEN TOP AND MIDDLE		(T/M)	2.20 cms.
DIFF. IN HEAD BETWEEN MIDDLE AND BOTTOM		(M/B)	2.60 cms.
VOLUME OF WATER FLOWING IN THIS TIME			640.0 mls.
DURATION OF TEST			60 sec.
VOLUME OF WATER / TIME			10.67 mls.
PERMEABILITY (BOTTOM / MIDDLE)	(lower)		0.66 cms./sec.
PERMEABILITY (MIDDLE / TOP)	(upper)		0.7811 cms./sec.
PERMEABILITY (BOTTOM / TOP)	(overall)		0.7160 cm/sec.
TEST 3			
MANOMETER READINGS			
BOTTOM 56.00	MIDDLE 59.800		TOP 61.70
DIFF. IN HEAD BETWEEN TOP AND BOTTOM		(T/B)	5.7 cms.
DIFF. IN HEAD BETWEEN TOP AND MIDDLE		(T/M)	1.9 cms.
DIFF. IN HEAD BETWEEN MIDDLE AND BOTTOM		(M/B)	3.8 cms.
VOLUME OF WATER FLOWING IN THIS TIME			745 mls.
DURATION OF TEST			60 sec.
VOLUME OF WATER / TIME			12.42 mls.
PERMEABILITY (BOTTOM / MIDDLE)	(lower)		0.5264 cms./sec.
PERMEABILITY (MIDDLE / TOP)	(upper)		1.0528 cms./sec.
PERMEABILITY (BOTTOM / TOP)	(overall)		0.7019 cm/sec.

MEAN OVERALL PERMEABILITY (k)	0.6838 cms./sec.

DIAMETER OF SAMPLE		8.89 cms.
CROSS SECTIONAL AREA		62.072 cms.^{2}
OVERALL LENGTH OF SAMPLE BETWEEN TOP & BOTTOM NIPPLE POINTS		20.00 cms.
LENGTH BETWEEN ANY TWO NIPPLE POINTS		10.00 cms.

TEST 1

MANOMETER READINGS		
BOTTOM 30.6	MIDDLE 32.10	TOP 33.60
DIFF. IN HEAD BETWEEN TOP AND BOTTOM	(T/B)	3.00 cms.
DIFF. IN HEAD BETWEEN TOP AND MIDDLE	(T/M)	1.50 cms.
DIFF. IN HEAD BETWEEN MIDDLE AND BOTTOM	(M/B)	1.50 cms.
VOLUME OF WATER FLOWING IN THIS TIME		367.0 mls.
DURATION OF TEST		60 sec.
VOLUME OF WATER / TIME		6.12 mls.
PERMEABILITY (BOTTOM / MIDDLE)	(lower)	0.6569 cms./sec.
PERMEABILITY (MIDDLE / TOP)	(upper)	0.6569 cms./sec.
PERMEABILITY (BOTTOM / TOP)	(overall)	0.6569 cm/sec.

TEST 2

MANOMETER READINGS		
BOTTOM 42.50	MIDDLE 44.90	TOP 47.20
DIFF. IN HEAD BETWEEN TOP AND BOTTOM	(T/B)	4.70 cms.
DIFF. IN HEAD BETWEEN TOP AND MIDDLE	(T/M)	2.30 cms.
DIFF. IN HEAD BETWEEN MIDDLE AND BOTTOM	(M/B)	2.40 cms.
VOLUME OF WATER FLOWING IN THIS TIME		580.0 mls.
DURATION OF TEST		60 sec.
VOLUME OF WATER / TIME		9.67 mls.
PERMEABILITY (BOTTOM / MIDDLE)	(lower)	0.65 cms./sec.
PERMEABILITY (MIDDLE / TOP)	(upper)	0.6771 cms./sec.
PERMEABILITY (BOTTOM / TOP)	(overall)	0.6627 cm/sec.

TEST 3

MANOMETER READINGS		
BOTTOM 52.30	MIDDLE 55.000	TOP 57.80
DIFF. IN HEAD BETWEEN TOP AND BOTTOM	(T/B)	5.5 cms.
DIFF. IN HEAD BETWEEN TOP AND MIDDLE	(T/M)	2.8 cms.
DIFF. IN HEAD BETWEEN MIDDLE AND BOTTOM	(M/B)	2.7 cms.
VOLUME OF WATER FLOWING IN THIS TIME		700 mls.
DURATION OF TEST		60 sec.
VOLUME OF WATER / TIME		11.67 mls.
PERMEABILITY (BOTTOM / MIDDLE)	(lower)	0.6961 cms./sec.
PERMEABILITY (MIDDLE / TOP)	(upper)	0.6713 cms./sec.
PERMEABILITY (BOTTOM / TOP)	(overall)	0.6835 cm/sec.

MEAN OVERALL PERMEABILITY (k)	0.6677 cms./sec.

Particle Size Distribution

B.S.Sieve Number	Aperture mm	Phi Value	Cumulative Weight	Weight Retained	Weight Percent	Cumulative % Finer	Cumulative % Coarser
	75.00	-6.2		0.00	0.000	100.00	0.000
	63.00	-6.0		0.00	0.000	100.00	0.000
	53.00	-5.7		0.00	0.000	100.00	0.000
	22.40	-4.5		0.00	0.000	100.00	0.000
	16.00	-4.0		0.00	0.000	100.00	0.000
	11.20	-3.5		0.00	0.000	100.00	0.000
	8.00	-3.0		0.00	0.000	100.00	0.000
	5.60	-2.5		0.00	0.000	100.00	0.000
	4.00	-2.0		0.00	0.000	100.00	0.000
6	2.80	-1.5		0.00	0.000	100.00	0.000
8	2.00	-1.0	5.75	5.75	4.569	95.43	4.569
12	1.40	-0.5	54.77	49.02	38.951	56.48	43.520
16	1.00	0.0	120.54	65.77	52.261	4.22	95.781
22	0.71	0.5	123.19	2.65	2.106	2.11	97.886
30	0.50	1.0	124.00	0.81	0.644	1.47	98.530
44	0.355	1.5	124.42	0.42	0.334	1.14	98.864
60	0.250	2.0	124.91	0.49	0.389	0.75	99.253
85	0.180	2.5	125.21	0.30	0.238	0.51	99.491
120	0.125	3.0	125.50	0.29	0.230	0.28	99.722
170	0.090	3.5	125.68	0.18	0.143	0.14	99.865
240	0.063	4.0	125.77	0.09	0.072	0.06	99.936
		PAN	125.85	0.08	0.064	0.00	100.000

Total weight of sample =	125.85	Grams
Weight of sample =	126.37	Grams
Sieving gain / loss =	-0.41%	

%	PHI
F5	**-1.00**
F16	**-0.85**
F25	**-0.72**
F50	**-0.42**
F75	**-0.20**
F84	**-0.10**
F95	**0.00**

MEDIAN DIAMETER =	**-0.42**
MEAN DIAMETER =	**-0.48**
GRAPHIC MEAN =	**-0.46**
STANDARD DEVIATION =	**0.38**
INCLUSIVE STANDARD DEVIATION =	**0.34**
PRIMARY SKEWNESS =	**-0.15**
SECONDARY SKEWNESS =	**-0.21**
INCLUSIVE GRAPHIC SKEWNESS =	**-0.15**
GRAPHIC KURTOSIS =	**0.79**

Shear Strength Determination

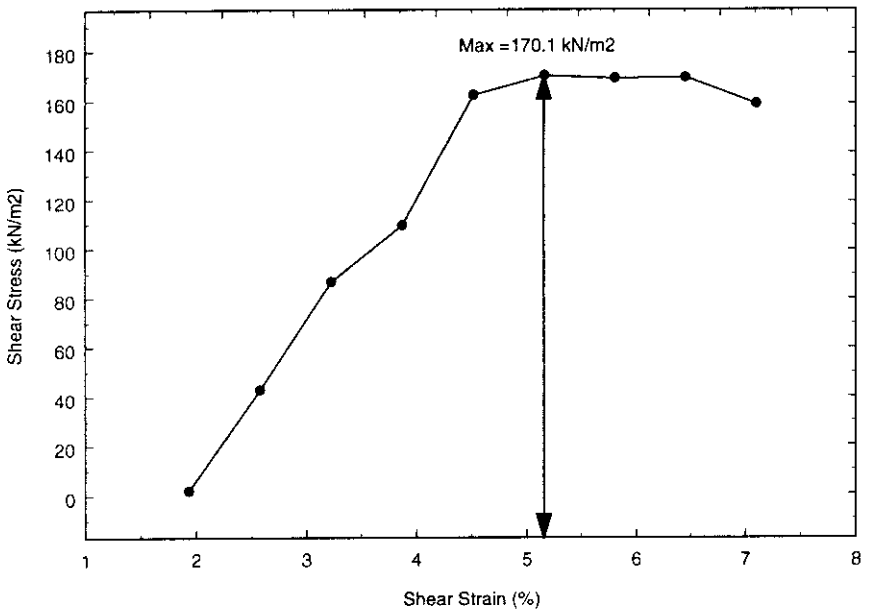

Plot of Shear Stress (kN/m^2) against Shear Strain (%). (Normal Stress = $200kN/m^2$)

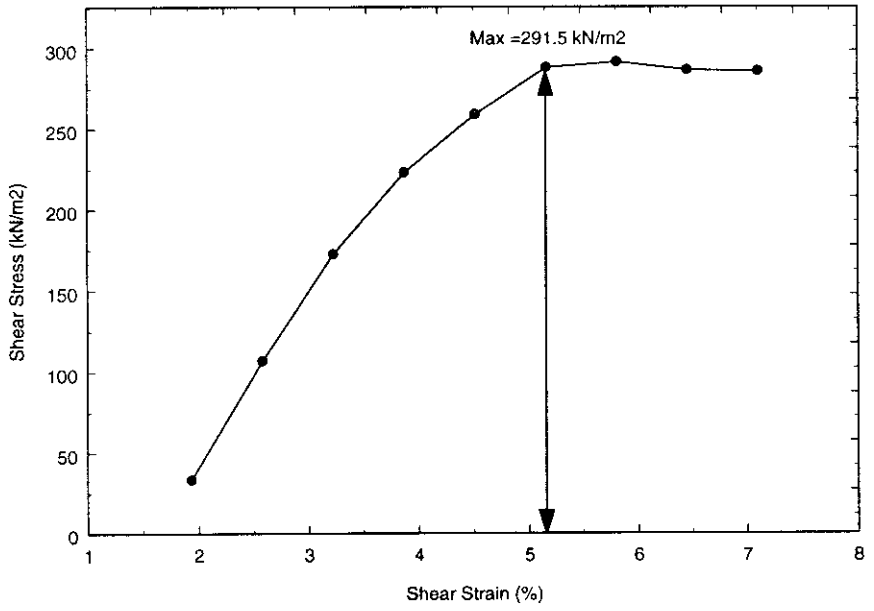

Plot of Shear Stress (kN/m^2) against Shear Strain (%). (Normal Stress = $400kN/m^2$)

AIR FLOW RIG TEST			HMC dried silica sand - grade 816						Test Date:	10/07/97
Material:		SAND	NOTES:							
Area (A) cm^2		28.58								
Depth (L)		5								
1	2	3	4	5	7	8	9	10		
LFE.	LFE.	Sample	Sample	LFE	Sample	Resistivity	Resistivity	Resistivity		
Pressure		pressure		volume	velocity					
Drop		drop		flow						
mmH_20	Volts	mmH_20	Volts	cu.cm/sec	cm/sec	cgs Rayls	MKS Ralys	$N.Sec/m^4$		
0.20	1.000	0.34	0.170	11.2360	0.3931	84.8106	16962.1181	16.9621		
0.30	1.500	0.50	0.249	16.8540	0.5897	83.1476	16629.5275	16.6295		
0.40	2.000	0.67	0.334	22.4720	0.7863	83.5634	16712.6752	16.7127		
0.50	2.500	0.84	0.420	28.0900	0.9829	83.8128	16762.5638	16.7626		
0.61	3.050	1.03	0.516	34.2698	1.1991	84.2381	16847.6197	16.8476		
0.70	3.480	1.17	0.586	39.1013	1.3681	83.8644	16772.8769	16.7729		
0.79	3.960	1.34	0.669	44.4946	1.5568	84.4074	16881.4749	16.8815		
0.89	4.460	1.51	0.755	50.1126	1.7534	84.4526	16890.5156	16.8905		
0.99	4.960	1.68	0.839	55.7306	1.9500	84.4887	16897.7336	16.8977		
1.55	0.773	2.58	1.288	86.8543	3.0390	83.2552	16651.0367	16.6510		
2.04	1.018	3.43	1.717	114.3825	4.0022	84.0461	16809.2150	16.8092		
2.56	1.278	4.360	2.181	143.5961	5.0244	85.0994	17019.8897	17.0199		
3.03	1.514	5.250	2.623	170.1130	5.9522	86.4977	17299.5456	17.2995		
3.53	1.764	6.190	3.095	198.2030	6.9350	87.5313	17506.2579	17.5063		
3.99	1..994	7.080	3.542	224.0458	7.8393	88.5685	17713.7025	17.7137		
4.51	2.253	8.120	4.061	253.1471	8.8575	89.9013	17980.2600	17.9803		
				Average Flow Resistivity with a sample velocity range of 0.7 - 4.0cm/sec						**16802.857**

AIR FLOW RIG TEST			HMC dried silica sand - grade 816						Test Date:	10/07/97
Material:		SAND	NOTES:							
Area (A) cm^2		28.58								
Depth (L)		5								
1	2	3	4	5	7	8	9	10		
LFE.	LFE.	Sample	Sample	LFE	Sample	Resistivity	Resistivity	Resistivity		
Pressure		pressure		volume	velocity					
Drop		drop		flow						
mmH_20	Volts	mmH_20	Volts	cu.cm/sec	cm/sec	cgs Rayls	MKS Ralys	$N.Sec/m^4$		
0.20	1.003	0.30	0.167	11.2697	0.3943	74.6091	14921.8199	14.9218		
0.30	1.508	0.51	0.257	16.9439	0.5929	84.3606	16872.1214	16.8721		
0.40	2.005	0.68	0.340	22.5282	0.7883	84.5990	16919.8035	16.9198		
0.50	2.505	0.85	0.426	28.1462	0.9848	84.6412	16928.2495	16.9282		
0.60	2.991	1.02	0.509	33.6069	1.1759	85.0657	17013.1454	17.0131		
0.69	3.469	1.10	0.550	38.9777	1.3638	79.0969	15819.3769	15.8194		
0.79	3.965	1.30	0.650	44.5507	1.5588	81.7846	16356.9270	16.3569		
0.89	4.462	1.47	0.734	50.1350	1.7542	82.1787	16435.7381	16.4357		
1.00	4.977	1.65	0.823	55.9216	1.9567	82.6965	16539.3048	16.5393		
1.54	0.768	2.52	1.262	86.2925	3.0193	81.8484	16369.6874	16.3697		
2.01	1.005	3.33	1.665	112.9218	3.9511	82.6512	16530.2468	16.5302		
2.54	1.268	4.33	2.163	142.4725	4.9850	85.1804	17036.0830	17.0361		
3.06	1.529	5.29	2.645	171.7984	6.0111	86.3017	17260.3442	17.2603		
3.54	1.770	6.22	3.112	198.8772	6.9586	87.6573	17531.4680	17.5315		
4.01	2.006	7.17	3.583	225.3942	7.8864	89.1578	17831.5590	17.8316		
4.5	2.252	8.17	4.086	253.0347	8.8536	90.4951	18099.0121	18.0990		
				Average Flow Resistivity with a sample velocity range of 0.7 - 4.0cm/sec						**16545.831**

Resonant Column Data Analysis

Location : Open University **Sample :** Indoor Tank **Date :** 27/11/98

JA : 0.0029 **MA :** 1.335

Test No.	Effective Stress (kPa)	Sample Length (mm)	Sample Dia. (mm)	Volume (cc)	Mass (kg)	Density (kg/m3)	Void Ratio	Porosity (%)	Length Change (%)	Volume Change (%)	Shear Velocity (m/s)	Shear Modulus (MPa)	Strain (E-5)	Shear Damping (%)	P-wave Velocity (m/s)	Young's Modulus (MPa)	Strain (E-5)	Long. Damping (%)
1	10	74.1	36.6	78.08	0.1276	1634.5	0.003	0.29	0.00	0.00	122.0	24.3	3.406	2.58				
2	10	74.1	36.6	78.08	0.1276	1634.5	0.003	0.29	0.00	0.00					267.0	66.5	3.021	3.17
3	20	74.1	36.6	78.08	0.1276	1634.5	0.003	0.29	0.00	0.00					266.0	90.4	2.406	2.86
4	20	74.1	36.6	78.08	0.1276	1634.5	0.003	0.29	0.00	0.00	146.9	35.3	3.184	1.86				
5	30	74.1	36.6	78.08	0.1276	1634.5	0.003	0.29	0.00	0.00	170.8	47.7	2.577	1.7				
6	30	74.1	36.6	78.08	0.1276	1634.5	0.003	0.29	0.00	0.00					296.5	119.4	1.475	3.48
7	40	74.1	36.6	78.08	0.1276	1634.5	0.003	0.29	0.00	0.00					305.3	137.2	1.416	3.23
8	40	74.1	36.6	78.08	0.1276	1634.5	0.003	0.29	0.00	0.00	187.0	57.2	2.192	1.53				
9	50	74.1	36.6	78.08	0.1276	1634.5	0.003	0.29	0.00	0.00	198.4	64.3	1.898	1.55				
10	50	74.1	36.6	78.08	0.1276	1634.5	0.003	0.29	0.00	0.00					316.5	151.3	1.298	3.21
11	70	74.1	36.6	78.08	0.1276	1634.5	0.003	0.29	0.00	0.00					343.8	180.7	0.790	4.14
12	70	74.1	36.6	78.08	0.1276	1634.5	0.003	0.29	0.00	0.00	217.9	77.6	1.885	1.3				
13	100	74.1	36.6	78.08	0.1276	1634.5	0.003	0.29	0.00	0.00	237.4	92.1	2.057	0.96				
14	100	74.1	36.6	78.08	0.1276	1634.5	0.003	0.29	0.00	0.00					468.6	244.5	0.726	3.26

Constant Head Permeameter

DIAMETER OF SAMPLE			8.89 cms.
CROSS SECTIONAL AREA			62.072 cms.^{2}
OVERALL LENGTH OF SAMPLE BETWEEN TOP & BOTTOM NIPPLE POINTS			20.00 cms.
LENGTH BETWEEN ANY TWO NIPPLE POINTS			10.00 cms.
TEST 1			
MANOMETER READINGS			
BOTTOM 24.4	MIDDLE 33.70		TOP 43.60
DIFF. IN HEAD BETWEEN TOP AND BOTTOM		(T/B)	19.20 cms.
DIFF. IN HEAD BETWEEN TOP AND MIDDLE		(T/M)	9.90 cms.
DIFF. IN HEAD BETWEEN MIDDLE AND BOTTOM		(M/B)	9.30 cms.
VOLUME OF WATER FLOWING IN THIS TIME			175.0 mls.
DURATION OF TEST			120 sec.
VOLUME OF WATER / TIME			1.46 mls.
PERMEABILITY (BOTTOM / MIDDLE)	(lower)		0.0253 cms./sec.
PERMEABILITY (MIDDLE / TOP)	(upper)		0.0237 cms./sec.
PERMEABILITY (BOTTOM / TOP)	(overall)		0.0245 cm/sec.
TEST 2			
MANOMETER READINGS			
BOTTOM 27.00	MIDDLE 43.80		TOP 60.00
DIFF. IN HEAD BETWEEN TOP AND BOTTOM		(T/B)	33.00 cms.
DIFF. IN HEAD BETWEEN TOP AND MIDDLE		(T/M)	16.20 cms.
DIFF. IN HEAD BETWEEN MIDDLE AND BOTTOM		(M/B)	16.80 cms.
VOLUME OF WATER FLOWING IN THIS TIME			225.0 mls.
DURATION OF TEST			120 sec.
VOLUME OF WATER / TIME			1.88 mls.
PERMEABILITY (BOTTOM / MIDDLE)	(lower)		0.02 cms./sec.
PERMEABILITY (MIDDLE / TOP)	(upper)		0.0186 cms./sec.
PERMEABILITY (BOTTOM / TOP)	(overall)		0.0183 cm/sec.
TEST 3			
MANOMETER READINGS			
BOTTOM 30.00	MIDDLE 53.700		TOP 77.20
DIFF. IN HEAD BETWEEN TOP AND BOTTOM		(T/B)	47.2 cms.
DIFF. IN HEAD BETWEEN TOP AND MIDDLE		(T/M)	23.5 cms.
DIFF. IN HEAD BETWEEN MIDDLE AND BOTTOM		(M/B)	23.7 cms.
VOLUME OF WATER FLOWING IN THIS TIME			405 mls.
DURATION OF TEST			120 sec.
VOLUME OF WATER / TIME			3.38 mls.
PERMEABILITY (BOTTOM / MIDDLE)	(lower)		0.0229 cms./sec.
PERMEABILITY (MIDDLE / TOP)	(upper)		0.0231 cms./sec.
PERMEABILITY (BOTTOM / TOP)	(overall)		0.0230 cm/sec.

MEAN OVERALL PERMEABILITY (k)	0.0219 cms./sec.

DIAMETER OF SAMPLE			8.89 cms.
CROSS SECTIONAL AREA			62.072 cms.^{2}
OVERALL LENGTH OF SAMPLE BETWEEN TOP & BOTTOM NIPPLE POINTS			20.00 cms.
LENGTH BETWEEN ANY TWO NIPPLE POINTS			10.00 cms.
TEST 1			
MANOMETER READINGS			
BOTTOM 23.4	MIDDLE 32.30		TOP 41.50
DIFF. IN HEAD BETWEEN TOP AND BOTTOM		(T/B)	18.10 cms.
DIFF. IN HEAD BETWEEN TOP AND MIDDLE		(T/M)	9.20 cms.
DIFF. IN HEAD BETWEEN MIDDLE AND BOTTOM		(M/B)	8.90 cms.
VOLUME OF WATER FLOWING IN THIS TIME			160.0 mls.
DURATION OF TEST			120 sec.
VOLUME OF WATER / TIME			1.33 mls.
PERMEABILITY (BOTTOM / MIDDLE)	(lower)		0.0241 cms./sec.
PERMEABILITY (MIDDLE / TOP)	(upper)		0.0233 cms./sec.
PERMEABILITY (BOTTOM / TOP)	(overall)		0.0237 cm/sec.
TEST 2			
MANOMETER READINGS			
BOTTOM 26.30	MIDDLE 41.30		TOP 56.70
DIFF. IN HEAD BETWEEN TOP AND BOTTOM		(T/B)	30.40 cms.
DIFF. IN HEAD BETWEEN TOP AND MIDDLE		(T/M)	15.40 cms.
DIFF. IN HEAD BETWEEN MIDDLE AND BOTTOM		(M/B)	15.00 cms.
VOLUME OF WATER FLOWING IN THIS TIME			225.0 mls.
DURATION OF TEST			120 sec.
VOLUME OF WATER / TIME			1.88 mls.
PERMEABILITY (BOTTOM / MIDDLE)	(lower)		0.02 cms./sec.
PERMEABILITY (MIDDLE / TOP)	(upper)		0.0196 cms./sec.
PERMEABILITY (BOTTOM / TOP)	(overall)		0.0199 cm/sec.
TEST 3			
MANOMETER READINGS			
BOTTOM 31.00	MIDDLE 56.400		TOP 81.10
DIFF. IN HEAD BETWEEN TOP AND BOTTOM		(T/B)	50.1 cms.
DIFF. IN HEAD BETWEEN TOP AND MIDDLE		(T/M)	24.7 cms.
DIFF. IN HEAD BETWEEN MIDDLE AND BOTTOM		(M/B)	25.4 cms.
VOLUME OF WATER FLOWING IN THIS TIME			440 mls.
DURATION OF TEST			120 sec.
VOLUME OF WATER / TIME			3.67 mls.
PERMEABILITY (BOTTOM / MIDDLE)	(lower)		0.0233 cms./sec.
PERMEABILITY (MIDDLE / TOP)	(upper)		0.0239 cms./sec.
PERMEABILITY (BOTTOM / TOP)	(overall)		0.0236 cm/sec.

MEAN OVERALL PERMEABILITY (k)	0.0224 cms./sec.

Particle Size Distribution

B.S.Sieve Number	Aperture mm	Phi Value	Cumulative Weight	Weight Retained	Weight Percent	Cumulative % Finer	Cumulative % Coarser
	75.00	-6.2		0.00	0.000	100.00	0.000
	63.00	-6.0		0.00	0.000	100.00	0.000
	53.00	-5.7		0.00	0.000	100.00	0.000
	22.40	-4.5		0.00	0.000	100.00	0.000
	16.00	-4.0		0.00	0.000	100.00	0.000
	11.20	-3.5		0.00	0.000	100.00	0.000
	8.00	-3.0		0.00	0.000	100.00	0.000
	5.60	-2.5		0.00	0.000	100.00	0.000
	4.00	-2.0		0.00	0.000	100.00	0.000
6	2.80	-1.5		0.00	0.000	100.00	0.000
8	2.00	-1.0	3.54	3.54	2.732	97.27	2.732
12	1.40	-0.5	4.17	0.63	0.486	96.78	3.218
16	1.00	0.0	5.67	1.50	1.158	95.62	4.376
22	0.71	0.5	8.92	3.25	2.508	93.12	6.884
30	0.50	1.0	20.22	11.30	8.720	84.40	15.604
44	0.355	1.5	45.15	24.93	19.239	65.16	34.843
60	0.250	2.0	88.13	42.98	33.169	31.99	68.012
85	0.180	2.5	114.54	26.41	20.381	11.61	88.393
120	0.125	3.0	125.91	11.37	8.775	2.83	97.168
170	0.090	3.5	128.47	2.56	1.976	0.86	99.143
240	0.063	4.0	129.09	0.62	0.478	0.38	99.622
		PAN	129.58	0.49	0.378	0.00	100.000

Total weight of sample =	129.58	Grams
Weight of sample =	130.43	Grams
Sieving gain / loss =	-0.65%	

%	PHI
F5	0.00
F16	1.05
F25	1.25
F50	1.70
F75	2.15
F84	2.40
F95	2.85

MEDIAN DIAMETER =	1.70
MEAN DIAMETER =	1.73
GRAPHIC MEAN =	1.72
STANDARD DEVIATION =	0.68
INCLUSIVE STANDARD DEVIATION =	0.77
PRIMARY SKEWNESS =	0.04
SECONDARY SKEWNESS =	-0.41
INCLUSIVE GRAPHIC SKEWNESS =	-0.08
GRAPHIC KURTOSIS =	1.30

Shear Strength Determination

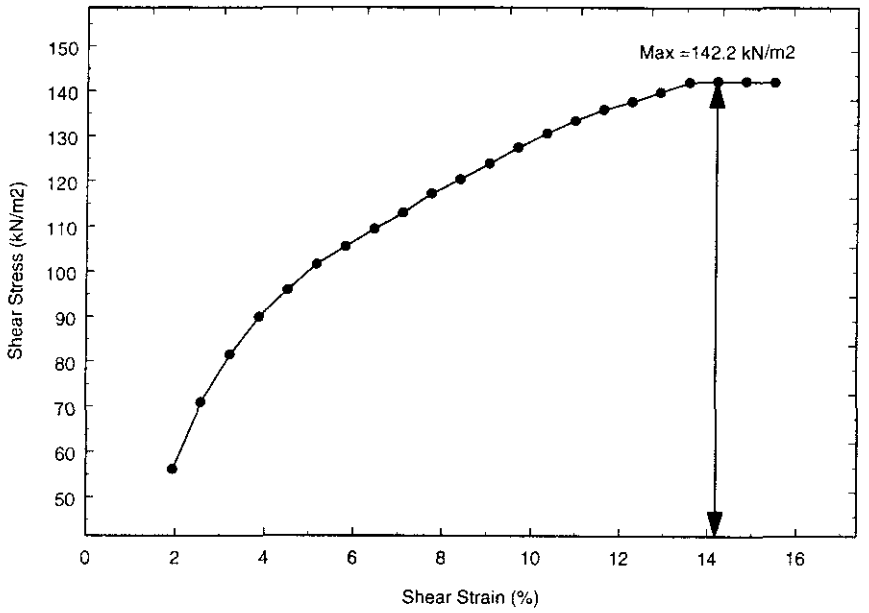

Plot of Shear Stress (kN/m^2) against Shear Strain(%). (Normal Stress = $200kN/m^2$)

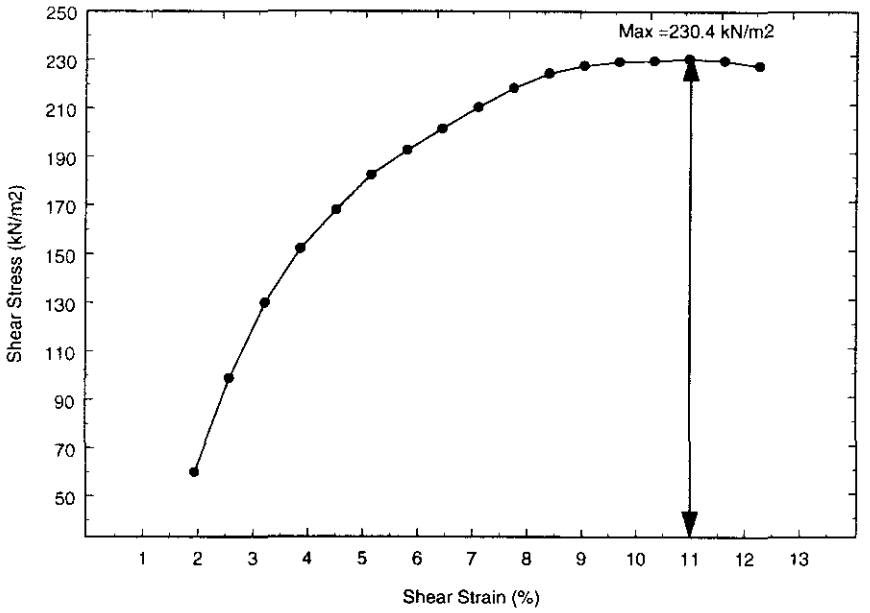

Plot of Shear Stress (kN/m^2) against Shear Strain (%). (Normal Stress = $400kN/m^2$)

AIR FLOW RIG TEST			SAMPLE TAKEN FROM HMC STONE LANE, HEATH AND REACH					Test Date: 09/10/97		
Material:		SAND	NOTES:							
Area (A) cm^2		28.58								
Depth (L)		5								
1	2	3	4	5	7	8	9	10		
LFE.	LFE.	Sample	Sample	LFE	Sample	Resistivity	Resistivity	Resistivity		
Pressure		pressure		volume	velocity					
Drop		drop		flow						
mmH_20	Volts	mmH_20	Volts	cu.cm/sec	cm/sec	cgs Rayls	MKS Ralys	$N.Sec/m^4$		
0.20	1.006	0.418	0.209	11.292	0.3951	103.7484	20749.6791	20.7497		
0.30	1.506	0.634	0.317	16.910	0.5917	105.0809	21016.1870	21.0162		
0.40	2.007	0.860	0.430	22.528	0.7882	106.9930	21398.5940	21.3986		
0.50	2.506	1.084	0.542	28.146	0.9848	107.9426	21588.5124	21.5885		
0.60	3.002	1.300	0.650	33.708	1.1794	108.0919	21618.3858	21.6184		
0.70	3.503	1.524	0.762	39.382	1.3780	108.4596	21691.9258	21.6919		
0.80	4.000	1.754	0.877	44.944	1.5726	109.3807	21876.1435	21.8761		
0.90	4.500	1.974	0.987	50.562	1.7691	109.4223	21884.4582	21.8845		
1.00	5.000	2.196	1.098	56.180	1.9657	109.5553	21911.0655	21.9111		
1.50	0.750	3.264	1.632	84.270	2.9486	108.5576	21711.5111	21.7115		
2.05	1.003	4.434	2.217	112.697	3.9432	110.2722	22054.4342	22.0544		
2.5	1.252	5.608	2.804	140.675	4.9221	111.7313	22346.2597	22.3463		
3	1.504	6.794	3.397	168.989	5.9129	112.6805	22536.1057	22.5361		
3.5	1.755	8.018	4.009	197.192	6.8996	113.9620	22792.4020	22.7924		
4	2.002	9.250	4.625	224.945	7.8707	115.2521	23050.4190	23.0504		
4.5	2.255	10.880	0.544	253.372	8.8654	120.3521	24070.4115	24.0704		
				Average Flow Resistivity with a sample velocity range of 0.7 - 4.0cm/sec						**21748.337**

AIR FLOW RIG TEST			SAMPLE TAKEN FROM HMC STONE LANE, HEATH AND REACH						Test Date:	08/01/98
Material:		SAND	NOTES:							
Area (A) cm^2		28.58								
Depth (L)		5								
1	2	3	4	5	7	8	9	10		
LFE.	LFE.	Sample	Sample	LFE	Sample	Resistivity	Resistivity	Resistivity		
Pressure		pressure		volume	velocity					
Drop		drop		flow						
mmH_20	Volts	mmH_20	Volts	cu.cm/sec	cm/sec	cgs Rayls	MKS Ralys	$N.Sec/m^4$		
0.20	0.970	0.41	0.151	11.2360	0.3931	102.2716	20454.3189	20.4543		
0.30	1.480	0.58	0.237	16.8540	0.5897	96.4513	19290.2519	19.2903		
0.40	1.960	0.74	0.314	22.4720	0.7863	92.2939	18458.7756	18.4588		
0.50	2.470	0.92	0.403	28.0900	0.9829	91.7950	18358.9984	18.3590		
0.60	2.940	1.09	0.484	33.7080	1.1794	90.6309	18126.1850	18.1262		
0.70	3.420	1.25	0.564	39.3260	1.3760	89.0868	17817.3509	17.8174		
0.80	3.950	1.43	0.658	44.9440	1.5726	89.1758	17835.1683	17.8352		
0.90	4.410	1.60	0.735	50.5620	1.7691	88.6908	17738.1627	17.7382		
1.00	0.510	1.79	0.861	56.1800	1.9657	89.3006	17860.1126	17.8601		
1.50	0.740	2.63	1.248	84.2700	2.9486	87.4713	17494.2630	17.4943		
2.05	0.990	3.54	1.704	112.3600	3.9314	88.3028	17660.5582	17.6606		
2.5	1.240	4.40	2.132	140.4500	4.9143	87.8039	17560.7811	17.5608		
3	1.480	5.30	2.565	168.5400	5.8971	88.1365	17627.2992	17.6273		
3.5	1.740	6.22	3.041	196.6300	6.8800	88.6591	17731.8276	17.7318		
4	1.960	7.14	3.451	224.7200	7.8628	89.0511	17810.2240	17.8102		
4.5	2.220	8.09	3.945	252.8100	8.8457	89.6886	17937.7170	17.9377		
				Average Flow Resistivity with a sample velocity range of 0.7 - 4.0cm/sec						**17927.731**

Resonant Column Data Analysis

Location : HMC, Stone Lane Quarry **Sample :** **Date :** 30/11/98

JA : 0.0029 **MA :** 1.335

Test No.	Effective Stress (kPa)	Sample Length (mm)	Sample Dia. (mm)	Volume (cc)	Mass (kg)	Density (kg/m3)	Void Ratio	Porosity (%)	Length Change (%)	Volume Change (%)	Shear Velocity (m/s)	Shear Modulus (MPa)	Strain (E-5)	Shear Damping (%)	P-wave Velocity (m/s)	Young's Modulus (MPa)	Strain (E-5)	Long. Damping (%)
1	10	80.8	35.5	77.70	0.117	1505.3	0.046	4.39	0.00	0.00					273.2	68.3	1.354	3.12
2	10	80.8	35.5	77.70	0.117	1505.3	0.046	4.39	0.00	0.00	129.3	25.2	3.520	2.36				
3	20	80.8	35.5	77.70	0.117	1505.3	0.046	4.39	0.00	0.00	161.6	39.3	3.492	1.81				
4	20	80.8	35.5	77.70	0.117	1505.3	0.046	4.39	0.00	0.00					306.9	102.8	1.562	2.76
5	30	80.8	35.5	77.70	0.117	1505.3	0.046	4.39	0.00	0.00					315.8	123.2	1.593	2.34
6	30	80.8	35.5	77.70	0.117	1505.3	0.046	4.39	0.00	0.00	180.3	49.0	2.598	1.30				
7	40	80.8	35.5	77.70	0.117	1505.3	0.046	4.39	0.00	0.00	195.8	57.7	2.565	1.30				
8	40	80.8	35.5	77.70	0.117	1505.3	0.046	4.39	0.00	0.00					360.9	149	1.255	2.09
9	50	80.8	35.5	77.70	0.117	1505.3	0.046	4.39	0.00	0.00					384.9	170.2	0.980	2.38
10	50	80.8	35.5	77.70	0.117	1505.3	0.046	4.39	0.00	0.00	209.4	66.0	2.975	1.26				
11	70	80.8	35.5	77.70	0.117	1505.3	0.046	4.39	0.00	0.00	231.4	80.6	2.616	1.18				
12	70	80.8	35.5	77.70	0.117	1505.3	0.046	4.39	0.00	0.00					427.3	208.3	1.037	2.35
13	100	80.8	35.5	77.70	0.117	1505.3	0.046	4.39	0.00	0.00					441.0	248.2	1.079	1.91
14	100	80.8	35.5	77.70	0.117	1505.3	0.046	4.39	0.00	0.00	257.9	100.1	2.480	0.97				

AIR FLOW RIG TEST			SAMPLE TAKEN FROM NCPA						Test Date:	10/07/97
Material:		Loam	NOTES: Crushed Loam used at NCPA for Tank experiments							
Area (A) cm^2		28.58								
Depth (L)		5								
1	2	3	4	5	7	8	9	10		
LFE.	LFE.	Sample	Sample	LFE	Sample	Resistivity	Resistivity	Resistivity		
Pressure		pressure		volume	velocity					
Drop		drop		flow						
mmH_20	Volts	mmH_20	Volts	cu.cm/sec	cm/sec	cgs Rayls	MKS Ralys	$N.Sec/m^4$		
0.20	1.017	11.28	0.564	11.4270	0.3998	2766.6854	553337.0724	553.3371		
0.30	1.510	17.10	0.855	16.9664	0.5936	2824.8104	564962.0868	564.9621		
0.40	1.996	22.18	1.109	22.4271	0.7847	2771.8602	554372.0396	554.3720		
0.50	2.480	28.02	1.401	27.8653	0.9750	2818.3006	563660.1133	563.6601		
0.60	2.979	39.90	1.995	33.4720	1.1712	3340.9820	668196.3955	668.1964		
0.69	3.465	47.50	2.375	38.9327	1.3622	3419.4951	683899.0210	683.8990		
0.81	4.029	24.78	1.239	45.2698	1.5840	1534.1776	306835.5121	306.8355		
0.89	4.474	27.90	1.395	50.2699	1.7589	1555.5325	311106.4948	311.1065		
1.00	4.982	32.04	1.602	55.9778	1.9586	1604.2039	320840.7900	320.8408		
1.55	0.773	31.46	1.573	96.8542	3.3889	910.3809	182076.1894	182.0762		
2.02	1.011	38.04	1.902	113.5960	3.9747	938.5564	187711.2773	187.7113		
				Average Flow Resistivity with a sample velocity range of 0.7 - 4.0cm/sec						**419855.315**

AIR FLOW RIG TEST			SAMPLE TAKEN FROM NCPA						Test Date:	10/07/97
Material:		Loam	NOTES: Crushed Loam used at NCPA for Tank experiments							
Area (A) cm^2		28.58								
Depth (L)		5								
1	2	3	4	5	7	8	9	10		
LFE.	LFE.	Sample	Sample	LFE	Sample	Resistivity	Resistivity	Resistivity		
Pressure		pressure		volume	velocity					
Drop		drop		flow						
mmH_20	Volts	mmH_20	Volts	cu.cm/sec	cm/sec	cgs Rayls	MKS Ralys	$N.Sec/m^4$		
0.20	1.003	8.86	0.443	11.2697	0.3943	2203.4554	440691.0823	440.6911		
0.30	1.514	12.78	0.639	17.0113	0.5952	2105.6018	421120.3669	421.1204		
0.40	2.005	16.42	0.821	22.5282	0.7883	2042.8175	408563.4907	408.5635		
0.50	2.493	19.72	0.986	28.0113	0.9801	1973.1338	394626.7688	394.6268		
0.60	2.976	21.72	1.086	33.4383	1.1700	1820.5329	364106.5795	364.1066		
0.69	3.468	24.08	1.204	38.9664	1.3634	1732.0048	346400.9656	346.4010		
0.80	3.979	27.58	1.379	44.7080	1.5643	1728.9878	345797.5527	345.7976		
0.90	4.476	29.16	1.458	50.2923	1.7597	1625.0582	325011.6420	325.0116		
1.00	4.992	32.44	1.622	56.0901	1.9626	1620.9795	324195.9066	324.1959		
1.54	0.769	29.78	1.489	86.4048	3.0233	965.9835	193196.7071	193.1967		
2.03	1.015	37.68	1.884	114.0454	3.9904	926.0107	185202.1470	185.2021		
2.54	1.272	39.080	1.954	142.9219	5.0008	766.3703	153274.0629	153.2741		
3.01	1.504	40.740	2.037	168.9894	5.9129	675.6853	135137.0569	135.1371		
3.53	1.763	43.680	2.184	198.0907	6.9311	618.0185	123603.6907	123.6037		
4.01	2.004	44.000	2.200	225.1694	7.8786	547.6791	109535.8295	109.5358		
				Average Flow Resistivity with a sample velocity range of 0.7 - 4.0cm/sec						**320789.084**

PERMEABILITY (K)

Sample Location:		HRI Wellesbourne					Date :	15/01/99
Sample No. :		Soil A					Analyst :	Nick Harrop

Diameter of Steffi :		0.032			Comments :			
Area of Steffi Filter :		0.082957681						
Length of Sample :		0.005						

Level in Manometer								
Level 1	Level 2	Head of Mercury	Head of Water	Level of Water	Volume of Water	Time of Reading	Time	Permeability
(m)	(m)			(m)	(m3)		(secs)	(m/s)
70.8	21.7	0.491		0.060		16:10:00		
			6.68197199		0.0007466		14505	4.64291E-10
71.4	22.2	0.492		0.051		21:05:00		
			6.70916211		0.0026546		45600	5.22982E-10
72.0	22.5	0.495		0.019		09:45:00		
							Average :	4.94E-10

Particle Size Analysis - Results Sheet - Hydrometer Test

Sample Location	HRI - SOIL A	Date	

Sample Preparation

Specific Gravity	**Average = 2.6480**	
mass bottle [g]	35.8773	35.8081
plus dry sed	54.7093	50.2069
plus dst. water	87.603	82.9502
plus water & sed	99.3506	91.8902
Specific Gravity	2.6582	2.6377

Moisture Content (%) =	**14.21**	
Tin	5.72	5.53
plus wet sediment	21.54	27.05
plus dry sediment	19.7	24.2
moisture Content	13.16	15.27

Dispersing Agent	
mass in 20ml	0.866
mass in 100ml	4.33

Sediment mass		
initial wet mass [g]	74.83	
calculated dry mas:	65.52	
Dry mass after hydrometer analysis		
mass of dry sed	18.2	
mass of disp agent	4.33	
sieved fraction	46.87	
Total dry mass	60.74	
LOSS =	4.78	7.29

Sieving analysis								
aperture [microns]	4000	2000	1000	500	250	125	62.5	**Total sieved**
dry weight [g]	0	1.25	1.14	3.43	25.69	14.13	2.48	**mass [g]**
%age retained	0.00	1.91	1.74	5.24	39.21	21.57	3.79	**46.87**

Hydrometer Calibration				
Length of bulb [cm]	16.00	Hx [cm]	Rh	Hr [cm]
length between 100 & 1000ml on cyl. [	25.80	1.50	30.00	8.43
Volume of hydrometer [ml]	75.00	2.00	25.00	10.43
Top of meniscus	1.50	4.00	20.00	12.43
Bottom of Meniscus	1.80	6.00	15.00	14.43
Temp of reading [deg C]	20.00	8.00	10.00	16.43
Meniscus correction (Cm)	**0.30**	10.00	5.00	18.43
Disp agent correction (x)	**1.81**	12.20	0.00	20.63

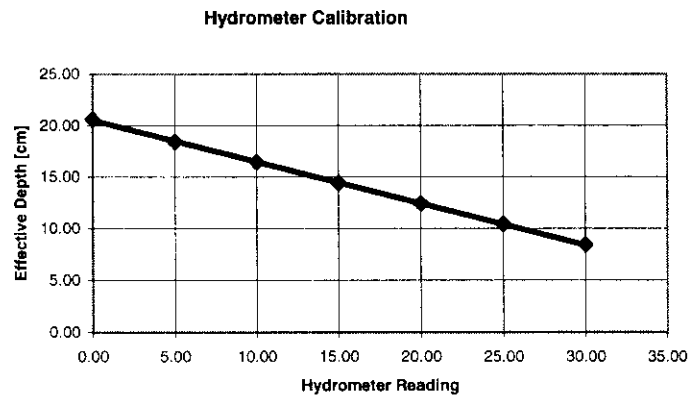

Please insert following values into boxes:	
Constant of equation:	20.518
Gradient of equation:	-0.4043

$$y = -0.4043x + 20.518$$

Time [min]	Rdg Rh	Temp [deg C]	meniscus corr	Eff. depth Hr	Equivalent diame	Disp agent corr	temp corr	%age finer than
0		21.6						
0.5	9.2	21.6	9.50	16.68	0.0774	7.69	8.01	19.63
1	8.7	21.6	9.00	16.88	0.0551	7.19	7.51	18.41
2	8.2	21.6	8.50	17.08	0.0392	6.69	7.01	17.18
4	7.9	21.6	8.20	17.20	0.0278	6.39	6.71	16.45
8	7.7	21.6	8.00	17.28	0.0197	6.19	6.51	15.96
15	7.5	21.6	7.80	17.36	0.0144	5.99	6.31	15.46
30	7.1	21.5	7.40	17.53	0.0103	5.59	5.89	14.43
80	6.7	21.5	7.00	17.69	0.0063	5.19	5.49	13.45
120	6.4	21	6.70	17.81	0.0052	4.89	5.09	12.48
240	6.2	20.5	6.50	17.89	0.0037	4.69	4.79	11.75
480	6.1	19.7	6.40	17.93	0.0027	4.59	4.55	11.15
1500								
1816								

SUMMARY DATA

Size [mm]	Size [phi]	%age finer than	Normalised%	%age coarser
8	-3.0	93.08		
4	-2.0	93.08		
2	-1.0	91.17	100.00	0.00
1	0.0	89.43	98.09	1.91
0.5	1.0	84.20	92.35	7.65
0.25	2.0	44.99	49.34	50.66
0.125	3.0	23.42	25.69	74.31
0.0774	3.7	19.63	21.53	78.47
0.0551	4.2	18.41	20.19	79.81
0.0392	4.7	17.18	18.85	81.15
0.0278	5.2	16.45	18.04	81.96
0.0197	5.7	15.96	17.50	82.50
0.0144	6.1	15.46	16.96	83.04
0.0103	6.6	14.43	15.83	84.17
0.0063	7.3	13.45	14.76	85.24
0.0052	7.6	12.48	13.69	86.31
0.0037	8.1	11.75	12.89	87.11
0.0027	8.6	11.15	12.23	87.77
0.0000	0.0	0.00	0.00	100.00
0.0000	0.0	0.00	0.00	100.00

Cumulative Curve

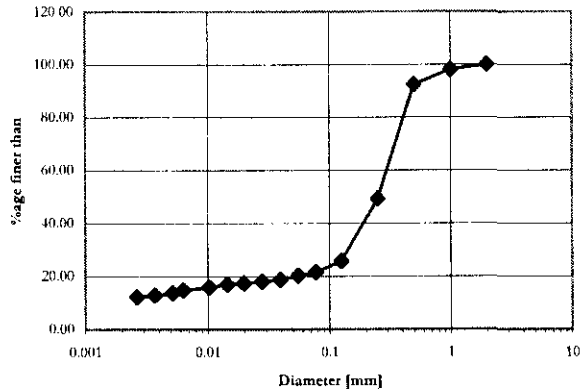

Shear Strength Determination

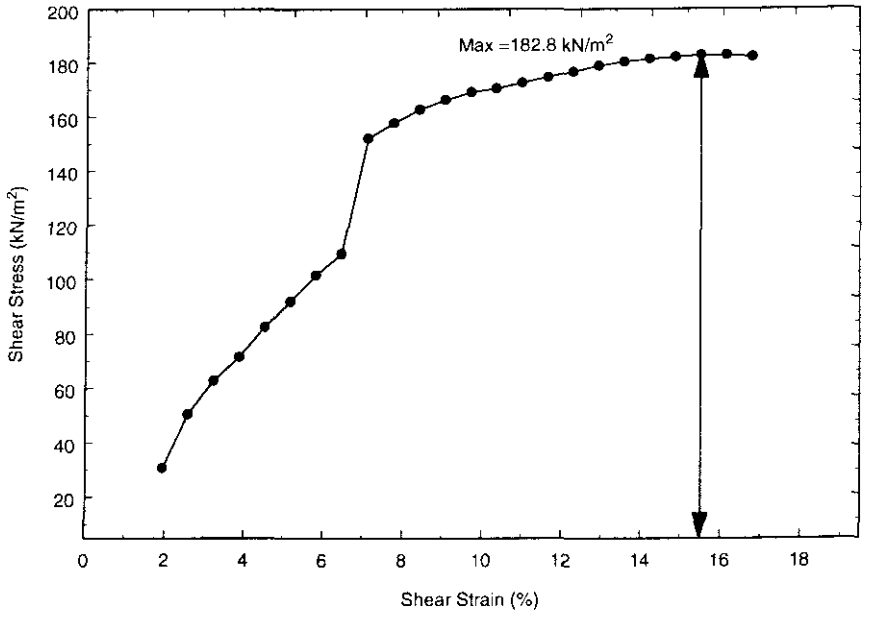

Plot of Shear Stress (kN/m^2) against Shear Strain(%). (Normal Stress = $200kN/m^2$)

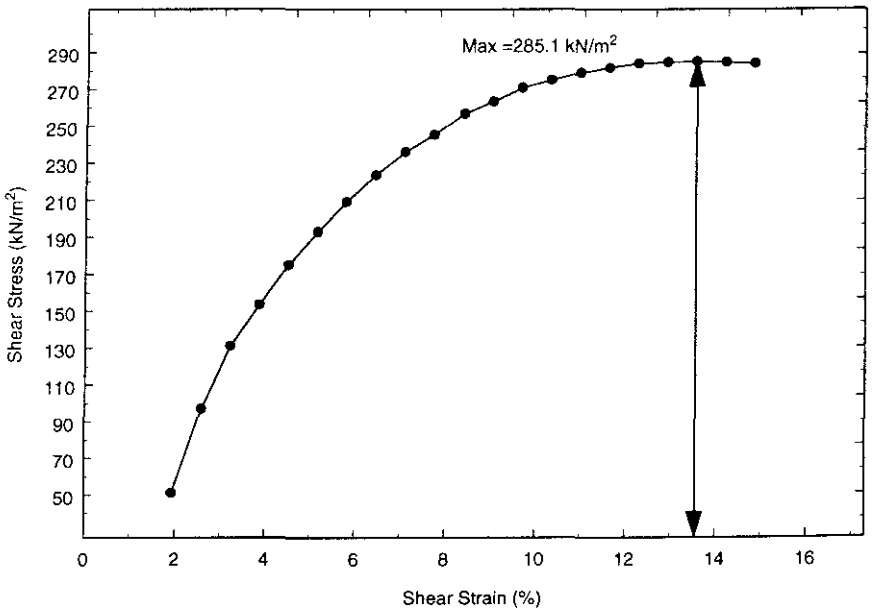

Plot of Shear Stress (kN/m^2) against Shear Strain(%). (Normal Stress = $400kN/m^2$)

Resonant Column Data Analysis

Location : HRI, Wellesbourne **Sample :** Soil A **Date :** 02/02/99

JA : 0.0029 **MA :** 1.335

Test No.	Effective Stress (kPa)	Sample Length (mm)	Sample Dia. (mm)	Volume (cc)	Mass (kg)	Density (kg/m3)	Void Ratio	Porosity (%)	Length Change (%)	Volume Change (%)	Shear Velocity (m/s)	Shear Modulus (MPa)	Strain (E-5)	Shear Damping (%)	P-wave Velocity (m/s)	Young's Modulus (MPa)	Strain (E-5)	Long. Damping (%)
1	10	76.2	37.6	84.54	0.1719	2033.6	0.312	23.76	0.00	0.00	44.5	4	13.725	7.64				
2	10	76.2	37.6	84.54	0.1719	2033.6	0.312	23.76	0.00	0.00					---	142.5	1.417	6.44
3	20	76.2	37.6	84.52	0.1719	2033.9	0.311	23.74	-0.01	0.03					---	163	1.106	7.21
4	20	76.2	37.6	84.52	0.1719	2033.9	0.311	23.75	-0.01	0.03	65.6	8.8	5.205	9.28				
5	30	76.2	37.6	84.46	0.1718	2034.7	0.310	23.69	-0.03	0.10	148.6	44.9	1.233	8.04				
6	30	76.2	37.6	84.45	0.1718	2034.7	0.310	23.68	-0.04	0.11					---	208.7	1.005	6.07
7	40	76.2	37.6	84.45	0.1718	2034.8	0.310	23.68	-0.04	0.11					---	225	0.991	5.68
8	40	76.2	37.6	84.45	0.1718	2034.7	0.310	23.68	-0.04	0.11	169.2	58.3	1.342	5.7				
9	50	76.2	37.6	84.42	0.1718	2035.2	0.310	23.65	-0.05	0.15	176.2	63.2	1.392	5.06				
10	50	76.2	37.6	84.42	0.1718	2035.2	0.310	23.65	-0.05	0.15					---	237.3	0.951	5.59
11	70	76.2	37.6	84.42	0.1718	2035.2	0.310	23.65	-0.05	0.15					---	254.3	0.896	5.45
12	70	76.2	37.6	84.42	0.1718	2035.2	0.310	23.65	-0.05	0.15	190.8	74.1	1.364	4.41				
13	100	76.2	37.6	84.42	0.1718	2035.2	0.310	23.65	-0.05	0.15	196.4	78.5	1.37	4.14				
14	100	76.2	37.6	84.42	0.1718	2035.2	0.310	23.65	-0.05	0.15					---	368.2	0.839	5.51
15	500	76.2	37.6	81.87	0.1693	2067.3	0.270	21.28	-1.06	3.16					---	466.8	0.381	6.69
16	500	76.2	37.6	81.87	0.1693	2067.3	0.270	21.28	-1.06	3.16	271.1	151.9	0.951	3.02				

PERMEABILITY (K)

Sample Location:	HRI Wellesbourne					Date :	15/01/99
Sample No. :	Soil B					Analyst :	Nick Harrop

Diameter of Steffi :	0.032			Comments :			
Area of Steffi Filter :	0.082957681						
Length of Sample :	0.005						

Level in Manometer								
Level 1	Level 2	Head of Mercury	Head of Water	Level of Water	Volume of Water	Time of Reading	Time	Permeability
(m)	(m)			(m)	(m3)		(secs)	(m/s)
0.800	0.136	0.66		0.06		14:00:00		
			9.02711984		0.0004148		3420	8.09776E-10
0.800	0.136	0.66		0.055		14:57:00		
			9.0407149		0.0004148		4140	6.67939E-10
0.801	0.135	0.67		0.05		16:06:00		
			9.04751243		0.0004148		3960	6.97775E-10
0.801	0.136	0.67		0.045		17:12:00		
			9.04751243		0.0007466		5160	9.63904E-10
0.801	0.135	0.67		0.036		18:38:00		
							Average :	7.85E-10

Particle Size Analysis - Results Sheet - Hydrometer Test

Sample Location	HR1 - SOIL B	Date	

Sample Preparation

Specific Gravity	**Average = 2.6406**	
mass bottle [g]	32.7609	33.4784
plus dry sed	47.328	49.2747
plus dst. water	82.0252	84.5179
plus water & sed	91.0669	94.3418
Specific Gravity	2.6364	2.6449

Moisture Content (%) =		**10.53**
Tin	5.58	5.49
plus wet sediment	24.96	22.4
plus dry sediment	23.17	20.74
moisture Content	10.18	10.89
Dispersing Agent		
mass in 20ml	0.866	
mass in 100ml	4.33	

Sediment mass		
initial wet mass [g]	49.06	
calculated dry mas:	44.39	
Dry mass after hydrometer analysis		
mass of dry sed	36.5	
mass of disp agent	4.33	
sieved fraction	10.34	
Total dry mass	42.51	
LOSS =	1.88	4.23

Sieving analysis								
aperture [microns]	4000	2000	1000	500	250	125	62.5	**Total sieved**
dry weight [g]	0	0.75	0.34	0.75	1.48	1.04	6.73	**mass [g]**
%age retained	0.00	1.69	0.77	1.69	3.33	2.34	15.16	**10.34**

Hydrometer Calibration				
Length of bulb [cm]	16.00	Hx [cm]	Rh	Hr [cm]
length between 100 & 1000ml on cyl. [	25.80	1.50	30.00	8.43
Volume of hydrometer [ml]	75.00	2.00	25.00	10.43
Top of meniscus	1.50	4.00	20.00	12.43
Bottom of Meniscus	1.80	6.00	15.00	14.43
Temp of reading [deg C]	20.00	8.00	10.00	16.43
Meniscus correction (Cm)	**0.30**	10.00	5.00	18.43
Disp agent correction (x)	**1.81**	12.20	0.00	20.63

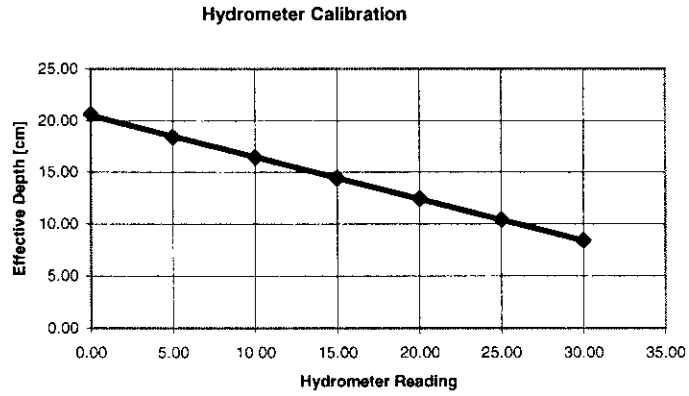

Please insert following values into boxes:	
Constant of equation:	20.518
Gradient of equation:	-0.4043

$y = -0.4043x + 20.518$

Time [min]	Rdg Rh	Temp [deg C]	meniscus corr	Eff. depth Hr	Equivalent diame	Disp agent corr	temp corr	%age finer than
0	17	21.6						
0.5	15.5	21.6	15.80	14.13	0.0714	13.99	14.31	51.88
1	14.5	21.6	14.80	14.53	0.0512	12.99	13.31	48.25
2	12	21.6	12.30	15.55	0.0374	10.49	10.81	39.18
4	9.7	21.6	10.00	16.48	0.0273	8.19	8.51	30.84
8	8.7	21.6	9.00	16.88	0.0195	7.19	7.51	27.22
15	8.1	21.6	8.40	17.12	0.0143	6.59	6.91	25.04
30	7.7	21.5	8.00	17.28	0.0102	6.19	6.49	23.52
80	7.5	21.5	7.80	17.36	0.0063	5.99	6.29	22.79
120	7.1	21	7.40	17.53	0.0052	5.59	5.79	20.99
240	6.9	20.5	7.20	17.61	0.0037	5.39	5.49	19.92
480	6.8	19.7	7.10	17.65	0.0026	5.29	5.25	19.02
1500								
1816								

SUMMARY DATA				
Size [mm]	Size [phi]	%age finer than	Normalised%	%age coarser
8	-3.0	76.86		
4	-2.0	76.86		
2	-1.0	75.17	100.00	0.00
1	0.0	74.41	98.98	1.02
0.5	1.0	72.72	96.73	3.27
0.25	2.0	69.38	92.30	7.70
0.125	3.0	67.04	89.18	10.82
0.0714	3.8	51.88	69.01	30.99
0.0512	4.3	48.25	64.19	35.81
0.0374	4.7	39.18	52.13	47.87
0.0273	5.2	30.84	41.03	58.97
0.0195	5.7	27.22	36.21	63.79
0.0143	6.1	25.04	33.31	66.69
0.0102	6.6	23.52	31.29	68.71
0.0063	7.3	22.79	30.32	69.68
0.0052	7.6	20.99	27.92	72.08
0.0037	8.1	19.92	26.50	73.50
0.0026	8.6	19.02	25.30	74.70
0.0000	0.0	0.00	0.00	100.00
0.0000	0.0	0.00	0.00	100.00

Cumulative Curve

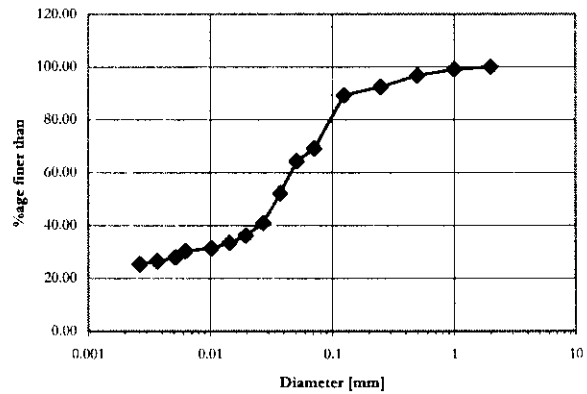

Shear Strength Determination

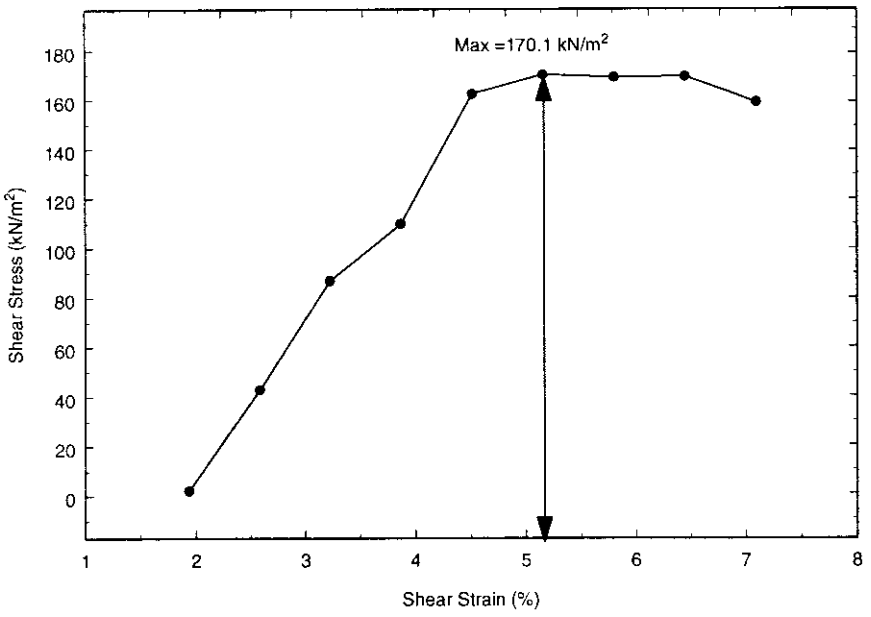

Plot of Shear Stress (kN/m^2) against Shear Strain(%). (Normal Stress = $200kN/m^2$)

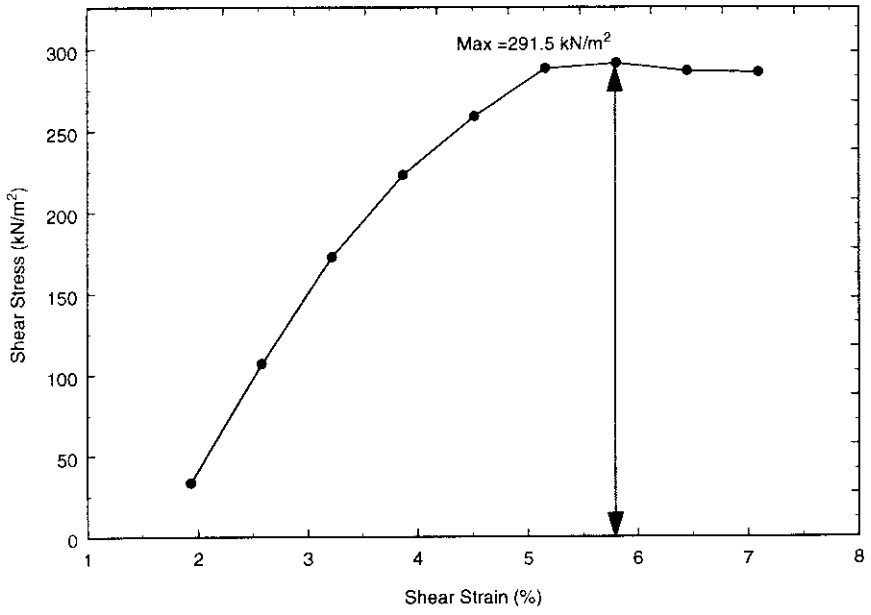

Plot of Shear Stress (kN/m^2) against Shear Strain(%). (Normal Stress = $400kN/m^2$)

Resonant Column Data Analysis

Location : HRI, Wellesbourne **Sample :** Soil B **Date :** 29/01/99

JA : 0.0029 **MA :** 1.335

Test No.	Effective Stress (kPa)	Sample Length (mm)	Sample Dia. (mm)	Volume (cc)	Mass (kg)	Density (kg/m3)	Void Ratio	Porosity (%)	Length Change (%)	Volume Change (%)	Shear Velocity (m/s)	Shear Modulus (MPa)	Strain (E-5)	Shear Damping (%)	P-wave Velocity (m/s)	Young's Modulus (MPa)	Strain (E-5)	Long. Damping (%)
1	10	76.4	37.6	84.73	0.1729	2040.2	0.219	17.94	0.00	0.00	175.6	62.9	0.517	13.67				
2	10	76.4	37.6	84.73	0.1729	2040.2	0.219	17.94	0.00	0.00					406.01889	183.6	0.372	18.71
3	20	76.4	37.6	84.73	0.1729	2040.2	0.219	17.94	0.00	0.00					431.07928	219.8	0.58	9.84
4	20	76.4	37.6	84.73	0.1729	2040.2	0.219	17.94	0.00	0.00	198.6	80.5	0.445	12.43				
5	30	76.4	37.6	84.73	0.1729	2040.2	0.219	17.94	0.00	0.00	206.5	87	0.486	10.51				
6	30	76.4	37.6	84.73	0.1729	2040.2	0.219	17.94	0.00	0.00					586.7395	248.7	0.585	8.48
7	40	76.4	37.6	84.73	0.1729	2040.2	0.219	17.94	0.00	0.00					755.31544	258.5	0.571	8.36
8	40	76.4	37.6	84.73	0.1729	2040.2	0.219	17.94	0.00	0.00	208.4	88.6	0.514	9.76				
9	50	76.4	37.6	84.73	0.1729	2040.2	0.219	17.94	0.00	0.00	212.2	91.8	0.567	8.54				
10	50	76.4	37.6	84.73	0.1729	2040.2	0.219	17.94	0.00	0.00					659.16069	270.3	0.538	8.42
11	70	76.4	37.6	84.73	0.1729	2040.2	0.219	17.94	0.00	0.00					1361.3798	296.4	0.482	8.47
12	70	76.4	37.6	84.73	0.1729	2040.2	0.219	17.94	0.00	0.00	221.1	99.7	0.522	8.54				
13	100	76.4	37.6	84.73	0.1729	2040.2	0.219	17.94	0.00	0.00	234.2	111.9	0.436	9.11				
14	100	76.4	37.6	84.73	0.1729	2040.2	0.219	17.94	0.00	0.00					718.54673	322.4	0.438	8.47
15	500	76.4	37.6	84.73	0.1729	2040.2	0.219	17.94	0.00	0.00					844.37706	498.9	0.31	7.41
16	500	76.4	37.6	84.73	0.1729	2040.2	0.219	17.94	0.00	0.00	292.2	174.2	0.429	5.94				

Sample Location:		HRI Wellesbourne					Date :	15/01/99
Sample No. :		Soil C					Analyst :	Nick Harrop

Diameter of Steffi :	0.032			Comments :			
Area of Steffi Filter :	0.082957681						
Length of Sample :	0.005						

Level in Manometer								
Level 1	Level 2	Head of Mercury	Head of Water	Level of Water	Volume of Water	Time of Reading	Time	Permeability
(m)	(m)			(m)	(m3)		(secs)	(m/s)
0.827	0.109	0.72		0.06		16:02:00		
			9.76125308		0.0010784		11160	5.96683E-10
0.827	0.109	0.72		0.047		19:08:00		
			9.76125308		0.0009125		18960	2.97179E-10
0.827	0.109	0.72		0.036		00:24:00		
							Average :	4.47E-10

Sample Location:	HRI Wellesbourne					Date :	15/01/99
Sample No. :	Soil C					Analyst :	Nick Harrop

Diameter of Steffi :	0.032			Comments :			
Area of Steffi Filter :	0.082957681						
Length of Sample :	0.005						

Level in Manometer								
Level 1	Level 2	Head of Mercury	Head of Water	Level of Water	Volume of Water	Time of Reading	Time	Permeability
(m)	(m)			(m)	(m3)		(secs)	(m/s)
0.827	0.109	0.72		0.06		16:02:00		
			9.76125308		0.0010784		11160	5.96683E-10
0.827	0.109	0.72		0.047		19:08:00		
			9.76125308		0.0009125		18960	2.97179E-10
0.827	0.109	0.72		0.036		00:24:00		
							Average :	4.47E-10

Particle Size Analysis - Results Sheet - Hydrometer Test

Sample Location	HRI - SOIL C	Date	

Sample Preparation

Specific Gravity	Average = 2.6331	
mass bottle [g]	33.074	32.2069
plus dry sed	47.043	47.3363
plus dst. water	83.0046	81.2923
plus water & sed	91.6794	90.6641
Specific Gravity	2.6385	2.6277

Moisture Content (%) =		12.62
Tin	5.36	5.5
plus wet sediment	22.95	23.61
plus dry sediment	21.01	21.55
moisture Content	12.40	12.83
Dispersing Agent		
mass in 20ml	0.866	
mass in 100ml	4.33	

Sediment mass		
initial wet mass [g]	52.63	
calculated dry mas:	46.73	
Dry mass after hydrometer analysis		
mass of dry sed	41.4	
mass of disp agent	4.33	
sieved fraction	7.06	
Total dry mass	44.13	
LOSS =	2.60	5.57

Sieving analysis								
aperture [microns]	4000	2000	1000	500	250	125	62.5	**Total sieved**
dry weight [g]	0	1.9	0.33	0.74	2.62	1.69	1.68	**mass [g]**
%age retained	0.00	4.07	0.71	1.58	5.61	3.62	3.59	**7.06**

Hydrometer Calibration				
Length of bulb [cm]	16.00	Hx [cm]	Rh	Hr [cm]
length between 100 & 1000ml on cyl. [	25.80	1.50	30.00	8.43
Volume of hydrometer [ml]	75.00	2.00	25.00	10.43
Top of meniscus	1.50	4.00	20.00	12.43
Bottom of Meniscus	1.80	6.00	15.00	14.43
Temp of reading [deg C]	20.00	8.00	10.00	16.43
Meniscus correction (Cm)	**0.30**	10.00	5.00	18.43
Disp agent correction (x)	**1.81**	12.20	0.00	20.63

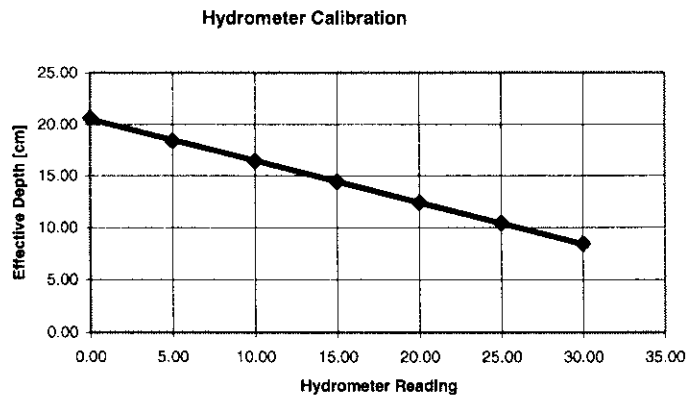

Please insert following values into boxes:	
Constant of equation:	20.518
Gradient of equation:	-0.4043

$y = -0.4043x + 20.518$

Time [min]	Rdg Rh	Temp [deg C]	meniscus corr	Eff. depth Hr	Equivalent diame	Disp agent corr	temp corr	%age finer than
0		21.6						
0.5	17.5	21.6	17.80	13.32	0.0695	15.99	16.31	56.25
1	17.5	21.6	17.80	13.32	0.0491	15.99	16.31	56.25
2	14.2	21.6	14.50	14.66	0.0364	12.69	13.01	44.87
4	11.5	21.6	11.80	15.75	0.0267	9.99	10.31	35.55
8	10.6	21.6	10.90	16.11	0.0191	9.09	9.41	32.45
15	9	21.6	9.30	16.76	0.0142	7.49	7.81	26.93
30	8.3	21.5	8.60	17.04	0.0102	6.79	7.09	24.45
80	7.7	21.5	8.00	17.28	0.0063	6.19	6.49	22.38
120	7.1	21	7.40	17.53	0.0052	5.59	5.79	19.97
240	6.8	20.5	7.10	17.65	0.0037	5.29	5.39	18.60
480	6.7	19.7	7.00	17.69	0.0026	5.19	5.15	17.75
1500								
1816								

SUMMARY DATA

Size [mm]	Size [phi]	%age finer than	Normalised%	%age coarser
8	-3.0	75.43		
4	-2.0	75.43		
2	-1.0	71.36	100.00	0.00
1	0.0	70.65	99.01	0.99
0.5	1.0	69.07	96.79	3.21
0.25	2.0	63.47	88.94	11.06
0.125	3.0	59.85	83.87	16.13
0.0695	3.8	56.25	78.83	21.17
0.0491	4.3	56.25	78.83	21.17
0.0364	4.8	44.87	62.88	37.12
0.0267	5.2	35.55	49.82	50.18
0.0191	5.7	32.45	45.47	54.53
0.0142	6.1	26.93	37.74	62.26
0.0102	6.6	24.45	34.26	65.74
0.0063	7.3	22.38	31.36	68.64
0.0052	7.6	19.97	27.98	72.02
0.0037	8.1	18.60	26.07	73.93
0.0026	8.6	17.75	24.88	75.12
0.0000	0.0	0.00	0.00	100.00
0.0000	0.0	0.00	0.00	100.00

Cumulative Curve

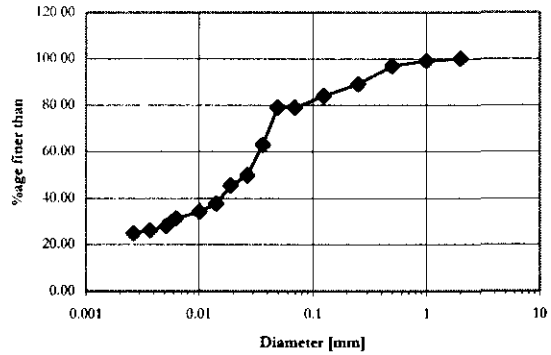

Shear Strength Determination

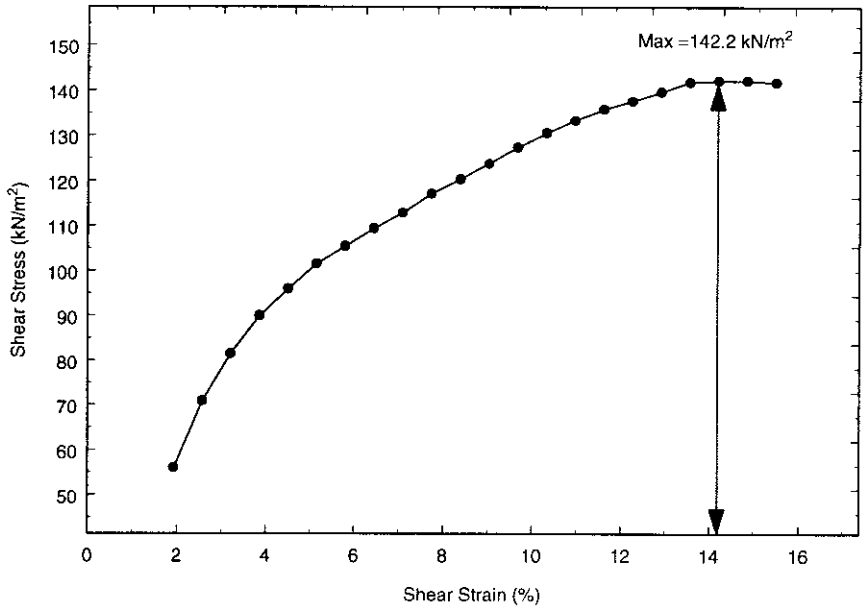

Plot of Shear Stress (kN/m^2) against Shear Strain(%). (Normal Stress = $200kN/m^2$)

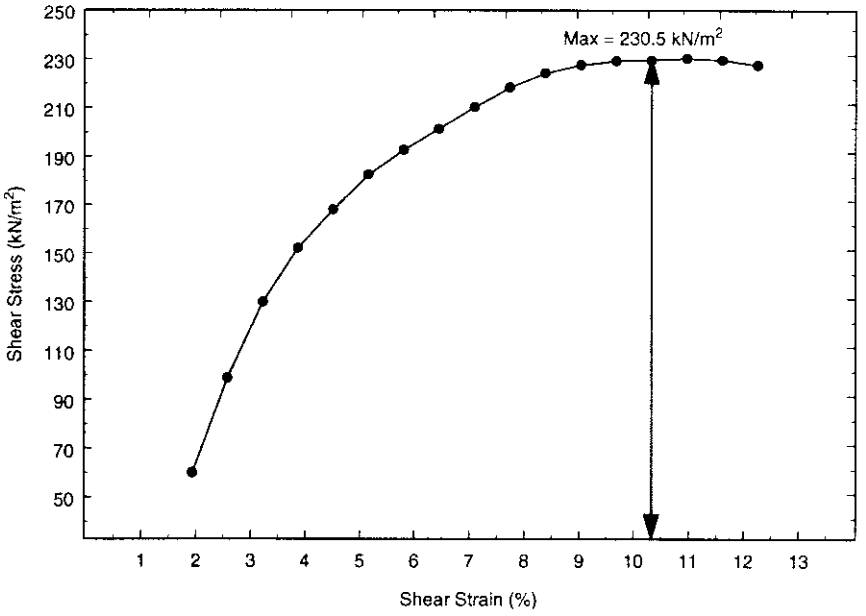

Plot of Shear Stress (kN/m^2) against Shear Strain(%). (Normal Stress = $400kN/m^2$)

Resonant Column Data Analysis

Location : HRI, Wellesbourne **Sample :** Soil C **Date :** 27/01/99

JA : 0.0029 **MA :** 1.335

Test No.	Effective Stress (kPa)	Sample Length (mm)	Sample Dia. (mm)	Volume (cc)	Mass (kg)	Density (kg/m3)	Void Ratio	Porosity (%)	Length Change (%)	Volume Change (%)	Shear Velocity (m/s)	Shear Modulus (MPa)	Strain (E-5)	Shear Damping (%)	P-wave Velocity (m/s)	Young's Modulus (MPa)	Strain (E-5)	Long. Damping (%)
1	10	78.2	37.8	87.94	0.1791	2036.9	0.142	12.43	0.00	0.00	130.1	34.5	1.664	4.93				
2	10	78.2	37.8	87.94	0.1791	2036.9	0.142	12.43	0.00	0.00					---	132.7	0.975	9.19
3	20	78.2	37.8	87.86	0.1790	2037.9	0.141	12.35	-0.03	0.09					---	155.6	0.885	8.56
4	20	78.2	37.8	87.86	0.1790	2037.9	0.141	12.35	-0.03	0.09	147.5	44.3	0.648	8.35				
5	30	78.2	37.8	87.79	0.1790	2038.7	0.140	12.28	-0.06	0.17	155.5	49.3	1.361	5.86				
6	30	78.2	37.8	87.79	0.1790	2038.7	0.140	12.28	-0.06	0.17					---	180.0	0.750	8.21
7	40	78.1	37.8	87.76	0.1789	2039.1	0.140	12.24	-0.07	0.21					---	197.0	0.714	7.97
8	40	78.1	37.8	87.76	0.1789	2039.1	0.140	12.24	-0.07	0.21	163.5	54.5	1.291	5.59				
9	50	78.1	37.8	87.73	0.1789	2039.4	0.139	12.21	-0.08	0.25	171.0	59.6	1.287	5.12				
10	50	78.1	37.8	87.73	0.1789	2039.4	0.139	12.21	-0.08	0.25					---	209.7	0.690	7.69
11	70	78.1	37.8	87.67	0.1789	2040.1	0.138	12.16	-0.10	0.31					---	233.0	0.613	7.44
12	70	78.1	37.8	87.67	0.1789	2040.1	0.138	12.16	-0.10	0.31	185.1	69.9	0.916	5.81				
13	100	78.1	37.8	87.65	0.1788	2040.4	0.138	12.13	-0.11	0.34	197.3	79.4	0.806	6.15				
14	100	78.1	37.8	87.64	0.1788	2040.5	0.138	12.12	-0.12	0.35					---	258.8	0.538	7.65
15	500	77.6	37.5	85.81	0.177	2062.7	0.114	10.25	-0.82	2.43					---	539.0	0.280	7.02
16	500	77.5	37.5	86.63	0.1768	2064.9	0.112	10.06	-0.88	2.63	296.8	182	0.396	5.59				

Appendix C

Indoor Tank Experiments

C Contents

Appendix C covers the results from the Indoor Tank experiments undertaken at The Open University. It includes:

a) Result of probe microphone experiments taken at Position B and normal incidence

b) Result of probe microphone experiments taken at Position A and 14° from normal

c) Result of probe microphone experiments taken at Position A and 21° from normal

d) Result of probe microphone experiments taken at Position A and 37° from normal

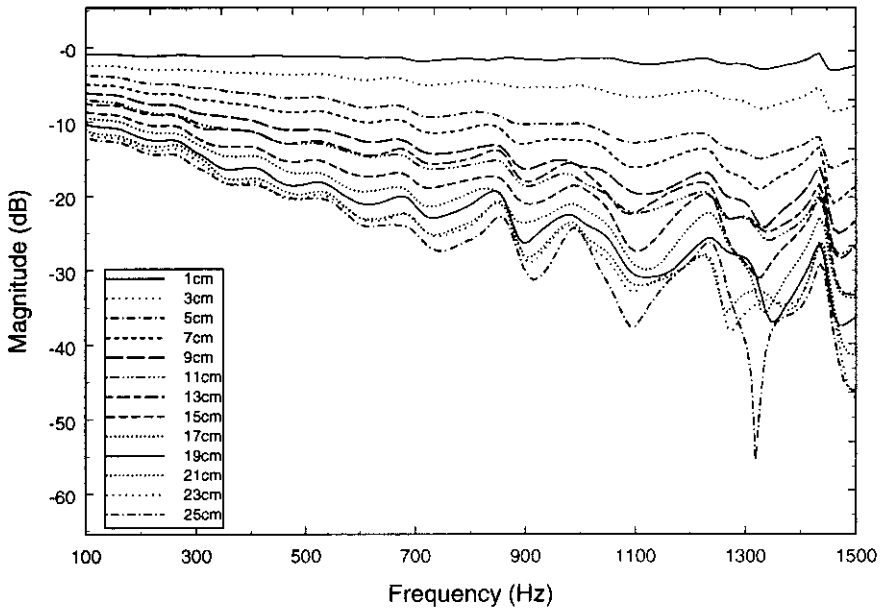

Figure C-1. Measured relative magnitude at Position B, between the probe microphone at various depths and a reference microphone situated at the sand surface

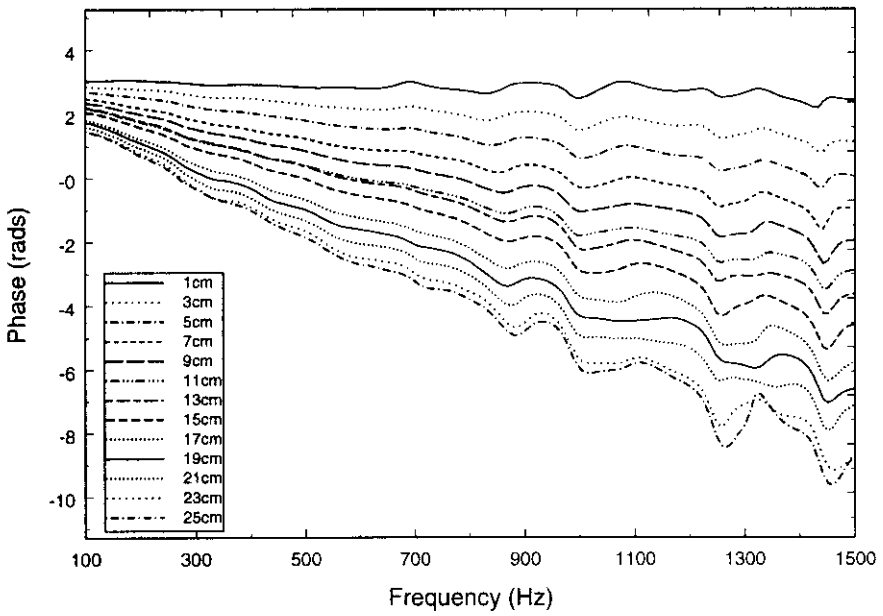

Figure C-2. Measured phase difference at Position B, between the probe microphone at various depths and a reference microphone situated at the sand surface.

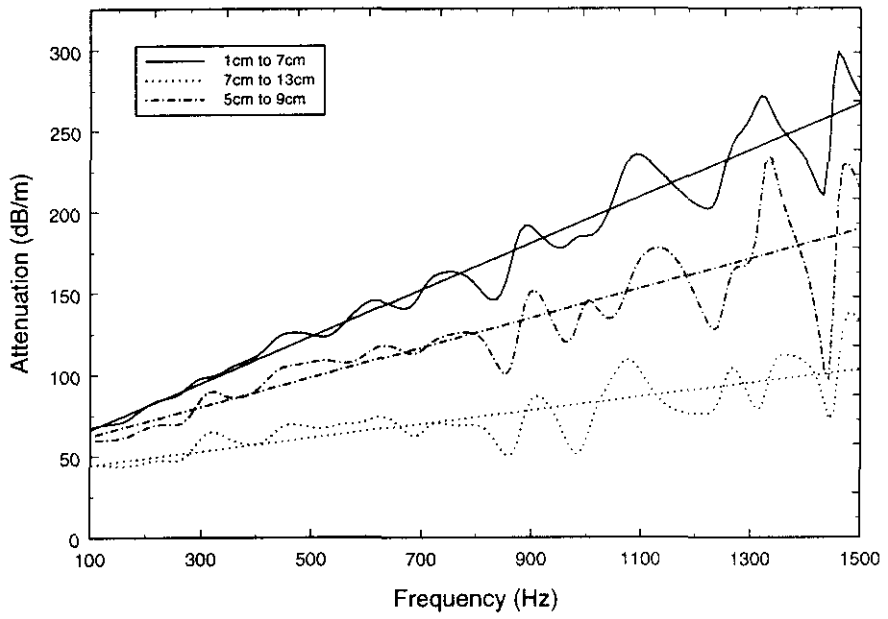

Figure C-3. Calculated attenuation at Position B over three different depth intervals. Best-fit regression has been applied to the data.

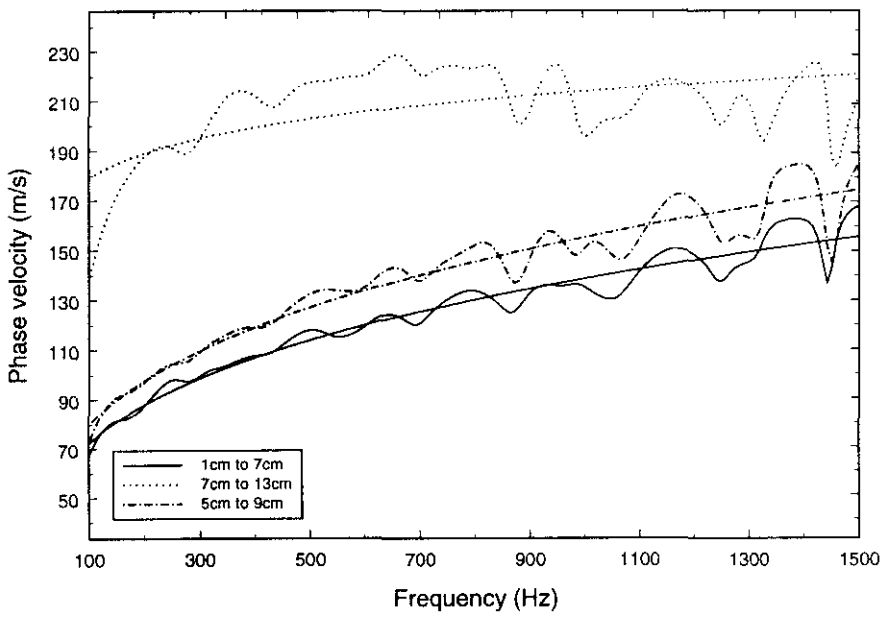

Figure C-4. Calculated phase velocity at Position B, over three different depth intervals. Best-fit regression has been applied to the data.

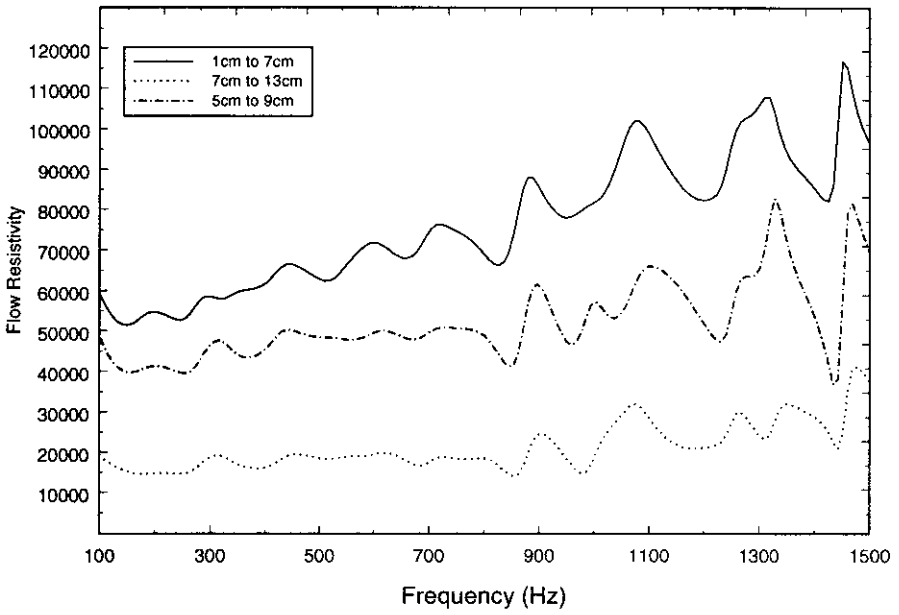

Figure C-5. Calculated flow resistivity at Position B, of the Tank Sand.

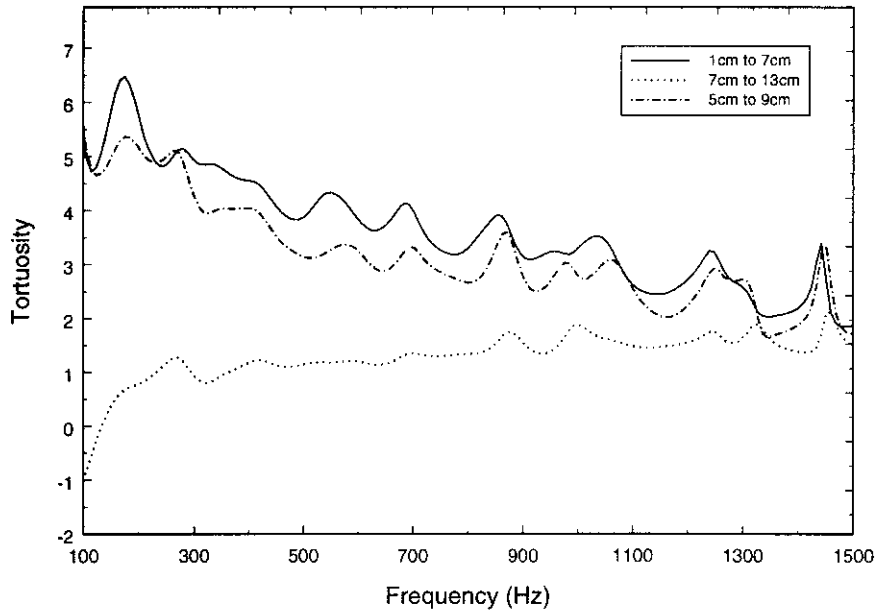

Figure C-6. Calculated tortuosity at Position B, of the Tank Sand.

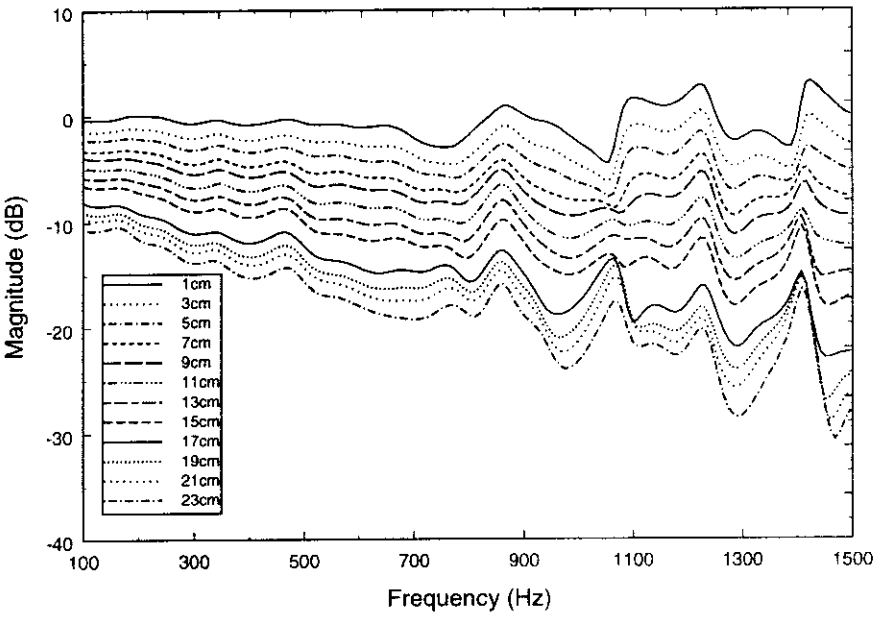

Figure C-7. Measured relative magnitude at Position A and Angle 1, between the probe microphone at various depths and a reference microphone situated at the sand surface

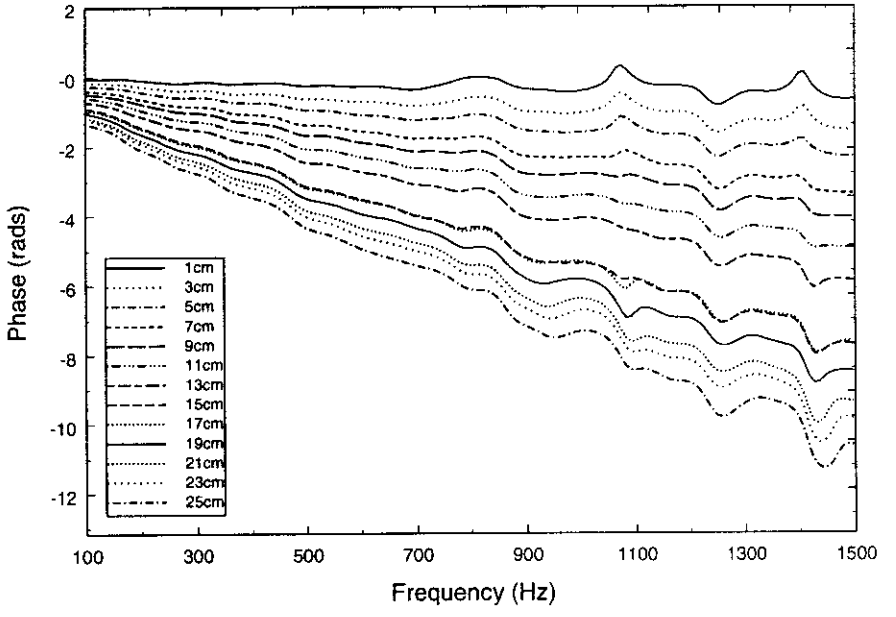

Figure C-8. Measured phase difference at Position A and Angle 1, between the probe microphone at various depths and a reference microphone situated at the sand surface.

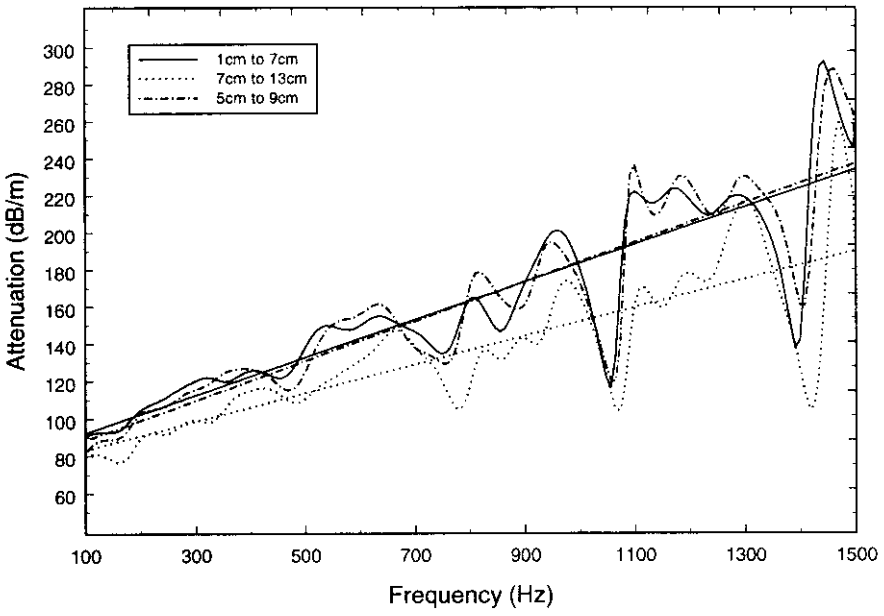

Figure C-9. Calculated attenuation at Position A and Angle 1 over three different depth intervals. Best-fit regression has been applied to the data.

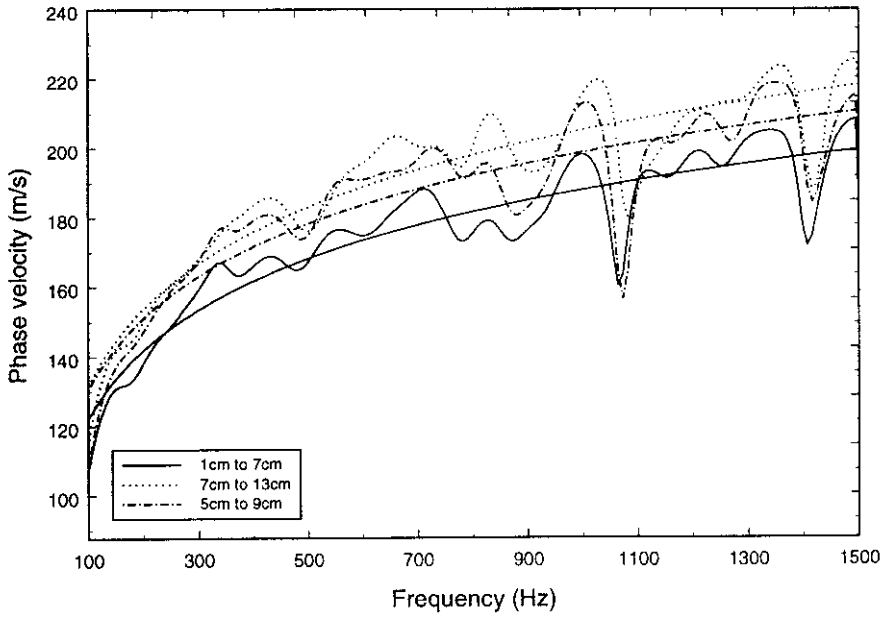

Figure C-10. Calculated phase velocity at Position A and Angle 1, over three different depth intervals. Best-fit regression has been applied to the data.

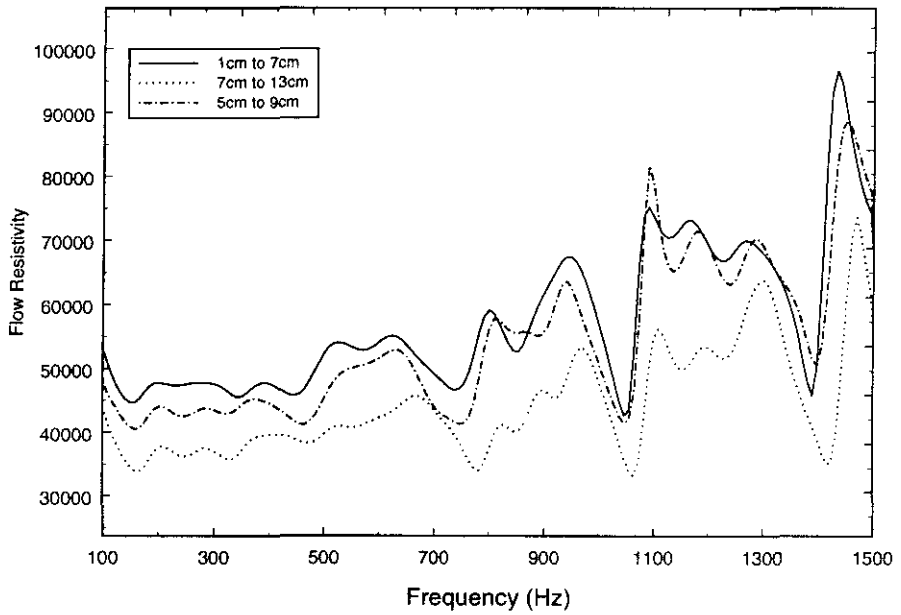

Figure C-11. Calculated flow resistivity at Position A and Angle 1, of the Tank Sand.

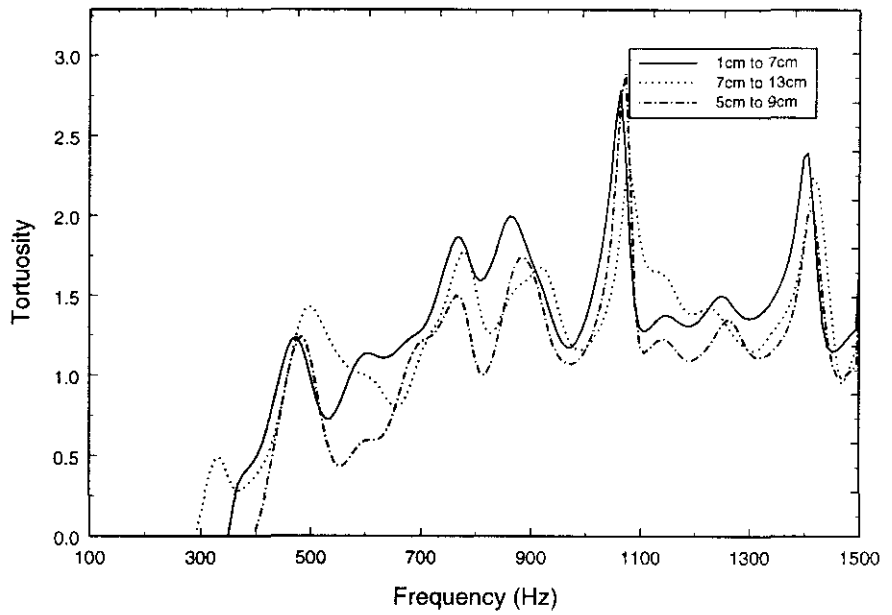

Figure C-12. Calculated tortuosity at Position A and Angle 1, of the Tank Sand.

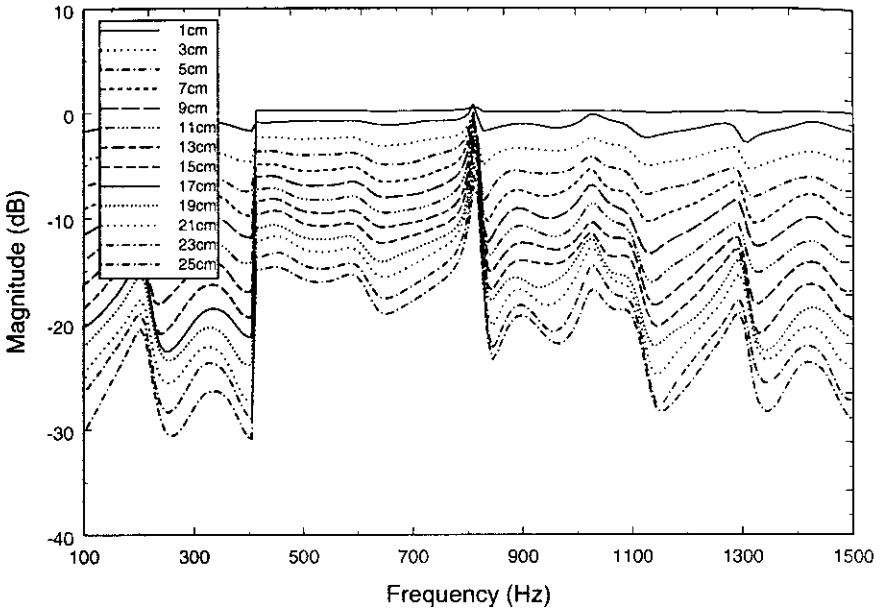

Figure C-13. Measured relative magnitude at Position A and Angle 2, between the probe microphone at various depths and a reference microphone situated at the sand surface

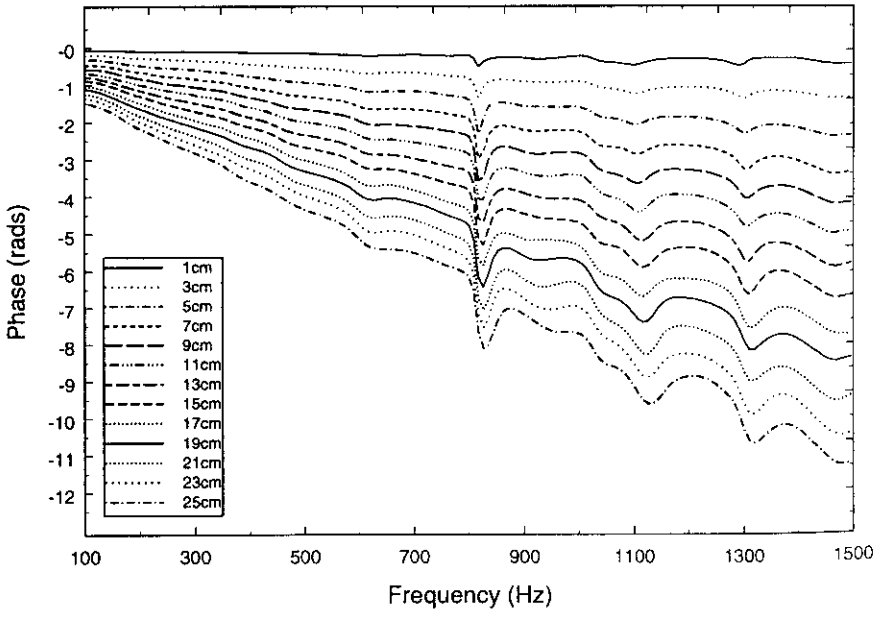

Figure C-14. Measured phase difference at Position A and Angle 2, between the probe microphone at various depths and a reference microphone situated at the sand surface.

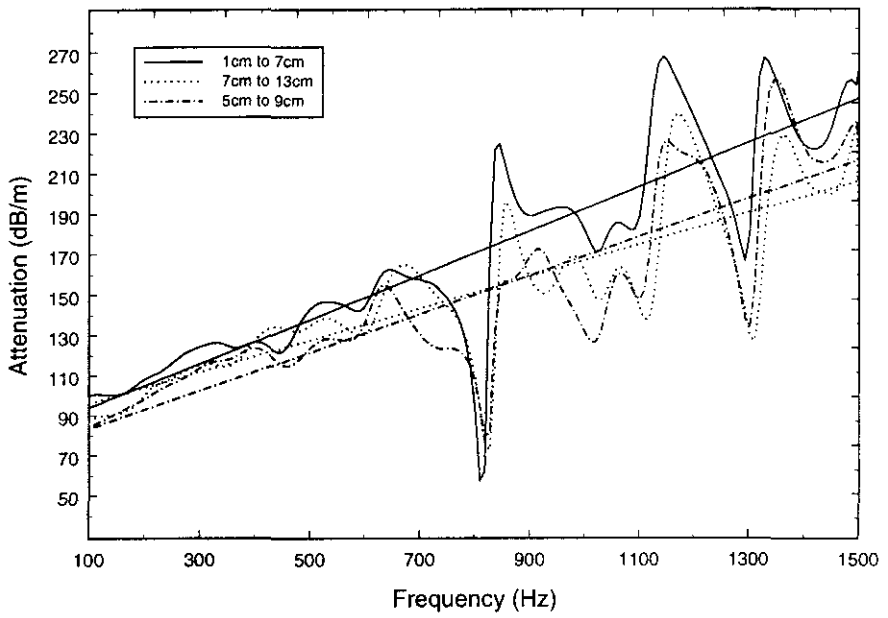

Figure C-15. Calculated attenuation at Position A and Angle 2 over three different depth intervals. Best-fit regression has been applied to the data.

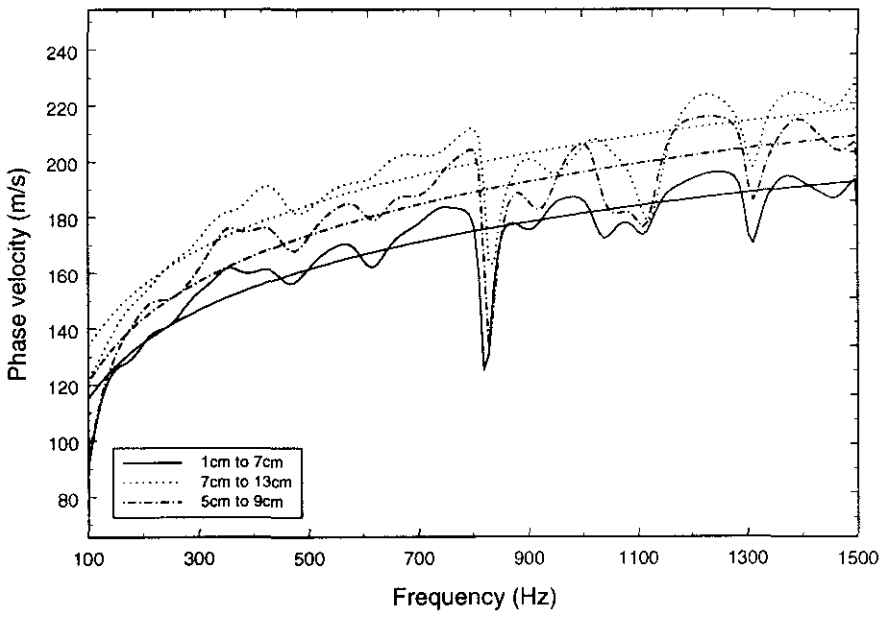

Figure C-16. Calculated phase velocity at Position A and Angle 2, over three different depth intervals. Best-fit regression has been applied to the data.

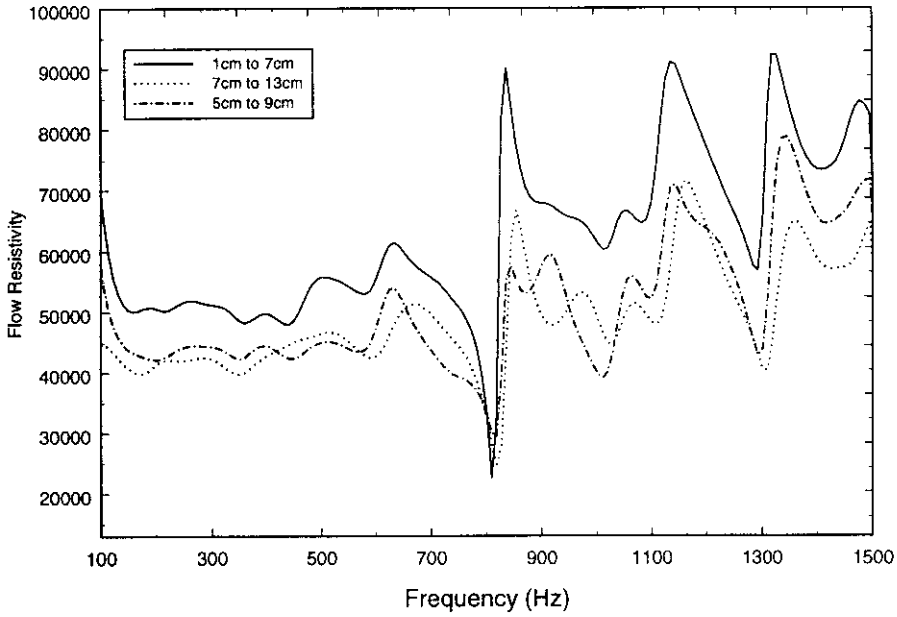

Figure C-17. Calculated flow resistivity at Position A and Angle 2, of the Tank Sand.

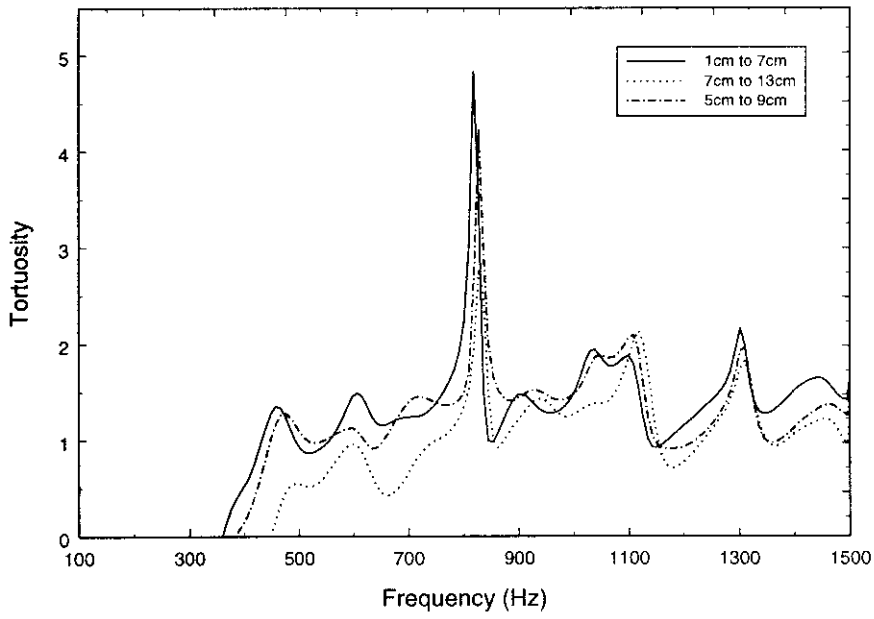

Figure C-18. Calculated tortuosity at Position A and Angle 2, of the Tank Sand.

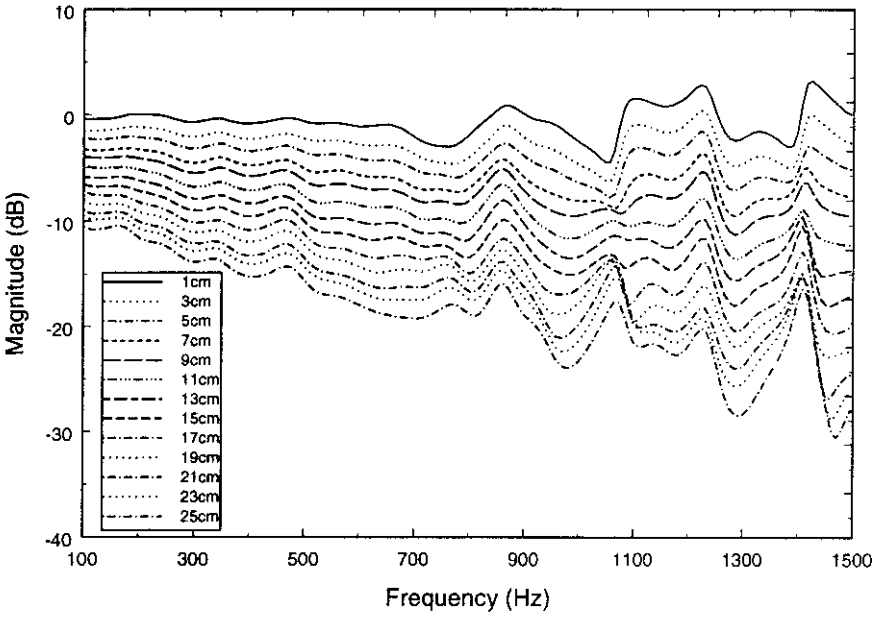

Figure C-19. Measured relative magnitude at Position A and Angle 3, between the probe microphone at various depths and a reference microphone situated at the sand surface

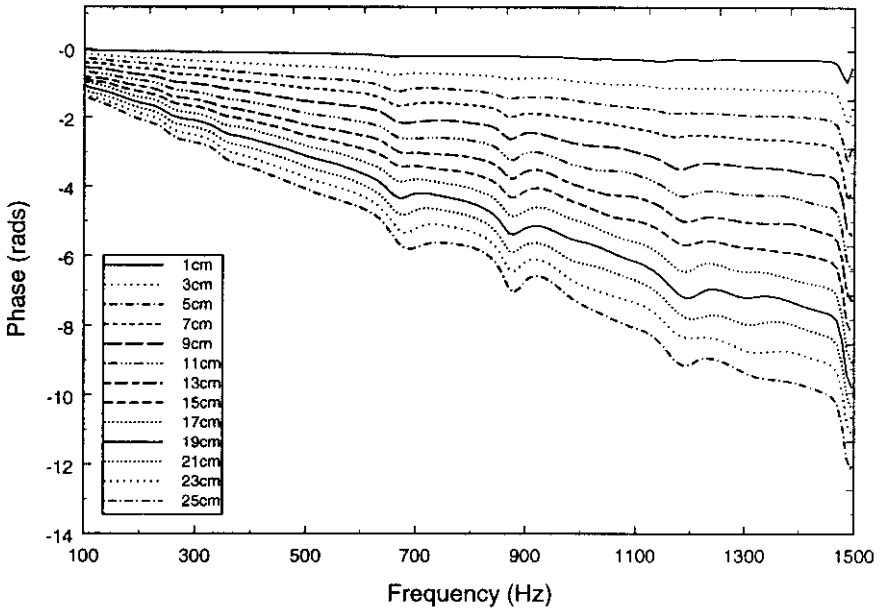

Figure C-20. Measured phase difference at Position A and Angle 3, between the probe microphone at various depths and a reference microphone situated at the sand surface.

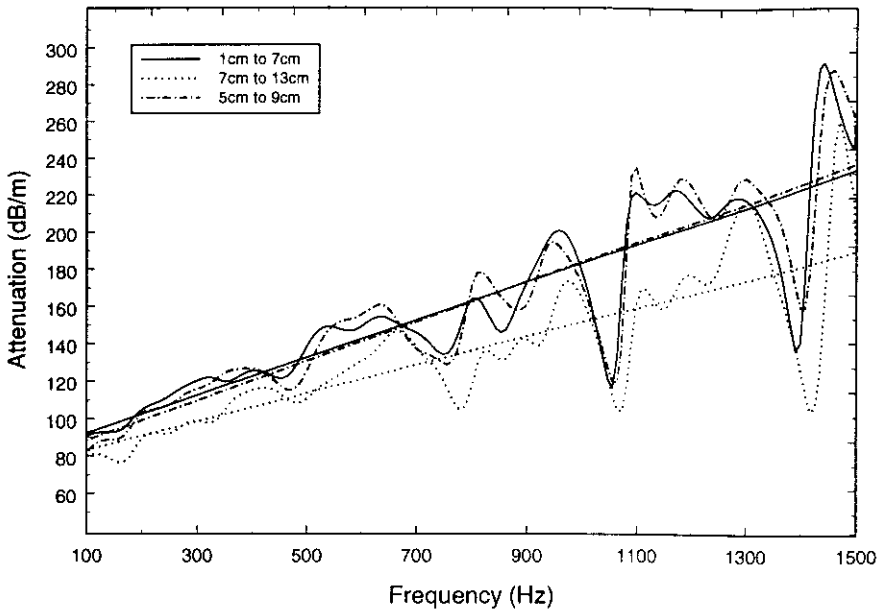

Figure C-21. Calculated attenuation at Position A and Angle 3 over three different depth intervals. Best-fit regression has been applied to the data.

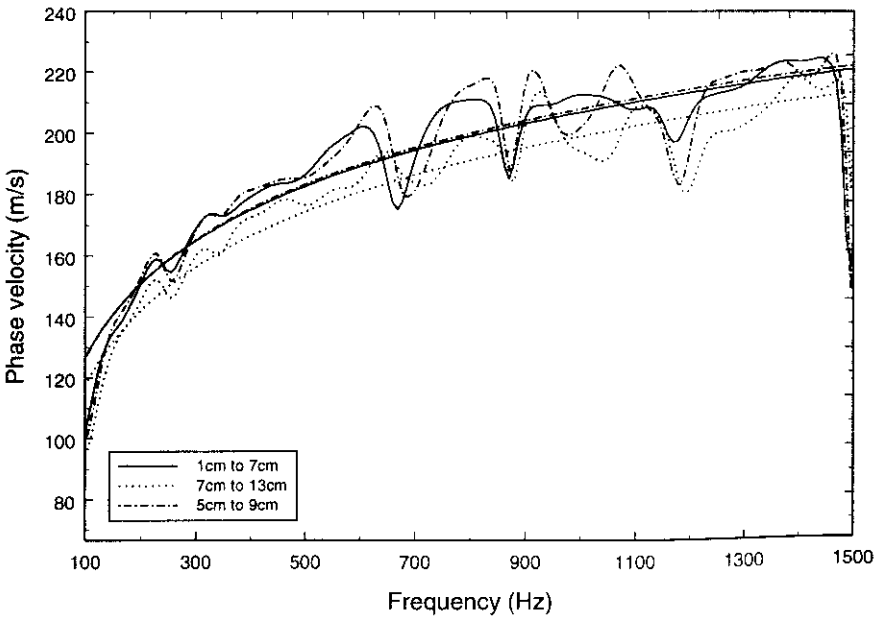

Figure C-22. Calculated phase velocity at Position A and Angle 3, over three different depth intervals. Best-fit regression has been applied to the data.

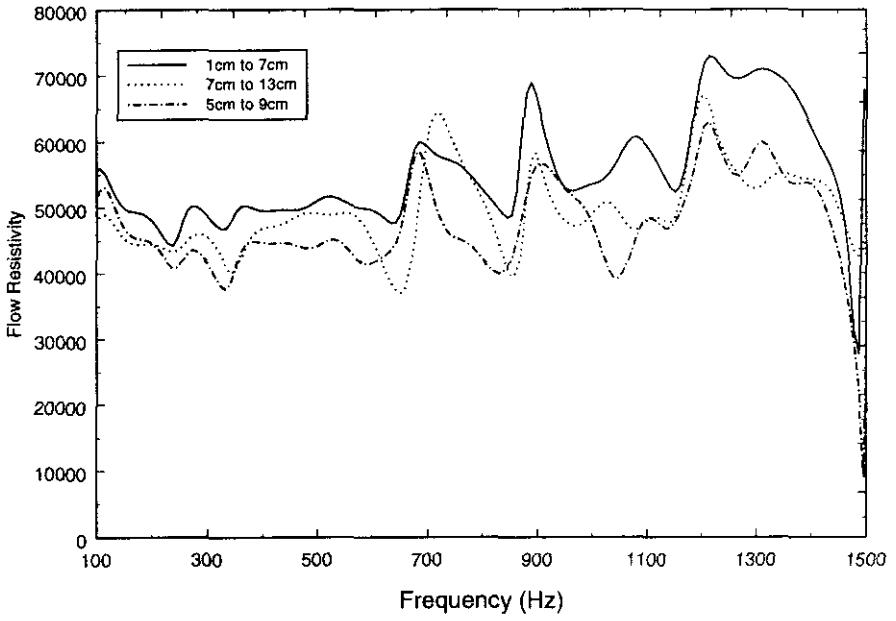

Figure C-23. Calculated flow resistivity at Position A and Angle 3, of the Tank Sand.

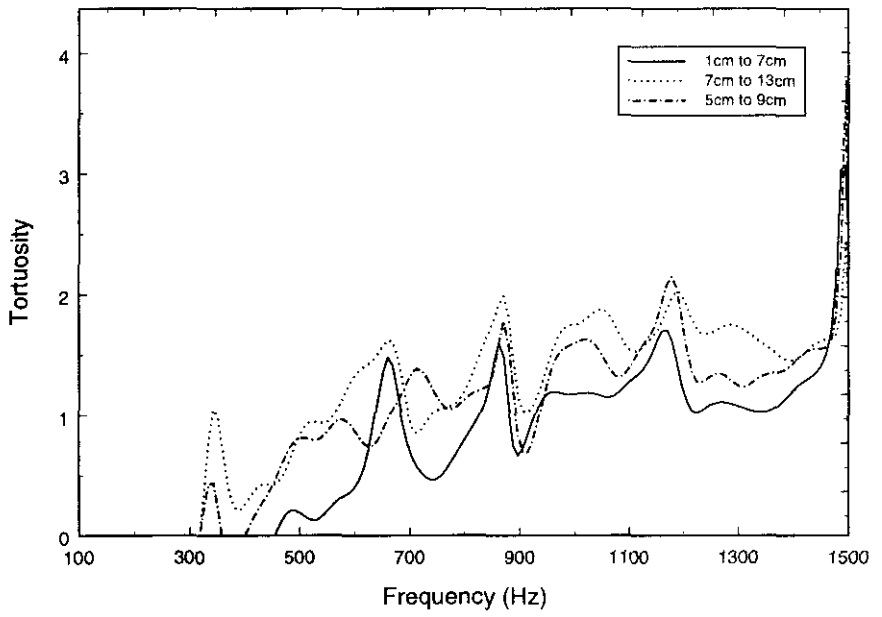

Figure C-24. Calculated tortuosity at Position A and Angle 3, of the Tank Sand.

Appendix D

Acoustic Research Group Test Site

D Contents

Appendix D covers the results from the Acoustic Research Group Test Site, The Open University. It includes:

a) Seismogram from the P-wave seismic refraction survey.

b) Example acoustic-to-seismic coupling ratio spectra and corresponding FFLAGS predictions.

c) Meteorological data taken concurrently with acoustic-to-seismic coupling measurements.

d) Example probe microphone measurements.

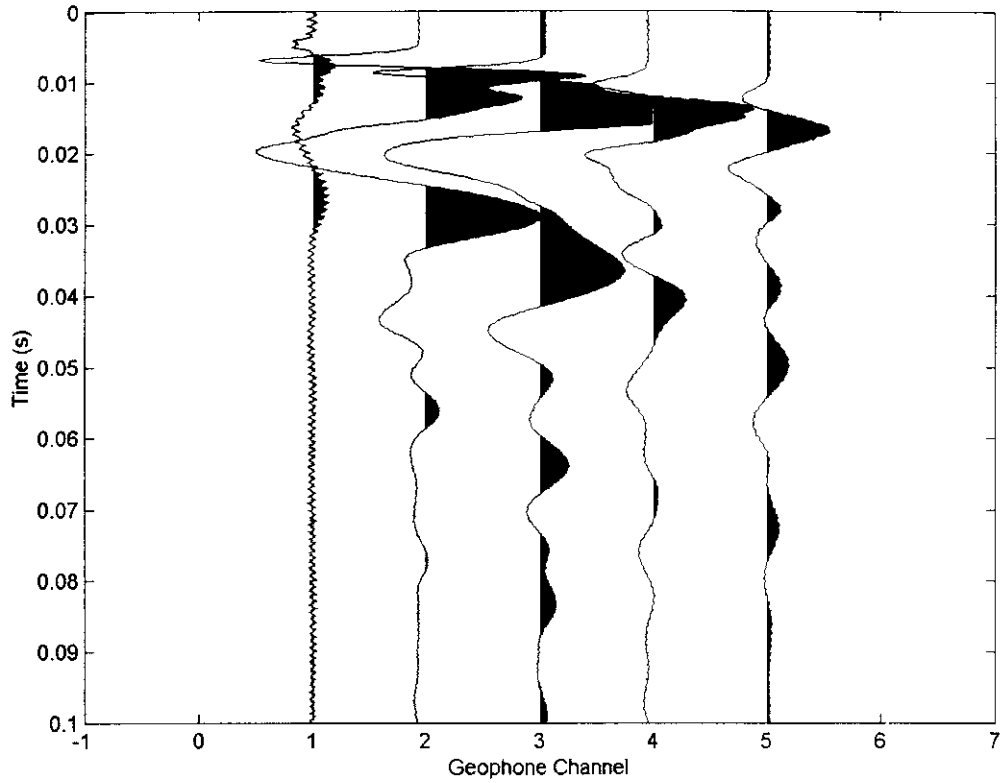

Figure D-1. Seismogram for P-wave survey.

Date	Range	Source Height	Receiver	Temperature	Wind Speed
		Position A			
16-Jul-98	1.0m	0.15	Microphone	21.7	0.959
16-Jul-98	1.0m	0.15	Geophone	21.5	1.300
16-Jul-98	1.0m	0.20	Microphone	20.9	1.470
16-Jul-98	1.0m	0.20	Geophone	20.6	1.420
16-Jul-98	1.0m	0.30	Microphone	20.5	1.740
16-Jul-98	1.0m	0.30	Geophone	20.2	1.270
16-Jul-98	1.0m	0.40	Microphone	20.7	1.090
16-Jul-98	1.0m	0.40	Geophone	20.8	1.280
16-Jul-98	1.0m	0.50	Microphone	20.5	1.290
16-Jul-98	1.0m	0.50	Geophone	19.9	0.685
16-Jul-98	1.0m	0.75	Microphone	19.9	1.430
16-Jul-98	1.0m	0.75	Geophone	20.7	0.837
16-Jul-98	1.0m	0.15	Microphone	19.9	1.430
16-Jul-98	1.0m	0.15	Geophone	19.5	1.630
16-Jul-98	1.0m	0.20	Microphone	20.6	1.080
16-Jul-98	1.0m	0.20	Geophone	20.5	0.833
16-Jul-98	1.0m	0.30	Microphone	19.8	1.240
16-Jul-98	1.0m	0.30	Geophone	19.2	0.925
16-Jul-98	1.0m	0.40	Microphone	19.3	1.360
16-Jul-98	1.0m	0.40	Geophone	19.4	0.832
16-Jul-98	1.0m	0.50	Microphone	19.9	1.320
16-Jul-98	1.0m	0.50	Geophone	19.4	0.961
16-Jul-98	1.0m	0.75	Microphone	19.3	0.745
16-Jul-98	1.0m	0.75	Geophone	19.4	0.581
		Position B			
16-Jul-98	1.0m	0.15	Microphone	19.2	1.080
16-Jul-98	1.0m	0.15	Geophone	18.9	1.240
16-Jul-98	1.0m	0.20	Microphone	18.9	0.751
16-Jul-98	1.0m	0.20	Geophone	18.9	0.695
16-Jul-98	1.0m	0.30	Microphone	18.9	0.864
16-Jul-98	1.0m	0.30	Geophone	18.6	0.474
16-Jul-98	1.0m	0.40	Microphone	18.7	0.697
16-Jul-98	1.0m	0.40	Geophone	18.6	0.860
16-Jul-98	1.0m	0.50	Microphone	18.7	0.461
16-Jul-98	1.0m	0.50	Geophone	18.5	1.350
16-Jul-98	1.0m	0.75	Microphone	18.6	0.526
16-Jul-98	1.0m	0.75	Geophone	18.4	0.685
16-Jul-98	1.0m	0.15	Microphone	18.6	0.369
16-Jul-98	1.0m	0.15	Geophone	18.8	1.730
16-Jul-98	1.0m	0.20	Microphone	18.6	1.310
16-Jul-98	1.0m	0.20	Geophone	18.7	0.804
16-Jul-98	1.0m	0.30	Microphone	18.5	0.729
16-Jul-98	1.0m	0.30	Geophone	18.6	0.781
16-Jul-98	1.0m	0.40	Microphone	18.4	0.691
16-Jul-98	1.0m	0.40	Geophone	18.6	0.665
16-Jul-98	1.0m	0.50	Microphone	18.3	0.934
16-Jul-98	1.0m	0.50	Geophone	18.4	1.080
16-Jul-98	1.0m	0.75	Microphone	18.4	0.960
16-Jul-98	1.0m	0.75	Geophone	18.2	1.170

Table D-1. Meteorological data for the acoustic-to-seismic coupling ratio measurements taken at the ARG test site.

Date	Range	Source Height	Receiver	Temperature	Wind Speed
		Position A			
02-Aug-98	1.0m	0.15	Microphone	30.2	0.836
02-Aug-98	1.0m	0.15	Geophone	28.4	1.440
02-Aug-98	1.0m	0.20	Microphone	27.5	1.980
02-Aug-98	1.0m	0.20	Geophone	28.0	1.540
02-Aug-98	1.0m	0.30	Microphone	28.5	1.540
02-Aug-98	1.0m	0.30	Geophone	28.0	1.900
02-Aug-98	1.0m	0.40	Microphone	28.4	1.140
02-Aug-98	1.0m	0.40	Geophone	29.2	0.871
02-Aug-98	1.0m	0.50	Microphone	30.3	0.869
02-Aug-98	1.0m	0.50	Geophone	31.4	0.689
02-Aug-98	1.0m	0.75	Microphone	30.5	0.937
02-Aug-98	1.0m	0.75	Geophone	30.8	0.937
02-Aug-98	1.0m	0.15	Microphone	30.7	0.992
02-Aug-98	1.0m	0.15	Geophone	30.4	0.883
02-Aug-98	1.0m	0.20	Microphone	28.5	1.720
02-Aug-98	1.0m	0.20	Geophone	29.0	1.200
02-Aug-98	1.0m	0.30	Microphone	29.8	1.110
02-Aug-98	1.0m	0.30	Geophone	31.2	0.562
02-Aug-98	1.0m	0.40	Microphone	32.0	0.617
02-Aug-98	1.0m	0.40	Geophone	29.9	1.180
02-Aug-98	1.0m	0.50	Microphone	30.1	0.883
02-Aug-98	1.0m	0.50	Geophone	31.1	0.650
02-Aug-98	1.0m	0.75	Microphone	30.0	0.820
02-Aug-98	1.0m	0.75	Geophone	30.9	0.683
		Position B			
02-Aug-98	1.0m	0.15	Microphone	29.8	0.946
02-Aug-98	1.0m	0.15	Geophone	31	0.555
02-Aug-98	1.0m	0.20	Microphone	31.7	0.459
02-Aug-98	1.0m	0.20	Geophone	32.6	0.518
02-Aug-98	1.0m	0.30	Microphone	30.4	0.860
02-Aug-98	1.0m	0.30	Geophone	32.1	0.689
02-Aug-98	1.0m	0.40	Microphone	28.7	1.160
02-Aug-98	1.0m	0.40	Geophone	30.3	0.699
02-Aug-98	1.0m	0.50	Microphone	30.3	0.728
02-Aug-98	1.0m	0.50	Geophone	28.6	1.300
02-Aug-98	1.0m	0.75	Microphone	28.5	1.120
02-Aug-98	1.0m	0.75	Geophone	29.8	0.775
02-Aug-98	1.0m	0.15	Microphone	31.7	0.359
02-Aug-98	1.0m	0.15	Geophone	31.8	0.587
02-Aug-98	1.0m	0.20	Microphone	30.1	0.892
02-Aug-98	1.0m	0.20	Geophone	30.2	0.817
02-Aug-98	1.0m	0.30	Microphone	29.5	0.586
02-Aug-98	1.0m	0.30	Geophone	30	0.519
02-Aug-98	1.0m	0.40	Microphone	30.5	0.577
02-Aug-98	1.0m	0.40	Geophone	32.1	0.290
02-Aug-98	1.0m	0.50	Microphone	33.4	0.424
02-Aug-98	1.0m	0.50	Geophone	28.9	1.170
02-Aug-98	1.0m	0.75	Microphone	30.7	0.676
02-Aug-98	1.0m	0.75	Geophone	29.6	0.853

Table D-2. Meteorological data for the acoustic-to-seismic coupling ratio measurements taken at the ARG test site.

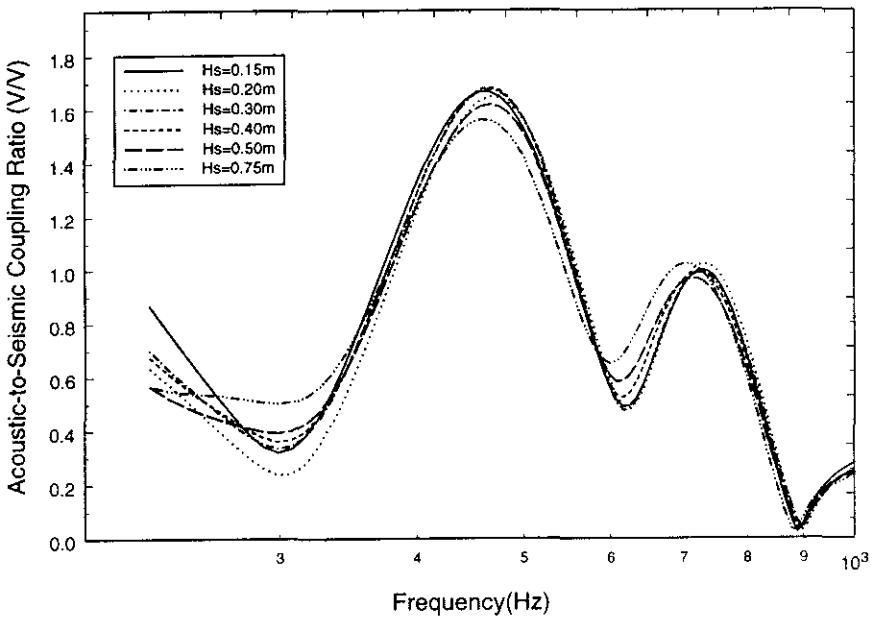

Figure D-2. Variation in acoustic-to-seismic coupling ratio with varying source height. Data taken at time T1 (Position A) and Range =2.0m.

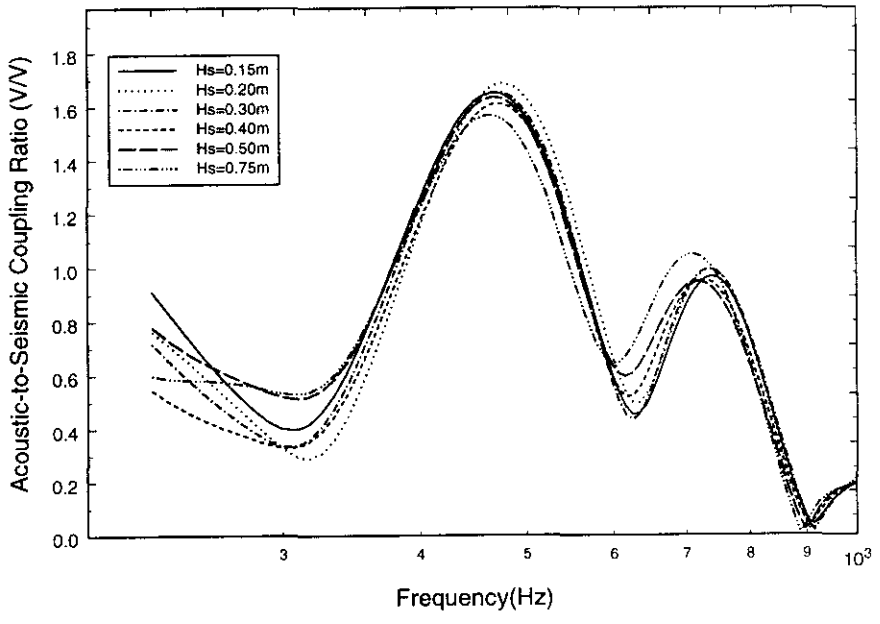

Figure D-3. Variation in acoustic-to-seismic coupling ratio with varying source height. Data taken at time T1+30 (Position A) and Range =2.0m.

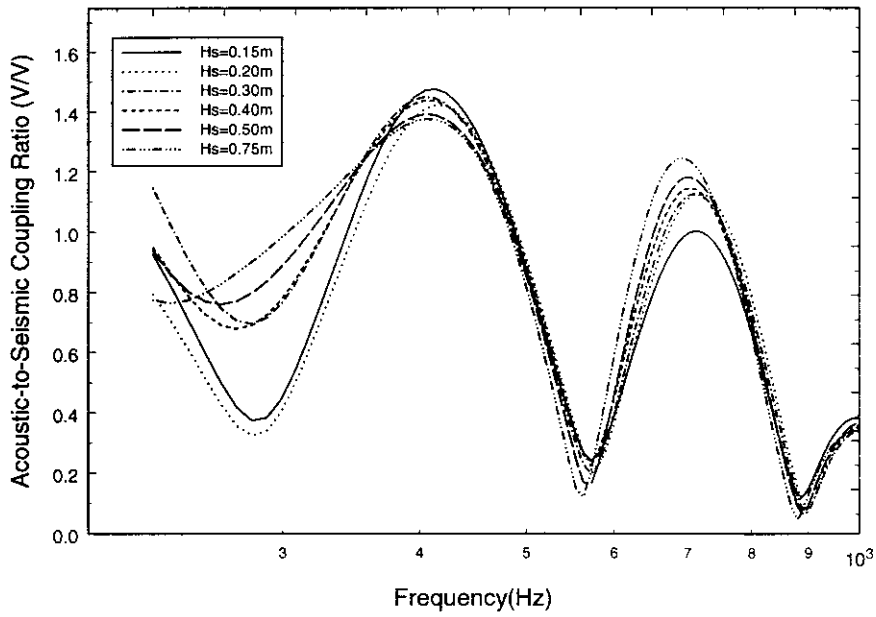

Figure D-4. Variation in acoustic-to-seismic coupling ratio with varying source height. Data taken at time T1 (Position B) and Range =2.0m.

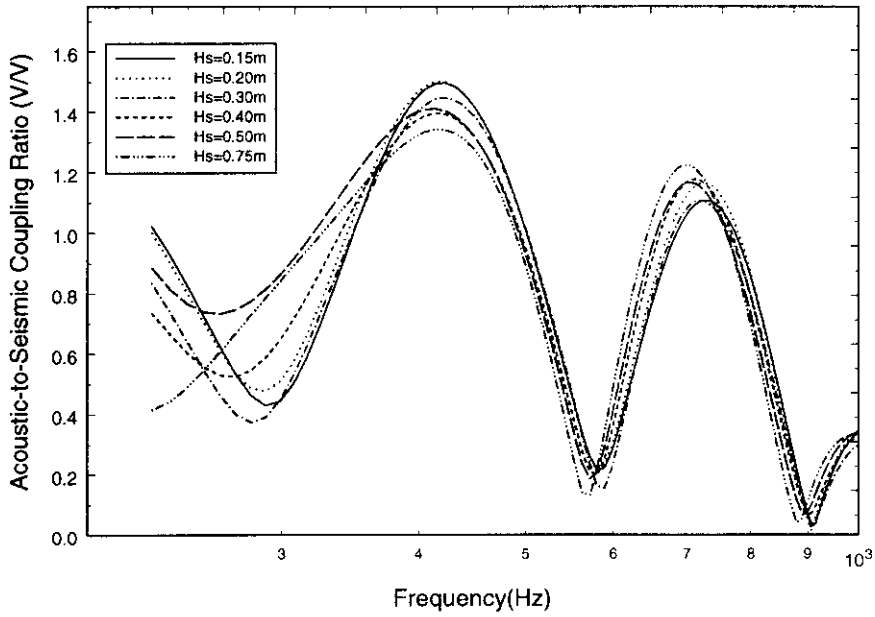

Figure D-5. Variation in acoustic-to-seismic coupling ratio with varying source height. Data taken at time T1+30 (Position B) and Range =2.0m.

Date	Range	Source Height	Receiver	Temperature	Wind Speed
		Position A			
26-Jul-98	2.0m	0.15	Microphone	21.9	0.438
26-Jul-98	2.0m	0.15	Geophone	20.9	1.040
26-Jul-98	2.0m	0.20	Microphone	21.3	0.650
26-Jul-98	2.0m	0.20	Geophone	22.5	0.441
26-Jul-98	2.0m	0.30	Microphone	23.4	0.535
26-Jul-98	2.0m	0.30	Geophone	21.5	1.120
26-Jul-98	2.0m	0.40	Microphone	22.8	1.070
26-Jul-98	2.0m	0.40	Geophone	22.8	0.956
26-Jul-98	2.0m	0.50	Microphone	22.7	0.904
26-Jul-98	2.0m	0.50	Geophone	22.8	0.418
26-Jul-98	2.0m	0.75	Microphone	20.9	1.840
26-Jul-98	2.0m	0.75	Geophone	20.2	1.640
26-Jul-98	2.0m	0.15	Microphone	22.0	0.916
26-Jul-98	2.0m	0.15	Geophone	21.0	0.790
26-Jul-98	2.0m	0.20	Microphone	21.7	0.957
26-Jul-98	2.0m	0.20	Geophone	20.6	1.360
26-Jul-98	2.0m	0.30	Microphone	23.1	0.629
26-Jul-98	2.0m	0.30	Geophone	23.5	0.605
26-Jul-98	2.0m	0.40	Microphone	23.2	0.866
26-Jul-98	2.0m	0.40	Geophone	22.8	1.440
26-Jul-98	2.0m	0.50	Microphone	23.5	0.854
26-Jul-98	2.0m	0.50	Geophone	22.0	1.260
26-Jul-98	2.0m	0.75	Microphone	22.2	1.010
26-Jul-98	2.0m	0.75	Geophone	21.8	0.316
		Position B			
26-Jul-98	2.0m	0.15	Microphone	22.0	0.922
26-Jul-98	2.0m	0.15	Geophone	22.1	0.546
26-Jul-98	2.0m	0.20	Microphone	22.8	0.565
26-Jul-98	2.0m	0.20	Geophone	23.5	0.786
26-Jul-98	2.0m	0.30	Microphone	23.8	0.908
26-Jul-98	2.0m	0.30	Geophone	23.0	0.822
26-Jul-98	2.0m	0.40	Microphone	22.9	1.100
26-Jul-98	2.0m	0.40	Geophone	22.7	0.871
26-Jul-98	2.0m	0.50	Microphone	23.4	0.730
26-Jul-98	2.0m	0.50	Geophone	21.9	0.967
26-Jul-98	2.0m	0.75	Microphone	20.5	1.030
26-Jul-98	2.0m	0.75	Geophone	21.4	0.639
26-Jul-98	2.0m	0.15	Microphone	21.2	0.936
26-Jul-98	2.0m	0.15	Geophone	24.2	0.245
26-Jul-98	2.0m	0.20	Microphone	26.2	0.363
26-Jul-98	2.0m	0.20	Geophone	22.7	0.565
26-Jul-98	2.0m	0.30	Microphone	25.6	0.293
26-Jul-98	2.0m	0.30	Geophone	23.1	0.916
26-Jul-98	2.0m	0.40	Microphone	25.3	0.577
26-Jul-98	2.0m	0.40	Geophone	23.0	0.878
26-Jul-98	2.0m	0.50	Microphone	22.5	0.611
26-Jul-98	2.0m	0.50	Geophone	21.6	1.240
26-Jul-98	2.0m	0.75	Microphone	21.5	1.380
26-Jul-98	2.0m	0.75	Geophone	22.1	0.834

Table D-3. Meteorological data for the acoustic-to-seismic coupling ratio measurements shown in Figure D-2 to Figure D-5 taken at the ARG test site.

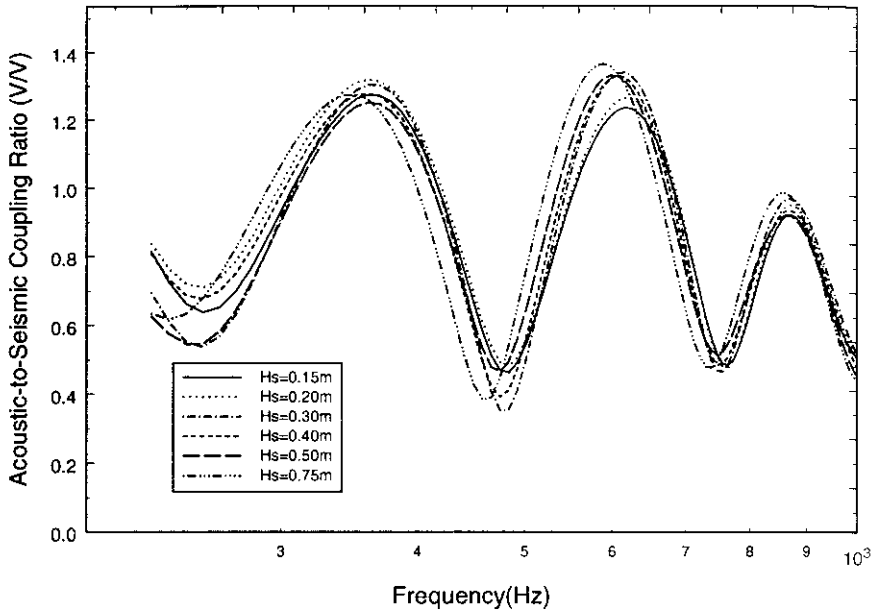

Figure D-6. Variation in acoustic-to-seismic coupling ratio with varying source height. Data taken at time T1 (Position A) and Range =3.0m.

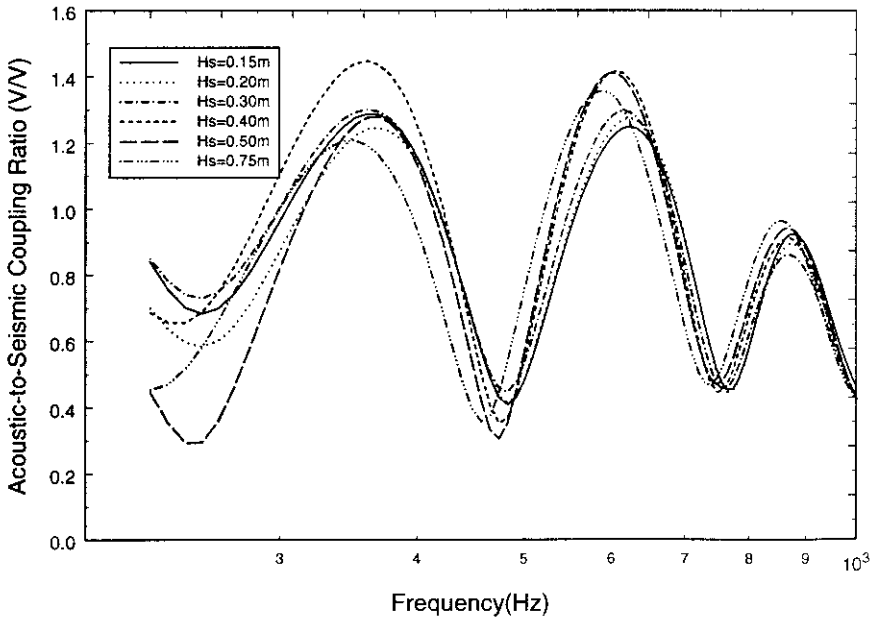

Figure D-7. Variation in acoustic-to-seismic coupling ratio with varying source height. Data taken at time T1+30 (Position A) and Range =3.0m.

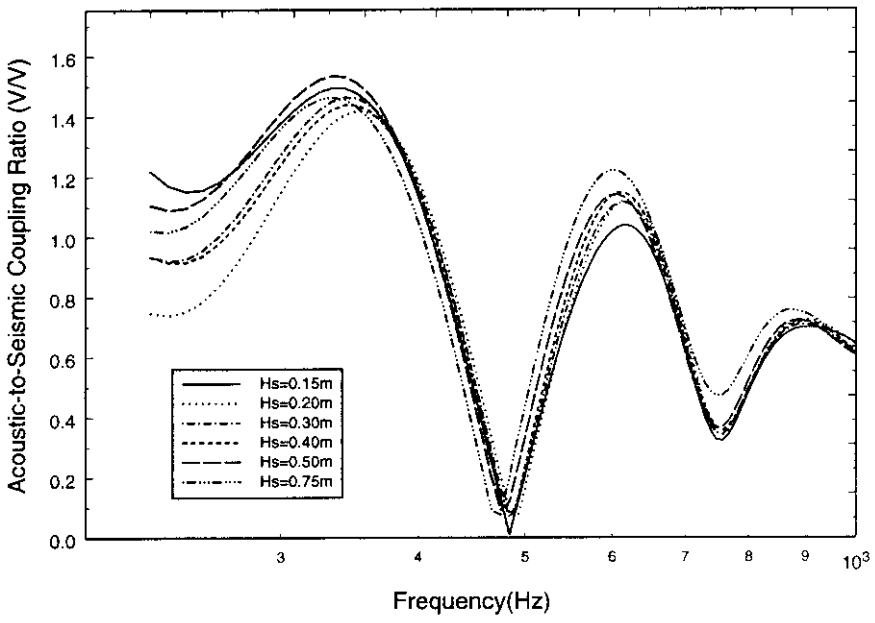

Figure D-8. Variation in acoustic-to-seismic coupling ratio with varying source height. Data taken at time T1 (Position B) and Range =3.0m.

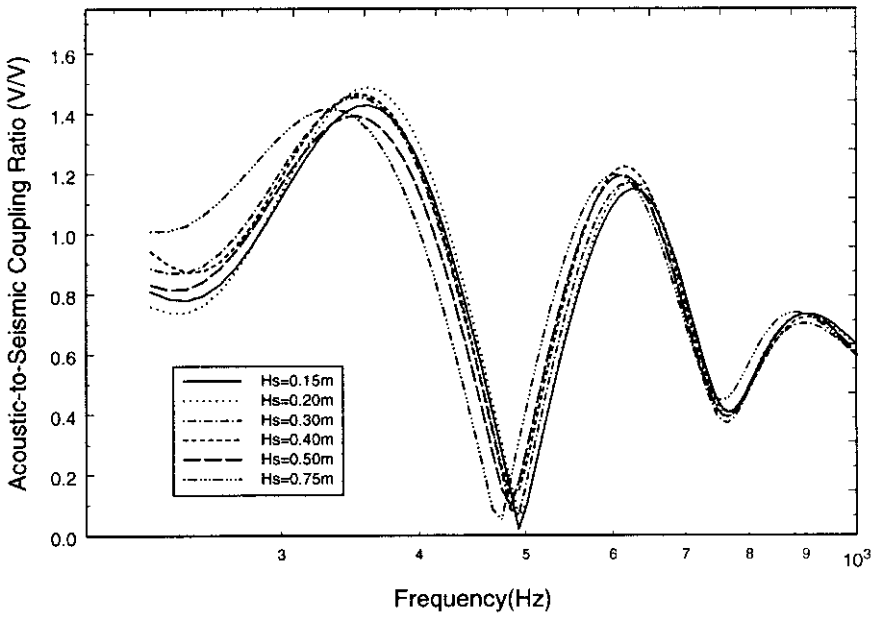

Figure D-9. Variation in acoustic-to-seismic coupling ratio with varying source height. Data taken at time T1+30 (Position B) and Range =3.0m.

Date	Range	Source Height	Receiver	Temperature	Wind Speed
		Position A			
28-Jul-98	3.0m	0.15	Microphone	18.9	1.270
28-Jul-98	3.0m	0.15	Geophone	18.8	1.200
28-Jul-98	3.0m	0.20	Microphone	18.5	1.300
28-Jul-98	3.0m	0.20	Geophone	18.7	1.310
28-Jul-98	3.0m	0.30	Microphone	18.4	1.130
28-Jul-98	3.0m	0.30	Geophone	18.4	1.130
28-Jul-98	3.0m	0.40	Microphone	17.7	1.190
28-Jul-98	3.0m	0.40	Geophone	18.7	1.160
28-Jul-98	3.0m	0.50	Microphone	18.6	1.430
28-Jul-98	3.0m	0.50	Geophone	18.5	1.440
28-Jul-98	3.0m	0.75	Microphone	18.2	2.340
28-Jul-98	3.0m	0.75	Geophone	18.0	2.290
28-Jul-98	3.0m	0.15	Microphone	18.5	1.430
28-Jul-98	3.0m	0.15	Geophone	18.3	1.730
28-Jul-98	3.0m	0.20	Microphone	18.2	2.700
28-Jul-98	3.0m	0.20	Geophone	18.2	2.610
28-Jul-98	3.0m	0.30	Microphone	18.3	1.930
28-Jul-98	3.0m	0.30	Geophone	18.4	2.090
28-Jul-98	3.0m	0.40	Microphone	18.4	2.020
28-Jul-98	3.0m	0.40	Geophone	18.6	1.930
28-Jul-98	3.0m	0.50	Microphone	18.5	2.210
28-Jul-98	3.0m	0.50	Geophone	18.5	2.500
28-Jul-98	3.0m	0.75	Microphone	18.6	1.670
28-Jul-98	3.0m	0.75	Geophone	18.5	1.910
		Position B			
28-Jul-98	3.0m	0.15	Microphone	18.5	2.130
28-Jul-98	3.0m	0.15	Geophone	18.4	1.880
28-Jul-98	3.0m	0.20	Microphone	18.2	2.210
28-Jul-98	3.0m	0.20	Geophone	18.1	2.150
28-Jul-98	3.0m	0.30	Microphone	18.4	2.080
28-Jul-98	3.0m	0.30	Geophone	18.3	2.090
28-Jul-98	3.0m	0.40	Microphone	18.3	1.940
28-Jul-98	3.0m	0.40	Geophone	18.4	1.960
28-Jul-98	3.0m	0.50	Microphone	18.5	1.390
28-Jul-98	3.0m	0.50	Geophone	18.2	2.090
28-Jul-98	3.0m	0.75	Microphone	18.3	1.770
28-Jul-98	3.0m	0.75	Geophone	18.3	1.370
28-Jul-98	3.0m	0.15	Microphone	18.2	2.150
28-Jul-98	3.0m	0.15	Geophone	18.1	2.010
28-Jul-98	3.0m	0.20	Microphone	18.0	2.670
28-Jul-98	3.0m	0.20	Geophone	17.9	2.380
28-Jul-98	3.0m	0.30	Microphone	17.9	2.650
28-Jul-98	3.0m	0.30	Geophone	18.1	1.990
28-Jul-98	3.0m	0.40	Microphone	18.1	1.830
28-Jul-98	3.0m	0.40	Geophone	18.1	1.953
28-Jul-98	3.0m	0.50	Microphone	18.1	1.920
28-Jul-98	3.0m	0.50	Geophone	18.0	2.410
28-Jul-98	3.0m	0.75	Microphone	18.1	2.620
28-Jul-98	3.0m	0.75	Geophone	18.0	2.600

Table D-4. Meteorological data for the acoustic-to-seismic coupling ratio measurements shown in Figure D-6 to Figure D-9 taken at the ARG test site.

	Layer		Substrate
P-wave speed (m/s)	Hs=0.20m	360	650
	Hs=0.30m	360	
	Hs=0.40m	360	
	Hs=0.50m	360	
S-wave speed (m/s)	Hs=0.20m	180	330
	Hs=0.30m	175	
	Hs=0.40m	175	
	Hs=0.50m	175	
Flow resistivity (Pa sm^{-2})	2000		36000000
Porosity	0.46		0.0046
Grain shape factor	0.5		0.5
Soil density (kg/m^3)	1700.0		2650.0
Layer thickness (m)	3.0		∞
Attenuation (V_p)	0.02		0.02
Attenuation (V_s)	0.01		0.01
Dynamic viscosity of air (Nsm^{-2})	1.81×10^{-5}		
Microphone height (m)	0.05		
Geophone depth (m)	-0.05		
Frequency range (Hz)	150 – 1000		
Speed of sound in air	344.0		
Coupling Resonant Frequency (Hz)	Hs=0.20m	452	
	Hs=0.30m	492	
	Hs=0.40m	443	
	Hs=0.50m	479	
Geophone Sensitivity (measured) (V / m/s)	Hs=0.20m	26	
	Hs=0.30m	26	
	Hs=0.40m	25	
	Hs=0.50m	26	
Microphone Sensitivity (measured) (V / Pa)	Hs=0.20m	13.4e-3	
	Hs=0.30m	13.4e-3	
	Hs=0.40m	13.4e-3	
	Hs=0.50m	13.4e-3	

Table D-5. Parameters used to predict the acoustic-to-seismic coupling ratio measurements taken at a range of 2m at the ARG test site.

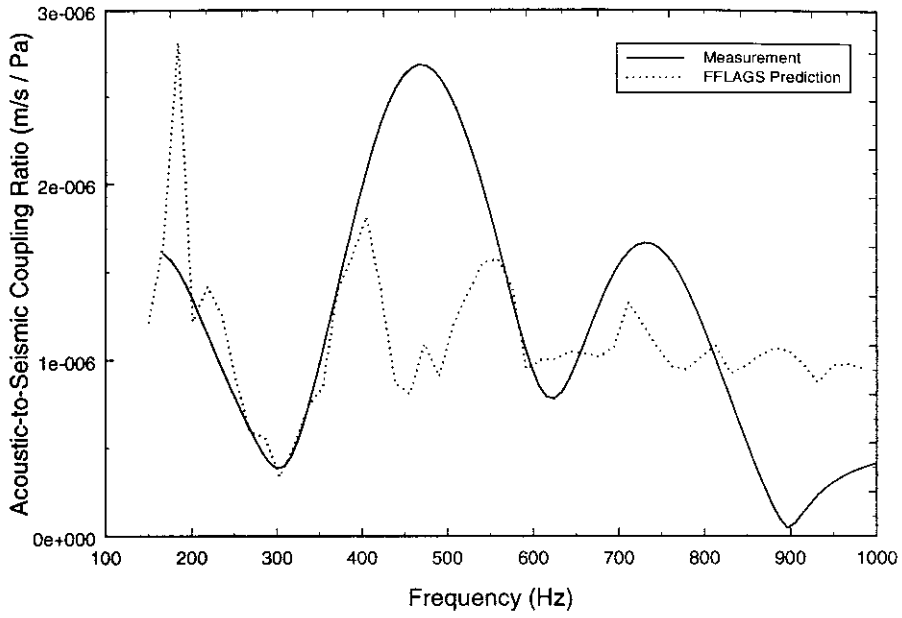

Figure D-10. Measured acoustic-to-seismic coupling ratio and FFLAGS prediction taken at the ARG test site (Range=2.0m, Hs=0.20m and f_0=452Hz).

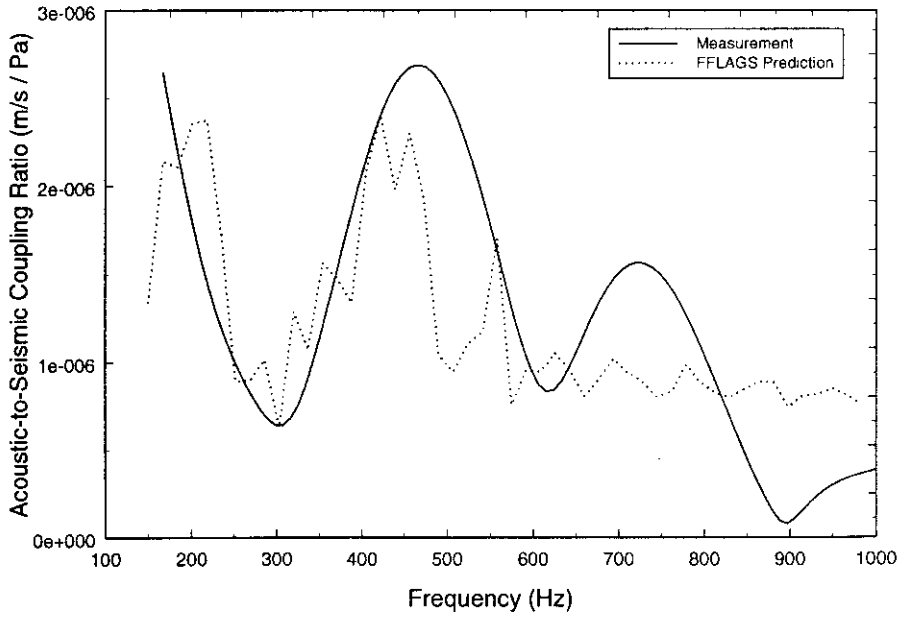

Figure D-11. Measured acoustic-to-seismic coupling ratio and FFLAGS prediction taken at the ARG test site (Range=2.0m, Hs=0.30m and f_0=492Hz).

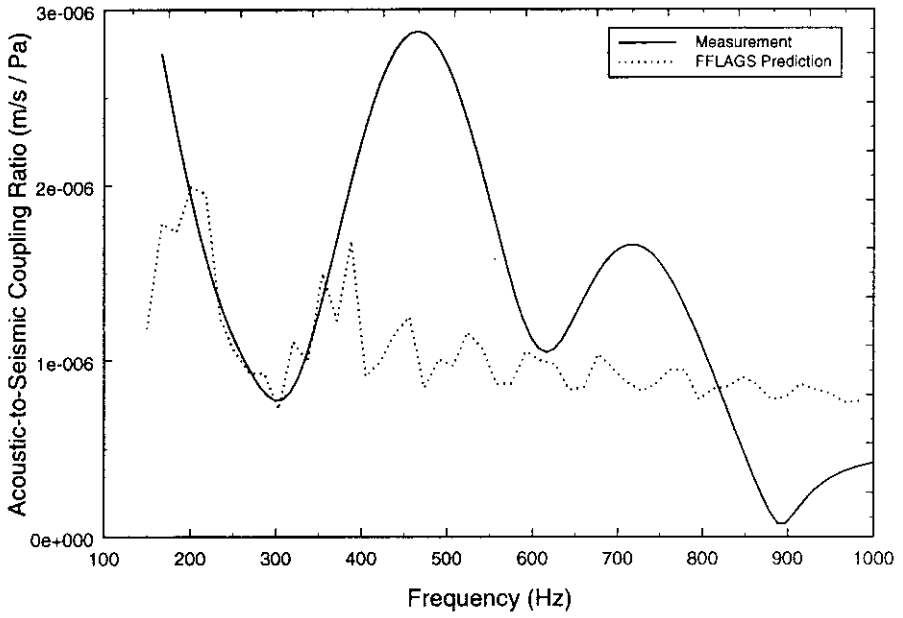

Figure D-12. Measured acoustic-to-seismic coupling ratio and FFLAGS prediction taken at the ARG test site (Range=2.0m, Hs=0.40m and f_0=443Hz).

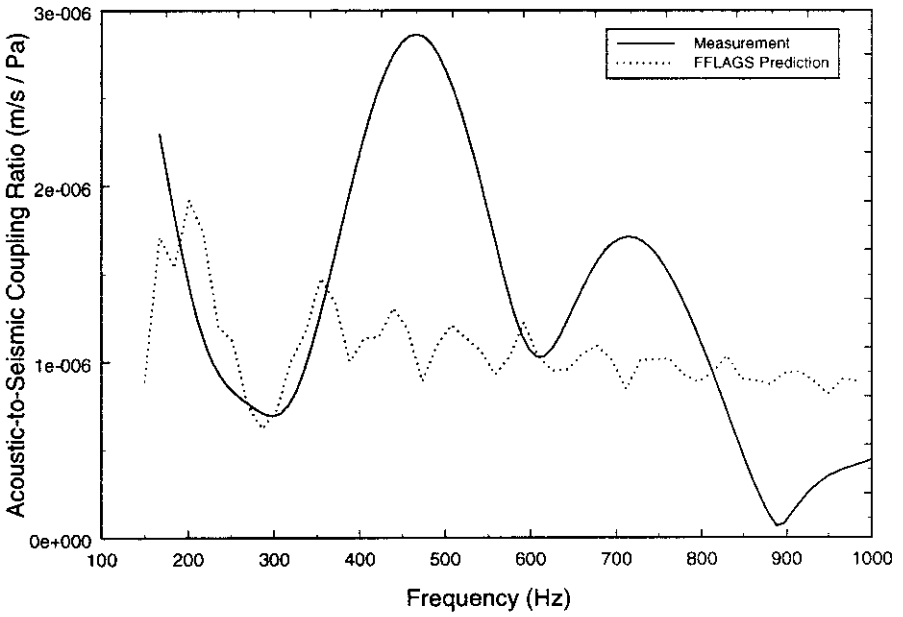

Figure D-13. Measured acoustic-to-seismic coupling ratio and FFLAGS prediction taken at the ARG test site (Range=2.0m, Hs=0.50m and f_0=479Hz).

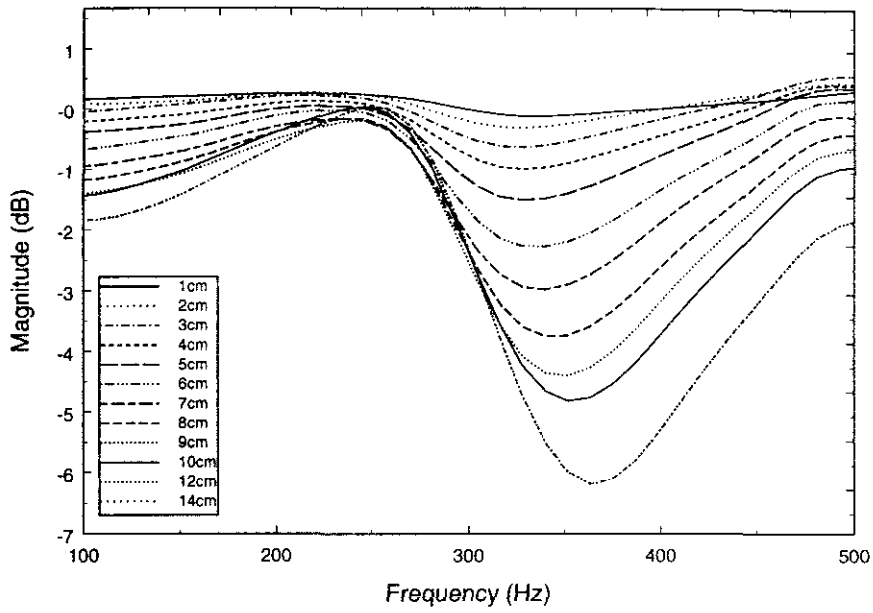

Figure D-14. Measured relative magnitude between the probe microphone at various depths and a reference microphone situated at the gravel surface.

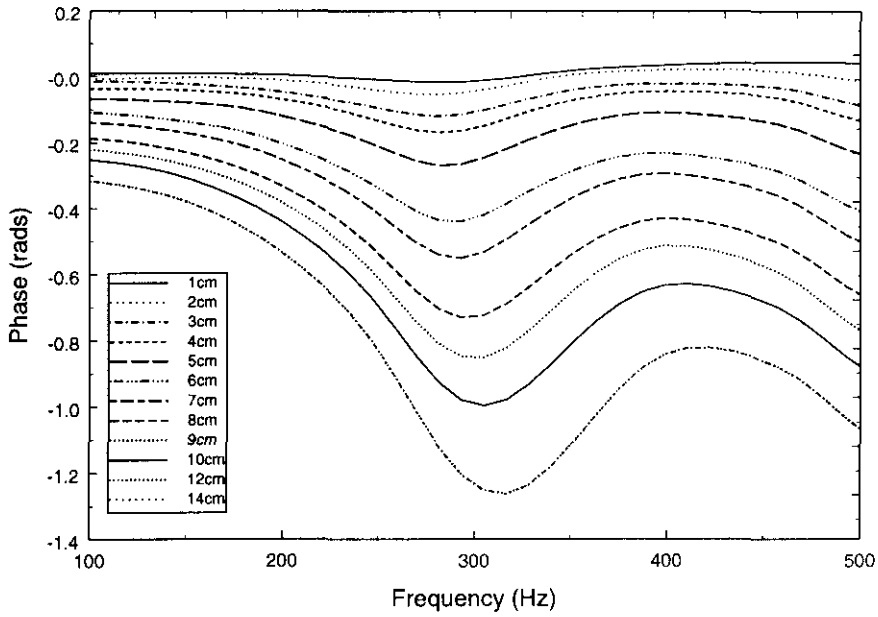

Figure D-15. Measured phase difference between the probe microphone at various depths and a reference microphone situated at the gravel surface.

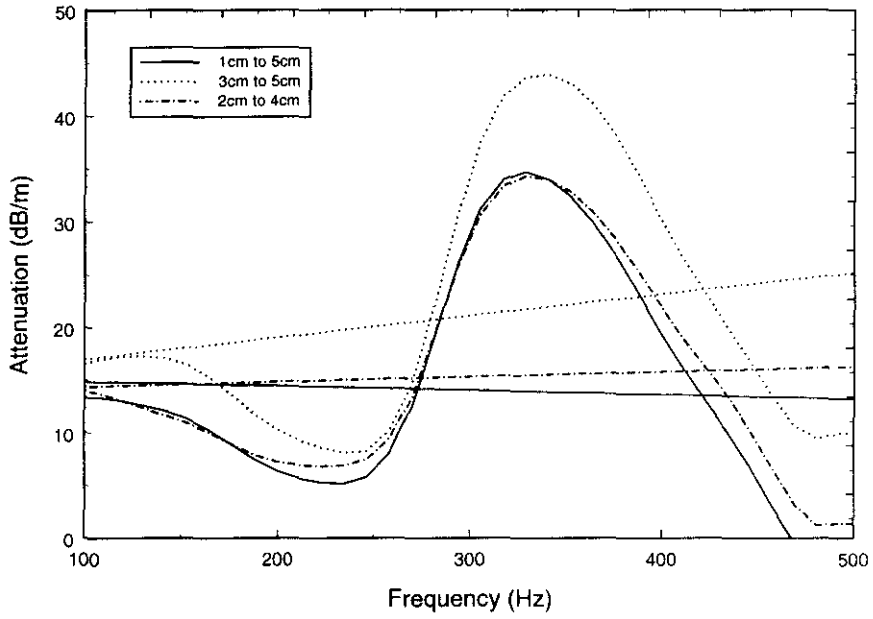

Figure D-16. Calculated attenuation over three different depth intervals. Best-fit regression has been applied to the data.

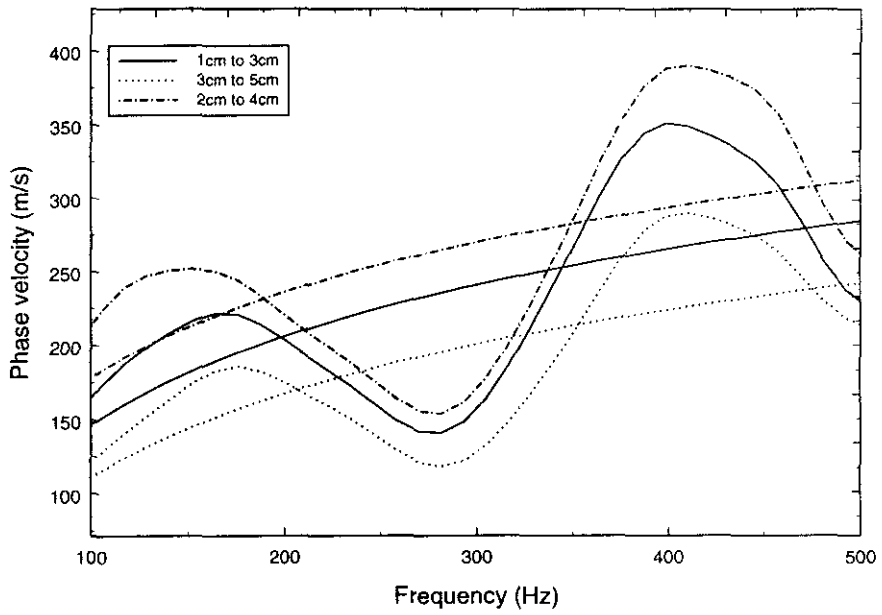

Figure D-17. Calculated phase velocity over three different depth intervals. Best-fit regression has been applied to the data.

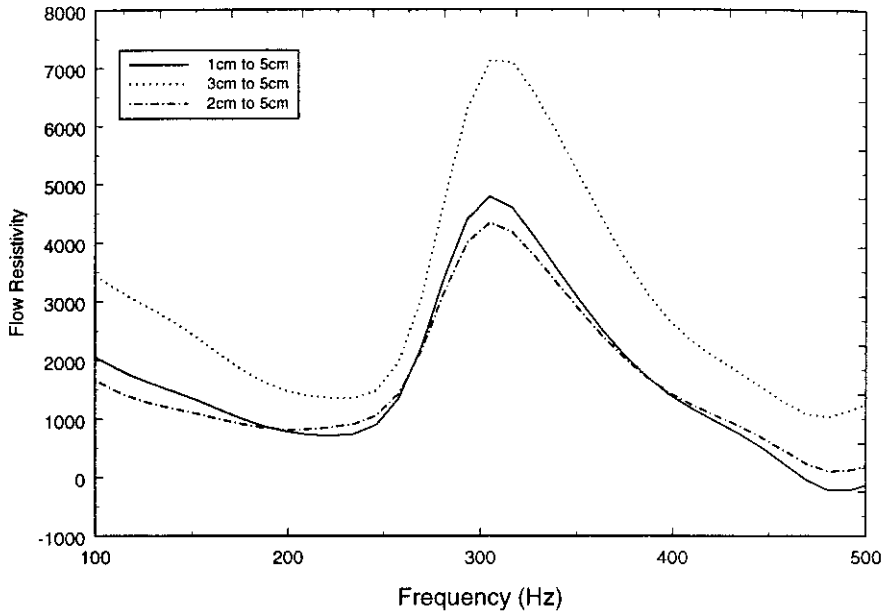

Figure D-18. Calculated flow resistivity of the ARG test site gravel.

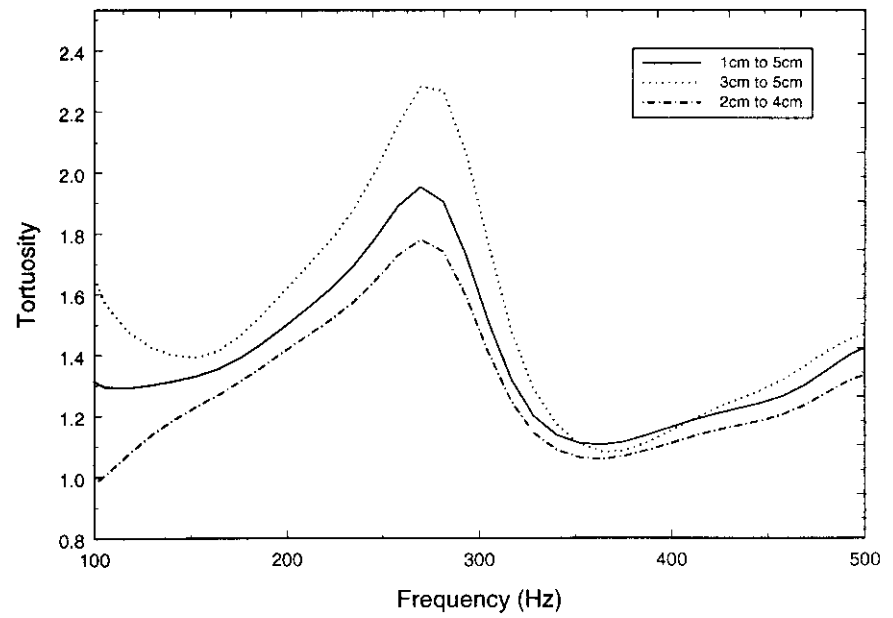

Figure D-19. Calculated tortuosity of the ARG test site gravel.

Appendix E

HMC Stone Lane Quarry, Heath and Reach

E Contents

Appendix E covers the results from HMC Stone Lane Quarry, Heath and Reach. It includes:

a) Seismograms from the P- and S-wave seismic refraction surveys.

b) Example acoustic-to-seismic coupling ratio spectra and corresponding FFLAGS predictions.

c) Meteorological data taken concurrently with acoustic-to-seismic coupling measurements.

d) Example probe microphone measurements

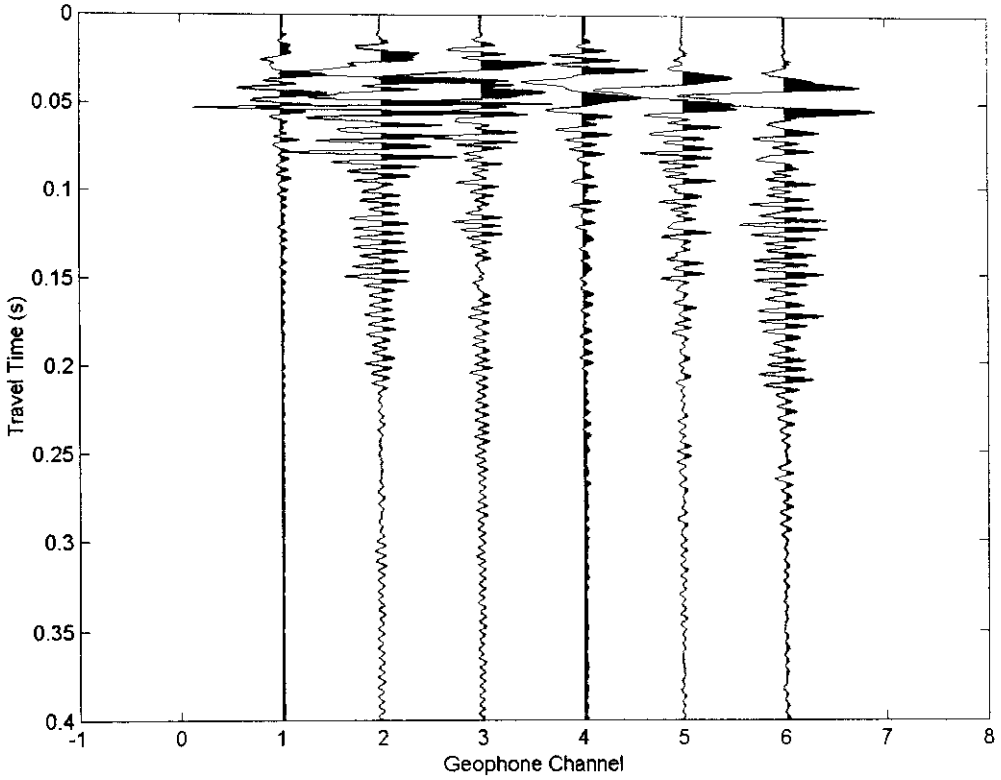

Figure E-1. Seismogram for P-wave survey (forward shot).

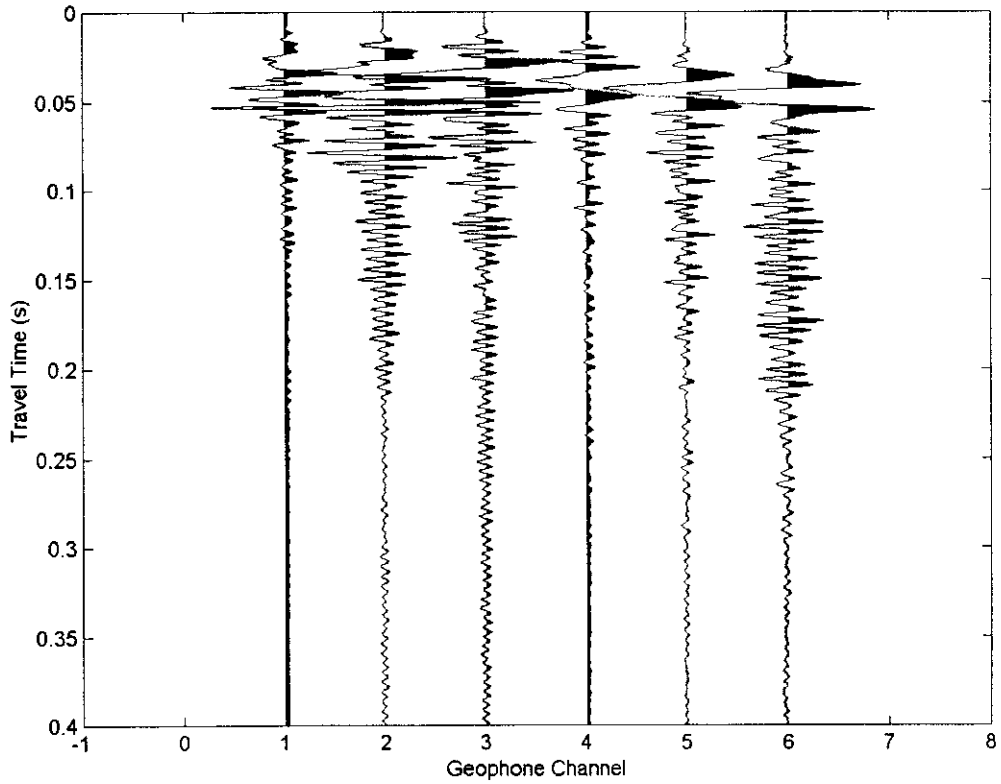

Figure E-2. Seismogram for P-wave survey (reverse shot).

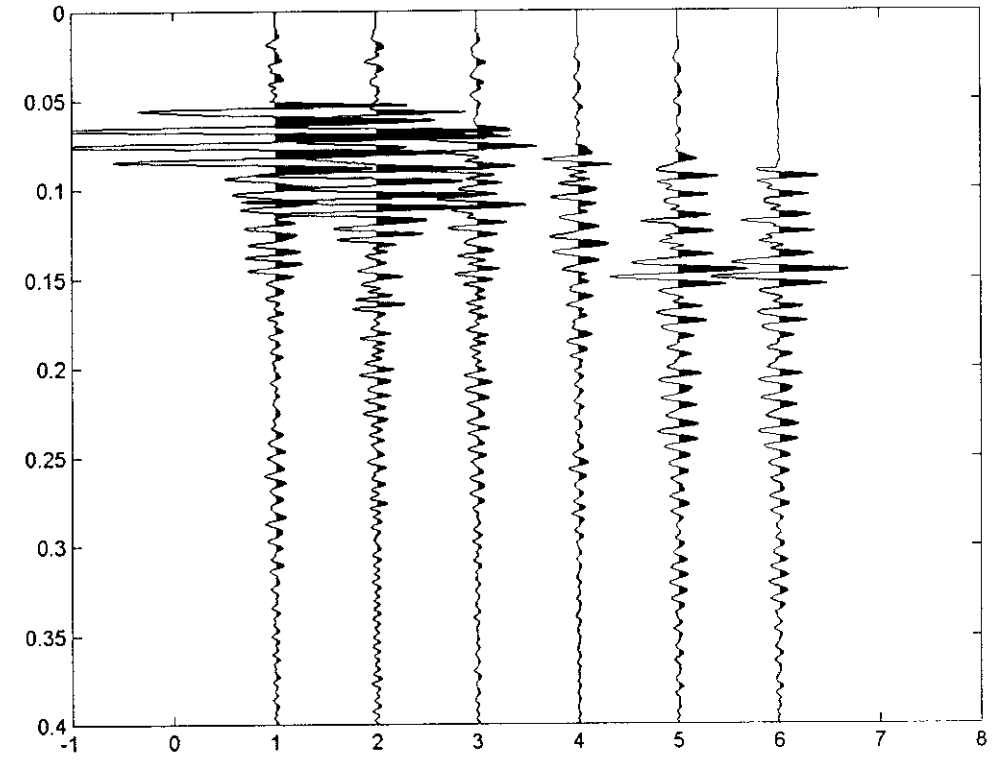

Figure E-3. Seismogram for S-wave survey (forward shot).

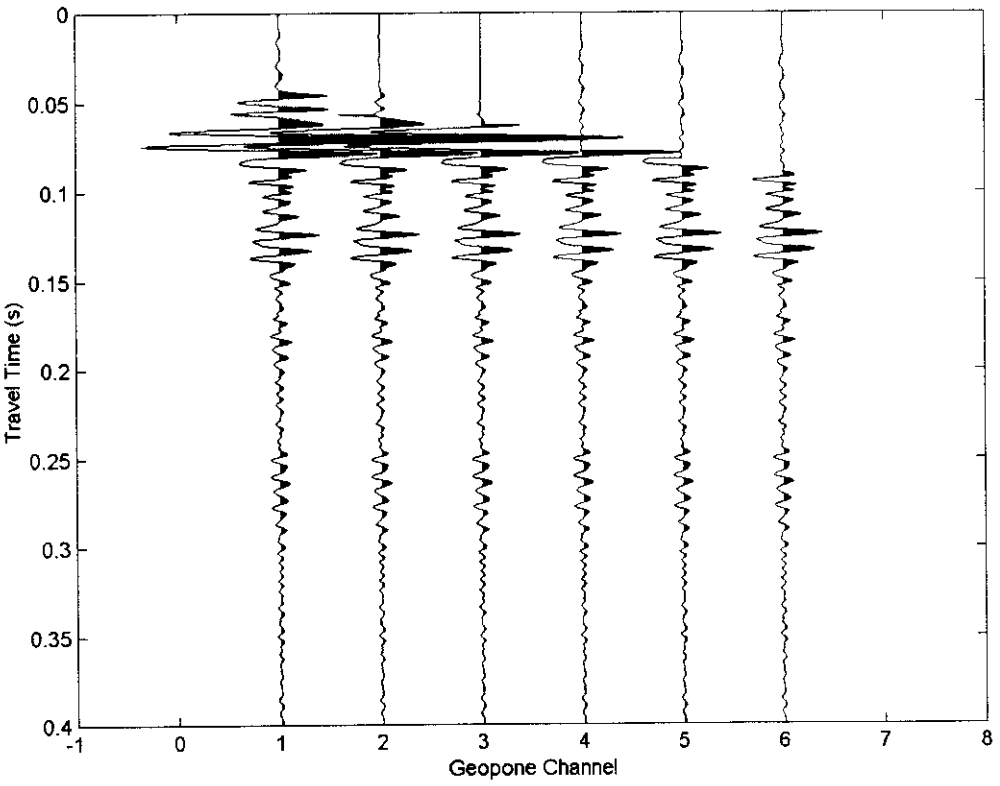

Figure E-4. Seismogram for S-wave survey (reverse shot).

Date	Range	Source Height	Receiver	Temperature	Wind Speed
		Position A			
10-Aug-98	1.0m	0.15	Microphone	29.9	1.650
10-Aug-98	1.0m	0.15	Geophone	29.8	1.740
10-Aug-98	1.0m	0.20	Microphone	30.0	1.590
10-Aug-98	1.0m	0.20	Geophone	30.2	1.430
10-Aug-98	1.0m	0.30	Microphone	31.4	1.020
10-Aug-98	1.0m	0.30	Geophone	30.4	1.610
10-Aug-98	1.0m	0.40	Microphone	29.8	1.540
10-Aug-98	1.0m	0.40	Geophone	313.4	0.887
10-Aug-98	1.0m	0.50	Microphone	31.2	1.040
10-Aug-98	1.0m	0.50	Geophone	29.8	1.210
10-Aug-98	1.0m	0.75	Microphone	29.2	1.980
10-Aug-98	1.0m	0.75	Geophone	29.7	1.400
10-Aug-98	1.0m	0.15	Microphone	30.4	1.100
10-Aug-98	1.0m	0.15	Geophone	29.8	1.270
10-Aug-98	1.0m	0.20	Microphone	29.9	1.160
10-Aug-98	1.0m	0.20	Geophone	30.5	0.877
10-Aug-98	1.0m	0.30	Microphone	29.8	1.650
10-Aug-98	1.0m	0.30	Geophone	29.5	1.880
10-Aug-98	1.0m	0.40	Microphone	30.4	1.240
10-Aug-98	1.0m	0.40	Geophone	30.6	0.934
10-Aug-98	1.0m	0.50	Microphone	30.1	1.140
10-Aug-98	1.0m	0.50	Geophone	29.8	1.390
10-Aug-98	1.0m	0.75	Microphone	30	1.220
10-Aug-98	1.0m	0.75	Geophone	29.7	1.230
		Position B			
10-Aug-98	1.0m	0.15	Microphone	30.2	1.120
10-Aug-98	1.0m	0.15	Geophone	30.3	0.811
10-Aug-98	1.0m	0.20	Microphone	29.9	1.190
10-Aug-98	1.0m	0.20	Geophone	29.2	1.010
10-Aug-98	1.0m	0.30	Microphone	30.0	1.110
10-Aug-98	1.0m	0.30	Geophone	30.3	0.540
10-Aug-98	1.0m	0.40	Microphone	29.2	1.460
10-Aug-98	1.0m	0.40	Geophone	30.2	1.020
10-Aug-98	1.0m	0.50	Microphone	29.1	1.480
10-Aug-98	1.0m	0.50	Geophone	29.5	1.130
10-Aug-98	1.0m	0.75	Microphone	29.1	1.200
10-Aug-98	1.0m	0.75	Geophone	28.6	1.990
10-Aug-98	1.0m	0.15	Microphone	28.8	1.340
10-Aug-98	1.0m	0.15	Geophone	29	1.100
10-Aug-98	1.0m	0.20	Microphone	28.9	1.460
10-Aug-98	1.0m	0.20	Geophone	28.9	1.520
10-Aug-98	1.0m	0.30	Microphone	29.3	1.180
10-Aug-98	1.0m	0.30	Geophone	28.9	1.390
10-Aug-98	1.0m	0.40	Microphone	29.6	0.811
10-Aug-98	1.0m	0.40	Geophone	29.1	0.942
10-Aug-98	1.0m	0.50	Microphone	29.2	0.933
10-Aug-98	1.0m	0.50	Geophone	29.2	0.902
10-Aug-98	1.0m	0.75	Microphone	28.6	1.070
10-Aug-98	1.0m	0.75	Geophone	28.7	0.754

Table E-1. Meteorological data for the acoustic-to-seismic coupling ratio measurements taken at the HMC Stone Lane Quarry.

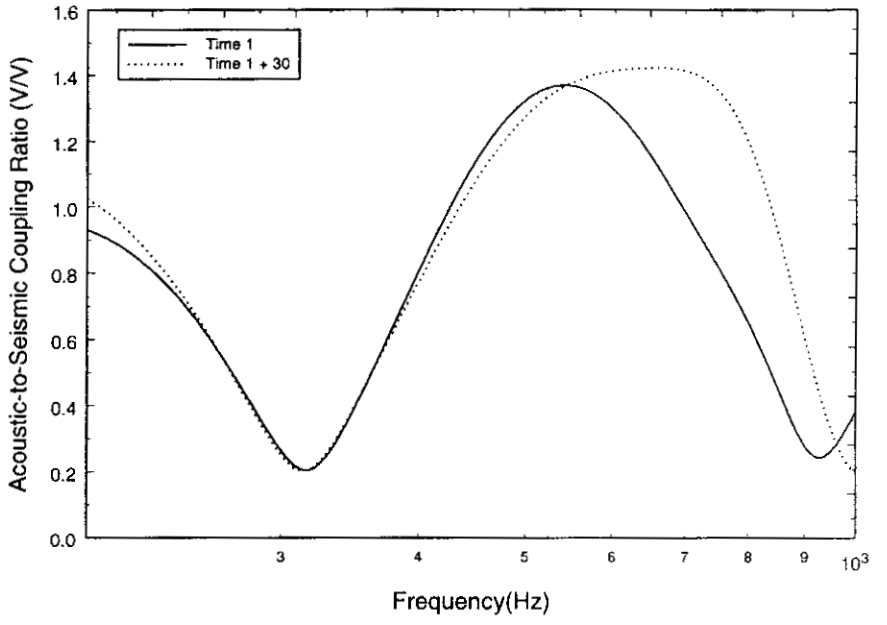

Figure E-5. Variation in acoustic-to-seismic coupling ratio with time. Measurements are 30mins apart and the sensors were removed. R=2.0m Hs=0.15m (Position A).

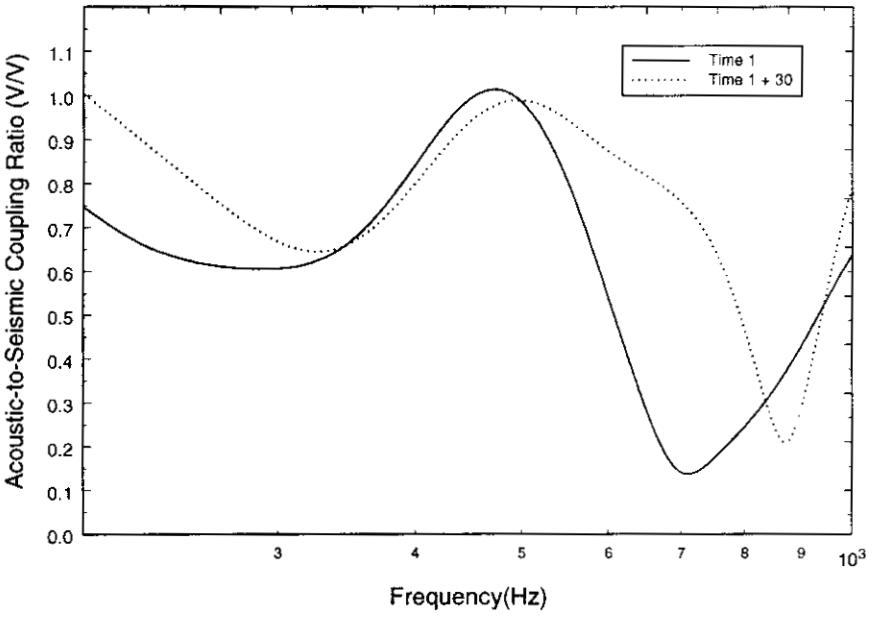

Figure E-6. Variation in acoustic-to-seismic coupling ratio with time. Measurements are 30mins apart and the sensors were removed. R=2.0m Hs=0.75m (Position A).

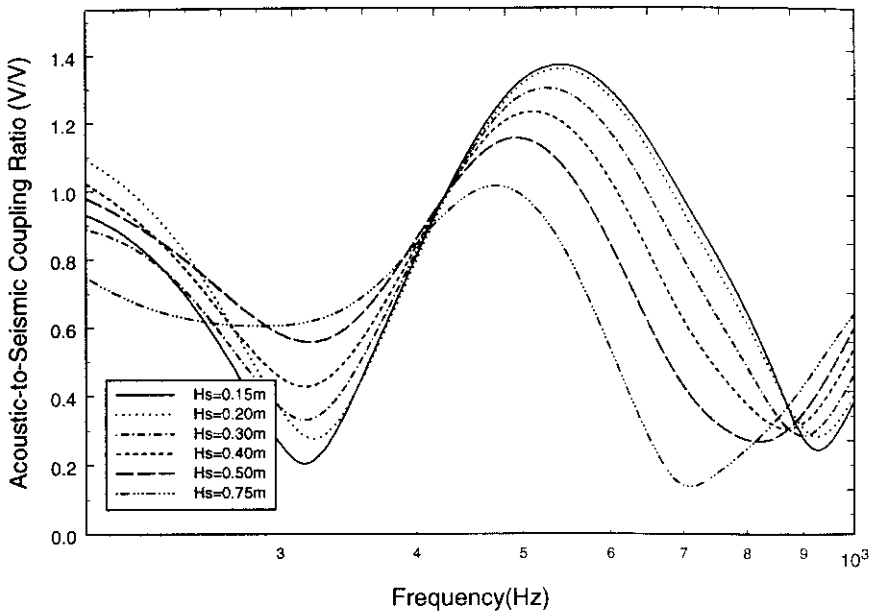

Figure E-7. Variation in acoustic-to-seismic coupling ratio with varying source height. Data taken at time T1 with no removal of geophone sensor between measurements (Pos.A).

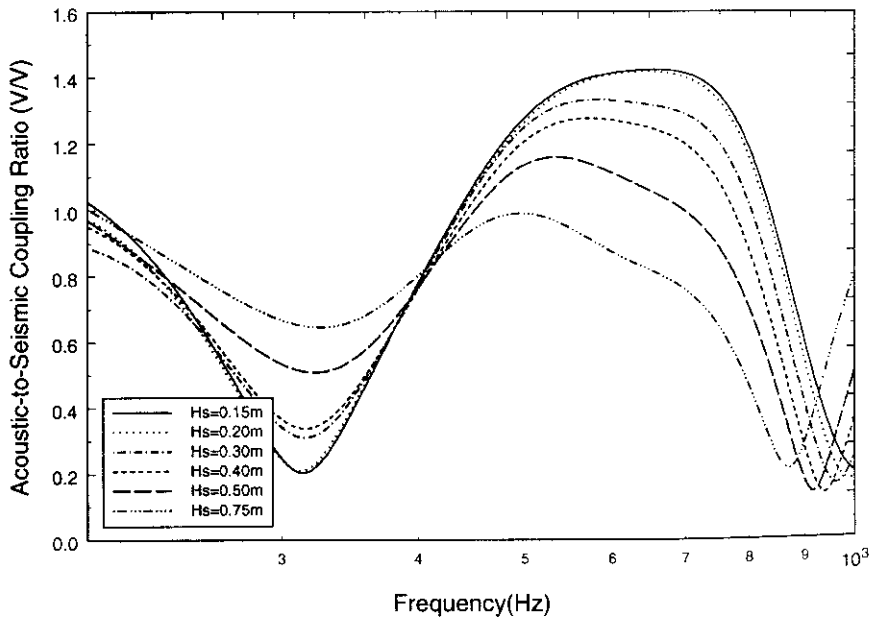

Figure E-8. Variation in acoustic-to-seismic coupling ratio with varying source height. Data taken at T1+30 minutes and the geophone sensor was re-positioned (Pos.A).

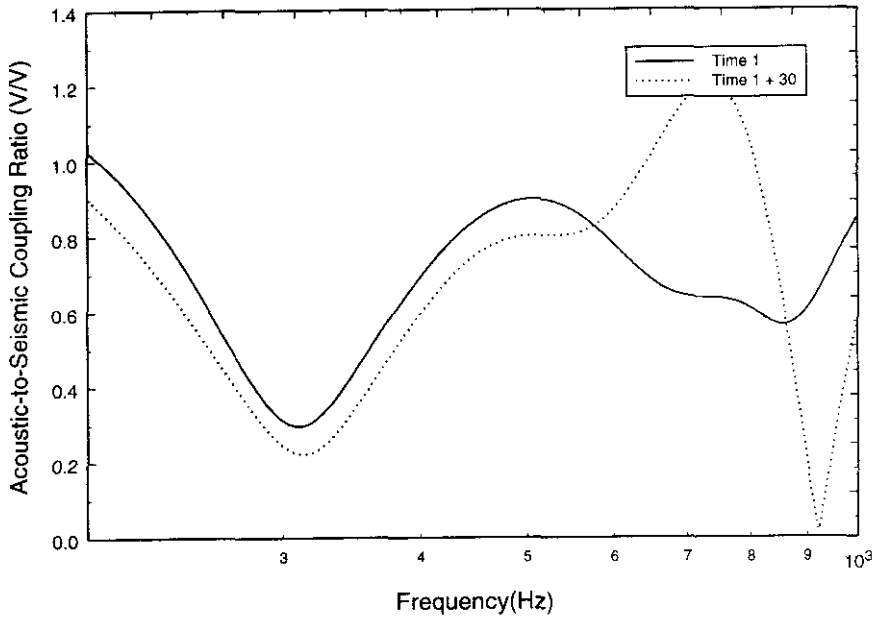

Figure E-9. Variation in acoustic-to-seismic coupling ratio with time. Measurements are 30mins apart and the sensors were removed. R=2.0m Hs=0.15m (Position B).

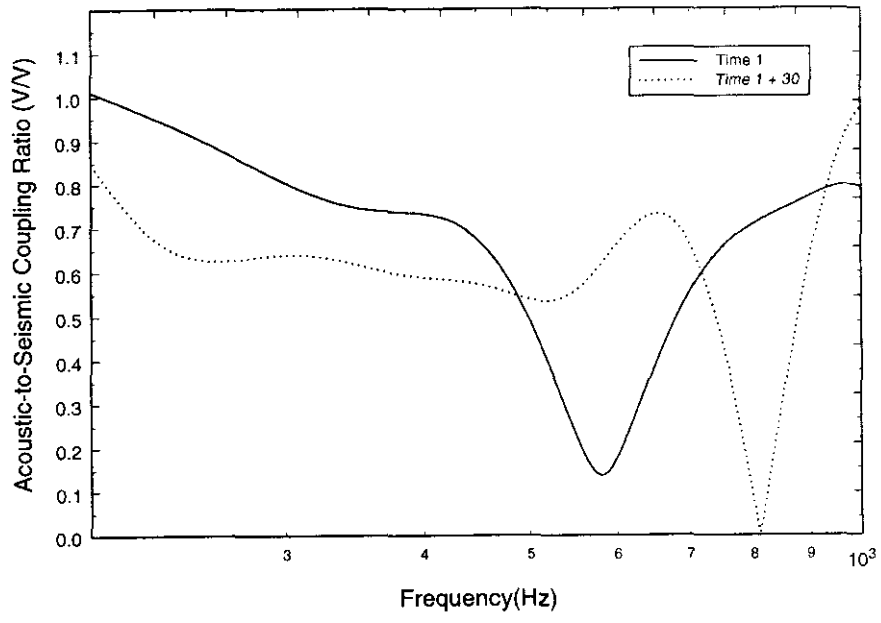

Figure E-10. Variation in acoustic-to-seismic coupling ratio with time. Measurements are 30mins apart and the sensors were removed. R=2.0m Hs=0.75m (Position B).

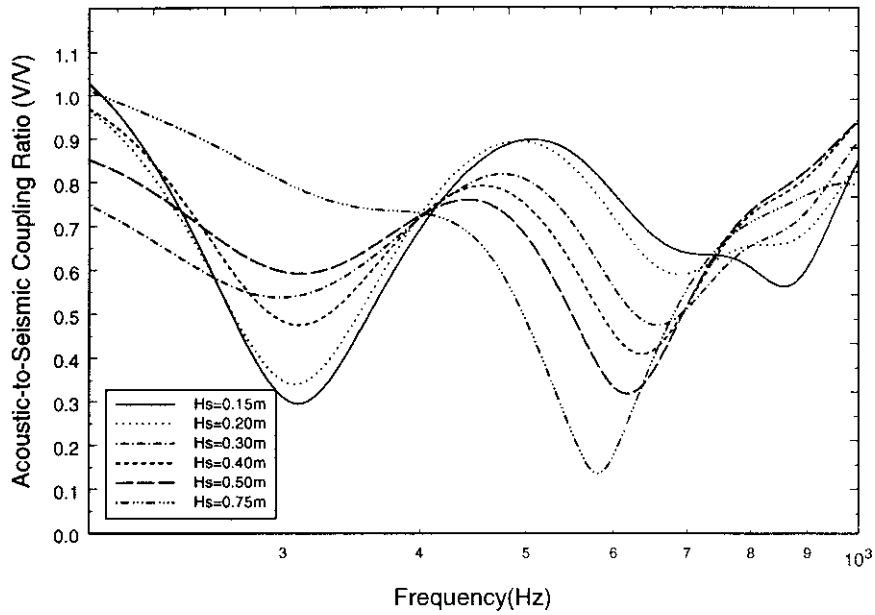

Figure E-11. Variation in acoustic-to-seismic coupling ratio with varying source height. Data taken at time T1 with no removal of geophone sensor between measurements (Pos.B).

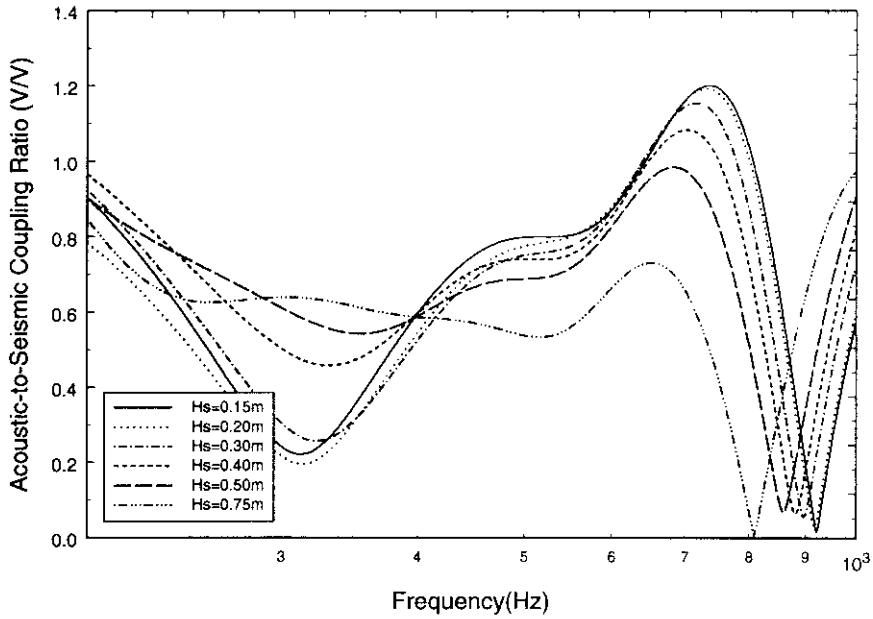

Figure E-12. Variation in acoustic-to-seismic coupling ratio with varying source height. Data taken at T1+30 minutes and the geophone sensor was re-positioned (Pos.B).

Date	Range	Source Height	Receiver	Temperature	Wind Speed
			Position A		
11-Aug-98	2.0m	0.15	Microphone	28.4	1.120
11-Aug-98	2.0m	0.15	Geophone	28.0	1.250
11-Aug-98	2.0m	0.20	Microphone	28.6	0.558
11-Aug-98	2.0m	0.20	Geophone	28.3	0.786
11-Aug-98	2.0m	0.30	Microphone	28.6	0.875
11-Aug-98	2.0m	0.30	Geophone	28.5	0.966
11-Aug-98	2.0m	0.40	Microphone	28.1	0.933
11-Aug-98	2.0m	0.40	Geophone	28.7	0.783
11-Aug-98	2.0m	0.50	Microphone	28.4	1.040
11-Aug-98	2.0m	0.50	Geophone	28.4	0.504
11-Aug-98	2.0m	0.75	Microphone	28.0	1.260
11-Aug-98	2.0m	0.75	Geophone	28.6	0.804
11-Aug-98	2.0m	0.15	Microphone	28.0	1.440
11-Aug-98	2.0m	0.15	Geophone	28.2	1.260
11-Aug-98	2.0m	0.20	Microphone	28.4	1.290
11-Aug-98	2.0m	0.20	Geophone	28.6	1.000
11-Aug-98	2.0m	0.30	Microphone	28.8	0.802
11-Aug-98	2.0m	0.30	Geophone	28.4	1.100
11-Aug-98	2.0m	0.40	Microphone	28.4	1.000
11-Aug-98	2.0m	0.40	Geophone	28.7	0.903
11-Aug-98	2.0m	0.50	Microphone	28.1	1.360
11-Aug-98	2.0m	0.50	Geophone	28.8	0.964
11-Aug-98	2.0m	0.75	Microphone	28.2	1.300
11-Aug-98	2.0m	0.75	Geophone	28.2	1.130
			Position B		
11-Aug-98	2.0m	0.15	Microphone	28.3	0.891
11-Aug-98	2.0m	0.15	Geophone	29.1	0.682
11-Aug-98	2.0m	0.20	Microphone	27.9	1.060
11-Aug-98	2.0m	0.20	Geophone	28.3	0.639
11-Aug-98	2.0m	0.30	Microphone	28.6	0.729
11-Aug-98	2.0m	0.30	Geophone	27.7	0.613
11-Aug-98	2.0m	0.40	Microphone	28.4	0.405
11-Aug-98	2.0m	0.40	Geophone	27.8	0.841
11-Aug-98	2.0m	0.50	Microphone	27.9	0.711
11-Aug-98	2.0m	0.50	Geophone	28.0	0.518
11-Aug-98	2.0m	0.75	Microphone	28.0	0.783
11-Aug-98	2.0m	0.75	Geophone	27.5	0.908
11-Aug-98	2.0m	0.15	Microphone	27.5	0.858
11-Aug-98	2.0m	0.15	Geophone	27.8	0.666
11-Aug-98	2.0m	0.20	Microphone	27.7	0.633
11-Aug-98	2.0m	0.20	Geophone	27.6	0.569
11-Aug-98	2.0m	0.30	Microphone	27.3	0.522
11-Aug-98	2.0m	0.30	Geophone	27.3	0.512
11-Aug-98	2.0m	0.40	Microphone	27.1	0.675
11-Aug-98	2.0m	0.40	Geophone	27.2	0.269
11-Aug-98	2.0m	0.50	Microphone	27.2	0.567
11-Aug-98	2.0m	0.50	Geophone	26.8	0.512
11-Aug-98	2.0m	0.75	Microphone	26.7	0.381
11-Aug-98	2.0m	0.75	Geophone	26.7	0.754

Table E-2. Meteorological data for the acoustic-to-seismic coupling ratio measurements taken at the HMC Stone Lane Quarry.

Date	Range	Source Height	Receiver	Temperature	Wind Speed
17-Sep-98	3.0m	0.75	V.Geophone	16.5	0.958
17-Sep-98	3.0m	0.75	Microphone	16.4	1.270
17-Sep-98	3.0m	1.50	V.Geophone	16.6	0.970
17-Sep-98	3.0m	1.50	Microphone	16.5	0.760
17-Sep-98	3.0m	1.50	V.Geophone	16.0	1.480
17-Sep-98	3.0m	1.50	Microphone	16.8	0.633
17-Sep-98	3.0m	0.75	V.Geophone	17.1	0.772
17-Sep-98	3.0m	0.75	Microphone	17.6	0.706
17-Sep-98	6.0m	0.75	V.Geophone	16.4	1.370
17-Sep-98	6.0m	0.75	Microphone	17.6	0.496
17-Sep-98	6.0m	1.50	V.Geophone	16.9	0.740
17-Sep-98	6.0m	1.50	Microphone	17.5	0.372
17-Sep-98	6.0m	1.50	V.Geophone	17.3	0.380
17-Sep-98	6.0m	1.50	Microphone	17.2	0.525
17-Sep-98	6.0m	0.75	V.Geophone	16.6	1.050
17-Sep-98	6.0m	0.75	Microphone	17.0	0.700
17-Sep-98	9.0m	0.75	V.Geophone	17.8	0.317
17-Sep-98	9.0m	0.75	Microphone	17.6	0.409
17-Sep-98	9.0m	1.50	V.Geophone	16.6	0.978
17-Sep-98	9.0m	1.50	Microphone	16.6	0.797
17-Sep-98	9.0m	1.50	V.Geophone	16.4	0.638
17-Sep-98	9.0m	1.50	Microphone	16.5	0.282
17-Sep-98	9.0m	0.75	V.Geophone	16.5	0.409
17-Sep-98	9.0m	0.75	Microphone	16.4	0.328
17-Sep-98	5.0m	0.75	V.Geophone	16.5	0.419
17-Sep-98	5.0m	0.75	V.Geophone	15.8	0.557
17-Sep-98	5.0m	0.75	V.Geophone	15.7	0.791
17-Sep-98	5.0m	0.75	V.Geophone	15.6	0.388
17-Sep-98	5.0m	0.75	V.Geophone	15.9	0.185
17-Sep-98	5.0m	0.75	Microphone	15.7	0.289
17-Sep-98	5.0m	0.75	H.Geophone	15.4	0.142
17-Sep-98	5.0m	0.75	H.Geophone	15.4	0.142
17-Sep-98	3.0m	0.75	H.Geophone	14.5	0.131
17-Sep-98	3.0m	0.75	H.Geophone	14.5	0.092
17-Sep-98	6.0m	0.75	H.Geophone	15.5	0.255
17-Sep-98	6.0m	0.75	H.Geophone	14.6	0.128
17-Sep-98	9.0m	0.75	H.Geophone	14.5	0.160
17-Sep-98	9.0m	0.75	H.Geophone	14.3	0.160
17-Sep-98	3.0m	1.50	H.Geophone	14.6	0.128
17-Sep-98	3.0m	1.50	H.Geophone	13.7	0.114
17-Sep-98	6.0m	1.50	H.Geophone	13.7	0.214
17-Sep-98	6.0m	1.50	H.Geophone	13.6	0.522
17-Sep-98	9.0m	1.50	H.Geophone	13.6	0.529
17-Sep-98	9.0m	1.50	H.Geophone	13.8	0.203

Table E-3. Meteorological data for the acoustic-to-seismic coupling ratio measurements taken using the loudspeaker at the HMC Stone Lane Quarry.

		Layer 1	Layer 2	Substrate
P-wave speed (m/s)	(Hs=0.75)	240	360	750
	(Hs=1.50)	240	360	750
S-wave speed (m/s)	(Hs=0.75)	85	160	320
	(Hs=1.50)	85	160	320
Flow Resistivity ((Pa sm^{-2})	(Hs=0.75)	40000	40000	3600000
	(Hs=1.50)	40000	40000	3600000
Porosity	(Hs=0.75)	0.36	0.36	0.036
	(Hs=1.50)	0.36	0.36	0.036
Grain shape factor		0.5	0.5	0.5
Soil density (kg/m^3)		1500.0	1700.0	2700
Layer thickness (m)	(Hs=0.75)	0.70	0.85	∞
	(Hs=1.50)	0.70	0.80	∞
Attenuation (V_p)		0.02	0.02	0.04
Attenuation (V_s)		0.01	0.01	0.02
Dynamic viscosity of air (Nsm^{-2})		$1.81x10^{-5}$		
Microphone height (m)		0.05		
Geophone depth (m)		-0.05		
Frequency range (Hz)		100 – 1000		
Speed of sound in air		344.0		
Coupling Resonant Frequency (Hz)		404		
Geophone Sensitivity (V / m/s) (measured)		27.4		
Microphone Sensitivity (V / Pa) (measured)		$13.4e^{-3}$		

Table E-4. Parameters used to predict the acoustic-to-seismic coupling ratio measurements taken at a range of 6m at HMC Stone Lane Quarry.

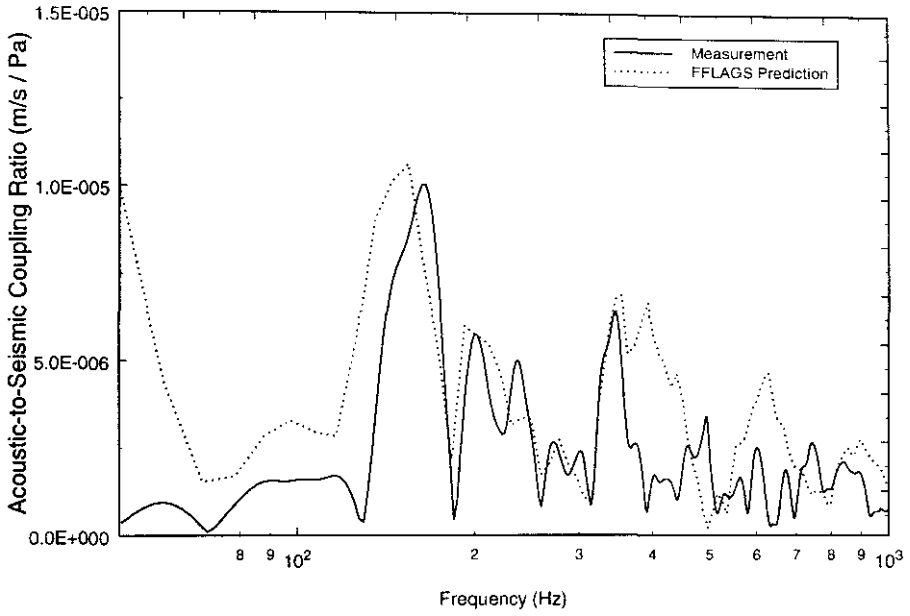

Figure E-13. Measured acoustic-to-seismic coupling ratio and FFLAGS prediction taken at HMC Stone Lane (Range=6.0m, Hs=0.75m and f_0=404Hz).

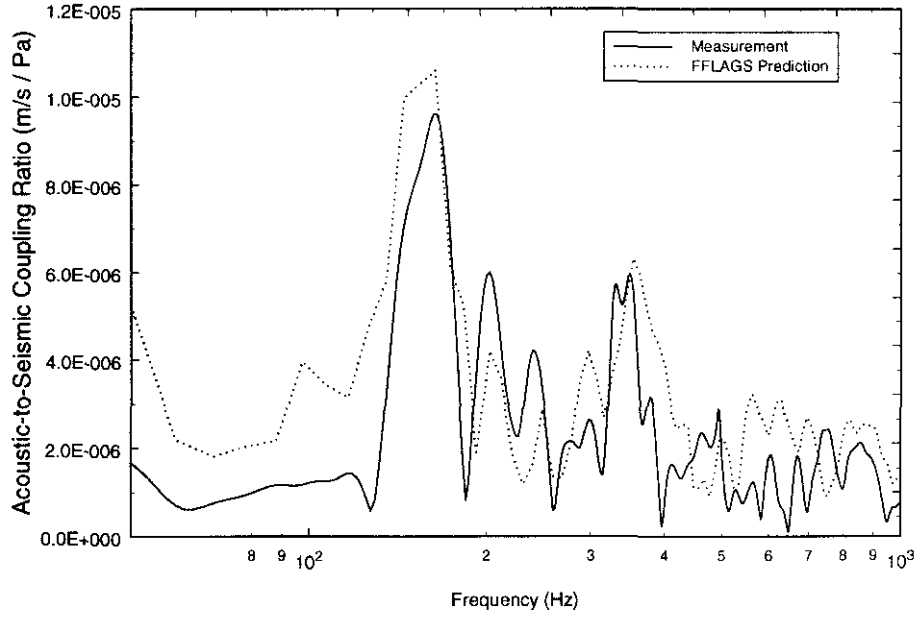

Figure E-14. Measured acoustic-to-seismic coupling ratio and FFLAGS prediction taken at HMC Stone Lane (Range=6.0m, Hs=1.50m and f_0=404Hz).

		Layer 1	Layer 2	Substrate
P-wave speed (m/s)	(Hs=0.75)	240	370	740
	(Hs=1.50)	250	370	740
S-wave speed (m/s)	(Hs=0.75)	90	160	320
	(Hs=1.50)	90	155	320
Flow Resistivity ((Pa sm^{-2})	(Hs=0.75)	40000	40000	360000
	(Hs=1.50)	40000	40000	360000
Porosity	(Hs=0.75)	0.36	0.36	0.036
	(Hs=1.50)	0.36	0.36	0.036
Grain shape factor		0.5	0.5	0.5
Soil density (kg/m^3)		1500	1700.0	2700
Layer thickness (m)	(Hs=0.75)	0.70	1.00	∞
	(Hs=1.50)	0.75	1.00	∞
Attenuation (V_p)		0.02	0.02	0.04
Attenuation (V_s)		0.01	0.01	0.02
Dynamic viscosity of air (Nsm^{-2})		$1.81x10^{-5}$		
Microphone height (m)		0.05		
Geophone depth (m)		-0.05		
Frequency range (Hz)		100 – 1000		
Speed of sound in air		344.0		
Coupling Resonant Frequency (Hz)		437		
Geophone Sensitivity (V / m/s) (measured)		28.5		
Microphone Sensitivity (V / Pa) (measured)		$13.4e^{-3}$		

Table E-5. Parameters used to predict the acoustic-to-seismic coupling ratio measurements taken at a range of 9m at HMC Stone Lane Quarry.

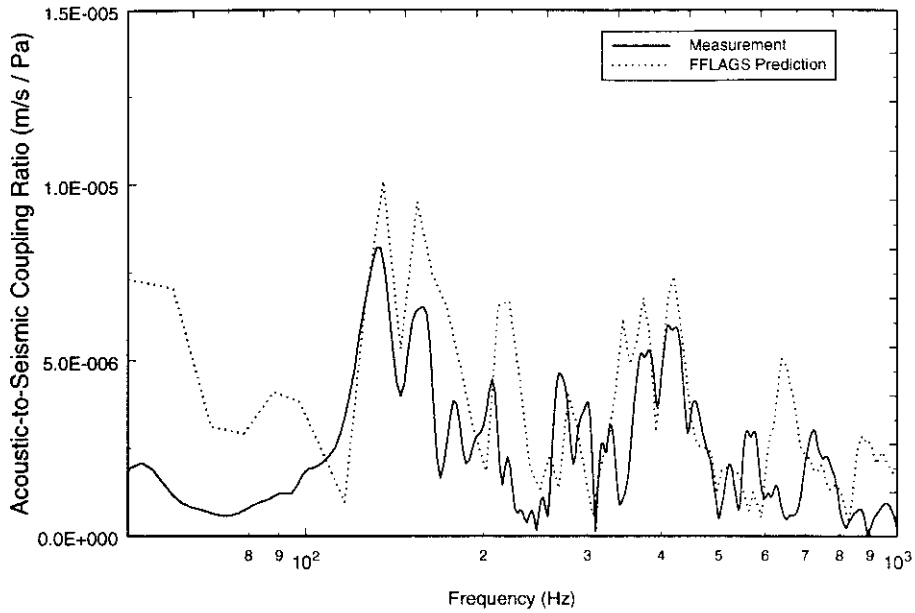

Figure E-15. Measured acoustic-to-seismic coupling ratio and FFLAGS prediction taken at HMC Stone Lane (Range=9.0m, Hs=0.75m and f_0=437Hz).

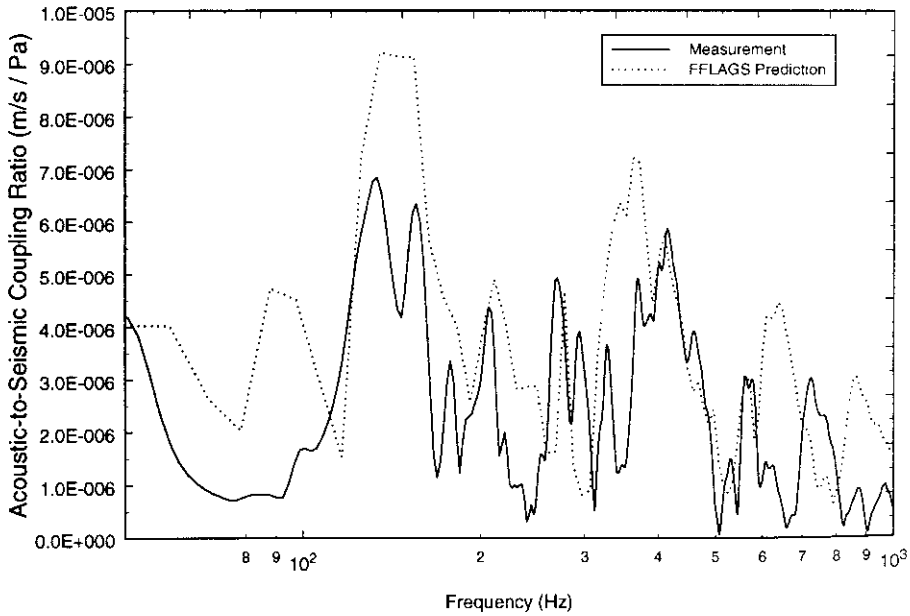

Figure E-16. Measured acoustic-to-seismic coupling ratio and FFLAGS prediction taken at HMC Stone Lane (Range=9.0m, Hs=1.50m and f_0=437Hz).

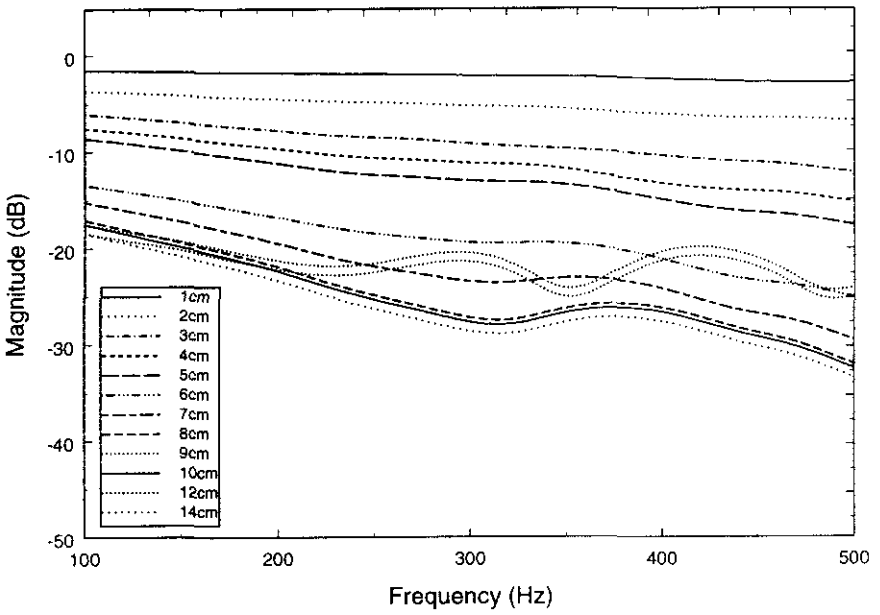

Figure E-17. Measured relative magnitude between the probe microphone at various depths and a reference microphone situated at the sand surface.

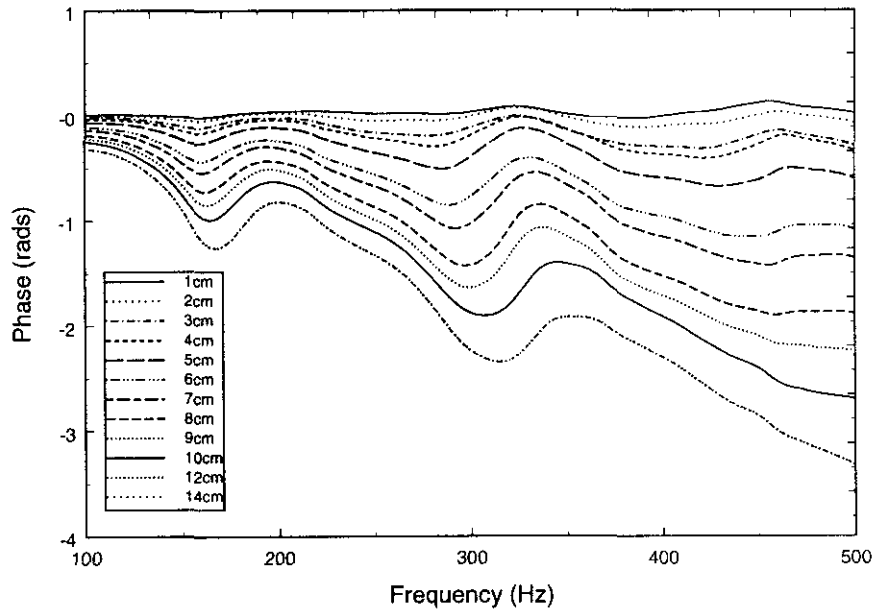

Figure E-18. Measured phase difference between the probe microphone at various depths and a reference microphone situated at the sand surface.

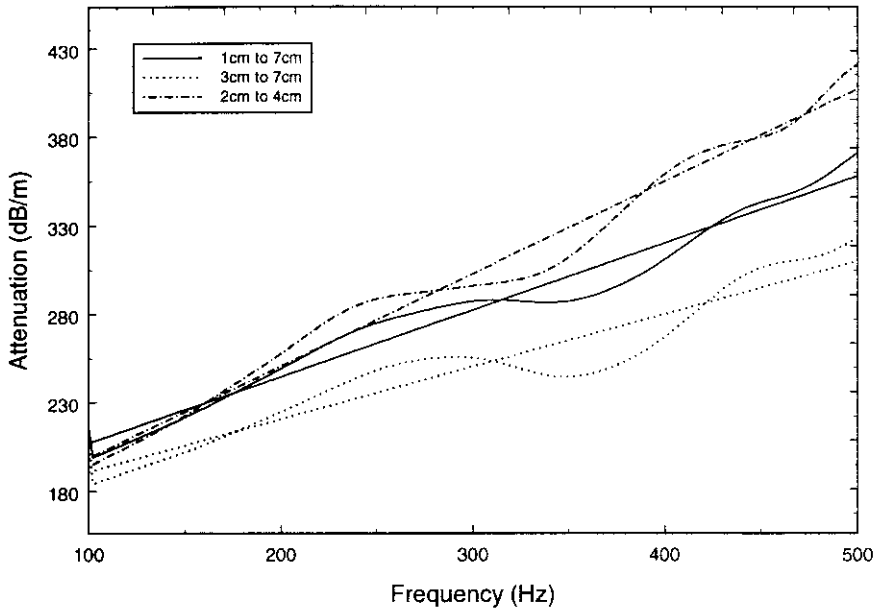

Figure E-19. Calculated attenuation over three different depth intervals. Best-fit regression has been applied to the data.

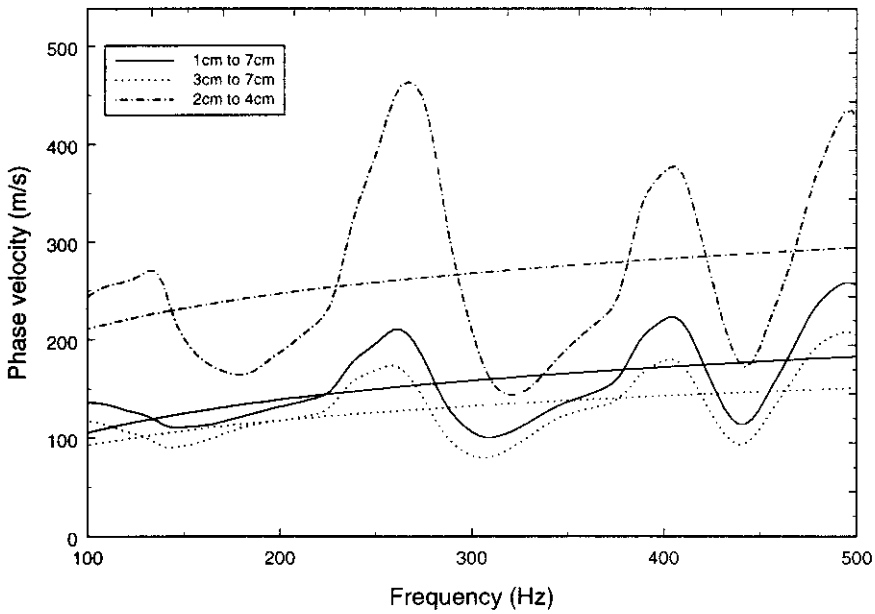

Figure E-20. Calculated phase velocity over three different depth intervals. Best-fit regression has been applied to the data.

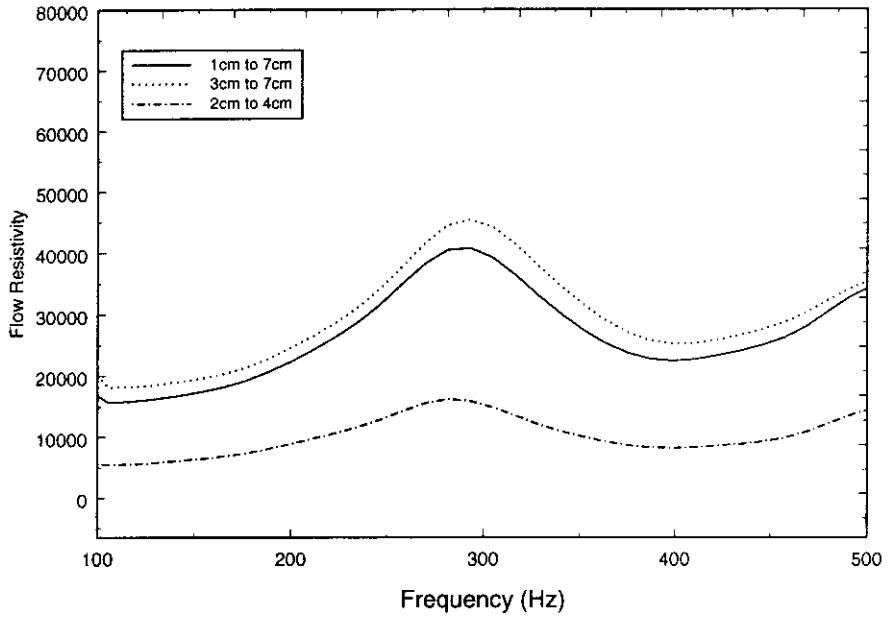

Figure E-21. Calculated flow resistivity of the Stone Lane Quarry sand.

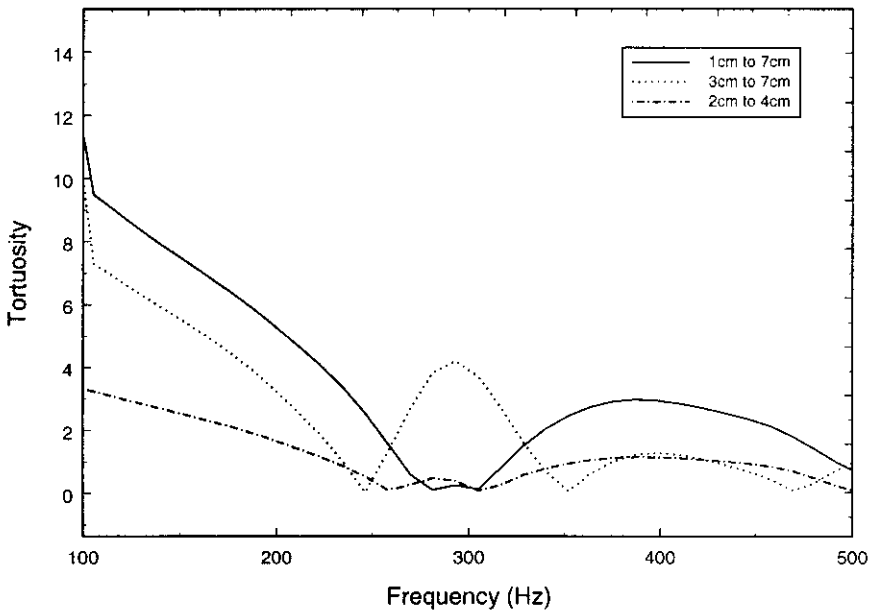

Figure E-22. Calculated tortuosity of the Stone Lane Quarry sand.

Appendix F

Horticultural Research International, Wellesbourne

F Contents

Appendix F covers the results from Horticultural Research International, Wellesbourne. It includes:

a) Seismograms from the P-wave seismic refraction surveys.

b) Example acoustic-to-seismic coupling ratio spectra and corresponding FFLAGS predictions.

c) Meteorological data taken concurrently with acoustic-to-seismic coupling measurements.

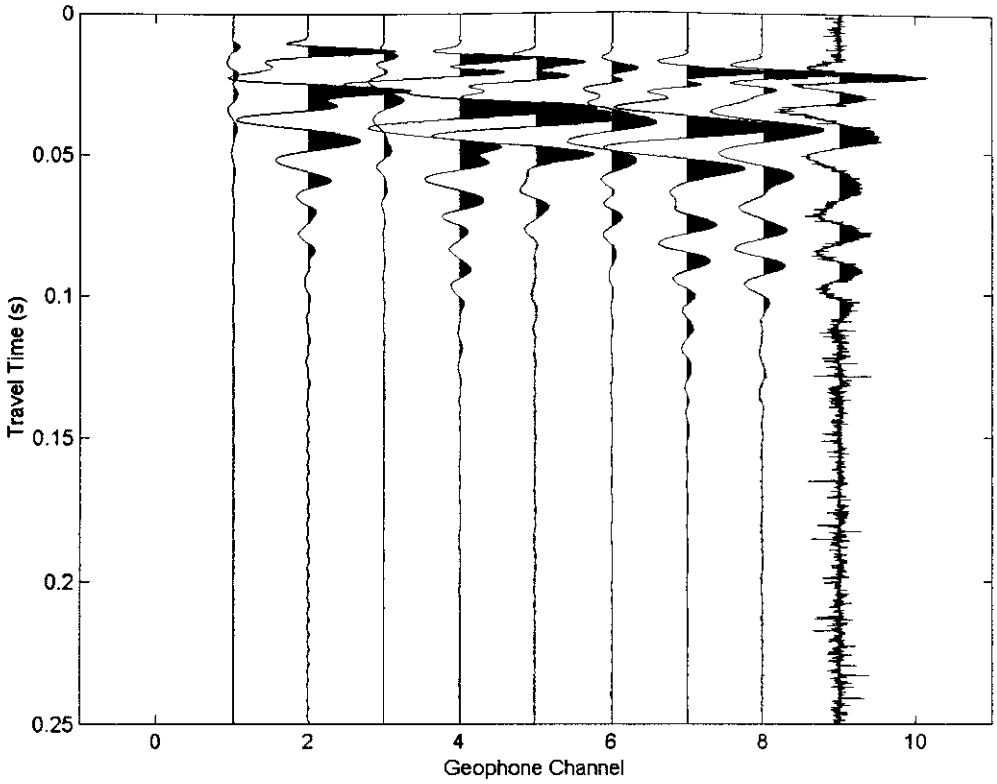

Figure F-1. Seismogram for P-wave survey on Soil A (forward shot).

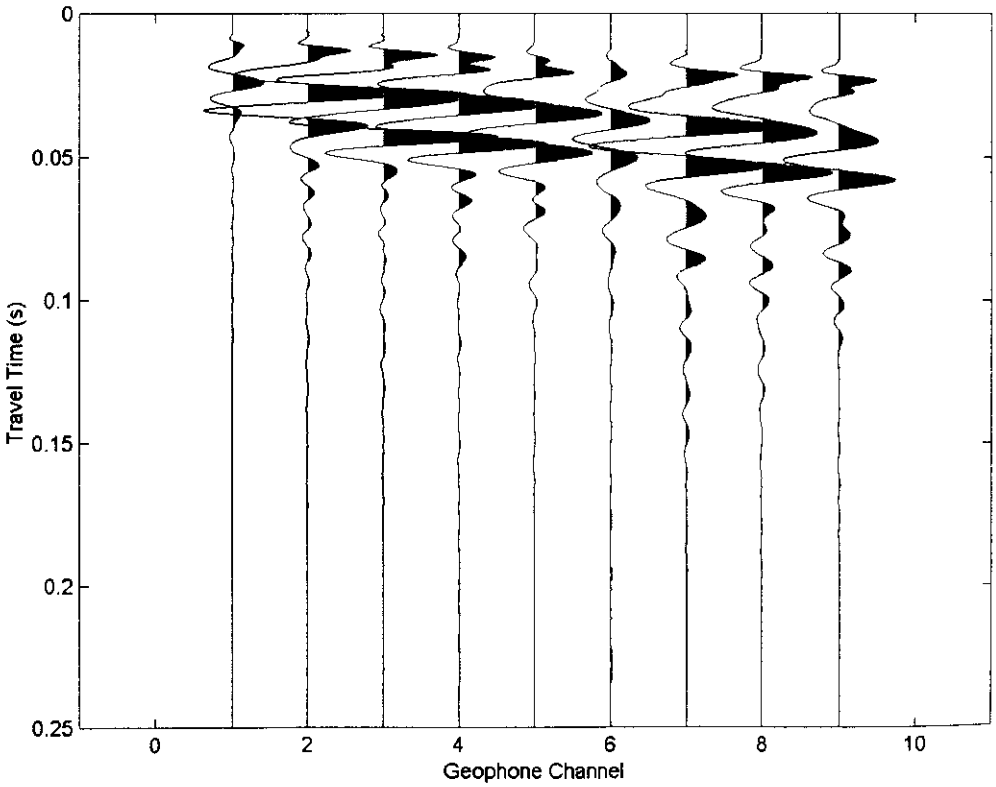

Figure F-2. Seismogram for P-wave survey on Soil A (reverse shot).

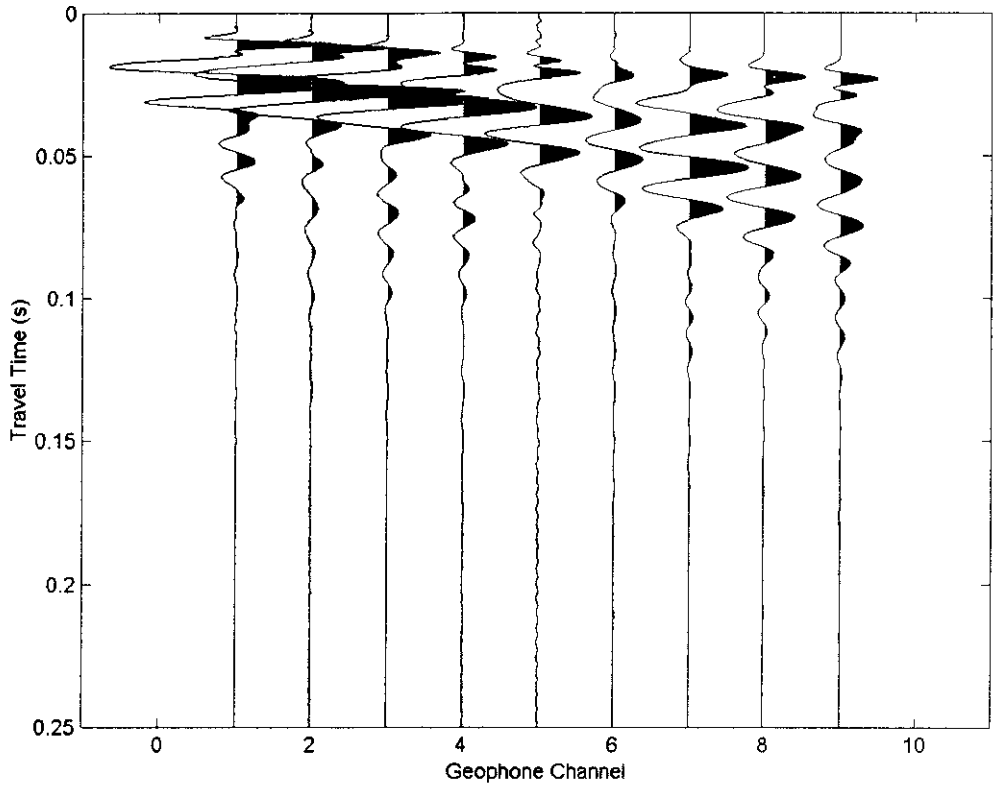

Figure F-3. Seismogram for P-wave survey on Soil B (forward shot).

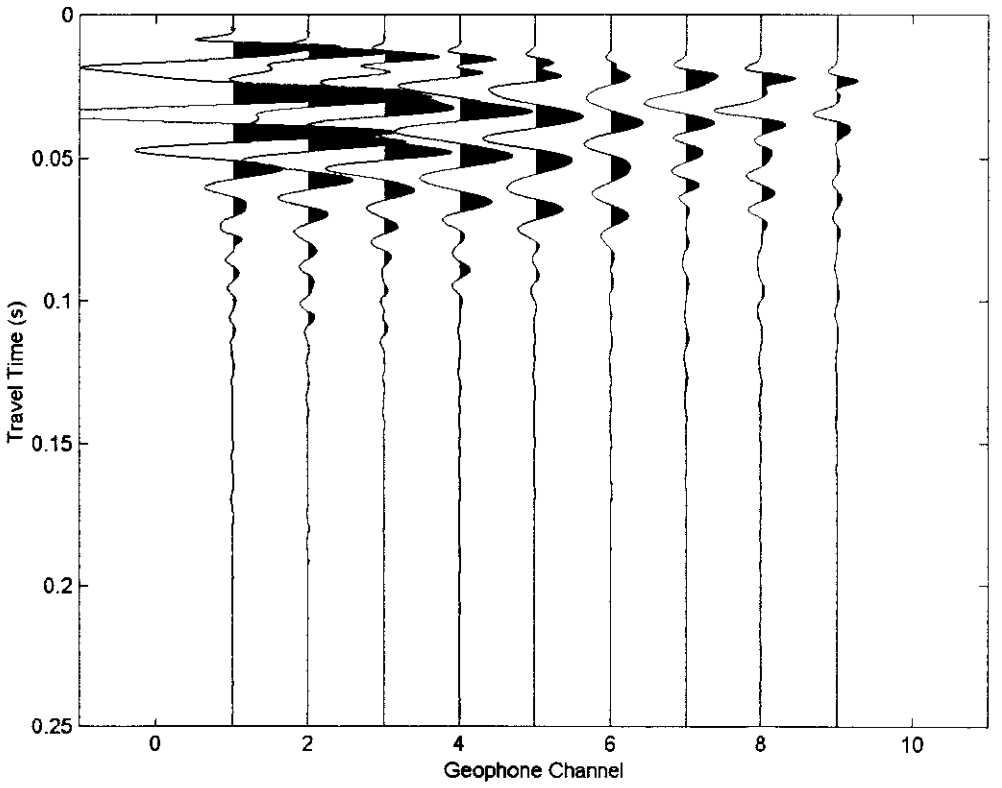

Figure F-4. Seismogram for P-wave survey on Soil B (reverse shot).

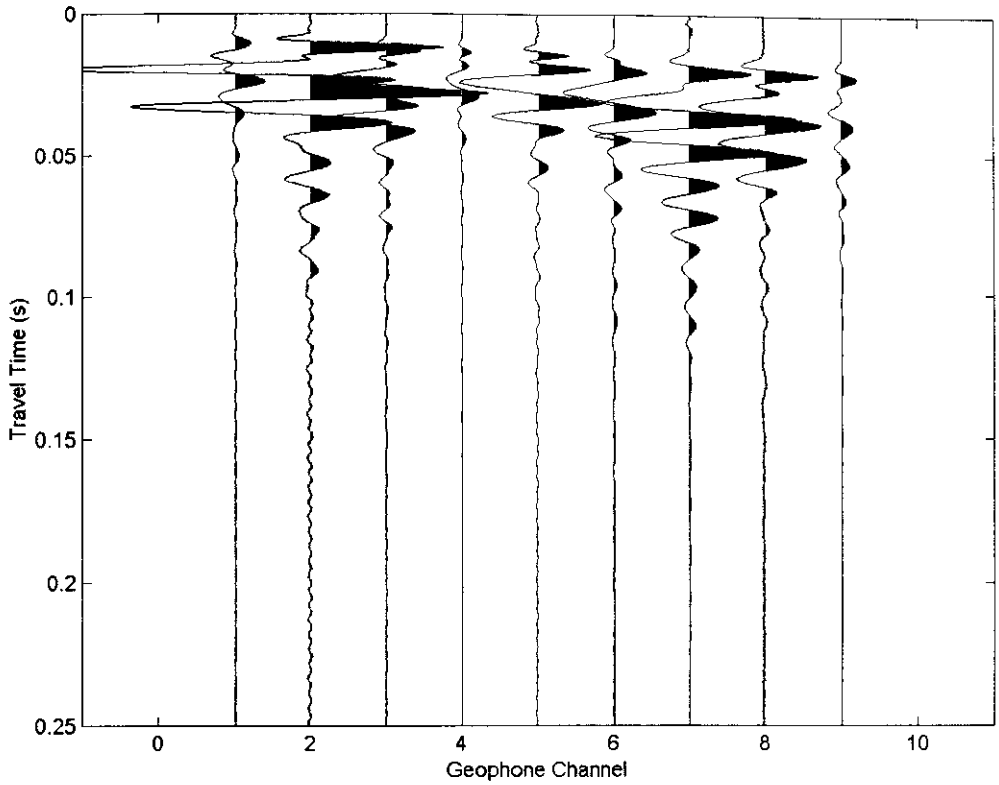

Figure F-5. Seismogram for P-wave survey on Soil C (forward shot).

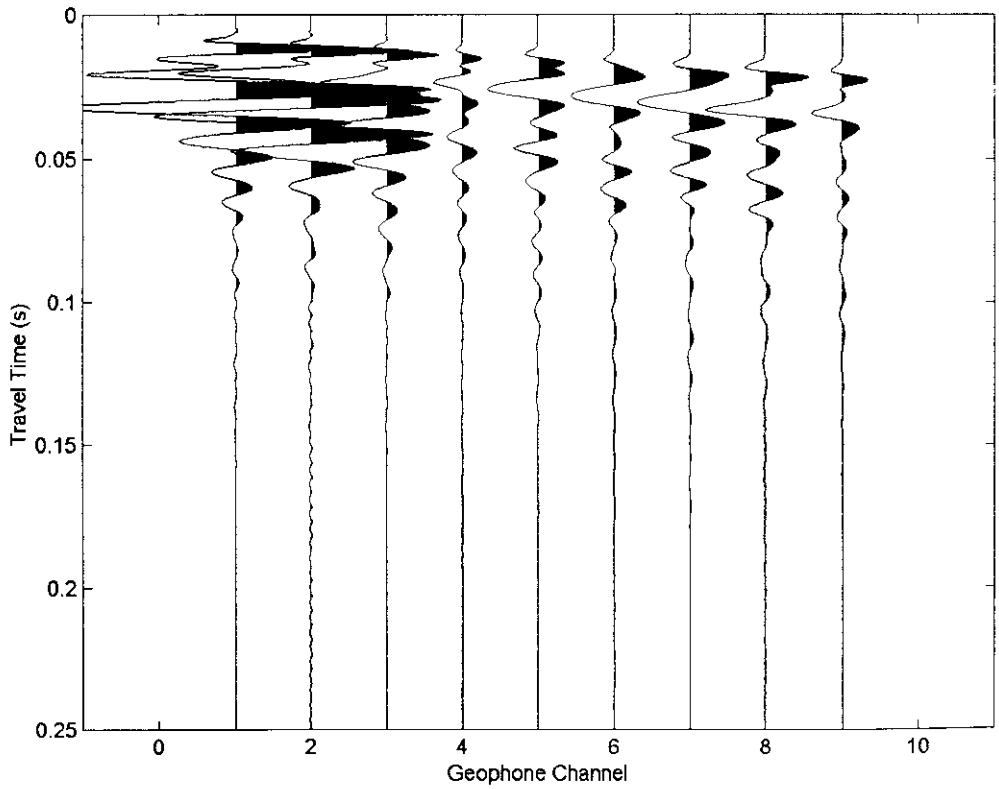

Figure F-6. Seismogram for P-wave survey on Soil C (reverse shot).

Range (m)	Receiver	Source Height (m)	Longitudinal Turbulance Intensity	Transverse Turbulance Intensity	Vertical Turbulance Intensity	Temp (°C)	Wind Speed (m/s)	Wind Direction (From North) (°)	Elevation (From Horiz.) (°)
1.0	Geophone	0.15(PS)	0.64	0.67	0.44	20.34	1.71	310.0	2.2
1.0	Microphone	0.15(PS)	0.55	0.40	0.36	20.19	1.99	301.7	0.4
1.0	Geophone	0.30(PS)	0.47	0.39	0.31	20.30	2.22	295.8	1.3
1.0	Microphone	0.30(PS)	0.43	0.35	0.28	20.14	2.68	295.8	-1.2
1.0	Geophone	0.45(PS)	0.56	0.61	0.43	20.51	1.66	304.5	2.2
1.0	Microphone	0.45(PS)	0.63	0.57	0.49	21.23	1.27	301.1	4.8
2.0	Geophone	0.15(PS)	0.50	0.42	0.37	21.14	2.14	294.8	3.1
2.0	Microphone	0.15(PS)	0.55	0.40	0.31	20.82	2.66	297.5	-0.6
2.0	Geophone	0.30(PS)	0.46	0.41	0.28	20.87	2.91	296.2	1.0
2.0	Microphone	0.30(PS)	0.79	0.73	0.53	21.09	1.30	309.1	5.0
2.0	Geophone	0.45(PS)	0.49	0.47	0.41	21.27	1.43	299.0	6.4
2.0	Microphone	0.45(PS)	0.60	0.45	0.31	21.20	1.96	297.8	2.7
2.0	Geophone	0.45(LS)	0.47	0.50	0.37	21.29	1.60	301.2	3.2
2.0	Microphone	0.45(LS)	0.44	0.30	0.29	21.32	2.57	292.9	-0.7
2.0	Geophone	0.68(LS)	0.42	0.42	0.32	21.15	2.08	298.2	-0.6
2.0	Microphone	0.68(LS)	0.45	0.52	0.31	21.16	2.59	296.6	-0.5
3.0	Geophone	0.45(LS)	0.56	0.50	0.40	21.33	1.56	295.8	0.4
3.0	Microphone	0.45(LS)	0.58	0.38	0.29	21.34	2.17	292.7	3.2
3.0	Geophone	0.68(LS)	0.50	0.48	0.35	21.22	2.46	302.5	1.0
3.0	Microphone	0.68(LS)	0.46	0.39	0.32	21.29	2.00	288.0	4.9

Table F-1. Meteorological Data taken concurrently with acoustic-to-seismic coupling ratio measurements (Soil A).

		Layer 1	Layer 2	Substrate
P-wave speed (m/s)	(R=2.0m)	180	480	900
	(R=3.0m)	190	460	900
S-wave speed (m/s)	(R=2.0m)	110	290	600
	(R=3.0m)	110	290	600
Flow Resistivity ((Pa sm^{-2})	(R=2.0m)	450000	450000	3600000
	(R=3.0m)	450000	450000	3600000
Porosity	(R=2.0m)	0.23	0.23	0.036
	(R=3.0m)	0.23	0.23	0.036
Grain shape factor		0.5	0.5	0.5
Soil density (kg/m^3)		2000	2200	2650
Layer thickness (m)	(R=2.0m)	0.58	2.00	∞
	(R=3.0m)	0.60	2.00	∞
Attenuation (V_p)		0.04	0.04	0.04
Attenuation (V_s)		0.02	0.02	0.02
Dynamic viscosity of air (Nsm^{-2})		1.81×10^{-5}		
Microphone height (m)		0.05		
Geophone depth (m)		-0.05		
Frequency range (Hz)		100 – 1000		
Speed of sound in air		344.0		
Coupling Resonant Frequency (Hz)	(R=2.0m)	802		
	(R=3.0m)	898		
Geophone Sensitivity (V / m/s) (measured)	(R=2.0m)	23.0		
	(R=3.0m)			
Microphone Sensitivity (V / Pa) (measured)	(R=2.0m)	$13.4e^{-3}$		
	(R=3.0m)	$13.4e^{-3}$		

Table F-2. Parameters used to predict the acoustic-to-seismic coupling ratio measurements taken in Soil A at HRI, Wellesbourne (source height=0.68m and range=2.0m, 3.0m).

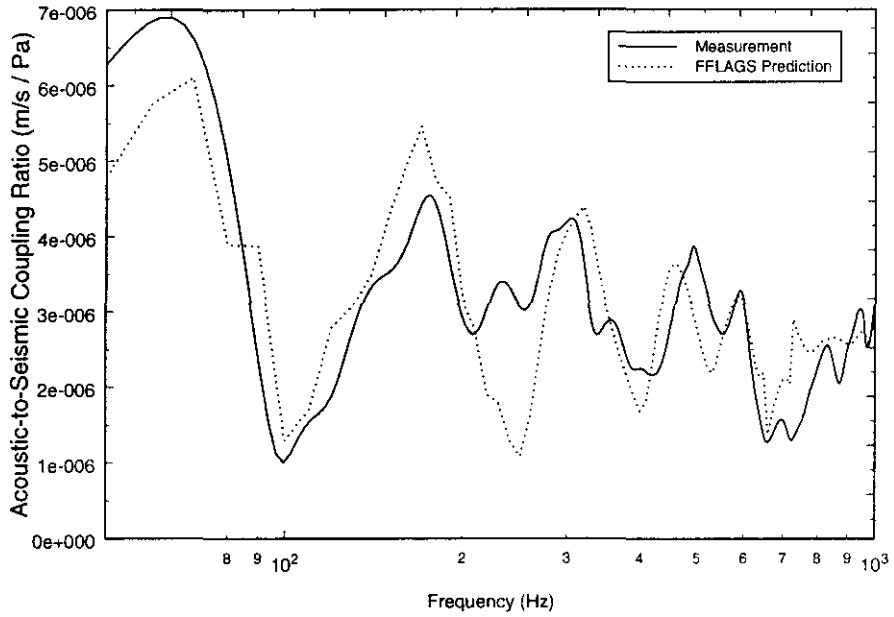

Figure F-7. Measured acoustic-to-seismic coupling ratio and FFLAGS prediction taken at HRI for Soil A (Range=2.0m, Hs=0.68m and f_0=802Hz).

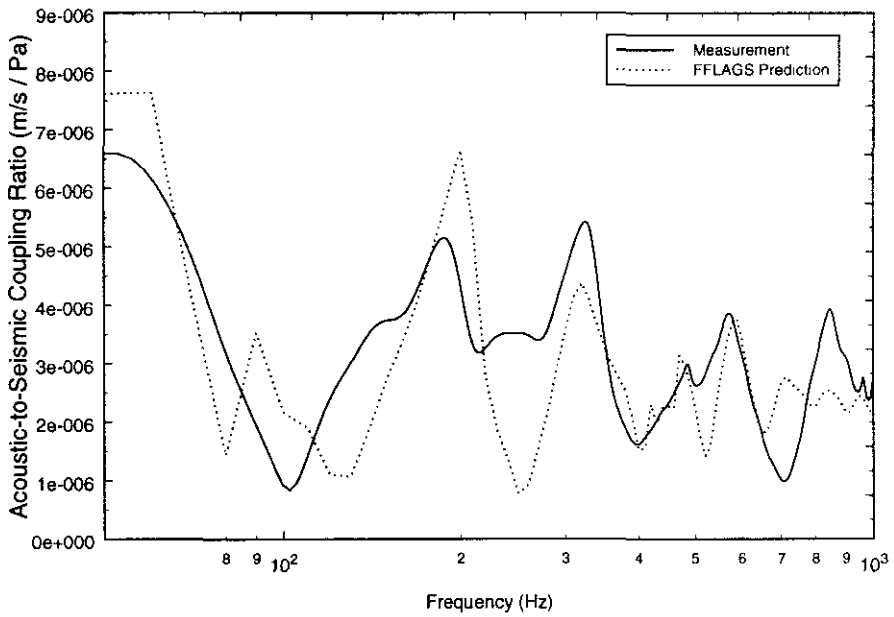

Figure F-8. Measured acoustic-to-seismic coupling ratio and FFLAGS prediction taken at HRI for Soil A (Range=3.0m, Hs=0.68m and f_0=898Hz).

Range (m)	Receiver	Source Height (m)	Longitudinal Turbulance Intensity	Transverse Turbulance Intensity	Vertical Turbulance Intensity	Temp (°C)	Wind Speed (m/s)	Wind Direction (From North) (°)	Elevation (From Horiz.) (°)
1.0	Geophone	0.15(PS)	0.96	2.09	1.14	23.85	0.38	252.0	15.6
1.0	Microphone	0.15(PS)	0.59	0.38	0.34	24.19	0.91	272.2	13.5
1.0	Geophone	0.30(PS)	0.39	0.66	0.46	23.66	0.38	36.7	35.3
1.0	Microphone	0.30(PS)	0.43	0.56	0.45	24.04	0.56	21.3	38.5
1.0	Geophone	0.45(PS)	0.28	0.48	0.34	24.25	0.54	4.5	45.9
1.0	Microphone	0.45(PS)	0.25	0.37	0.23	23.99	1.31	139.0	13.8
2.0	Geophone	0.15(PS)	0.64	1.29	0.65	24.22	0.42	242.0	21.0
2.0	Microphone	0.15(PS)	0.69	0.76	0.47	24.23	0.36	3.9	41.1
2.0	Geophone	0.30(PS)	0.43	0.44	0.33	24.36	0.63	54.1	19.8
2.0	Microphone	0.30(PS)	0.43	36.00	0.35	24.57	0.66	48.7	18.3
2.0	Geophone	0.45(PS)	0.37	0.51	0.41	24.66	0.79	54.8	21.1
2.0	Microphone	0.45(PS)	0.25	0.23	0.19	24.66	1.43	14.6	11.5
2.0	Geophone	0.45(LS)	0.45	0.58	0.54	25.16	0.77	18.1	25.4
2.0	Microphone	0.45(LS)	0.30	0.50	0.48	24.83	0.64	14.9	43.0
2.0	Geophone	0.68(LS)	0.04	0.51	0.56	25.23	0.72	16.6	31.3
2.0	Microphone	0.68(LS)	0.43	0.37	0.34	24.78	1.04	39.7	9.2
3.0	Geophone	0.45(LS)	0.49	0.52	0.32	25.17	1.39	3.9	13.0
3.0	Microphone	0.45(LS)	0.51	0.56	0.50	24.93	0.90	14.9	12.5
3.0	Geophone	0.68(LS)	0.45	0.59	0.39	25.01	1.18	17.0	18.6
3.0	Microphone	0.68(LS)	0.47	0.57	0.49	25.17	1.26	20.6	9.7

Table F-3. Meteorological Data taken concurrently with acoustic-to-seismic coupling ratio measurements (Soil B).

		Layer 1	Layer 2	Substrate
P-wave speed (m/s)	(R=2.0m)	265.0	390.0	900.0
	(R=3.0m)	255.0	400.0	900.0
S-wave speed (m/s)	(R=2.0m)	145.0	230.0	600.0
	(R=3.0m)	150.0	230.0	600.0
Flow Resistivity ((Pa sm^{-2})	(R=2.0m)	475000	475000	3600000
	(R=3.0m)	475000	475000	3600000
Porosity	(R=2.0m)	0.18	0.18	0.036
	(R=3.0m)	0.18	0.18	0.036
Grain shape factor		0.5	0.5	0.5
Soil density (kg/m^3)		2000	2200	2650
Layer thickness (m)	(R=2.0m)	0.60	1.50	∞
	(R=3.0m)	0.58	1.50	∞
Attenuation (V_p)		0.04	0.04	0.04
Attenuation (V_s)		0.02	0.02	0.02
Dynamic viscosity of air (Nsm^{-2})		$1.81x10^{-5}$		
Microphone height (m)		0.05		
Geophone depth (m)		-0.05		
Frequency range (Hz)		100 – 1000		
Speed of sound in air		344.0		
Coupling Resonant Frequency (Hz)	(R=2.0m)	763		
	(R=3.0m)	882		
Geophone Sensitivity (V / m/s) (measured)	(R=2.0m)	24.6		
	(R=3.0m)	25.1		
Microphone Sensitivity (V / Pa) (measured)	(R=2.0m)	$13.4e^{-3}$		
	(R=3.0m)	$13.4e^{-3}$		

Table F-4. Parameters used to predict the acoustic-to-seismic coupling ratio measurements taken in Soil B at HRI, Wellesbourne (source height=0.68m and range=2.0m, 3.0m).

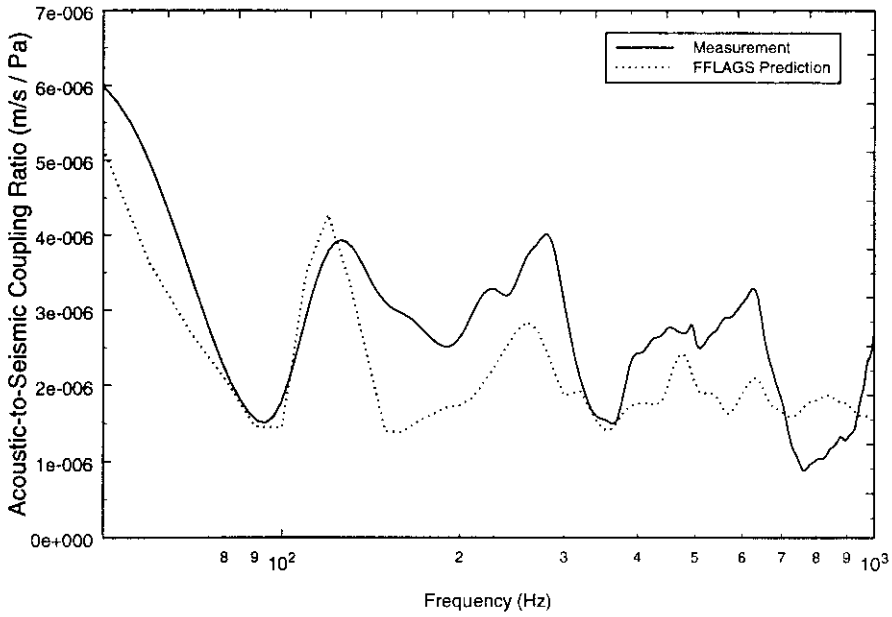

Figure F-9. Measured acoustic-to-seismic coupling ratio and FFLAGS prediction taken at HRI for Soil B (Range=2.0m, Hs=0.68m and f_0=763Hz).

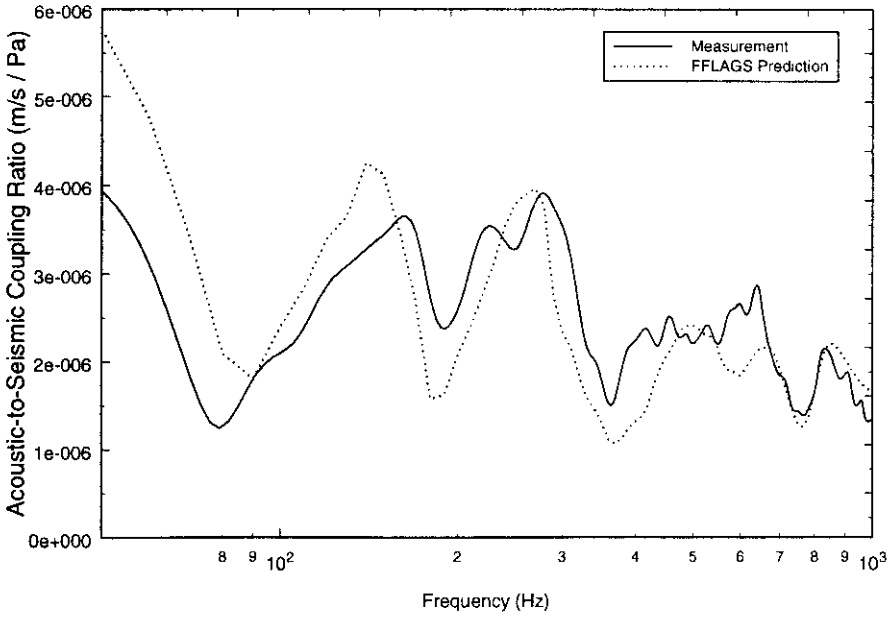

Figure F-10. Measured acoustic-to-seismic coupling ratio and FFLAGS prediction taken at HRI for Soil B (Range=3.0m, Hs=0.68m and f_0=882Hz).

Range (m)	Receiver	Source Height (m)	Longitudinal Turbulance Intensity	Transverse Turbulance Intensity	Vertical Turbulance Intensity	Temp (°C)	Wind Speed (m/s)	Wind Direction (From North) (°)	Elevation (From Horiz.) (°)
1.0	Geophone	0.15(PS)	0.75	0.86	0.65	23.56	1.03	243.5	0.3
1.0	Microphone	0.15(PS)	0.85	0.75	0.54	23.80	1.05	265.2	0.5
1.0	Geophone	0.30(PS)	0.94	0.78	0.65	23.62	1.22	235.1	0.7
1.0	Microphone	0.30(PS)	0.92	0.86	0.58	23.41	0.88	248.2	-0.2
1.0	Geophone	0.45(PS)	0.91	0.94	0.49	23.77	0.53	242.5	1.1
1.0	Microphone	0.45(PS)	0.87	0.86	0.70	23.82	0.22	265.0	2.3
2.0	Geophone	0.15(PS)	0.92	1.19	1.12	24.28	0.55	208.6	2.7
2.0	Microphone	0.15(PS)	0.95	0.81	0.68	24.24	1.03	231.9	0.7
2.0	Geophone	0.30(PS)	0.90	0.84	0.67	24.24	1.05	231.9	-1.0
2.0	Microphone	0.30(PS)	0.53	0.54	0.44	24.23	1.11	267.5	-5.3
2.0	Geophone	0.45(PS)	1.16	1.30	1.37	24.65	0.33	221.7	48.5
2.0	Microphone	0.45(PS)	1.33	0.97	1.39	24.68	0.37	78.4	31.2
2.0	Geophone	0.45(LS)	1.02	1.46	1.75	24.79	0.28	204.3	13.5
2.0	Microphone	0.45(LS)	1.04	1.29	1.30	24.81	0.30	223.1	40.0
2.0	Geophone	0.68(LS)	0.71	1.42	1.08	25.20	0.39	186.5	59.9
2.0	Microphone	0.68(LS)	1.16	0.86	0.74	25.35	0.37	243.1	102.0
3.0	Geophone	0.45(LS)	1.08	1.29	2.05	25.50	0.25	216.4	93.9
3.0	Microphone	0.45(LS)	1.01	1.33	1.25	25.51	0.33	318.3	95.9
3.0	Geophone	0.68(LS)	1.23	1.41	1.40	25.50	0.54	219.6	19.7
3.0	Microphone	0.68(LS)	0.92	1.06	0.92	25.66	0.44	284.1	160.5

Table F-5. Meteorological Data taken concurrently with acoustic-to-seismic coupling ratio measurements (Soil C).

		Layer 1	Layer 2	Substrate
P-wave speed (m/s)	(R=2.0m)	255.0	390.0	900.0
	(R=3.0m)	245.0	385.0	900.0
S-wave speed (m/s)	(R=2.0m)	140.0	230.0	600.0
	(R=3.0m)	145.0	225.0	600.0
Flow Resistivity ((Pa sm^{-2})	(R=2.0m)	500000	500000	3600000
	(R=3.0m)	500000	500000	3600000
Porosity	(R=2.0m)	0.12	0.12	0.036
	(R=3.0m)	0.12	0.12	0.036
Grain shape factor		0.5	0.5	0.5
Soil density (kg/m^3)		2000	2200	2650
Layer thickness (m)	(R=2.0m)	0.55	1.50	∞
	(R=3.0m)	0.55	1.45	∞
Attenuation (V_p)		0.04	0.04	0.04
Attenuation (V_s)		0.02	0.02	0.02
Dynamic viscosity of air (Nsm^{-2})		$1.81x10^{-5}$		
Microphone height (m)		0.05		
Geophone depth (m)		-0.05		
Frequency range (Hz)		100 – 1000		
Speed of sound in air		344.0		
Coupling Resonant Frequency (Hz)	(R=2.0m)	744		
	(R=3.0m)	705		
Geophone Sensitivity (V / m/s) (measured)	(R=2.0m)	33.0		
	(R=3.0m)	25.6		
Microphone Sensitivity (V / Pa) (measured)	(R=2.0m)	$13.4e^{-3}$		
	(R=3.0m)	$13.4e^{-3}$		

Table F-6. Parameters used to predict the acoustic-to-seismic coupling ratio measurements taken in Soil C at HRI, Wellesbourne (source height=0.68m and range=2.0m, 3.0m).

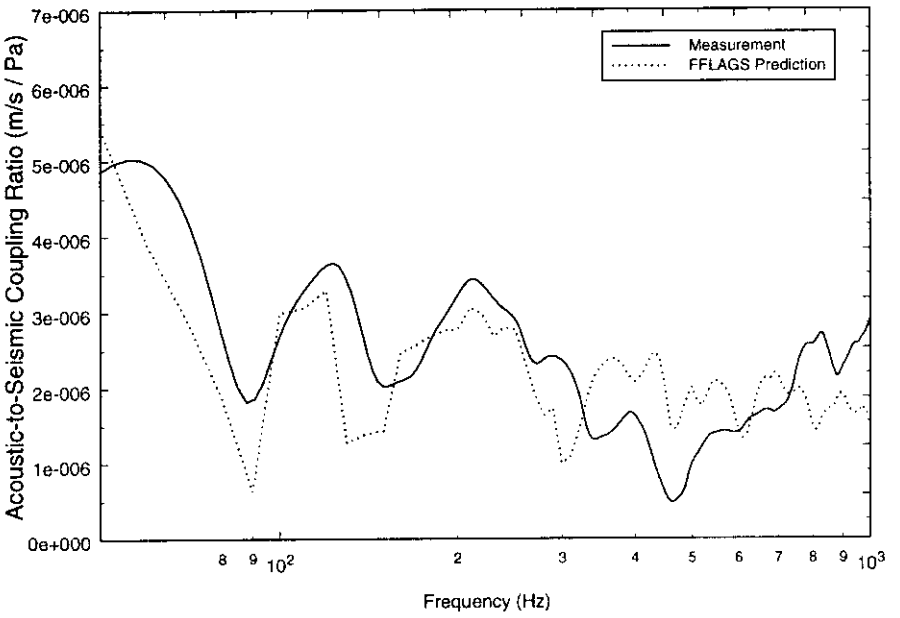

Figure F-11. Measured acoustic-to-seismic coupling ratio and FFLAGS prediction taken at HRI for Soil C (Range=2.0m, Hs=0.68m and f_0=744Hz).

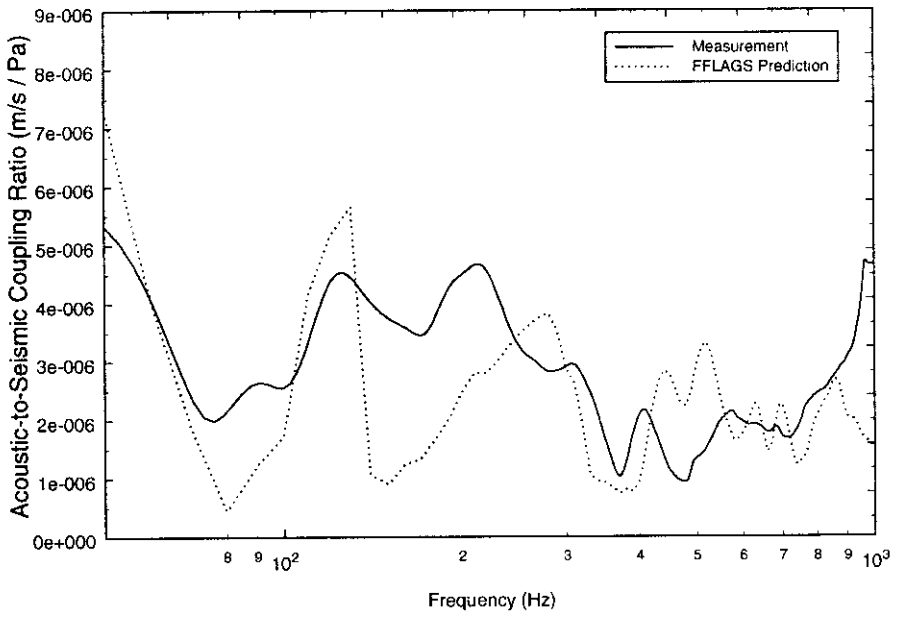

Figure F-12. Measured acoustic-to-seismic coupling ratio and FFLAGS prediction taken at HRI for Soil C (Range=3.0m, Hs=0.68m and f_0=505Hz).